JOURNAL OF APPLIED PHYSICS

Vol. 31, No. 11 November, 1960

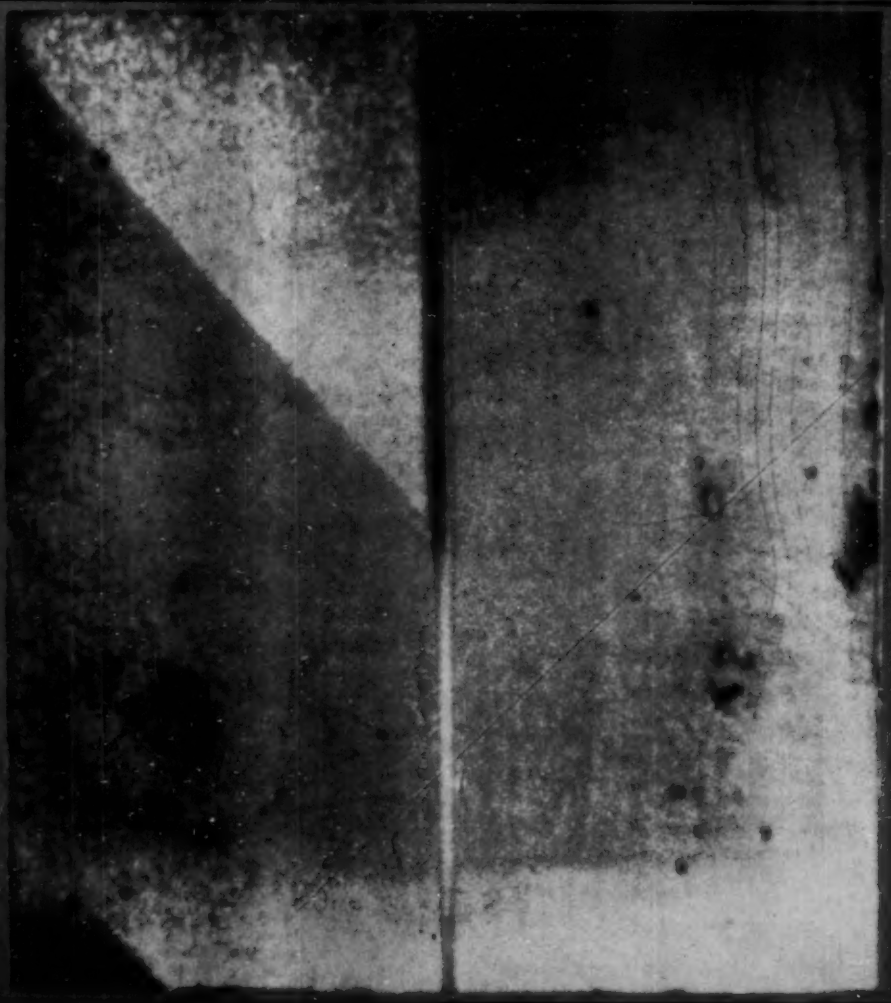

Antiferromagnetic Domains in Nickel Oxide.
See Page 2000.

HARSHAW MANUFACTURES A COMPLETE LINE OF SCINTILLATION AND OPTICAL CRYSTALS

SCINTILLATION *Mounted* NaI(T1) *Crystals*

Crystal detectors designed for the most sophisticated counting problems. Our physics and engineering group are available to assist you in your special detector problems.

More detailed information is contained in our 32-page book, "Harshaw Scintillation Phosphors." We invite you to write for your free copy!

STANDARD LINE
(Hermetically Sealed Crystal Assemblies)
- The accepted standard of the industry
- Proven through years of service in research, medical and industrial applications
- unparalleled performance
- dependability
- consistent good quality.

INTEGRAL LINE
(Crystal photo multiplier tube combination assembly)
- Improved resolution
- Ready to use plug-in unit
- Permanently light sealed
- Capsule design facilitates decontamination
- Close dimensional tolerances
- Harshaw guaranteed

***Large Crystal* MATCHED WINDOW LINE**
(Designed primarily for crystals 4" dia. and larger)
- "Small crystal" performance achieved through improved optical design
- Low mass containers
- Available in standard aluminum or complete low background assemblies
- Convenient mounting flange
- Ready to use

Every Harshaw crystal is a product of our experience in crystal growing technology since 1936

Other Phosphors Available from The Harshaw Chemical Company

ROUGH CUT THALLIUM ACITVATED SODIUM IODIDE CRYSTAL BLANKS • EUROPIUM ACTIVATED-LITHIUM IODIDE (NORMAL) • EUROPIUM ACTIVATED LITHIUM IODIDE (96% Li^6 ENRICHED) • THALLIUM ACTIVATED CESIUM IODIDE • THALLIUM ACTIVATED POTASSIUM IODIDE • ANTHRACENE • PLASTIC PHOSPHORS

OPTICAL *Crystals*

For Infrared and Ultra Violet Transmitting Optics

"HARSHAW QUALITY" INHERENT IN EACH HARSHAW-GROWN CRYSTAL GUARANTEES THE MOST EFFICIENT OPTICAL TRANSMISSION POSSIBLE THROUGH:

1) Negligible light scattering in crystals, permitting higher sensitivity and improved resolution
2) Freedom from absorptions caused by trace impurities in crystal optics
3) Minimum strain

"HARSHAW QUALITY" meets the demand for uniformity of optical properties such as dispersion and refractive index.

Prices, specifications, or other information will be sent in answer to your inquiry.

The following infrared and ultra violet transmitting crystals are available; others are in the process of development:

SODIUM CHLORIDE • SODIUM CHLORIDE MONOCHROMATOR PLATES POTASSIUM BROMIDE • POTASSIUM BROMIDE PELLET POWDER • (through 200 on 325 mesh) • POTASSIUM CHLORIDE • OPTICAL SILVER CHLORIDE • THALLIUM BROMIDE IODIDE • LITHIUM FLUORIDE • LITHIUM FLUORIDE MONOCHROMATOR PLATES • CALCIUM FLUORIDE • BARIUM FLUORIDE • CESIUM BROMIDE • CESIUM IODIDE

Additional information on the physical and optical properties of the above crystals is available in our 36-page booklet "Synthetic Optical Crystals". Send for your free copy.

THE HARSHAW CHEMICAL CO.
Crystal Division • Cleveland 6, Ohio

JOURNAL OF APPLIED PHYSICS

Vol. 31, No. 11 NOVEMBER, 1960

In This Issue

Special Issue on High Polymer Physics

NMR Absorption in Teflon Fibers . . . D. Hyndman and G. F. Origlio 1849
Kinetic Theory of Thermal Diffusion in Dilute Polymer Solutions . . . Joe S. Ham 1853
Experimental Study of Thermal Diffusion in Dilute Solutions of High Polymers . . . Frank C. Whitmore 1858
Defects in Polyethylene Crystals . . . W. P. Slichter 1865
Effect of Reactor Irradiation on the Tensile Strength of Uniaxially Oriented Polyethylene Terephthalate . . . C. C. Hsiao and S. T. Chow 1869
Effect of Temperature and Reactor Irradiation on the Strength of Biaxially Oriented Polyethylene Terephthalate . . . A. Haynes and C. C. Hsiao 1871
Photographic Light Scattering by Polyethylene Films . . . Richard S. Stein and Marion B. Rhodes 1873
Stress as a Reduced Variable: Stress Relaxation of SBR Rubber at Large Strains . . . Robert F. Landel and Paul J. Stedry 1885
Time and Temperature Dependence of the Ultimate Properties of an SBR Rubber at Constant Elongations . . . Thor L. Smith and Paul J. Stedry 1892
Determination of the Anisotropy of Bond-Polarizability of Liquids Using Flow-Birefringence Measurements . . . W. Philippoff 1899
Hollow Pyramidal Crystals of Polyethylene and a Mechanism of Growth . . . Walter D. Niegisch and Paul R. Swan 1906
Theoretical Calculation of the Birefringence of Polypropylene Crystals . . . D. A. Keedy, J. Powers, and R. S. Stein 1911
Morphology of Polymer Single Crystals . . . D. H. Reneker and P. H. Geil 1916
Wave Functions and Energy Eigenvalues for the Polytetrafluoroethylene Chain . . . Yoh-Han Pao and R. F. Bjorklund 1925
Chain Folding and Free Energy Density in Polymer Crystals . . . Anton Peterlin 1934

Regular Articles

Effect of Random Inhomogeneities on Electrical and Galvanomagnetic Measurements . Conyers Herring 1939
Structural Study of the Compound $AgSbTe_2$ . . . R. W. Armstrong, J. W. Faust, Jr., and W. A. Tiller 1954
Anomalous Hall Effect in $AgSbTe_2$ . . . R. Wolfe, J. H. Wernick, and S. E. Haszko 1959
Diffusion of Ag^+, Cl^-, and Cd^{++} in Silver Chloride Single Crystals . . . Richard F. Reade and Don S. Martin, Jr. 1965
Measurement of Orientation in Polypropylene Film . . . Zigmond W. Wilchinsky 1969
Transformation Studies of Gray Tin Single Crystals . . . R. G. Wolfson, M. E. Fine, and A. W. Ewald 1973
Effect of Magnetic Fields on Thermionic Power Generators . . . Alfred Schock 1978
Conservation Laws of Uniform Linear Homogeneous Systems . . . M. C. Pease 1988
Orientation-Dependent Dissolution of Germanium . . . F. C. Frank and M. B. Ives 1996
Neutron and Optical Studies of Domains in NiO . . . W. L. Roth 2000
Temperature Dependence of the Debye Temperatures of Aluminum, Lead, and Beta Brass by an X-Ray Method . . . D. R. Chipman 2012
Adiabatic Collapse of a Relativistic Electron Beam . . . T. F. Godlove and D. C. dePackh 2016
Hole Mobility and Crystal Size in Lead Sulfide Photoconductive Films . H. E. Spencer and J. V. Morgan 2024
Conservation Laws of an Interacting Electron Beam . . . Marshall C. Pease 2028
Secondary Electron Emission of MgO Crystals Bombarded by Relativistic Electrons . . . Martin A. Pomerantz, Romas A. Shatas, and William C. Schieve 2036
Growth from the Melt. Part II. Cellular Interface Morphology . . . G. F. Bolling and W. A. Tiller 2040
Effect of Neutron Bombardment on the Magnetic Properties of Very High Permeability Iron . . . G. Biorci, A. Ferro, and G. Montalenti 2046
Determination of Streaming Velocity and the Flow of Heat and Mass in High-Current Arcs . T. B. Reed 2048
In What Sense Do Slow Waves Carry Negative Energy? . . . P. A. Sturrock 2052
On the Incorporation of Neodymium in Mixed Yttrium-Neodymium-Iron Garnets . . . G. Goldring, M. Schieber, and Z. Vager 2057
Nonlinear Effects of Crystalline Anisotropy on Ferrimagnetic Resonance . . . Peter Gottlieb 2059

Letters to the Editor:

Modification in Technique for Growing Single Crystals of ZnF_2:Mn . . . L. M. Matarrese and F. L. Hughes 2063
Alkali Vapor Plasmas . . . M. A. Hakeem and Harry S. Robertson 2063
Effect of Interelectrode Spacing on Cesium Thermionic Converter Performance . . . R. L. Hirsch 2064
Influence of Arsenic Pressure on the Doping of Gallium Arsenide with Germanium . . . J. O. McCaldin and Roy Harada 2065
Noise Propagation in Drifting Multivelocity Electron Beams . . . J. A. Morrison 2066
Solvent Evaporation Technique for the Growth of Arsenic-Doped Germanium Single Crystals for Esaki Diodes . . . F. A. Trumbore and E. M. Porbansky 2068

Books Reviewed . . . 2069
Index to Advertisers . . . xxxiv

JOURNAL OF APPLIED PHYSICS

A journal of general physics and its applications to other sciences and to industry

Published by the

American Institute of Physics

GOVERNING BOARD

Members

Ralph A. Sawyer, *Chairman*
James G. Baker
R. H. Bolt
W. R. Brode
Harvey Brooks
Dirk Brouwer
J. W. Buchta
Vernet E. Eaton
J. H. Elliott
Herbert A. Erf
S. A. Goudsmit
W. W. Havens, Jr.
Winston E. Kock
R. Bruce Lindsay
H. V. Neher
C. J. Overbeck
G. E. Pake
Ray Pepinsky
F. W. Sears
Frederick Seitz
John Strong
George E. Uhlenbeck
M. E. Warga
Victor F. Weisskopf
W. R. Willets

ADMINISTRATION

Elmer Hutchisson
Director

Wallace Waterfall
Secretary and Treasurer

Henry A. Barton
Administrative Consultant

W. C. Kelly
Director of Education

Eugene H. Kone
Director of Public Relations

Hugh C. Wolfe
Director of Publications

Kathryn Setze
Assistant Treasurer

Norma Frankel
Publications Editor

Sistina Greco
Circulation Manager

Edward Tober
Manager, Production and Distribution

Theodore Vorburger
Advertising Manager

Emily Wolf
Manager, Special Services

Editor
J. H. Crawford

Assistant Editor
Ethel McMillan

Editorial Board

Arthur Kantrowitz
A. F. Kip
J. E. Goldman
J. L. Tuck
C. A. Wert
Herman A. Haus
C. Lester Hogan
R. S. Rivlin

THE JOURNAL OF APPLIED PHYSICS is devoted to general physics and its applications to other sciences, to engineering, and to industry. Previous to 1937, this journal was called PHYSICS.

The JOURNAL OF APPLIED PHYSICS welcomes articles of two distinct kinds: (1) Descriptions of new results in experimental or theoretical physics which are of general interest to physicists. The author should explain his contribution in such a way that a physicist or engineer in another field of specialization can appreciate its objectives and essential features. (2) Critical reviews of particular areas of physics or surveys of extensive investigations at a single laboratory. Authors contemplating writing such should correspond with the Editor before they begin writing.

The JOURNAL OF APPLIED PHYSICS welcomes Letters to the Editor which are short [approximately four (4) typewritten pages] communications without abstracts. Timeliness, briefness, and degree of current importance of the subject matter will be of primary concern in the publication of Letters. Letters should not be looked upon as partial publication or announcement of more comprehensive work, but rather self-contained presentations in themselves.

Manuscripts should be submitted to the Editor, J. H. Crawford, Solid State Division, Oak Ridge National Laboratory, Oak Ridge, Tennessee. Authors should read the "Information for Contributors," facing page 1 of the January issue, before writing articles or letters. The *Style Manual* of the American Institute of Physics is also helpful to writers preparing manuscripts for journals published by the American Institute of Physics. It can be obtained for $1.00 from the American Institute of Physics, 335 East 45 Street, New York 17, New York.

Corrected proofs and all correspondence concerning papers in the process of publication should be addressed to the Publication Manager, American Institute of Physics, 335 East 45 Street, New York 17, New York.

Subscriptions, renewals, and orders for back numbers should be addressed to the American Institute of Physics, 335 East 45 Street, New York 17, New York.

Subscription Price	U.S. and Canada	Elsewhere
To members of member organizations of the American Institute of Physics and Affiliated Societies ..	$12.00	$13.00
To all others	14.00	16.00

Back Number Prices

Yearly back number rate when complete year is available: $17.00.
Single copies: $1.75 each (exception: March, 1958—$3.00 each).

Changes of address should be sent to the American Institute of Physics.

Advertising rates supplied on request. Orders, advertising copy, and cuts should be sent to the American Institute of Physics.

The Journal of Applied Physics is published monthly at Prince and Lemon Streets, Lancaster, Pennsylvania.
Second-class postage paid at Lancaster, Pa.

For the ultimate in — **RELIABILITY**
REPEATABILITY
SUPERIOR PERFORMANCE

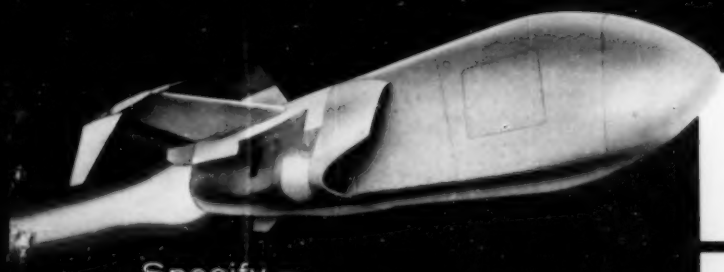

Specify —

"MAG MOD"®

miniaturized

MAGNETIC MODULATORS

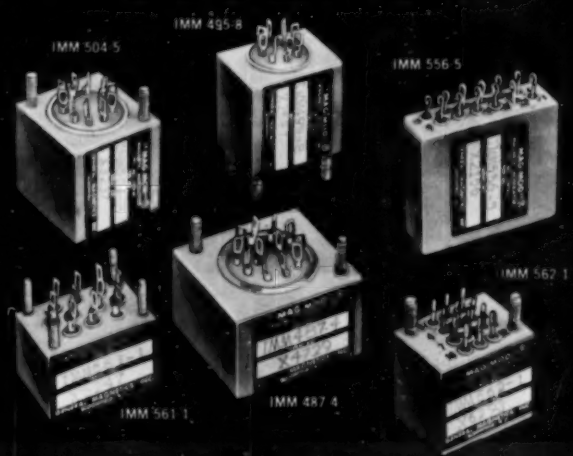

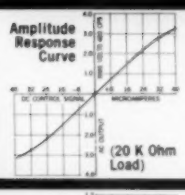

Input Magnetic Modulator
Type No. IMM 487-4

Subminiature "MAG MOD"® featuring high input signal sensitivity and high AC output impedance. Male or female mounting.

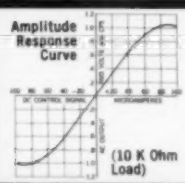

Input Magnetic Modulator
Type No. IMM 495-8

Subminiature "MAG MOD"® featuring wide band width, multiple signal input circuits, extreme zero stability from −65°C to +135°C, low null amplitude or noise level. Mounting available male or female.

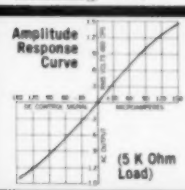

Input Magnetic Modulator
Type No. IMM 504-5

Subminiature "MAG MOD"® featuring low input and output impedance, resistance vs. temperature compensated input, extreme zero stability, repeatability and insignificant hysteresis. Supplied with male or female mounting.

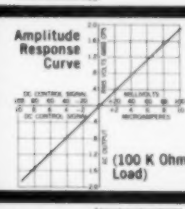

Input Magnetic Modulator
Type No. IMM 562-1

Subminiature "MAG MOD"® featuring 4 KC carrier operation, wide frequency band width, high output impedance and voltage range. Mounting male or female.

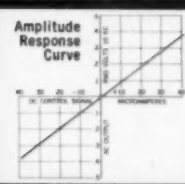

Input Magnetic Modulator
Type No. IMM 561-1

Subminiature "MAG MOD"® featuring low carrier energy level operation, very wide frequency band width, wide output operating range, minimum size and weight. Mounting male or female. May be mounted directly on printed circuit boards.

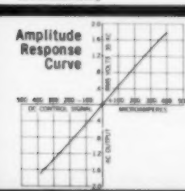

Input Magnetic Modulator
Type No. IMM 556-5

Subminiature "MAG MOD"® featuring high frequency carrier operation (35 KC), flat construction for printed circuit mounting, low output impedance and clean output fundamental frequency wave form. Mounting supplied male or female.

Designed for Subminiature
Circuit Assemblies and Printed Circuit Card Configurations

New miniature designs of these reliable "MAG MODS"® make them ideal for incorporation into transistorized printed circuit assemblies. There is no sacrifice of dynamic response. They offer the engineer/designer the solution to problems involved in a wide range of data systems where analog circuit operations are encountered. To insure complete flexibility, the mechanical mounting on any "MAG MOD" may be modified to conform to your particular packaging requirements.

- **1% repeatability throughout entire service life**
- **Negligible hysteresis**
- **Faster response time**
- **Extreme stability over a wide temperature range**
- **Infinite service life**
- **Extremely lightweight — compact design**

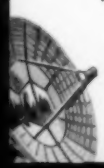

GENERAL MAGNETICS • INC
135 BLOOMFIELD AVENUE, BLOOMFIELD, NEW JERSEY, U. S. A.

GM INC.

See reverse side for specifications

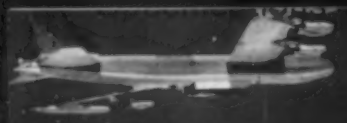

"MAG MOD" miniaturized MAGNETIC MODULATORS

TYPE NUMBER	IMM 487-4	IMM 495-8	IMM 504-5	IMM 562-1	IMM 561-1	IMM 556-5
Excitation Carrier Voltage and Frequency	115 V @ 400 cps	115 V @ 400 cps	115 V @ 400 cps	2.5 V RMS @ 4 KC	1.0 V RMS @ 10 KC	6 to 10 V RMS @ 35 KC
Control Signal Winding DC Resistance	Winding No. 1 6200 ohms Winding No. 2 7400 ohms	Signal Winding No. 1 550 ohms Signal Winding No. 2 600 ohms	1000 ohms	Signal Winding 1300 ohms Feedback Winding 180 ohms	200 ohms	5000 ohms
Input Control Signal Range	0 to ±40 μa Each Winding	0 to ±100 μa (Both Sig. Windings in Series)	0 to ±100 μa	0 to ± 100 μa 0 to ± 1 V Bipolar	0 to ±400 μa	0 to ±400 μa
Amplitude Modulated AC Output Range	3 V RMS @ 400 cps Phase Reversing	0 to 1 V RMS @ 400 cps Phase Reversing	0 to 1.5 V RMS @ 400 cups Phase Reversing	0 to 6 V RMS @ 4000 cps Phase Reversing	0 to 3 V RMS @ 4 KC Phase Reversing	0 to 1.8 V RMS @ 35 KC Phase Reversing
Differential Gain RMS mv AC Out/ μa Signal In	100 mv/μa	15 mv/μa	10 mv/μa	200 mv/μa	10 mv/μa	4.2 mv/μa
Null Amplitude (Noise Level) mv RMS	25 mv RMS Maximum	5 mv RMS Maximum	10 mv RMS Maximum	30 mv RMS Maximum	10 mv RMS Maximum	20 mv RMS Maximum
Output Impedance	Approx. 30 K ohms	1000 ohms	1000 ohms	Approx. 70 K ohms	Approx. 40 K ohms	900 ohms Each Output Wind.
External Load (Suggested)	Approx. 20 K ohms	Approx. 10 K ohms	Approx. 5 K ohms	Approx. 100 K ohms	Approx. 100 K ohms	1000 ohms Each Output Wind.
Null Drift (In terms of Input Signal) −65°C to +135°C	Less than ±0.25 μa Over Temp. Range	Less than ±0.25 μa Over Temp. Range	±1 μa Maximum Over Temp. Range	±0.5 μa Maximum Over Temp. Range	±1 μa Over Temp. Range	±2 μa Over Temp. Range
Hysteresis (% of Input Control Signal)	0.5% Maximum	0.5% Maximum	0.5% Maximum	Approx. 0.5%	0.5% Maximum	0.5% Maximum
% Harmonic Distortion in Output AC Modulated Envelope	Approx. 40% (3rd Harmonic)	Approx. 25% (3rd Harmonic)	Approx. 30% (3rd Harmonic)	Approx. 15% (3rd Harmonic)	Less Than 10% (3rd Harmonic)	Approx. 5% (3rd Harmonic)
Overall Dimensions (In Inches)	1¼ x 1½ x ¾	¾ x 1 x 1	1 x 1 x 1	1 x 11/16 x ⅞	11/16 x 1 x ⅝	7/16 x 1⅜ x 1¼
Type of Mounting	4-40 Studs or Inserts	4-40 Studs or Inserts	4-40 Studs or Inserts	4-40 Studs or Inserts	2-56 Studs	4-40 Tapped Holes or Studs
Weight in Ounces	Approx. 1.25	Approx. 1	Approx. 1.1	0.75	0.6	1
Response Time (Band Width cps)	0.01 sec. for 15 K Sig. Source Imp. (17 cps Corner Frequency)	20 cps for 10 K Sig. Source Imp. 25 cps for 20 K Sig. Source Imp. (Both Sig. Windings in Series)	5 cps for 1 K Sig. Source Imp. 10 cps for 5 K Sig. Source Imp. 20 cps for 10 K Sig. Source Imp.	70 cps for 10 K Sig. Source Imp. (Time Constant Approx. 2 Milli-Seconds)	Corner Frequency 2 KC for Sig. Source Imp. of Approx. 6 K ohms	Corner Frequency 200 cps for 600 ohm Signal Source Imp. or 1000 cps for 5 K Source

Magnetic Multiplying Modulator Model MCM 515-1

The MAGNETIC MULTIPLIER is a miniaturized magnetic modulator specifically designed to deliver an analog output voltage which is the continuous product of two variable input voltages. One of these is an excitation voltage which varies over a pre-determined range; in this case, 0 to 1 VRMS 400 cycles per second. The other signal is a DC current which varies between 0 and ±400 μa. The output voltage is 400 cycles AC, and is always in phase or 180° out of phase with the variable excitation or fixed reference, i.e., in phase when the variable amplitude DC signal is positive, and 180° out of phase when the DC signal is negative. The general schematic is illustrated in Fig. 1. The relationship between variable alternating supply signal voltage E_S, variable direct current control signal E_C, and the alternating load voltage E_L having a sinusoidal wave shape is denoted by the equation—

$E_L = \text{Constant} \times E_S \times E_C$.

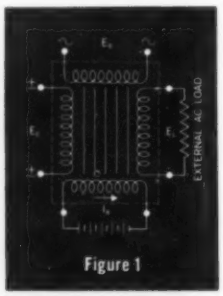

Figure 1

This expression, which defines the fundamental principle of the four quadrant MAGNETIC MULTIPLYING MODULATOR, can be clearly illustrated by linear transfer response curve families as shown at right, in Figure 2-A and Figure 2-B.

Illustrating:

(1) **Load voltage E_L as a function of alternating supply signal voltage E_S with control DC signal voltage E_C as a parameter.**

(2) **Load voltage E_L as a function of control DC signal voltage E_C with alternating supply voltage, E_S as a parameter.**

With linearity response curves held to within approximately 1 to 2% of theoretical straight lines, the product accuracy of the fundamental equation will be within 2 to 5% of the theoretical product.

SPECIFICATIONS MODEL MCM 515-1

Variable Excitation Carrier Voltage and Frequency	Variable AC Signal 0 to 1 V RMS 400 cps
Control Signal Winding DC Resistance	DC Signal Winding Resistance 2650 ohms
Input Control Signal Range	Variable DC Signal 0 to ±400 μa
Amplitude Modulated AC Output Range	0 to 0.9 V RMS @ 400 cps Phase Reversing
Null Amplitude (Noise Level) mv RMS at Max. AC Excitation	5 mv RMS
Output Impedance	Approx. 3500 ohms
External Load (Suggested)	Approx. 25 K ohms
Null Drift (In terms of Input Signal) −65°C to +135°C	±2 μa over Temperature Range
Hysteresis (% of Input Control Signal)	0.5% Maximum
% Harmonic Distortion in Output AC Modulated Envelope	Less than 5%
Overall Dimensions (In Inches)	27/32 x 27/32 x 1 3/16
Type of Mounting	4-40 Insert or Stud
Weight	Approx. 1 Ounce

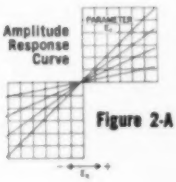

Figure 2-A

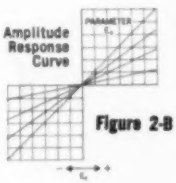

Figure 2-B

Typical "Mag Mod"® Applications—Circuit applications for MAGNETIC MODULATORS include algebraic addition, subtraction, multiplying, raising to a power, controlling amplifier gain, mechanical chopper replacement in DC to fundamental frequency conversion, filtering and low signal level amplification.

Consult General Magnetics—For magnetic amplifier components of proven reliability. These dependable instruments are widely employed in automatic flight systems, fire control, analog computers, guided missiles, nuclear equipment, antennas, gun turrets, commercial power amplifiers and complete control systems. Miniature, subminiature, standard and customized types available.

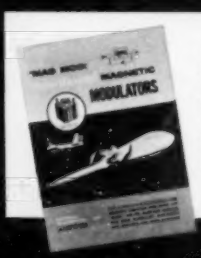

Call or write for new Brochure 102 on "MAG MOD" Miniaturized Magnetic Modulators and Magnetic Multiplying Modulators. Please address inquiries on company letterhead.

GENERAL MAGNETICS • INC
135 BLOOMFIELD AVENUE, BLOOMFIELD, NEW JERSEY, U.S.A.

DELAY LINES, INDUCTORS, FILTERS AND CHOKES... ARNOLD IRON POWDER CORES CUT COSTS

Iron powder cores are commonly specified for such applications as delay lines (illustrated below), inductors, filters and filter chokes because of their inherent low cost. And Arnold cores are your logical choice, for the principal reasons of superior dependability and the wide selection available to you.

Arnold's overall magnetic knowledge, and unequalled facilities for manufacture and test, are of prime importance in assuring you a source of cores that are highly uniform, shipment after shipment. You'll find them dependable, not only in permeability and resultant inductance at high frequencies, but in high mechanical strength and dimensional accuracy as well.

The Arnold line also offers a wider range of shapes and sizes of iron powder cores for your selection than any other one brand on the market. It includes bobbin cores, cups, toroids, plain, sleeve and hollow cores, threaded cores and insert cores, etc. Facilities for special cores to your order. Ask for new Bulletin PC-109A. ● Write *The Arnold Engineering Company, Main Office and Plant, Marengo, Illinois.*

ADDRESS DEPT. J-11

ARNOLD

SPECIALISTS in MAGNETIC MATERIALS

BRANCH OFFICES and REPRESENTATIVES in PRINCIPAL CITIES • *Find them FAST in the YELLOW PAGES*

2284

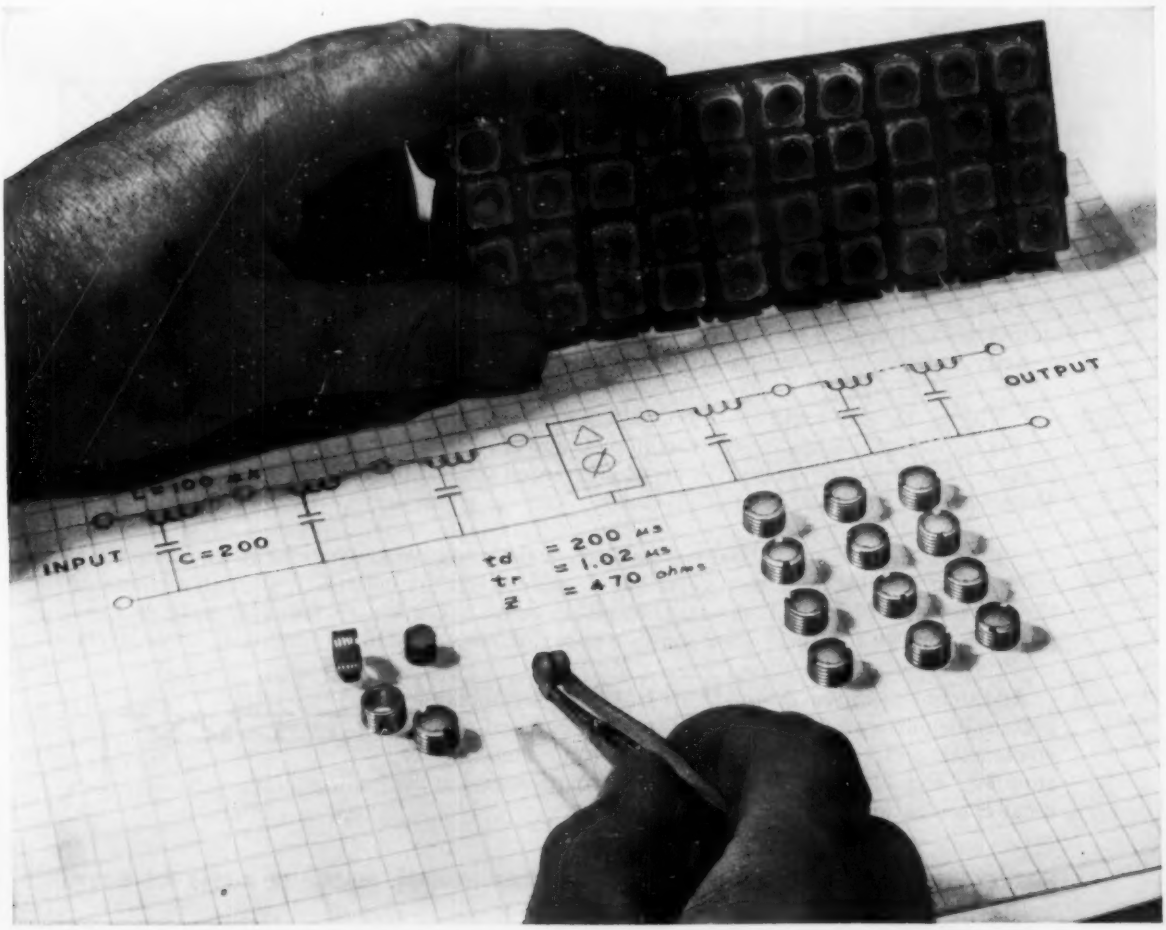

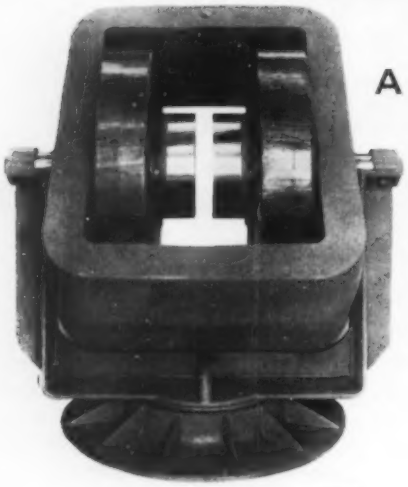

A NEW STANDARD OF EXCELLENCE

An exacting investigation into optimum methods for the design and fabrication of precision laboratory electromagnets has produced definite proof that the casting of magnet yokes affords positive advantages in performance. Many laboratories now benefit from this "new standard of excellence" made possible in part by these new design concepts.

FIGURE A. BOLTED AND MACHINED MAGNET YOKE
FIGURE B. HARVEY-WELLS CAST MAGNET YOKE
FIGURE C. YOKE CROSS SECTION CAST MAGNET
FIGURE D. YOKE CROSS SECTION MACHINED AND BOLTED MAGNET

FIGURE A

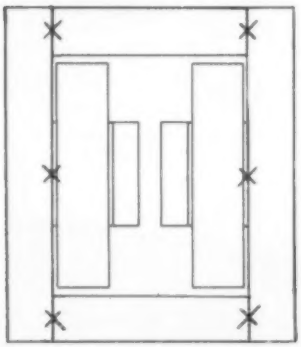

FIGURE B

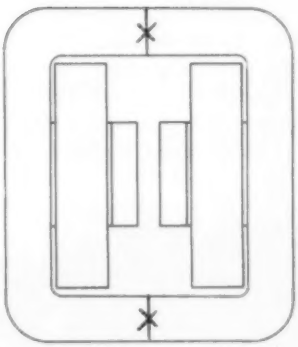

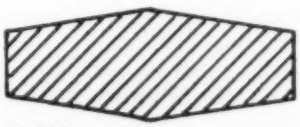

FIGURE C

FIGURE D

Figure A illustrates the older method of constructing a magnet yoke by machining and bolting a number of pieces of metal. This allows a number of joints, shown by the X's, which cumulatively allow a build-up of machine tolerances, with subsequent variations in parallelism at the pole faces and a tendency to stress at high field strengths. Figure B shows the Harvey-Wells cast magnet yoke. Casting requires fewer such joints permitting far greater rigidity and stability. This in turn allows improved homogeneity through changing fields and greater homogeneous volumes at fixed fields.

The greater strength of the hexagonal cross section of the cast magnet yoke, shown in Figure C as compared to the rectangular cross section of the older method shown in Figure D is a further example of the increased inherent rigidity of cast magnets, with the attendant virtues as described above.

By casting the entire magnet yoke from the same batch of metal at the same time, there is no possibility of any variation in characteristics between different sections of the same magnet. In fact, the magnetization curve for a low carbon cast yoke as compared to a curve for 10-10 steel shows a superior resistance to saturation at lower levels.

Additional features of the Harvey-Wells electromagnet system include wafer coils for increased power and cooling efficiencies and continuously regulated solid state power supplies. Please write for complete information and technical specifications.

HW

HARVEY-WELLS CORPORATION P.O. BOX 189 FRAMINGHAM, MASS. TR 2-4365 CE 5-7370

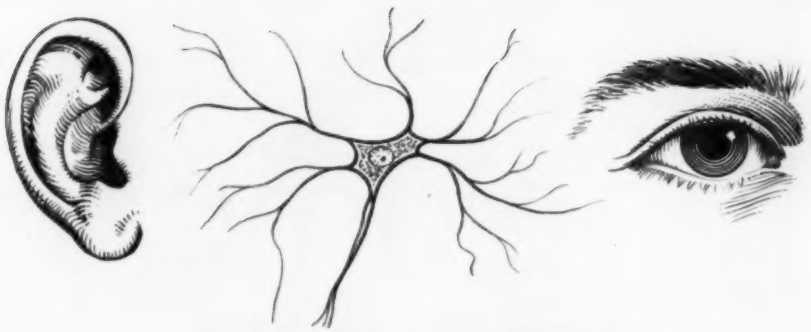

WHAT GOES ON HERE?

Bell Laboratories' new electronic "nerve cell" is a step toward finding out.

One fascinating area of communications has long resisted exploration—what happens inside the nervous system when you see, or when you hear. It is of special interest to telephone science; knowledge of how the nervous system handles sound and picture signals can help determine what information is essential to perception. This in turn may lead to more efficient communication instruments and systems.

To probe the mystery of nerve activity, Bell Telephone Laboratories scientists have developed an electronic model of a living nerve cell or neuron. Consisting of transistors, resistors, capacitors and diodes, the "artificial neuron" exhibits many of the characteristics of a living neuron; for instance, "all-or-none" response and fatigue.

In one experiment at Bell Laboratories, a network of artificial neurons is subjected to a stimulus from light through a set of photocells. The network can distinguish specific patterns of light and dark, thus duplicating roughly some of the eye's basic reactions to light. Similar studies are underway to explore our hearing processes.

At present, too little is known about neural action to permit exact electronic duplication. But experiments with artificial neurons can provide suggestive clues, thus helping to develop a stimulating interplay between electronics and neurophysiology which may help workers in both disciplines.

The human nervous system, including the brain, is the most efficient and versatile data processing system known; and data processing is an essential part of communications. The artificial neuron provides a new approach to investigating and understanding basic nerve network functions. It is a fresh example of how Bell Telephone Laboratories constantly explores new frontiers to improve America's communications system, now and in the years ahead.

Network of neurons is assembled by L. D. Harmon of Bell Laboratories, the initiator of this new research. Many assemblies are possible.

BELL TELEPHONE LABORATORIES

WORLD CENTER OF COMMUNICATIONS RESEARCH AND DEVELOPMENT

some men see only gulls...

but a man of imagination named Otto Lilienthal saw more, and conceived an idea of consequence to the future of the world. The sources of world-shaping ideas are myriad; the men capable of conceiving these ideas, few.

In this age, more than ever before, there is a need for men of ideas. Now, at the new Autonetics Research Center in Whittier, California, a group of men are working to apply advanced physical concepts to the electromechanical technology of tomorrow. More men with advanced degrees are needed for this important work. Men to do research in moletronics, micromagnetics, advanced materials, and cryogenics.

Perhaps you are a man with new ideas... a man of imagination... one who requires the stimulation of new challenges. If you are, we invite you to share in the work at the new Autonetics Research Center.

Write: A. P. Knutson, Autonetics Research Center, 12000 E. Washington Boulevard, Whittier, California.

Current Openings for Experienced Ph.D's:

Solid State Physicists • Physical Chemists • Electrochemists • Physical Metallurgists • High Vacuum Technologists.

Autonetics

A DIVISION OF NORTH AMERICAN AVIATION, INC.

SILICON NEWS from Dow Corning

(PART 1)

The Untouchables

Hyper-Pure Silicon... Silicon So Pure Just a Touch Contaminates Its Quality

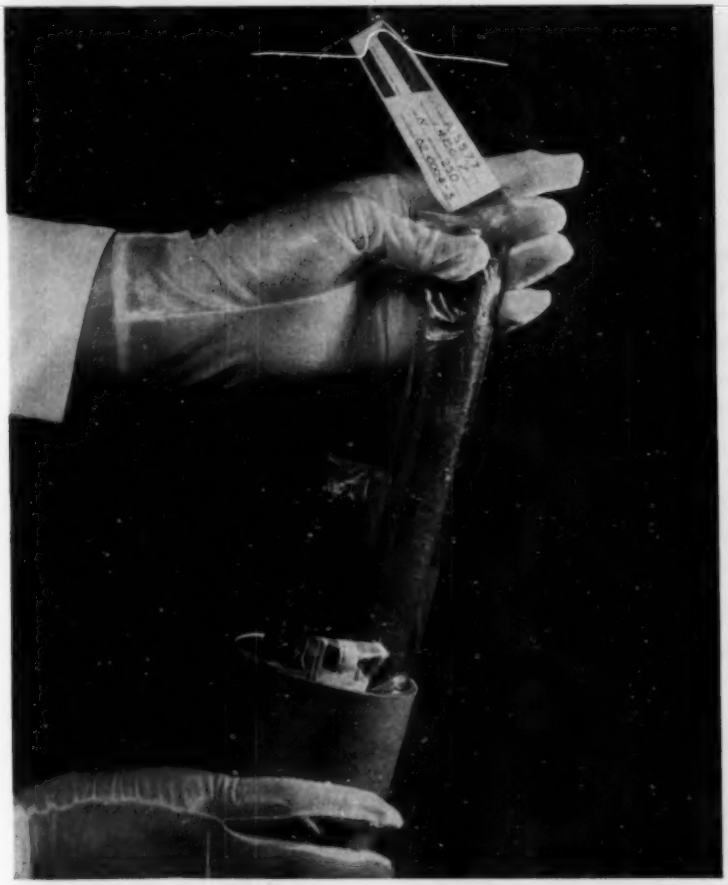

The highest purity attained in any element refined by man . . . purer than any element found in nature! That's Hyper-Pure Silicon.

With less than one part per billion of boron, Dow Corning Silicon is so pure that just the touch of a finger tip causes contamination — destroys its high quality.

To assure this untouchable purity when you receive them, Dow Corning polycrystalline rods are wrapped in special unbleached cellophane and sealed in airtight polyethylene envelopes.

Purity pays off in quality — in uniformity of properties . . . in relatively flat resistivity and lifetime profiles for the entire length of single crystal silicon grown from Dow Corning polycrystalline rod and chunk . . . in maximum yield.

Specify polycrystalline rod if you use the zone refining process for conversion to single crystal — polycrystalline chunk if the Czochralski method is used. Both are of the same high quality.

Why is Dow Corning able to supply this untouchable quality?

Dow Corning has nearly twenty years experience in the production and purification of trichlorosilane, a chemical basic to both *Silicones* and *Hyper-Pure Silicon*. This experience, plus a fully integrated production facility, assures uniformly high quality — minimizes batch to batch variations.

For more information contact our nearest regional office, or write direct.

Typical properties of Dow Corning polycrystalline silicon, together with resistivity and life-time curves for an evaluation crystal, are shown below.

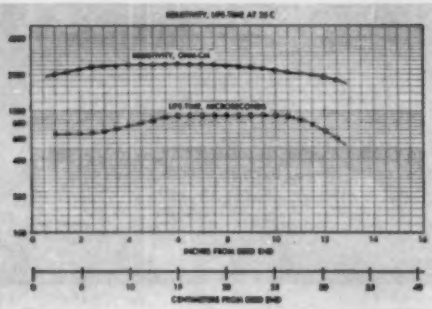

Typical Properties of Polycrystalline Silicon

Acceptor Impurity Content:	0.15 part/billion
Donor Impurity Content:	0.5 part/billion
Rod Diameter:	up to 26 mm (1.0 in.)
Rod Length:	up to 450 mm (17.7 in.)
Resistivity (vacuum zoned evaluation crystal):	>1000 ohm cm
Lifetime (vacuum zoned evaluation crystal):	>400 micro sec.

Free brochure — "Hyper-Pure Silicon for Semiconductor Devices." Write Dept. 4711.

HYPER-PURE SILICON DIVISION

Address: HEMLOCK, MICHIGAN

Dow Corning CORPORATION

MIDLAND, MICHIGAN

ATLANTA BOSTON CHICAGO CLEVELAND DALLAS LOS ANGELES NEW YORK WASHINGTON, D.C.

NOTABLE ACHIEVEMENTS AT JPL...

pioneering work in worldwide communication via satellites

PROJECT
ECHO

On August 12th, 1960, JPL scientists at Goldstone, California, radioed the world's first transcontinental microwave message to be relayed by a passive, artificial earth satellite. This satellite was the 100 ft. plastic balloon Echo I orbiting around the Earth at an altitude of approximately 1,000 miles. A pre-recorded statement by President Eisenhower was received 2,300 land miles away by scientists of the Bell Telephone Laboratories at Holmdel, New Jersey, as clearly as any conventional telephone call, in a fraction of a second.

Later in the course of the Echo experiment, the scientists at Goldstone and Holmdel conducted 2-way voice communication via the balloon satellite, Goldstone transmitting at 2,390 megacycles and Holmdel at 960 megacycles. This successful experiment has demonstrated the feasibility of worldwide communication and is typical of many pioneering achievements of the Jet Propulsion Laboratory.

jpl

CALIFORNIA INSTITUTE OF TECHNOLOGY

JET PROPULSION LABORATORY

A Research Facility operated for the National Aeronautics and Space Administration

PASADENA, CALIFORNIA

Employment opportunities for Engineers and Scientists interested in basic and applied research in these fields:

COMMUNICATIONS • INSTRUMENTATION • INFRARED • ASTROPHYSICS • GEOPHYSICS • GEOCHEMISTRY • ASTRONOMY • PROPULSION • MASER • STRUCTURES • PHYSICS •

Send professional resume, with full qualifications and experience, for our immediate consideration

Kodak reports on:

materials that are not blinded by hot wind . . . the sweetest little old solid-state amplifier and transducer known to man . . . polyester electrically upgraded

For little pots or big peepholes

If you want to make a useful little pot for putting things in that are to be poked with infrared or microwave radiation; or if you want to make an object move through the air at speeds like Mach 6 and need something to keep the hot wind out of the peephole while admitting infrared *and* microwaves to steer by, you must investigate *Kodak Irtran* material or face charges of that heinous sin, ignoring the "state of the art."

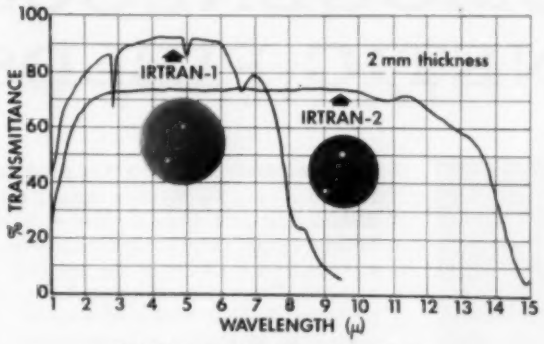

Kodak Irtran merchandise: an *Irtran-1* dome and an *f*/1.0 *Irtran-2* molded asphere

There are now two kinds of *Irtran* optical material, neither of them intended for wavelengths that your old dictionary would call "optical."

The newer, *Irtran-2*, has as its point of pride the transmittance curve displayed above, combined with a remarkable mechanical and chemical ruggedness. Its refractive index is around 2.2. Note the tremendous wavelength span over which transmittance losses are nearly all due to reflection. Heating to 600°C in air does nothing more than improve the transmittance—by formation of an anti-reflection coating. We can apply a much better coating, though, by evaporation.

*Irtran-1** material, the other one, needs no anti-reflection coating because its refractive index is only 1.38 at 1μ. *Its* big glory, aside from high infrared transmittance at 2 to 7μ even when very hot, stems from a 9.4 kmc dielectric constant of 5 and a loss tangent of 10^{-4}.

Decibel loss per meter for low-loss materials is

$$\frac{8.686\pi}{\lambda_o}\sqrt{K}\tan\delta$$

where K = dielectric constant
λ_o = wavelength in vacuum
tan δ = loss tangent
δ is the complement of the vector angle whose cosine the power engineer calls "power factor."

One untuned *Irtran-1* sample .012" thick we tested in the X-band frequency range introduced an attenuation of less than 0.3db and exhibited a maximum standing wave ratio of 1.5 over the band.

The ideal radome material would have a kilomegacycle dielectric constant of unity, i.e. to microwaves it would be the same as nothing at all. Plastics commonly used for radomes run around 2 or 3, but they don't transmit infrared rays. On the other hand, there are materials that are good for infrared transmission but have dielectric constant around 13.

Another way the *Irtran* materials shine figuratively is their very low tendency to glow literally when hot and thus to blind themselves by swamping transmittance with emissivity. They survive undamaged through the conventional torture tests of temperature-humidity cycling for 28 days, vacuum-steam pressure for 2,000 cycles in saline solution, sand and dust blast, acids, alkalis, organic solvents, plunges from hot to cold, etc.

Currently we can supply either of these polycrystalline Irtran *materials as optical elements up to 6½" in diameter, among other forms. Let us have no jurisdictional disputes among opticker, micro-wavers, and infraredders as to who sends for the supporting data from Eastman Kodak Company, Special Products Division, Rochester 4, N. Y.*

*Formerly designated "Irtran AB-1."

Rapid-access photography

The silver halide crystal of suitable size and suitable dislocations, with a suitable organic compound or two clinging to it, makes the sweetest little old solid-state amplifier and transducer known to man. It is doing just fine, despite a few misconceptions that have arisen due to the following circumstances:

1) The idea was developed by artists before words like "solid-state physics," "amplifier," and "transducer" were coined and even before science was recognized as profitable.

2) The crystal is employed in very large numbers, dispersed in a dried-down broth from hides and bones. Superficially regarded, this seems archaic. By referring to the preparation as a "photographic emulsion," the notion is dispelled.

3) Memories from childhood suggest that after a photographic emulsion is exposed, one must wait until Dad brings the results home from downtown the week after next. This is no longer true.

Purpose of this message is to make it perfectly clear that today the delivery of photographic results within virtually any desired time interval after exposure is wholly feasible technologically. There are many ways of accomplishing quick delivery, some currently on the market and others on the way. The manufacturer wagers on what the public will buy. As far as goods for the general public are concerned, that's the way it has to be. But on goods for the professionally technical public—rational, organized, deliberate, articulate—*must* the betting be so blind?

We have had a flash of genius. Let's ask them first what they want! Then, as patterns appear in the answers, markets can be defined and gauged. If this works, rapid-access and simplified technical photography will encounter fewer custom problems to be solved at custom prices or else given up for less satisfactory alternatives.

Responsible organizations confronted with technical problems, major or minor, where rapidly or instantaneously available photographic images would be helpful, are invited to describe their wants to Eastman Kodak Company, Special Sensitized Products Division, Rochester 4, N. Y.

New recipe

We have a new polyester resin recipe. It results in a dielectric constant that is really constant up to 130°C, which could not be said of earlier polyester. Its dissipation factor is 0.3% at 100°C, where the old ran to 1.2%. Since it also better resists humidity, acid, and bases, it is excellent for insulation. As a capacitor film at 2000 v/mil, it outlasts the old 8 to 1.

Eastman Chemical Products, Inc. our subsidiary, sells the resin. Acme Backing Corporation, Canal and Ludlow Streets, Stamford, Conn., turns it to what others call film and we (for whom "film" has another meaning) call sheeting. Acme will gladly expatiate.

Kodak
TRADE MARK

This is another advertisement where Eastman Kodak Company probes at random for mutual interests and occasionally a little revenue from those whose work has something to do with science

FROM VARIAN

12-INCH PRECISION LABORATORY MAGNETS

LARGE HOMOGENEOUS MAGNETIC FIELDS

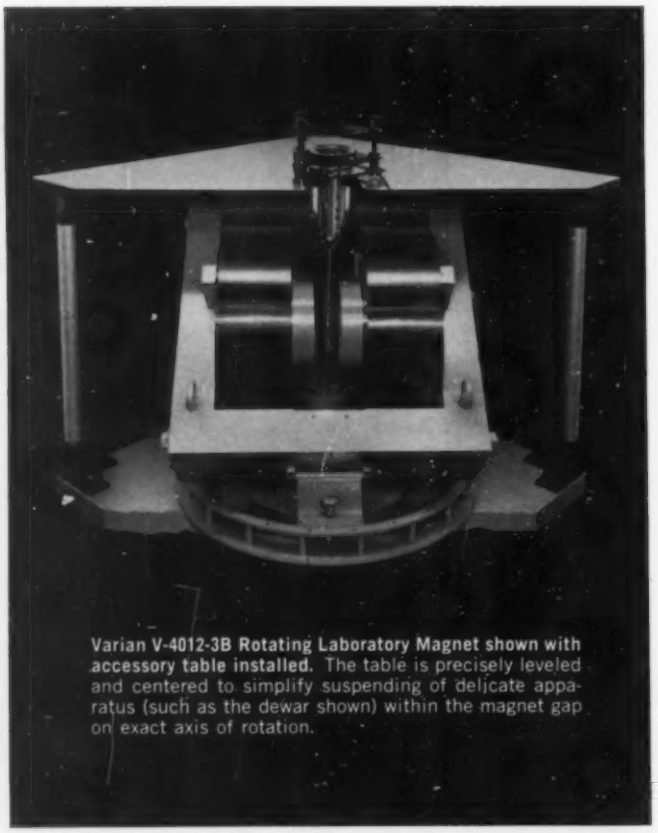

Varian V-4012-3B Rotating Laboratory Magnet shown with accessory table installed. The table is precisely leveled and centered to simplify suspending of delicate apparatus (such as the dewar shown) within the magnet gap on exact axis of rotation.

Field homogeneity in a useful third dimension

Presented here for the first time, a three-dimensional plot from a 12-inch Varian Magnet reveals over 100 cc of highly homogeneous field available to the experimental physicist. This volume is a technical accomplishment because field homogeneity normally falls off rapidly with increasing gap width. It demonstrates again how Varian's long experience puts extra value into these magnet systems.

Easy accommodation of bulky experimental apparatus

The large field shown is highly useful in two respects. The over-all air gap width of nearly three inches is sufficient to hold glass dewars and other apparatus surrounding the field-sensitive sample or object. And your sample itself may be of any bulk and dimensions up to those shown and still fall inside a field homogeneous within ± 0.07 gauss of the 3550 gauss central field strength. Outstanding performance is also attainable at other field strengths.

A versatile range of other capabilities

Much higher magnetic field strengths are available by purchase of additional pole cap configurations for smaller air gaps. The extra cost is nominal. And the magnet provides a useful volume of homogeneous field at these higher strengths. Thus as a long-range investment a Varian Magnet is adaptable to needs unforeseen at time of purchase.

Write today for the new 32-page magnet brochure which gives specifications on Varian's full magnet line. Address Instrument Division.

IN WIDE AIR GAPS

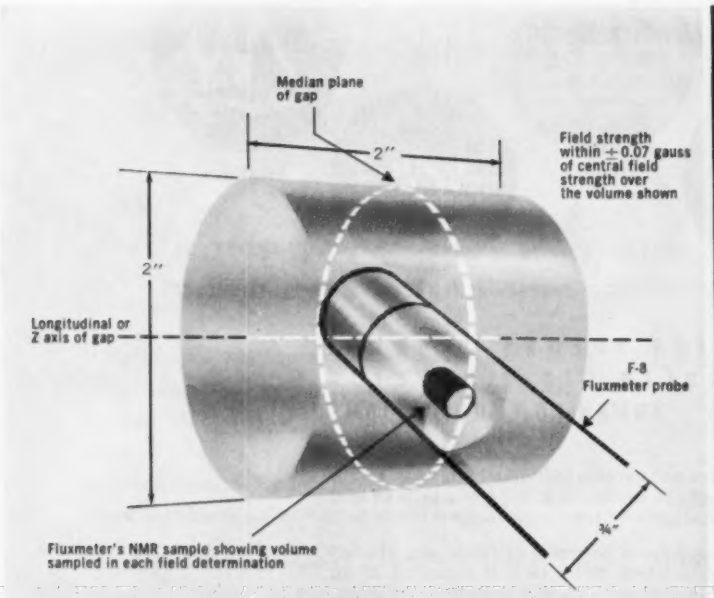
Median plane of gap
2″
Field strength within ± 0.07 gauss of central field strength over the volume shown
2″
Longitudinal or Z axis of gap
F-8 Fluxmeter probe
¾″
Fluxmeter's NMR sample showing volume sampled in each field determination

More than 100 cc of homogeneous magnetic field within 3-inch central air gap. Three-dimensional cylindrical field of Varian 12-inch magnet shown full scale in oblique view; ring shim pole caps used; field strength 3550 gauss.

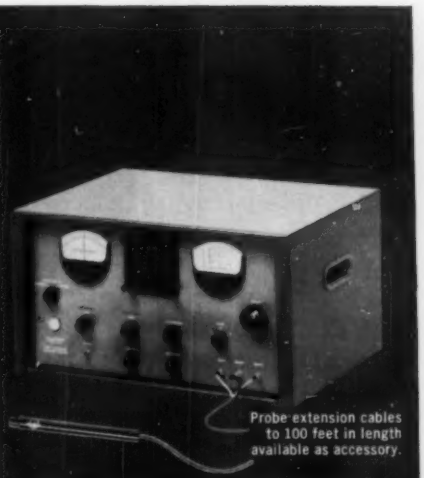

VARIAN F-8 FLUXMETER with new crystal frequency control. Time stability and accuracy enable the Varian Fluxmeter to make homogeneity field plots. The fluxmeter probe (at left) is shown extended into the magnet gap as actually done in making the field plot.

The F-8 can provide direct stabilization of magnetic fields by utilization of the D.C. error signal output. The F-8 is perfectly matched to the Varian 6- and 12-inch magnet system power supplies, and readily adapts to others.

VARIAN associates
PALO ALTO 36, CALIFORNIA

NMR & EPR SPECTROMETERS, MAGNETS, FLUXMETERS, GRAPHIC RECORDERS, MAGNETOMETERS, MICROWAVE TUBES, MICROWAVE SYSTEM COMPONENTS, HIGH VACUUM EQUIPMENT, LINEAR ACCELERATORS, RESEARCH AND DEVELOPMENT SERVICES

Scientists

AN INVITATION TO EXPLORE THE COMMUNICATIONS SCIENCES

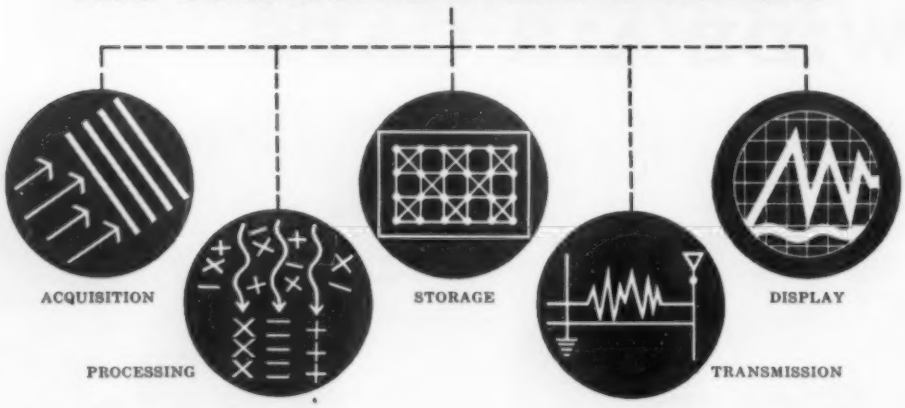

INFORMATION THEORY / CODING
LOGIC / SOLID STATE PHYSICS
PROPAGATION / HUMAN COMMUNICATIONS

Invitation to explore and develop individual interests within the broad reaches of the communications sciences is offered by the Research Division of Stromberg-Carlson.

Recognizing the need for a program of basic and applied research in a field in which technology is changing at an explosive rate, Stromberg-Carlson Division of General Dynamics gives its research people unrestricted opportunity to pursue their own investigations in a free, academic atmosphere.

If you would like to discuss your field of interest with the head of this research group, write informally to Mr. Maurice Downey. Background at the doctoral level or equivalent is prerequisite to a staff appointment.

STROMBERG-CARLSON
A DIVISION OF **GENERAL DYNAMICS**
1488 North Goodman Street, Rochester 3, New York

dial any output from 0-1000V within 1%

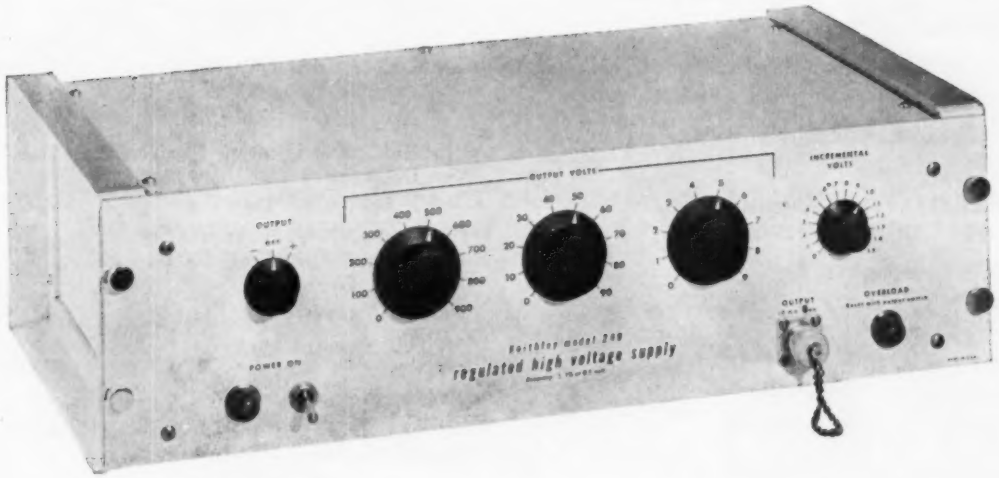

KEITHLEY Model 240 High-voltage Supply combines convenience, accuracy, wide range

This convenient supply brings new speed, ease and accuracy to laboratory tests. Typical applications include calibration of meters and dc amplifiers, supplying potentials for photomultiplier tubes and ionization chambers. Other uses include furnishing potentials for high resistance measurements, and for diode and capacitor leakage resistance tests.

The Model 240 output delivers 0 to 1000 volts at up to 10 milliamperes. Three calibrated dials on the front panel select the desired output voltage in one volt steps, with accuracy of 1% or 100 millivolts. Greater accuracy may be obtained with a potentiometer provided for setting the output with an accurate voltmeter.

Polarity is selectable. The switch includes an "OFF" position, facilitating timed measurements. An overload relay cuts off the output at 12 milliamperes within 50 milliseconds. Connectors are provided on front and rear panels.

SPECIFICATIONS

DC OUTPUT VOLTAGE: Positive or negative, 0 to 1000 volts, in one volt steps.

OUTPUT CURRENT: 0 to 10 milliamperes.

ACCURACY: Within 1% above 10 volts, within 100 millivolts below 10 volts.

LOAD REGULATION: 0.02% for 0 to 10 ma.

RIPPLE: Less than 3 mv RMS above 5 cps.

OUTPUT IMPEDANCE: Less than 15 ohms.

STABILITY: After a 20-minute warmup, within 0.02 volts $\pm$ 0.02% the first hour, or in any subsequent 8-hour period, with line voltage changes within $\pm$ 10%.

LINE REGULATION: Output change is less than 0.02 volts + 0.02% for a 10% change in line voltage.

RACK mounting, shown above with accessory end frames, bench mounting.

PRICE $325.00

SEND TODAY FOR COMPLETE DETAILS

KEITHLEY INSTRUMENTS, INC.
12415 EUCLID AVENUE • CLEVELAND 6, OHIO

Wiley BOOKS

OREAR: Fundamental Physics.
1961. Approx. 456 pages. Prob. $7.00.

BUBE: Photoconductivity of Solids.
1960. 461 pages. $14.75.

FRÉCHETTE: Non-Crystalline Solids.
1960. 536 pages. $15.00.

EGLI: Thermoelectricity.
1960. 407 pages. $10.00.

LIVERHANT: Elementary Introduction to Nuclear Reactor Physics.
1960. 447 pages. $9.75.

ZUCKER–HALBERT–HOWARD: Proceedings of the Second Conference on Reactions Between Complex Nuclei.
1960. 319 pages. $7.00.

BURTON: Comparative Effects of Radiation.
1960. 427 pages. $8.50.

CORBEN–STEHLE: Classical Mechanics, Second Edition.
1960. 396 pages. $12.00.*

GRAY: The Dynamic Behavior of Thermoelectric Devices.
1960. 136 pages. $3.50.

GATOS–FAUST: The Surface Chemistry of Metals and Semiconductors.
1960. 526 pages. $12.50.

WELSBY: The Theory and Design of Inductance Coils.
1960. In Press.

HAUS–PENHUNE: Case Studies in Electromagnetism.
1960. 335 pages. $6.50.

PENFIELD: Frequency Power Formulas.
1960. Approx. 256 pages. $4.00.

MESAROVIC: Control Theory of Multivariable Systems.
1960. Approx. 128 pages. $3.50.

JONSCHER: Principles of Semiconductor Device Operation.
1960. 168 pages. $5.00.

LIEBHAFSKY–PFEIFFER–WINSLOW–ZEMANY: X-Ray Absorption and Emission in Analytical Chemistry.
1960. 357 pages. $13.50.

LOUISELL: Coupled Mode and Parametric Electronics.
1960. 268 pages. $11.50.

VAN VALKENBURG: Introduction to Modern Network Synthesis.
1960. 512 pages. $11.75.*

TOBOLSKY: Properties and Structures of Polymers.
1960. 331 pages. $14.50.

MEYERHOFF: Digital Applications of Magnetic Devices.
1960. Approx. 656 pages. Prob. $14.00.

AIGRAIN: Electronic Processes in Solids.
1960. 67 pages. $4.00.

SANGREN: Digital Computers and Nuclear Reactor Calculations.
1960. 208 pages. $8.50.

DE WITT–DETOEUF: The Theory of Neutral and Ionized Gases.
1960. 469 pages. $17.50.

BATTELLE MEMORIAL INSTITUTE: Semiconductor Abstracts. Vol. VI, 1958 Issue.
(C. S. Peet, Editor.) 1960. In Press.

BUNDY–HIBBARD–STRONG: Progress in Very High Pressure Research.
1960. In Press.

**Textbook edition available for college adoption.*

Send for your examination copies.

JOHN WILEY & SONS, INC., 440 Park Avenue South, New York 16, N. Y.

X-RAY DIFFRACTION AND SPECTROSCOPY

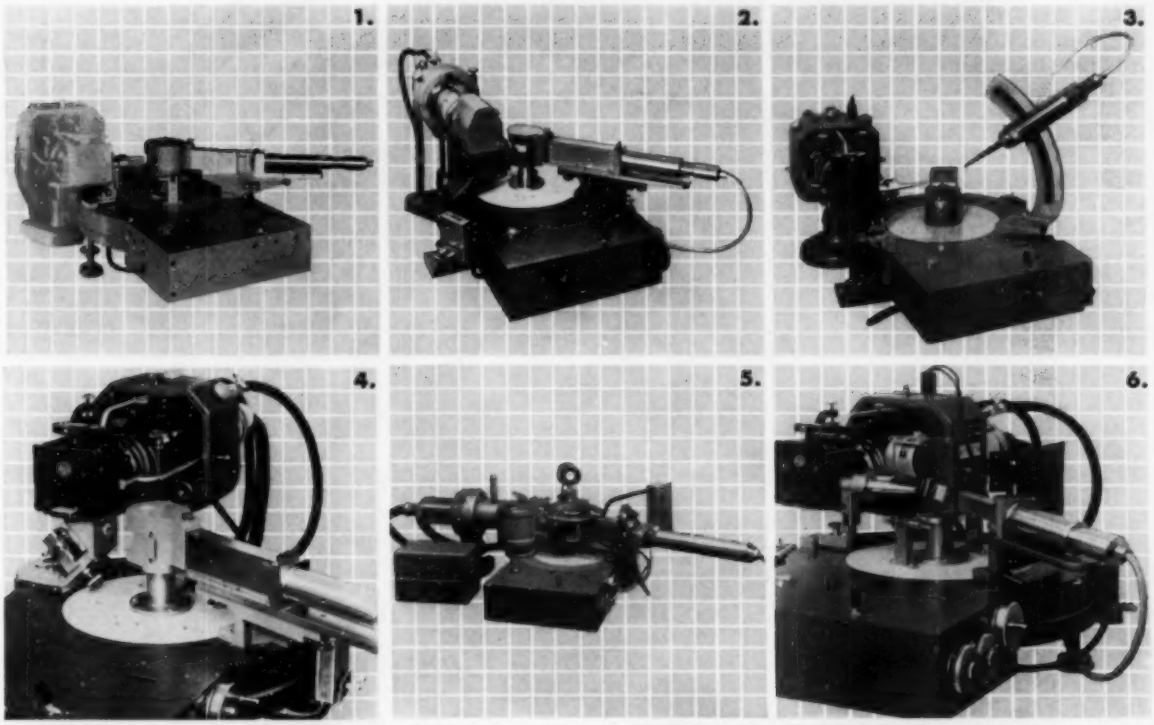

1. Counter Tube Diffractometry. 2. Spectroscopy. 3. Single Crystal Studies. 4. Spectroscopy of Small Areas. 5. Vacuum Spectroscopy of Light and Heavy Elements. 6. Studies of Orientation.

VERSATILITY!

RCA's horizontal goniometer performs 6 functions

Unusual versatility is an important distinguishing characteristic of RCA's X-Ray Diffraction and Spectroscopy Equipment. This versatility is graphically demonstrated by the horizontal goniometer which can perform six different functions merely by adding accessories, as illustrated above.

RCA X-Ray Diffraction and Spectroscopy Equipment offers many other outstanding features which make it one of today's most specified lines. For example, the DC regulated and filtered power supply; the option of mounting two tube stands on the Crystalloflex IV; a kit which permits conversion from diffraction to spectroscopy in minutes; and the new vacuum spectrometer for analysis of light and heavy elements. For those engaged in film studies of all kinds, the RCA Table Model Crystalloflex II can be bought, complete with cameras, for as little as $4000.

A NEW LEASING PLAN now makes it possible to obtain all RCA scientific instruments, including the Electron Microscope, with no down payment, low monthly terms, and a favorable option to buy.

For complete information write to RCA, Dept. N-65, Bldg. 15-1, Camden, N.J.

Crystalloflex IV and Electronic Circuit Panel with Vacuum Spectrometer and Diffractometer mounted on the generator.

RCA®

The Most Trusted Name in Electronics

RADIO CORPORATION OF AMERICA

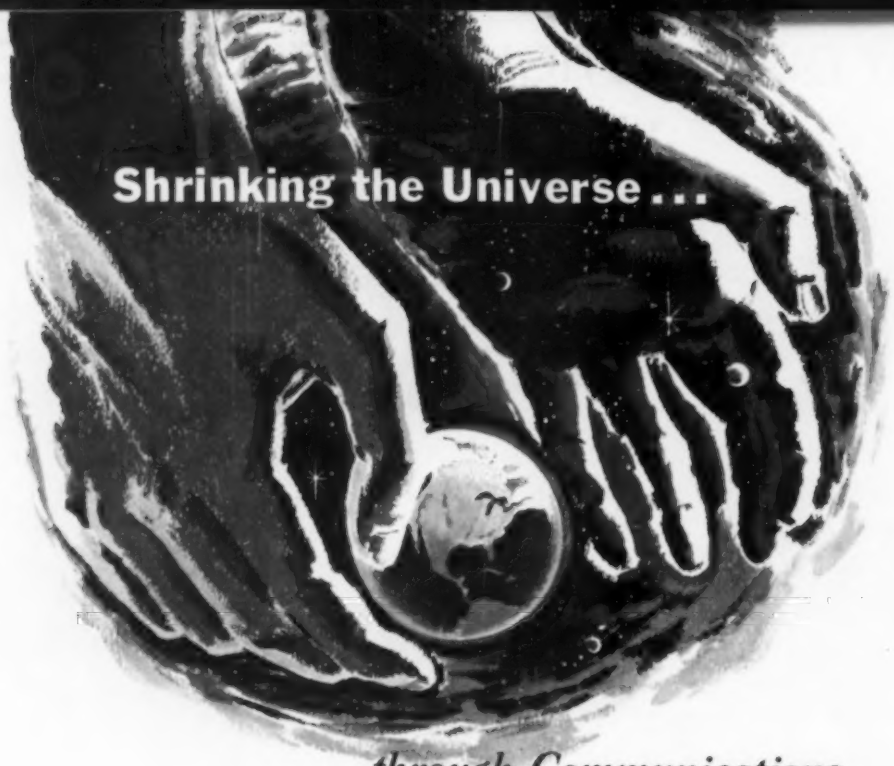

through Communications

BY APPLYING TOMORROW'S CONCEPTS TODAY... AT AMHERST LABORATORIES

today's dynamic R & D mission also includes creative opportunities in Navigation, Microwave Data Handling, ECM and Radar Systems

Man's vision of future exploration in the infinity of outer space is predicated on pertinent data that can be gathered by each space probe today. As the probe distances increase... our universe becomes smaller and communications are the vital link that proves success or failure of each venture into the unknown. It is imperative that new systems of communications be developed well in advance of other facets of space technology. At Amherst Laboratories new solutions are sought to communications problems even before they are encountered. Creative ideation is not compromised by conventionally accepted conclusions.

Amherst Laboratories is currently anticipating tomorrow's electronics needs in areas of advanced Ground, Air and Space Communication.

PROFESSIONAL STAFF AND MANAGEMENT OPPORTUNITIES *are unlimited for Electronics Engineers, Physicists and Mathematicians with advanced degrees and creative desire.*

You are invited to direct inquiries in confidence to Mr. W. Serniuk, Director, Amherst Laboratories... or call NF 3-8315 for information. All inquiries will be acknowledged promptly.

SYLVANIA ELECTRONIC SYSTEMS
A Division of SYLVANIA
Subsidiary of GENERAL TELEPHONE & ELECTRONICS
1183 Wehrle Drive, Williamsville, New York

AMHERST LABORATORIES

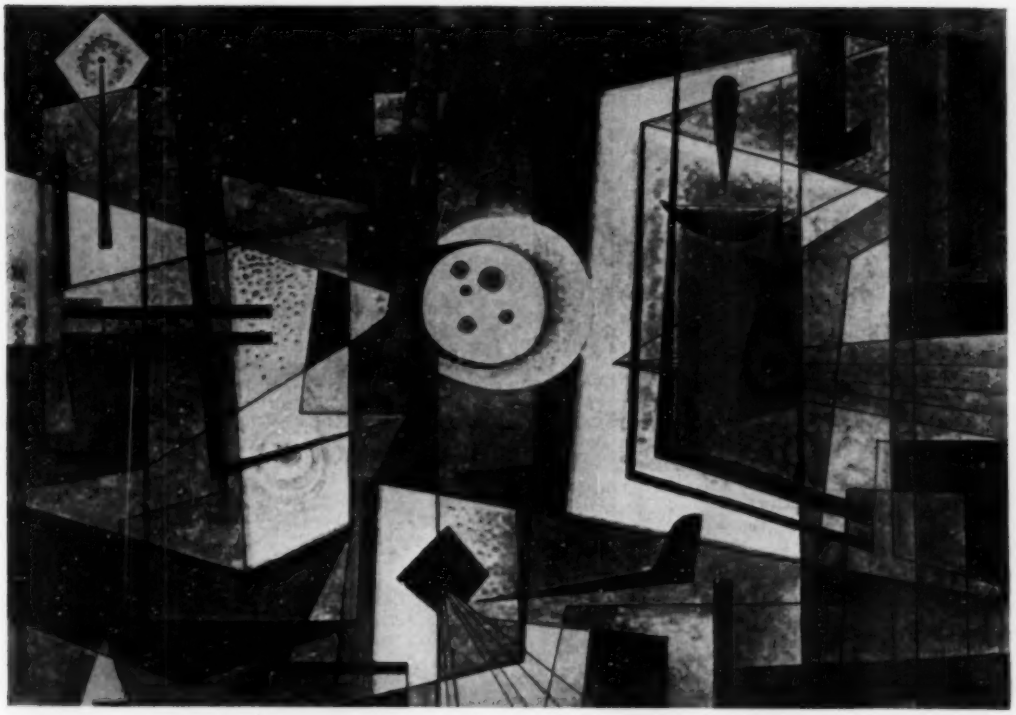

ORIENTATION LECTURES

GRADUATE TRAINING CENTER

FREQUENT SCIENTIFIC COLLOQUIA

ASSOCIATION WITH LEADING SCIENTISTS

GRADUATE THESIS PROGRAM

ADVANCE STUDY PROGRAM

SUMMER GRADUATE STUDENT PROGRAM

. . . these are some of the Doorways to Knowledge at Los Alamos.

For employment write to Personnel Director Division 60-108

los alamos
scientific laboratory
OF THE UNIVERSITY OF CALIFORNIA
LOS ALAMOS, NEW MEXICO

Valuable McGraw-Hill books . . .

Ready in January

RETRIEVAL GUIDE TO THERMOPHYSICAL PROPERTIES RESEARCH LITERATURE

Edited by Y. S. Touloukian

Thermophysical Properties Research Center
Purdue University

Ten thousand scientific and technical research papers have been coded as to property, substance, subject, language, physical state, etc. and the information stored on magnetic tapes of a computer at Purdue University. The thermophysical properties of 14,500 substances are reported. This work represents the print out of a special computer program and will provide the engineer, scientist, or reference librarian with quick access to the world literature on the following seven thermophysical properties: thermal conductivity, thermal diffusivity, diffusion coefficient, specific heat, viscosity, emissivity and Prandtl number. Volume I, ***The Three Book Set,*** (10,000 bibliographic references), $120.00

MODERN MATHEMATICS FOR THE ENGINEER, Vol. II

By Edwin F. Beckenbach, University of California, Los Angeles. Ready in January, 1961.

GERMAN-ENGLISH SCIENCE DICTIONARY, Third Edition

By Louis De Vries, Iowa State University. 592 pages, $7.00.

TIME-HARMONIC ELECTRO-MAGNETIC FIELDS

Roger V. Harrington, Syracuse University. Ready in January, 1961.

DIGITAL COMPUTER AND CONTROL ENGINEERING

By Robert S. Ledley, The George Washington University. 864 pages, $14.50.

TRAVELING WAVE ENGINEERING

By Richard K. Moore, University of New Mexico. 368 pages, $11.00.

INTRODUCTION TO NUCLEAR PHYSICS

By Otto Oldenberg, Harvard University. Ready in January, 1961.

WAVE PROPAGATION IN A TURBULENT MEDIUM

By V. I. Tatarski, Academy of Sciences, U. S. S. R. Translated by Richard A. Silverman, New York University. Ready in January, 1961.

THEORY OF ELASTIC STABILITY, *Second Edition*

By Stephen P. Timoshenko and James M. Gere, Stanford University. Ready in January, 1961.

send for on-approval copies

McGRAW-HILL BOOK COMPANY, Inc.

330 West 42nd Street New York 36, N.Y.

Collins men are working late tonight...

exploring a new method of communication

Although the initial excitement over Echo I has subsided, Collins engineers and scientists still seek additional information vital to the nation's space effort. So far, they have:

- ... bounced intelligible signals in north-south direction
- ... transmitted and received live voice messages
- ... established a two-way voice circuit
- ... transmitted and received a teletype signal
- ... transmitted and received a wirephoto
- ... collected valuable propagation and orbit data

One of the most difficult obstacles for Collins to overcome was that of accurately tracking the Echo I satellite. 800 miles, roughly speaking, separate Collins Radio Company in Cedar Rapids, Iowa, and its subsidiary, Alpha Corporation in Dallas, Texas. Both locations were prepared to send and receive radio signals bounced off Echo. Because Echo I was speeding through space at approximately 15,000 miles per hour some 900 miles above the Earth, its time above the horizon of both Collins locations was brief. However, Collins engineers perfected an automatic tracking device which permitted both the sending and receiving units to maintain constant contact from the time Echo I appeared on the horizon until it disappeared some 15 minutes later.

The radio signals actually traveled a minimum of about 2000 miles. Power loss was of staggering proportions . . . with received signal strength approximately 10^{-16} watts.

These contributions to the new world of space communications were completely company sponsored — and represent an investment in the future by Collins Radio Company and its subsidiary, Alpha Corporation. It was worth it . . . in the warm feeling of accomplishment alone.

Collins provides freedom of activity in basic research for the engineer, physicist and mathematician . . . and is able to offer unique professional opportunities. Your inquiry is invited.

The Echo project is being coordinated with the National Aeronautics and Space Administration. Data collected by Collins is being submitted to NASA to be used in the evaluation of this communications technique.

COLLINS

COLLINS RADIO COMPANY • CEDAR RAPIDS, IOWA • DALLAS, TEXAS • BURBANK, CALIFORNIA

TESLA ELECTRON MICROSCOPE—Desk Model BS243

Guaranteed
Local Service

Installation
and
Instruction
Included in Price

TESLA

The Little
Giant
60 kV
30,000X
30Å

TESLA

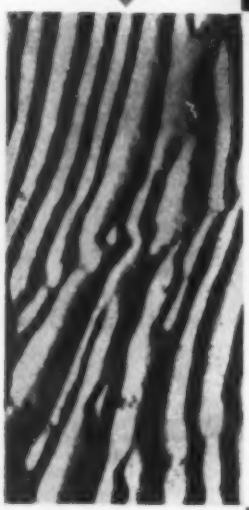

FEATURES

- Resolving power 30Å to 50Å in routine operation, optimal resolution 25Å
- Magnification 1,000X to 30,000X, adjustable in steps
- Accelerating voltage 60 kV ±0.01%
- High-voltage stability better than 10^{-4}, ripple less than 2.5×10^{-5}
- Specimen inserted under vacuum
- Specimen motion controlled from microscope platform
- Microscope may be tilted for stereo-photography
- Viewing port usable for diffraction patterns
- Uses standard 35 mm film (36 pictures) or ten 2" x 2" plates
- Dimensions of basic instrument: 14½" wide, 18" deep, 34½" high
- Low initial cost and minimal maintenance

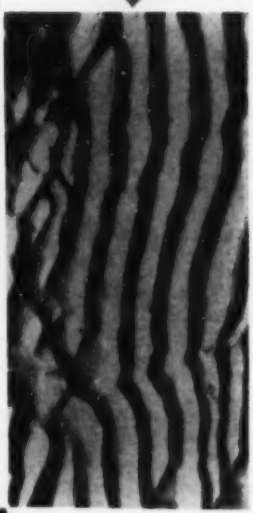

Made in
Czechoslovakia

Worldwide
Distribution
by

KOVO

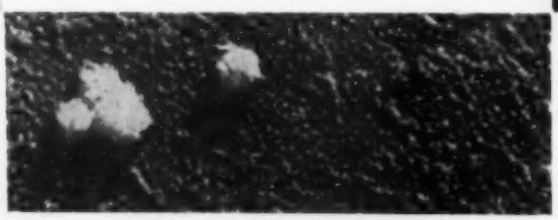

For complete
description, technical
data, and ordering
information, write for
BULLETIN 8-2000

Exclusive Sales and Service in U.S.A.

NATIONAL INSTRUMENT LABORATORIES, Inc.

828 Evarts St., Washington 18, D.C.

Tel. NOrth 7-7582

How Do You Measure Achievement?

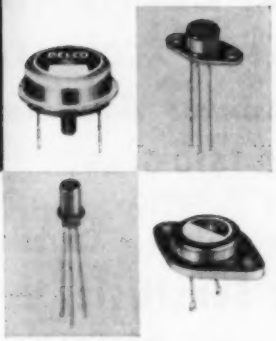

These transistors—representing the proven capability of Delco Radio to develop and mass produce the highest power transistor in the industry—are a measure of achievement.

TALENT—bold, imaginative talent stimulated by the constant challenge of new concepts—was responsible for this achievement.

However, past achievements are significant only insomuch as they indicate the path of the future. At DELCO, this path is clearly charted. We are committed—and dedicated—to uphold and maintain our position of leadership in the fields of electronics and Solid State Physics.

Fulfilling this challenge requires a constant infusion of new ideas and new talent—*aggressive new talent.* That's what we're looking for.

We are vitally interested in ambitious men with experience in the following areas:

SEMICONDUCTOR DEVICE DEVELOPMENT

—We need men with experience in the techniques of semiconductor device development including alloying and diffusion.

—We need a man with experience in the chemistry of semiconductor devices.

—We need a man with experience in semiconductor materials to lead a program on metallurgical research of new semiconductor materials.

—We need a man with experience in semiconductor device encapsulation.

PROCESS ENGINEERING

—We need several men for production set-up and trouble shooting.

EQUIPMENT DEVELOPMENT

—We need men to develop automatic and semi-automatic fabrication equipment.

The applications we see for Delco Radio capabilities in electronics and Solid State Physics are staggering. We're therefore eager to find more, experienced personnel; responsible positions are available for those who qualify.

If you're interested in becoming a member of our Delco—GM team of outstanding scientists and engineers, send your resume today to the attention of Mr. Carl Longshore, Supervisor Salaried Employment.

DELCO RADIO
DEPENDABILITY
RELIABILITY

Division of General Motors • Kokomo, Indiana

• Convenient • Efficient • Economical

Welch TRIPLE-BEAM TRIP-SCALE

SPEEDY, ACCURATE WEIGHING

Stainless Steel Beam and Pan

• ***Large Capacity-1610 Grams*** (With Extra Weight-2110 Grams) • ***Sensitivity to 0.1 Gram***

Wide Range · Stable · Corrosion-Resistant · Low Cost

Excellent Sensitivity — Enduring Service

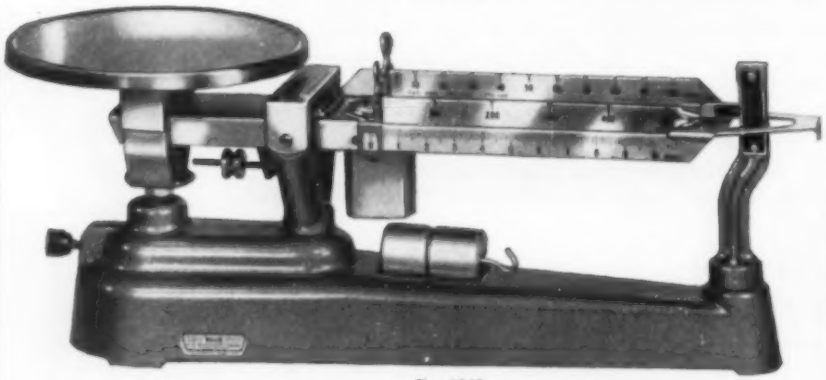

No. 4048

Each
$21.00

3 Graduated Scale Levels for easy reading. Riders move easily. Hard, Cobalite Knife Edges maintain true edge indefinitely.

Grooved Agate Bearings are protected against damage, yet highly resistant to corrosive action of laboratory fumes.

One-Piece Beam Construction—Silver-Gray Hammerloid Finish—Rapid Zero Setting—Beam Arrest for faster weighing.

No. 4048. LOW FORM SCALE, WITH TWO EXTRA WEIGHTS	$21.00
No. 4048C. PLASTIC COVER, For No. 4048	Each, $1.10
No. 4048W. EXTRA WEIGHT. For increasing the capacity of No. 4048 to 2110 grams	Each, $1.45

W. M. WELCH SCIENTIFIC COMPANY

DIVISION OF W. M. WELCH MANUFACTURING COMPANY

ESTABLISHED 1880

1515 SEDGWICK STREET, DEPT. C-I, CHICAGO 10, ILLINOIS, U.S.A.

Manufacturers of Scientific Instruments and Laboratory Apparatus

Journal
of
Applied Physics

Volume 31, Number 11 November, 1960

Special Issue on High Polymer Physics

The following fifteen papers were presented at the meeting of the Division of High Polymer Physics of the American Physical Society at Detroit, Michigan, March 21–24, 1960.

NMR Absorption in Teflon Fibers

D. Hyndman and G. F. Origlio
American Viscose Corporation, Marcus Hook, Pennsylvania

Nuclear magnetic resonance absorption in oriented polytetrafluoroethylene fibers has been investigated in the temperature range 170°–380°K. The sample, in the form of a parallel bundle of fibers, showed a marked dependence of line shape on the direction of the applied magnetic field over the temperature range studied, although the observed anisotropy was much greater above 285°K than below. Changes occurring in the linewidth and second moment at around 285°K indicate a rotational disorder transition in the crystalline regions of the polymer, and serve to illustrate the advantages of using oriented fibers in the NMR investigation of semicrystalline polymers.

INTRODUCTION

MANY excellent papers have appeared in the last few years on the study of crystalline and amorphous polymers by wide line NMR, and extensive review articles are available on the subject.[1,2] However, very little work has been reported on oriented fibers of crystalline polymers and, as pointed out by Slichter,[2] this results in the sacrifice of available information. The magnetic interactions responsible for NMR absorption contain terms which are dependent on the angular disposition of internuclear vectors with respect to the applied magnetic field. In a polycrystalline material, containing no preferred molecular direction, these internuclear vectors are distributed randomly in space and the observed spectrum can be regarded as the spatial average of the spectra from the individual crystallites. Obviously the use of a single crystal specimen introduces a new experimental variable, since a study can be made of the anisotropy of the absorption as a function of the direction of the magnetic field. A good example is the work of Pake[3] on a single crystal of gypsum. Unfortunately, single crystals of polymers of sufficient dimensions are not available for NMR studies. However, it is possible to approximate a single crystal by an oriented fiber since in the stretching process the polymer chains align with the direction of drawing and therefore give rise to a preferred molecular orientation.

It is the purpose of this paper to show that a study of the line shapes, linewidths and second moments of oriented Teflon fibers leads to a clearer interpretation of NMR absorption in this particular polymer.

EXPERIMENTAL

F^{19} magnetic resonance measurements were made at 30 Mc/sec using a Varian model V-4300-2 Dual-Purpose Spectrometer and a Varian V-4007 6-in. electromagnet. The fibers were held in a small, thin-walled nylon cylinder fixed at right angles to one end of a nylon rod. The other end of the rod was supplied with a nylon cap which fitted snugly over the end of the glass insert holding the receiver coil in the Varian probe. When in position, the axis of the cylinder coincided with the median plane of the receiver coil. The fibers were packed axially in the cylinder and by rotating the rod it was possible to obtain any desired angle between the fiber

[1] J. A. Sauer and A. E. Woodward, Revs. Modern Phys. **32**, 88 (1960).
[2] W. P. Slichter, Makromol. Chem. **34**, 67 (1959).
[3] G. E. Pake, J. Chem. Phys. **16**, 327 (1948).

Copyright © 1960 by the American Institute of Physics.

axes and the magnetic field. The temperature of the specimen was controlled by a gasflow cryostat similar in design to the one described by Brownstein,[4] except that the dimensions were such as to retain the Varian 15-mm broad line insert. This cryostat has the advantage over the commercially available temperature assembly[5] in that the receiver coil is inside the Dewar and thus in close proximity to the sample with an attendant improvement in filling factor. Dry nitrogen was used as a refrigerant for temperatures down to 150°K. Temperatures from room temperature to 400°K were obtainable by passing the gas over a heating coil. It was found that the temperature of the sample could be held to within 1°K for a time appreciably longer than that required to record a resonance spectrum.

The Teflon fiber used in the experiments was obtained from E. I. du Pont de Nemours and Company. This material was dark brown in color, and it was suggested earlier[6] that this might be due to degradation. However, comparison of the temperature dependence of NMR absorption of a sample of finely divided fibers with that of undegraded polymer shows virtually no difference between the two specimens. It is thought, perhaps, that the color results from the oxidation of some material added to the polytetrafluoroethylene to aid in extrusion. It was assumed, therefore, that the fiber represented pure polymer as far as these studies were concerned.

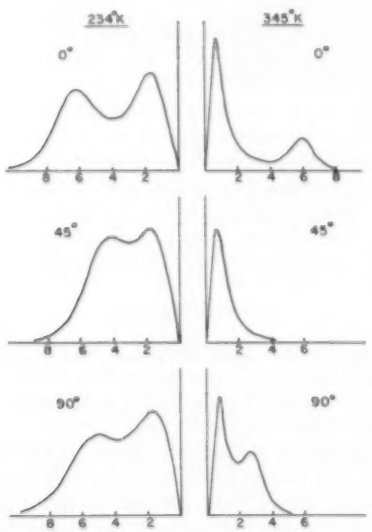

FIG. 1. Fluorine derivative line shapes for drawn Teflon fibers at fiber-magnetic field angles of 0°, 45°, and 90° at 234°K and 345°K (abscissa in gauss).

[4] S. Brownstein, Can. J. Chem. **37**, 1119 (1959).
[5] Varian Associates, Palo Alto, California.
[6] W. P. Slichter, J. Polymer Sci. **24**, 173 (1957).

RESULTS AND DISCUSSION

Several workers[6–9] have reported NMR measurements in Teflon. However, some discrepancies exist which have been attributed by Powles[9] to differences in crystallinity of the samples studied. Wilson and Pake,[8,10] in their original work on Teflon, reported a composite line shape consisting of a narrow line superimposed on a broad line, over a wide temperature range, indicating the presence of two magnetic resonance phases corresponding to the amorphous and crystalline areas of the polymer. This was substantiated by the work of Smith,[7] whereas neither Slichter[6] nor Powles[9] observed a two-component system. Perhaps this difference can be resolved by an examination of the line shapes obtained from oriented fibers. Figure 1 shows one-half of the derivative of the F^{19} resonance lines of Teflon fiber at three orientations to the magnetic field recorded at two temperatures, 234°K and 345°K. The three curves at the lower temperature are easily separable into two components, a broad line attributed to the oriented crystalline areas and a narrow component attributed to the amorphous areas. The anisotropy of the broad line with magnetic field direction lends support to the assumption that this component results from the crystalline areas, since it is known[11] from x rays that, in an oriented fiber, the crystallites are aligned with the fiber axis.

At 345°K distinct changes were observed in the width of the broad component. At 45° orientation, for instance, the broad line has narrowed to the point where it has merged with that of the amorphous areas, resulting in a structureless curve. This would suggest that at some temperature between 234°K and 345°K the crystalline phase has undergone a transition. The nature of this transition will become more apparent when we consider the temperature dependence of the linewidths and second moments. The discrepancies in the reported line shapes can perhaps be explained in terms of our experimental curves shown in Fig. 1. Since the previous workers used polycrystalline specimens, their observed spectra were the sum of the spectra of the individual crystallites randomly oriented in space, i.e., a sum of spectra of the type shown in Fig. 1. Since the relative intensities of the two components, at a particular temperature, will depend on the degree of crystallinity, it can easily be shown that a composite curve made up of these individual spectra can range from a single broad line (high crystallinity) through a two-component system (intermediate crystallinity) to a single narrow line with extensive tails (low crystallinity). This has been supported experimentally by observing the spectrum of a sample of finely divided fiber, effectively polycrystalline, where the crystalline component ap-

[7] J. A. Smith, Discussions Faraday Soc. **19**, 207 (1955).
[8] C. W. Wilson, III, and G. E. Pake, J. Chem. Phys. **27**, 115 (1957).
[9] J. G. Powles and J. A. E. Kail, J. Polymer Sci. **31**, 183 (1958).
[10] C. W. Wilson, III, and G. E. Pake, J. Polymer Sci. **10**, 503 (1953).
[11] C. W. Bunn and E. R. Howells, Nature **174**, 549 (1954).

pears as an indistinct shoulder on the curve at certain temperatures. Therefore, this evidence lends support to Powles' suggestion that crystallinity plays an important part in the shape of the observed NMR spectra of Teflon.

The main interest of the present work, however, lay in the study of the crystalline transition referred to above. Rigby and Bunn[12] have shown a first-order thermodynamic transition in Teflon around room temperature accompanied by a change in the x-ray diffraction pattern. This has been substantiated by many authors employing a variety of techniques. For example, a λ transition was observed at 293°K in the heat capacity,[13] and dynamic mechanical measurements[14] show a damping peak at room temperature which has been associated with a crystalline phase change. This transition appears to be quite sharp and is consistent with the onset of dynamic disorder in the crystal, presumably reorientation about the chain axis taking place. NMR studies[6–9] have also indicated a transition, or transitions, in polytetrafluoroethylene. However, there are differences in the extent and number of transitions observed which appear to depend on whether or not a composite line was observed. Smith[7] reports one linewidth transition in the range 200°K to 250°K but observes two second-moment changes, one between 210°K and 230°K, the other between 280°K and 310°K, and suggests that the 280–310°K transition is associated with the crystalline phase. Wilson and Pake[8] observed two linewidth changes, one at 180°K associated with the narrow amorphous component, and an abrupt narrowing of the broad line at 290°K. However, Slichter,[6] observing a noncomposite line, saw only one change in both linewidth and second moment extending from about 250°K to over 350°K. Powles[9] also demonstrated one linewidth transition, the character of which depended greatly on crystallinity, and he suggests that the transition observed in a highly crystalline sample at about 285°K is probably associated with the crystalline areas. Therefore, it would appear that the NMR data does not clearly indicate the room temperature transition in Teflon, since we would expect relatively sharp changes to occur in both linewidth and second moment in this temperature region.

The identification of the crystalline transition is quite evident when the linewidths and second moment of a parallel bundle of fibers are examined as functions of both temperature and orientation with respect to the magnetic field. Figure 2 shows the linewidths vs temperature plot of the broad component for three orientations of the fibers in the magnetic field, the linewidth being taken as the interval between corresponding maxima and minima of the recorded derivatives of the

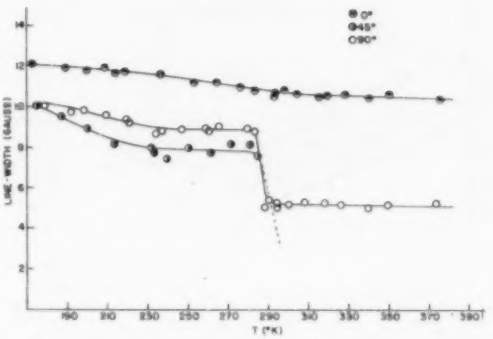

FIG. 2. Variation with temperature of the linewidth for three orientations of Teflon fibers with respect to the magnetic field.

absorption lines. The narrow central line appeared about 200°K, grew narrower as the temperature increased, and showed no anisotropy with field direction, i.e., typical behavior of amorphous regions.[14] There is a marked transition in the 45° and 90° plots at 285°K. Above this temperature the broad line is no longer observable for a 45° orientation, whereas a linewidth change of about 3.5 gauss takes place in the 90° case. However, when the fibers are lying along the magnetic field no change is observed in the linewidth at 285°K. If the transition is one of rotational disorder about the chain axes this would be the expected behavior of the linewidth. When the axis of rotation (fiber axis) coincides with the direction of the magnetic field the angles between internuclear vectors and the magnetic field direction remain unchanged, and therefore no line narrowing would result. For any other fiber orientation in the magnetic field, however, these angles must be averaged over the motion and, in general, would result in a reduced linewidth.

A more quantitative interpretation of the crystal transition can be obtained from second-moment measurements. Figure 3 shows second-moment vs temperature plots for the three fiber orientations. Although not shown in the plots, the second moments leveled off at about 180°K and remained constant to the lowest temperature of measurement, 150°K. The general decrease in second moment from low temperature to 280°K is associated with the narrowing of the central component of the absorption lines which, as mentioned above, appeared around 200°K. As in the linewidth plot, a sharp transition is observed at 285°K in the 45° and 90° curves but not for the 0° orientation. The observed second moments can be compared to theoretical values calculated from the known structure of Teflon.[11] The calculation of the rigid lattice second moment of a fiber has already been treated for polyethylene.[15] The Teflon case is somewhat more complicated owing to the helical structure[11] of the chains and the uncertainty in the relative positions of the fluorine nuclei on neighboring chains. Using Bunn's model, however, and assuming

[12] H. A. Rigby and C. W. Bunn, Nature **164**, 583 (1949).
[13] G. T. Furukawa, R. E. McCoskey, and G. J. King, Natl. Bur. Standards J. Research **49**, 273 (1952).
[14] A. E. Woodward and J. A. Sauer, Fortschr. Hochpolym. Forsch. **1**, 114 (1958).
[15] L. H. Meyer, thesis, University of Illinois, 1953.

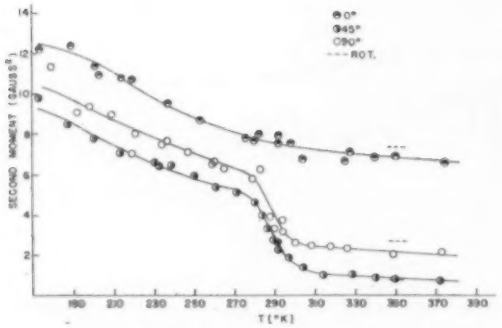

FIG. 3. Variation with temperature of the second moment for three orientations of Teflon fibers with respect to the magnetic field. (Dashed lines show calculated values for rotating chains.)

perfect orientation of the chain in the fiber, the calculated rigid lattice values showed good agreement with the low temperature experimental second moments. It has been shown recently[16] that the second moment of an NMR spectrum should be invariant with respect to thermal motion and should therefore be unaffected by the dynamic transition under consideration. This invariance depends on including sideband spectra, resulting from the molecular motion, in the measurement on the second moment. If these sidebands are weak, which is usually the case, they can be neglected and the second moment will vary in a manner described by Gutowsky and Pake,[17] provided that comparisons between theory and experiment are made at a temperature where there is no further decrease of experimental second moment with increasing temperature.[16] From Fig. 3 it would appear that 350°K is a suitable temperature. Theoretical second moments are shown for the case where the chains in the crystal are free to rotate about their axes. In the calculation the fibers were assumed to have 65% crystallinity, in agreement with the manufacturer's data and also with a measured estimate obtained by the NMR method where, following the method of Wilson and Pake,[5] decomposition of the derivative curves led to 62±5% for the percentage of nuclei contributing to the broad component of the observed composite lines. The chains were also assumed perfectly aligned with the fiber axes in accordance with the x-ray data of Bunn. The agreement between theory and experiment is good and we are led, therefore, to the conclusion that the crystal-crystal transition at 285°K is one of dynamic rotational disorder. However, it is impossible to state whether the motion is one of free rotation or hindered rotation since both forms would account for the observed results. Energetically the latter type of motion is, perhaps, more probable and this interpretation would also agree with some recent x-ray work by Clark and Muus.[18]

It is significant that the observed NMR transition is sharp covering a small temperature range. This is in keeping with the character of the transition observed by the other techniques[13,14] and is similar to the rotational transition seen by Andrew[19] in dicetyl, a long chain hydrocarbon.

There is, perhaps, one more significant piece of information to be obtained from the linewidth data shown in Fig. 2. Between 180°K and 210°K there is a decrease in the linewidth of the broad component coinciding with the appearance of the narrow amorphous line. This effect was also apparent for a finely divided, i.e., polycrystalline, fiber sample. This might suggest that the glassy configuration of the Teflon chains gives rise to a wider line than a wholly crystalline packing implying some very close fluorine-fluorine distances in the glass. One explanation is afforded if we consider the possibility of a fraction of the chains in the glass not having the helical structure but assuming a planar zigzag similar to polyethylene. Obviously more work is required to substantiate this conclusion.

To summarize, the data presented here illustrate the advantages of using oriented fibers to investigate certain semicrystalline polymers by NMR. Although the conclusions arrived at are not new it is felt that the interpretation of changes in line shapes, linewidths, and second moments is greatly facilitated by this approach, and in the specific case of Teflon has helped to explain some of the discrepancies reported previously and to support the conclusions of x-ray work on a specific crystalline transition.

[16] E. R. Andrew and R. A. Newing, Proc. Phys. Soc. (London) **72**, 959 (1958).
[17] H. S. Gutowsky and G. E. Pake, J. Chem. Phys. **18**, 163 (1950).
[18] E. S. Clark and L. T. Muus (private communication).
[19] E. R. Andrew, J. Chem. Phys. **18**, 607 (1950).

JOURNAL OF APPLIED PHYSICS VOLUME 31, NUMBER 11 NOVEMBER, 1960

Kinetic Theory of Thermal Diffusion in Dilute Polymer Solutions*

JOE S. HAM
Department of Physics, A. & M. College of Texas, College Station, Texas

A simple Brownian motion model is used to discuss thermal diffusion in dilute polymer solutions. The thermal diffusion coefficient is found to be independent of polymer at sufficiently large molecular weights and to be given by $D_T = -(D_s E_s)/RT^2$ where D_s is the self-diffusion of the solvent and E_s is the activation energy for this diffusion. This suggests that the thermal diffusion ratio $\alpha = TD_T/D_0$ should show a marked temperature dependence, a molecular weight dependence proportional to $M^{\frac{1}{2}}$, and a concentration dependence governed for the most part by that of D_0. The results are shown to agree with published data in most respects and are contrasted to the results of other theoretical models. The results indicate that thermal diffusion is not a particularly promising method of fractionating various molecular weight molecules.

THE thermal diffusion of solutions, which is sometimes called the Soret Effect, has been known ever since the middle of the last century, yet it is still poorly understood. This is partly due to its being a second-order effect, the rate of entropy production depending upon both the gradient of the temperature and the gradient of concentration, and partly due to the unfavorable theoretical situation in regard to transport processes in liquids in general. Nevertheless, it will be shown in this paper that from a few reasonable assumptions a simple theory of thermal diffusion can be obtained that will be applicable to dilute polymer solutions.

After first touching upon some general statements relating to such a theory, a model will be developed. This will be compared to the existing experimental data where possible and to previous theories of thermal diffusion. Finally, the implications of this theory to the utilization of thermal diffusion to form a practical method of polymer fractionation or analysis will be discussed.

The best understood example of thermal diffusion is found in the kinetic theory of gases,[1,2] where the diffusive flow depends in a complicated manner upon the details of the intermolecular force laws. For example, molecules with a force law varying as the inverse fifth power of the intermolecular distance show no thermal diffusion effect. A kinetic theory for liquids, if modeled after that for gases, would have not only these complications of the details of the force law, but all the other complications inherent in the description of the liquid state. Therefore, there has existed great pessimism that a molecular theory could be developed for thermal diffusion in liquids which would be physically meaningful. Chapman[3] attacked several early theoretical attempts and showed that these models were incapable of giving the proper sign to the effect, let alone quantitative results. In this paper, a method of attack will be used which avoids the complications of a kinetic theory model, but at the expense of restricting the range of applicability.

The paucity of careful experimental studies of thermal diffusion in liquids has been both the result and the cause for the lack of a usable theory. Yet, the data that are available do indicate some of the complexities which must be considered. In solutions of small molecules, the direction of flow is so sensitive to the conditions that it may be altered by changes in the relative concentration in some cases. In polymer solutions, though, the direction of flow of the polymer seems always to be in the direction of heat flow.[4,5] This generalization suggests that there is an effect arising from the great disparity in size between the polymer and solvent molecules which produces thermal diffusion but that in solutions of small molecules, not only this effect but possibly others come into play, producing a complex relationship for small molecules. The present theory takes into account the effect which will be large in polymer solutions but, while present in solutions of small molecules, may not be the total picture in those cases.

Model

The model used in this treatment is the Brownian motion model described by Chandrasekhar[6] and extended by Yang[7] to include thermal diffusion. While Yang discusses thermal diffusion, his final result is left in a form which makes comparison to experiment difficult. The theory will derive an integral equation governing diffusion processes and then the differential equation for diffusion will be deduced from it.

The model breaks down the diffusive flow into three separate fluxes in a manner that is similar to the elementary treatments of diffusion in gases. First, there is a flow of polymer molecules into the solution; second,

* This work supported by a grant from Convair, a division of General Dynamics Corporation.

[1] S. Chapman and T. G. Cowling, *The Mathematical Theory of Nonuniform Gases* (Cambridge University Press, Cambridge, England, 1939).

[2] J. O. Hirschfelder, *Molecular Theory of Gases and Liquids* (John Wiley & Sons, Inc., New York, 1954).

[3] S. Chapman, Phil. Mag. **5**, 630 (1928).

[4] A. H. Emery and H. G. Drickamer, J. Chem. Phys. **23**, 2252 (1955).

[5] F. C. Whitmore, J. Appl. Phys. **31**, 1858 (1960).

[6] S. Chandrasekhar, Revs. Modern Phys. **15**, 1 (1943), which has been reprinted in *Selected Papers on Noise and Stochastic Processes*, edited by N. Wax (Dover Publications, New York, 1954).

[7] L. M. Yang, Proc. Roy. Soc. (London) **A198**, 94 (1949). See also H. S. Green, *The Molecular Theory of Fluids* (Interscience Publishers, Inc., New York, 1952).

there is a flow of solvent into the solution; and third, there is a mass motion superimposed so that no pressure gradient can develop. Although the superposition of fluxes has been used to discuss diffusion in liquids,[8,9] it seems to be the weakest point in the present theory so that some discussion will be in order.

In materials where a lattice model may be used, the meaning of this superposition is simple. The two molecular fluxes are relative to the lattice and if not equal, then the lattice will move to prevent pressure gradients. The Kirkendall effect in crystals illustrates that the motion of the lattice may be real and measurable. In the simple kinetic theory of gases a similar superposition of fluxes is used which predicts a marked dependence of diffusion constant upon concentration in gas mixtures. Neither experiment nor the more exact kinetic theory show such a large concentration dependence so that in gases, at least, the use of the superimposed fluxes is unrealistic.[10] This is supported by the use of two theoretical diffusion coefficients, whereas only one can be determined experimentally.

Thus, a justification of the superposition of fluxes in a liquid seems to hinge upon the question of whether the diffusion mechanism in a liquid is more like that in a solid, where the superposition is valid, or in a gas, where it is not. Since the other transport processes in a liquid are more solidlike than gaslike in their character, it seems likely that superposition will be valid. It would clearly be valid with a lattice model of a liquid. But lattice models have been criticized because, although correctly predicting some properties of liquids, they fail completely to predict some of the details.[11] Although the present theory does not involve a lattice model explicitly, some of its properties are implicit in the separation of the fluxes that is assumed. It remains an open question whether the present model would be free of the objections raised against the lattice model of liquids.

The breakdown of the problem into two diffusive flows superimposed upon a mass flow permits the description of one component diffusing at a time. First, consider the motion of the center of mass of a polymer molecule. It will undergo Brownian motion as the other molecules in the liquid collide with it. A time interval, Δt, is assumed to exist which is quite long compared to the time between collisions, but quite small compared to the intervals between measurements. The existence of such a time interval Δt makes it possible to treat the motion using only asymptotic solutions, so that a detailed picture of the collision processes is immaterial. This assumption should be quite realistic when dealing with liquids.

It is assumed that the motion of this molecule from a region near $\mathbf{x}$ by a distance $\Delta\mathbf{x}$ in the time Δt can be described by the transition probability $W(\mathbf{x},\Delta\mathbf{x},\Delta t)$. It is assumed that this transition probability depends only upon the original position of the molecule and not upon any prior history or internal configuration that it may have. The first part of this assumption is the usual one to obtain a Markov stochastic process and is realistic, but the assumption about independence of internal configuration is quite unrealistic and is made only to simplify the model. It is thought that the definition of a more detailed transition probability would only complicate the model without changing the final results. Thus, the probability of a particular molecule's being near a given position may be given in terms of all the positions possible for this particle at a prior time $t-\Delta t$ and the transition probability W. Rather than follow a single molecule, we can follow the concentration $n(\mathbf{x},t)$ so that the concentration at a point $\mathbf{x}$ is given in terms of the concentration distribution at a time Δt earlier by

$$n(\mathbf{x}, t+\Delta t)=\int n(\mathbf{x}',t)W(\mathbf{x}',\Delta x,\Delta t)d\mathbf{x}', \qquad (1)$$

where

$$\mathbf{x}'=\mathbf{x}-\Delta\mathbf{x}.$$

Since W is a transition probability there is a normalization condition,

$$\int W(\mathbf{x}',\Delta\mathbf{x},\Delta t)d\mathbf{x}'=1, \qquad (2)$$

stating that a molecule must go somewhere and so cannot be generated or disappear. In order to convert the integral equation for diffusion into the differential equation, the left hand side of Eq. (1) is expanded as a function of Δt and the integrand is expanded as a function of $\Delta\mathbf{x}$. The equation then becomes

$$n(\mathbf{x},t)+\frac{\partial n}{\partial t}\Delta t+0(\Delta t^2)$$

$$=n(\mathbf{x},t)\int W(\mathbf{x}-\Delta\mathbf{x},\Delta\mathbf{x},\Delta t)d(\Delta\mathbf{x})$$

$$-\frac{\partial}{\partial\mathbf{x}}\cdot\int n\Delta\mathbf{x}Wd(\Delta\mathbf{x})+\frac{1}{2}\frac{\partial^2}{\partial\mathbf{x}\partial\mathbf{x}}$$

$$\cdot\int n\Delta\mathbf{x}\Delta\mathbf{x}Wd(\Delta\mathbf{x})+0(\Delta\mathbf{x}^3). \qquad (3)$$

The first term on the right cancels the first term on the left because of Eq. (2). Although the mean square displacement is strictly a tensor quantity of second order, the part that is first order in Δt is proportional to the unit tensor. If higher order terms than those linear in

[8] S. Prager, J. Chem. Phys. **21**, 1344 (1953).
[9] L. S. Darken, Trans. AIME **175**, 184 (1948).
[10] E. H. Kennard, *Kinetic Theory of Gases* (McGraw-Hill Book Company, Inc., New York, 1938), p. 196.
[11] For example, see article by J. H. Hildebrand in *Growth and Perfection of Crystals* (John Wiley & Sons, Inc., New York, 1958).

Δt are neglected, then

$$\frac{\partial n}{\partial t}=\frac{\partial}{\partial \mathbf{x}}\cdot-\boldsymbol{\alpha} n+\frac{\partial \beta n}{\partial \mathbf{x}} \tag{4}$$

results where

$$\boldsymbol{\alpha}\Delta t=\int \Delta \mathbf{x} W d(\Delta \mathbf{x})$$
$$\boldsymbol{\beta}\mathbf{I}\Delta t=\int \Delta \mathbf{x}\Delta \mathbf{x} W d(\Delta \mathbf{x}). \tag{5}$$

Equation (4) has the form of a continuity equation if the current is defined by

$$\mathbf{J}=\boldsymbol{\alpha} n-\frac{\partial \beta n}{\partial \mathbf{x}}, \tag{6}$$

which consists of two parts. The first part, $\boldsymbol{\alpha} n$, is a steady drift produced in the asymmetry of the transition probability, and the second part, $(\partial/\partial \mathbf{x})\boldsymbol{\beta} n$, is produced by the diffusion resulting from the random walk nature of the motion of the center of mass of the molecule. With an identical argument, a similar equation can be found for the diffusion of solvent into the solution.

The mutual diffusion velocity becomes

$$\frac{\mathbf{J}_p}{n_p}-\frac{\mathbf{J}_s}{n_s}=(\boldsymbol{\alpha}_p-\boldsymbol{\alpha}_s)-\frac{\partial}{\partial \mathbf{x}}(\beta_p-\beta_s)-\frac{\beta_p}{n_p}\frac{\partial n_p}{\partial \mathbf{x}}+\frac{\beta_s}{n_s}\frac{\partial n_s}{\partial \mathbf{x}}, \tag{7}$$

where the first term on the right is the difference of the rates of drift of the two kinds of molecules due to asymmetry of the transition probability W, the second term is the gradient of the difference of the rates of dispersion, and the third term is the mutual velocity due to the concentration gradients.

The first term depends upon the asymmetry of the transition probability function W, and so depends upon a nonequilibrium distribution function. Since it has been found satisfactory in theories of transport processes in many cases to use the equilibrium distribution functions in evaluating transport processes, this term will be neglected. Whether, in fact, it is negligible can only be determined when a better understanding of the liquid state is achieved. The third term is the term that gives rise to normal diffusion, and the β's have the role of diffusion constants. The second term vanishes if the β's do not depend upon position or variables which depend upon position. The temperature dependence of the β's will cause this term to contribute to the mutual diffusion velocity when a thermal gradient is present. This contribution is taken to be the source of thermal diffusion flux in polymer solutions.

When the mass flow is superimposed upon the two separate molecular flows, so that there are no resulting pressure gradients, the net flux in volume fraction of polymer component is given as

$$\boldsymbol{\Gamma}_p=\frac{\mathbf{J}_p}{n_p}\phi_p-\left(\frac{\mathbf{J}_p}{n_p}\phi_p+\frac{\mathbf{J}_s}{n_s}\phi_s\right)\phi_p=\phi_p\phi_s\left(\frac{\mathbf{J}_p}{n_p}-\frac{\mathbf{J}_s}{n_s}\right)$$
$$=\phi_p\phi_s\left(\frac{\partial}{\partial \mathbf{x}}(\beta_p-\beta_s)+\frac{\beta_p}{n_p}\frac{\partial n_p}{\partial \mathbf{x}}-\frac{\beta_s}{n_s}\frac{\partial n_s}{\partial \mathbf{x}}\right),$$

in terms of the hypothetical fluxes and the volume fractions

$$\phi_p=\frac{n_pV_p}{n_sV_s+n_pV_p};\quad \phi_s=\frac{n_sV_s}{n_sV_s+n_pV_p}.$$

This equation is derived under the assumptions that the volumes are additive and there are no compressions.

It is seen from the usual definitions of the normal diffusion coefficient, D_0, the thermal diffusion coefficient, D_T, and the thermal diffusion ratio α that

$$\boldsymbol{\Gamma}_p=-D_0\frac{\partial \phi_p}{\partial \mathbf{x}}+D_T\phi_p\phi_s\frac{\partial T}{\partial \mathbf{x}},\quad \alpha=T\frac{D_T}{D_0} \tag{8}$$

when combined with Eq. (7),

$$D_0=\frac{\dfrac{\beta_p}{n_p}\dfrac{\partial n_p}{\partial \mathbf{x}}-\dfrac{\beta_s}{n_s}\dfrac{\partial n_s}{\partial \mathbf{x}}}{\dfrac{1}{n_p}\dfrac{\partial n_p}{\partial \mathbf{x}}-\dfrac{1}{n_s}\dfrac{\partial n_s}{\partial \mathbf{x}}}+\frac{\dfrac{\partial(\beta_p-\beta_s)}{\partial n_p}\dfrac{\partial n_p}{\partial \mathbf{x}}+\dfrac{\partial(\beta_p-\beta_s)}{\partial n_s}\dfrac{\partial n_s}{\partial \mathbf{x}}}{\dfrac{1}{n_p}\dfrac{\partial n_p}{\partial \mathbf{x}}-\dfrac{1}{n_s}\dfrac{\partial n_s}{\partial \mathbf{x}}} \tag{9a}$$

and

$$D_T=\frac{\partial(\beta_p-\beta_s)}{\partial T}. \tag{9b}$$

For dilute polymer solutions, $1/n_p\ \partial n_p/\partial \mathbf{x}$ will be larger than $1/n_s\ \partial n_s/\partial \mathbf{x}$. If the β's are assumed to have an exponential dependence upon $1/T$ with an activation energy defined in the usual manner, then Eq. (9) becomes

$$D_0=\beta_p+n_p\frac{\partial(\beta_p-\beta_s)}{\partial n_p}$$
$$D_T=\frac{E_p\beta_p-E_s\beta_s}{RT^2}. \tag{10}$$

It is seen that D_0, the normal diffusion coefficient, is closely connected to β_p so that if the concentration dependence of $\beta_p-\beta_s$ is neglected they are identical. The thermal diffusion coefficient becomes a difference between two terms, each of which involve an activation energy times the corresponding β. If the β_s is associated with the diffusion of solvent within itself and therefore to the self-diffusion coefficient of the solvent, then it can be seen that β_s will be several orders of magnitude larger than β_p for a fairly large molecular weight polymer. The activation energies E_p and E_s will be comparable since diffusion of a polymer takes place by a segmental

motion. The result of this is

$$D_T=\frac{E_sD_s}{RT^2};\quad \alpha=\frac{E_sD_s}{RTD_p}, \tag{11}$$

which contains the rather surprising result that for sufficiently high molecular weights, the thermal diffusion coefficient depends only upon the properties of the pure solvent and, in particular, is independent of the molecular weight of the polymer. Equation (11) predicts that thermal diffusion of polymer will always take place toward the cold wall.

DISCUSSION OF RESULTS

The factors of most concern in the results of the theory are the molecular weight, concentration, temperature and solvent dependence of D_T and α. From Eq. (11) it can be seen that D_T depends only upon the properties of the solvent and not upon any properties of the polymer once a sufficiently high molecular weight has been attained.

The molecular weight dependence of D_0 has been studied extensively and it is found to vary approximately as the inverse one-half power of the molecular weight. In most solvents, due to excluded volume effects, the dependency varies a little bit faster. Therefore, according to the present theory, α should vary directly as the one-half power of the molecular weight with possible small deviations from this law in various solvents. Experimentally, the data are not consistent. A direct measurement of D_T by Hoffman and Zimm[12] using a moving boundary technique showed that polystyrene in toluene of molecular weights 60 000 and 1 100 000 had D_T that differed by less than 20%. Similar results were found using butyl acetate as a solvent. The extrapolated values of α measured by Emery and Drickamer[4] varied approximately as $M^{\frac{1}{2}}$ with the exception of one low molecular weight sample. On the other hand, Whitmore[5] has not been able to verify the concentration dependence found by Emery and Drickamer and so, also, does not confirm their extrapolated values. In addition, studies with a Clusius-Dickel column seem to disagree with the present theory.[13] According to the theory of the operation of the column, the separation should be made by D_T rather than α, and yet considerable molecular weight dependence is found experimentally. The resolution of these discordant results may lie in the theory of the column operation, since this is generally treated as if D_0 and D_T were independent of concentration. These assumptions are far from valid in the ranges used in a typical column experiment so that more complicated interactions may affect the results.

[12] J. D. Hoffman and B. H. Zimm, J. Polymer Sci. **15**, 405 (1955).

[13] G. Langhammer, H. Pfenning, and K. Quitzsh, Z. Electrochem. **62**, 458 (1958) and G. Langhammer and H. Forster, Z. physik. Chem. (Frankfurt) **15**, 212 (1958).

It is a rather delicate matter to discuss the concentration dependence of D_T, as the association of the β's with experimental quantities applies only in the limit of high dilutions. Nevertheless, if one proceeds optimistically, and makes the association even at finite concentration, then the concentration dependence is found in D_0 and not in D_T. It can enter in two ways. From thermodynamic considerations, the driving force is more properly measured in terms of the gradient of chemical potential rather than the gradient of concentration. These can be different even at rather low concentrations of polymer and so a concentration dependence of D_0 can result. In addition to this purely thermodynamic term, there is probably an interference term resulting from the motion of a polymer molecule being impeded by other polymer molecules. It is quite possible that this second effect will give rise to some concentration dependence of D_T as well as D_0.

Experimentally, the situation is not clear. Zimm and Hoffman[12] found no concentration dependence for D_T for polystyrene in butyl acetate, a poor solvent, but a rather marked dependence for polystyrene in toluene, a good solvent. Emery and Drickamer[4] used the thermodynamic dependence of D_0 upon concentration to fit their curves of α. The concentration dependence seems to be given within the limits of their experimental error by the thermodynamic terms. But Whitmore[5] at somewhat higher temperatures was not able to fit his data of α vs concentration to the curve containing only the thermodynamic term. This may be the result of operating at different temperature ranges since, as discussed below, temperature is expected to have a marked effect on D_T and α. Nevertheless, using the experimental concentration dependence of D_0, most of the concentration dependence of α was taken care of so that in his data D_T is largely, although not completely, concentration independent. Thus, the data tend to support the present theory of a concentration independent D_T in many cases but not in all.

The temperature dependence of D_T is given by the temperature dependence of self-diffusion of the solvent. The ratio α will tend to decrease with increasing temperature since activation energies for the polymer diffusion will be higher, in general, than that for solvent self-diffusion. This last conclusion has been confirmed by Whitmore, who found an apparent activation energy for α of -8000 to $-22\,000$ cal/mole for polystyrene in toluene for various molecular weights and $-35\,000$ cal/mole for polystyrene in cyclohexane. The much larger termperature dependence in cyclohexane solvent is thought to be the result of being very close to the critical temperature so that many of the solution properties are changing very rapidly. The temperature extrapolation was carried out over only a very short temperature range in cyclohexane due to this fact.

The solvent dependence of D_T will be quite large since the self-diffusion in liquids can be changed radically with different substances. On the other hand, α

may not be altered so radically because any structural changes in the solvent which decrease self-diffusion will probably also decrease the normal diffusion of polymer in much the same way.

In summary, the theoretical results agree with the experimental data as to right order of magnitude and direction and molecular weight dependence. The concentration dependence seems either more complex than given by the theory or else some experimental data is misleading. It is hoped that the present theory will be sufficiently concrete in its results so that it will stimulate more experimental work on thermal diffusion. Since the present theory neglects any excluded volume effects, only qualitative results can be expected at best.

Comparison with Previous Theories

There exist in the literature a number of molecular theories for thermal diffusion, all of which have many points in common. The present theory is quite similar to many of these in predicting the thermal diffusion ratio to depend upon the difference of two activation energies. The results differ primarily in the manner of taking into account the discrepancy in size between the solvent and polymer molecules which results in the activation energies for diffusion being weighted in the present theory by the diffusion constants. Various other activation energies have been used and various weighting forces have been suggested or derived.

Debye and Bueche[14] described thermal diffusion in terms of a Brownian motion model but they considered only the polymer molecules undergoing motion. They showed that the temperature coefficient of diffusion is only large enough to account for about 10% of the observed thermal diffusion effect and so that the asymmetry in the velocity distribution function must be considered if only polymer motion is considered. The present treatment includes the motion of the solvent, in which case the temperature coefficient of the mean square displacements become large enough to explain the thermal diffusion effect. Therefore, the asymmetry need not be involved in the proposed model.

In 1946, Wirtz and Hiby[15] developed a theory of thermal diffusion in liquids and crystals based upon a lattice model where the thermal gradient biases the transitions between neighboring sites so that there is a net motion of one component relative to the other. This theory predicts a thermal diffusion ratio which depends upon the difference of two activation energies which are defined in terms of the lattice model. There seems to be no method that can measure these two activation energies separately, or estimate them with enough confidence to predict the sign of the effect unambiguously. The lattice model has fallen into disfavor as a model for liquids partly because of such problems.

Prager and Eyring[16] have used a much more detailed lattice model and get results quite similar to those obtained in the present paper. They point out the simplifications possible when one component diffuses much slower than the other, as is the case for dilute polymer solutions, which enables an unambiguous prediction for the sign of the effect. Their results are equivalent to ours.

The general theory of irreversible thermodynamics[17] predicts the form of the thermal diffusion ratio as being proportional to the difference between two energies of transport but is unable to define these in a manner that they are separately measurable. In an attempt to remedy this situation, Emery and Drickamer[4] have interpreted these energy terms as activation energies for diffusion and later as activation energies for viscous flow. They were able to fit their experimental data on this basis and to predict the correct sign and order of magnitude in many cases, even for molecules of comparable size. But the differences between these two terms are so small that the experimental errors in the measured energies of activation are comparable with the differences. For polymer solutions, they used the experimental data on thermal diffusion to compute the activation energy for the polymer. While their results are reasonable, the method of calculation is insensitive to any defects in their theory. From their theory, there is no apparent reason why the direction of the effect should be in the same direction for all polymer solutions.

Bearman, Kirkwood, and Fixman[18] have extended the fundamental theory of liquids to include thermal diffusion by some rather drastic approximations. Their result contains a number of terms but if these are estimated as to relative size, which should be possible for a solvent-polymer system, and the term which involves a nonequilibrium radial distribution function is neglected, the result predicts the wrong direction for the thermal diffusive flux. This is somewhat surprising, as the relative sizes of the terms from the solvent and polymer should be as estimated and one does not expect the effect to be so sensitive upon the nonequilibrium part of the radial distribution function. It may be that the approximations which were made in the development of this theory, which was directed toward its use with small simple molecules, are just not valid for a polymer solvent system.

Fractionation

A number of elution and precipitation methods have been described to fractionate dilute solutions of polymer molecules according to their molecular weights. Caplon[19] has described a method using precipitation chromatog-

[14] P. Debye and A. M. Bueche in *High Polymer Physics* (Remsen Press, Brooklyn, New York, 1948).

[15] K. Wirtz and J. W. Hiby, Physik. Z. **44**, 369 (1943).

[16] S. Prager and H. Eyring, J. Chem. Phys. **21**, 1347 (1953).

[17] I. Prigogine, *Introduction to Thermodynamics of Irreversible Processes* (Charles C. Thomas, Springfield, Illinois, 1955).

[18] R. J. Bearman, J. G. Kirkwood, and M. Fixman, Advances in Chem. Phys. **1**, 1 (1958).

[19] S. R. Caplon, J. Polymer Sci. **35**, 409 (1959).

raphy which is particularly promising. Nevertheless, a method which does not involve a precipitation might have an advantage with some polymeric materials. The original studies on thermal diffusion of polymer solutions[12] showed the potentiality of fractionating high molecular weight materials. The present theory indicates that the method will not be too practical because D_T, which governs the flux produced by the thermal gradient, becomes independent of molecular weight for moderately high molecular weights. To be sure, α depends upon molecular weight and so if a steady state is attained, a molecular weight separation can be achieved but since the separation comes primarily from D_0 governing the back diffusion, then any other method of producing a concentration gradient would be as effective in fractionating polymer molecular weights.

Nevertheless, it should be mentioned that several experimenters with Clusius-Dickel columns are optimistic about the practicability of their use in fractionating molecular weights.[13,39] According to theory, the columns should operate using D_T and so should show a very slight molecular weight dependence. This is contradicted by the data, which may be a result of a failure of the simple column theory rather than an indication of a marked molecular weight dependence of D_T.

[39] I. Kossler and J. Krejsa, J. Polymer Sci. 35, 308 (1959).

JOURNAL OF APPLIED PHYSICS VOLUME 31, NUMBER 11 NOVEMBER, 1960

Experimental Study of Thermal Diffusion in Dilute Solutions of High Polymers*

FRANK C. WHITMORE†
Department of Physics, A. & M. College of Texas, College Station, Texas

Ham [J. Appl. Phys. 31, 1853 (1960) (preceding paper)] has derived a simplified theory for thermal diffusion in dilute solutions of high polymers. It is of interest to apply this theory to two different types of polymer solutions: (a) dilute solutions in a good solvent, and (b) dilute solutions in a poor solvent. By studies of the concentration, temperature, and molecular weight dependence of the thermal diffusion ratio in these two different types of polymer solutions, it has been possible to obtain a detailed test of the theory.

I. EXPERIMENTAL METHOD

THE defining equation for thermal diffusion is taken to be

$$J_1 = -D\rho\{\text{grad}c_1 - \alpha c_1(1-c_1)\ \text{grad}\ \ln T\}, \qquad (1)$$

where J_1 is the material flux of the polymer, D is the normal diffusion coefficient of the polymer, c_1 is the concentration of the polymer, α is the thermal diffusion ratio for the polymer-solvent system, and ρ is the density of the solution. At the steady state, the material flux vanishes and we find

$$\alpha = \text{grad}\ \ln(c_1)/\text{grad}\ \ln(T), \qquad (2)$$

where we have assumed small concentrations; i.e., we have taken $(1-c_1)\sim 1$. Equation (2) has been used as the defining equation for the thermal diffusion ratio for this work.

In the actual experiments, a homogeneous sample of the polymer solution was introduced into a cylindrical sample cell. The ends of the sample cell were cemented into an upper and a lower aluminum plate. The lower aluminum end plate was maintained at a constant temperature T, while the upper end plate was maintained at a constant temperature of $T+\Delta T$, where $\Delta T/L$ was the thermal gradient applied across the cell. The temperature at each end of the cell was monitored continuously by thermocouples embedded into the ends of the sample cell. After the sample was introduced into the cell, the cell was sealed with a brass screw fitted with a Teflon washer. Since the time required to establish the steady state was quite long, many experiments were run at the same time—using 20 identical cells cemented between the same pair of end plates.

When the run was complete, several samples were removed from the thermal gradient in order to establish the steady-state concentration gradient. In the interest of greater reliability, some eight to 12 samples were withdrawn from carefully determined positions within the thermal gradient. The samples were taken with a Hamilton 100-lambda microsyringe. The position from which the sample was taken was determined with a micrometer that screwed into the cell top and which was carefully machined to hold the barrel of the Hamilton syringe in a very rigid grip. The accuracy of position measurements was about 1%, whereas the accuracy of the volume measurements was about 0.5%.

After the sample had been withdrawn from the thermal gradient, it was transferred to a previously tared aluminum balance pan, allowed to dry, and again weighed with a Microchemical Specialties quartz microbalance. The over-all accuracy (reproducibility) of the concentration measurements was found to be about 3%.

* This work was supported by a grant from Convair, a division of General Dynamics Corporation.

† This paper is based, in part, on a dissertation submitted in partial fulfillment of the requirements for the Ph.D. degree, A. & M. College of Texas.

If the concentration gradient that is measured is known to be the steady-state concentration gradient, we may then use Eq. (2) to find the thermal diffusion ratio. At this point we also note that Eq. (2) yields the result that $\ln c$ depends linearly upon the position x within the cell at equilibrium. We may use this fact to obtain a good value of the concentration gradient by plotting $\ln c$ vs x to obtain a straight line. A typical example of such a plot is shown in Fig. 1. All the data have been plotted in this manner in order to find a smoothed concentration gradient.

To establish the time required for the system to come to the steady state, we find a solution to the diffusion equation in terms of a series of relaxation processes, each characterized by a characteristic time τ_n. The time

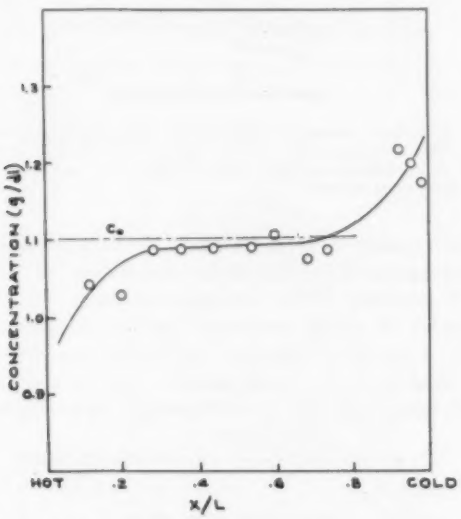

FIG. 1. A plot of the steady-state concentration versus position in a typical thermal diffusion cell.

that is required to reach equilibrium is then controlled by the longest of these relaxation times,

$$\tau_n = D^{-1}\{(\beta/2)^2 + (n\pi/L)^2\}^{-1}, \quad (n = 1, 2, \cdots), \quad (3)$$

where $\beta = -\alpha \text{ grad } \ln T$, and D is the normal diffusion coefficient for the polymer (assumed to be concentration-independent). For the experiments described in this work, the longest characteristic time became $\tau_1 \sim 10^6 L^2$ sec, where L is in centimeters. In the cells for which L was 0.75 cm, the time required to establish the steady state should have been about 160 hr, whereas for those cells with $L = 1.6$ cm, the time required should have been about 720 hr. The experimental data that are presented here represent running times that are approximately twice that required for establishing the steady state, and thus Eq. (2) should be valid.

The data have been obtained on a series of fractions of polystyrene ranging in molecular weight from 60 000 to 600 000. The samples were fractionated from a sample of Dow Styron 666 supplied by the Dow Chemical Company.

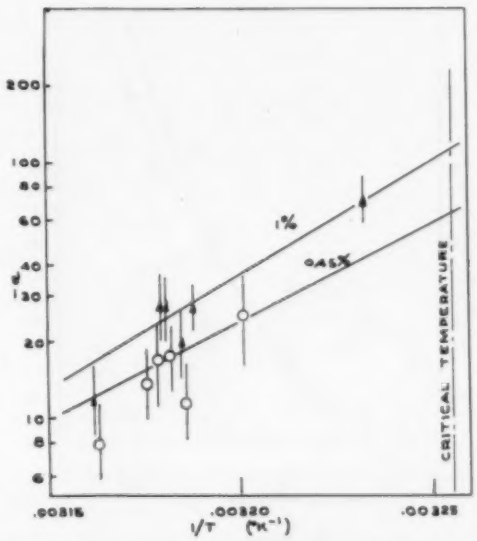

FIG. 2. Temperature extrapolation, thermal diffusion ratio. Polystyrene (MW 374 000) in cyclohexane. Each point represents the average of from five to eight experiments. Note the different slope for the different concentrations.

II. EXPERIMENTAL RESULTS

In the interest of simplicity, it appears best to divide the discussion of the experimental results into two

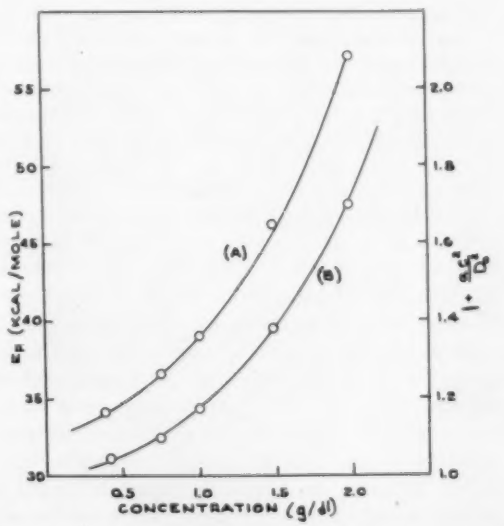

FIG. 3. Curve A—the measured activation energy for thermal diffusion of polystyrene (MW 374 000) in cyclohexane showing concentration dependence. Curve B—the concentration dependence of the factor $(1+ac^2/D_0^2)$ from Eq. (9).

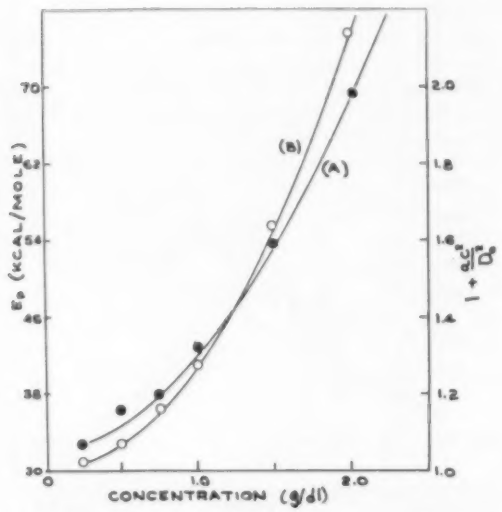

FIG. 4. Curve A—the measured activation energy for thermal diffusion of polystyrene (MW 603 000) in cyclohexane showing concentration dependence. Curve B—the concentration dependence of the factor $(1+ac^2/D_0^2)$ from Eq. (9).

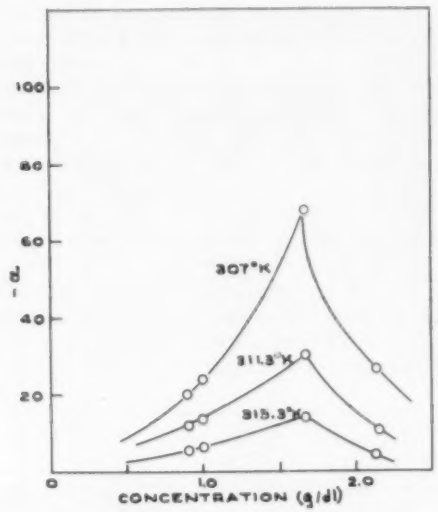

FIG. 5. Experimental thermal diffusion ratio, polystyrene (MW 248 000) in cyclohexane at 315.3° and at 311.3°K showing concentration dependence. The curve at 307°K was found by temperature extrapolation.

sections: (a) Sec. A will deal with the experimental results obtained with polystyrene in cyclohexane near the critical solution temperature, and (b) Sec. B will deal with the experimental results in solutions of polystyrene in toluene taken at temperature far above the critical solution temperature.

Section A

A large number of experiments were run with this system; in every case, the polymer concentration was found to increase at the cold wall in agreement with the general prediction of the theory. In all these experiments the base (lowest) temperature was within a degree of the critical solution temperature, 307°K. In order to determine the temperature effect on the thermal diffusion ratio, the thermal gradient ranged from 1 to about 25 deg/cm. In Fig. 2 we have plotted the measured thermal diffusion ratio, at a variety of measured temperatures, vs $(1/\bar{T})$, where $\bar{T}$ is the mean temperature, for the MW 374 000 polystyrene sample in cyclohexane. The form of the temperature dependence appears to be of the usual activation energy form with an activation energy that is a function of the concentration of the polymer. When such plots were prepared for a variety of concentrations and molecular weights, the observed activation energies take the form as indicated in Figs. 3 and 4. Although an activation energy of 30 000 to 60 000 cal/mole seems very large, this is not too surprising, since the apparent activation energy is often large when measurements are made near a critical temperature. In view of this large temperature effect, it is necessary to correct all data to the same average temperature for the data to be comparable.

A summary of the experimental data, taken on samples of several molecular weights, is shown in Figs. 5 through 7. The curves at 307°K were obtained by temperature extrapolation. The other two curves in each figure represent the averaged data from a number

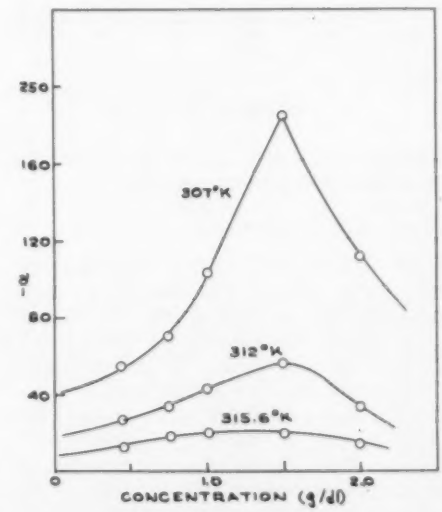

FIG. 6. Experimental thermal diffusion ratio, polystyrene (MW 374 000) in cyclohexane at 312° and 315.6°K showing concentration dependence. The curve at 307°K was found by temperature extrapolation.

of experimental runs. Each point represents the average of from five to eight experiments.

If we now use the normal diffusion data from Cantow[1] for the polystyrene-cyclohexane system, we may compute the thermal diffusion coefficient D_T at the critical solution temperature for this system. The results of these calculations are shown in Fig. 8. It is seen from Fig. 8 that there is no systematic variation of D_T with either molecular weight or polymer concentration. The slight concentration dependence is probably not real since the data have been carried through several extrapolations and are thus subject to rather large uncertainties. For comparison, D_T for the polystyrene-cyclohexane system should be approximately 10^{-7} cm²/sec°K if Ham's[2] Eq. (11) were correct; the approximate values of 10^{-5} cm²/sec and 1800 cal/mole have been used for

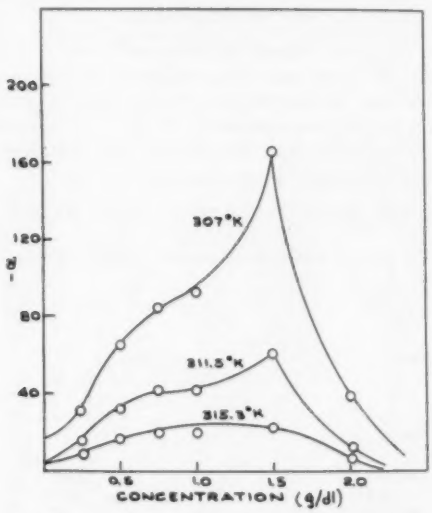

FIG. 7. Experimental thermal diffusion ratio, polystyrene (MW 603 000) in cyclohexane at 311.5° and at 315.3°K showing concentration dependence. The curve at 307°K was found by temperature extrapolation.

the normal diffusion coefficient and the activation energy for normal diffusion of cyclohexane, respectively.[3]

Section B

A large number of experiments were run with the polystyrene-toluene system; in every case the polymer concentration was found to increase at the cold end of the diffusion cell in agreement with the general prediction of the theory. A summary of some of the data taken is presented in Figs. 9 and 10. Figure 9 represents, in curve B, the composite data from some 30 experiments on samples with molecular weight varying from 64 000

[1] H. J. Cantow, Makromol. Chem. **30**, 169 (1959).
[2] J. S. Ham, preceding paper.
[3] *American Institute of Physics Handbook* (McGraw-Hill Book Company, Inc., New York, 1959).

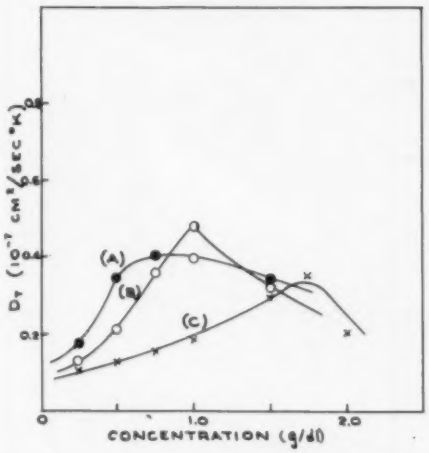

FIG. 8. Concentration dependence of D_T for polystyrene in cyclohexane. Curve A—MW 603 000; curve B—MW 374 000; curve C—MW 248 000.

to 78 000. For the sake of comparison with other published data on this system, we have also reproduced in Fig. 9 the curve that Emery and Drickamer[4] fitted to their data on a sample of MW 50 000. It is perfectly clear that the agreement between these two sets of data is very poor. The data represented by curve B were taken at an average temperature of 314°K, whereas those which lead to curve A were taken at an average temperature of 298°K. This disagreement indicates that here

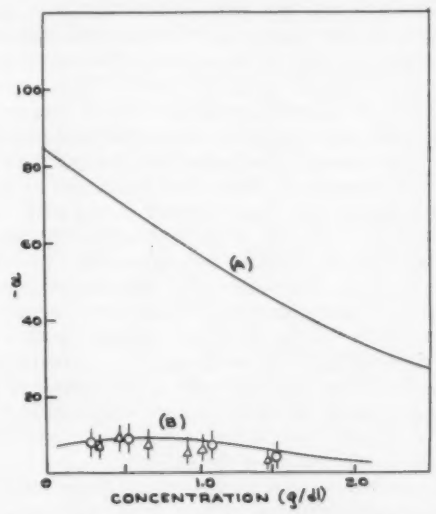

FIG. 9. Curve A—Thermal diffusion ratio, polystyrene (MW 50 000) in toluene at 298°K taken from Emery and Drickamer[4] showing concentration dependence. Curve B—Thermal diffusion ratio polystyrene (MW 64 500 to 79 000) in toluene at 314°K, from this work, showing concentration dependence.

[4] A. H. Emery and H. G. Drickamer, J. Chem. Phys. **23**, 2252 (1955).

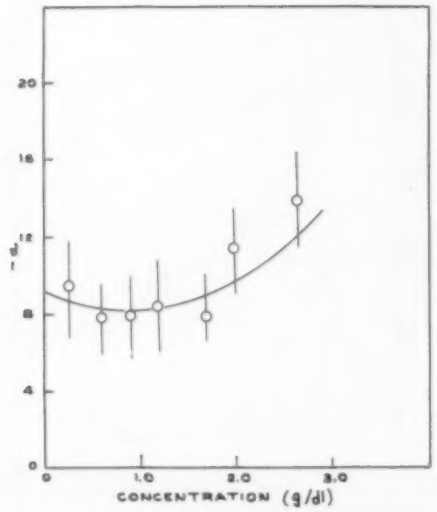

FIG. 10. Thermal diffusion ratio, polystyrene (MW 374 000) in toluene at 313.5°K showing concentration dependence.

again there is a strong temperature dependence to be found in the thermal diffusion ratio. To examine this point we refer to Fig. 11, where the observed thermal diffusion ratio is plotted against $(1/\bar{T})$, where $\bar{T}$ is the mean temperature, on a semilog plot. It is quite clear that these data are in excellent agreement with the assumption that there is an exponential temperature dependence to be found in the thermal diffusion ratio. It is also interesting to note that the two filled points in Fig. 11 are taken from the work of Emery and Drickamer[4] and are seen to fit quite well with the extrapolated thermal diffusion ratio measurements from this work. The excellent agreement between this work and that of Emery and Drickamer is not obtained at concentrations below 1%. In the low concentration region the thermal diffusion ratio measurements of Emery and Drickamer are consistently higher than those reported in this work. This difference is a reflection of the significant difference in the observed concentration dependence that is clearly shown in Fig. 9. Returning to the temperature dependence of α, we have summarized the observed activation energy, which for the polystyrene-toluene system appears to be independent of the polymer concentration, in Fig. 12. There appears to be a dependence of the activation energy on the molecular weight, indicating that the segmental length does increase with an increase in the molecular weight of the polymer.

We now use the normal diffusion coefficient data on the polystyrene-toluene system from the work of Tsvetkov[5] and compute the thermal diffusion coefficient D_T at 298°K (we have first reduced α to 298°K by temperature extrapolation in the manner indicated in Fig. 11). The results of these calculations are shown in Figs. 13 and 14. In Fig. 14 we have also included a summary of the thermal diffusion coefficient data found by Hoffman and Zimm,[6] obtained by studies of the motion of a boundary layer between two regions of different concentration when the system is placed in a thermal gradient, and the data of Debye and Bueche,[7] taken from a thermal diffusion column. It is clear that the general agreement is quite good, and it is particularly interesting to note that the concentration dependence of D_T found in this work is remarkably similar to that observed by Debye and Bueche.

[5] V. N. Tsvetkov, *Simposio Internazionale di Chimica Macromolecolare*, Milano-Torino, 1954 (Spa Arti Grafiche Panetto and Petrelli, Spoleto-Roma, Italy), pp. 413 ff.

III. DISCUSSION OF THE EXPERIMENTAL RESULTS

In general, the normal diffusion coefficient for a dilute polymer solution may be written in the form

$$D_p = D_0(1+2A_2Mc), \tag{4}$$

where D_0 is the normal diffusion coefficient at infinite dilution, M is the molecular weight of the polymer, A_2 is the second virial coefficient for the osmotic pressure, and c is the polymer concentration. If Eq. (4) is substituted into Ham's[2] Eq. (11) and the result simplified, we find, for sufficiently dilute solutions,

$$\alpha = -(E_z D_z/D_0RT)(1-2A_2Mc) = -\alpha_0(1-2A_2Mc). \tag{5}$$

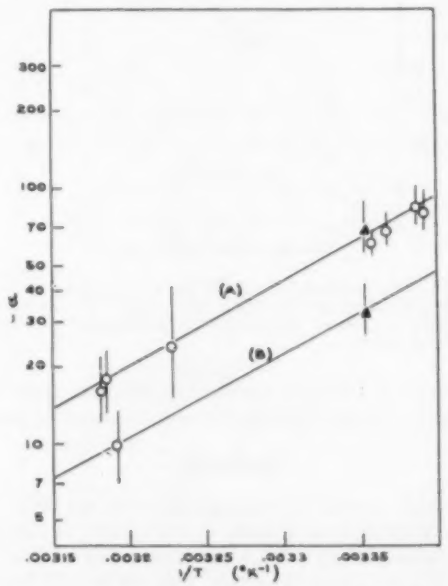

FIG. 11. Temperature dependence of thermal diffusion ratio for polystyrene (MW 311 000) in toluene. The filled points are taken from Emery and Drickamer.[4] Curve A—solution with initial concentration of 1 g/dl; curve B—solution with initial concentration of 2.25 g/dl.

[6] J. D. Hoffman and B. H. Zimm, J. Polymer Sci. **15**, 405 (1955).

[7] P. Debye and A. M. Bueche, *High Polymer Physics*, edited by H. A. Robinson (Chemical Publishing Company, Brooklyn, New York, 1948), pp. 497 ff.

From Eq. (5), one would expect to find the concentration dependence of α to be included in the term that involves the second virial coefficient A_2. Further, it appears that $-\alpha$ should be a linear function of the concentration with a slope that is equal to $-2M\alpha_0 A_2$. Then, in a poor solvent, at the critical solution temperature where the second virial coefficient vanishes, the thermal diffusion α should be independent of the concentration of the polymer. On the other hand, in a good solvent the thermal diffusion ratio should increase linearly with the concentration of the polymer.

In a poor solvent, at the critical solution temperature, one would expect to find the molecular weight dependence of α to be determined by the molecular weight dependence of the normal diffusion coefficient at infinite dilution. On the other hand, there will be two contributions to the molecular weight dependence of α in a good

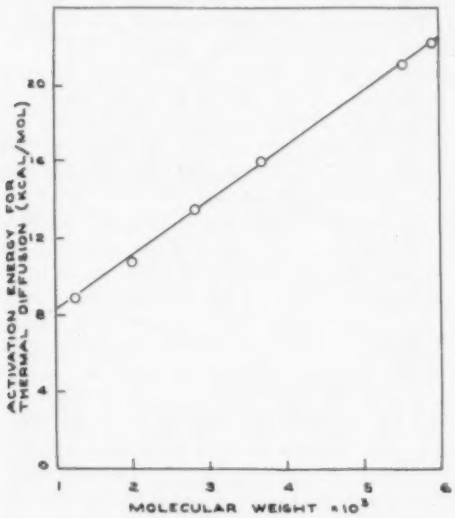

FIG. 12. Observed activation energy for thermal diffusion of polystyrene in toluene as a function of the molecular weight of the polymer.

solvent—that contained in the normal diffusion coefficient at infinite dilution and that derived from the factor that involves the second virial coefficient,

$$\frac{\partial(-\alpha/\alpha_0)}{\partial M} = -2A_2c, \qquad (6)$$

where we have used Eq. (5) and neglected the molecular weight dependence of A_2.[8] It would appear that it should be possible to determine the second virial

[8] In a poor solvent, near the critical solution temperature, A_2 is accurately independent of the molecular weight of the polymer. In a good solvent, if the molecular weight range is not too great, the approximation used in Eq. (6) should still be moderately good. See P. J. Flory, *Principles of Polymer Chemistry* (Cornell University Press, Ithaca, New York, 1953), pp. 537 ff.

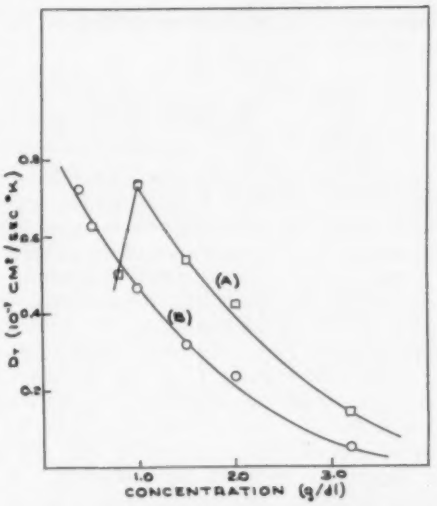

FIG. 13. Curve A—D_T for polystyrene (MW 126 000) in toluene at 298°K showing concentration dependence; curve B—D_T for polystyrene (MW 64 000) in toluene at 298°K showing concentration dependence.

coefficient in a good solvent from the thermal diffusion data using Eq. (6).

The temperature dependence of α may also be approximated from Eq. (5) [or from Ham's[2] Eq. (11)]. In a good solvent, far from the critical solution temperature, the second virial coefficient is essentially independent of the temperature so that the temperature dependence of α should be that of D_0. If we take the tempera-

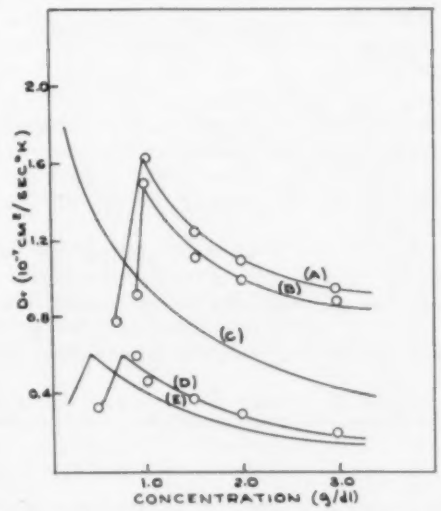

FIG. 14. D_T for polystyrene in toluene at 298°K. Curve A—MW 634 000; curve B—MW 552 000; curve C—taken from Hoffman and Zimm,[5] MW 1 100 000; curve D—MW 371 000; curve E—taken from Debye and Bueche[6] for MW 509 000.

ture dependence of D_0 to be given by the usual Eyring[9] model, we find

$$\frac{\partial \ln(-\alpha)}{\partial(1/T)} = T - E_a/R + E_p/R, \tag{7}$$

where E_p is the activation energy for normal diffusion of the polymer. So we expect to find that the apparent activation energy for thermal diffusion in a good solvent is independent of the concentration of the polymer.

In a poor solvent, the temperature dependence of α is essentially different from the temperature dependence in a good solvent. In a solution near the critical temperature the second virial coefficient is rapidly changing as the temperature changes. If we take this effect into account, we find that the activation energy for thermal diffusion is strongly concentration dependent. In the absence of experimental data dealing with this particular dependence of A_2 on the temperature in the vicinity of the critical solution temperature, we use the empirical formula of Cantow[1] for the normal diffusion coefficient of the polystyrene-cyclohexane system near the critical temperature. His results may be put in the form

$$D_p = D_0 - ac^2/D_0, \tag{8}$$

where c is the polymer concentration in g/cc and D_0 is the normal diffusion coefficient at infinite dilution in cm^2/sec and $D_0 = 1.21\times10^{-4}(\bar{M})^{-0.49}$. The constant a in Eq. (8) is given by $a = 9\times10^{-11}$. If we now consider Eq. (8) into Ham's[2] Eq. (11) and take the derivative of $\ln(-\alpha)$ with respect to $(1/T)$, assuming that a is a constant, we find

$$\frac{\partial \ln(-\alpha)}{\partial(1/T)} = T - E_a/R - (E_p/R)(1+ac^2/D_0^2), \tag{9}$$

where we have used the fact that $D_0^{-2} \gg D_0^{-1}$. From Eq. (9) we see that the apparent activation energy for thermal diffusion of polystyrene in cyclohexane near the critical solution temperature should depend on the concentration of the polymer through the factor $(1+ac^2/D_0^2)$.

In Figs. 3 and 4 we have plotted the factor $(1+ac^2/D_0^2)$ as a function of the concentration of the polymer. The agreement with the experimental curve is very gratifying. It is also seen that the factor E_p/R is about 17 500 for both molecular weights. The experimental evidence would then indicate that the activation energy, at infinite dilution, for normal diffusion of polystyrene in cyclohexane is about 35 000 cal/mole and is independent of the molecular weight of the polymer.

[9] S. Glasstone, K. J. Laidler and H. Eyring, *Theory of Rate Processes* (McGraw-Hill Book Company, Inc., New York, 1941).

IV. DISCUSSION

In the poor solvent, cyclohexane, the experimental results are in excellent agreement with the theory. The concentration dependence as well as the temperature dependence of the thermal diffusion ratio appear to be in almost exact agreement with the theoretical predictions. The thermal diffusion ratio increases with increasing concentrations up to a concentration of about 1.5%. The abrupt decrease in the thermal diffusion ratio at concentration above 1.5% does not appear to be in agreement with the theory, but perhaps this experimental result reflects the range of concentration for which the approximations present in the theory are valid. The temperature dependence of α is in excellent agreement with the theoretical expression Eq. (9) with an activation energy that is concentration dependent. The prediction that D_T should be independent of the properties of the polymer appears to be borne out rather well by the experimental data. In summary, the theory is very effective in describing the experimental results in the case of a critical solution.

The agreement between the theory and the experimental data in the good solvent is not especially good. The concentration dependence of α appears to be good for concentrations above 1.5%, but for concentrations below this concentration there appears to be considerable deviation. This deviation seems to be a real effect in view of the excellent agreement between the calculated D_T data and the experimental data of Debye and Bueche.[7] The temperature dependence of the thermal diffusion ratio appears to be in substantial agreement with the theory as given by Eq. (7). The experimental results on D_T show that D_T depends on the concentration of the polymer and to a lesser extent, depends on the molecular weight of the polymer. The theory requires that D_T depend only on the nature of the solvent. The very good agreement between these data and those of Debye and Bueche[7] as well as the general agreement between these results and those of Hoffman and Zimm[6] lend considerable credence to the validity of the experimental data reported here.

It appears that the assumptions introduced in the development of the theory apply better in a poor solvent than in a good solvent. Possibly a more careful description of the concentration dependence in the theory would remove this difficulty.

JOURNAL OF APPLIED PHYSICS VOLUME 31, NUMBER 11 NOVEMBER, 1960

Defects in Polyethylene Crystals

W. P. SLICHTER
Bell Telephone Laboratories, Murray Hill, New Jersey

Nuclear magnetic resonance measurements have been made of the development of chain motion in linear polyethylene and polymethylene crystallized from solution. It is shown that segmental mobility is produced at room temperature when the compounds are heated below the melting point. The changes are rapid and irreversible, and are independent of crystallization temperature and concentration, except at high concentration. The effects are ascribed to the development of defects in the crystalline structure.

TRADITIONAL concepts of polymer morphology have been greatly changed in the past few years. The discovery that many polymers can form single crystals composed of folded chains, when crystallization occurs from solution,[1] has led to suggestions that similar structures underlie the morphology of polymer solids formed from the melt.[2] The viewpoint has been expressed that the "amorphous" content in the older fringed micelle concept is to be reinterpreted in terms of defects arising from chain folds, branch points, and other faults in the crystalline structure.[2,3]

Peterlin *et al.*[4] have shown, through the use of nuclear magnetic resonance (NMR) spectroscopy, that solution-grown microcrystals of polyethylene irreversibly develop segmental mobility at room temperature when they have been heated to temperature not far below the melting point. Statton and Geil[3] have shown from studies by x-ray diffraction and electron microscopy that such heating produces recrystallization, and that this recrystallization is accompanied by a major increase in the thickness of the microcrystals. They have emphasized that chain mobility becomes sizable when these crystals are heated. The present paper extends Peterlin's studies with NMR and offers some new results that bear upon aspects of morphology and crystallization kinetics.

EXPERIMENTAL

Samples of two polymeric *n*-paraffins, Marlex 50 (a product of the Phillips Petroleum Company) and polymethylene, were crystallized from various solvents. The polymethylene, made by Professor W. J. Bailey of the University of Maryland, from the decomposition of diazomethane, obviously had an extremely high molecular weight, although no attempt was made to measure the value. The polymer was dissolved in the boiling solvent. Heating was continued for several hours (overnight with the polymethylene). The solution was then transferred to one-liter flasks immersed in a thermostat. No special means were taken to hasten the cooling of the hot solutions to the temperature of the thermostat, and therefore it may well be that some crystallization occurred in the interval between the temperature of the boiling solution and that of the thermostat. A layer of crystals formed on the walls of the flasks. These crystals doubtlessly were formed by heterogeneous nucleation. Perhaps the crystallization in the bulk of the solution involved heterogeneous processes too, since no extraordinary effort was made to free the solvent and solute of impurities that might cause nucleation. Still, for the sake of uniformity, an effort was made to collect only the crystals formed in the body of the solution, not those deposited on the walls. After crystallization, usually overnight, the precipitated polymer was collected by rapid filtration. The residual solvent was removed by gently heating the precipitate (*ca.* 50–60°C) for several days in a vacuum oven.

Heat treatment was achieved by warming about 0.3 g of a given precipitate in a nitrogen-filled test tube immersed in a thermostat regulated to ±0.1°C. Heating times varied from ½ to 24 hr.

Treatment of the NMR Results

Wilson and Pake, studying some melt-crystallized polymers by NMR, noted that the absorption curve seemed to be a superposition of a narrow envelope upon a broad envelope.[5] They identified these components with the "crystalline" and "amorphous" regions, respectively, of the traditional two-phase structure. It has since been shown[6] that ambiguities may result from such a simple assignment, since the separation of the resonance envelope into two components depends directly upon the existence of two categories of chain mobility and only indirectly upon two categories of chain order. Thus, it is something of a coincidence that one can find a temperature at which the NMR envelope can be separated into components corresponding to the crystalline-amorphous ratios seen by other techniques.

Marlex 50 crystallized from the melt exhibits this compound resonance envelope,[6,7] but the polymer when crystallized from solution appears to yield only a broad envelope [Fig. 1(a)]. When the sample is heated to a high enough temperature, a narrow component develops

[1] A. Keller, Makromol. Chem. **34**, 1 (1959); references.
[2] H. A. Stuart, Ann. N. Y. Acad. Sci. **83**, 1 (1959); references.
[3] W. O. Statton and P. H. Geil, paper presented at the 137th Meeting of the American Chemical Society, Cleveland, Ohio, April 6, 1960; J. Appl. Polymer Sci. **3**, 357 (1960).
[4] A. Peterlin, F. Krasovec, E. Pirkmajer, and I. Levstek, paper presented before the Symposium on Macromolecules, I.U.P.A.C., Wiesbaden, Germany, October 12, 1959.
[5] C. W. Wilson, III, and G. E. Pake, J. Polymer Sci. **10**, 503 (1953).
[6] W. P. Slichter and D. W. McCall, J. Polymer Sci. **25**, 230 (1957).
[7] R. L. Collins, J. Polymer Sci. **27**, 75 (1958).

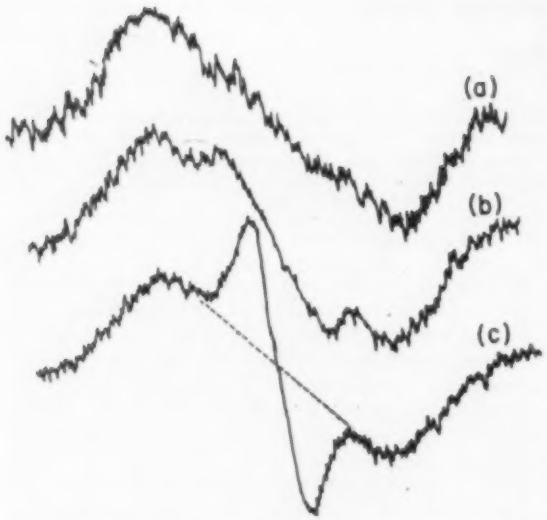

FIG. 1. Effect of heat treatment upon the shape of the derivative curves in nuclear magnetic resonance measurements of Marlex 50 crystallized at 90°C from 0.5% xylene solution. (a) Original material; (b) after heating at 130°C; (c) after heating at 135°C.

permanently, as in Figs. 1(b) and 1(c). It should be emphasized that these traces, and likewise all the rest of the data given in the following, refer to NMR measurements at *room temperature*, following heating of the sample to an elevated temperature.

The separation of the resonance into a narrow and a broad component is done readily with the derivative curve.[5] The method used here is somewhat arbitrary and involves drawing a straight line [Fig. 1(c)] between the outer peaks of the derivative curve. The justification for this choice is that the broad portion thus separated closely resembles the resonance for the unheated sample [Fig. 1(a)]. It is also essentially the same as the resonance for a pure *n*-paraffin of low molecular weight, such as n-$C_{35}H_{72}$.

Use of such a decomposition for morphological studies requires that a temperature interval exist within which the ratio of the narrow to the broad component remains constant. It was shown earlier[6] that this condition is met with melt-crystallized Marlex 50, fortunately in a temperature region that includes room temperature. In the present studies, this condition has been found to apply also to solution-crystallized Marlex 50 and polymethylene. The detailed morphological interpretations that are drawn from the decomposed resonances may be open to some argument. In any case, it is clear that these changes correspond to the development of segmental mobility, for NMR measurements at liquid nitrogen temperature upon heat-treated samples show only the broad component, the narrow component being quenched at low temperature. To avoid offering a morphological interpretation at this point, it is convenient to express the data in terms of the fraction of the narrow component F_n, which is the ratio of the integrated intensity of the narrow component to that of the whole resonance.

RESULTS

Figure 2 shows the variation of F_n with temperature of heating for Marlex 50, crystallized at 90°C from xylene solution containing 0.5% by volume of polymer. The results in Fig. 2 resemble to a degree those reported by Peterlin.[4] There is a marked increase in F_n with increasing temperature of heating. The value of F_n attained at a given temperature is irreversible, for subsequent heating at a lower temperature fails to alter the higher value of F_n. Each of the points in Fig. 2 represents a separate sample. However, essentially the same curve is produced if a single sample is heated by stages through a range of increasing temperatures and is subjected to NMR measurement following each stage of heating. The value of F_n does not seem to depend upon the time of heating after about 30 min. Indeed, when the heating time is much less than 30 min, one is really not sure that temperature equilibrium has been reached throughout the sample. Thus, on the rather gross time scale of this experiment, the thermal transformation is quite fast.

A qualitative measure of the rapidity of this change was made by rapidly heating a sample of crystals to a temperature within this critical range and then quickly cooling the sample after a short time. To do this, a thin layer of the crystallized polymer was sprinkled into a dry flask which was already immersed in a thermostat at 131°C. After a chosen interval, the sample was dumped into an ice-cooled vessel. It was found that the narrow component developed very quickly, reaching a steady-state value within an interval of a couple of minutes, set by the rather crude time scale of this experiment.

The results in Fig. 2 differ from those of Peterlin in that the transformations begin at higher temperatures, and the ultimate values of F_n are higher than in his studies. Peterlin observed development of the narrow component somewhere between 70° and 90°C, whereas in the present studies the transformation did not appear until nearly 110° and did not become appreciable until about 120°C. Peterlin found a maximum of 0.085 for F_n, whereas in the present work F_n reached 0.15 for Marlex 50. There seems to be no obvious reason for these differences.

Figure 2 also shows the level of F_n obtained with the same polymer which had been crystallized from the melt, heated overnight at 128°C, and then cooled at the rate of a few degrees per hour. This sample could be characterized as a fairly well-annealed polymer.[7] It is interesting to note that F_n for Marlex 50 crystallized from solution attains permanent values that are much higher than for this well-annealed sample made from the

melt. It would appear that the regions permitting segmental mobility in these two categories of crystalline polymer are not equivalent.

Figure 3 shows the variation of F_n with temperature of heating for polymethylene crystallized from two solvents, xylene and perchloroethylene, at a volume concentration of 0.1% and a temperature of 90°C. Also shown are results for polymer crystallized from very dilute solution, 0.01% by volume. In the latter case the temperature of crystallization was uncontrolled and must be regarded as having occurred within some range between the boiling point of xylene and room temperature. We see that NMR results show no dependence upon the solvent used or upon the concentration for these very dilute solutions. This independence from the identity of the solvent is not surprising, since one expects[8,9] that the important parameter in the crystallization should be the temperature, and that identity of the solvent should be felt mainly through the crystallization temperatures that can be realized. Independence

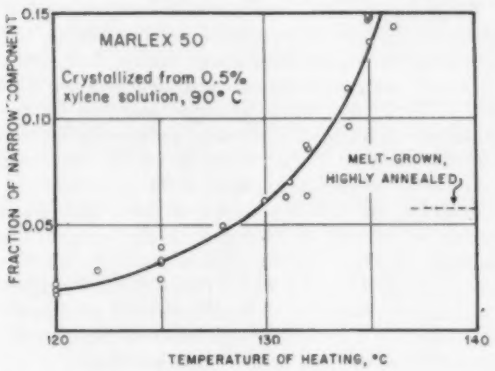

FIG. 2. Variation of the fraction of the narrow component in the nuclear resonance envelope with temperature of heat treatment for Marlex 50 crystallized from 0.5% xylene.

from the concentration (even up to 0.5%, cf. Fig. 2) is at least in keeping with the prediction[9] that crystallization occurs homogeneously in sufficiently dilute solutions.

The high molecular weight of the polymethylene shifts the peak value of F_n to about 136°C, which is close to the reported value of the thermodynamic melting point.[10] The magnitude of F_n approaches 0.30. In terms of the traditional picture of a two-phase structure, this figure corresponds to the development of a sizable extent of amorphous material. However, below about 136°C this component of mobile chain segments is permanent, unaltered by heat treatment at lower temperatures, whereas the narrow component developed

[8] F. P. Price, J. Chem. Phys. **31**, 1679 (1959).
[9] J. I. Lauritzen, Jr. and J. D. Hoffman, J. Chem. Phys. **31**, 1680 (1959); J. Research Natl. Bur. Standards **64A**, 73 (1960).
[10] F. A. Quinn, Jr., and L. Mandelkern, J. Am. Chem. Soc. **80**, 3178 (1958).

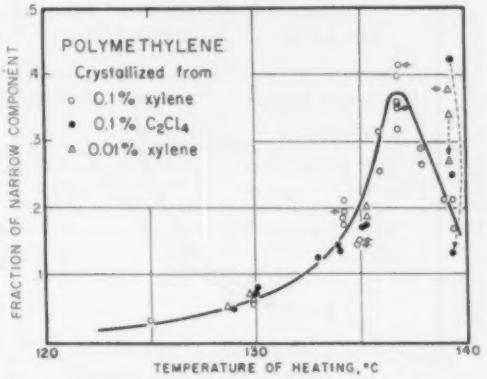

FIG. 3. Variation of the fraction of the narrow component with temperature of heat treatment for polymethylene crystallized from xylene and perchloroethylene.

in the resonance envelope after heating at temperatures above 136°C is nonpermanent and is influenced by annealing. The point is illustrated in Fig. 3. Here a representative pair of points is shown (a) shortly after heat treatment above 136°C and (b) after subsequent annealing for 20 hr at 125°C. The dashed lines show the changes caused by this annealing. The same sort of annealing effect occurs with melt-crystallized samples of linear polyethylene.[7]

Except for the fact that the polymethylene samples sustained higher temperatures, without obvious fusion, than did the Marlex 50 samples, the results were the same for the two compounds below about 135°C. Evidently the segmental mobility caused by the heat treatment does not arise from low molecular weight components, for the two kinds of polymer were clearly very different in molecular weight.

It is well to remark upon the possibility that thermal degradation, rather than morphological change, caused

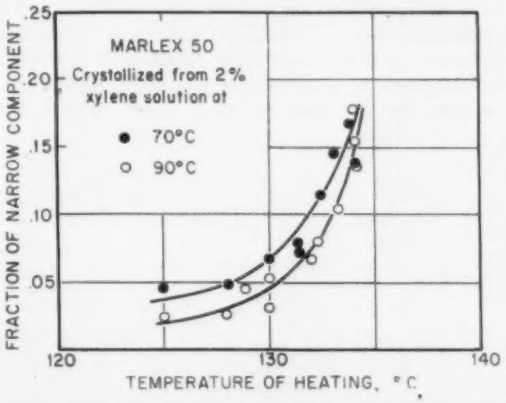

FIG. 4. Variation of the fraction of the narrow component with temperature of heat treatment for Marlex 50, crystallized from 2% xylene solution at 70° and 90°C.

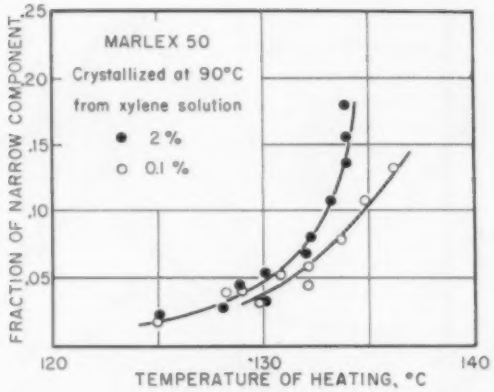

FIG. 5. Variation of the fraction of the narrow component with temperature of heat treatment for Marlex 50, crystallized at 90°C from 0.1% and 2% xylene solution.

these alterations in the NMR spectra. In Fig. 3, the points marked with arrows represent heat treatments of about 1 hr, while the unmarked points represent heat treatments of 24 hr. Since F_n does not depend perceptibly upon the duration of heat treatment, we conclude that thermal decomposition played a negligible role in these results.

The temperature of crystallization and the concentration produce discernible differences in these studies only when the concentration is quite high, of the order of 2% in the case of Marlex 50. Figure 4 shows the variation of F_n with temperature of heating for samples crystallized from 2% solution, at 70° and at 90°C. The segmental mobility developed in the former appears to be somewhat greater than in the latter.

Figure 5 compares the temperature dependence of F_n for two samples crystallized at 90°C, one from 2% solution and one from 0.1% solution. Again, the segmental mobility developed in the former exceeds that in the latter. It may be significant that this sensitivity to concentration and temperature, seen in Figs. 4 and 5, occurs only when the concentration falls into the range predicted, to yield bundlelike nucleation. We have to be cautious in studying very concentrated solutions, however, for the question must arise whether the crystallization occurred from a solution or from a well-plasticized solid.

DISCUSSION

Studies by x-ray diffraction and electron microscopy have suggested that heat treatment of microcrystals of polyethylene causes a recrystallization characterized by the development of voids[3] or corrugations.[11] The NMR results show that the process is accompanied by the rapid development of mobility in a portion of the chain segments within the crystals. Following the evidence from other sources,[3,11] we ascribe the NMR results to morphological changes, with the suggestion that the chain mobility is permitted by the development of defects in the crystalline structures. The folded-chain structure possessed by polyethylene crystals grown from solution inherently possesses defects in the surfaces where the chains fold, but evidently these regions do not constitute the portions seen directly by NMR, for the narrow component of the resonance develops only after heating.

We postulate therefore that heat treatment of the microcrystals introduces fairly extensive defects, sufficient to permit appreciable chain motion. It is well to emphasize two morphological consequences of the NMR results. First, the sizable changes produced by heat treatment are rapid. This finding underscores the considerable mobility, translational as well as rotational, possessed by polyethylene chains in the solid state.[2]

Secondly, the lack of response of these heat-treated crystals to further annealing at lower temperatures contrasts with the behavior of these materials following crystallization from the melt. This difference suggests caution is necessary in the development of proposals[2,11] regarding a tieup in morphology between single crystals obtained from solution and the bulk polymer.

ACKNOWLEDGMENT

I am grateful to Professor A. Peterlin of the J. Stefan Institute, Ljubljana, Yugoslavia, to Dr. W. O. Statton of the du Pont Company, and to Dr. D. Hyndman of the American Viscose Corporation, for helpful discussions.

[11] D. C. Bassett and A. Keller, J. Polymer Sci. 40, 565 (1959).

Effect of Reactor Irradiation on the Tensile Strength of Uniaxially Oriented Polyethylene Terephthalate*

C. C. Hsiao and S. T. Chow
University of Minnesota, Minneapolis, Minnesota

A series of uniaxially oriented polyethylene terephthalate fibers irradiated in a nuclear reactor have been investigated. On the basis of tensile studies the ultimate tensile strength is found to decrease as the dose of reactor irradiation increases. However, the ultimate tensile strength is found to increase when the degree of molecular orientation increases. But after the samples have received a relatively high dose of irradiation the tensile strength approaches practically zero. The x-ray diffraction scans of the nonirradiated samples with low degrees of orientation indicate very little crystallinity, whereas the very definite diffraction peaks associated with the irradiated and oriented samples indicate a definite trend toward crystallinity.

IT is known that the orientation of the molecular structure of linear high polymers produces remarkable changes in their physical and mechanical properties,[1–3] whether the materials are irradiated or not.[4] However, little or no attention has been given to this effect in most available literature on the investigation of irradiation effect upon solid polymers.[4] It is the purpose of this brief report to describe the effect of reactor irradiation on some mechanical and physical properties of oriented and unoriented polyethylene terephthalate fibers.

The oriented polyethylene terephthalate yarns were prepared and supplied by "Dacron" Research Laboratory of du Pont Company. The orientation of these samples was determined by obtaining the ratio between the cross-sectional areas of the unoriented and oriented samples. They were found to range from 1.00 to 5.35, as shown in Table I. These samples were irradiated in sealed aluminum containers for the same length of time in different regions in a graphite hole in the MTR (Material Testing Reactor) at about 100°F with a total reactor irradiation of 420 megawatt-days at 40 megawatts. The thermal neutron flux traverse was determined from measurements of 23½% Co-Al alloy wire sections irradiated together with the samples. The average accumulated thermal nvt values and some available information on the estimated fast neutron and gamma photons from individual sample containers are given in Table II. Since the thermal neutron doses were actually determined, their nvt values are used for this report as an index although the thermal neutron radiation alone is not the prime contributor to the irradiation effect.

Each bundle of the specimen consists of 34 fibers. The diameter of each fiber for the unoriented sample was found to be about $1\frac{5}{32}\times10^{-3}$ in. All the samples were

TABLE I. Oriented samples of polyethylene terephthalate.

Oriented sample	Oriented and irradiated sample	Degree of orientation in terms of strain change
A	*A'*	0.00
B	*B'*	0.22
C	*C'*	0.63
D	*D'*	1.03
E	*E'*	2.10
F	*F'*	3.43
G	*G'*	4.35

TABLE II. Irradiation doses for drawn and undrawn polyethylene and terephthalate.[a]

Number of container	Accumulated perturbed thermal neutron dose	Estimated accumulated fast neutron transverse ($\Sigma_R \geq 1$ mev)	Estimated roentgens of gamma photons
1	4.3×10^{17} nvt	3.3×10^{14} nvt	8.6×10^{10}
2	7.4 nvt	5.6 nvt	1.3×10^{11}
3	1.2×10^{18} nvt	1.0×10^{15} nvt	1.8
4	2.0 nvt	1.6 nvt	2.8
5	3.4 nvt	2.7 nvt	4.3
6	5.7 nvt	4.6 nvt	6.6
7	8.6 nvt	7.8 nvt	9.6
8	1.1×10^{19} nvt	1.3×10^{16} nvt	1.3×10^{12}
9	1.3 nvt	2.2 nvt	1.4

[a] The experiment was carried out in *VG-20* hole of MTR for a total of 420 megawatt-days at 40 megawatts. Data were supplied by the technical staff of the MTR, Idaho Falls, Idaho.

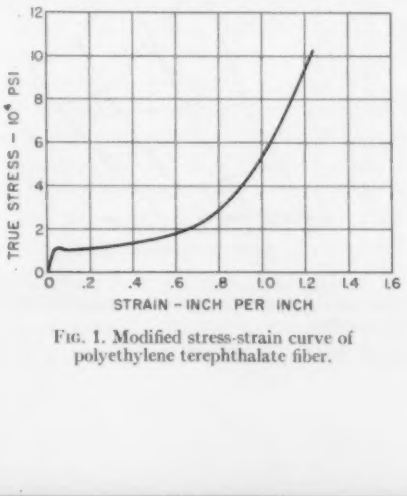

FIG. 1. Modified stress-strain curve of polyethylene terephthalate fiber.

* Supported in part by the U. S. Atomic Energy Commission.

[1] C. C. Hsiao, J. Appl. Phys. **30**, 1492 (1959).
[2] J. Bailey, India Rubber World, **118**, 225 (1948).
[3] K. J. Cleereman, H. J. Karam, and J. L. Williams, Modern Plastics, **30**, 119 (1953).
[4] C. C. Hsiao, Y. C. Das, and A. Haynes, Technical Report 2, AEC AT(11-1)-532, University of Minnesota (1959); Brit. J. Appl. Phys. **11**, 277 (1960).

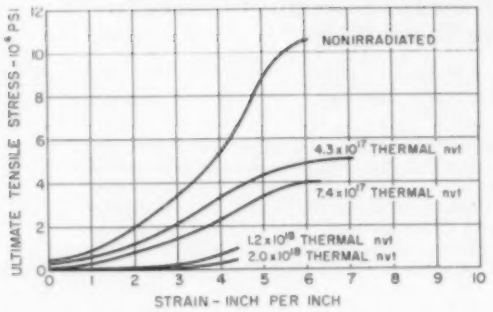
ULTIMATE TENSILE STRESS - 10⁴ PSI
NONIRRADIATED
4.3 x 10¹⁷ THERMAL nvt
7.4 x 10¹⁷ THERMAL nvt
1.2 x 10¹⁸ THERMAL nvt
2.0 x 10¹⁸ THERMAL nvt
STRAIN - INCH PER INCH

FIG. 2. Ultimate tensile strength of unoriented polyethylene terephthalate fiber as affected by irradiation.

investigated at room temperature by simple tension. The nominal strain rate of testing used was 2 per min. During testing the total deformation was found to be fairly large. In order to take into account the orientation as a result of the large deformation, the assumption of constant volume of the material was used. As there were 34 fibers in each specimen an average value of the true breaking stress was determined by assuming that all the 34 fibers fail when the 17th fiber fails. Figure 1 shows a modified true stress-strain curve of a bundle of polyethylene terephthalate fibers.

In order to compare more closely the breaking strength for unoriented samples receiving different degrees of reactor irradiation, Fig. 2 shows the ultimate tensile strength of polyethylene terephthalate fiber as affected by reactor irradiation. For the irradiated but unoriented sample the ultimate tensile strength was observed to decrease significantly as compared with that of the nonirradiated and unoriented sample. This agrees with the result reported earlier by Little.[5]

However, when the samples have been preoriented before irradiation, it has appeared that the high degree of molecular orientation was able to maintain the

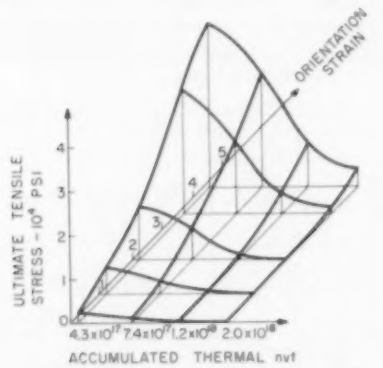

FIG. 3. Strength surface showing both effects of molecular orientation and reactor irradiation on the strength of polyethylene terephthalate fiber.

[5] K. Little, Nature **173**, 680 (1954).

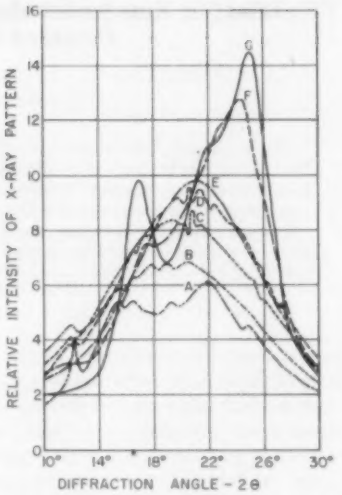

FIG. 4. X-ray photometer curves of oriented polyethylene terephthalate.

ultimate strength a great deal higher than that of the unoriented sample. This effect is clearly brought out by Fig. 3, which shows the variation of the strength as affected by both molecular orientation[1] and reactor irradiation.[4] It is interesting to note that after the highly oriented specimen (orientation strain 4.35) has received a reactor irradiation indicated by 2×10^{18} thermal nvt, it still possesses a strength higher than that of the unoriented specimen, which has received a reactor irradiation indicated by only 4.3×10^{17} thermal nvt. It seems reasonable to suspect that a sample with prior molecular orientation has a much better ability to resist chain

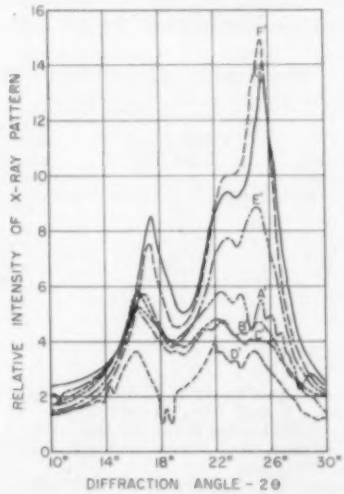

FIG. 5. X-ray photometer curve of oriented and irradiated polyethylene terephthalate.

scission resulting from irradiation than that without. In general the ultimate tensile strength is found to decrease as the dose of reactor irradiation increases. But the ultimate tensile strength is found to increase when the degree of molecular orientation increases. At fairly high doses, however, the tensile strength vanishes completely.

In order to obtain a little more understanding of the structure of the samples, both irradiated and nonirradiated as well as oriented and unoriented specimens have been subjected to x-ray diffraction examination. The samples were scanned from $30°-2\theta$ to about $10°-2\theta$. Samples were inserted into the specimen holder with fiber axis coincident to the axis of the specimen shaft. The diffraction scans of the nonirradiated samples indicate very little crystallinity associated with these samples except the two highly oriented samples as shown in Fig. 4. The very definite diffraction peaks associated with the irradiated samples shown in Fig. 5 indicate a definite trend toward crystallinity. For the purpose of getting a more complete picture of the diffraction pattern, two flat plate films were used for both the irradiated sample and its nonirradiated counterpart. The film for the nonirradiated and unoriented sample shows a broad amorphous halo as shown in Fig. 6(a), whereas in Fig. 6(b) the film for the irradiated and unoriented sample shows two definite rings.

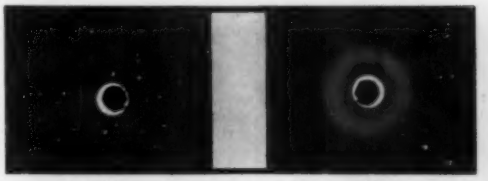

FIG. 6. X-ray transmission diffraction pattern of polyethylene terephthalate. (a) Nonirradiated and unoriented (orientation strain 0). (b) Irradiated and oriented (orientation strain 2.10).

The shift of the peaks and the variation of the sharpness of the diffracted rings indicate the existence of orientation and crystallization of the sample. However, in view of the complexity of the problem, an explicit correlation between the strength and the orientation and crystallization of the molecules was not attempted.

JOURNAL OF APPLIED PHYSICS VOLUME 31, NUMBER 11 NOVEMBER, 1960

Effect of Temperature and Reactor Irradiation on the Strength of Biaxially Oriented Polyethylene Terephthalate*

A. HAYNES AND C. C. HSIAO
University of Minnesota, Minneapolis, Minnesota

Samples of biaxially oriented polyethylene terephthalate irradiated in a nuclear reactor have been investigated at five temperature levels ranging from −150°F to 350°F. In general, from tensile studies, the ultimate tensile strength was found to decrease markedly to a relatively low magnitude upon receiving a reactor irradiation dose having a thermal neutron bombardment component of 10^{18} nvt and over. The modulus of elasticity for both the irradiated and nonirradiated samples was found to increase with the decrease of the temperature.

The fracture surfaces of the biaxially oriented polyethylene terephthalate samples obtained at −15°F are also recorded for reference.

THE purpose of this investigation was to study the effect of temperature and reactor irradiation on the strength properties of biaxially oriented polyethylene terephthalate. Samples 4 in. long with a uniform effective test section of $\frac{1}{2}$ in.$\times\frac{1}{4}$ in.$\times$0.0105 in. were punched out of a Mylar sheet along one of the biaxial orientation directions. The irradiation of these samples were carried out in sealed aluminum containers by putting them in different sections of a graphite hole in the Material Testing Reactor. Table I gives the irradiation data supplied by the engineering office of the MTR. The mean thermal neutron irradiation component of this reactor irradiation was determined from measurements of Co-Al alloy wire sections irradiated together with the samples. Since the thermal neutron doses were actually determined for different sections of the graphite hole in the reactor, their nvt values are used as an index in this report. It is evident that the thermal neutron irradiation alone is not the prime contributor to the irradiation effect.

All of the irradiated samples were studied by simple tension in an automatically controlled temperature chamber with a constant nominal strain rate of 0.2 per minute. Liquid nitrogen was forced into the testing chamber for obtaining the low temperatures. The testing chamber has built-in thermal elements for conducting high-temperature tests. Because of the high anisotropic nature of the biaxially oriented samples, the dimensions in two cross-sectional directions were measured during the test. In determining the true stress values, it was

* Supported in part by the U. S. Atomic Energy Commission.

TABLE I. Irradiation doses for biaxially oriented polyethylene terephthalate.[a]

Capsule number	Accumulated perturbed thermal neutron dose	Estimated accumulated fast neutron traverse ($\Sigma_R \geq 1$ mev)	Estimated roentgens of gamma photons
1	4.3×10^{17} nvt	3.3×10^{14} nvt	8.6×10^{10}
2	7.4 nvt	5.6 nvt	1.3×10^{11}
3	1.2×10^{18} nvt	1.0×10^{15} nvt	1.8
4	2.0 nvt	1.6 nvt	2.8
5	3.4 nvt	2.7 nvt	4.3
6	5.7 nvt	4.6 nvt	6.6
7	8.6 nvt	7.8 nvt	9.6
8	1.1×10^{19} nvt	1.3×10^{16} nvt	1.3×10^{12}
9	1.3 nvt	2.2 nvt	1.4

[a] The experiment was carried out in *VG-20* hole of MTR for a total of 420 megawatt-days at 40 megawatts. Data were supplied by the engineering office of the MTR, Idaho Falls, Idaho.

assumed that the volume of the material remained constant during the test.

In order to compare more closely the stress-strain properties of these irradiated and nonirradiated samples, Fig. 1 is plotted for five different temperature levels. For the irradiated samples the ultimate tensile strength was found to decrease appreciably as compared with those of the nonirradiated ones at all the temperature levels. The destruction of the preferred orientation of the sample as a result of scission of the long polymer chains was suspected to be the mechanism of the reduction of the mechanical strength.[1,2] From Little's report it was found that the results of the effect of irradiation on polyethylene terephthalate are consistent with a straightforward breakdown on the main polymer chain instead of any crosslinking effect. This effect can be clearly seen in Fig. 2, in which the ultimate tensile strength is plotted against the logarithm of thermal neutron irradiation at different temperature levels. It is interesting to note that beyond a thermal neutron dose of about 2×10^{18} nvt the ultimate tensile strength of the

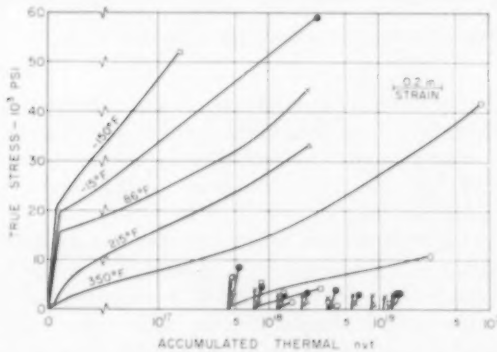

FIG. 1. True stress-strain curves of irradiated and nonirradiated biaxially oriented polyethylene terephthalate.

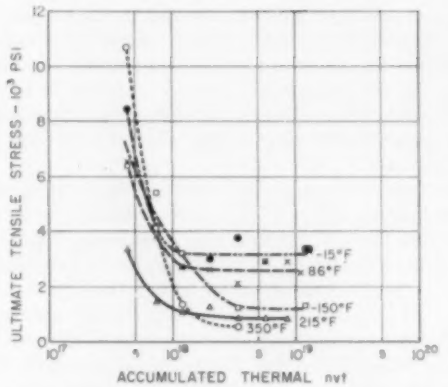

FIG. 2. Ultimate tensile stress vs irradiation level at different temperatures of irradiated biaxially oriented polyethylene terephthalate.

samples at all temperature levels has shown little variation in its magnitude.

In the unoriented and nonirradiated sample, the stress-strain relations consist of perhaps two or three stages; the initial, the orientation, and the final stage[3]; whereas in an irradiated sample it seems that only one stage occurs. When irradiation doses become greater and greater, the effect of molecular orientation seems to be gradually destroyed and little variation of the ultimate tensile strength can be observed. However, the strength was not entirely lost and the material did not begin to powder although it was quite brittle.[1] The slight improvement in strength might be the indirect result of having prior molecular orientation before subjecting it to irradiation.

As for the temperature effect, it can be seen that the total strain for the nonirradiated samples is approximately constant within the temperature range of 215°F to −15°F. Within this range the ultimate strength increases as the temperature decreases. At a higher temperature the total strain increases. As a result of this increase of strain, the strength is also increased. At a low temperature beyond −15°F, the total strain decreases, thus the breaking strength is also reduced. Similarly, the modulus of elasticity increases with a decrease in temperature, as shown in Fig. 3 for the nonirradiated samples. For the irradiated sample, a similar general trend holds. However, there is a slight variation of the modulus of elasticity as affected by reactor irradiation within the temperature range between 215°F and −15°F.

Beyond the range at a higher temperature, the modulus of elasticity simply reduces as the thermal nvt value increases. On the other hand, at a lower temperature beyond the temperature range, a somewhat similar trend is also observed. It is suspected that at a relatively low temperature the mechanism of the microscopic

[1] K. Little, Nature **173**, 680 (1954); K. H. Sun, Modern Plastics **32**, 141 (1954).

[2] C. C. Hsiao, Y. C. Das, and A. Haynes, Brit. J. Appl. Phys. **11**, 277 (1960).

[3] C. C. Hsiao and S. T. Chow, AEC AT(11-1)-532 T.R. 10, University of Minnesota.

crack propagation in the material may have caused the increase of the macroscopic strain values and thus the reduction of the modulus of elasticity. Perhaps the rapid propagation of the fine cracks is also a factor of the reduction of the ultimate tensile strength of the material.

In order to see the irradiation effect on the variation of the fracture surfaces of biaxially oriented polyethylene terephthalate, Fig. 4 shows a series of photomicrographs of fracture surfaces obtained at −15°F. For the nonirradiated fracture surface it appears that a fairly uniform failure has resulted. For any of the relatively highly irradiated samples the texture of the fracture surface shows a large number of circular dots. These dots might be originally associated with the microscopic cracks. At the initial stage of these microscopic cracks little or no evidence of separation of the material in the vicinity of the cracks could be detected. However, after these cracks had propagated to a certain size, they then became visible. For the duration of testing used it seems that there was sufficient time for a large number of these microscopic cracks to develop into visible ones as shown in the figure. For the sample irradiated with a relatively low irradiation dose the fracture surfaces have shown a very interesting texture. Fairly large, long, and smooth strips seem to prevail on the surface after the failure of the samples. This perhaps indicates that there is little or no propagation of fine cracks in the material during testing until fracture occurs. This phenomenon seems to be further supported by the slight increase of the modulus of elasticity of the material observed within this range of irradiation as shown in Fig. 3.

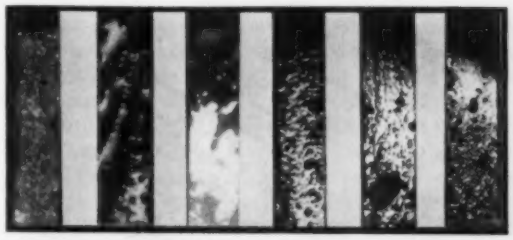

FIG. 4. Reactor surfaces with thermal neutron component in nvt; fracture surfaces of biaxially oriented polyethylene terephthalate at −15°F.

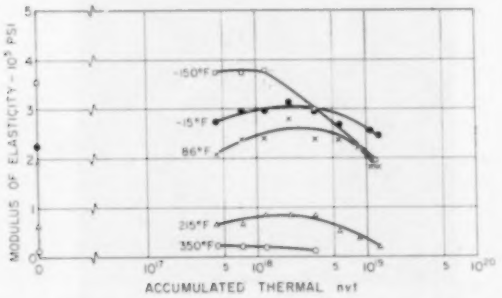

FIG. 3. Modulus of elasticity as a function of irradiation and temperature of biaxially oriented polyethylene terephthalate.

JOURNAL OF APPLIED PHYSICS VOLUME 31, NUMBER 11 NOVEMBER, 1960

Photographic Light Scattering by Polyethylene Films*

RICHARD S. STEIN AND MARION B. RHODES†
Department of Chemistry, University of Massachusetts, Amherst, Massachusetts

The photographic light scattering technique permits a measurement of the size, anisotropy, radial periodicity, packing, and internal structure of polymer spherulites. The theory of some of these effects is described, and experiments are presented showing changes occurring in the melting and growth of spherulites.

INTRODUCTION

THE study of the scattering of light from crystalline polymeric films has been the subject of a number of papers from this[1–5] and other[6,7] laboratories. The technique described involved photometric measurement of the scattered intensity as a function of sample and scattering angle. It was concluded that scattering arises principally from orientation fluctuations among aggregates of crystals. The scattering patterns are complex, especially with polarized light and oriented samples.

* Supported in part by a contract with the Office of Naval Research, grants from the National Science Foundation and the Plax Corporation, and by assistance from the Monsanto Chemical Company.

† National Science Foundation Faculty Research Fellow. Part of this work constitutes a portion of a Master of Science thesis at the University of Massachusetts.

[1] R. S. Stein and J. J. Keane, J. Polymer Sci. **17**, 21 (1955).
[2] J. J. Keane and R. S. Stein, J. Polymer Sci. **20**, 327 (1956).
[3] F. H. Norris and R. S. Stein, J. Polymer Sci. **27**, 87 (1958).
[4] R. S. Stein, in *Growth and Perfection of Crystals*, edited by R. H. Doremus, B. W. Roberts, and D. Turnbull (John Wiley & Sons, Inc., New York, 1958), p. 549.
[5] R. S. Stein *et al.*, Ann. N. Y. Acad. Sci. **83**, 37 (1959).
[6] S. W. Hawkins and R. B. Richards, J. Polymer Sci. **4**, 515 (1949).
[7] F. Price, in *Growth and Perfection of Crystals*, edited by R. H. Doremus, B. W. Roberts, and D. Turnbull (John Wiley & Sons, Inc., New York, 1958), p. 533.

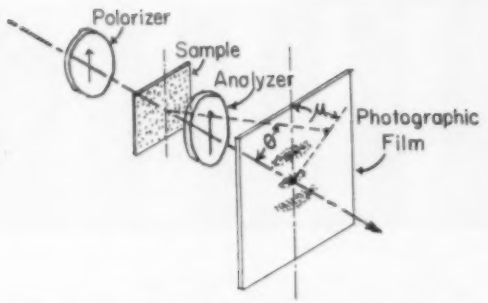

FIG. 1. The experimental arrangement for photographic light scattering from films.

Recently, a photographic method for observing film scattering at low angles has been proposed.[8] This method has the advantage of simplicity of equipment, rapidity, and presentation of the entire low-angle scattering pattern for surveillance. In this paper, the theory and experimental techniques for this method are described.

EXPERIMENTAL

The apparatus has been described previously[8] and is sketched in Fig. 1. In the former work, the incident beam was collimated to about 0.3 deg, and a 5-mm diam beam was used so that the scattering represented an average of the structure within an area of the sample of about this diameter. A recent innovation has been the introduction of a smaller pinhole, 0.3 mm in diam, giving a microbeam which makes possible the examination of the scattering from a small region of a sample or from a portion of a large spherulite. The samples are mounted between microscope slides and held in a universal stage so that the incident beam may be aligned with a region of the sample which is of interest. A low-power microscope is of value in locating and aligning such a region of the sample. By using Ansco Super Hypan film, light scattering photographs are obtained with exposure times of 1 to 5 min. With a higher-intensity light source, faster optics, and faster film, appreciably shorter exposure times should be possible and would permit kinetic studies. Smaller slit sizes down to 50 μ may be used permitting examination of structure in very small regions of samples. The smallest slit size is limited by diffraction from the slit.

Some typical scattering patterns from an unoriented medium density polyethylene film are presented in Fig. 2. The circles are drawn to indicate 5 deg of scattering angle. Two types of polarized patterns are discussed: (1) V_v patterns obtained when the polarizer in the incident beam and the analyzer in the scattered beam are both vertical, and (2) V_H patterns where the polarizer is vertical and the analyzer is horizontal.

[8] A. Plaza and R. S. Stein, J. Polymer Sci. **40**, 267 (1959).

THEORY

A qualitative analysis of the scattering patterns will be made first. It is observed that the V_v scattering patterns are elongated in the direction of polarization. An anisotropic scattering pattern of this sort is usually interpreted in terms of an oriented scattering object.[9] This cannot be the case with an unoriented polyethylene sample, particularly since the direction of extension of the scattering pattern is dependent upon the direction of polarization. Consequently, the interpretation may be made in terms of an anisotropic but unoriented arrangement of principal polarizability directions.

Polyethylene crystallites are known to be arranged in spherical aggregates called spherulites[10] with differing radial and tangential refractive indices denoted by n_r

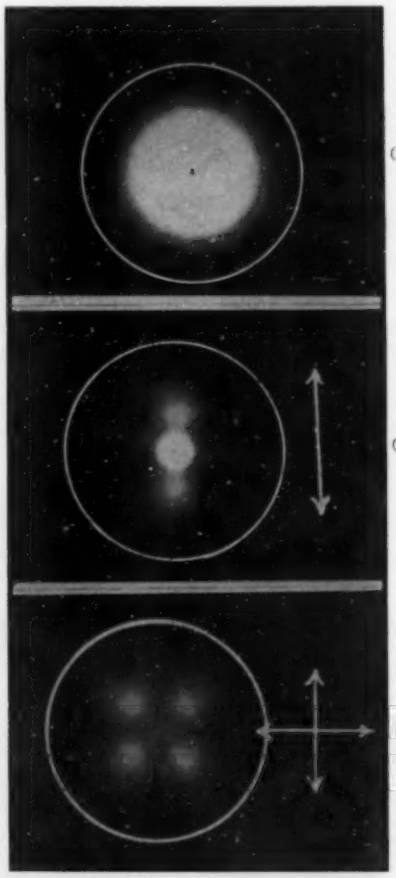

FIG. 2. Typical light scattering photographs for (a) unpolarized light, (b) V_v polarization, and (c) H_v polarization. The circles represent 5 deg of scattering angle, and the arrows represent directions of polarization.

[9] A. Gunier *et al.*, *Small Angle Scattering of X Rays* (John Wiley & Sons, Inc., New York, 1955), p. 29.

[10] W. M. D. Bryant, J. Polymer Sci. **2**, 552 (1947).

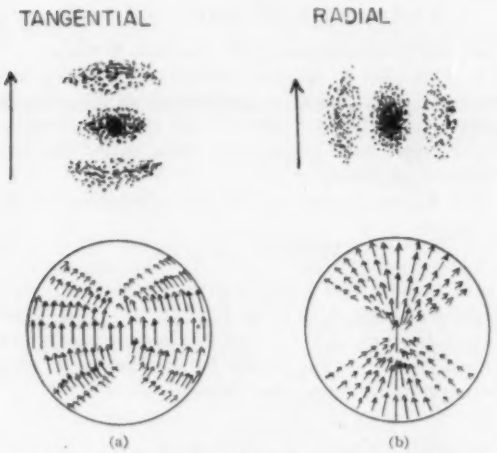

FIG. 3. The arrangement of induced dipoles and the expected V_v scattering patterns for spherulites which are (a) only polarizable tangentially and (b) only polarizable radially.

and n_t, respectively. Typical values ascribed to these by Bryant are $n_r = 1.514$ and $n_t = 1.516$ for low-density polyethylene. This optical anisotropy is a consequence of the arrangement of the anisotropic crystallites within the spherulites. The orthorhombic crystals have principal refractive indices of 1.514, 1.519, and 1.575 along their *a*, *b*, and *c* axes, respectively.[11] The high-refractive index direction is that of the *c* axis along which lies the polyethylene chain. The crystals are believed to be oriented within the spherulites with their *b* axes radial and their *a* and *c* axes tangential.[12] Consequently, assuming complete crystallinity and perfect orientation of crystals within spherulites, this would give $n_r = 1.519$ and $n_t = (1.514 + 1.575)/2 = 1.545$. The difference between these, -0.026, is about ten times as great as the spherulite birefringence. This may be attributed to (a) partial crystallinity of the spherulite, (b) imperfect orientation of crystals within spherulites, (c) orientation of amorphous regions of spherulites, and (d) form birefringence.[13]

Let us consider two idealized cases illustrated in Fig. 3. In (a) it is assumed that the electrons within the spherulite may only be displaced in a tangential direction. It is apparent that for vertically polarized light, dipoles are induced in only the equatorial regions of the spherulite. The scattering pattern, which is most elongated in the direction of smallest extension of the spherulite,[9] is extended in the vertical direction. In case (b), where the electrons may move only along the radii of the spherulite, the induced dipoles are principally in the polar regions and the scattering pattern is extended horizontally. For isotropic spherulites, radial and tangential motion of the electrons is equally easy, and induced dipoles are uniformly arranged throughout the spherulite. The scattering pattern will be the sum of those for cases (a) and (b) and will have circular symmetry. The observed extension of the V_v scattering pattern in the polarization direction corresponds to case (a) and indicates that it is the tangential component of polarizability which gives rise to scattering. The low intensity of scattering in the direction perpendicular to polarization observed in Fig. 2(b) indicates that the radial polarizability contribution is negligible. This probably arises because of destructive interference among adjacent spherulites.

The cloverleaf type pattern obtained with crossed polaroids may also be understood in terms of spherulite anisotropy. For vertical polarization of the incident light, the induced dipoles are distributed as in Fig. 3(a). If these are viewed through a horizontally oriented analyzer, the large dipoles along the equator will be oriented perpendicularly to the analyzer and will not contribute to the scattered light passed by the analyzer. It will be the dipoles in planes of the spherulite oriented at 45 deg to both the polarizer and analyzer that will make the maximum contribution to scattering. The arrangement of these is indicated in Fig. 4. The cloverleaf arrangement of these is apparent.

It is also apparent that in isotropic spherulites, the induced dipole will be oriented in the direction of polarization of the incident light, and no scattered light will be transmitted through an analyzer perpendicular to this. Consequently, the H_v component of scattering for isotropic spherulites will be zero.

The qualitative predictions may be quantitatively justified in a calculation similar to that of Goldstein.[14]

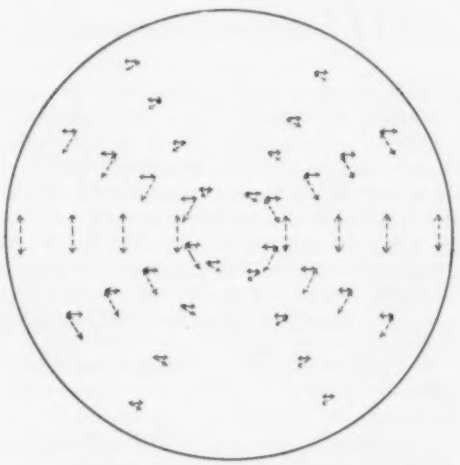

FIG. 4. The arrangement of induced dipoles in a tangentially polarizable spherulite which will contribute to H_v scattering. The dotted arrows represent the strength of the induced dipoles, while the solid arrows represent the component of this passing through a horizontal analyzer.

[11] C. W. Bunn and R. de Daubeny, Trans. Faraday Soc. **50**, 1173 (1954).
[12] A. Keller, J. Polymer Sci. **17**, 291 (1955).
[13] A. Keller, J. Polymer Sci. **17**, 351 (1955).
[14] M. Goldstein, J. Polymer Sci. **20**, 413, 578 (1956).

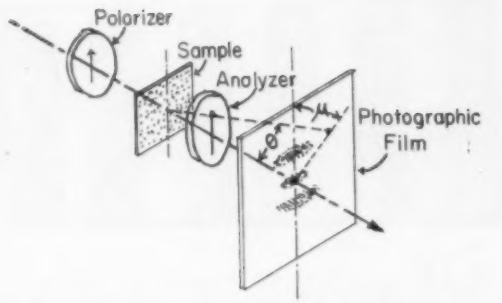

FIG. 1. The experimental arrangement for photographic light scattering from films.

Recently, a photographic method for observing film scattering at low angles has been proposed.[8] This method has the advantage of simplicity of equipment, rapidity, and presentation of the entire low-angle scattering pattern for surveillance. In this paper, the theory and experimental techniques for this method are described.

EXPERIMENTAL

The apparatus has been described previously[8] and is sketched in Fig. 1. In the former work, the incident beam was collimated to about 0.3 deg, and a 5-mm diam beam was used so that the scattering represented an average of the structure within an area of the sample of about this diameter. A recent innovation has been the introduction of a smaller pinhole, 0.3 mm in diam, giving a microbeam which makes possible the examination of the scattering from a small region of a sample or from a portion of a large spherulite. The samples are mounted between microscope slides and held in a universal stage so that the incident beam may be aligned with a region of the sample which is of interest. A low-power microscope is of value in locating and aligning such a region of the sample. By using Ansco Super Hypan film, light scattering photographs are obtained with exposure times of 1 to 5 min. With a higher-intensity light source, faster optics, and faster film, appreciably shorter exposure times should be possible and would permit kinetic studies. Smaller slit sizes down to 50 μ may be used permitting examination of structure in very small regions of samples. The smallest slit size is limited by diffraction from the slit.

Some typical scattering patterns from an unoriented medium density polyethylene film are presented in Fig. 2. The circles are drawn to indicate 5 deg of scattering angle. Two types of polarized patterns are discussed: (1) V_v patterns obtained when the polarizer in the incident beam and the analyzer in the scattered beam are both vertical, and (2) V_H patterns where the polarizer is vertical and the analyzer is horizontal.

[8] A. Plaza and R. S. Stein, J. Polymer Sci. **40**, 267 (1959).

THEORY

A qualitative analysis of the scattering patterns will be made first. It is observed that the V_v scattering patterns are elongated in the direction of polarization. An anisotropic scattering pattern of this sort is usually interpreted in terms of an oriented scattering object.[9] This cannot be the case with an unoriented polyethylene sample, particularly since the direction of extension of the scattering pattern is dependent upon the direction of polarization. Consequently, the interpretation may be made in terms of an anisotropic but unoriented arrangement of principal polarizability directions.

Polyethylene crystallites are known to be arranged in spherical aggregates called spherulites[10] with differing radial and tangential refractive indices denoted by n_r

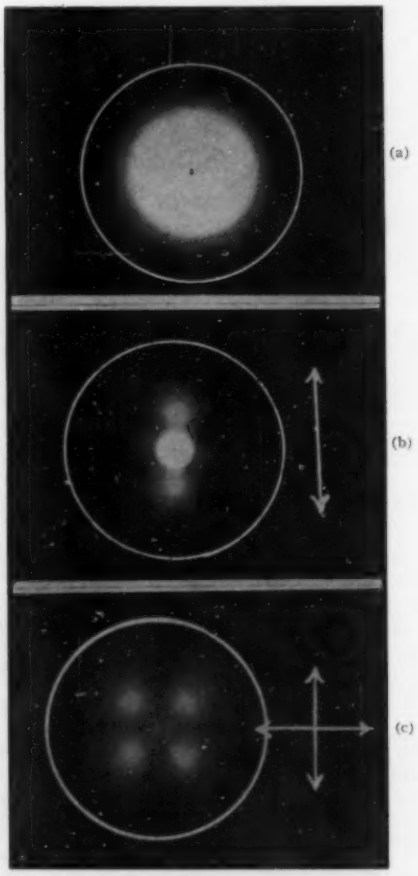

FIG. 2. Typical light scattering photographs for (a) unpolarized light, (b) V_v polarization, and (c) H_v polarization. The circles represent 5 deg of scattering angle, and the arrows represent directions of polarization.

[9] A. Gunier *et al.*, *Small Angle Scattering of X Rays* (John Wiley & Sons, Inc., New York, 1955), p. 29.

[10] W. M. D. Bryant, J. Polymer Sci. **2**, 552 (1947).

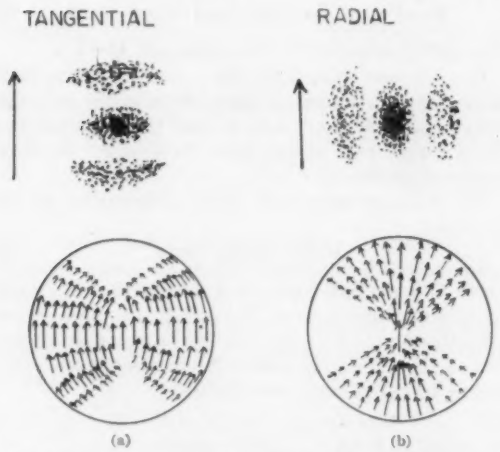

FIG. 3. The arrangement of induced dipoles and the expected V_v scattering patterns for spherulites which are (a) only polarizable tangentially and (b) only polarizable radially.

and n_t, respectively. Typical values ascribed to these by Bryant are $n_r = 1.514$ and $n_t = 1.516$ for low-density polyethylene. This optical anisotropy is a consequence of the arrangement of the anisotropic crystallites within the spherulites. The orthorhombic crystals have principal refractive indices of 1.514, 1.519, and 1.575 along their *a*, *b*, and *c* axes, respectively.[11] The high-refractive index direction is that of the *c* axis along which lies the polyethylene chain. The crystals are believed to be oriented within the spherulites with their *b* axes radial and their *a* and *c* axes tangential.[12] Consequently, assuming complete crystallinity and perfect orientation of crystals within spherulites, this would give $n_r = 1.519$ and $n_t = (1.514 + 1.575)/2 = 1.545$. The difference between these, -0.026, is about ten times as great as the spherulite birefringence. This may be attributed to (a) partial crystallinity of the spherulite, (b) imperfect orientation of crystals within spherulites, (c) orientation of amorphous regions of spherulites, and (d) form birefringence.[13]

Let us consider two idealized cases illustrated in Fig. 3. In (a) it is assumed that the electrons within the spherulite may only be displaced in a tangential direction. It is apparent that for vertically polarized light, dipoles are induced in only the equatorial regions of the spherulite. The scattering pattern, which is most elongated in the direction of smallest extension of the spherulite,[9] is extended in the vertical direction. In case (b), where the electrons may move only along the radii of the spherulite, the induced dipoles are principally in the polar regions and the scattering pattern is extended horizontally. For isotropic spherulites, radial and tangential motion of the electrons is equally easy, and induced dipoles are uniformly arranged throughout the spherulite. The scattering pattern will be the sum of those for cases (a) and (b) and will have circular symmetry. The observed extension of the V_v scattering pattern in the polarization direction corresponds to case (a) and indicates that it is the tangential component of polarizability which gives rise to scattering. The low intensity of scattering in the direction perpendicular to polarization observed in Fig. 2(b) indicates that the radial polarizability contribution is negligible. This probably arises because of destructive interference among adjacent spherulites.

The cloverleaf type pattern obtained with crossed polaroids may also be understood in terms of spherulite anisotropy. For vertical polarization of the incident light, the induced dipoles are distributed as in Fig. 3(a). If these are viewed through a horizontally oriented analyzer, the large dipoles along the equator will be oriented perpendicularly to the analyzer and will not contribute to the scattered light passed by the analyzer. It will be the dipoles in planes of the spherulite oriented at 45 deg to both the polarizer and analyzer that will make the maximum contribution to scattering. The arrangement of these is indicated in Fig. 4. The cloverleaf arrangement of these is apparent.

It is also apparent that in isotropic spherulites, the induced dipole will be oriented in the direction of polarization of the incident light, and no scattered light will be transmitted through an analyzer perpendicular to this. Consequently, the H_v component of scattering for isotropic spherulites will be zero.

The qualitative predictions may be quantitatively justified in a calculation similar to that of Goldstein.[14]

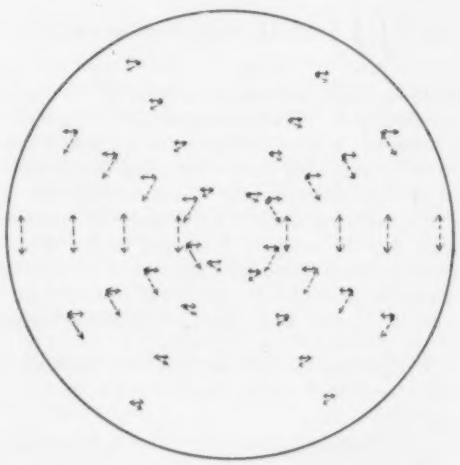

FIG. 4. The arrangement of induced dipoles in a tangentially polarizable spherulite which will contribute to H_v scattering. The dotted arrows represent the strength of the induced dipoles, while the solid arrows represent the component of this passing through a horizontal analyzer.

[11] C. W. Bunn and R. de Daubeny, Trans. Faraday Soc. **50**, 1173 (1954).
[12] A. Keller, J. Polymer Sci. **17**, 291 (1955).
[13] A. Keller, J. Polymer Sci. **17**, 351 (1955).
[14] M. Goldstein, J. Polymer Sci. **20**, 413, 578 (1956).

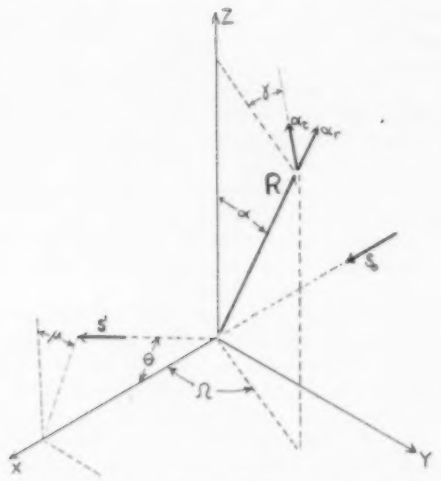

FIG. 5. The coordinate system used in describing the scattering from an anisotropic spherulite.

The scattering is described in terms of the coordinate system shown in Fig. 5. The vertical direction is taken as the z axis and the incident light beam propagates in the x direction. The scattering element has radial and tangential polarizabilities, α_r and α_t, respectively, and is located in the spherulite by the polar coordinates r, α, and Ω. The direction of the scattered ray is described in terms of the conventional scattering angle θ and the azimuthal angle μ.

The amplitude of the scattered ray is expressed in terms of the conventional type integral[15]

$$E=K\int\int\int(\mathbf{M}\cdot\mathbf{O})\cos k(\mathbf{r}\cdot\mathbf{S})r^2\sin\alpha d\alpha d\Omega dr, \quad (1)$$

where $\mathbf{M}$ is the dipole moment induced by the incident electric field in the volume element of the spherulite at vector distance $\mathbf{r}$ from the center of the spherulite. $\mathbf{O}$ is a unit vector lying in the direction of the electric vector of the scattered wave transmitted by the analyzer. k is the wave number $2\pi/\lambda$, where λ is the wavelength within the medium. $\mathbf{S}$ is equal to $\mathbf{S}_0-\mathbf{S}'$ where $\mathbf{S}_0$ is a unit vector in the direction of the incident light beam and $\mathbf{S}'$ is a unit vector in the direction of the scattered light beam. In terms of the coordinate system,

$$\mathbf{r}=r[(\sin\alpha\cos\Omega)\mathbf{i}+(\sin\alpha\sin\Omega)\mathbf{j}+(\cos\alpha)\mathbf{k}], \quad (2)$$

$$\mathbf{S}=(1-\cos\theta)\mathbf{i}-(\sin\theta\sin\mu)\mathbf{j}-(\sin\theta\cos\mu)\mathbf{k}. \quad (3)$$

For vertical orientation of the analyzer, $\mathbf{O}=\mathbf{k}$.

It is simplest to consider the scattering arising from the radial and tangential components of the polarizability separately, and then to add the amplitudes of the scattered rays arising from them to get the total scattered amplitude.

For V_v scattering and radial polarization of the spherulite,

$$(\mathbf{M}\cdot\mathbf{O})V_v=E_0\alpha_r\cos^2\alpha, \quad (4)$$

where E_0 is the field strength of the incident light wave at the scattering element. If Eqs. (2), (3), and (4) are substituted into Eq. (1) and the integration is performed [by expanding $\cos\mathbf{k}(\mathbf{r}\cdot\mathbf{S})$ in a series and integrating term by term], one obtains

$$Ev_v(\text{radial})=K'v_0\alpha_r\cdot\frac{3}{U^3}\Big[(SiU-\sin U)-\frac{1}{25}\cos^2\frac{\theta}{2}\cos^2\mu(4\sin U-U\cos U-3SiU)\Big], \quad (5)$$

where v_0 is the spherulite volume. SiU is the sin integral defined by

$$SiU=\int_0^U\frac{\sin x}{x}dx.$$

This amplitude is a maximum at $\mu=90$ deg where the second term (which is negative) is zero. This corresponds to maximum scattering in a plane perpendicular to the polarization direction, as was predicted in the qualitative discussion.

In the case of a tangentially polarizable spherulite, Eq. (4) must be replaced by

$$(\mathbf{M}\cdot\mathbf{O})V_v=E_0\alpha_t\sin^2\gamma\sin^2\alpha, \quad (6)$$

where γ is the angle of rotation of the tangential principal polarizability direction about the radius vector (Fig. 5). If this angle is taken as random, $\langle\sin^2\gamma\rangle=\frac{1}{2}$ and

$$(\mathbf{M}\cdot\mathbf{O})V_v=\tfrac{1}{2}E_0\alpha_t\sin^2\alpha. \quad (7)$$

For a system having cylindrical symmetry in tangential polarizability, where α_t has the same value in all directions perpendicular to the radius,

$$(\mathbf{M}\cdot\mathbf{O})V_v=E_0\alpha_t\sin^2\alpha. \quad (8)$$

If Eq. (8) is substituted into Eq. (1), one finds upon integrating that

$$Ev_v(\text{tangential})=K'v_0\alpha_t\frac{3}{U^3}\Big[(2\sin U-U\cos U-SiU)+\frac{1}{25}\cos^2\frac{\theta}{2}\cos^2\mu(4\sin U-U\cos U-3SiU)\Big]. \quad (9)$$

This amplitude will be greatest at $\mu=0$ giving rise to the most intense scattering in the polarization (vertical) direction.

The total V_v scattering is then found by adding Eqs. (5) and (9), giving

[15] See, for example, Chap. 2 of work cited in footnote 9.

$$E_{V_v}=K'v_0\frac{3}{U^3}\left\{\alpha_t[2\sin U-U\cos U-SiU]+\alpha_r[SiU-\sin U]+(\alpha_t-\alpha_r)\cos^2\frac{\theta}{2}\cos^2\mu[4\sin U-U\cos U-3SiU]\right\}. \quad (10)$$

For isotropic spherulites where $\alpha_t=\alpha_r=\alpha_0$, this reduces to

$$E_{V_v}=K'v_0\alpha_0\frac{3}{U^3}[\sin U-U\cos U], \quad (11)$$

which is the familiar equation for scattering from an isotropic sphere which is independent of the azimuthal angle μ.

For V_H scattering (which is equal to H_v at small angles), $\mathbf{O}=\mathbf{j}$ and Eq. (4) is modified to give for radial polarizability

$$(\mathbf{M}\cdot\mathbf{O})_{V_H}=E_0\alpha_r\sin\alpha\cos\alpha\sin\Omega. \quad (12)$$

For tangential polarizability, one substitutes for Eq. (8)

$$(\mathbf{M}\cdot\mathbf{O})_{V_H}=-E_0\alpha_t(\sin\alpha\cos\alpha\sin\Omega). \quad (13)$$

On proceeding as before, one finds for the scattering amplitude

$$E_{V_H}=K'v_0\frac{3}{U^3}(\alpha_r-\alpha_t)\cos^2\frac{\theta}{2}\sin\mu\cos\mu \times[4\sin U-U\cos U-3SiU]. \quad (14)$$

This will be zero in the isotropic case where $\alpha_t=\alpha_r$ and will be zero at both $\mu=0$ deg and $\mu=90$ deg. The term $\sin\mu\cos\mu$ is a maximum at $\mu=45$ deg. Consequently, this accounts for the observed cloverleaf type scattering pattern.

The foregoing equations are derived for isolated spherulites in a vacuum. In samples studied, the spherulites are imbedded in an amorphous matrix or are in intimate contact with each other. The details of the interference of the scattering of different spherulites with each other depends upon their arrangement. If one makes the approximation that the spherulite is surrounded by an isotropic uniform medium of polarizability α_s, the foregoing equations may be modified by substituting $(\alpha_t-\alpha_s)$ and $(\alpha_r-\alpha_s)$ for α_t and α_r, respectively.

The intensity of scattering is proportional to the square of the amplitude, consequently

$$I_{V_v}=Av_0^2\left(\frac{3}{U^3}\right)^2\Big[(\alpha_t-\alpha_s)(2\sin U-U\cos U-SiU)+(\alpha_r-\alpha_s)(SiU-\sin U) +(\alpha_t-\alpha_r)\cos^2\frac{\theta}{2}\cos^2\mu(4\sin U-U\cos U-3SiU)\Big]^2, \quad (15)$$

and

$$I_{H_v}=Av_0^2\left(\frac{3}{U^3}\right)^2\Big[(\alpha_t-\alpha_r)\cos^2\frac{\theta}{2}\sin\mu\cos\mu(4\sin U-U\cos U-3SiU)\Big]^2. \quad (16)$$

It is apparent that I_{V_H} arises entirely from the anisotropy of the spherulite and depends strongly upon the azimuthal angle μ. I_{V_v} contains three terms, the last of which arises from anisotropy and is dependent upon μ. The first two terms in I_{V_v} depend upon the difference between the spherulite polarizabilities and that of the surroundings and are independent of μ. The experimental observation that the V_v scattering pattern is strongly oriented in the polarization direction indicates that the last term in I_{V_v} is as large or larger than the first two. That is, the difference between the radial and tangential polarizabilities is greater than the difference between either one of them and the effective polarizability of the surroundings of the spherulite (which in this case consist of other spherulites). Thus, spherulite anisotropy is the principal cause of low-angle scattering in this case.

Typical calculated scattering patterns are presented in Figs. 6 and 7 for the case of $\alpha_t-\alpha_s=0.001$, $\alpha_r-\alpha_s=0.002$, and $\alpha_t-\alpha_r=0.003$. This would correspond to assuming (1) the spherulite birefringence reported by Bryant,[10] and (2) that the effective polarizability of the surroundings which consist of spherulites is equal to the average of the spherulite polarizabilities. The resemblance to the experimental patterns is apparent. The central region of the V_v pattern arises from the first two terms of Eq. (15) and has a density which depends upon the difference between the polarizability of the spherulite and its surroundings, while the two vertical lobes depend upon the anisotropy. The relative magnitude of these two contributions depends upon the sample and its treatment as is illustrated in the series of V_v photographs in Fig. 8.

It is apparent from the experimental H_v scattering pattern [Fig. 2(c)] and from the theory [Eq. (16)] that at a particular μ (say, $\mu=45$ deg), the intensity of scattering will go through a maximum with increasing scattering angle θ. The intensity is zero at zero angle ($U=0$) and at large angles ($U\rightarrow\infty$). This results from the dependency of the term $3/U^3(4\sin U-U\cos U-3SiU)$ of Eq. (16) on U.[16] A maximum is observed at about $U=4.0$. This corresponds to a scattering angle θ_m given

[16] This calculation was carried out by Philip Wilson.

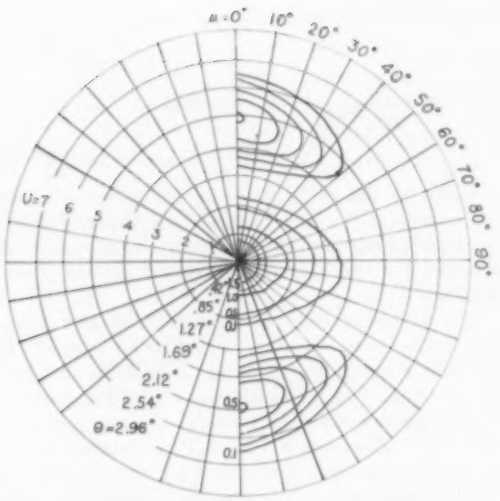

FIG. 6. One-half the calculated scattered intensity contour for V_v scattering.

by

$$4\pi\left(\frac{R}{\lambda}\right)\sin\frac{\theta_m}{2}=4.0. \tag{17}$$

Thus, the determination of the angular position of the scattering maximum serves to characterize the ratio R/λ and affords a rapid means for determining the average spherulite size. For example, for the geometry of our camera where the sample-to-film distance is about 30 cm and where the mercury green line is used,

$$R(\text{microns})=70/d(\text{mm}), \tag{18}$$

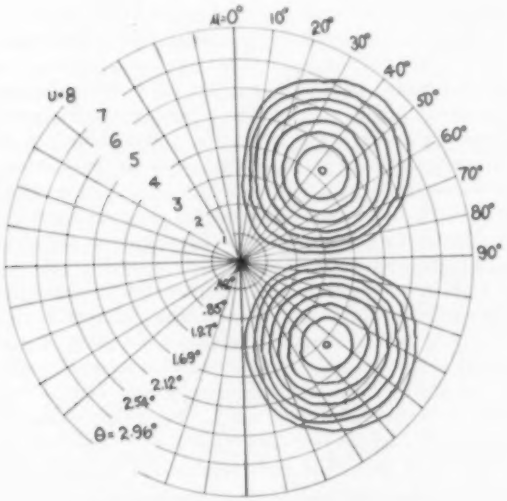

FIG. 7. One-half the calculated scattered intensity contour for V_H scattering.

where d is the distance on the H_v photograph from the incident beam to the maximum. Since values of d from 3 to 100 mm may be measured readily in this manner, spherulites having radii in the range of 25 μ down to 1 μ may be measured in this manner. Figure 9 gives a plot of some spherulite radii measured by this method compared with radii estimated from measurements of average size using a microscope with a micrometer eyepiece.

Spherulites smaller than 1 μ should give similar scattering patterns at greater angles, and these could be studied most conveniently using a similar theoretical interpretation with photometric data.

CHANGES ON HEATING AND COOLING

It has been pointed out[2,3,6,17,18] that on heating a polyethylene sample, the scattering gradually decreases; however, on cooling, the scattering rapidly

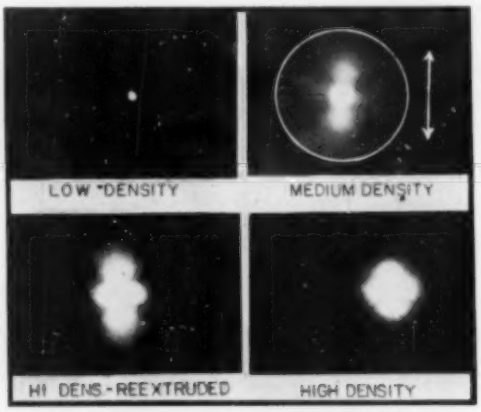

FIG. 8. Some typical V_v scattering patterns for a number of polyethylene samples.

increases from the low value of melt scattering, decreases, and then increases again with decreasing temperature. The photographic V_v scattering patterns accompanying the cooling are presented in Fig. 10. The patterns do not represent equilibrium states of the material, and there is about a 15-min time interval between each picture. On cooling to about 121°C, the pattern which first develops is not oriented with respect to the vertical polarization direction. This intensifies until about 117.5°C, after which the scattering decreases to a minimum at about 114°C. With further cooling, a new pattern develops which is extended in the polarization direction. This is typical of the room temperature scattering which results principally from spherulite anisotropy. With H_v polarization, no scattering is observed until the sample has cooled to about

[17] M. B. Rhodes and R. S. Stein, J. Polymer Sci. (to be published).
[18] F. Zernicke and J. A. Prins, Z. Physik 41, 184 (1927).

114°C, after which the typical cloverleaf pattern gradually develops.

The changes occurring may be explained readily in terms of Eq. (15). The crystallization is believed to occur in two steps: (1) a growth of spherulites from nuclei which have a degree of crystallinity characteristic of the growth temperature and which grow until they are volume filling, and (2) an intraspherulitic crystallization occurring as the temperature is lowered, resulting in an increase of the degree of crystallinity of the spherulites without change in size. The changes occurring in process (1) are indicated in (A), (B), and (C) of Fig. 11. State (B), where the polymer is about half-filled with spherulites, corresponds to the scattering maximum at about 117.5°C. The scattering of an isolated spherulite in this state is given by Eq. (15) where α_s is the polarizability of the amorphous phase. Under

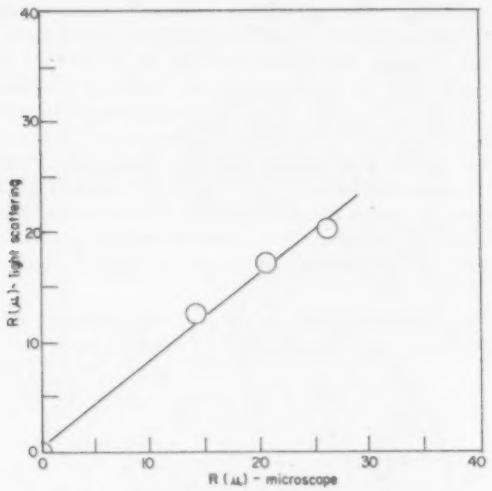

FIG. 9. A comparison of spherulite radii measured by microscope and by light scattering.

these conditions $(\alpha_t-\alpha_s)$ and $(\alpha_r-\alpha_s)$ are each about 0.01 as compared with $(\alpha_t-\alpha_r)$, which is about 0.001 (assuming the spherulites are at about 50% of their room temperature crystallinity). Consequently, the first two terms of Eq. (15) dominate, and the scattering will be independent of μ (the scattering pattern will not be oriented with respect to the polarization direction).

The effect of interspherulitic interference in this state may be semiquantitatively interpreted in terms of the equation of Zernicke and Prins[18]:

$$I_{V_v}=NVI^0{}_{V_v}\left\{1-N\int_0^\infty[1-P(r)]\frac{\sin hr}{hr}4\pi r^2dr,\right. \quad (19)$$

where N is the number of spherulites per unit volume, $I^0{}_{V_v}$ is the intensity scattering from the isolated spherulite, V is the volume of the sample, $P(r)$ is the radial distribution function of spherulite centers separated by distance r, and $h=4\pi\sin(\theta/2)/\lambda$. An approximate form for this is[19]

$$I_{V_v}=\frac{NVI^0{}_{V_v}(U)}{1+8N\mathfrak{v}_0\epsilon F_0(2U)}, \quad (20)$$

where ϵ is a constant close to one, $\mathfrak{v}_0$ is the volume of the spherulite and

$$F_0(x)=(3/x^3)(\sin x-x\cos x). \quad (21)$$

$U=4\pi(R/\lambda)\sin(\theta/2)$ as before.

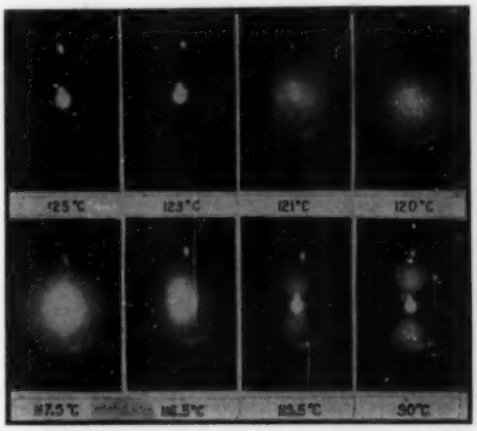

FIG. 10. The change in the V_v scattering pattern on slowly cooling a polyethylene sample from the melt. The polarization direction is vertical.

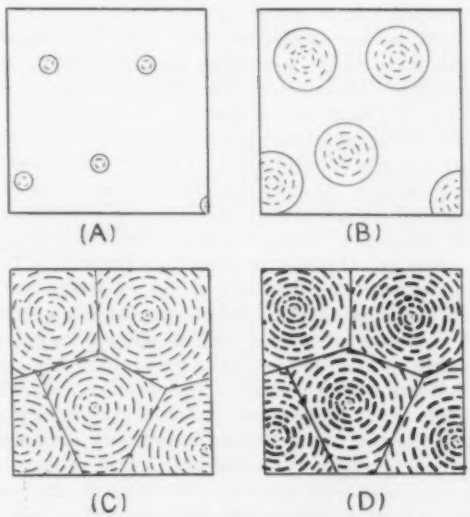

FIG. 11. The changes occurring during the slow crystallization of a polymer as the temperature is lowered.

[19] G. Fournet, Compt. rend. 228, 1421, 1801 (1949).

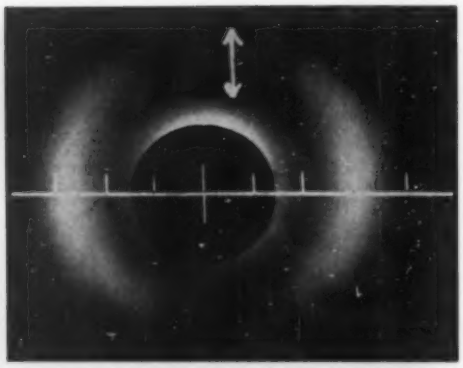

FIG. 12. The V_v scattering pattern for a polyethylene sample having "ringed" spherulites. Five-degree angular divisions are marked. The polarization direction is vertical.

As the spherulite grows, the scattering intensity first increases because of the increase in $I^0 v_v$ but then decreases with increasing interspherulitic interference with the increase of $v_0 F_0(2U)$ in the denominator.

In state (C), where the spherulites are in intimate contact, the Zernicke-Prins equations are no longer valid, and the surroundings of a given spherulite are other spherulites. Under these conditions, the simplest approach is to use Eq. (15), where now $\alpha_s = (\alpha_r + 2\alpha_t)/2$, which is about 0.001. This state corresponds to the scattering minimum at 114°C. The scattering here would be expected to be only about 1% of that at the maximum. The anisotropy scattering represented by the third term of Eq. (15) is still not large because $(\alpha_t - \alpha_r)$ is low at the low degree of crystallinity of the spherulites. Since I_{VH} depends only upon this term, its value is low in this state.

With further cooling to state (D), the degree of crystallinity of the spherulites increases, and $(\alpha_t - \alpha_r)$ correspondingly increases. The third (anisotropic) term of Eq. (15) increases, as does I_{Hv} given by Eq. (16). With subsequent heating back to the melting point, there is a gradual decrease in degree of crystallinity of the spherulites without reduction in size. This corresponds to a uniform decrease in $(\alpha_t - \alpha_r)$ in Eqs. (15) and (16) with a corresponding gradual fading away of the oriented scattering pattern (as is observed). There is a change in the intensity of the scattering pattern without change in size, indicating that the polarizabilities rather than the size of the spherulites are changing.

Swelling with a variety of solvents has little effect on the room temperature patterns. The amorphous regions of the spherulite which swell are presumably appreciably smaller than the wavelength of light and do not contribute much to scattering in the small angle region. Consequently, both α_t and α_r will be shifted about the same amount by the swelling liquid, and $(\alpha_t - \alpha_r)$ (which principally affects the scattering) does not change much.

It is believed that stages (A)—(C) of the crystallization process are irreversible while (C)—(D) is reversible. If a sample is crystallized isothermally at a temperature just under the melting point, scattering will increase and then decrease again as the spherulites grow until they fill the volume. Such spherulites will have a very low degree of crystallinity, however.

THE RING STRUCTURE OF POLYETHYLENE SPHERULITES—EXPERIMENTAL

The observed ring structure of polyethylene spherulites has been attributed to radial periodicity of crystallite orientation.[20–22] This conclusion has been confirmed by light scattering studies.[23,24] A typical light scattering photograph with V_v polarization for an unoriented polyethylene sample having "ringed" spherulites is presented in Fig. 12.[25] The lines on the horizontal scale indicate 5-deg divisions. Most of the low-angle scattering of the type discussed in the previous sections occurs at angles less than 5 deg and is blocked out by a central mask. The diffraction ring at about 13 deg is much weaker in intensity than the low-angle scattering and required about an hour exposure time. The maximum occurs along the equator of the pattern, indicating that it arises from a periodicity in a plane of the spherulite perpendicular to the polarization direction (Fig. 13). Since the tangential polarizability determines the dipole moment in this plane, it must be the tangential polarizability which is periodic and the radial which is constant.

FIG. 13. The pattern of induced dipoles in a spherulite having a constant radial polarizability but periodic tangential polarizability. The length of the solid lines represents the magnitude of the tangential dipoles, and the length of the dotted lines represents the magnitude of the induced radial dipole moment.

[20] A. Keller, J. Polymer Sci. **17**, 291 (1955); **39**, 151 (1959).
[21] F. Price, J. Polymer Sci. **37**, 71 (1959); **39**, 139 (1959).
[22] H. D. Keith and F. J. Padden, J. Polymer Sci. **39**, 101, 123 (1959).
[23] R. J. Clark, R. L. Miller, R. S. Stein, and P. R. Wilson, J. Polymer Sci. **42**, 275 (1960).
[24] R. S. Stein and A. Plaza, J. Polymer Sci. (to be published).
[25] These experiments were conducted by A. Plaza.

One cannot conceive of a model involving periodically varying density or degree of crystallinity which would result in periodicity of tangential polarizability and not radial. The results are nicely explained in terms of the Keller-Price proposal, in which the b axis of the crystal is radial, and the a and c axes are tangential and rotate about the radius in a helicoidal manner. Since the refractive index in the c direction is greater than that in the a, this gives rise to a periodicity in tangential polarizability with changing distance from the center of the spherulite.

THEORY FOR RING SCATTERING

Only the V_v type scattering will be considered. The radial polarizability contribution to scattering, $(Ev_v)_b$, is given by Eq. (5), where now $\alpha_r = f\alpha_b$. α_b is the crystal polarizability along the z axis, and f is a factor less than one to correct for imperfect crystal orientation and amorphous content of the spherulite.

There will be two contributions to the tangential polarizability. One of these arises from the principal polarizability along the a axis of the crystal, and is given by modifying Eq. (6) to give

$$(\mathbf{M}\cdot\mathbf{O})v_v = E_0 f\alpha_a \sin^2\gamma \sin^2\alpha. \tag{22}$$

The other contribution arises from the principal polarizability along the c axis which is perpendicular to the a and b axes and is

$$(\mathbf{M}\cdot\mathbf{O})v_v = E_0 f\alpha_c \cos^2\gamma \sin^2\alpha. \tag{23}$$

It is assumed that f is identical for the principal directions. The amplitudes of the scattered ray arising from these three components of principal polarizability may be calculated separately and added together.

In this case the angle γ does not vary randomly but is a periodic function of r, the distance from the center of the spherulite. γ is assumed to vary with r according to the equation

$$\gamma = 2\pi r/d = 2\pi n r/R, \tag{24}$$

where d is the radial distance for a complete rotation of the crystal, and n is the number of periods of rotation in the radius of the spherulite R. If Eqs. (24), (23), (3), (2), and (1) are combined, one obtains for the V_v component of scattered field strength arising from the polarization of the crystals along their c axes

$$(Ev_v)_c = KE_0 f\alpha_c \int_{r=0}^{R}\int_{\Omega=0}^{2\pi}\int_{\alpha=0}^{\pi} \Big\{ \sin^3\alpha \cos^2\Big(\frac{2\pi n r}{R}\Big) \times \cos k[(1-\cos\theta)\sin\alpha\cos\Omega - \sin\theta\sin\mu\sin\alpha\sin\Omega - \sin\theta\cos\mu\cos\alpha] \Big\} r^2 d\alpha d\Omega dr. \tag{25}$$

After integrating and adding to a similar integral for $(Ev_v)_a$ and to the result for $(Ev_v)_b$, this gives for the total V_v scattered field strength in the special case of $\mu = 90$ deg (equatorial scattering)

$$Ev_v = \frac{K''}{h^2}\Big\{\alpha_b[SiU - \sin U] + \Big(\frac{\alpha_a+\alpha_c}{2}\Big)[2\sin U - SiU - U\cos U] + \Big(\frac{\alpha_c-\alpha_a}{2}\Big)\Big[\frac{2\sin U}{(b^2-1)^2} + \frac{U\cos U}{b^2-1} - \tfrac{1}{2}Si[(b+1)U] + \tfrac{1}{2}Si[(b-1)U]\Big]\Big\}, \tag{26}$$

where $b = 4\pi n/U$ and, as before, $U = 4\pi(R/\lambda)\sin(\theta/2)$. In the special case where $\alpha_a = \alpha_c = \alpha_t$ and $\alpha_b = \alpha_r$, this reduces to Eq. (10), where $\mu = 90$ deg. If $\alpha_a = \alpha_b = \alpha_c$, this reduces to Eq. (11) for an isotropic sphere. The third term of Eq. (26) is the one which depends upon the periodicity in crystal orientation through the parameter b. This term becomes large when $b = 1$, in which case the denominators of some of the terms become zero. This condition leads to

$$b = \frac{4\pi n}{U} = \frac{4\pi(R/d)}{4\pi(R/\lambda)\sin(\theta/2)} = \frac{\lambda}{d\sin(\theta/2)},$$

or

$$\lambda = d\sin(\theta/2) \tag{27}$$

as the condition for an equatorial scattering maximum.[26]

[26] It should be noted that this is an approximate condition. The correct procedure would involve differentiating Eq. (25) with respect to U and equating to zero.

Since each half-rotation of the crystal will bring the crystal into optically equivalent positions, there will be two rings visible per rotation of the crystal. Therefore, the spacing between rings is $\rho = d/2$, so that Eq. (27) becomes

$$\lambda = 2\rho\sin(\theta/2). \tag{28}$$

This is the analog of Bragg's diffraction equation for diffraction from the inter-ring identity period ρ. The Bragg diffraction angle is equivalent to half the scattering angle. An experimental check of this prediction indicates approximate agreement between the angular position of the scattering maximum and that calculated from the microscopically measured ring spacing. For example, a sample exhibiting ring spacing of 1.8 μ exhibits a scattering maximum[20] at 13 deg. The θ calculated from Eq. (28) is 12 deg.

Equation (26) contains three terms, the first two of which represent scattering from a uniform anisotropic

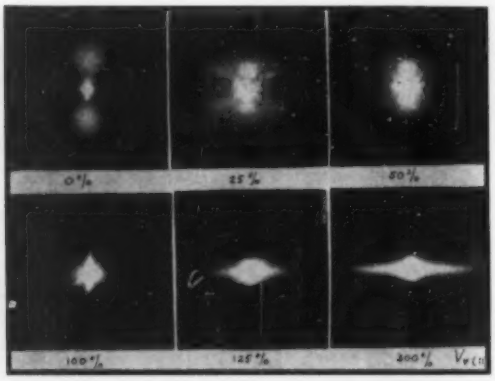

FIG. 14. The change in the V_v scattering pattern for polyethylene with percentage elongation. The stretching direction is vertical.

sphere, while the third represents the contribution from the "ring" structure. For an isolated sphere, the first two terms will be much larger than the third so that the diffraction maximum from the rings will not be observable. However, for a sphere imbedded in a uniformly polarizable environment of polarizability α_s, the polarizabilities $f\alpha_a$, $f\alpha_b$, and $f\alpha_c$ in Eqs. (22) and (23) should be replaced by $(f\alpha_a-\alpha_s)$, $(f\alpha_b-\alpha_s)$, and $(f\alpha_c-\alpha_s)$, respectively. This will, as in the previous case, reduce appreciably the contribution of the first two terms in Eq. (26), but not that of the third term.

EFFECT OF STRETCHING

Figures 14, 15, and 16 are typical scattering patterns for a polyethylene sample which has been stretched. Figures 14 and 15 are V_v patterns in which the polarization direction is vertical. In Fig. 14 the stretching direction is vertical, while in Fig. 15 it is horizontal. Figure 16 is an H_v pattern with the stretching direction horizontal. It is apparent that the pattern changes from

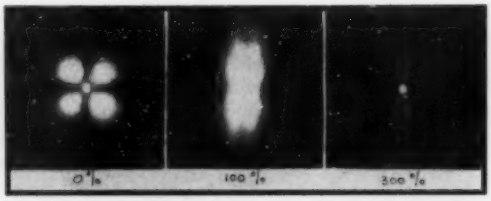

FIG. 16. The change in the H_v scattering pattern for polyethylene with percentage elongation. The stretching direction is horizontal.

the typical low-angle scattering patterns of Fig. 2 to a pattern which is extended perpendicular to the stretching direction. This would indicate that the greatest dimension of the scattering object is in the stretching direction. The pattern for the stretched sample is most intense when the polarization corresponds to the stretching direction indicating that this is the direction of greatest polarizability.

Thus, on stretching, the system changes from one of spherical symmetry with greatest polarizability in a tangential direction to one which is extended and has its greatest polarizability in the stretching direction. This represents a change from spherulite to fiber morphology, and a quantitative interpretation of these patterns will serve to characterize the details of this transformation.

The over-all reduction in scattering on stretching is apparent, which is in agreement with the observed clarification of samples. The reduction in the amount of H_v scattering on stretching is particularly striking. This is related to the fact that the dipoles contributing principally to H_v are those at about 45 deg to the stretching direction [which makes $\sin\alpha\cos\alpha$ a maximum in Eqs. (12) and (13)]. On stretching, the principal polarizability direction becomes aligned in the stretching direction (α approaches 0 deg) and the contribution to scattering decreases.

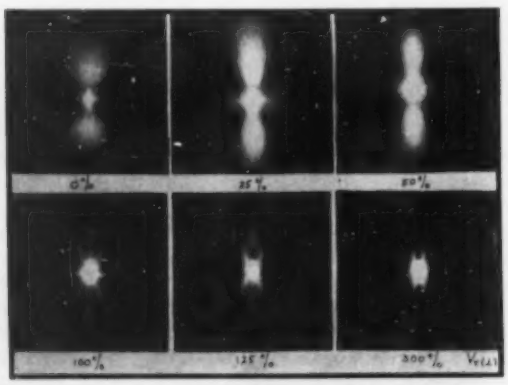

FIG. 15. The change in the V_v scattering pattern for polyethylene with percentage elongation. The stretching direction is horizontal.

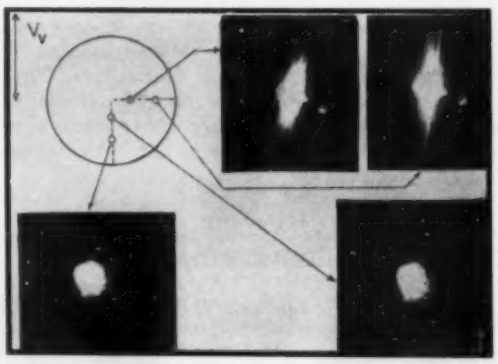

FIG. 17. Typical horizontal and vertical radial scattering photographs for V_v polarization from the indicated positions within a single polyethylene oxide spherulite.

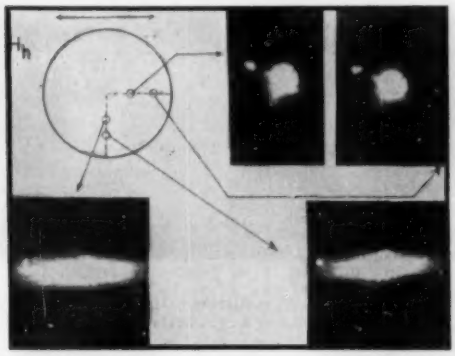

FIG. 18. Typical horizontal and vertical radial scattering photographs for H_H polarization from the indicated positions within a single polyethylene oxide spherulite.

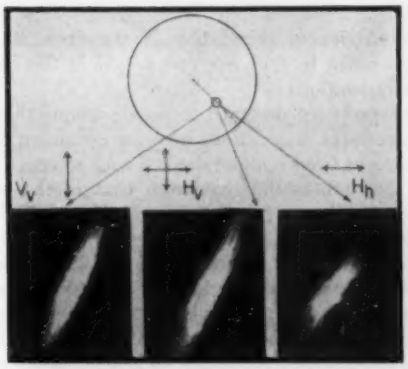

FIG. 20. A typical 45-deg scattering photograph for V_v, H_H, and H_v polarization.

SINGLE SPHERULITE SCATTERING

In this study, photographic light scattering experiments on large spherulites of polyethylene oxide 5–10 mm in diameter are reported. (These were selected Carbowax samples furnished through the kindness of Dr. F. P. Price of the General Electric Research Laboratories.) The large spherulites were grown isothermally between microscope slides and cover glasses at 50°C (for a sample with a melting point of 63°C). They formed coherent films of abutting two-dimensional spherulites about 20 μ thick.

By moving the sample relative to the light beam, which was small compared with the spherulites, patterns were obtained by scanning a spherulite along a horizontal radius, a vertical radius, and a 45-deg radius for V_v, H_H, and H_v polarization. These are presented in Figs. 17—20.

It is apparent that all scattering patterns have preferential elongation in a direction tangential to the spherulite. The intensity and elongation of the pattern is greatest when the direction of polarization is tangential. There is not much variation of the pattern with distance from the center of the spherulite.

The anisotropic shape of the scattering pattern indicates a scattering entity which is anisotropic in a reciprocal direction.[9] Since the scattering pattern has its greatest dimension tangentially, the scattering object must be most extended radially. The polarization dependency indicates that the scattering object is anisotropic in polarizability. Since the intensity of scattering is appreciable only when the direction of polarization is tangential, the polarizability fluctuations must be greatest in this direction. The tangential direction has been observed to be that of greatest polarizability for these[18] as well as other polymeric spherulites.

These scattering patterns indicate that the local polarizability varies in the radial and tangential direction of the spherulite in the manner indicated in Fig. 21. This would be consistent with a fiber or plate-like structure of the spherulite where the long direction of the fiber or plate is radial and where the greatest refractive index is perpendicular to this direction. The tangential fluctuation in polarizability may result from low refractive index material between platelets or fibers, or

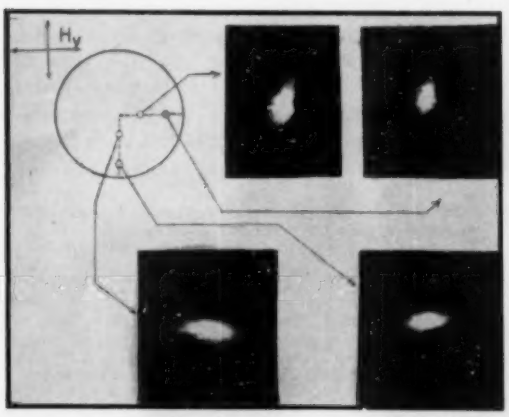

FIG. 19. Typical horizontal and vertical radial scattering photographs for H_v polarization from the indicated positions within a single polyethylene oxide spherulite.

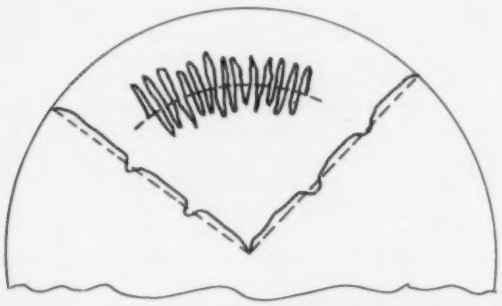

FIG. 21. The postulated variation of the local spherulite polarizability in the radial and tangential direction.

from imperfect radial orientation with a periodic angular fluctuation of orientation of the fibers or plates corresponding to the observed period of the polarizability fluctuations.

An experiment designed to decide among these possible causes of fluctuations involves obtaining scattering patterns from samples swollen with solvents having refractive indices different from that of the sample. Solvents used were methyl phenyl ether, carbon tetrachloride, acetone, propylene glycol, cyclohexanone, nitrobenzene, and a number of silicone fluids representing a refractive index range of 1.35 to 1.55 as compared with an approximate sample refractive index of 1.46. Some solvents such as acetone practically dissolved the sample. Typical results for an unswollen sample and one swollen in carbon tetrachloride are presented in Fig. 22. In no case was there an appreciable change in the scattering pattern.

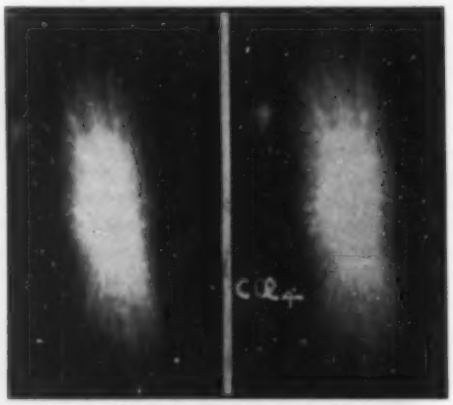

(a) (b)

FIG. 22. The V_v scattering pattern for (a) an unswollen sample, and (b) one swollen with carbon tetrachloride.

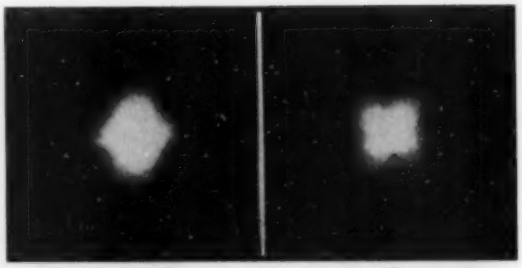

V_v H_v

FIG. 23. The V_v and H_v scattering patterns for quenched polyethylene oxide samples using a light beam large as compared with the spherulites.

It is known that partly crystalline polymers are swollen preferentially in their amorphous regions. If the refractive index fluctuation causing scattering is due to refractive index differences between crystalline and amorphous regions or between sample and microvoids, swelling should change this difference appreciably and greatly affect the scattering. Therefore, it would appear that orientational differences are the most probable cause of scattering. This would be in agreement with the conclusions arrived at for scattering by polyethylene spherulites and by the shorter-range macrostructure in polyethylene.

Scattering patterns for quenched samples of polyethylene oxide having spherulite sizes smaller than the light beam have been obtained (Fig. 23). These were obtained using the earlier apparatus.[8] It is noted that these are similar to patterns obtained with polyethylene samples having microscopic spherulites.[8] Consequently, it is probable that the polyethylene spherulites have an internal structure similar to polyethylene oxide. It has not been possible to grow large enough spherulites of polyethylene to make single spherulite light scattering studies using the present techniques.

Stress as a Reduced Variable: Stress Relaxation of SBR Rubber at Large Strains*

ROBERT F. LANDEL AND PAUL J. STEDRY
Jet Propulsion Laboratory, California Institute of Technology, Pasadena 3, California

Stress relaxation measurements on SBR were carried out at temperatures from −5 to +60°C and at initial strains of up to 550%. The effects of strain and time were found to be factorable, so that the isochronal stress-strain curve may be written as a modified Hooke's law with a time dependent modulus: $S=E(t)ef(\alpha)$, where $f(\alpha)$ is an appropriate function of the strain. By defining a strain-reduced stress $S^*=S/f(\alpha)$, i.e., a strain-reduced modulus $E^*(t)=E(t)f(\alpha)$, it can be shown that Ferry's method of reduced variables may be extended to large deformations. An appropriate strain function was obtained from the empirical Martin-Roth-Stiehler equation [Trans. Inst. Rubber Ind. **32**, 189 (1956)] as $f(\alpha)=\alpha^{-2}\exp A(\alpha-\alpha^{-1})$ with $A=0.40$. Although it cannot yet be certain that A is truly a constant and the same for all elastomers, this equation has the advantage of being valid right out to the breaking strain.

INTRODUCTION

THE reduced variable concept for linear viscoelastic behavior covering the effects of time, temperature, and concentration (for solutions) proposed by Ferry[1] ten years ago has proven to be eminently successful as a method of showing the interactions between these parameters and of correlating data obtained over wide ranges in them.[2] In principle this treatment is limited to deformations sufficiently small for an isochronal stress-strain relationship to be considered linear. Nevertheless, it has been found that ultimate properties have the same time and temperature interdependence as small deformation properties.[3,4] Therefore, one would like to be able to extend the reduced variable treatment to the nonlinear region, i.e., to larger deformations. A most promising start in this direction has been reported by Mason[5] since the inception of this work. We report these results on the basis of a somewhat different outlook on the same problem and an extension to even higher strains.

Linear behavior is here taken to represent behavior which can be described in terms of an array of Hookean springs and Newtonian dashpots. The total response of the array may not be linear in that the stress may not be proportional to the strain or rate of strain, particularly under dynamic conditions, but that of the individual elements is. Extension to nonlinear elements is possible, but leads to mathematical difficulties which are not easily solved.[6,7] The restriction to linearity is now examined and a method of circumventing it is proposed.

The most general expression of the tensile stress-strain law simply states that the stress based on the initial cross-sectional area S is proportional to the strain e through some function f of time t, absolute temperature T, and strain e or extension ratio $\alpha(=e+1)$.

$$S=ef(t,T,\alpha). \tag{1}$$

For small deformations the effects of time and temperature are factorable, though interrelated through the Ferry shift factor a_T. Thus Eq. (1) can be rewritten as

$$S=ef(\alpha)g(T)h(t/a_T), \tag{2}$$

where for small deformations $f(\alpha)$ is unity and $g(T)h(t/a_T)$ is the time and temperature dependent Young's modulus $E(T,t/a_T)$. The latter is directly proportional to T, so $g(T)$ is simply T and $h(t/a_T)$ equals $T^{-1}E(t/a_T)$. But if the effects of large strains are also factorable, then at any given temperature there results a modified Hooke's law

$$S=E(t)ef(\alpha). \tag{3}$$

Therefore this equation can be linearized by defining a strain-reduced stress S^* as $S/f(\alpha)$ and the resulting expression can be used in the standard equations for viscoelastic behavior derived for spring-dashpot arrays. This factorization is tacitly assumed but not explicitly demonstrated by Mason.[5]

What we propose to try then, is to choose the proper form of $f(\alpha)$ in order to be able to calculate S^*, and then employ this reduced-stress, stress-strain curve in subsequent calculations. Therefore, as a first step in this process the various proposed forms of $f(\alpha)$ must be evaluated to see which expression will most adequately describe experimental results and so give the required analytic representation. Note, however, that this evaluation must be carried out at constant $E(t)$. This can be done in one of two ways: either by making stress relaxation or creep measurements and considering isochronal data, or by making actual stress-strain measurements at such high temperatures and low strain rates that $E(t)$ will be at its equilibrium value and constant throughout the course of the experiment.

One of the first difficulties encountered in attempting to describe nonlinear viscoelastic systems is the require-

* This paper presents the results of one phase of research carried out at the Jet Propulsion Laboratory, California Institute of Technology, under contract sponsored by the National Aeronautics and Space Administration.

[1] J. D. Ferry, J. Am. Chem. Soc. **72**, 3746 (1950).

[2] For a recent summary discussion of the reduced variable treatment, see *Die Physik der Hochpolymeren*, edited by H. A. Stuart (Springer-Verlag, Berlin, 1956), especially p. 56 *et seq.* in Chap. 1 by A. J. Staverman and F. Schwarzl, and Chap. 6 by J. D. Ferry.

[3] F. Bueche, J. Appl. Phys. **26**, 1133 (1955).

[4] T. L. Smith, J. Polymer Sci. **32**, 99 (1958).

[5] P. Mason, J. Appl. Polymer Sci. **1**, 63 (1959); Trans. Faraday Soc. **440**, 1461 (1959).

[6] M. S. Green and A. V. Tobolsky, J. Chem. Phys. **14**, 80 (1946).

[7] P. J. Blatz and A. V. Tobolsky, J. Chem. Phys. **14**, 113 (1946).

ment of a suitable analytic representation of the stress-strain curve of a rubber. Although there have been a large number of equations proposed for this purpose, few are adequate over wide ranges in experimental test conditions.

In general, the proposed stress-strain equations can be subdivided into two categories, theoretical and empirical or semiempirical. In the former class we may list the modified Hooke's law, the kinetic theory expression,[8] and the Mooney-Rivlin expression.[9,10] The modified Hooke's law,

$$\alpha S = E(t)e, \tag{4}$$

can be justified on the assumption that Poisson's ratio is one-half, and so the measured stress should be corrected to a true stress by the factor α. The more fundamentally significant kinetic theory expression

$$S = (E(t)/3)[\alpha - (1/\alpha^2)] \tag{5}$$

is nonlinear, but on multiplying through by the quantity α and expanding $\alpha^2 - 1/\alpha$ in a power series an equation analogous to Eq. (1) is obtained which is approximately linear to 50% strain. This observed linearity can also be offered in support of the use of Eq. (1). A more recent improvement on the kinetic theory is the Mooney-Rivlin expression

$$S = \frac{E(t)}{6}\left(\alpha - \frac{1}{\alpha^2}\right) + 2C_2\left(1 - \frac{1}{\alpha^3}\right), \tag{6}$$

where C_2 is an additional time dependent constant which should go to zero at truly equilibrium test conditions for a well crosslinked network.[11]

Of the empirical or semiempirical equations, we should like to mention only two—that proposed by Blanchard and Parkinson[12]:

$$S = E(t)\left(\frac{1}{\alpha} - \frac{1}{\alpha^2}\right)\exp B(\alpha - 1), \tag{7}$$

and a purely empirical expression discovered by Martin, Roth, and Stiehler (MRS)[13]:

$$S = E(t)\left(\frac{1}{\alpha} - \frac{1}{\alpha^2}\right)\exp A\left(\alpha - \frac{1}{\alpha}\right). \tag{8}$$

Equation (8) was devised as a curve fitting scheme for isochronal stress-strain data obtained from creep curves by replotting the strain increments observed at a given time. One of the more interesting conclusions of this study was the fact that the parameter A had a nearly constant value of 0.38 for all the rubbers studied: natural, butyl, styrene-butadiene, and nitrile.

In a separate study[14] on the actual stress-strain behavior at high temperatures and low strain rates of a polyurethane rubber, and from SBR data of Smith,[4] it has been found that of all the suggested equations only the MRS equation, Eq. (8), adequately describes the behavior. Moreover, it does so over the whole stress-strain curve, right out to the breaking strain. It is surprising to us that so simple an expression—it really contains only two arbitrary parameters—can describe the stress behavior over the complete range of strain. Since Eq. (8) can be rearranged to

$$\log(\alpha^2 S/e) = \log E(t) + 0.434A(\alpha - 1/\alpha), \tag{9}$$

a plot of $\log \alpha^2 S/e$ vs $\alpha - 1/\alpha$ should be linear with the slope $0.434A$, provided $E(t)$ is constant.

As an illustration, Fig. 1 shows such a plot for three samples of polyurethane tested as ring-shaped specimens. The breaking strain in this case was 225%. The plot is linear as required and $E(t)$ is found to have essentially the same value as found from the use of Eqs. (2) and (3) on the same data at smaller strains. However, these experiments indicated a value of A which, though reasonably constant for a given rubber, varied between 0.4 and 0.5. This is in contrast to the reported value of 0.38. On the other hand, the experiments may not have been carried out under conditions

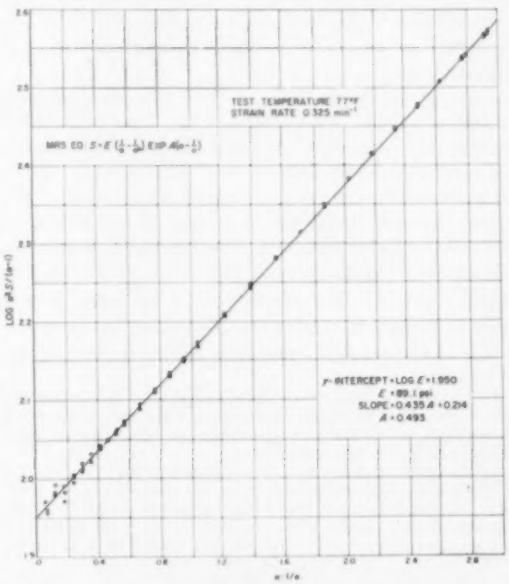
TEST TEMPERATURE 77°F
STRAIN RATE 0.325 min⁻¹
MRS EQ S=E(1/α − 1/α²) EXP A(α − 1/α)
y-INTERCEPT = LOG E = 1.950
E = 89.1 psi
SLOPE = 0.435 A = 0.214
A = 0.493
LOG α²S/e (psi)
α − 1/α

FIG. 1. Stress-strain data for a polyurethane elastomer, plotted as suggested by Eq. (9).

[8] P. J. Flory, *Principles of Polymer Chemistry* (Cornell University Press, Ithaca, New York, 1953).
[9] M. Mooney, J. Appl. Phys. **11**, 582 (1940).
[10] R. S. Rivlin and D. W. Saunders, Phil. Trans. **A243**, 251 (1951).
[11] A. Ciferri and P. J. Flory, J. Appl. Phys. **29**, 1498 (1959).
[12] A. F. Blanchard and D. Parkinson, Ind. Eng. Chem. **44**, 799 (1952).
[13] G. M. Martin, F. L. Roth, and R. D. Stiehler, Trans. Inst. Rubber Ind. **32**, 189 (1956).
[14] R. F. Landel, P. J. Stedry, and T. L. Smith (unpublished).

sufficiently close to equilibrium, so that $E(t)$ may not have been constant as assumed. Therefore it became imperative to test the expression on isochronal data.

Such data were obtained as stress relaxation moduli measured during the course of a study whose primary aim was simply to examine the influence of strain on the time to rupture.[15] The present work was included as a corollary to test the MRS equation as indicated above and to provide data for an experimental test of the reduced variable concept.

EXPERIMENTAL

The styrene-butadiene rubber was obtained from the National Bureau of Standards. It contains 23.5% styrene and has an average molecular weight between crosslinks of 15 800, as determined by swelling experiments in several solvents. A more complete description is given in footnote 15.

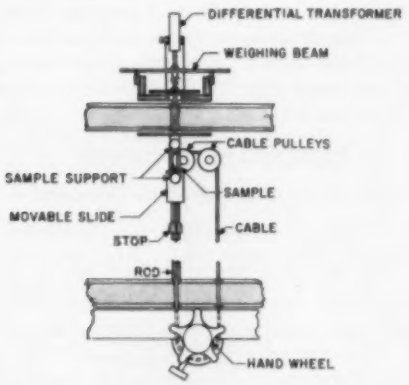

FIG. 2. Sketch of the stress relaxometer.

The test specimens were rings cut from the rubber sheets with a circular die having an inside diameter of 1.400 in. and an outside diameter of 1.650 in. The outer cut edges of the rings were always slightly concave. This slight imperfection was disregarded in calculating the cross-sectional area of the samples, and the directly observed width as measured with a micrometer was employed. The ring dimensions were 0.078(+0.002, −0.003) in. thick by 0.125(+0.004, −0.003) in. wide, the indicated deviations being the maximum observed. In any given run the average dimension for all samples employed in that run was used in calculating the stress.

The stress relaxometer was a specially constructed apparatus shown in Fig. 2. The load cell was a simply supported beam whose motion under load was detected by a linear variable differential transformer. A Wiancko carrier system provided a stable 1000 cps excitation

[15] T. L. Smith and P. J. Stedry, J. Appl. Phys. **31**, 1892 (1960).

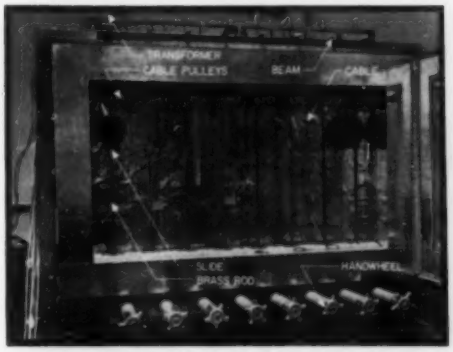

FIG. 3. Over-all view of the stress relaxometer and the air thermostat.

signal and rectified the transformer output so that the latter could be recorded with a standard recorder. The load cell was calibrated before each run by suspending a series of known weights from the beam and recording the transformer signal. The output was a linear function of the applied force, within about 1%. A small, freely rotating nylon pulley was supported from the center of the beam and a matching pulley was mounted on a slide movable along a brass rod by means of a cable and handwheel located outside the apparatus. Ring specimens could be looped over both pulleys and then extended by pulling the slide down the desired extent with the handwheel. By adjusting the position of a metal stop on the rod, the desired strain could be attained in two seconds or less. The calculation of strain was based on the inside diameter D of the ring, $e=2\Delta C/\pi D$, where ΔC is the pulley displacement.

An assembly of eight of these stress relaxometers was enclosed in a circulating air, constant temperature chamber as shown in Fig. 3. Heating was provided by a series of nichrome elements; cooling, by a mechanical refrigerator unit and a set of cooling coils. These units are mounted on the back of the chamber shown in Fig. 3. Temperature control was provided by a bimetallic thermoregulator. At temperatures near room temperature and below, the referigerator was allowed to run continuously and the requisite amount of balancing heat was provided by the heaters. The maximum spread between various points within the chamber was about 1°C. At any given point the temperature was constant within ±0.5°C over many hours, but only to within about 1.5°C over a period of days. During a test, it was necessary to bleed a stream of dry nitrogen continuously into the system to prevent condensation on the refrigerated cooling coils, because even slight condensation interfered sufficiently with the heat transfer rate to prevent the system from operating at a stable temperature. The nitrogen was also intended to reduce the possibility of oxygen and ozone attack on the stretched SBR specimens. However, a mass spectro-

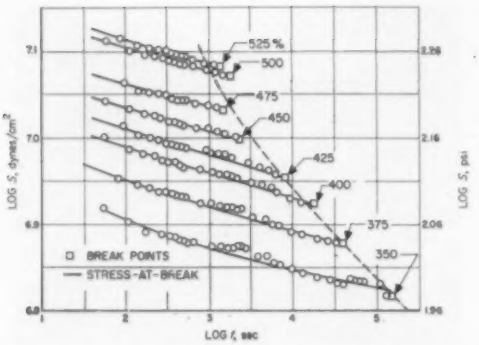

FIG. 4. Stress relaxation to break in SBR under large strains at 1.7°C. The figures indicate the percent strain initially applied.

graphic analysis[16] of the air withdrawn from the chamber showed that the oxygen content had been reduced to only about 7%, so this purpose was not fulfilled. Ozone cannot be detected as such by the mass spectrometer, since it reacts in the spectrometer to form oxygen.

The over-all accuracy of the results is limited by several factors: sample-to-sample variability; the ability to measure the sample dimensions accurately; the variation in strain rate employed during the initial elongation; the sensitivity and drift of the load measuring system, including the recorder; and temperature fluctuation. The first three factors affect the accuracy; the remainder, the precision. The most important factors are the apparatus sensitivity and, particularly at lower temperatures, the differences in the rate at which the initial strain is applied. For any given stress relaxation experiment, the precision is estimated to be $\pm 5\%$, while the over-all accuracy at any given temperature is estimated to be $\pm 10 = 20\%$.

The experiments were carried out at ten temperatures between -15 and $+60$°C and at several strains between 50 and 550%, as indicated in Table I. The results at

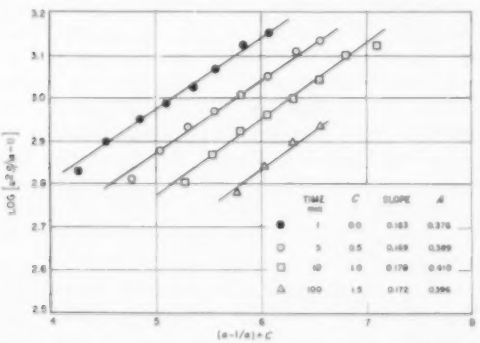

FIG. 5. Data of Fig. 4 cross plotted as indicated by Eq. (9) to find A of the MRS equation.

[16] We are indebted to Dr. William DeMore of this Laboratory for making these measurements.

TABLE I. Initial strains applied at the various temperatures.

t, °C	Strain range,[a] %
−5	275–550
1.7	325–525
7.2	325–525
12.8	200–500
18.3	150–450
40	100–350
50	50–300
60	50–300

[a] The strains were varied in 25% increments over this range.

−15 and +29.4° are omitted from subsequent discussion in this paper because the reduced modulus data are inconsistent with the data at other temperatures.

In addition, a limited number of constant strain rate tensile tests were made in order to apply the MRS equation to tensile data for this same rubber, both to obtain a value of A by this method for comparison with that obtained from isochronal data, and also to be able to construct a reduced stress-strain curve in the manner of Smith.[17] The latter is important because $E(t)$ can be calculated from such a curve and should serve as a basis of comparison with $E(t)$ obtained directly from the stress relaxation data.

RESULTS AND DISCUSSION

Determination of the MRS Constant A

Typical stress relaxation curves are shown in Fig. 4. The constant A can be evaluated from these data by interpolating the stress values at times of 1, 5, 10, and 100 minutes and crossplotting as indicated by Eq. (9). The results for the curves of Fig. 4 are shown in Fig. 5 and the value of A thus obtained is given in the figure. The value of A cannot be determined with precision.

The results for the determination of A at all temperatures are given in Table II. It can be seen that there is a slight dependence of A on both the temperature and on the time at which readings are taken. Figure 6 compares the temperature dependence of the average value of A given in Table II with that obtained in the constant strain rate experiments. Although the data, when taken

TABLE II. Constant A in MRS equation.

Temp. °C	S_1	S_5	S_{10}	S_{100}	S_{1000}	$S_{10\,000}$	Average
−5.0	0.40	0.42	0.42	0.42	0.43	0.45	0.42
1.7	0.38	0.39	0.41	0.40	···	···	0.39
7.2	0.40	0.41	0.40	0.41	0.39	0.39	0.40
12.8	0.35	0.35	0.36	0.36	0.37	0.37	0.36
18.3	0.39	0.40	0.40	0.41	0.43	0.44	0.41
40.0	···	0.43	0.43	0.44	···	···	0.43
50.0	···	0.40	0.40	0.39	0.44	···	0.41
60.0	···	0.42	0.43	0.42	0.46	···	0.42
Average	0.38	0.41	0.41	0.41	0.42	0.41	0.40 / 0.41

[17] T. L. Smith, J. Polymer Sci. **20**, 89 (1956).

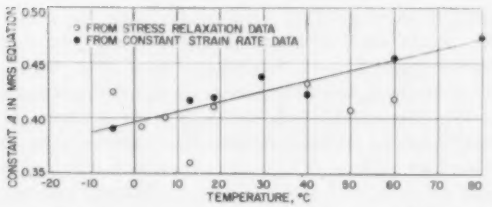

FIG. 6. Temperature dependence of the average value of A of Table I and the value found in constant strain rate experiments.

together, apparently indicate a uniform increase with temperature at a rate somewhat less than directly proportional to the absolute temperature, the constant strain rate data are suspect at lower temperatures because of the assumption of equilibrium behavior and the constancy of $E(t)$. If log $E(t)$, the intercept of plots such as Fig. 1, is decreasing while the stress-strain curve is being measured, then the effect will be to decrease the apparent value of A with decreasing temperature, as observed. The values obtained in the stress relaxation experiments do not suffer from such a defect but on the other hand, the experimental scatter is so great that one cannot decide whether or not A is temperature dependent.

The average values of A, at each temperature, also show a consistent increase with log time. If true, this would represent a serious drawback to the utility of the MRS equation. However, in view of the experimental error in determining A (see Fig. 5), it seems reasonable to use an average value of 0.40 for subsequent calculations.

Reduced Variable Treatment in Terms of Strain-Reduced Stress

Assuming that the required function of α is given by the MRS equation, and taking the value of A to be 0.40, the expression for the strain-reduced stress relaxation modulus is given by

$$E(t)=\frac{S^*}{e}=\frac{\alpha^2 S}{e}\exp -0.40\left(\alpha-\frac{1}{\alpha}\right). \qquad (10)$$

Figure 7 shows the results using the data of Fig. 4. The family of stress relaxation curves shown there has been compressed to a single modulus curve within experimental error. The latter shows up all too clearly on a plot to this scale. Nevertheless, one may draw an average curve through the results at all six strains. Figure 8 shows this average curve and the corresponding curves for other temperatures. The curve at 12.8°C seems to contain a systematic error, since it is too high relative to the other curves. The sharp drop in log $E(t)$ at 10^5 to 10^6 sec at 50° and 60° is attributed to oxidative degradation of the rubber.

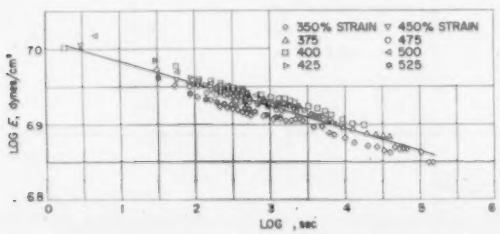

FIG. 7. Strain-reduced stress relaxation modulus calculated from the data of Fig. 4.

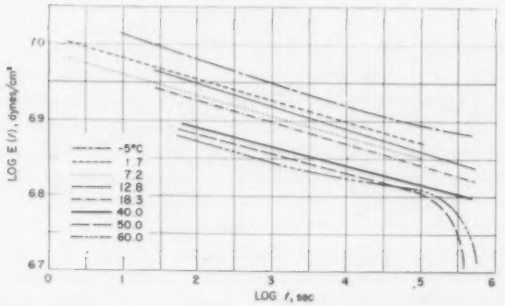

FIG. 8. Strain-reduced stress relaxation modulus of SBR at temperatures from −5 to +60°C. The initial strains range from 50 to 550%, as indicated in Table I.

These averaged curves can be superposed in the normal fashion by first converting the measured modulus to the reduced modulus[18] $E_r(t)=E(t)286°K/T$ and then subjecting these reduced modulus plots to a suitable horizontal translation along the time scale. The extent of the translation is defined as $1/a_T$. Values of a_T so obtained, as well as values from the time-to-break data,[15] are shown in Fig. 9 where they are com-

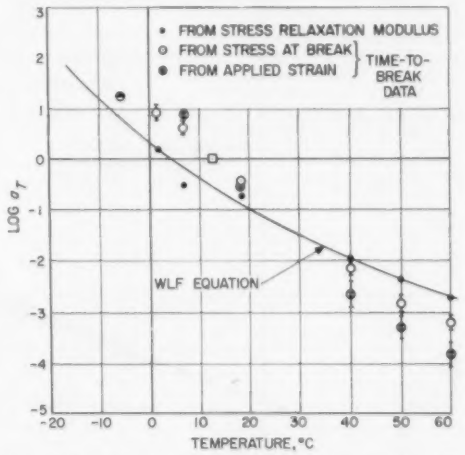

FIG. 9. Log a_T determined from superposing the data of Fig. 8. Also shown are a_T values obtained from the ultimate property and time-to-break data of footnote 15. The square shows that 12.8°C was chosen as the reference temperature for superposition.

[18] As originally defined,[2] $E_r(t)=E(t)T_0\rho_0/T\rho$, where ρ is the corresponding density. The small density correction has been omitted in these calculations.

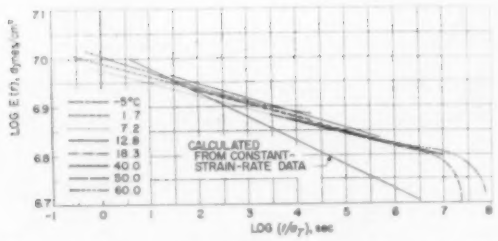

FIG. 10. Superposed strain-reduced modulus for SBR. $T_0 = 12.8°C$. Also shown are the results calculated from the constant strain rate data of Fig. 11.

pared with the values predicted by the WLF equation[19]

$$\log a_T = \frac{-17.44(T-T_g)}{51.6+T-T_g}, \qquad (11)$$

where T_g is the glass transition temperature. The agreement is rather good for the modulus data, but poor for the points from ultimate property data. The latter show a much greater dependence on T than does the WLF function. Since the reason for this discrepancy has not yet been established, the WLF curve is drawn for a best fit to the modulus results. T_g is estimated by this procedure to be $-55°C$, vs an experimental determination of $-59°C$ based on linear thermal expansion measurements.

Average log a_T values were read from Fig. 9 and used to superpose the data of Fig. 8. The results are shown in Fig. 10. Note that the sharply decreasing portions of the 50° and 60° curves do not superpose, as indeed they cannot if the effect is due to degradation.

The curves are too flat to afford a positive test of superposition. A better test is afforded by the comparison of moduli data obtained at different ranges of the real time scale. For this purpose we compare the stress relaxation modulus calculated from a reduced

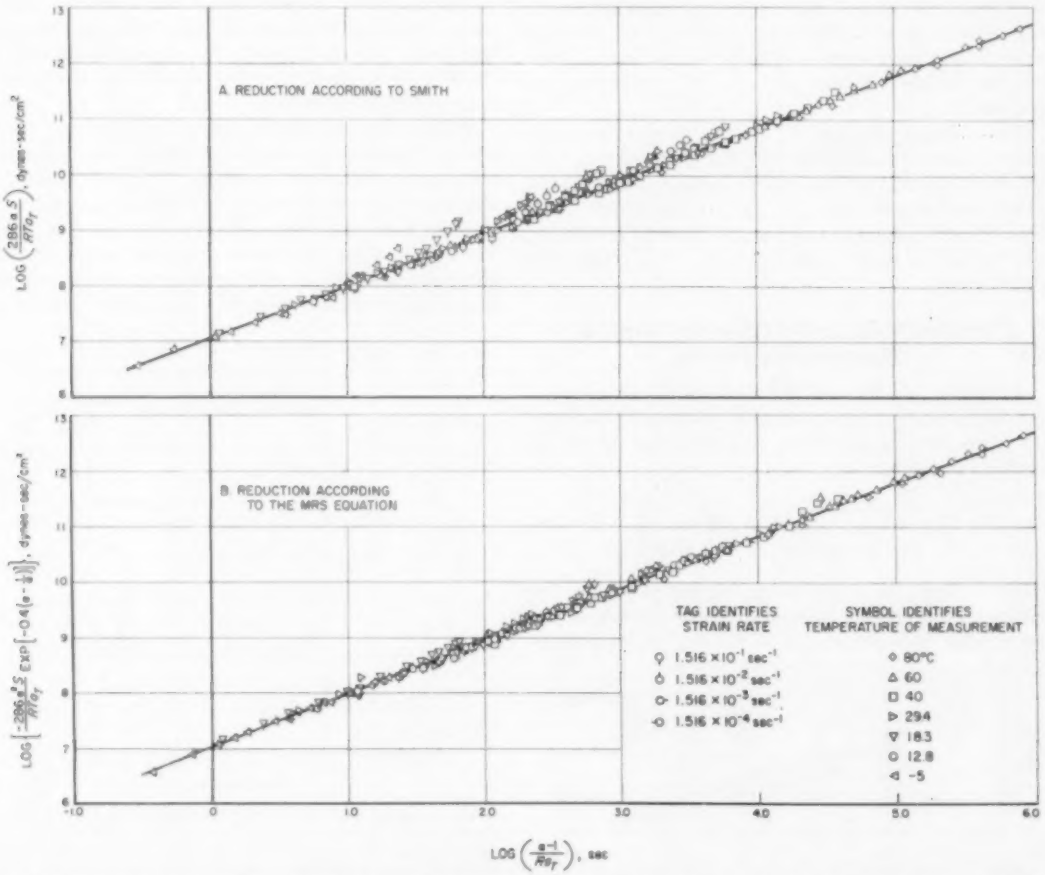

FIG. 11. Stress-strain data on SBR at various temperatures and strain rates, reduced to a composite stress-strain curve at 12.8°C. A. Reduction according to Smith,[17] $f(\alpha)=\alpha^{-1}$; B. Reduction according to the MRS eq., $f(\alpha)$ given by Eq. (10).

[19] M. L. Williams, R. F. Landel, and J. D. Ferry, J. Am. Chem. Soc. 77, 3701 (1955).

stress-strain curve with the more directly measured results of Fig. 10.

The stress-strain data can be superposed in the original manner of Smith[17] to give a composite stress-strain curve by simply plotting log $\alpha ST/T_0Ra_T$ vs log e/Ra_T, where R is the strain rate. Thus the reduced stress is αS and $f(\alpha)=\alpha^{-1}$. Figure 11(a) shows the results for such a superposition using a_T values calculated from Eq. (11), with $T_g=-59$°C. The individual stress-strain curves are concave upward and their initial portions define the envelope of all of the curves, as previously noted by Smith. In the present instance the envelope is essentially a straight line over this region of the reduced time scale.

The MRS equation can similarly be used to reduce the data, except of course that the reduced stress is that indicated in Eq. (10). The superposed plot thus obtained is shown in Fig. 11(b). The MRS function has now converted all of the stress-strain curves into straight line segments, and practically all of the points now lie on a single line. This line is of course the same as the envelope in Fig. 11(a), since at low strains the results become independent of the reduced stress employed. The stress relaxation modulus $E(t)$ can be obtained from the slope of either of these plots at any desired value of reduced time $t_\tau=e/Ra_T$, as

$$E(t)=(S^*/t_\tau)(d\log S^*/d\log t_\tau). \qquad (12)$$

If the use of the reduced stress concept and the MRS equation is correct, then these values of the stress relaxation modulus should fall on the superposed curve of Fig. 10. Instead, the results cross over and fall progressively below the superposed curves. However, when it is considered that the maximum discrepancy between the two results is 0.1 log units, no more than the diameter of the data points shown in Fig. 11, the agreement can be considered very satisfactory.

CONCLUSIONS

Since experimental data obtained at quite different times, temperatures, and strains showed reasonable agreement, it may be concluded that the concept of strain-reduced stress as a reduced variable is generally valid. Thus Ferry's method of reduced variables may be extended to large deformations by employing a strain-reduced modulus $E(t)f(\alpha)$, where $f(\alpha)$ is an appropriate function of the strain. Such a function was obtained from the Martin-Roth-Stiehler equation, but the validity of its use in this reduction was not definitely established. The constant A in the MRS equation is clearly related to the finite extensibility of polymer chains, since its magnitude controls the rate of rise of stress at higher strains. The implications of a possible time and temperature dependence of A are not clear at this time.

On the other hand, it should be recognized that this concept of a strain-reduced stress cannot hold at very short reduced times. Ferry[20] has recently shown that if strain produces a free volume change, then there will exist a time-strain shift factor analogous to the time-temperature shift factor a_T. In this case, superposition of isothermal data such as stress relaxation curves will require a translation of the curves along both the time and modulus axis. Such an effect would be expected to occur at temperatures near T_g, where Poisson's ratio is decreasing from the value of $\frac{1}{2}$, characteristic of a rubber, to a value of about $\frac{1}{3}$, characteristic of the glassy state.

ACKNOWLEDGMENTS

The authors wish to acknowledge the contributions of C. T. Weekley, who assisted in the performance of the experiments, and the cooperation of the Computer and Design groups of the Jet Propulsion Laboratory. We are indebted to Dr. Thor L. Smith for valuable discussions.

[20] J. D. Ferry and R. A. Stratton, Kolloid Z. 171, 107 (1960).

JOURNAL OF APPLIED PHYSICS VOLUME 31, NUMBER 11 NOVEMBER, 1960

Time and Temperature Dependence of the Ultimate Properties of an SBR Rubber at Constant Elongations*

THOR L. SMITH† AND PAUL J. STEDRY
Jet Propulsion Laboratory, California Institute of Technology, Pasadena, California

The ultimate properties of amorphous rubbers at temperatures above T_g are considered in terms of stress-strain curves to rupture measured at different strain rates and temperatures. The consideration indicates that a specimen held at a fixed elongation should break eventually, provided the elongation exceeds a critical value. This expected behavior was found by studying an SBR rubber. For samples maintained at different elongations for up to seven days, both the time to break and the stress at break were measured at eight temperatures from 1.7° to 60°C. For comparison, the ultimate properties were also measured at different strain rates and temperatures. The comparison indicates that for a given ultimate elongation and stress at break, the time to break under conditions of constant elongation is less than under conditions of constant strain rate.

I. INTRODUCTION

A STUDY was made previously of the temperature and strain rate dependence of the stress at break (tensile strength) and the ultimate elongation of an unfilled SBR rubber.[1] In that study, stress-strain curves to the point of rupture were measured with an Instron tensile tester on ring type specimens at 14 temperatures between −67.8° and 93.3°C, and at 11 strain rates between 0.158×10^{-3} and 0.158 sec^{-1} at most temperatures. The tensile strength was found to increase with both increasing strain rate and decreasing temperature. At all temperatures above −34.4°C, the ultimate elongation was likewise found to increase with increasing strain rate and decreasing temperature but at lower temperatures the opposite dependence on rate was observed; at −34.4°C, the ultimate elongation passed through a maximum with increasing rate.

Values of the ultimate properties at each temperature were plotted against $\log 1/R$, where R is the strain rate. The resulting curves were then superposed by shifting them along the $\log 1/R$ axis, the shift distance required to effect superposition being $\log a_T$. Values of $\log a_T$ obtained from superposing the tensile strength data were equal, within experimental error, to those obtained from superposing the ultimate elongation data. Further, these values of $\log a_T$ were found to fit the Williams, Landel, and Ferry (WLF) equation[2]

$$\log a_T = -\frac{8.86(T-T_s)}{101.6+T-T_s}, \qquad (1)$$

with the standard reference temperature T_s equal to 263°K. In this form of the WLF equation, T_s is normally about 50°C above the glass temperature T_g of a material. Thus, the value obtained for T_s indicated T_g should be 213°K, in close agreement with 210°K obtained from dilatometric measurements. Values of a_T given by Eq. (1) were used to construct two reduced curves which showed all ultimate property data plotted against $\log 1/Ra_T$. These curves showed the strain rate dependence of the tensile strength and the ultimate elongation, over many decades, at the standard reference temperature.

In studying the linear viscoelastic properties of amorphous polymers above T_g, many workers have found the shift factor a_T to be extremely useful for interconverting the effects of temperature and experimental time scale. The conclusion from the study of the SBR rubber was that a_T can also be used to interconvert the effects of temperature and strain rate on the ultimate properties of certain types of polymeric materials. Prior to this work, F. Bueche[3] presented a theory which predicted that values of the tensile strength measured at different temperatures and under either constant loads or strain rates can be interrelated by using a_T values. To check the theory, Bueche measured the tensile strength of polybutyl methacrylate under constant loads at temperatures above T_g and applied time-temperature superposition to reduce the data to a single temperature.

The shift factor is given by the relation $a_T=(T_0/T)\times(\eta/\eta_0)$, where η is the viscosity (or internal viscosity for crosslinked polymers) at temperature T and η_0 is the viscosity at some arbitrary reference temperature T_0. Because T_0/T differs from unity by a relatively small amount, a_T equals approximately the viscosity ratio η/η_0, and consequently the temperature dependence of a_T is essentially the same as that of the viscosity. Thus, the observation that a_T can be used to interconvert the effects of strain rate and temperature on the ultimate properties—at least for materials like SBR rubber—leads to the following conclusions: (1) The ultimate properties vary with temperature because the internal viscosity varies with temperature; (2) the ultimate properties vary with strain rate because the viscous resistance to network deformations increases

* This paper represents the results of one phase of research carried out at the Jet Propulsion Laboratory, California Institute of Technology, under contract sponsored by the National Aeronautics and Space Administration.

† Present address: Stanford Research Institute, Menlo Park, California.

[1] T. L. Smith, J. Polymer Sci. **32**, 99 (1958).

[2] M. L. Williams, R. F. Landel, and J. D. Ferry, J. Am. Chem. Soc. **77**, 3701 (1955).

[3] F. Bueche, J. Appl. Phys. **26**, 1133 (1955).

with the rate; and (3) the temperature dependence of factors such as the rate of bond rupture have no significant effect on the temperature dependence of the ultimate properties.

Values of the ultimate properties shown by the reduced curves in a previous paper[1] have now been replotted in Fig. 1 against the time to break (t_b) expressed in seconds and reduced to 263°K; t_b equals γ_b/Ra_T where γ_b is the strain at break measured at a strain rate R and temperature T, and S_b is the stress at break based on the initial cross-sectional area of the specimen. Figure 1 shows that the ultimate properties become relatively insensitive to strain rate at sufficiently low rates; the shapes of the curves suggest that asymptotes may exist which have near-zero slopes. Because of kinetic effects which must be associated with the chain scissions which lead to specimen rupture, it is unlikely that asymptotes of zero slope exist. However, the asymptotic or long-time values of the ultimate properties are of major significance because such values are nearly independent of the testing conditions and are characteristic of the network in the absence of viscous effects.

An important qualitative conclusion above the time-dependent ultimate properties can be reached by examining Fig. 1. For example, this figure shows that a specimen will break at 300% elongation provided the strain rate is selected so that 10^5 sec are required to reach this elongation. Let us suppose, however, that a specimen is stretched at the strain rate needed to produce a 300% elongation in 100 sec and that the elongation is subsequently held constant. Immediately after the sample is stretched, the stress will begin to relax because the sample was not stretched under equilibrium conditions. Although the stress decays, the sample will break eventually because it can withstand an elongation of only about 100% when the network chains are in an equilibrium condition. As a rough approximation, it might be expected that the sample will break after a total of 10^5 sec, as indicated by the curve which shows the ultimate strain plotted against log t_b. However, this curve represents data measured under conditions of constant strain rate, and it is to be expected that values of the ultimate properties, like other time-dependent mechanical properties, will depend on the path.

Important conclusions about the time dependence of the ultimate properties can also be reached by considering the diagram in Fig. 2. This diagram shows schematically stress-strain curves, including the rupture points, measured at various strain rates and temperatures. The variation of the stress at break and the strain at break with either strain rate or temperature is shown by the envelope ABC. The curve OA represents equilibrium stress-strain conditions, except possibly in the vicinity of point A. Although curve OA represents stress-strain values in the absence of viscous effects, true equilibrium—especially in the vicinity of A—undoubtedly does not exist because under suitable conditions stress leads to breakage of chemical bonds. Thus, values of the ultimate properties are not expected to be unique but to depend on the temperature and stress history. However, for present purposes, we can ignore such degradation effects and assume that A represents the ultimate properties measured under equilibrium conditions.

Suppose now that a specimen is stretched at the strain rate and temperature required to traverse curve

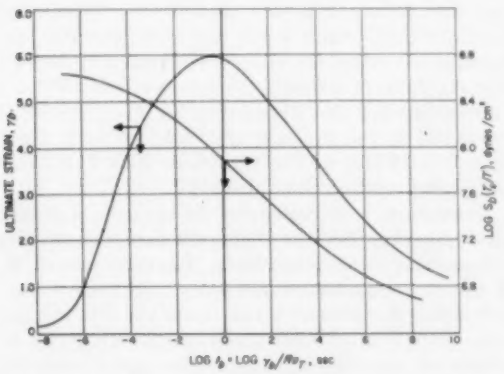

FIG. 1. Ultimate properties of an SBR rubber measured at different strain rates and temperatures. Data plotted against the logarithm of the time to break (t_b) reduced to −10° C. (Data from work cited in footnote 1.)

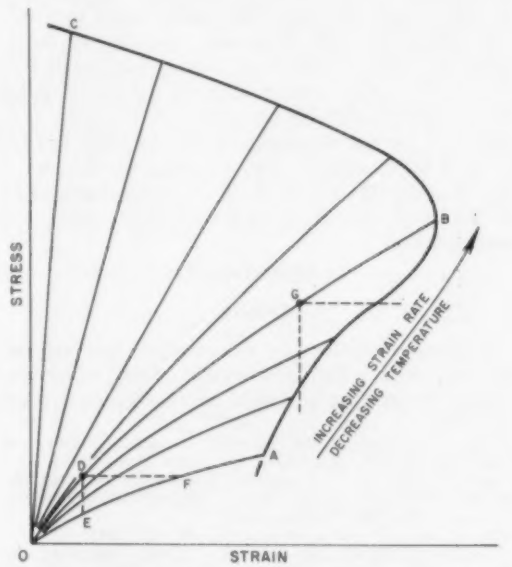

FIG. 2. Schematic representation of the variation of stress-strain curves with strain rate and temperature. Envelope connects rupture points and the dotted lines illustrate stress relaxation and creep under different conditions.

OB, and that the strain is held constant after point *D* is reached. At the constant strain the stress relaxes, as indicated by the dotted vertical line, until it reaches *E*, which is on the equilibrium stress-strain curve. On the other hand, if the stress is held constant after point *D* is reached, the strain increases, as indicated by the dotted line, until it reaches point *F*, which is also on the equilibrium stress-strain curve.

Next suppose that curve *OB* is traversed until point *G* is reached and thereafter the strain is held constant. The stress again relaxes, but because no equilibrium stress exists for the strain represented by point *G*, the specimen should eventually break. Likewise, if the stress is held constant after point *G* is reached, the strain increases, and the specimen should eventually break because no equilibrium strain exists for the stress represented by point *G*.

Studies have been made of the time to break for various materials under constant loads,[4] although with several possible exceptions,[3,5] most studies have been made of rigid materials. Apparently, no studies have been made of ultimate properties under constant strain conditions. Thus, the primary purpose of the present work was to obtain experimental confirmation of the prediction that certain rubbers when held at constant elongation will rupture eventually, provided the elongation exceeds some critical value; the secondary purpose was to see how values for the ultimate elongation and stress at break,[6] measured under constant strain conditions, compare with values measured under constant strain-rate conditions. To obtain the desired data, measurements were made at various temperatures of the stress-relaxation of an SBR rubber under relatively large elongations; the apparatus used and the stress-relaxation data obtained are discussed in detail elsewhere.[7] This paper presents data on the time required for the rupture of specimens subjected to various elongations at various temperatures and the stress existing at the time of rupture. For comparative purposes, a limited study was also made of the ultimate properties of the SBR rubber at different strain rates and temperatures.

II. EXPERIMENTAL

Material

Ultimate properties were measured of a gum vulcanizate of a styrene-butadiene rubber (SBR) which was supplied in the form of ASTM tensile sheets (*ca.* 0.080 in. thick) by the Rubber Section of the National Bureau of Standards. The base polymer was NBS reference sample 387 (X-768), which contained 23.5% bound styrene and had been prepared by emulsion polymerization at 50°C. The gum vulcanizate, which was cured for 60 min at 150°C, contained the following parts by weight: SBR, 100 parts; zinc oxide, 5 parts; sulfur, 2 parts; benzothiazyl disulfide, 1.75 parts. The sheets of the vulcanizate were stored in a freezer prior to being used. The vulcanizate used in the previous study[1] was the same except that 1 part of mercaptobenzothiazole was used in place of 1.75 parts of benzothiazyl disulfide and cure was for 45 instead of 60 min.

The average molecular weight between crosslinks M_c for the vulcanizate was determined from swelling measurements in four solvents. Duplicate weighed pieces of SBR were immersed in the solvents for four days at 25°C, and the swollen samples were weighed after removing excess solvent from their surfaces with filter paper. Values of M_c were calculated using the equation

$$\ln(1-v_2)+v_2+\chi_1 v_2^2=-\rho\frac{V_1}{M_c}\left(v_2^{\frac{1}{3}}-\frac{v_2}{2}\right),$$

where v_2 is the volume fraction of polymer in the swollen gel, ρ is the density of SBR, V_1 the molar volume of the solvent, and χ_1 the solvent-polymer interaction parameter. Values of χ_1, approximated as described previously,[1] are given in Table I along with the values of M_c for both the present vulcanizate and the vulcanizate used in the previous study.

A value of M_c was also calculated from the tensile modulus E derived from stress-strain data measured at 80°C with the Instron tensile tester. The modulus was evaluated, as described elsewhere,[8] from the slope of a plot of αS vs γ, where αS is the stress based on the stressed cross-sectional area of a specimen and γ is the strain. At 80°C, the modulus was found to decrease from 7.35 to 6.58×10^6 dynes/cm² as the strain rate of the test was decreased from 1.516×10^{-2} to 1.516×10^{-4} sec^{-1}. At 60°C and a strain rate of 1.516×10^{-3}, the modulus was 6.96×10^6 dynes/cm². These data indicate that the value measured at the lowest rate at 80°C is a near-equilibrium one. By substituting $E=6.58\times10^6$ at $T=353$°K in the equation $M_c=3\rho RT/E$, it is found that $M_c=13\,100$, in fair agreement with 15 800 obtained from swelling data (Table I).

Unfortunately, M_c values for the vulcanizate studied previously were 8020 and 9250 as obtained from swelling and modulus data, respectively. The difference in M_c of the two vulcanizates precludes quantitative comparisons of the ultimate properties of the first vulcanizate, studied at constant strain rates, with those observed on the present vulcanizate under constant strain conditions. Because of the desire to compare

[4] See, for example, R. N. Haward, *Strength of Plastics and Glasses* (Interscience Publishers, Inc., New York, 1949). Also, F. Schwarzl and A. J. Staverman, *Die Physik der Hochpolymeren*, edited by H. A. Stuart (Springer-Verlag, Berlin, Germany, 1956), Vol. IV, Chap. III.

[5] R. N. Haward, Trans. Faraday Soc. **39**, 267 (1943).

[6] Because tensile strength is usually defined as the maximum stress developed during certain types of tests, it seems desirable here to speak of the stress at break, and to call the stress at break the tensile strength only when it equals the maximum stress developed during a test.

[7] R. F. Landel and P. J. Stedry, J. Appl. Phys. **31**, 1885 (1960).

[8] T. L. Smith and A. B. Magnusson, J. Polymer Sci. **42**, 391 (1960).

results obtained under these different conditions, some measurements under constant strain rates were also made on the present vulcanizate.

Apparatus

Data under both constant strain rate and constant strain conditions were measured on rings which were cut from the sheets of SBR with a circular die which had an inside diameter of 1.400 in. and an outside diameter of 1.650 in. The edges of the die-cut rings were dished slightly, although this slight imperfection was disregarded in measuring the dimensions of specimens. Tensile data were measured at different temperatures, and strain rates with an Instron tensile tester equipped as briefly described previously.[1]

The constant strain apparatus[7] contained eight racks for stretching ring specimens. These racks were mounted in an air thermostat whose temperature was controlled by the continuous circulation of heated or refrigerated air from an external source. Temperature control devices maintained the temperature at any given point to within ±0.5°C for many hours; the maximum temperature difference between various points in the thermostat was about 1°C. When the temperature was regulated below ambient for several days or more, the over-all temperature variation, as indicated by three thermocouples, was about ±1.5°C, this large variation being due to certain operational changes produced by frosting of the refrigeration coils. During operation, a stream of dry nitrogen was bled continuously into the system to delay frosting.

Each rack for stretching a specimen consisted of a vertically mounted brass rod on which two movable supports were attached. Each support had a freely rotating nylon pulley whose diameter was 0.150 in., and a ring type specimen was placed over the pulleys. The upper support was connected to a heat treated steel beam which rested on knife edges mounted on top of the thermostat, and the lower support was connected by a cable to a wheel mounted under the thermostat. By adjusting the position of a metal stop on the brass rod, the specimen could be stretched manually by the wheel and cable device to a predetermined elongation in 2 sec or less. The force exerted by a stretched specimen was determined by measuring the small deflection of the beam with a linear variable differential transformer whose output was recorded by a Brown potentiometer; the output was determined to be a linear function of the applied force within about 1%.

Ultimate properties under constant strain conditions were measured on eight samples simultaneously. To carry out tests, unstrained rings of SBR were placed over the pulleys on the racks and allowed to come to temperature equilibrium. The rings were then rapidly stretched to predetermined elongations, the elongation increment of adjacent specimens normally being 25%. The elongations were calculated from the final distance between the centers of the pulleys, the diameter of the pulleys, and the initial inside diameter of a ring. The inside diameter was used to obtain the maximum elongation existing in a stretched ring. Other experimental work has indicated that the maximum elongation, instead of some average value, correlates best with the ultimate elongation measured on tensile specimens in which the strain is uniform. To obtain the stress, the measured load on the supporting beam was divided by twice the initial cross-sectional area of the ring. Because of some uncertainties in determining the absolute value of the load during a measurement and in determining the cross-sectional area of a specimen, the error in the stress may at times have been as great as 10%.

TABLE I. Values of M_c from equilibrium swelling data.

Solvent	χ_1	Previous vulcanizate	Present vulcanizate
Carbon tetrachloride	0.300	8000	15 957
Xylene	0.305	8657	16 647
Toluene	0.316	8000	15 998
Benzene	0.345	7424	14 802
		av 8020	av 15 851

III. RESULTS AND DISCUSSION

Stress-relaxation measurements were made at various elongations at eight temperatures between 1.7° and 60°C, most measurements being continued until rupture occurred. (A few measurements were also made at −5° and −15°C, but the rupture data were erratic and thus are not presented.) Stress-relaxation data obtained during a typical run are shown in Fig. 3. These data were measured at 1.7°C and at eight elongations between 350 and 525%. The solid points indicate when rupture occurred and the dotted curve through these points shows the stress at break at the various elongations.

Plots are shown in Fig. 4 of the percent elongation against the logarithm of the time to break (t_b) for re-

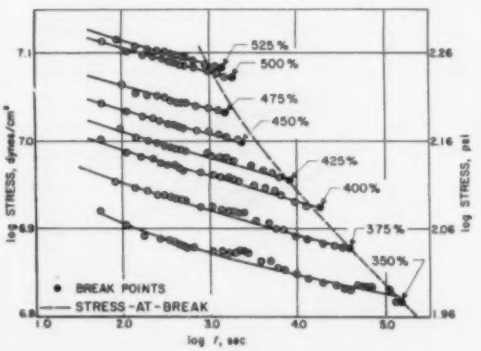

FIG. 3. Stress-relaxation of an SBR rubber at 1.7° C under elongations from 350 to 525%. Solid points indicate rupture.

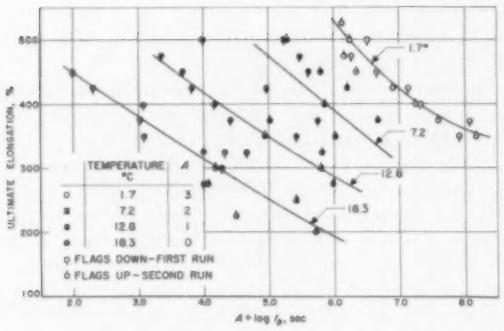

FIG. 4. Variation of ultimate elongation with log t_b under constant elongations (values of A are arbitrary).

sults obtained at 1.7°, 7.2°, 12.8°, and 18.3°C; data obtained at 29.4°, 40°, and 50°C are shown in Fig. 5. Two sets of measurements were made at each temperature and the results from each are differentiated by flags on the points. Figures 6 and 7 show plots of log S_b 286/T vs log t_b, where S_b is the stress at break and T is the absolute temperature of measurement. As shown in Fig. 6, only one set of stress measurements was made at 1.7°C, although as shown in Fig. 4, two sets of time-to-break measurements were made at this temperature. (For clarity, the data in Figs. 4 and 6 are shifted along the abscissa by arbitrary amounts A and, similarly, along the ordinate in Figs. 5 and 7.) Because elastic retractive forces are directly proportional to the absolute temperature, all values of the stress at break are multiplied by 286/T to reduce them to 286°K. (The ultimate property data obtained at 60°C under the constant strain conditions are shown later by the points in Figs. 10 and 11.) Because values of the ultimate properties are by nature rather nonreproducible, the scatter of the points about the lines shown in the figures is not unduly great, except for the data at 7.2°C.

Both the ultimate elongation and stress-at-break data at the various temperatures were superposed by shifting along the log t_b axis to obtain values of the shift factor a_T. The shape of some curves representing data at the higher temperatures changes markedly with temperature, and the shift distance required to superpose these curves was selected somewhat arbitrarily. For the 29.4° and 40°C data, the best over-all superposition—which actually is rather poor—is effected by an unusually large shift. Because this large shift was inconsistent with that required to give superposition of other data separated by 10°C, superposition was effected by considering only the first three or four points at the low end of the time scale at 40°C. This procedure gave a reasonably realistic value of the shift factor. In general, however, the accuracy of the a_T values is markedly lower than of those presented previously,[1] obtained by superposing ultimate property data measured at different strain rates. However, values obtained for log a_T are compared in Fig. 8 with the WLF equation. The solid square point in Fig. 8 shows that 12.8°C was selected as the reference temperature for the experimental determination of a_T values by shifting data.

Figure 8 shows that at 29.4°C and higher temperatures the values of log a_T obtained from the stress-at-break data are not in close agreement with those from the ultimate elongation data. Actually, values of log a_T from the stress-at-break data seem to be in moderate agreement with the WLF equation except at 50° and 60°C, whereas values from the elongation data begin to depart markedly from the WLF equation at temperatures above 29.4°C. A small deviation from the WLF equation might be expected at temperatures above about 40°C because this equation often applies only at temperatures less than T_s+50; for the SBR, T_s+50 equals 40°C.

Because of the poor accuracy of the a_T values, the only conclusion that can be drawn is that they are not grossly inconsistent with the WLF equation. However, the data certainly do not prove that rupture under conditions of constant strain is controlled entirely by the internal viscosity, as would be shown if the values agreed closely with the WLF equation. Actually, the

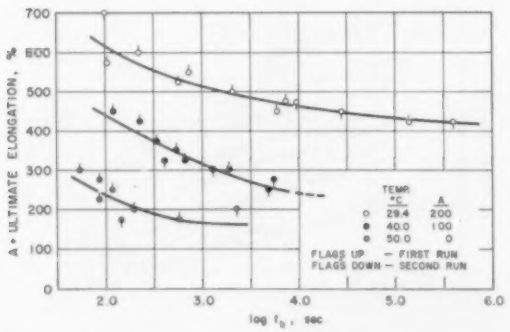

FIG. 5. Variation of ultimate elongation with log t_b under constant elongations (values of A are arbitrary)

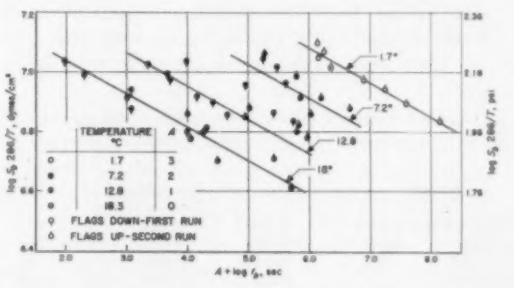

FIG. 6. Logarithm of the stress at break reduced to 286° K (S_b 286/T) plotted against log t_b. Data obtained under constant elongations (values of A are arbitrary).

stress-relaxation data, discussed elsewhere,[7] suggest that some chemical degradation occurred during the experiments at 50° and 60°C. Although the thermostat was flushed continuously with dry nitrogen, as mentioned in Sec. II, the oxygen concentration in the thermostat was only one-third that in air. Thus, the nitrogen purge was ineffective to prevent possible degradation. If degradation occurred, the values of $\log a_T$ obtained by superposing ultimate property data would be expected to differ from those predicted by the WLF equation. However, the stress-relaxation data showed degradation only after about 6×10^4 sec at 50° and 60°C; under these conditions, only two values of the ultimate properties were obtained (see Figs. 10 and 11). Thus, there is no definite evidence that rupture times were influenced by degradation, although it is conceivable that ultimate property data are affected to a greater extent by small amounts of degradation than stress-relaxation data.

Because of the difficulty in choosing a reliable set of $\log a_T$ values, the ultimate properties at the various temperatures are not shown plotted against the time to break reduced to a common temperature. Although such reduced plots can be constructed, their reliability for predicting values of the ultimate properties over an extended time scale at different temperatures would be questionable. Values of the ultimate properties observed under constant strain conditions at a given temperature will thus be compared directly with the values measured at different strain rates.

The ultimate properties at different strain rates were measured at seven temperatures between −5° and 80°C and at three strain rates at most of these temperatures. The strain rates ranged from 1.52×10^{-4} to 1.52×10^{-1} sec^{-1}, although this range was not covered at any single temperature. The few data obtained at each temperature coupled with the poor reliability of individual values of the ultimate properties precluded the determination of accurate values of $\log a_T$ by shift plots of the data at each temperature to effect superposition. Because the previous study[1] showed that

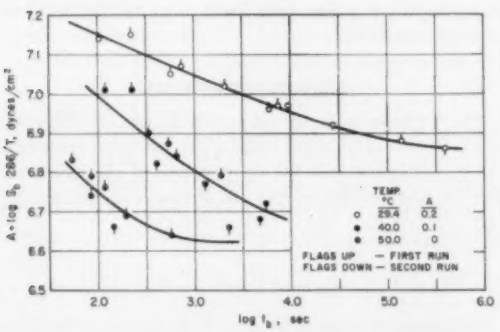

FIG. 7. Log S_b 286/T plotted against log t_b. Data obtained under constant elongations (values of A are arbitrary).

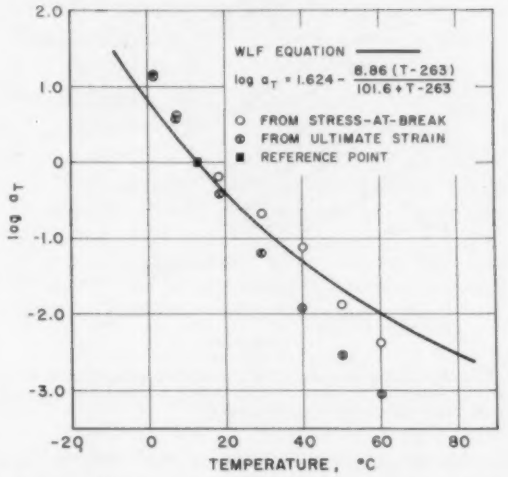

FIG. 8. Shift factor $\log a_T$ obtained by superposing ultimate property data compared with the WLF equation.

values of a_T given by the WLF equation can be used to effect superposition, the present data were superposed by using the a_T values shown by the plot of the WLF equation in Fig. 8. The resulting curves are shown in Fig. 9, where the ultimate strain and $\log S_b$ 286/T are plotted against $\log t_b/a_T$, the quantity t_b/a_T being the time to break reduced to 286°K.

To compare the data measured at constant strain rates with those at constant strains, the curves in Fig. 9 were reduced to each of the temperatures at which constant strain measurements were made; this reduction was made by using values of $\log a_T$ given by the WLF equation in Fig. 8 to change the time scale.

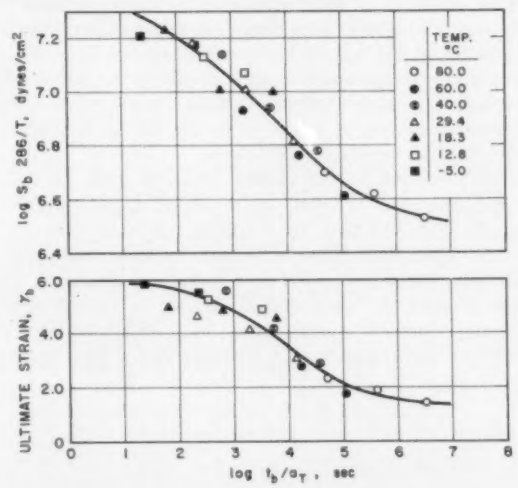

FIG. 9. Ultimate properties measured at different strain rates and temperature plotted against log t_b. Data reduced to 13° C.

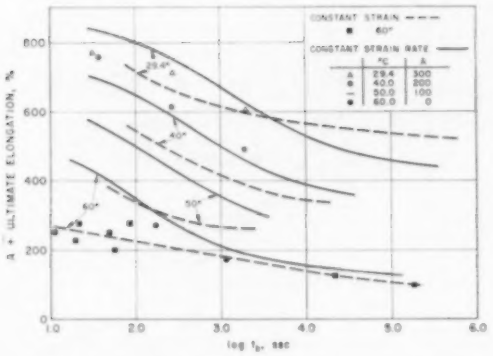

FIG. 10. Comparison of ultimate elongation vs log t_b data measured at constant elongations with values measured at different strain rates (values of A are arbitrary).

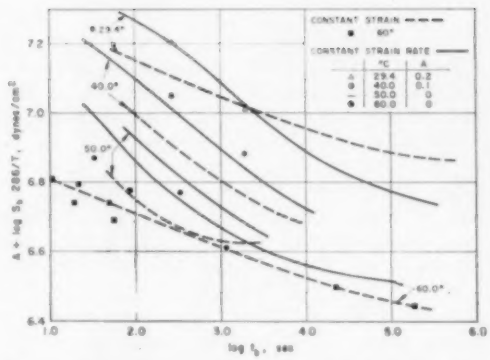

FIG. 11. Comparison of log S_b 286/T vs log t_b data measured at constant elongations with values measured at different strain rates (values of A are arbitrary).

Sections of the curves reduced to 29.4°, 40°, 50°, and 60°C are compared in Figs. 10 and 11 with the constant strain data measured at these temperatures. In the figures, sections of the reduced curves are shown by solid lines and the individual values measured at constant strain rates at 29.4°, 40°, and 60°C (measurements were not made at 50°) are shown by points; the dotted lines show the constant strain data, and individual values obtained under these conditions are shown at 60°C. Plots like those in Figs. 10 and 11 were also prepared from data at 1.7°, 7.2°, 12.8°, and 18.3°C. Because these plots did not show any trends not shown by Figs. 10 and 11, they are not presented.

Figures 10 and 11 show that most individual values obtained at constant strain rates lie to the right of the curves showing values measured at constant strain. Although the curves showing the constant strain rate data lie to the right of those showing constant strain data—at least at shorter times—the curves at 29.4°C intersect so that at long times the constant strain rate data lie to the left of the constant strain data. This crossover is unexpected and probably is not real, especially since no individual values measured at constant strain rate lie below or to the left of the curves showing the constant strain data.

A crossover of the curves indicates that at long times the time to break for a sample under constant strain is greater than for a sample subjected to a constant strain rate. However, under constant strain conditions, the energy input to a sample as measured by the product of stress and elongation is considerably greater than the energy input to a sample which is strained continuously at a constant rate until rupture occurs. This factor suggests that the time to break for samples under constant strain should not be longer than for samples subjected to a constant strain rate. Thus, the crossover is tentatively attributed to some error in either the experimental data or its reduction.

An attempt was made to measure ultimate properties under constant elongations at −5° and −15°C. The results were erratic and thus are not presented. At these low temperatures, it is possible that during the stretching of a specimen to certain elongations, the left side of the bell-shaped curve—like that shown in Fig. 1—was often approached rather closely. If this were true, the time of stretching a specimen could affect the results because a small difference in time would change markedly the closeness of approach to the bell-shaped curve. Thus, in some tests, damage may have been done to the network when a specimen was stretched; this damage could cause the specimen to break almost immediately or to break at times considerably different than expected; both types of behavior were observed. When the bell-shaped curve is not closely approached during the stretching of a specimen, no damage should be done to the specimen. However, the time to break might now be greater than the four to five days normally used for a test and no rupture of the specimen would be observed.

ACKNOWLEDGMENTS

The authors wish to acknowledge the contributions of C. W. Weekly, who assisted in the performance of the experiments, and the cooperation of the Computer and Design Groups of the Jet Propulsion Laboratory.

Determination of the Anisotropy of Bond-Polarizability of Liquids Using Flow-Birefringence Measurements

W. PHILIPPOFF
Esso Research and Engineering Company, Linden, New Jersey

INTRODUCTION

THE interaction of light and transparent matter can be described in terms of the electrical field of the incident beam and dipoles in initially neutral molecules. The electric dipoles may be permanent ones—the dipole moment μ—or induced ones, determined by the field and the polarizability of the molecule. When the polarizability of a molecule is isotropic, even under the influence of orienting fields, no optical effects are observable. If, however, it is anisotropic, polarized light can detect orientation effects in applied fields; this is called accidental birefringence. The anisotropy of the polarizability, which is small (of the order of 10% of the mean polarizability), can be also measured by the depolarization of scattered light according to the theory of Gans and by the Kerr effect. This has been used extensively in the past, especially by Stuart and his school.[1]

Flow birefringence gives us a further independent method for its determination. The light-scattering measurements in gases are extremely difficult to perform because of the very small effects (one-millionth part of the intensity of the incident light) observable and in the evaluation of the Kerr effect, due allowance has to be made to the influence of μ, which for polar molecules is larger than that of the anistropy of the polarizability. Flow birefringence is caused solely by this anisotropy and is not influenced by μ; further, the effect is much larger than the former ones and therefore can be determined with more precision. It has, however, other uncertainties in its theory.

A special interest in these measurements was a new determination of the contribution of the CH_2 link to the anistropy of a paraffin chain. This value would allow one to calculate the flexibility of polymer chains using flow birefringence.

In previous publications, it was shown that flow birefringence can be described by the stress optical coefficient C in Brewsters Br (10^{-13} cgs),

$$C=\Delta n/\Delta p=\Delta n \sin 2\chi/2\eta D, \tag{1}$$

where Δn is the observed birefringence, Δp the difference in the principal stresses, η the viscosity in poises, and D the rate of shear in sec^{-1}. This is true for normal liquids as well as for polymer solutions. The existing values for the contribution of the CH_2-link or bond polarizabilities have been determined from depolarization studies[2] or paraffin crystals.[3] It has been proved that C is essentially the same in the 100% rubbery state or in solutions of polymers. Therefore, it seemed that values for the CH_2-link determined from measurements in liquids would be better applicable to the problem.

THEORY

In 1928, Raman and Krishnan[4] developed the first theory of the flow birefringence in liquids. In their calculations there was an error of a factor two that was corrected by Paldhikar.[5] Their general statement was that flow birefringence can occur when the molecules, assumed to be triaxial ellipsoids, are both mechanically and optically anisotropic. Their theory leads to the following expression:

$$\frac{\Delta n}{n\eta D}=\frac{(n^2-1)(n^2+2)}{10\,n^2N_0kT}\,\frac{(a_1-a_2)(\alpha_{11}-\alpha_{22})+(a_2-a_3)(\alpha_{22}-\alpha_{33})+(a_3-a_1)(\alpha_{33}-\alpha_{11})}{(a_1+a_2+a_3)(\alpha_{11}+\alpha_{22}+\alpha_{33})}, \tag{2}$$

where n = index of refraction; N_0 = number of particles per cubic centimeter; k = Boltzmann's constant, T = absolute temperature in °K; α_{ii} = principal polarizabilities of the triaxial ellipsoids; a_{ii} = geometrical axes of the triaxial ellipsoid.

This paper will proceed to evaluate the experimental results according to the Raman-Krishnan formula. Previous checks of this theory have been done essentially with the experimental results for *n*-octanol, *assuming* a ratio of the polarizabilities $\alpha_{11}:\alpha_{22}=1.15$ and $\alpha_{22}=g_{23}$.

Our idea was to determine experimentally the anisotropy $(\alpha_1-\alpha_2)$ for the normal alcohols, using as wide a range for X, the number of carbon atoms, as possible. A check of the literature revealed that only a few alcohols were measured. Alcohols are better suited for this type of work than paraffins, as their viscosities are higher and they can be investigated to C_{16} in a reasonable temperature range.

The Raman-Krishnan formula can be changed to a simpler expression[6] by introducing the mean polar-

[1] Latest summary: H. A. Stuart, *Die Struktur des freien Molekülls; Vol. I, Die Physik der Hochpolymeren* (Springer-Verlag, Berlin, 1952), Chaps. 5, 6, and 7.

[2] K. G. Denbigh, Trans. Faraday Soc. **36**, 936 (1940).

[3] C. W. Bunn and R. de P. Daubeny, Trans. Faraday Soc. **50**, 1173 (1954).

[4] C. V. Raman and K. S. Krishnan, Phil. Mag. **5**, 769 (1928).

[5] R. Paldhikar, Phil. Mag. **21**, 1125 (1936).

[6] A. Peterlin in *Rheology: Theory and Application I* by F. Eirich (Academic Press, Inc., New York, 1956), Chap. 15.

izability α_m according to the Lorenz-Lorentz equation

$$\alpha_m=\frac{\alpha_1+\alpha_2+\alpha_3}{3}=\frac{3}{4\pi N_0}\cdot\frac{n^2-1}{n^2+2}, \tag{3}$$

and inserting into Eq. (2):

$$C=\frac{\Delta n}{2\eta D}=\frac{\pi}{45kT}\cdot\frac{(n^2+2)^2}{n}\cdot\frac{(\alpha_1-\alpha_2)(a_1-a_2)+(\alpha_2-\alpha_3(a_2-a_3)+(\alpha_3-\alpha_1)(a_3-a_1)}{a_1+a_2+a_3}. \tag{4}$$

Rotational symmetry of both the mechanical and optical properties of the molecule is assumed: $\alpha_2=\alpha_3$ and $a_2=a_3$. On introducing $p=a_1/a_2$, the axial ratio, the final formula becomes

$$C=\frac{2\pi}{45kT}\cdot\frac{(n^2+2)^2}{n}(\alpha_1-\alpha_2)\frac{p-1}{p+2}$$

$$=\frac{2\pi}{45kT}\cdot\frac{(n^2+2)^2}{n}(\alpha_1-\alpha_2)\cdot f. \tag{5}$$

The index of refraction n is easily measured. The temperature T is known, and axial ratio p can be calculated from x-ray measurements. This allows the calculation of $(\alpha_1-\alpha_2)$ from C.

The theory of Kuhn and Gruen[7] as well as that of Hermans[8] give the following expression for the stress-optical coefficient C of a rubberlike molecular network:

$$C=\frac{2\pi}{45kT}\cdot\frac{(n^2+2)^2}{n}(\alpha_1-\alpha_2). \tag{6}$$

The difference between the two equations is obviously only in the geometric form factor "f."

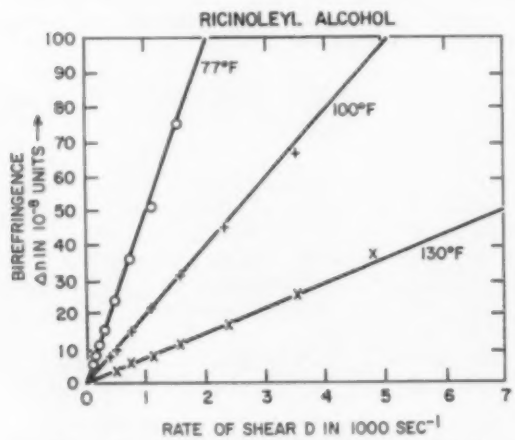

FIG. 1. Flow-birefringence measurements on ricinoleyl alcohol at three temperatures.

[7] W. Kuhn and F. Grün, Kolloid-Z. **101**, 248 (1942).
[8] J. J. Hermans, Kolloid-Z. **103**, 210 (1943). See also F. H. Müller, Kolloid-Z. **95**, 138 (1941).

Having determined the increment per CH_2 group from the measurements of the normal alcohols and the increment for a C=C double bond from the comparison of the undecylic and undecylenic acid, one can proceed to calculate $(\alpha_1-\alpha_2)$ for a monomer link of such materials as polyisobutylene or Hevea rubber. The ratio "q"$=(\alpha_1-\alpha_2)$ for the polymer (calculated from measurements on solutions of polymers or on the 100% polymer in the rubbery state) and the calculated value of $(\alpha_1-\alpha_2)$ for the monomer unit gives, according to Treloar[9] and Saunders,[10] a measure for the number of monomer links in the statistical unit or a measure for the flexibility of the chain. It is important to note that the conclusion from the last equation is the independence of C from both the concentration c of the polymer solution, and the molecular weight M of the polymer, a conclusion that could be proved both by our previous measurements and by the recalculation of Schmidli's results[11] by Lodge.[12] C depends, according to the existing theory, only on the structure of the monomer unit. However, a difference of the index of refraction of polymer and solvent causes a departure from this rule.

The Raman-Krishnan theory has been recently rejected for two theoretical reasons: (1) Boltzmann statistics should not be applied to a flow phenomenon where the molecules are performing a complicated motion, and (2) the theory predicts that the extinction angle χ is always 45°, whereas experimentally in polymer solutions the angle may be between 45° and 0°. However, we believe it has been shown that the theory need not predict that the angle be always 45°: the direction of the principal tensile stress may vary from 45° to 0° referred to the direction of flow, depending on the magnitude of the recoverable shear s in the flow of viscoelastic liquids. s is the total recoverable shear after stationary flow and removal of the shear stress. For normal liquids $s=0$ and $\chi=45°$.

[9] L. R. G. Treloar, *The Physics of Rubber Elasticity* (Oxford University Press, New York, 1949), p. 150; Trans. Faraday Soc. **43**, 277 (1947).
[10] D. W. Saunders, Trans. Faraday Soc. **53**, 860 (1957).
[11] B. Schmidli, thesis, University of Zürich (1952). See A. Peterlin and R. Signer, Helv. Chim. Acta **36**, 1572 (1953).
[12] A. Lodge, Nature **176**, 838 (1955); Trans. Faraday Soc. **52**, 120 (1956).

TABLE I. Flow-birefringence results on alcohols.

Alcohol	Author	Temperature °C	Viscosity P	$K\times10^{-12}$	$K'\times10^{10}$	C Br	$C\cdot T/298$	C mean
Heptyl	Stuart	16	0.0466	2.72	0.59	285	276	315
	Sadron	20	0.070	4.5	0.64	320	315	
	Björnståhl	20	0.070	4.5	0.64	320	315	
	Philippoff	25	0.0585	3.7	0.64	320	320	
Octyl	Philippoff	13.6	0.116	8.75	0.754	377	363	
	Sadron	20	0.089	6.5	0.73	365	360	
	Björnståhl	20	0.0905	7.4	0.82	410	403	380
	Philippoff	25	0.0746	5.8	0.78	390	390	
Nonyl	Björnståhl	20	0.114	10.6	0.94	470	470	470
Decyl	Björnståhl	20	0.144	16.7	1.16	580	590	590
Undecyl	Björnståhl	20	0.170*	22.8	1.50	750	750	780
	Philippoff	25	0.1402	22.5	1.60	800	800	
Dodecyl	Sadron	22	0.185*	29.6	1.60	800	800	
	Philippoff	25	0.1648	32.0	1.93	965	965	
	Philippoff	37.8	0.1008	19.2	1.90	950	985	900
	Philippoff	54.5	0.0572	8.8	1.54	770	845	
Tetradecyl	Philippoff	37.8	0.1402	29.0	2.07	940	1075	1150
	Philippoff	54.5	0.0774	17.2	2.22	1010	1270	
Hexadecyl	Philippoff	54.5	0.0967	24.6	2.57	1290	1410	1410
Ricinoleyl	Philippoff	25	2.510	525	2.10	1050	1050	
	Philippoff	37.8	1.050	218	2.07	1035	1080	1070
	Philippoff	54.5	0.400	79.8	2.00	1000	1095	
Hexadecane	Philippoff	25	0.0306	6.3	2.06	1030	...	...
Undecylenic acid	Philippoff	25	0.0993	38.6	3.89	1945	1945	1952
		37.8	0.0695	26.1	3.76	1880	1960	
Undecylic acid	Philippoff	37.8	0.0803	27.8	3.45	1730	1800	1800
Nonylic acid	Sadron	20	0.082	33.3	4.1	2030	...	
Octylic acid	Sadron	20	0.0576	25.8	4.5	2250	...	
Heptylic acid	Sadron	20	0.0436	23.0	5.3	2640	...	

EXPERIMENTAL

The birefringence instrument has been previously described.[13] The *n*-alcohols and the undecylic acid were CP purchased from Matheson & Cole Company. The undecylenic acid and the ricinoleyl alcohol were from the Baker Castor Oil Company. Only the undecylenic acid was redistilled in vacuum before use. This purity was apparently adequate, as two separately purchased samples of dodecanol gave identical results. The viscosities and densities were measured by conventional means, the refractive index n_D by an Abbé refractometer at the operational temperature.

The first experiments were made in order to prove the proportionality of Δn and D and that the orientation angle $\chi=45°$. In some cases these measurements were performed at three temperatures, as shown in Fig. 1 for ricinoleyl alcohol. This alcohol has a comparatively high viscosity and the effects were more easily and precisely measurable than with the normal alcohols. However, the results on the other substances were very much the same. The angle χ was always 45° as the theory required, and, as seen from the figure, the proportionality between Δn and D was within the precision of the measurements. This checks the results of previous investigators.[14]

All the values measured and taken from literature are listed in Table I, including $K=\Delta n/D$, $K'=\Delta n/\eta D=\Delta n/\tau$, and C, together with the temperature and viscosity. The direct experimental results—K as a function of X at different temperatures—are shown in Fig. 2. Δn was always positive.

If the viscosity η is taken into account, as is done in the expression for K' and C, these curves nearly coincide. However, in Eq. (7) the absolute temperature T appears in the denominator. In order to compare values at different temperatures, not only has one to correct K for

[13] W. Philippoff and F. H. Gaskins, Ind. Eng. Chem. **51**, 871 (1959); J. Appl. Polymer Sci. **2**, 143 (1959).

[14] Ricinoleyl alcohol is slightly optically active, giving in our instrument a rotation of +4.0°. This did not influence the values of Δn, but it made measurements of small effects impossible, due to a general illumination of the field of vision.

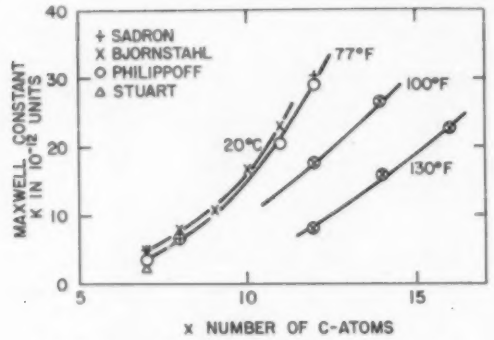

FIG. 2. $K=\Delta n/D$ for the alcohols as a function of the number of carbon atoms X.

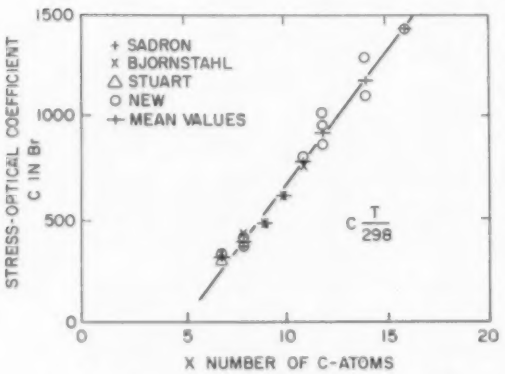

FIG. 3. $C\cdot T/298$—the stress-optical coefficient reduced to 25°C as a function of X.

viscosity, but the value $C\times T$ should be used. The reference temperature was 298°K, so the values measured at a temperature T were multiplied by $T/298$. This has been also included in Table I and has been previously suggested by Stein[15] for rubberlike polymers. Figure 3 shows the relation between C and X, which is more or less linear. Björnståhl[16] has stated that $K'(=2C)$ is a function of $(X+1)^2$. However, the extension of the experiments from $X=11$ to $X=16$ showed the linear relation.

A study of Table I shows that $CT/298$ does not always give a better check than C at different temperatures (tetradecanol). However, the differences are small and probably caused by experimental errors. See the results on polymer solutions.[17] From Björnståhl's Fig. 3.9, $C=830Br$ for dodecanol can be obtained; no experimental details are given; it checks, however, with the listed values. Sadron's[18] values are included, using the interpolated viscosities.

[15] R. S. Stein, F. H. Holmes, and A. V. Tobolsky, J. Polymer Sci. **14**, 443 (1954).
[16] O. Snellman and Y. Björnståhl, Kolloid-Beih. **52**, 403 (1941).
[17] W. Philippoff, Trans. Soc. Rheol. **3**, 153 (1959).
[18] C. Sadron, J. phys. radium **7**, 263 (1936).

In Table I, the measurements on the corresponding acids are also included. Three of them are taken from literature[16] and the undecyl and undecylenic acids are added. Also, the value for cetane is included.

The viscosity values given in Table I were obtained as follows: In Fig. 4, the temperature dependence of the viscosity of the normal alcohols is shown. The values for propanol through hexanol are taken from the literature (ICT Tables and Landolt-Börnstein). The ones from heptanol to hexadecanol have been measured and the curves drawn to form a family. This allows one to interpolate values that have not been measured. Our three reference temperatures were 25°, 37.8°, and 55.4°C. In order to prove that the results are consistent, these values are replotted as isotherms over X in Fig. 5. These curves, together with the ones in Fig. 4, show a very great regularity of the increase of viscosity both with decreasing temperature and X. The resulting values from these two curves were used to calculate C from the literature data. Some viscosity measurements of Björnståhl were erroneous, probably due to typo-

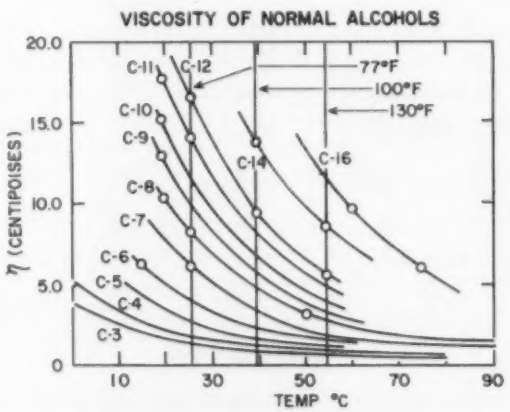

FIG. 4. Viscosity-temperature relation for n-alcohols.

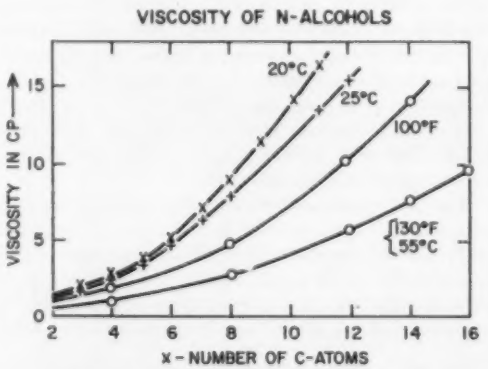

FIG. 5. Viscosity isotherms as a function of X.

graphical errors; the interpolated values are marked with an asterisk.

EVALUATION

In order to calculate the form factor f, x-ray measurements of alcohol molecules in crystalline form have been taken from the literature.[19] It is therefore assumed that the alcohol molecules investigated in the liquid state will retain their solid-crystal shape. The measurements of alcohols and acids are shown in Fig. 6. The x-ray "c" spacing is double the molecular length, as is well known. The slope of both lines gives the value of 1.27 A for each CH_2 group and, for the alcohols, a contribution of 1.5 A for the terminal OH group. Furthermore, the distance between the chains in the crystal give us the breadth of the molecule. This was assumed to be 4.5 A. In Table II, the geometric factor (f) for the series of alcohols is shown. This factor does not change very much in the range of measurement.

Further, the factor $A=(n^2+2)^2/n$ is evaluated and shown in Table III. It varies only by 1% with the index of refraction n for the normal alcohols. Using the factor A, the stress-optical coefficient C, and the geometric form factor f, calculated in the foregoing, the anisotropy of the polarizability $(\alpha_1-\alpha_2)$ for the normal alcohols can be calculated from Eq. (7), and the values

TABLE II. Calculation of geometric factor $f=(p-1)/(p+2)$; $L_{\text{calc}}=1.50+1.27X$ A.

Alcohol	L_{calc} A	b A	$p=L/b$	f
Heptyl	10.39	4.5	2.310	0.304
Octyl	11.66	4.5	2.595	0.347
Nonyl	12.93	4.5	2.875	0.385
Decyl	14.20	4.5	3.160	0.418
Undecyl	15.47	4.5	3.440	0.448
Dodecyl	16.74	4.5	3.720	0.475
Tetradecyl	19.28	4.5	4.285	0.522
Cetyl	21.82	4.5	4.850	0.562
Ricinoleyl	24.36	4.5	5.410	0.595

TABLE III. Calculation of the anisotropy of polarizability of n-alcohols.

Alcohol	CB_r	n_D	A	f	$\alpha_1-\alpha_2$ A³
Heptyl	315	1.428	11.42	0.304	2.67
Octyl	380	1.432	11.45	0.347	2.87
Nonyl	470	1.431	11.44	0.385	3.15
Decyl	590	1.437	11.49	0.418	3.62
Undecyl	780	1.439	11.51	0.448	4.46
Dodecyl	900	1.441	11.53	0.475	4.84
Tetradecyl	1150	1.4387	11.51	0.522	5.64
Cetyl	1410	1.4376	11.46	0.562	6.44
Ricinoleyl	1070	1.4702	11.78	0.595	4.50

$$(\alpha_1-\alpha_2)f=29.45\,\frac{1}{A}\,\frac{C}{1000}\text{ in A}^3$$

$$\alpha_1-\alpha_2=-0.57+0.44X$$

[19] E. Hertel, *Landolt-Börnstein Physical Chemical Table 15022* (Springer-Verlag, Berlin, 1955), 6th ed., Vol. I, part 4.

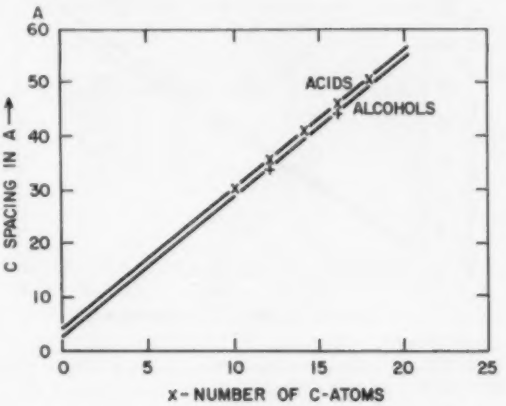

FIG. 6. X-ray "c" spacings for n-acids and n-alcohols.

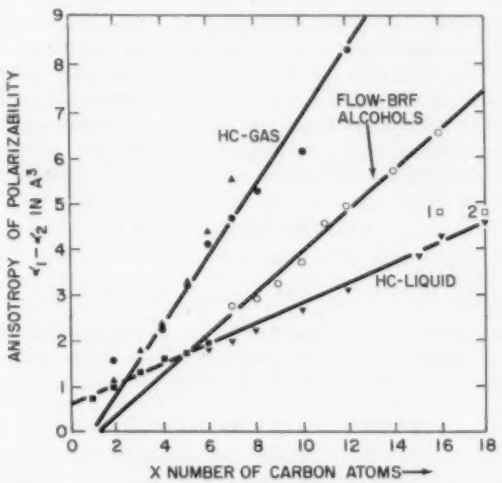

FIG. 7. Anisotropy of the polarizability $\alpha_1-\alpha_2$ in A³ as a function of X calculated from different experiments. ▲ Stein—depolarization of scattered light hydrocarbons as gas; ● Stuart—same; ▼ Stuart—same liquid hydrocarbons; ■ LeFevre—alcohols in solution; □ 1—Cetane; □ 2—Ricinoleyl alcohol.

are listed in Table III. These values are plotted in Fig. 7 and give a linear relationship:

$$\alpha_1-\alpha_2=-0.57+0.44X. \tag{7}$$

It has been thus proved experimentally that $\alpha_1-\alpha_2$ for the normal alcohols is proportional to the chain length. The increment for one CH_2 group is 0.44 A³.

One can now proceed to calculate the separate values α_1 and α_2 by using an expression for the mean polarizability of the alcohol molecule. Such measurements have been made and listed in the literature, and α_m is extrapolated to infinite wavelengths to eliminate the dispersion contribution in the visible range. These measurements are shown in Fig. 8, together with our independently determined values. The polarizability P,

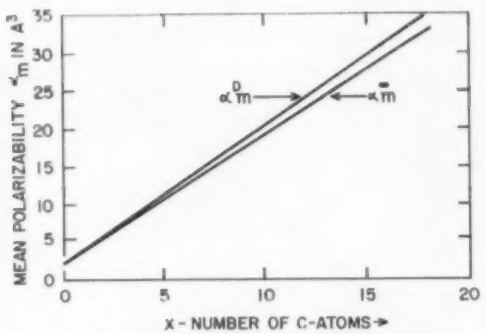

FIG. 8. Mean polarizability α_m measured experimentally in Table III, and literature values extrapolated to $\lambda \to \infty$ (α_m^∞) as a function of X for n-alcohols.

in cubic centimeters, is converted to A^3 by multiplying by $0.3956 = 3\times10^{24}/(4\pi N)$, where $N = 6.03\times10^{23}$, the Avogadro number. This gives an expression for the mean polarizability of the alcohol (see the values in Table IV): $\alpha_m = 2.00 + 1.79X$. Thus, the mean polarizability for one CH_2 is 1.79 A^3. Now, having both the mean polarizability α_m and $\alpha_1-\alpha_2$, and assuming the molecule to have a rotational symmetry (i.e., $\alpha_2=\alpha_3$), α_1 and α_2 for a CH_2 group are calculated in the following way:

$$\alpha_m = (\alpha_1+2\alpha_2)/3 = 1.79,$$
$$\alpha_1-\alpha_2 = 0.44,$$
$$\alpha_1 = 2.08\ \text{A}^3; \quad \alpha_2 = 1.64\ \text{A}^3.$$

According to Sack[20] and LeFevre,[21] one can calculate the anisotropy of the C−C bond under the assumption that the C−H bond is isotropic, $\alpha_1=\alpha_2=\alpha_m=0.635$ A^3. Then,

$$(\alpha_1+2\alpha_2)/3 = (\alpha_1+2\alpha_2)_{C-C}/3 + 2\alpha_{mCH},$$
$$(\alpha_1+2\alpha_2)/3 = 1.79 - 2\times0.635 = 0.52\ \text{A}^3, \qquad (8)$$
$$\alpha_1-\alpha_2 = 0.44\ \text{A}^3,$$

introducing the values, one obtains for the C−C bond

$$\alpha_1 = 0.81\ \text{A}^3; \quad \alpha_2 = 0.37\ \text{A}^3.$$

A comparison of these values with those from the literature (Bunn and Daubeny,[3] Denbigh,[2] and the theoretical calculation of Bolton[22]) are shown in Table V. Our values check best with the Bolton values.

In his publication,[10] Saunders uses a value for the anisotropy $\alpha_1-\alpha_2$ of the CH_2 group of 0.155 A^3 determined from the values of Bunn and Daubeny. At the end of his paper he presents a calculation of Sack which gives a different value of 0.31 A^3. Our value is 0.44 A^3. Saunders does not explain the discrepancy of these two calculated values. However, our value checks with the Sack value as well as could be expected.

[20] R. A. Sack, Trans. Faraday Soc. **53**, 860 (1957).
[21] C. G. LeFevre and R. J. W. LeFevre, Revs. Pure and Appl. Chem. (Australia) **5**, 261 (1955).
[22] H. G. Bolton, Trans. Faraday Soc. **50**, 1261 (1954).

As is seen from Table I, the undecyl and undecylenic acid were investigated to obtain the contribution of a double bond in the chain. By using a geometric factor $f=0.448$, the same as undecylenic acid and undecanol, undecylic acid gave an anisotropy $\alpha_1-\alpha_2=10.31$ A^3. The undecylenic acid gave $\alpha_1-\alpha_2=11.16$ A^3. The difference is 0.85 A^3. Two CH_2 groups in the chain are replaced by a double bond. As previously, the CH bond is assumed to be isotropic and therefore does not influence the optical properties. The contribution of the double bond in a chain is

$$(\alpha_1-\alpha_2)_{C=C} = 0.85 + 0.44 = 1.29\ \text{A}^3.$$

The values of the literature, namely these of Denbigh,[2] Bunn and Daubeny,[3] and Bolton,[22] all give

$$(\alpha_1-\alpha_2)_{C=C} = 1.83\pm0.03\ \text{A}^3.$$

Our value is, however, determined by the difference of two fairly large experimental values. The relative precision is therefore not great. We think the value of 1.83 A^3 is probably right, the discrepancy of about 0.5 A^3 possibly being due to unavoidable experimental errors.

These evaluations showed that the contribution $\alpha_1-\alpha_2$ of the C−C and C=C bonds, determined using the Raman-Krishnan theory and the experimental values of the alcohol series, are reasonable and well within the limits expected from the other measurements. It seems, therefore, that our objective has been obtained: to determine the contribution of these bonds from new experimental values. The limitations are: the use of the Boltzmann statistics for flow birefringence, the Lorenz-Lorentz equation, LeFevre's assumption[21] of the isotropic C−H bond, the rotational symmetry of the alcohol molecule (that it has the same shape in the crystal as in the liquid state), and the validity of Silberstein's theory[23] concerning the additivity of the bond increments. However, this theory is not always right. The series of acids measured in literature (Table I) and extended by the new measurements showed that the anisotropy *decreases* with the number of carbon atoms. It is not clear how this can happen. This result has, until now, not been discussed in the literature.

The next test of the theory was done on data for the ricinoleyl alcohol. It has a double bond in the 9–10 position and a side OH group in the 11 position. As before, the contribution for 18-chain carbon atoms including the terminal OH group can be assumed to be the one for hexadecanol plus the increment for two CH_2 groups $= 6.44 + 2\times0.44 = 7.32$ A^3. The double bond increases this value by 1.29 and the side OH group decreases it by 0.57, giving a total anisotropy of 8.04 A^3. By using an f factor of 0.595, an optical factor of $A = 11.78$ (calculated from the index of the refraction $n=1.4702$), and the mean stress optical coefficient $C = 1070$ *Br* determined at three temperatures, the experimental value of $\alpha_1-\alpha_2 = 4.50$ A^3 is

[23] L. Silberstein, Phil. Mag. **33**, 92, 215, 521 (1917).

TABLE IV. Calculation of the mean polarizability of the normal alcohols.

Alcohol	M.W.	ρ_{25}	M/ρ	$n_{D_{25}}$	n_D^2	$(n_D^2-1)/(n_D^2+2)$	P cc	α_m A³	Tables
Heptyl	116.19	0.8196	141.8	1.4280	2.040	0.2570	36.50	14.47	
Octyl	130.22	0.827	157.5	1.432	2.045	0.2580	40.60	16.11	40.58
Nonyl	144.25	0.8279	174.3	1.431	2.050	0.2590	45.15	17.90	
Decyl	158.27	0.8297	191.0	1.437	2.065	0.2620	50.00	19.80	
Undecyl	172.30	0.8293	208.0	1.4390	2.070	0.2630	54.70	21.70	
Dodecyl	186.32	0.8295	224.8	1.4410	2.080	0.2650	59.60	23.55	
Tetradecyl (100°F)	214.37	0.824	260.0	1.4366	2.065	0.2620	68.90	27.00	
Cetyl (130°F)	242.43	0.8145	295.5	1.4376	2.065	0.2620	77.40	30.70	

calculated. This is only about ½ the theoretically calculated value. Apparently, the side OH group influences the anisotropy of the molecule much more than had been assumed.

For cetane $C=1030\,Br$ was measured. In using $n=1.4335$, $A=11.46$ and $f=0.562$, like cetylalcohol, $\alpha_1-\alpha_2=4.70$ A³ is calculated. This is somewhat smaller than the value for cetylalcohol. The measurement is not as reliable as the alcohol measurements due to the low viscosity and, therefore, high rates of shear necessary for the measurement. An extension to higher X seems impractical, as the melting point of n-paraffins increases rapidly with X, requiring high temperatures for measurements in the liquid state.

By using the value for the increment in the chain direction of 0.44 A³, the experimental values for polyethylene and polymethylene obtained by Saunders[10] can be re-evaluated. His value of the anisotropy was 7.5 A³. This gives a ratio "q"=16.7 as compared to 48.5 derived by Saunders. By using the calculation of Kubo,[24] mentioned by Saunders, an activation energy for the rotation of the polymethylene chain of 1545 cal/mole, or about 2 RT is obtained, as compared with 2340 cal/mole calculated by Saunders (R—gas constant). Values quoted by Saunders from heat capacities and spectroscopic data give 800 cal/mole, or 1 RT. It seems, however, that our value is sensible.

Should LeFevre's[21] assumption of the isotropy of the C−H bond be always true, as the new results suggest, then measurements of C give a characteristic value for the C-skeleton. This is a clear-cut reason for further investigation on polymers and polymer solutions.

COMPARISON WITH OTHER RESULTS

A study of the literature showed that most of the significant values are summarized in Stuart's new book.[1] However, the higher alcohols, suitable for a comparison with flow-birefringence values, have not been investigated. Recently LeFevre and his school published extensive measurements[25] on the Kerr effect, the depolarization of scattered light, and the dielectric polarization of the n-alcohols in solution in CCl_4 and benzene. The Kerr effect was investigated up to C_{18}, the depolarization of scattered light, however, only to C_6. LeFevre calculated the triaxial polarizability-ellipsoid for the alcohols. By taking the two smaller axes as roughly equal, his values are plotted in Fig. 8 and give a reasonable check with the results of flow birefringence measurements. One must await further extensions of these measurements to higher alcohols.

Recently Stein[26] and co-workers performed a more precise check of the depolarization of scattered light on paraffins in the vapor state, using a photomultiplier technique. They evaluated their measurements assuming, as was done here, rotational symmetry of the molecule. Their values are also plotted in Fig. 7. The existing data on depolarization on alcohol vapors are not consistent, probably because of the extreme difficulty of making the measurements. One does not even have the possibility of deciding if the anisotropy of the molecule increases, remains constant, or decreases with a change in X. For hydrocarbons in the vapor state it apparently increases, according to Stein, *et al.*, but values in Stuart's book may also be interpreted as being constant. In the liquid state or in solution the depolarization decreases with X, as listed in Stuart's book and recently found by LeFevre *et al.* In Fig. 7, $\alpha_1-\alpha_2$ determined by different methods is plotted as a function of X. LeFevre's values for the alcohols in solution are used directly, as mentioned. The depolarization values are calculated assuming $\alpha_2=\alpha_3$ according to the well-known equation:

$$\alpha_1-\alpha_2=3\alpha_m(\delta^2)^{\frac{1}{2}}$$
$$\delta^2=5\Delta/(6-7\Delta), \tag{9}$$

where Δ=ratio of the intensity of scattered light in two

TABLE V. C−C bond polarizabilities.

Value	Exp.	Bunn-D	Denbigh	Bolton	CH_2 gas	CH_2 liq
α_1	0.81	1.00	1.88	0.70	1.02	0.67
α_2	0.37	0.25	0.02	0.38	0.27	0.45
α_m	0.52	0.50	0.64	0.49	0.52	0.52
$\alpha_1-\alpha_2$	0.44	0.75	1.86	0.32	0.75	0.22
α_1/α_2	2.19	4.00	94	1.84	3.8	1.5

[24] R. Kubo, J. Phys. Soc. Japan **4**, 319 (1949).

[25] R. J. W. LeFevre and A. J. Williams, J. Chem. Soc. **1960**, 108, 115, 128; R. J. W. LeFevre and B. P. Rao, *ibid.* 119; C. G. LeFevre, R. J. W. LeFevre, B. P. Rao, and A. J. Williams, *ibid.* 123.

[26] R. S. Stein, D. A. Keedy, and J. Powers, Office of Naval Research Tech. Rept., Project NR 356-378 (July, 1959).

perpendicular directions = depolarization factor. The values for the liquid hydrocarbons are recalculated using Eq. (9) and δ from Table 110 of Stuart's book. It is seen that any of the series of measurements conform more or less to a linear relationship as a function of X. From the slopes the values listed in Table V are calculated, using the same procedure as given for the flow-birefringence measurements. The values of LeFevre for the alcohols and the ones for the liquid hydrocarbons match very well; they are, however, about half as great as the ones for the hydrocarbons in the gaseous state. The values from flow-birefringence are between the two other sets of results.

At the moment, no final decision seems possible. One must await further measurements, especially depolarization studies of higher alcohols in the vapor state.

JOURNAL OF APPLIED PHYSICS VOLUME 31, NUMBER 11 NOVEMBER, 1960

Hollow Pyramidal Crystals of Polyethylene and a Mechanism of Growth

WALTER D. NIEGISCH AND PAUL R. SWAN
Union Carbide Plastics Company, Bound Brook, New Jersey

A hollow pyramidal model for diamond-shaped single crystals of polyethylene is proposed which accounts for the electron microscope observations and electron diffraction effects presented in this paper and in the literature. The pyramidal shape occurs because the rows of folded molecules along the (110) growth face in each quadrant of the crystal are translated along the molecular chain direction by two carbon-carbon distances relative to the previous row. This translation presumably occurs in order to relieve steric interferences at the folds or loops of the polymer chain. The resulting triclinic cell, of which the familiar orthorhombic cell is in reality a subcell, has a c dimension equal to the constant fold length of the polymer chain, and remaining parameters of $a = 7.84$ A, $b = 5.56$ A, $\alpha = (90\text{–}27.3)°$, $\beta = (90\text{–}19.0)°$ and $\gamma = 81.5°$. The values 19.0 and 27.3 degrees are, respectively, arctan (c/a) and arctan (c/b) of the orthorhombic subcell, so that the (001) planes of the triclinic cell which contain the folds on the surface of the pyramids are (111) planes relative to the orthorhombic subcell.

INTRODUCTION

WE recently reported that single crystals of polyethylene were hollow pyramids instead of flat tabular platelets as commonly believed.[1,2] Since that time, Bassett, Frank, and Keller independently came to the same conclusion,[3] but the evidence they presented did not conclusively establish the pyramidal model since at least two other morphological configurations might explain their data. For this reason we present additional evidence which establishes the pyramidal model, and also propose a mechanism for the growth of hollow pyramidal crystals.

EXPERIMENTAL

Polymer Description

The polymer used in this investigation was a very linear experimental polyethylene, characterized by a narrow high molecular weight distribution.[4] Various high molecular weight fractions were dissolved in xylene or trichloroethylene at concentrations from 0.001% to 2%. The crystals were obtained by cooling a refluxed solution at a rate of approximately 10°/hr through the cloud point. This proved to be more effective in producing single crystals than a procedure of quenching to a predetermined temperature and crystallizing isothermally, because undesirable picture-framelike growth developed at the perimeter of the crystals in many cases during isothermal crystallization. The suspension was cooled to room temperature and deposited by means of an air brush upon a carbon substrate premounted on standard electron microscope specimen screens.

Experimental Results

Many investigators have observed wrinkles in single crystals of polyethylene which are generally b-axis oriented, although occasionally they are either a-axis or even randomly oriented. Keller has suggested that the folding or rolling up of thickened centers of lozenge-shaped crystals along the b axis is related to the orientation of polyethylene spherulite fibrils.[5] This has been substantiated[2] by the discovery of truncated diamond-shaped crystals which possess b-axis oriented overgrowth which in later stages develops into spherulite arms.

If we consider only the crystals in which the wrinkles have apparently reached a maximum width, Fig. 1, it is possible to determine approximately the maximum angle of inclination of the hollow pyramidal crystal. The width of the wrinkle in the collapsed crystal gives

[1] W. D. Niegisch, "The nucleation of polyethylene spherulites," presented at the Polymer and Fiber Microscopy Society Meeting, Textile Research Institute, Princeton, New Jersey, September 26, 1959.
[2] W. D. Niegisch, J. Polymer Sci. **40**, 263 (1959).
[3] D. C. Bassett, F. C. Frank, and A. Keller, Nature **184**, 810 (1959).
[4] J. J. Smith, E. F. Bonner, F. M. Rugg, L. H. Wartman, and W. L. Carrick, J. Am. Chem. Soc. **82**, 3883 (1960).
[5] A. Keller, Phil. Mag. **2**, 1171 (1957).

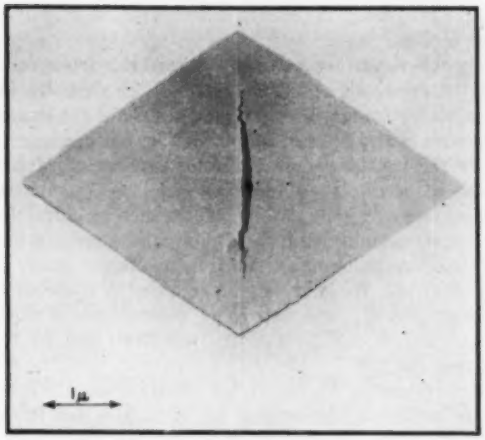

FIG. 1. A diamond-shaped single crystal showing a wrinkle along the *b* axis.

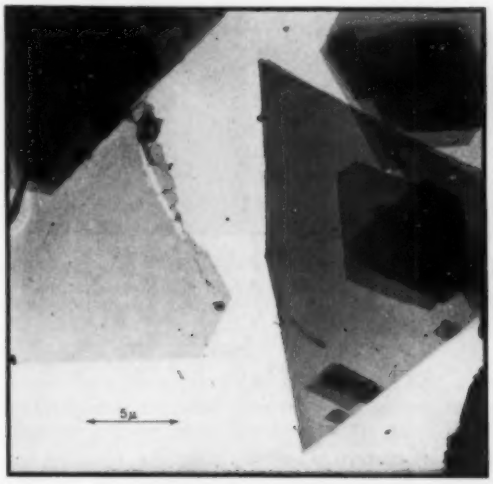

FIG. 2. A truncated diamond-shaped crystal which has folded on itself along the *b* axis.

directly a measure of the inclination along the *a* axis of the pyramidal form. We find this angle to be 19±2°. The reason for the collapse of the pyramid is due to the great compressive force of the surface tension of the solvent as the specimen is dried prior to electron microscopic examination. Further collapse takes place during the early stages of examination of the specimen due to effects of the highly energetic electron beam.

The angle of inclination of about 19° along the *a* axis by no means establishes the pyramidal shape of the crystal. Although it is intuitively tempting to consider these crystals to be pyramidal, at least two other configurations are possible. One is roof-shaped and the other is a saddle-shaped. Both these shapes are conveniently eliminated from the present discussion on the basis of Fig. 2. Here is shown one of several crystals which folded over on itself along the *b* (minor) axis. The shape of the fold is convex, which obviously eliminates the roof-shaped configuration, and it can be shown that a saddle-shaped crystal would fold in a concave fashion.

The fact that several crystals have folded as shown in Fig. 2 does not preclude the possibility of the existence of configurations other than pyramidal, but at least some crystals have been proven to be pyramidal, a fact which is supported by the overwhelming crystallographic dark-field evidence to be presented later. This evidence will show that a roof-shaped or planar model is essentially nonexistent. There is some indication, however, that saddle-shaped crystals may exist.[6]

In the light of this evidence in support of the pyramidal configuration, we have obtained from the shape of the fold of crystals such as shown in Fig. 2 an approximate value for the angle of inclination along the *b* axis of the crystal. If we assume that the base of this truncated diamond crystal is planar, the angle of inclination along the *b* axis is about 26°.

[6] W. D. Niegisch and P. R. Swan (to be published).

Crystallographic Dark-Field Illumination

The existence of four quadrants in single crystals was first established from bright-field images photographed at low intensity,[7] and more recently by a technique which we prefer to call crystallographic dark-field illumination,[1,8] but which has also been referred to as diffraction microscopy.[9] This method of illumination is most interesting in that it enables one to identify those portions of the field of view which produce a particular diffraction spot. In brief, the method consists of selecting one of the diffracted beams by proper positioning of the objective aperture, and of magnifying that beam instead of the central beam. The diffracted beam carries with it, of course, a dark-field image of the material which diffracted into that particular reflection.

When this technique is applied to the 110 reflection from a single polyethylene crystal such as in Fig. 3(a), the image obtained is that of Fig. 3(b). In order to define properly the observed effect, it is necessary first to determine the orientation on the fluorescent screen of the bright-field and crystallographic dark-field images with respect to the orientation of the diffraction pattern. When this is accomplished, we find that the 110 spot is primarily produced by sectors bounded by $(\bar{1}10)$ and $(1\bar{1}0)$ growth faces, provided that the crystal is normal to the beam direction. This of course constitutes further evidence for the nonplanar nature of the crystals under discussion.

This method is related to one reported by Bassett,

[7] A. W. Agar, F. C. Frank, and A. Keller, Phil. Mag. 4, 32 (1959).

[8] P. R. Swan and W. D. Niegisch, "Structure of single crystals of polyethylene," presented at the Meeting-in-Miniature of the American Chemical Society, North Jersey Subsection, Seton Hall, New Jersey, February 1, 1960.

[9] J. H. Reisner, RCA Scientific Instrument News 3, 1 (1958).

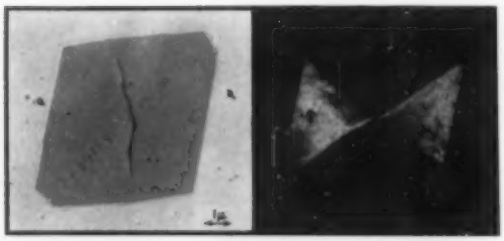

(a) (b)

FIG. 3. (a) A truncated single crystal in bright-field illumination. (b) A crystallographic dark-field image from a single 110 reflection of the crystal in Fig. 3(a).

Frank, and Keller,[3] in which they selected a portion of a crystal and found that this produced a partial diffraction pattern. However, the absence of a complete diffraction pattern is not unambiguous, since we have observed in many instances, particularly in tilted crystals, that an entire crystal will produce only a partial pattern. This is due to the fact that only a portion of the crystal is in the correct Bragg orientation to record low index ($hk0$) reflections.

The determination of the particular portions of the crystal which diffract into each diffraction spot can be established by an even more effective procedure. First, select a single crystal and record the diffraction pattern of this crystal [Fig. 4(a)]. Then magnify simultaneously each of the diffraction spots by underfocusing the intermediate lens sufficiently to obtain the image shown in Fig. 4(b). This is a simultaneous record of all crystallographic dark-field images on a single exposure. In the center of the pattern we have outlined the overexposed bright-field image in order to show better the magnification of Fig. 4(b).

By this means we are able to record in a few seconds all the crystallographic images. This is virtually impossible by standard techniques because of the limited exposure time available before the electron beam cross-links the crystal. After the composite micrograph is obtained there is still ample time subsequently to record other crystallographic effects such as diffraction patterns, proof of orientation, images of tilted crystals, normal crystallographic dark-field images such as Fig. 5(a), etc. We have, in fact, recorded 22 consecutive micrographs of these and other effects from a single crystal before the crystallinity was destroyed by the electron beam.[6]

Before leaving Fig. 4(b), we should draw attention to the outline of the intersection of sectors seen in the 020 reflections, which further establishes the presence of six sectors in truncated crystals. Also, the 200 reflections are illuminated by the diamond-shaped contours observed by Agar, Frank, and Keller.[7] Since these crystallographic images may be thought of as being diffraction contour lines, the 200 reflections indicate that the central portion of the crystal is not flat, but forms a crater of which the contour lines form the rim.

One is also prompted to suggest that considerable slip occurs along planes such as (100) and (010). Figure 5(a) is a portion of the crystallographic dark-field image of the crystal shown in Fig. 5(b). We define the large, brightly illuminated sector as a 110 sector and the narrow isosceles sector as a 100, because of the related growth faces. The fine texture in the 110 sector appears

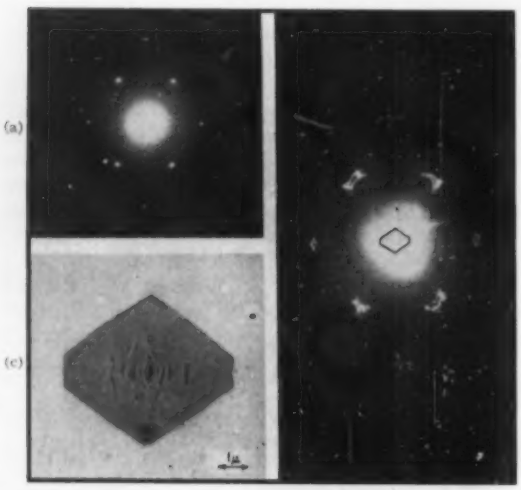

(a) (c) (b)

FIG. 4. (a) Electron diffraction pattern of the crystal in Fig. 4(c). (b) Underfocused image of Fig. 4(a). (c) Bright-field image oriented correctly with respect to its diffraction pattern, Fig. 4(a).

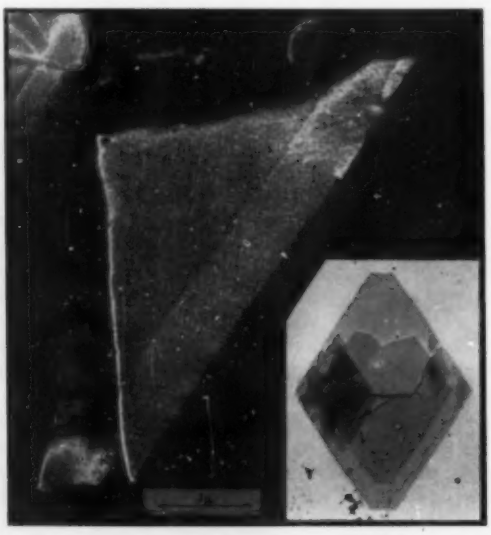

FIG. 5. (a) Texture in a 110 sector by crystallographic dark-field illumination. The adjacent 100 sector is partially visible. (b) The bright-field image of the entire crystal (insert). Figure 5(a) is the lower right-hand portion of the crystal.

to be oriented approximately along the a and b axes. This fine structure may be formed as a result of localized slip along the (100) and (010) planes. The angle between these slip planes is approximately 82° to 85° near the center of the crystal. Also of interest is the extremely bright line of intersection of the adjacent 100 and 110 sectors.

MODEL AND MECHANISM OF GROWTH

We feel that the evidence which has been presented unequivocally establishes the existence of hollow pyramidal crystals. The crystal must be hollow since the transmittance of electrons through the crystal is essentially constant over the entire (001) face. Thus, we visualize a shallow hollow pyramid inclined about 19° and 26° along the a and b axes, and with a thickness equal to the fold repeat distance of about 125 A.

The question which now arises is, how and why do these crystals grow in this unusual fashion? We propose the following hypothesis to explain this phenomenon. The angles of inclination of 19° and 26° along the a and b axes, respectively, as determined in the foregoing observations, are to be compared with the values of arctan $(c/a)=19.0°$ and arctan $(c/b)=27.3°$ for the familiar orthorhombic cell [Fig. 6(a), (b)]. This suggests that a stepwise translation of orthorhombic cells occurs in the c direction for each new cell added in the a and b directions during the growth process.[1] This stepwise translation is shown schematically in Fig. 6(c), where only the top layer of orthorhombic unit cells in one sector of the diamond-shaped crystal is shown. This means that each additional row of folded molecules along the (110) growth face is translated one unit cell, or two CH_2 groups, relative to the previous row of molecules.

This point may be clarified by examining a portion of a growing hollow pyramidal crystal in detail. The precise orientation of the region under scrutiny is shown as the shaded region of Fig. 7(a), which is a projection on a plane normal to the c axis of the crystal. An orthorhombic cell in this ab basal projection is singled out for further reference.

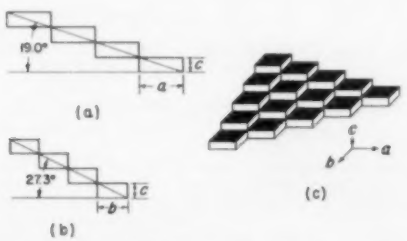

FIG. 6 (a) Stepwise translation of unit cells in the ac plane. (b) Stepwise translation of unit cells in the bc plane. (c) Schematic representation of the stepwise translation of orthorhombic cells in a 110 sector.

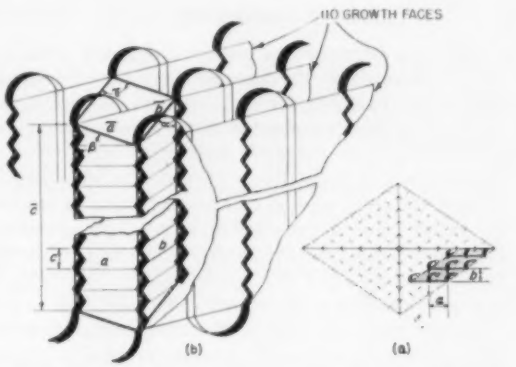

FIG. 7. (a) Projection of unit cells normal to the c axis. (b) A schematic isometric view of a portion of a growing crystal, showing the (111) plane of folds, the folding in (110) planes, and the proposed triclinic cell.

The schematic isometric view of the shaded projection is shown in Fig. 7(b). The positions of the molecules in the folded chain configuration are indicated by the ribbons folding on (110) growth faces. The stacked orthorhombic cells are shown, as is the stepwise translation of unit cells at the top and bottom of the large cell. Thus the planes containing all the molecular folds in one sector of the crystal are (111) planes relative to the orthorhombic cell.

From these arguments, it follows that the true unit cell is a triclinic cell with the c dimension equal to the folded chain repeat distance and with the following cell parameters:

$\bar{a}=7.843$ A	$\alpha=90-27.3°$
$\bar{b}=5.563$ A	$\beta=90-19.0°$
$\bar{c}\sim 125$ A	$\gamma=81.5°$

These values for the triclinic cell were calculated from cell parameters of the orthorhombic cell determined at 30°C, which differ slightly from the corrected values of Bunn's original data.[10] The existence of a large unit cell was first proposed by Keller and O'Conner in reference to flat lozenge-shaped crystals,[11] but the concept holds equally true for pyramidal crystals. The angle γ between the a and b axes of the triclinic cell may be related to the 82–85° gridlike pattern observed in Fig. 5(a). This suggests that the crystals flatten by a simultaneous collapse and slip mechanism, as will be discussed later.

In our model of stepwise translation of orthorhombic subcells, the folding polymer molecule has ample room to complete the bend since it does so at an empty lattice site. Any possible steric hindrance caused by a large number of carbon atoms in the fold which would prevent the formation of a flat tabular crystal is circumvented in the pyramidal model.

[10] C. W. Bunn, Trans. Faraday Soc. **35**, 482 (1939).
[11] A. Keller and A. O'Conner, Discussions Faraday Soc. **25**, 114 (1958).

CONCLUSIONS

We have attempted to present a detailed model for the structure of only the diamond-shaped single crystals. Truncated diamonds are more difficult to explain because of the appearance of the sector bounded by a (100) growth face. The degree of truncation can be varied continuously by regulating such variables as molecular weight, choice of solvent and concentration. Therefore the intersection between 110 sectors and 100 sectors is not a low index crystallographic plane, and so constitutes a unique kind of twin boundary. Moreover, a stepwise translation of orthorhombic unit cells in the 100 sector would necessarily generate a large monoclinic cell, so that we have the crystallographically unique situation of a single (multiply twinned) crystal containing simultaneously triclinic and monoclinic modifications.

A somewhat speculative extension of these truncated crystals is the observation that the ultimate in truncation would be a *b*-axis oriented fibril bounded by (001) and (100) faces. This may not be too farfetched, since it can be shown that the appearance of the truncated face is indicative of nonequilibrium crystallization conditions,[12] and the spherulites grown from dilute solution have been observed in this Laboratory to be nonstable forms.[6] Any detailed correlation, however, would be quite premature at this time.

There are many unexplained phenomena occurring which are brought to light by the crystallographic dark-field observations reported here. We have not as yet arrived at a satisfactory explanation for the preferred formation of crystallographic images of diametrically opposite sectors from a single 110 reflection. Also, we know that many crystals which diffract have collapsed, as shown by the wrinkles in Figs. 1, 3(a), and 5(b). Bragg requirements are such that the crystals must be correctly oriented with respect to the incident electron beam to within less than 1°. If the crystals are hollow pyramids and collapse so as to tilt the *c* axis 19° along the *a* direction, then no low-index reflections could be observed. To this extent our model and evidence are in conflict, and we propose that the collapse of a hollow pyramid occurs by a combination of tilting and slippage in localized regions. The detailed diffraction effects to be expected from such a combination have not been worked out at present.[13]

The stepwise translation model is not without precedence. For instance, the translation of adjacent chains by one CH_2 length was postulated by Schoon in 1938 as a general phenomenon in the field of long chain compounds.[14] The simplest case is that of the *n*-paraffins, which crystallize in three or four different crystalline forms and are thought to vary by translations of one or two CH_2 lengths between adjacent molecules in various directions. The polyethylene case is simple compared to the requirements for forming single crystals by the folded chain configuration with, say, polyamides, where the "subcell" is already triclinic and the relative amount of adjacent-chain translation is fixed by intermolecular hydrogen bonds. However, we expect that similar behavior of the planes of folds being not normal to the chain direction occurs in polymer crystals other than polyethylene.

ACKNOWLEDGMENTS

The authors wish to thank Dr. G. E. Myers and Mr. J. R. Dagon of this Laboratory who kindly supplied the numerous high molecular weight fractions used in this investigation. The assistance of Mr. S. Crisafulli in the experimental portions of this work is also gratefully acknowledged.

[12] P. Hartman, Acta Cryst. **11**, 459 (1958).

[13] *Note added in proof*. Subsequent consideration of the details of folding and collapse has led us to a qualitative understanding which bridges the gap between the apparent anomalies cited here. These data are unpublished.

[14] T. Schoon, Z. physik. Chem. **39B**, 385 (1938).

A Theoretical Calculation of the Birefringence of Polypropylene Crystals*

D. A. KEEDY, J. POWERS, AND R. S. STEIN
Department of Chemistry, University of Massachusetts, Amherst, Massachusetts

In the course of some investigations on the effect of carbon-carbon and carbon-hydrogen bond polarizabilities on the optical properties of hydrocarbon polymers, a theoretical calculation of the polypropylene chain principal polarizabilities was performed. The polypropylene chain model given by Natta was used. Results were expressed in terms of carbon-carbon and carbon-hydrogen bond polarizabilities. Two sets of values of bond polarizabilities, one given by Denbigh, the other by Bunn and Daubeny, were substituted into the polarizability equation. Values of chain principal polarizabilities were then used to calculate the refractive index and birefringence using the Lorentz-Lorenz equation. Better agreement was found between experimental and theoretical birefringence values using Denbigh's data. Three explanations are suggested which might account for the differences between the two sets of bond polarizabilities.

INTRODUCTION

TWO sets of values[1,2] for the carbon-carbon bond polarizability exist in the literature. This casts some doubt on the principle of the additivity of bond polarizabilities which these authors used in their calculations. Bunn[1] has questioned the Denbigh values of C−C bond polarizabilities on the basis of the unreasonably low value of transverse polarizability. A means for checking the plausibility of the two sets of carbon-carbon bond polarizabilities is to calculate the principal polarizabilities for the polypropylene chain. This was done and the results are compared with experimental values.

MODEL OF THE POLYPROPYLENE CHAIN

Natta and co-workers[3] have concluded from x-ray diffraction studies on crystalline isotactic polypropylene that it possesses a helical structure with three monomers in each repeat distance. The repeat distance is 6.5 A measured along the helix axis. The axes of the pendant methyl groups are at an angle of 120° with respect to each other in the plane perpendicular to the chain axis. The angle between adjacent carbon-carbon atoms in the main chain is 114°.

An idealized polypropylene chain, used in the calculation, is shown in Fig. 1(a) and (b). For the purpose of this calculation, C_1 represents the position of a carbon atom expressed in Cartesian coordinates, etc.; $\mathbf{a}_1$ is the bond vector from carbon atom 1 to carbon atom 2. The component of the atom coordinate in the X direction is x, that in the Y direction y, and that in the Z direction a. L is the period of the helix.

CALCULATION OF ATOM COORDINATES AND BOND VECTORS FROM THE MODEL

The coordinates of the carbon atoms of the main chain are given in Table I. Bond vectors are then obtained by taking the difference between two adjacent carbon atom coordinates. The result is given in Table II.

To evaluate x, y, and a, three simultaneous equations are set up by taking the dot product of $\mathbf{a}_1$ with itself, $\mathbf{a}_2$ with itself, and $\mathbf{a}_3$ with itself, then equating the result in each case with the square of the carbon-carbon bond length. Equations (1) to (3) follow:

$$\mathbf{a}_1\cdot\mathbf{a}_1 = x^2+a^2 = l_{CC}^2, \tag{1}$$

$$\mathbf{a}_2\cdot\mathbf{a}_2 = (\tfrac{1}{3}L-a)^2 = l_{CC}^2, \tag{2}$$

$$\mathbf{a}_3\cdot\mathbf{a}_3 = \tfrac{1}{4}x^2+y^2+a^2 = l_{CC}^2, \tag{3}$$

where l_{CC} is the carbon-carbon single bond distance 1.54 A and L is the helix repeat distance. Solution of the foregoing equations gives values of $a=0.6267$, $y=1.2182$, and $x=1.4067$.

The numerical values for the main chain atom coordinates and bond vectors are given in the Appendix.

TABLE I. Coordinates of the main chain carbon atoms.

$C_1=0, 0, 0$	$C_4=\frac{1}{2}x, y, (\frac{1}{3}L+a)$
$C_2=x, 0, a$	$C_5=\frac{1}{2}x, y, \frac{2}{3}L$
$C_3=x, 0, \frac{1}{3}L$	$C_6=0, 0, (\frac{2}{3}L+a)$
$C_7=0, 0, L$	

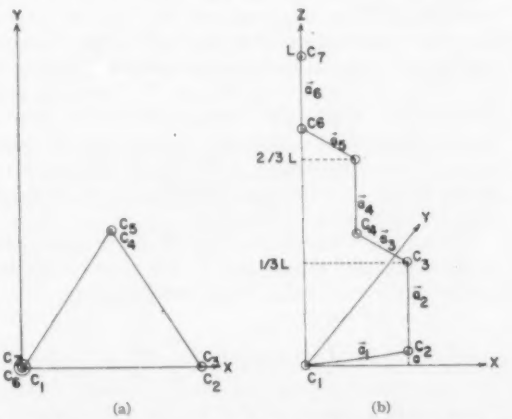

FIG. 1. Idealized polypropylene chain used in assignment of vector coordinates: (a) top view, (b) side view.

* This work was supported in part by a contract from the Office of Naval Research and a grant from the Plax Corporation. It was presented in part at the Detroit meeting of the American Physical Society, March 22, 1960.

[1] C. W. Bunn and R. Daubeny, Trans. Faraday Soc. **50**, 1173 (1954).

[2] K. G. Denbigh, Trans. Faraday Soc. **36**, 936 (1940).

[3] G. Natta, P. Corradini, and M. Cesari, Rend. accad. nazl. Lincei VIII **21**, 365 (1956).

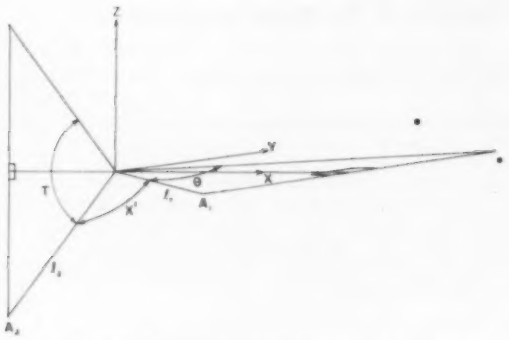

FIG. 2. Diagram of geometrical relationships used in the derivation of Eq. (8).

TABLE II. Coordinates of main chain bond vectors.

$\mathbf{a}_1 = x, 0, a$	$\mathbf{a}_4 = 0, 0, (\frac{1}{2}L - a)$
$\mathbf{a}_2 = 0, 0, (\frac{1}{2}L - a)$	$\mathbf{a}_5 = \frac{1}{2}x, -y, a$
$\mathbf{a}_3 = -\frac{1}{2}x, y, a$	$\mathbf{a}_6 = 0, 0, (\frac{1}{2}L - a)$

As a check on the calculations, the carbon-carbon bond angle was obtained by taking the dot product between two adjacent bond vectors. Since all the bond vectors are taken in a positive direction, the direction of one vector has to be reversed so that the bond angle will fall in the second quadrant. Solving Eq. (4) for θ,

$$-\mathbf{a}_1 \cdot \mathbf{a}_2 = l_{CC}^2 \cos\theta \tag{4}$$

yields a value for the bond angle of 114° 1′. This result compares very well with Natta's value[3] of 114°.

The main chain carbon-carbon bond angle is distorted 4° 33′ from the tetrahedral angle. The effect of this distortion on neighboring carbon-hydrogen and carbon-methyl bond angles can be calculated from the following considerations. In Fig. 2, X, Y, and Z are the axes of the polypropylene chain, θ the carbon-carbon bond angle, T the angle between the two substituents on a main chain carbon atom, and χ the angle between a bond vector lying on the main chain and one lying between the carbon atom and a substituent. T is assumed to be a tetrahedral angle. This assumption can be justified by consideration of a molecule such as ethylene, which has a carbon atom with a double bond and two single bonds. In this case, the angle between the two hydrogen bonds is very nearly tetrahedral.

The angle χ is found by taking the dot product of the vectors associated with A_1 and A_2, the atom coordinates of the substituent atoms. Their coordinates are

$$A_1 = \left(l_1 \cos\frac{\theta}{2}, -l_1 \sin\frac{\theta}{2}, 0\right), \tag{5}$$

$$A_2 = \left(-l_2 \cos\frac{T}{2}, 0, -l_2 \sin\frac{T}{2}\right). \tag{6}$$

If $\mathbf{D}_1$ and $\mathbf{D}_2$ are the bond vectors of A_1 and A_2, respectively, then

$$\mathbf{D}_1 \cdot \mathbf{D}_2 = l_1 l_2 \cos\chi. \tag{7}$$

By substituting Eqs. (5) and (6) into Eq. (7), one obtains

$$-\cos\frac{\theta}{2}\cos\frac{T}{2} = \cos\chi. \tag{8}$$

On solving Eq. (8) for χ, one obtains a value of 108° 15′.

The value for the angle χ having been calculated, one can readily obtain the bond vectors between the hydrogen and methyl group carbon atoms and the main chain carbon atoms by solving three simultaneous equations:

$$\mathbf{b}_1 \cdot \mathbf{b}_1 = x^2 + y^2 + z^2 = l_{CH}^2 \tag{9}$$

$$-\mathbf{a}_1 \cdot \mathbf{b}_1 = -\mathbf{a}_1 \cdot (x,y,z) = l_{CC} l_{CH} \cos\chi \tag{10}$$

$$\mathbf{a}_2 \cdot \mathbf{b}_1 = \mathbf{a}_2 \cdot (x,y,z) = l_{CC} l_{CH} \cos\chi. \tag{11}$$

The unknown vector, $\mathbf{b}_1$, is the bond vector between C_2 and the substituent atom in question. l_{CH} is the carbon-hydrogen bond length, 1.09 A. The x, y, and z components of the bond vector $\mathbf{b}_1$ can be determined from these equations. Two solutions are obtained from these equations. These solutions represent the atom coordinates of the substituent atom on the main chain atom. If the atom coordinates of C_2 are added to the bond vector $\mathbf{b}_1$, the atom coordinates of the hydrogen atom in question are obtained. The same procedure, as outlined in the foregoing, is followed in order to determine the atom coordinates of the other hydrogen and methyl-carbon atoms lying along the main chain. The resulting values are listed in the Appendix.

The hydrogen bond vectors of the methyl groups may be calculated by the following procedure: The carbon-methyl-carbon bond vector is extended 1.09 A. The resulting vector $\mathbf{d}$ is the methyl-hydrogen bond vector with coordinate axes (x'',y'',z'') of length 1.09 A (Fig. 3). The vector $\mathbf{d}$ is rotated 70° 32′ towards the Z axis keeping ϕ constant. The vector $\mathbf{b}$ with coordinate axes x', y', z', the result of the rotation of $\mathbf{d}$, is the methyl-hydrogen bond vector and has the same length as $\mathbf{d}$. The vector $\mathbf{b}$ forms a tetrahedral bond angle with the carbon-methyl carbon bond vector. By referring to Fig. 3, the following equations may be deduced in order to evaluate the coordinates of $\mathbf{b}$.

$$\theta_1 = \theta + 70° 32', \tag{12}$$

where

$$\theta = \sin^{-1}(z/1.09),$$

and

$$\theta_1 = \sin^{-1}(z'/1.09),$$

$$z' = l_{x'y'} \tan\theta_1, \tag{13}$$

since

$$\tan\phi = y/z. \tag{14}$$

Then, on using Eq. (14) to evaluate ϕ,

$$x' = l_{x'y'} \cos\phi, \tag{15}$$

$$y' = l_{x'y'} \sin\phi. \tag{16}$$

TABLE III. Values of polypropylene chain polarizability ($\times 10^{25}$ cm^3).

	Denbigh	Bunn and Daubeny
P_x	168.73	159.17
P_y	168.73	159.17
P_z	186.35	163.12
$P_{\parallel}-P_{\perp}$	17.62	3.95

The other two hydrogen bond vectors and atom coordinates of the methyl group are determined by the same type of calculation. The results of this calculation are given in the Appendix.

CALCULATION OF THE POLYPROPYLENE CHAIN POLARIZABILITY

If $P_{\parallel}$ is the chain polarizability parallel to the helical axis (0,0,1), and $P_{\perp}$ is the average polarizability perpendicular to the helical axis (1,0,0) and (0,1,0), then $P_{\parallel}=P_z$, and $P_{\perp}=(P_x+P_y)/2$. P_x and P_y are equal because of the cylindrical symmetry of the model.

The chain anisotropy $(P_{\parallel}-P_{\perp})$ is related to the bond anisotropy $(b_{\parallel}-b_{\perp})$ by Eq. (17):

$$P_{\parallel}-P_{\perp}=n_{CC}(b_{\parallel}-b_{\perp})_{CC}f_{CC}+n_{CH}(b_{\parallel}-b_{\perp})_{CH}f_{CH}. \quad (17)$$

n_{CC} and n_{CH} are the number of carbon-carbon and carbon-hydrogen bonds, respectively, in a repeat distance along the helical axis.

f_{CC} and f_{CH}, the average orientation functions, are defined by

$$f_{CC}=\frac{3\langle\cos^2\theta_{CC}\rangle_{av}-1}{2}, \quad (18)$$

$$f_{CH}=\frac{3\langle\cos^2\theta_{CH}\rangle_{av}-1}{2}. \quad (19)$$

The average of the cosine of the bond angle squared is given by

$$\langle\cos^2\theta_{CC}\rangle_{av}=\frac{\Sigma_i[\mathbf{a}_i\cdot(0,0,1)]^2}{l_{CC}^2 n_{CC}}; \quad (20)$$

$[\mathbf{a}_i\cdot(0,0,1)]$ is the z component of the ith carbon-carbon bond. Similarly,

$$\langle\cos^2\theta_{CH}\rangle_{av}=\frac{\Sigma_i[\mathbf{b}_i\cdot(0,0,1)]^2}{l_{CH}^2 n_{CH}}; \quad (21)$$

$[\mathbf{b}_i\cdot(0,0,1)]$ is the z component the ith carbon-hydrogen bond.

The polarizability along an axis (in this case, X) of the chain may be calculated by using Eq. (22):

$$P_x=(b_{\parallel}-b_{\perp})_{CC}\sum_{\substack{\text{All C—C}\\ \text{bonds}}}\cos^2\theta_{CC}+b_{\perp CC}$$
$$+(b_{\parallel}-b_{\perp})_{CH}\sum_{\substack{\text{All C—H}\\ \text{bonds}}}\cos^2\theta_{CH}+b_{\perp CH}. \quad (22)$$

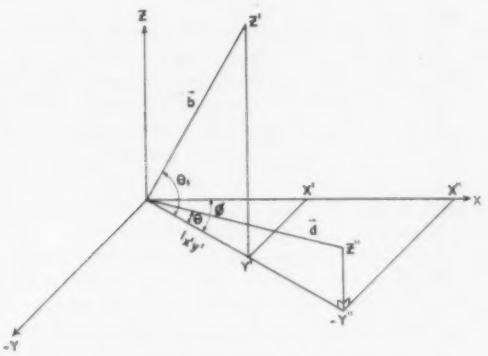

FIG. 3. Diagram of geometrical relationships used in the derivation of Eqs. (12)–(16).

The results of these calculations are shown in Table III.

The birefringence of the polypropylene unit cell may now be calculated from the following considerations. Since the polypropylene chains have cylindrical symmetry,

$$P_x'_{\text{u.c.}}=nP_x, \quad (23)$$

$$P_y'_{\text{u.c.}}=nP_y, \quad (24)$$

$$P_z'_{\text{u.c.}}=nP_z. \quad (25)$$

n is the number of chains per unit cell. Natta[3] has concluded that there are four chains per unit cell. Upon substituting the values of P_x, P_y, and P_z into Eqs. (23) to (25), the unit cell polarizabilities, shown in Table III, are obtained. Interactions between helices and between bond polarizabilities have been neglected in the foregoing calculation.

The refractive index of polypropylene crystals may be calculated from the Lorentz-Lorenz equation,

$$\frac{\bar{n}^2-1}{\bar{n}^2+2}=\frac{4\pi}{3}\bar{P}, \quad (26)$$

where $\bar{n}$ = the average refractive index and $\bar{P}$ = the average unit cell polarizability per unit volume. Now

$$\bar{P}=(P_{\parallel}+2P_{\perp})/3V_C, \quad (27)$$

where V_C = the unit cell volume $=894.0\times10^{-24}$ cm^3.

For small polarizability differences, the relationship between the birefringence and the difference in principal polarizability may be obtained by differentiating Eq. (26). This gives

$$(n_{\parallel}-n_{\perp})=\Delta_{\text{u.c.}}=\frac{2\pi(\bar{n}^2+2)^2(P_{\parallel}-P_{\perp})_{\text{u.c.}}}{9\bar{n}V_C}. \quad (28)$$

The theoretical birefringence values, based upon 100% crystallinity, using Denbigh's[2] and Bunn's[1] bond polarizability values in the foregoing equations, are 0.067 and 0.015, respectively.

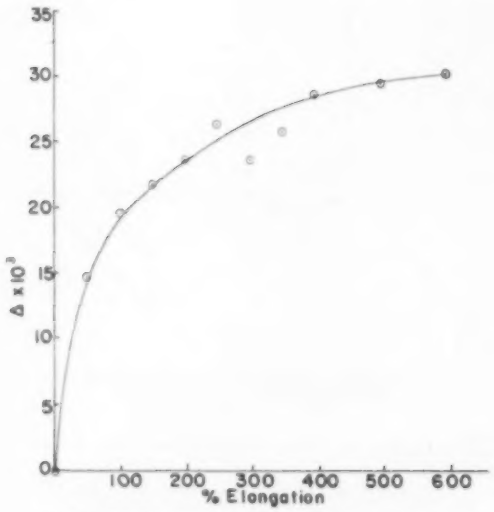

FIG. 4. Birefringence versus percentage elongation for quenched polypropylene.

DISCUSSION

Padden and Keith[4] reported a polypropylene film refractive index of 1.510 measured with an Abbé refractometer. Their film was 70% crystalline and was unoriented. We have observed a refractive index of 1.508 in this laboratory using a Becke Line method on unoriented film of 50–70% crystallinity. The observed value (1.51) agrees better with the refractive index calculated on the basis of Bunn's bond polarizability data[1] (1.51) than that calculated from Denbigh's[2] (1.57).

A more exacting test of the validity of the bond polarizability additivity concept lies in the comparison between the observed and the calculated birefringence values. Z. W. Wilchinsky[5] has observed, on stretched polypropylene films (40–70% crystallinity), a birefringence of +(0.02–0.03) birefringence unit. Measurements of birefringence versus percentage elongation performed in this laboratory give the same result (Fig. 4). Keith and Padden[6] reported a value of +0.027 birefringence unit for a highly oriented polypropylene film.

If the observed birefringence +(0.02–0.03) is assumed due entirely to chain orientation in the crystalline region, the birefringence values calculated from Denbigh's and Bunn's bond polarizability values are 0.033 and 0.007 birefringence units, respectively, for 50% crystalline polypropylene.

The substitution of Bunn's bond polarizability would be expected to show the better agreement in the calculation of polypropylene crystal birefringence if the assumption of bond polarizability additivity holds. The better agreement of Denbigh's values indicates a breakdown in this assumption. Other evidence bearing on this question may be cited from the literature.

Smith and Mortensen[8] recently reviewed the work of previous authors who have made bond polarizability calculations. They derived general tensor expressions for molecular anisotropy and showed that for tetrahedrally bonded hydrocarbons, the anisotropy γ is given by

$$\gamma = C\Gamma_{CC},$$

where

$$\Gamma_{CC} = (b_1 - b_2)_{CC} - 2(b_1 - b_2)_{CH},$$

and b_1 and b_2 are the polarizabilities parallel and perpendicular to the bond, respectively.

C is a theoretical constant dependent upon the structure of a particular molecule. They obtain a value for Γ_{CC} of 1.7 A³, as compared to 1.4 A³ calculated from Denbigh's bond polarizability values and 0.3 A³ from Bunn's values.

Using a similar approach, Stein and co-workers[7] have calculated Γ_{CC} from their measurements of the depolarization of scattered light by gaseous *n*-paraffins between ethane and heptane. They find, in contradiction to the additivity assumption, that Γ_{CC} is not constant but varies between 1.1 and 2.4 A³ in this series, again favoring the Denbigh results.

To summarize, it appears that (a) Denbigh's values of Γ_{CC} are approximately correct for *n*-paraffins in the vapor state, but the values are not independent of molecular size, and (b) the value of Γ_{CC} for polypropylene crystals is closer to the Denbigh value than to the value of Γ_{CC}, proposed by Bunn for *n*-paraffin crystals, which is valid for polyethylene. Thus, it would seem that bond polarizabilities are not simply additive but dependent upon configuration and state, being different in the environment of a polypropylene crystal from that of a polyethylene crystal. Further evidence for this may be obtained from measurements of the stress-optical coefficient of amorphous polyethylene (above the melting point of the crystals).

Saunders,[9] using Bunn's bond polarizability values, has calculated from measurements of the stress-optical coefficient of molten polyethylene that a polyethylene statistical segment contains about 48 monomer units. The experimental result is independently confirmed by Stein and Volungis.[9] About ten monomer units per statistical segment are calculated if Denbigh's values are substituted in Saunders' calculation. This latter figure is in better agreement with a value of about five monomer units per statistical segment (q) calculated from the data of Flory and co-workers[10] on stress-

[4] F. J. Padden and H. D. Keith, J. Appl. Phys. **30**, 1479, 1485 (1959).

[5] Z. W. Wilchinsky, Meeting of the North Jersey Section, American Chemical Society, East Orange, New Jersey, January, 1959.

[6] R. P. Smith and E. M. Mortensen, J. Chem. Phys. **32**, 502, 508 (1960).

[7] J. Powers, D. A. Keedy, and R. S. Stein, "The scattering of light by *n*-paraffin vapors," Office of Naval Research Tech. Rept. No. 11 (July 23, 1959); J. Powers, M. S. thesis, University of Massachusetts, 1959.

[8] D. W. Saunders, Trans. Faraday Soc. **52**, 1414 (1956).

[9] R. S. Stein and R. J. Volungis, J. Chem. Phys. **23**, 1179 (1955).

[10] P. J. Flory, C. A. J. Hoeve, and A. Ciferri, J. Polymer Sci. **34**, 337 (1959).

temperature measurements on lightly crosslinked polyethylene in the temperature range of 127°–202°C.

The theories of Kubo[11] and of Sack[12] on the anisotropy of paraffin chains indicate that a $q=48$ would correspond to an energy difference of 2400 cal/mole between the trans and the gauche conformations of the paraffin chain. The value of 800 cal/mole determined by spectroscopic and other data on short-chain paraffins corresponds to a $q=6.5$.

If the Saunders result is taken to indicate that the Denbigh polarizabilities are more appropriate in amorphous polyethylene, then it would appear that the proper polarizability values would depend upon whether the polyethylene was crystalline or amorphous, and that amorphous polyethylene has polarizability values similar to *n*-paraffin vapors.

It would seem that there are at least three factors which may influence the polarizability values: (a) internal field effects between portions of a single molecule which may differ, for example, depending on whether the two C—C bonds neighboring a given bond are in trans or gauche conformation, (b) internal field effects between adjacent molecules which depend on the state of aggregation, and (c) deviations in bond polarizability resulting from departure from tetrahedral bonding, as occur, to a small degree in polypropylene crystals. The importance of these factors should be investigated.

[11] R. Kubo, J. Phys. Soc. Japan **4**, 319 (1949).
[12] R. A. Sack, J. Chem. Phys. **25**, 1087 (1956).

APPENDIX

TABLE AI. Numerical values for atom coordinates and bond vectors of the main chain and substituent atoms.[a]

Vectors	Bond vectors x	y	z		Atom coordinates x	y	z
$-\mathbf{a}_1$	−1.4067	0	−0.6267	C_1	0	0	0
$\mathbf{a}_2$	0	0	1.54	C_2	1.4067	0	0.6267
$-\mathbf{a}_3$	0.7034	−1.2182	−0.6267	C_3	1.4067	0	2.1667
$\mathbf{a}_4$	0	0	1.54	C_4	0.7034	1.2182	2.7934
$-\mathbf{a}_5$	0.7034	1.2182	−0.6267	C_5	0.7034	1.2182	4.3333
$\mathbf{a}_6$	0	0	1.54	C_6	0	0	4.9600
$-\mathbf{a}_7$	−1.4067	0	−0.6267	C_7	0	0	6.5
$\mathbf{a}_8$	1.46238	−0.02318	0.48218	C_8	2.86908	−0.02318	2.64888
$\mathbf{a}_9$	−0.71094	1.27815	0.48218	C_9	−0.00754	2.49635	4.81548
$\mathbf{a}_{10}$	−0.75142	−1.25478	0.48218	C_{10}	−0.75142	−1.25478	6.98218
				C_{11}	1.4067	0	7.1267
$\mathbf{b}_2^1$	0.5257	0.8918	−0.3413	H_2^1	1.9324	0.8918	0.2854
$\mathbf{b}_2^2$	0.5257	−0.8918	−0.3413	H_2^2	1.9324	−0.8918	0.2854
$\mathbf{b}_3$	−0.50935	−0.9012	0.3413	H_3	0.89735	−0.9012	2.5080
$\mathbf{b}_4^1$	0.50935	0.9012	−0.3413	H_4^1	1.21275	2.1194	2.4521
$\mathbf{b}_4^2$	−1.03514	0.00935	−0.3413	H_4^2	−0.33174	1.22755	2.4521
$\mathbf{b}_5$	1.03514	0.00935	0.3413	H_5	1.73854	1.22755	4.6746
$\mathbf{b}_6^1$	0.50935	−0.9012	−0.3413	H_6^1	0.50935	−0.9012	4.6187
$\mathbf{b}_6^2$	−1.03514	−0.00935	−0.3413	H_6^2	−1.03514	−0.00935	4.6187
$\mathbf{b}_7$	−0.5257	0.8918	0.3413	H_7	−0.5257	0.8918	6.8413

[a] The superscripts refer to the hydrogens and the subscripts refer to the carbon atom to which the hydrogen in question is bonded.

TABLE AII. Numerical values for the atom coordinates and bond vectors for the hydrogens for methyl groups.[a]

	Bond vectors x	y	z		Atom coordinates x	y	z
$\mathbf{b}_1^1$	0.02314	−0.00037	1.08975	H_1^1	2.89222	−0.02355	3.73863
$\mathbf{b}_1^2$	0.49141	−0.89816	−0.37408	H_1^2	3.36049	−0.92134	2.27480
$\mathbf{b}_1^3$	0.51987	0.88198	−0.37408	H_1^3	3.38895	0.85880	2.27480
$\mathbf{b}_9^1$	−0.01125	0.02023	1.08975	H_9^1	−0.01879	2.51658	5.90523
$\mathbf{b}_9^2$	−1.02376	0.00925	−0.37408	H_9^2	−1.03130	2.50560	4.44140
$\mathbf{b}_9^3$	0.53214	0.87464	−0.37408	H_9^3	0.52460	3.37099	4.44140
$\mathbf{b}_{10}^1$	−0.01189	−0.01986	1.08975	H_{10}^1	−0.76331	−1.27464	8.07193
$\mathbf{b}_{10}^2$	0.50413	−0.89108	−0.37408	H_{10}^2	−0.24729	−2.14586	6.60810
$\mathbf{b}_{10}^3$	−1.02353	0.02322	−0.37408	H_{10}^3	−1.77495	−1.23156	6.60810

[a] The superscripts refer to the hydrogens and the subscripts refer to the carbon atom to which the hydrogen in question is bonded.

JOURNAL OF APPLIED PHYSICS VOLUME 31, NUMBER 11 NOVEMBER, 1960

Morphology of Polymer Single Crystals

D. H. Reneker and P. H. Geil
E. I. du Pont de Nemours & Company, Wilmington, Delaware

Evidence is presented indicating that polyethylene crystals grow in the form of hollow pyramids as well as lamellar crystals. Modes of packing the folded molecules consistent with the nonplanar structure are proposed. Observed electron diffraction patterns and dark-field micrographs are related to the pyramidal morphology. Various sources are described for the screw dislocations which result in spiral growths on crystals of polyethylene and polyoxymethylene.

I. INTRODUCTION

THE fact that polymeric molecules can crystallize from solution as lamellar crystals in which the molecules are folded has been established for a number of different polymers.[1–8] Certain secondary structural features of these lamellar crystals recur regularly throughout these observations. For instance, thickening of polymer crystals occurs through the development of spiral growths from screw dislocations. Two other secondary structural features observed on some polyethylene crystals are triangular central folds or pleats[2] and regular corrugations forming a diamond pattern.[9] Finally, adjacent sections of a crystal may reflect an incident electron beam in different directions so that the sections appear with different intensities in a dark-field electron micrograph.[10,11]

The pleats, corrugations, and dark-field micrographs have been interpreted[10,11] as indicating that polyethylene crystals are not always flat lamellas but that they frequently grow as hollow pyramids, the faces of which are flat lamellas. In this paper we present quantitative evidence for the hollow pyramidal structure as well as a hypothesis as to how this type of growth may occur and its effect on electron diffraction patterns. Evidence is also presented concerning the nature of some of the imperfections in the basal lamella which results in the development of spiral growths on polymer crystals.

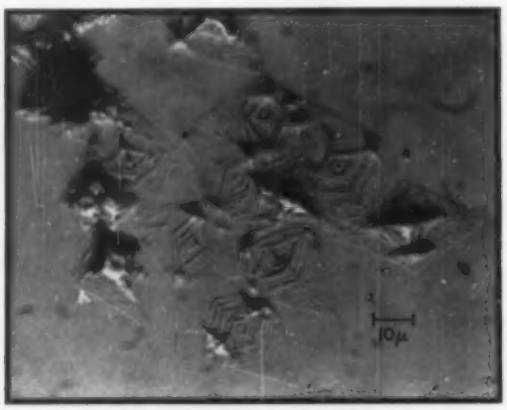

FIG. 1. Optical micrograph of polyethylene crystals having corrugated surfaces. The corrugations were still present several months after removal of the tetrachloroethylene solvent by evaporation. The fold domain boundaries, which are parallel to the **a** and **b** axes of the crystal, lie along the diagonals of these crystals (incident steep oblique illumination).

II. EXPERIMENTAL OBSERVATIONS

A. Nonplanar Growth

In the optical microscope corrugations have been observed on single-crystal lamellas of polyethylene precipitated from dilute tetrachloroethylene solution (Fig. 1). These corrugations can be seen before the crystal is completely uncovered by the retreating edge of the evaporating solvent. Electron micrographs show that the corrugations result from the wrinkling of single lamellas. Not all crystals in a given preparation have this corrugated appearance and, in some preparations, no crystals show the phenomenon. Those which do not may have either a pleated structure, which will be discussed later, or no apparent surface structure.

The corrugations in these crystals are similar to those described previously by Agar, Frank, and Keller.[9] In contrast to their observations, however, these corrugations do not disappear with time. The corrugations in Fig. 1 were still present several months after the preparation of the slide. The angle of intersection of these corrugations with the long and short diagonals of the crystal are, respectively, slightly larger and slightly smaller than the angles of intersection of the {310} planes with the same diagonals in a flat crystal. The angle of intersection of a corrugation with the long diagonal usually is smallest near the apices and gradually increases toward the center of the crystal. A second set of striations was clearly displayed in a few of the

[1] P. H. Till, J. Polymer Sci. **24**, 301 (1957).
[2] A. Keller, Phil. Mag. **2**, 1171 (1957).
[3] E. W. Fischer, Z. Naturforsch. **12a**, 753 (1957).
[4] P. H. Geil, N. K. J. Symons, and R. G. Scott, J. Appl. Phys. **30**, 1516 (1959).
[5] B. G. Ränby, F. F. Morehead and N. M. Walter, J. Polymer Sci. **44**, 349 (1960).
[6] P. H. Geil, J. Polymer Sci. **44**, 449 (1960).
[7] F. C. Frank, A. Keller, and A. O'Connor, Phil. Mag. **4**, 200 (1959).
[8] R. Eppe, E. W. Fischer, and H. A. Stuart, J. Polymer Sci. **34**, 721 (1959).
[9] A. Agar, F. C. Frank, and A. Keller, Phil. Mag. **4**, 32 (1959).
[10] W. Niegisch, Polymer and Fiber Microscopy Society Meeting, Princeton, New Jersey, September 1959.
[11] D. C. Bassett, F. C. Frank, and A. Keller, Nature **184**, 810 (1959).

crystals examined. Their angles of intersection have a similar relationship with the directions of the {530} planes.

As discussed later, the diagonals of the crystals in Fig. 1 are boundaries between fold domains, which are regions that differ from each other only in the orientation of the folds.[12] Some polyethylene crystals, as described by Agar *et al.*,[9] grow by repeated formation of fold domain boundaries. In such crystals the corrugations change direction across each boundary.

A second type of surface structure observed for polyethylene crystal lamellas consists of a pleat through or near the center (Fig. 2). Usually the pleat is parallel to the minor diagonal of the crystal. In a few cases, as in the larger crystal in Fig. 2, pleats lying along the major diagonal were observed. The larger pleats usually consist of two extra layers. The matching irregularities of the fractured edges on the larger pleats (Fig. 2) indicate that they were at one time joined and that the pleats formed after crystal growth had ceased. In some crystals the stresses involved in creating the pleats also result in tearing of the crystal near the ends of the minor diagonal. Fibers about 50 A in diam are drawn across the tears near the corners of the crystal. Similar pleats have occasionally been found on crystals of polyoxymethylene, crystallized from a dilute cyclohexanol solution.

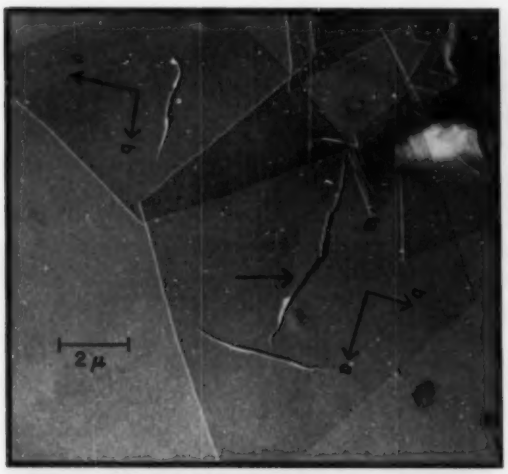

FIG. 2. Pleated polyethylene crystals precipitated more rapidly and from a more concentrated tetrachloroethylene solution than the crystals in Fig. 1. The smaller of these crystals is typical, the pleat being parallel to its minor axis. The matching irregularities of the fractured edges of the pleat in the larger crystal are indicated by an arrow. Pt-Pd shadowed at $\tan^{-1} 5/7$.

Figure 3 is an electron micrograph of a polyethylene crystal folded back on itself along its shorter fold domain boundaries. The appearance of the broken edges indi-

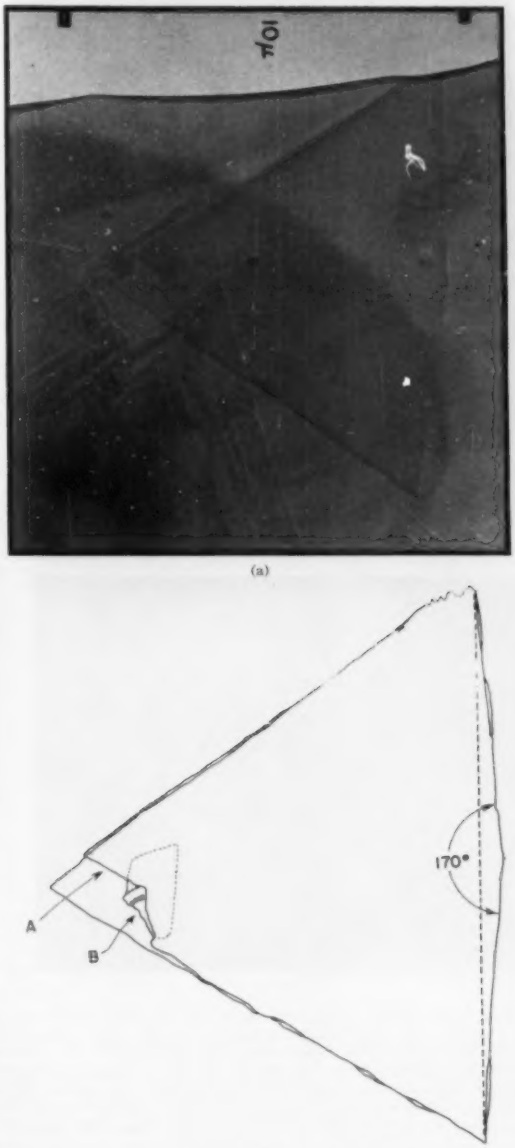

(a)

(b)

FIG. 3. (a). Electron micrograph of a hollow pyramidal polyethylene crystal which folded back on itself along its shorter fold domain boundaries. Pt-Pd shadowed at $\tan^{-1} 5/7$. (b). Tracing of Fig. 3(a) showing the folded crystal. The material in the obtuse triangle formed by the fold domain boundaries and the dotted line could not be incorporated into a flat diamond-shaped lamella. Fracture of a small piece of the crystal has occurred along line A which is parallel to a nongrowth face {110} plane, and tearing along an irregular line at B has resulted in drawing fibers across the break.

[12] These boundaries have been described as twin boundaries by Agar *et al.*[9] They separate regions related by a translation of $(\mathbf{a}/2+\mathbf{b}/2)$ followed by reflection in a (010) or (100) plane. We prefer the more specific terms, fold domain and fold domain boundary, since the lattice in the bulk of the crystal is continuous across the domain boundaries.

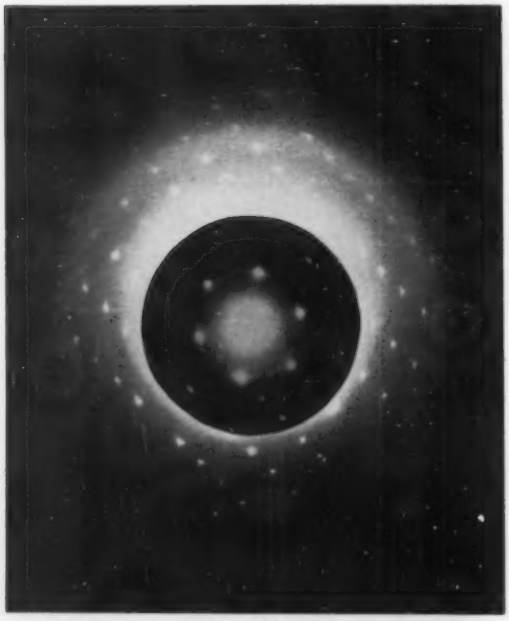

(a)

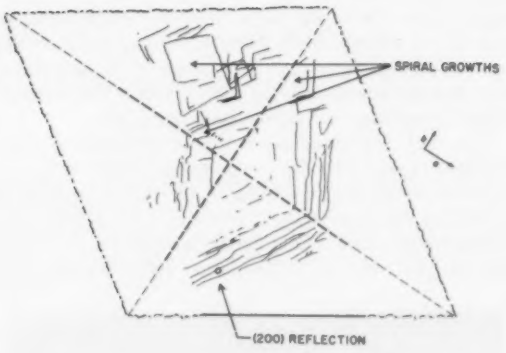

(c)

(b)

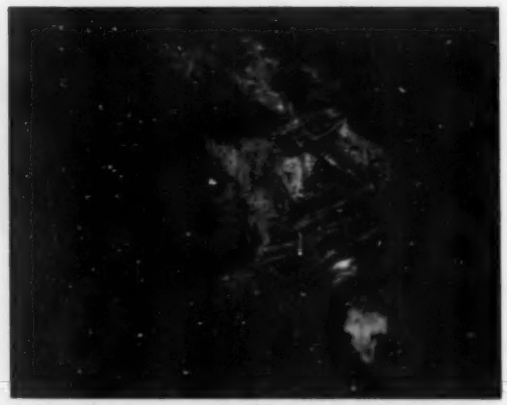

(d)

FIG. 4. (a) Diffraction pattern shown is a composite of two exposures from the same crystal. Reflections with h and k indices as high as 6 and 7, respectively, could be observed on the original negative. Forbidden reflections, such as the {100}, {010} and higher orders, were also visible. Small angle x-ray diffraction indicates that crystals prepared under similar conditions have a thickness of 104 A. (b) Portions of the corrugated material in all fold domains contribute electrons to the (200) reflection used for this micrograph. (c) Line tracing of the material in Fig. 4(b) which is scattering into the (200) reflection. Spiral growths are present in the first and second quadrant. The approximate position of the boundaries of the crystal and the arbitrarily chosen positive axis directions are shown. (d) The first and third quadrants of this crystal are bright. The ($\bar{1}10$) planes in these quadrants which contribute to the Bragg reflection used are nearly radial. In the other two quadrants only those portions of the corrugations are bright in which the molecules are nearly vertical.

cates that fracture occurred after crystallization had ceased, probably during removal of the solvent. The quadrant angles formed by the fold domain boundaries of the pyramid are about 85°. The material present after collapse in the obtuse triangle formed by the shorter fold domain boundaries and a straight line joining their ends could not be incorporated into a flat, diamond-shaped lamella. The "extra" material amounts to 5.4% of the total material in the crystal. Measurement of the extra material in other crystals with large pleats yields values between 3% and 4%.

Electron diffraction patterns from polyethylene crystals similar to those in Figs. 1 and 2 show up to seven orders of ($hk0$) reflections and no reflections from planes

with $l \neq 0$. Certain reflections such as (100) and (010), which are forbidden by the orthorhombic symmetry of the crystals, are clearly visible. The narrow width of the diffraction spots, each of which receives electrons reflected from portions of each fold domain, indicates that the fold domains are rotated about [001] by only a few degrees at most during collapse.

By inserting an aperture near the objective lens of the microscope it is possible to select only the electrons which contribute intensity to a particular diffraction spot and cause them to form an image of the crystal. Figure 4 shows a complete electron diffraction pattern from a corrugated crystal along with a series of such "dark-field" electron micrographs. (The Bragg reflection used for each micrograph was superimposed on the negative. The portion of the crystal which is bright was scattering electrons into the reflection shown. The objective aperture of the microscope limited the area of the crystal which could be observed. The observed area is shifted slightly in two exposures shown.) By using extremely low beam intensities it has been possible to obtain as many as six dark-field pictures of a crystal (each picture from a separate diffraction spot) before the crystal is destroyed by the beam.

In Fig. 4(b) only small portions of the corrugated material in all of the fold domains are contributing electrons to the (200) reflection used for this micrograph. Where two fold domains overlap, as in a spiral growth, the corrugations are at angles to each other [Fig. 4(c)]. Each lamella collapses as a separate entity.

In Fig. 4(d) almost all of the area in the first and third fold domains is reflecting into the $(\bar{1}10)$ reflection used for the micrograph. In the other two quadrants only portions of the corrugated material are visible. Using the $(1\bar{1}0)$ reflection instead, the same results are found. If, however, a (110) or $(\bar{1}\bar{1}0)$ reflection is used, the situation is reversed, corrugations being visible in the quadrants which are bright in Fig. 4(d) and the other quadrants being bright only along contour lines of the corrugations.

In a few rare cases involving preparations in which the solvent was removed at an elevated temperature, a central, diamond-shaped portion of the crystal separated from the remainder (Fig. 5). The area of the resulting

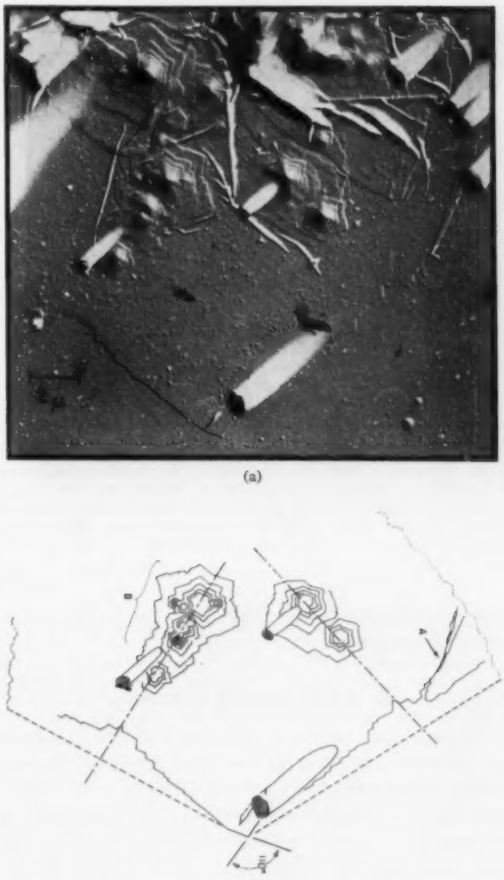

FIG. 6. (a) Electron micrograph of a region near one apex of a star-shaped polyoxymethylene crystal grown in a cyclohexanol solution. The large electron dense objects are globular polyoxymethylene particles. Cr shadowed at $\tan^{-1} 5/7$. (b) Tracing of Fig. 6(a). The dotted lines show the approximate location of lines connecting adjacent apices. The dash-dot lines indicate the directions of slow growth lines along which spiral growths frequently develop. In the region near A the crystal has wrinkled and fractured along a zigzag line. Notches are present where the slow growth line intersects the edge of the crystal.

FIG. 5. A polyethylene crystal which developed a diamond-shaped hole at its center when it collapsed onto the slide. There is a 4.1% deficiency of material at the center of the crystal. Pt-Pd shadowed at $\tan^{-1} 5/7$.

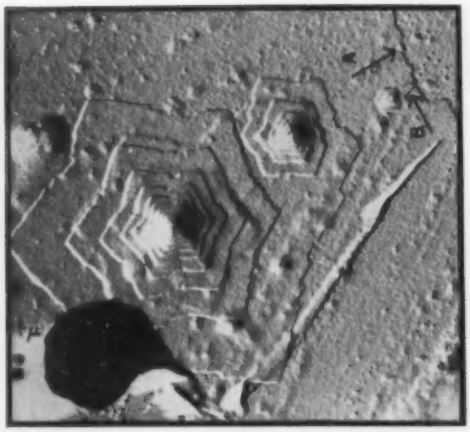

FIG. 7. Spiral growths on a polyoxymethylene crystal similar to that in Fig. 6(a). The arrow A points in the direction of advance of a portion of the growth face near its intersection with a slow growth line. A pair of spiral growths about screw dislocations of opposite sign are shown. The arrow B points to a fault surface which has given rise to a third spiral growth. Cr shadowed at $\tan^{-1} 7/24$.

diamond-shaped hole was larger than that of the material which separated.

B. Spiral Growth Sources

The basal lamella of a polymer crystal usually develops without any mechanism for growing thicker. Lateral growth occurs by adding material to its edges. Screw dislocations develop normal to the basal lamella and provide a means by which additional lamellas can grow, resulting in a structure many layers thick. Observations relevant to the formation of screw dislocations and the resulting spiral growths in polyethylene and polyoxymethylene are presented in the following.

(*a*) *Polyoxymethylene*

Regular hexagonal crystals of polyoxymethylene, similar to those crystallized from phenol,[4] have been obtained from dimethyl phthalate solutions. In addition, six-pointed starlike crystals have been obtained from cyclohexanol and 1–2 propanediol solutions of polyoxymethylene. All of these crystals were so large and flexible that they tended to fold and collapse on the substrate during drying. A portion of one of the starlike crystals from cyclohexanol is shown in Fig. 6.

The star shape of the lamellas, which is most apparent in the larger lamellas of the spiral growths in Fig. 6, develops from an originally hexagonal shape during growth. This indicates that the apices of the hexagonal crystal grow outward at a more rapid rate than the edges between two apices. A line approximately normal to the line connecting two adjacent apices as shown in Fig. 6(b) is referred to as a slow growth line. The apex angles of both the basal lamella and the larger lamellas in the spiral growth are approximately 110°. The growth faces are slightly irregular and frequently have a sharp notch where they intersect the slow growth line. Globular particles of polyoxymethylene were also formed during the crystallization (see Fig. 6).

Most spiral growths on polyoxymethylene crystals from cyclohexanol solutions originate at pairs of screw dislocations of opposite sign (Fig. 7). The lines joining the dislocation pairs usually lie along a slow growth line.

All the dislocations whose origins can be traced result from an exposed fault surface along a slow growth line, as shown at point B in Fig. 7. Only one-half of the expected double spiral has developed. Presumably, if growth had continued, another screw dislocation of equal but opposite Burgers vector would have formed, resulting in healing of the fault and growth of the second half of the spiral. The double spiral would then be similar to the one already formed.

The development of spiral growths on polyoxymethylene crystals is usually accompanied by an apparent rotation of the successive lamellas around the dislocation axis (Fig. 8). This rotation can be smooth, slightly irregular as in this figure, or abrupt, as shown in a previous publication.[4] Double or higher-order electron diffraction patterns are obtained from these crystals. Moiré patterns resulting from rotation have been observed both in crystals of polyethylene[9] and polyoxymethylene.[4] There is some indication, from the shadow density and, as shown in Fig. 8, the warpage of the underlying basal lamella, that some polyoxymethylene crystals may also be nonplanar.

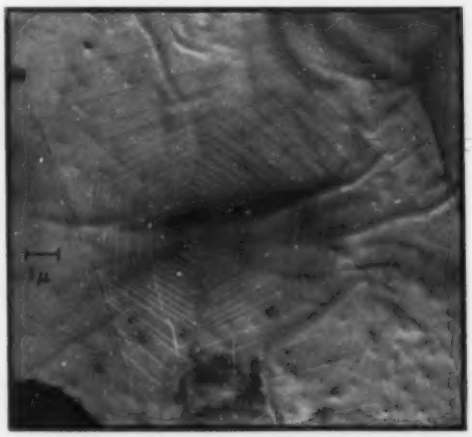

FIG. 8. Spiral growth on a polyoxymethylene crystal grown in a dimethyl phthalate solution. Defects at the apices of the fifth, sixth, and last layer from the top occurred during its growth. An irregular rotation of the lamellas about the screw dislocation axis is also apparent. Cr shadowed at $\tan^{-1} 5/7$.

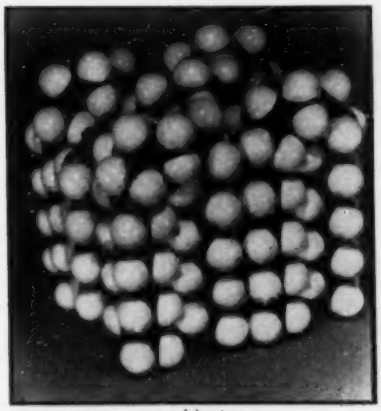

(a)

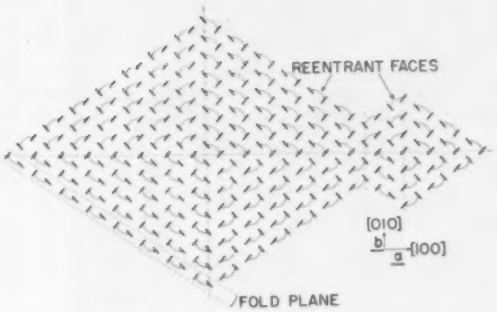

(c)

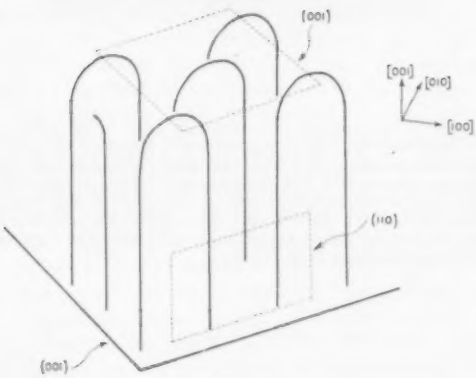

(b)

FIG. 9. (a) Photograph of a Stuart-Briegleb model showing the orientation of the folds in successive fold planes which results in the growth of a flat lamellar polyethylene crystal. (b) A sketch showing the crystallographic planes and axis directions of the model in Fig. 9(a). (c) A projection of the crystal onto the (001) planes showing the arrangement of the folds in a Case 1 crystal. Planar zigzag of molecular backbone /. Fold at top of lamella ◡. Folds at bottom of lamella are not shown. A fold plane and re-entrant faces are indicated. The dotted lines are fold domain boundaries.

(*b*) *Polyethylene*

Many of the growth spirals on polyethylene crystals are centered on fold domain boundaries associated with reentrant faces.[12] Similar arrangements of the spiral growths can be seen on micrographs of 6-nylon crystals.[6] During crystallization neighboring re-entrant faces apparently become displaced in the [001] direction with respect to each other. The screw dislocation thus formed permits the subsequent development of a spiral growth. Occasionally another displacement of the lamella will cause the fault to heal and generate a spiral growth of opposite sense as observed more frequently in polyoxymethylene crystals, and shown in Figs. 6 and 7.

The overlapping of lamellas, which occurs when secondary dendrites meet, provides another source of the spiral growths observed in polyethylene crystals. Other nucleating sites for spiral growths on a polyethylene lamella result from the tearing, fracture, or separation by other means of the lamella along a line roughly normal to the growth face. These imperfections have not been observed to heal during further growth.

[12] See, for instance, figures in works cited in footnotes 1 and 2.

III. DISCUSSION

A. Hollow Pyramidal Structure

The evidence presented indicates that some polyethylene crystals grow in the form of hollow pyramidal lamellas rather than flat lamellas. The observations indicate that each lamellar sector bounded by a growth face and two fold domain boundaries is a flat lamella, but that, in the case of the hollow pyramidal crystals, the central angles of the sectors do not total 360°. Measurement of the length of the sides permits one to calculate the angle between the longer fold domain boundary and the basal plane. This angle for the crystal in Fig. 3 is nearly 17°. The elevation of the apex of this 100-A thick, 16-μ long, hollow pyramidal crystal was about 2.5 μ.

The explanation for this phenomenon lies in the packing of the folds. The orientation of the growth faces and brittle fracture planes indicates that the fold planes in polyethylene diamond-shaped crystals are {110} planes. There are two ways for identical folds in successive fold planes to pack. The alternate possibilities are described below with reference to the sector lying be-

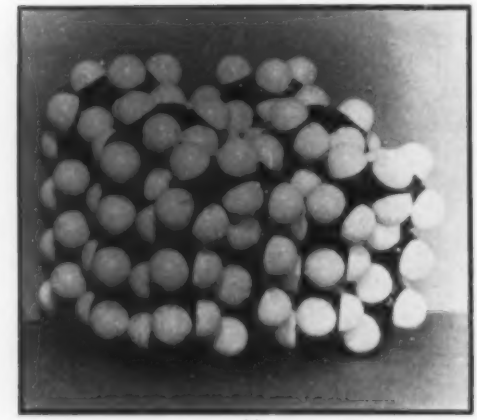

(a)

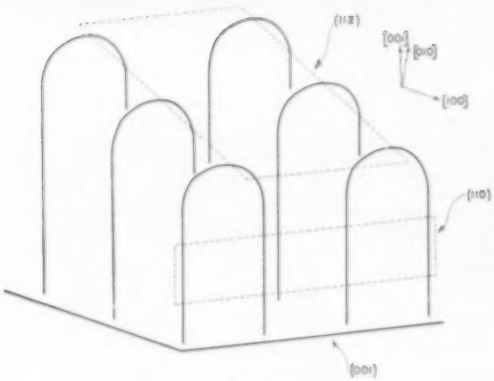

(b)

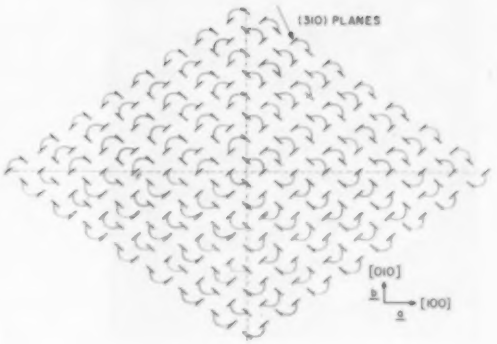

(c)

FIG. 10. (a) Photograph of a Stuart-Briegleb model showing the orientation of the folds in successive fold planes which results in the growth of hollow pyramidal polyethylene crystals with the fold planes displaced by $\mathbf{c}/2$. (b) Diagram showing the crystallographic planes and axis directions for the model in Fig. 10(a). (c) Diagram showing the arrangement of the folds on the top surface of a Case 2 pyramidal crystal. The symbols on the drawing have the same meaning as in Fig. 9(c).

tween the [100] and [010] directions, but a similar treatment applies to each of the other sectors.

Case 1. In successive (110) fold planes [Fig. 9(a), (b), (c)] the neighboring folds line up along the [100] and [010] directions. The packing of the molecules in the interior of the lamella requires that the folds in successive fold planes be tangent to (001) planes [planes parallel to the plane of Fig. 9(c)] displaced from one another by n repeat distances. For $n=0$, a flat lamellar crystal will develop. For $n=1$, folds are displaced by one repeat distance in the [001] direction in successive fold planes. The slope of the resulting pyramid is 31.6° and the longer lateral edge has a slope of 18.9°. This agrees reasonably well with the slope observed for the crystal in Fig. 3, indicating that the packing of the folds and the direction of displacement was propagated throughout the crystal during growth.[14]

Case 2. In successive (110) fold planes the folds [Fig. 10(a), (b), (c)] lie along lines in the ($\bar{1}10$) and (310) planes. In this case, which differs from Case 1 in that every other fold plane is rotated by 180° about a chain axis, the packing of the molecules in the interior of the lamella also requires that each successive fold plane be displaced by $(n+\frac{1}{2})$ repeat distances in the [001] direction. If the displacement is always in one direction a hollow pyramidal crystal develops. For $n=0$ the slope of the pyramid is 17.2°, and the longer fold domain boundary has a slope of 9.8°. The folds are tangent to (112) planes. Both of these pyramidal morphologies are similar to "oblique" modifications of the normal paraffins described by Kitaigorodskii.[15]

The two cases previously described appear to apply if the same number of chain atoms is involved in each fold. Manipulation of Stuart-Briegleb atomic models suggests that the detailed conformation of the several possible folds which involve the same number of chain atoms, does not affect their packing. However, it is also possible to produce folds which involve more chain atoms. In Case 2, for instance, flat crystals can develop if the folds in adjacent fold planes involve three and five chain atoms alternately. Small differences between the

[14] Case 1 crystals have also been described independently by W. D. Niegisch and P. R. Swan [Bull. Am. Phys. Soc. **5**, 192 (1960)].

[15] A. I. Kitaigorodskii, Soviet Phys. Cryst. **2**, 637 (1959).

various types of folds and fold packing thus have a large effect on the structure of the crystal.

Surface tension forces during solvent removal produce bending and compressive stresses in the lamellar faces of pyramidal crystals. These stresses are relieved, to some extent, by the formation of either pleats or corrugations. Our observations suggest that if the successive fold planes are displaced by one repeat distance (Case 1), pleats are formed during solvent removal, whereas is the fold planes are displaced by half a repeat distance (Case 2), corrugations are formed.

Consider first the fold packing of Case 2. Figure 10(c) shows that the folds which connect segments of molecules in adjacent (310) planes in the first fold domain are alternately all on the top or all on the bottom of the lamellas. Therefore, one might expect that the crystals would bend most easily along these lines. The presence of folds makes it necessary to distinguish between {110} planes which are growth faces and {110} planes which are not. Adjacent {110} planes which were growth faces are not connected by folds so that a crystal will pull apart along these planes if subjected to the appropriate stress. Adjacent {110} planes which are not growth faces, such as $(1\bar{1}0)$ planes in the first fold domain, are connected in the same manner as described above for the (310) planes. The moment arm of the forces involved in the collapse of pyramidal crystals is approximately radial. The moment arm in the first and third fold domains is nearly normal to the (310) planes, but almost parallel to the nongrowth face $(1\bar{1}0)$ planes. Corrugations parallel to (310) planes in the first and third domains and parallel to $(\bar{3}10)$ planes in the second and fourth domains can relieve these moments and allow the pyramidal crystal to collapse.

The relative positions of the corners of the crystal are not changed during collapse so that after collapse the intersections of a {310} plane with the crystal axes are displaced toward the center of the crystal by unequal amounts. This results in a rotation of the {310} planes about [001] toward the observed angles of intersection of the corrugations with the crystal axes (Fig. 1).

Another set of higher index planes in the first fold domain, in which adjacent planes are connected alternately at the top and bottom by folds, are the (530) planes. The second set of corrugations sometimes observed is probably related to these planes in a similar fashion.

When pyramidal crystals collapse, ($hk0$) planes which are approximately tangential to the crystal tilt to a much greater degree than those which are more nearly radial. The tilt of the fold planes in pyramids with Case 2 ($n=0$) fold packing, for instance, can be on the order of 18° in regions which lie down on the substrate without distortion. In the corrugations and other distorted regions, these and similar planes will have a wide range of orientations. However, the {110} planes which are not fold planes are approximately radial and therefore their orientation is not greatly changed during pyramid collapse.

In the dark-field micrographs only portions of corrugations are bright when {200} reflections are used, the visible portions being those in which these planes are nearly parallel to the beam [Fig. 4(b)]. With a $(\bar{1}10)$ reflection, as in Fig. 4(d), the uniformly bright fold domains are those in which the (110) planes are nearly radial, that is, the first and third fold domain. In the other domains only small portions brought into the correct orientation by corrugations and other distortion are bright.

For the other possible arrangement of folds, as described in Figs. 9(a), (b), (c), the planes which are connected alternately at top and bottom by folds are the {100} and {010} planes. Collapse of pyramidal crystals with integer displacements of successive fold planes would be expected to result in pleats parallel to {100} and {010} planes. Even though pleats form, dark-field micrographs indicate that additional lattice distortion occurs during collapse so that some regions in all fold domains may be reflecting.

For both alternatives of fold packing, another mode of collapse of the crystals is conceivable. The stresses may cause shearing parallel to the chain axis of some of the fold planes with respect to each other. If this occurs uniformly throughout the crystal the molecular axis remains normal to the substrate. The thickness of the lamella normal to the faces increases and no indication remains that the crystal was originally pyramidal. These regions should contribute intensity to all of the low-order reflections.

Agar, Frank, and Keller[9] have shown that one should obtain reflections only out to Bragg angles corresponding to approximately 2.5 A from flat polymer crystals oriented normal to a well collimated, monoenergetic 80-kv electron beam. This expected type of pattern is obtained from nylon crystals[6] and from some types of polyethylene and polyoxymethylene crystals. Tilting such a crystal can cause additional reflections to become visible, but the center of intensity is displaced from the center of symmetry of the diffraction pattern.

From some crystals of polyethylene and polyoxymethylene, reflections have been obtained out to angles corresponding to spacings of less than one angstrom. In the corrugated polymer crystals and even in those with pleats, there is sufficient lamella distortion to bring some portion of the lattice into proper position for the high order reflections. Although changing the collimation of the beam does not significantly affect the number of orders observed, imperfect collimation of the beam and spread in electron energy will increase the effective area of the crystal in producing the higher-order reflections. In the unstrained portions of collapsed pyramidal

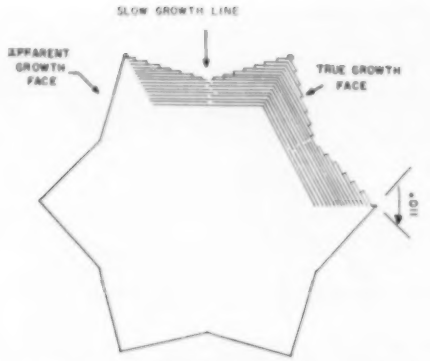

FIG. 11. Diagram of a star-shaped crystal of polyoxymethylene. The true growth face is made up of fold planes growing from adjacent apices toward each other. (The fold planes are indicated for $\frac{1}{3}$ of the crystal by the parallel lines in the upper right of the diagram).

crystals the angle of tilt of the molecules should be sufficient to permit the observation of reflections from planes with nonzero values of l. We have not observed these reflections. The forbidden reflections found on many of the polyethylene diffraction patterns indicate the presence of imperfections in the crystal which disrupt the orthorhombic symmetry of the lattice. In the case of paraffins the appearance of forbidden reflections has been ascribed to secondary scattering in imperfect crystals.[16]

Regular or irregular alternation in the fold plane displacement direction and in the type of fold packing during growth would result in the formation of apparently flat crystals and pyramids with shallower slopes. It is impossible to determine the original shape of such crystals after the solvent has been removed. Although we have discussed only polyethylene crystals with {110} faces, folding along other growth faces could also result in hollow pyramidal lamellas with different slopes.

If, instead of adding the material in the obtuse triangle shown in Fig. 3(b), the crystals had grown so that when folded a similar obtuse triangular area would contain no material, the resulting three-dimensional structure would be saddle-shaped, with sides having the same slope as the sides of a pyramid. The arrangement of folds in a saddle-shaped crystal is similar to that in a pyramidal crystal. Several crystals have been found which developed holes in their centers when dried on a slide (as in Fig. 5). In the crystal shown, however, the simultaneous presence of a pleat and a hole leaves some doubt as to whether this crystal was actually saddle-shaped.

[16] J. M. Cowley, A. L. G. Rees, and J. A. Spink, Proc. Phys. Soc. (London) **A64**, 609 (1951).

B. Spiral Growth Sources

Spiral growths on a lamellar crystal develop around regions (screw dislocations) where a part of the lamella has slipped parallel to the chain axis, thereby exposing a new face on which growth can occur. The slip can be due to forces exerted on the crystal during growth by convection currents, interference of two lamellas, interference by particles of foreign matter, or the like. This type of slip can occur anywhere along the edge of the growing crystal. The basal lamella usually does not heal after a fault of this type forms. A single spiral growth develops about such a fault on each side of the basal lamella.

A favored location for the generation of screw dislocations in both polyethylene and polyoxymethylene crystals is the region near the intersection of two re-entrant growth faces. In polyethylene this region lies near the fold domain boundaries discussed earlier, and is a region in which the orientation of the fold plane changes. In a perfect polyoxymethylene crystal there is no abrupt change in the arrangement of the folds on either side of a slow growth line. The re-entrant apparent growth faces are the result of faster growth of the apices.

Growth of crystals with re-entrant faces appears to proceed by formation of new fold planes near an external apex which then grow laterally until they meet. The apparent growth faces are not low index planes but consist of a stack of low index planes of decreasing width, as shown for polyoxymethylene in Fig. 11. In polyethylene the apparent growth faces are usually more nearly parallel to the low index planes than they are in the polyoxymethylene crystals.

If the growth faces advance rapidly, impurities which tend to remain in the liquid phase will accumulate near the intersection of the re-entrant faces. When the concentration becomes high enough, the impurities are incorporated into the crystal perforce and distort the crystal lattice. Distortion also results from imperfections such as improper folds and edge dislocations. In polyoxymethylene, formation of a screw dislocation seems to relieve the accumulated stress and, after a few microns or less of lateral growth, permit a second screw dislocation of opposite sign from the first to form, thereby healing the fault.

In some of the growths observed on polyoxymethylene crystals, the two screw dislocations responsible for the growth are only a few hundred angstroms apart. If a complete lamellar thickness is exposed in this short distance, the lattice must be severely strained. Alternatively, it is possible that only a fraction of the lamella has been exposed by the slip, and the succeeding lamellas have grown from it with the same thickness as the original lamellas.

Only a few of the more prominent imperfections in polymer crystals have been discussed. These secondary

features provide many possibilities for complicated structures to develop from a single lamella. As is the case in metals and crystals of lower molecular weight, secondary features of the type discussed doubtless play a dominant role in the strength, creep, and many of the other physical properties of polymeric solids.

ACKNOWLEDGMENTS

The authors are pleased to acknowledge many helpful discussions with Drs. Y. H. Pao and L. T. Muus. We are also grateful to R. Schatz and R. McLaughlin for their assistance in performing the experiments from which these observations resulted.

JOURNAL OF APPLIED PHYSICS VOLUME 31, NUMBER 11 NOVEMBER, 1960

Wave Functions and Energy Eigenvalues for the Polytetrafluoroethylene Chain

YOH-HAN PAO AND R. F. BJORKLUND*
Polychemicals Department, E. I. du Pont de Nemours & Company, Inc., du Pont Experimental Station, Wilmington, Delaware

The paper reports on a quantum mechanical investigation of an isolated polytetrafluoroethylene molecule. The purpose of this investigation is twofold: to find the energy gap between filled and empty electronic bands and to determine the energy required to change the conformation of the molecule. For reasons of simplicity, the carbon atoms are assumed to have the planar zigzag conformation in the ground state of the molecule. Molecular wave functions are constructed from Bloch sums taken along the four rows of fluorine atoms. The basis functions used are Gaussian approximations to $2p$ and $3s$ atomic orbitals. The suitability of this choice is tested in a preliminary calculation of the dissociation energy of the hydrogen fluoride molecule.

In polytetrafluoroethylene, the molecular orbitals form bands. The energy gap between the filled $2p$ band and the empty $3s$ band is calculated as 10.07 ev, suggesting negligible intrinsic semiconduction. The width of the $2p$ band is 0.0625 ev, signifying that chain conformation may change easily at room temperature, for example from a right-handed helical conformation to the conformation of the opposite hand.

I. INTRODUCTION

TO obtain some idea of the molecular wave functions and energy eigenvalues which might characterize a linear (nonbranched) polymer molecule, some preliminary calculations have been carried out for a polytetrafluoroethylene chain.

In the formation of a polytetrafluoroethylene molecule, only one of the five $2p$ electrons of the fluorine atoms contributes appreciably to the CF bond. The orbitals of the remaining four $2p$ electrons overlap mutually to some extent, and it is questionable whether it is useful to think of their being in $2p$ states.

In view of the symmetry of the molecule, it is perhaps reasonable to think of a great number of molecular orbitals with energy levels so closely spaced that they form a band. The gap between a filled band arising from, say, the $2p$ orbitals, and an empty band constructed from $3s$ orbitals is of interest in view of implications with respect to resistance to ultraviolet and gamma radiation and also with respect to electrical conductivity problems.

The width of the filled $2p$ band provides an estimate of the energy required to "disorder" the chain intramolecularly, that is, for example, to transform a left-handed helix into a right-handed helix.

One of the real bottlenecks in such calculations lies in the evaluation of the molecular integrals. The various methods of calculation contemplated initially all involved the use of atomic orbitals as elementary functions from which molecular orbitals would eventually be constructed. Slater orbitals would have been quite suitable for providing representations of the atomic orbitals except that calculation of many-center interelectronic repulsion integrals is extremely difficult when Slater orbitals are used. Considerable progress has been made in developing computer programs for the two-center case, but little headway has been made in the calculation of three- and four-center integrals. As has been pointed out previously,[1] this difficulty is removed completely if one uses Gaussian approximations to Slater's orbitals. In contrast to the situation for Slater orbitals, to date little use has been made of Gaussians in molecular calculations. In order to test their suitability for this purpose, the dissociation energy for the hydrogen fluoride molecule was evaluated using Slater orbitals initially and then using Gaussians in place of the Slater functions.

The hydrogen fluoride calculations are of semiempirical nature in that the experimentally obtained value of the dipole moment was used in the calculation to give the appropriate linear combination of the $2p_z$ and $1s$ orbitals to be used in the basis functions. These calculations are described in Sec. II, and the calculations and results for the polytetrafluoroethylene chain are presented in Sec. III.

II. WAVE FUNCTIONS AND ENERGY EIGENVALUES FOR THE HF MOLECULE

The configuration considered for fluorine is $(1s)^2(2s)^2(2p)^5$ and that for hydrogen is $1s$. The experimental

* Present address: Western Regional Research Laboratory, Albany, California.

[1] S. F. Boys, Proc. Roy. Soc. (London) **A200**, 542 (1950).

equilibrium internuclear distance is 0.9171 A or 1.733 atomic units.

For the calculations with the Slater orbitals, the orbitals are:

Fluorine

$$2p_z = p_z = (a^5/\pi)^{\frac{1}{2}} r_{A1} \exp(-ar_{A1}) \cos\theta_{A1}$$
$$2p_x = p_x = (a^5/\pi)^{\frac{1}{2}} r_{A1} \exp(-ar_{A1}) \sin\theta_{A1} \cos\phi_{A1}$$
$$2p_y = p_y = (a^5/\pi)^{\frac{1}{2}} r_{A1} \exp(-ar_{A1}) \sin\theta_{A1} \sin\phi_{A1}.$$

Hydrogen

$$h = (b^3/\pi)^{\frac{1}{2}} \exp(-br_{B1}).$$

The basis functions used are

$$\psi_1 = (6!)^{-\frac{1}{2}} \begin{vmatrix} p_x\alpha(1) & p_x\alpha(2)\cdots p_x\alpha(6) \\ p_x\beta(1) & p_x\beta(2)\cdots p_x\beta(6) \\ p_y\alpha(1) & p_y\alpha(2)\cdots p_y\alpha(6) \\ p_y\beta(1) & p_y\beta(2)\cdots p_y\beta(6) \\ (c_1p_z+c_2h)\alpha(1) & \cdots (c_1p_z+c_2h)\alpha(6) \\ (c_1p_z+c_2h)\beta(1) & \cdots (c_1p_z+c_2h)\beta(6), \end{vmatrix}$$

and

$$\psi_2 = (6!)^{-\frac{1}{2}} \begin{vmatrix} p_x\alpha(1) & p_x\alpha(2)\cdots p_x\alpha(6) \\ p_x\beta(1) & p_x\beta(2)\cdots p_x\beta(6) \\ p_y\alpha(1) & p_y\alpha(2)\cdots p_y\alpha(6) \\ p_y\beta(1) & p_y\beta(2)\cdots p_y\beta(6) \\ (d_1p_z-d_2h)\alpha(1) & \cdots (d_1p_z-d_2h)\alpha(6) \\ (d_1p_z-d_2h)\beta(1) & \cdots (d_1p_z-d_2h)\beta(6). \end{vmatrix}$$

As implied by the preceding notation, the fluorine orbitals are centered about A and the hydrogen orbital is centered about B, the internuclear distance is AB, and a and b are the screening parameters. The value of a is taken to be 2.55, which is the value given by Duncanson and Coulson,[2] and b is taken to be 1.

The 1s and 2s closed shells of fluorine are assumed not to contribute appreciably to the molecular binding energy, and the problem is consequently reduced to a six-electron problem instead of the full ten-electron problem treated by Kastler[3] and Hurley.[4]

The Hamiltonian for the six-electron problem is

$$H = \frac{Z_AZ_B}{AB} - \sum_i^6 \left[\tfrac{1}{2}\Delta^2(i) + \frac{Z_A}{r_{Ai}} + \frac{Z_B}{r_{Bi}}\right] + \sum_i \sum_{j>i} \frac{1}{r_{ij}}$$
$$i, j = 1, 2, \cdots 6.$$

Z_A represents the nuclear charge of fluorine and Z_B represents the nuclear charge of hydrogen. Since 1s and 2s electrons of the fluorine atom are not treated explicitly, the nuclear charge Z_A cannot be taken to be 9 but rather 5. The details of this type of calculation are well known and are omitted here. The parameters c_1, d_1, and d_2 are determined from the conditions that the orbitals $c_1p_z+c_2h$ and $d_1p_z=d_2h$ be normalized and orthogonal to each other. These conditions are sufficient to determine the magnitude of three of these parameters relative to the fourth one; the value of the fourth parameter is determined by the requirement that the calculated dipole moment be equal to the observed one.

With

$$c_1 = 0.6682, \quad d_1 = 0.8097;$$
$$c_2 = 0.5680 \quad d_2 = 0.8828.$$

The two roots to the detrimental equation are found to be

$$E_1 = -7.0565 \text{ au},$$

and

$$E_2 = -5.9147 \text{ au},$$

and the wave function for the ground state is

$$\Omega_1 = 0.9962\psi_1 - 0.0749\psi_2.$$

The definition and values for the integrals used in this calculation are given in Appendix I.

In the present scheme, the dipole moment is given by

$$\int \Omega_1(1, \cdots 6)[Z_5+Z_6]\Omega_1(1, \cdots 6)dv_1 \cdots dv_6$$
$$= 2\int (0.9972\psi_1 - 0.0748\psi_2) \times Z(0.9972\psi_1 - 0.0748\psi_2)dv = 0.759.$$

The dipole moment in Debyes is obtained by multiplying by $(0.52917\times10^{-8}\times4.8029\times10^{-10})/10^{-8} = 2.54155$ to give a value of 1.93 Debyes. For the present purpose, this was considered to be in satisfactory agreement with the observed value of 1.91 Debyes. The binding energy is E_1 minus the sum of the atomic energies of the neutral fluorine and hydrogen atoms, i.e.,

$$D_e = E_1 - 6.7831 = -0.2734 \text{ au}$$
$$= -7.4364 \text{ ev}.$$

The zero point vibrational energy is 0.257 electron volts and the dissociation energy is consequently obtained to be

$$D_0 = 7.4364 - 0.257 = 7.179 \text{ ev}.$$

The experimental value is $\leq$6.4 ev. The hydrogen fluoride molecule has been well studied theoretically, two of the most recent investigations being those of Kastler and Hurley.

Hurley gives a summary of the results obtained by his previous methods. These and the present results are exhibited in Table I.

The procedure used in making the calculation with the Gaussians is essentially the same as that used for the Slater orbitals. There are several possible ways of choosing the screening parameters for the orbitals. One

[2] W. E. Duncanson and C. A. Coulson, Proc. Roy. Soc. Edinburgh **62**, 37 (1944).
[3] D. Kastler, J. chim. phys. **50**, 556 (1953).
[4] A. C. Hurley, Proc. Phys. Soc. (London) **69A**, 301 (1956).

TABLE I.

	Orbital [2 terms]	Orbital [6 terms]	AIM[a] [2 terms]	KM[b] [2 terms]	KM [6 terms]	LCC[c] [2 terms]	LCC [6 terms]	Exp[6,7]	Present
D_0(ev)	1.03	1.96	8.33	5.05	5.77	5.39	5.84	>5.8 <6.4	7.19

[a] AIM = atoms in molecules (Moffit's method).
[b] KM = Kastler's modified theory (Kastler's modification of Moffitt's method).
[c] LCC = Intra-atomic correlation corrections (Hurley's method).

method would be to choose the parameters so that they maximize the overlap of the Gaussian with the corresponding Slater orbital. Another method would be to select the parameters so that the individual orbitals satisfy the virial theorem. The latter method was selected, although a calculation showed that the difference in the binding energy obtained using the two methods is negligible.

The analytic expressions and numerical values of the integrals for the Gaussian wave functions are listed in Appendix II. In addition, the values of the atomic and molecular energies are given. For comparison, the results for Gaussians are listed together with those obtained previously using Slater orbitals in Table II.

TABLE II.[a]

Total atomic energy[b] Gaussian	Slater	Total molecular energy[c] Gaussian	Slater	Binding energy Gaussian	Slater
−5.9691	−6.7831	−6.2426	−7.0565	0.2735	0.2734

[a] In atomic units.
[b] $E(H)+E(F)$.
[c] Except for zero point vibrational energy.

When the zero point vibrational energy of 0.257 ev is subtracted from the binding energies, the values of 7.19 ev and 7.18 ev are obtained for the dissociation energies for the two cases.

The most striking feature about these results is that the atomic and molecular energies obtained with the two types of orbitals are markedly different; but the binding energies differ only very slightly. The probable explanation of this result is that in the region between the nuclei (which is the region which makes the largest contribution to the binding energy), the Gaussians and Slater orbitals are about equally good (or bad); but in the immediate vicinity of the nuclei and also at large distances from the nuclei the Gaussians are much less satisfactory.

III. WAVE FUNCTIONS AND ENERGY EIGENVALUES FOR THE POLYTETRAFLUOROETHYLENE CHAIN MOLECULE

To simplify the calculation, it was assumed that the carbons in the polytetrafluoroethylene chain have a planar zigzag conformation. This assumption was then used to determine the position of the fluorine atoms, but the carbon atoms themselves were neglected in constructing approximate molecular wave functions.

Bloch sums along the four rows of fluorine atoms were chosen as the molecular basis functions. They were constructed from Gaussian approximations to $2p$ and $3s$ orbitals. With this choice of basis functions, it was not necessary to make the common approximation of neglecting all but the nearest neighbor interactions ("tight binding" approximation). The potential was assumed to be constant along the chain so that only the overlap and kinetic energy integral had to be evaluated. Although this might at first glance seem to be a drastic assumption, it is actually fairly realistic.[5]

The expressions for the Bloch sums and the analytical expressions for the molecular integrals are given in Appendix III.

To gain insight into the possible symmetry types for the molecular wave functions, the irreducible representations of the space group of the infinite chain for $k=0$ and π/a were determined (Appendix IV). With these representations available it was not necessary to solve a secular equation to determine the optimum phases between Bloch sums along the rows of fluorine atoms. It was only necessary to find functions which transform according to the different irreducible representations. However, if the energies for a great number

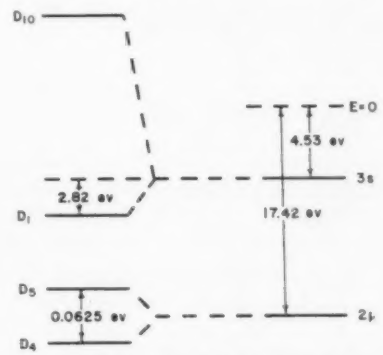

FIG. 1. Energy levels for the modified polytetrafluoroethylene molecule.

[5] This assumption made it unnecessary to evaluate electronic exchange integrals, but the use of Gaussians nevertheless facilitated the calculations to a significant degree.
[6] T. L. Cottnell, *The Strength of Chemical Bonds* (Academic Press, Inc., New York, 1954).
[7] G. Herzberg, *Spectra of Diatomic Molecules* (D. Van Nostrand Company, Inc., Princeton, New Jersey, 1950).

of values of k are required, it is perhaps less time-consuming to have the appropriate secular equations solved by machine.

Energy eigenvalues for this molecule are listed in Appendix V for $k=0$ and $k=\pi/a$.

The relative spacings of some of these levels are shown in Fig. 1. It is seen that the width of the $2p$ band is 0.0625 ev or 1.44 kcal/mole. This is interpreted to mean that thermal energy at or slightly above room temperature is sufficient to produce a significant amount of disordering of chain conformations. In the absence of more detailed analysis of the density of states in this band, it is not possible to obtain further information from this result. We also see that there is a state in the $3s$ band which is at least 2.82 ev below that of the $3s$ state for the isolated fluorine atom. This reduces the gap between the two bands to 10.07 ev but suggests nevertheless that there is little intrinsic semiconduction.

APPENDIX I

Definitions of and Values for the Molecular Integrals Used in the Calculations for the HF Molecule (with Slater Orbitals)

$$\langle 1\rangle = \int P_x(1)(-\tfrac{1}{2}\Delta_1)P_x(1)dV_1 \equiv \langle P_x|-\tfrac{1}{2}\Delta|P_x\rangle = 3.2513.$$

$$\langle 2\rangle = \int P_x(1)\frac{1}{A1}P_x(1)dV_1 \equiv \left\langle P_x\left|\frac{1}{r_{A1}}\right|P_x\right\rangle = 1.2750.$$

$$\langle 3\rangle = \left\langle P_x\left|\frac{1}{r_B}\right|P_x\right\rangle = 0.5329, \qquad (K_{2x2x})\ \text{K.A.I.K. p. 82.}$$

$$\langle 4\rangle = \int P_x(1)P_x(1)\frac{1}{r_{12}}P_y(2)P_y(2)dV_1dV_2 \equiv \left\langle P_xP_x\left|\frac{1}{r_{12}}\right|P_yP_y\right\rangle = 0.9443.$$

$$\langle 5\rangle = \left\langle P_xP_x\left|\frac{1}{r_{12}}\right|P_xP_x\right\rangle = \left\langle P_yP_y\left|\frac{1}{r_{12}}\right|P_yP_y\right\rangle = 0.9981.$$

$$\langle 6\rangle = \langle P_x|-\tfrac{1}{2}\Delta|P_x\rangle = 3.2513.$$

$$\langle 7\rangle = \langle h|-\tfrac{1}{2}\Delta|P_x\rangle = 0.2270.$$

$$\langle 8\rangle = \langle h|-\tfrac{1}{2}\Delta|h\rangle = 0.5000.$$

$$\langle 9\rangle = \left\langle P_x\left|\frac{1}{r_{A1}}\right|P_x\right\rangle = 1.2750.$$

$$\langle 10\rangle = \left\langle h\left|\frac{1}{r_{A1}}\right|P_x\right\rangle = 0.2384, \qquad (J_{xh})\ \text{K.A.I.K. p. 218.}$$

$$\langle 11\rangle = \left\langle h\left|\frac{1}{r_{A1}}\right|h\right\rangle = 0.5278, \qquad (K_{hh})\ \text{K.A.I.K. p. 219.}$$

$$\langle 12\rangle = \left\langle P_x\left|\frac{1}{r_{B1}}\right|P_x\right\rangle = 0.6505, \qquad (K_{2x2x})\ \text{K.A.I.K. p. 82.}$$

$$\langle 13\rangle = \left\langle h\left|\frac{1}{r_{B1}}\right|P_x\right\rangle = 0.3800, \qquad (J_{hx})\ \text{K.A.I.K. p. 218.}$$

$$\langle 14\rangle = \left\langle h\left|\frac{1}{r_H}\right|h\right\rangle = 1.0000.$$

$$\langle 15\rangle = \left\langle P_xP_x\left|\frac{1}{r_{12}}\right|P_xP_x\right\rangle = \left\langle P_yP_y\left|\frac{1}{r_{12}}\right|P_xP_x\right\rangle = 0.9443.$$

$\langle 16\rangle = \left\langle P_x P_x \left| \frac{1}{r_{12}} \right| hP_x \right\rangle = 0.2030,$ (L_{xxxh}) K.A.I.K. p. 214.

$\langle 17\rangle = \left\langle P_x P_x \left| \frac{1}{r_{12}} \right| hh \right\rangle = \left\langle P_y P_y \left| \frac{1}{r_{12}} \right| hh \right\rangle = 0.4900,$ (M_{xx}) K.A.I.K. p. 208.

$\langle 18\rangle = \left\langle P_s P_s \left| \frac{1}{r_{12}} \right| P_s P_s \right\rangle = 0.9981.$

$\langle 19\rangle = \left\langle P_s P_s \left| \frac{1}{r_{12}} \right| P_s h \right\rangle = 0.2294,$ (L_{sssh}) K.A.I.K. p. 213.

$\langle 20\rangle = \left\langle P_s P_s \left| \frac{1}{r_{12}} \right| hh \right\rangle = 0.5295,$ (M_{ss}) K.A.I.K. p. 208.

$\langle 21\rangle = \left\langle P_s h \left| \frac{1}{r_{12}} \right| P_s h \right\rangle = 0.1151,$ (N_{ss}) K.A.I.K. p. 210.

$\langle 22\rangle = \left\langle P_s h \left| \frac{1}{r_{12}} \right| hh \right\rangle = 0.2319,$ (L_{hhsh}) K.A.I.K. p. 216.

$\langle 23\rangle = \left\langle hh \left| \frac{1}{r_{12}} \right| hh \right\rangle = 0.6250,$ Roothan, *Tables for Two Center Coulomb Integrals* (University of Chicago Press, Chicago, 1955), p. 9.

$\langle 24\rangle = \langle h | Z | P_z \rangle = 0.5317,$ ($Z_{1s2s} = Z_{2s1s}$) K.A.I.K. p. 81.

$\langle 25\rangle = \langle P_s | h \rangle = 0.3044,$ (S_{sh}) K.A.I.K. p. 217.

$\langle 26\rangle = \left\langle P_x P_y \left| \frac{1}{r_{12}} \right| P_x P_y \right\rangle = 0.0538,$ Roothan, *Tables*.

$\langle 27\rangle = \left\langle P_x P_z \left| \frac{1}{r_{12}} \right| P_z h \right\rangle = 0.0097,$ (L_{xxzh}) K.A.I.K. p. 214.

$\langle 28\rangle = \left\langle P_z h \left| \frac{1}{r_{12}} \right| P_z h \right\rangle = 0.0283,$ (N_{xx}) K.A.I.K. p. 210.

In the list, the letters K.A.I.K. refer to the *Table of Molecular Integrals*, by M. Kotani, A. Amemiza, E. Ishiguro, and T. Komura (Marwzen Company, Ltd., Tokyo, 1955). The symbol in parenthesis preceding the letters K.A.I.K. refers to the notation used by Kotani *et al.* for the specific integral. Those integrals which are not followed by the symbols K.A.I.K. or Roothan were evaluated directly by integration. Integral $\langle 25\rangle$ is involved only in calculations for c_1, c_2, d_1, and d_2.

APPENDIX II

Analytical Expressions for and Values of Molecular Integrals for the HF Molecule Using Gaussians

$a = 1.132 \quad b = 0.283 \quad Z_B - Z_A = 1.733 \equiv \langle AB \rangle$ (a positive quantity).

$\langle 1\rangle = \langle P_x | -\Delta/2 | P_x \rangle = \frac{5}{2}a = 0.2830.$

$\langle 2\rangle = \left\langle P_x \left| \frac{1}{r_A} \right| P_x \right\rangle = \frac{4}{3}\left(\frac{2a}{\pi}\right)^{\frac{1}{2}} = 1.1319.$

$$\langle 3\rangle=\left\langle P_s\left|\frac{1}{r_B}\right|P_s\right\rangle=2\left(\frac{2}{\pi a}\right)^{\frac{1}{2}}\left\{\left[a-\frac{1}{4(Z_B-Z_A)^2}\right]F(\alpha)+\frac{1}{4(Z_B-Z_A)^2}e^{-\alpha}\right\}=0.5346,$$

$$\alpha=2aAB^2\quad F(\alpha)\equiv\alpha^{-\frac{1}{2}}\int_0^{\alpha^{\frac{1}{2}}}e^{-u^2}du.$$

$$\langle 4\rangle=\left\langle P_xP_x\left|\frac{1}{r_{12}}\right|P_yP_y\right\rangle=\frac{43}{30}\left(\frac{a}{\pi}\right)^{\frac{1}{2}}=0.8604.$$

$$\langle 5\rangle=\left\langle P_sP_s\left|\frac{1}{r_{12}}\right|P_xP_x\right\rangle=\left\langle P_yP_y\left|\frac{1}{r_{12}}\right|P_yP_y\right\rangle=\frac{49}{30}\left(\frac{a}{\pi}\right)^{\frac{1}{2}}=0.9806.$$

$$\langle 6\rangle=\langle P_s|-\Delta/2|P_s\rangle=\tfrac{5}{2}a=0.2830.$$

$$\langle 7\rangle=\langle P_s|-\Delta/2|h\rangle=\frac{2^{5/2}a^{5/4}b^{3/4}}{(a+b)^{3/2}}\langle AB\rangle\exp\left(-\frac{ab}{a+b}AB^{-2}\right)\left\{\frac{5ab^2}{(a+b)^2}-\frac{2a^2b^2}{(a+b)^3}\langle AB\rangle^2\right\}=0.2203.$$

$$\langle 8\rangle=\langle h|-\Delta/2|h\rangle=0.4245.$$

$$\langle 9\rangle=\left\langle P_s\left|\frac{1}{r_A}\right|P_s\right\rangle=\frac{4}{3}\left(\frac{2a}{\pi}\right)^{\frac{1}{2}}=1.1319.$$

$$\langle 10\rangle=\left\langle P_s\left|\frac{1}{r_A}\right|h\right\rangle=\frac{2^{7/2}a^{5/4}b^{3/4}}{\pi^{1/2}(a+b)}\exp\left(-\frac{ab}{a+b}AB^{-2}\right)\left\{\left[\frac{b}{a+b}\langle AB\rangle-\frac{1}{2b\langle AB\rangle}\right]F(\alpha)+\frac{2^{-\alpha}}{2b\langle AB\rangle}\right\}=0.2314,$$

$$\alpha=[b^2\langle AB\rangle^2]/[a+b].$$

$$\langle 11\rangle=\left\langle h\left|\frac{1}{r_A}\right|h\right\rangle=2(2b/\pi)^{\frac{1}{2}}F\{2b\langle AB\rangle^2\}=0.5395.$$

$$\langle 12\rangle=\left\langle P_s\left|\frac{1}{r_B}\right|P_s\right\rangle=2(2a/\pi)^{\frac{1}{2}}\left[1+\frac{1}{2a\langle AB\rangle^2}\right]\{F[ab\langle AB\rangle^2]-\exp[-2a\langle AB\rangle^2]\}=0.6596.$$

$$\langle 13\rangle=\left\langle P_s\left|\frac{1}{r_B}\right|h\right\rangle=\frac{8(2^{1/2})a^{5/4}b^{3/4}}{\pi^{1/2}(a+b)}\exp\left[-\frac{ab\langle AB\rangle^2}{a+b}\right]\left\{\left[\frac{b}{a+b}\langle AB\rangle+\frac{1}{2a\langle AB\rangle}\right]F(\alpha)-\frac{1}{2a\langle AB\rangle}e^{-\alpha}\right\}=0.3107,$$

$$\alpha=[a^2/(a+b)]\langle AB\rangle^2.$$

$$\langle 14\rangle=\left\langle h\left|\frac{1}{r_B}\right|h\right\rangle=2(2b/\pi)^{\frac{1}{2}}=0.8489.$$

$$\langle 15\rangle=\left\langle P_xP_x\left|\frac{1}{r_{12}}\right|P_zP_z\right\rangle=\left\langle P_yP_y\left|\frac{1}{r_{12}}\right|P_zP_z\right\rangle=\frac{43}{30}(a/\pi)^{\frac{1}{2}}=0.8604.$$

$$\langle 16\rangle=\left\langle P_xP_x\left|\frac{1}{r_{12}}\right|hP_z\right\rangle=\frac{16a^{\frac{1}{2}}b^{\frac{1}{2}}}{(a+b)[\pi(3a+b)]^{\frac{1}{2}}}\left[\left\{\frac{7a^2+4ab+b^2}{4b(3a+b)\langle AB\rangle}-\frac{3(a+b)^2}{8b^3\langle AB\rangle^3}\right\}e^{-\alpha}\right.$$
$$\left.+\left\{\frac{ab\langle AB\rangle}{a+b}-\frac{3a+b}{4b\langle AB\rangle}+\frac{3(a+b)^2}{8b^3\langle AB\rangle^3}\right\}F(\alpha)\right]\exp\left[-\frac{ab}{a+b}\langle AB\rangle^2\right]=0.1962,$$

$$\alpha=[2ab^2\langle AB\rangle^2]/[(a+b)(3a+b)].$$

$$\langle 17\rangle=\left\langle P_xP_x\left|\frac{1}{r_{12}}\right|hh\right\rangle=2\left[\frac{2ab}{\pi(a+b)}\right]^{\frac{1}{2}}\left[\left\{1-\frac{1}{4a\langle AB\rangle^2}\right\}F(\alpha)+\frac{e^{-\alpha}}{4a\langle AB\rangle^2}\right]=0.4959,$$

$$\alpha=[2ab\langle AB\rangle^2]/[a+b].$$

$$\langle 18\rangle=\left\langle P_sP_s\left|\frac{1}{r_{12}}\right|P_sP_s\right\rangle=\frac{49}{30}(a/\pi)^{\frac{1}{2}}=0.9806.$$

$$\langle 19\rangle=\left\langle P_sh\left|\frac{1}{r_{12}}\right|P_sP_s\right\rangle=\frac{8(ab)^{\frac{1}{2}}}{[\pi(a+b)(3a+b)]^{\frac{1}{2}}}\left\{\left[\frac{3(a+b)^2}{2b^3\langle AB\rangle^3}+\frac{2a^2-ab-b^2}{b(3a+b)\langle AB\rangle}-\frac{2ab(a+b)}{(3a+b)^2}\langle AB\rangle\right]e^{-\alpha}\right.$$
$$\left.+\left[-\frac{3(a+b)^2}{2b^3\langle AB\rangle^3}+\frac{1}{AB}+\frac{2ab\langle AB\rangle}{a+b}\right]F(\alpha)\right\}\exp\left[-\frac{ab}{a+b}\langle AB\rangle^2\right]=0.2233,$$

$$\alpha=[2b^2a\langle AB\rangle^2]/[(a+b)(3a+b)].$$

$$\langle 20\rangle=\left\langle hh\left|\frac{1}{r_{12}}\right|P_sP_s\right\rangle=2\left[\frac{2ab}{\pi(a+b)}\right]^{\frac{1}{2}}\left\{\left[1+\frac{1}{2a\langle AB\rangle^2}\right]F(\alpha)-\left[\frac{b}{a+b}+\frac{1}{2a\langle AB\rangle^2}\right]e^{-\alpha}\right\}=0.5287,$$

$$\alpha=[2ab/(a+b)]\langle AB\rangle^2.$$

$$\langle 21\rangle=\left\langle P_sh\left|\frac{1}{r_{12}}\right|P_sh\right\rangle=\frac{32a^{\frac{1}{2}}b^{\frac{1}{2}}}{(2\pi)^{\frac{1}{2}}(a+b)^{\frac{1}{2}}}\left[\frac{2b^2}{(a+b)^2}\langle AB\rangle^2+\frac{1}{6(a+b)}\right]\exp\left[\frac{2ab}{a+b}\langle AB\rangle^2\right]=0.1011.$$

$$\langle 22\rangle=\left\langle hh\left|\frac{1}{r_{12}}\right|P_sh\right\rangle=\frac{8a^{\frac{1}{2}}b^{\frac{1}{2}}}{(a+b)[\pi(3b+a)]^{\frac{1}{2}}}\left\{\left[\frac{2ab\langle AB\rangle}{a+b}+\frac{1}{\langle AB\rangle}\right]F(\alpha)-\frac{e^{-\alpha}}{AB}\right\}\exp\left[-\frac{ab}{a+b}\langle AB\rangle^2\right]=0.1987,$$

$$\alpha=[2a^2\langle AB\rangle^2]/[(a+b)(3b+a)].$$

$$\langle 23\rangle=\left\langle hh\left|\frac{1}{r_{12}}\right|hh\right\rangle=0.6003.$$

$$\langle 24\rangle=\langle P_s|Z|h\rangle=0.1265.$$

$$\langle 25\rangle=\langle P_s|h\rangle=\frac{2^{5/2}a^{5/4}b^{7/4}}{(a+b)^{5/2}}\langle AB\rangle\exp\left[-\frac{ab}{a+b}\langle AB\rangle^2\right]=0.2673.$$

$$\langle 26\rangle=\left\langle P_xP_y\left|\frac{1}{r_{12}}\right|P_xP_y\right\rangle=0.1(a/\pi)^{\frac{1}{2}}=0.0600.$$

$$\langle 27\rangle=\left\langle P_xP_z\left|\frac{1}{r_{12}}\right|P_xh\right\rangle=\frac{2a^{\frac{1}{2}}b^{\frac{1}{2}}}{[\pi(3a+b)]^{\frac{1}{2}}}\left[\frac{3(a+b)}{b^2\langle AB\rangle^2}F(\alpha)-\left\{\frac{3(a+b)}{b^3\langle AB\rangle^3}+\frac{4a}{b(3a+b)\langle AB\rangle}\right\}e^{-\alpha}\right]\exp\left[-\frac{ab\langle AB\rangle^2}{a+b}\right]=0.0124,$$

$$\alpha=[2ab^2\langle AB\rangle^2]/[(a+b)(3a+b)].$$

$$\langle 28\rangle=\left\langle P_zh\left|\frac{1}{r_{12}}\right|P_zh\right\rangle=\frac{8\sqrt{2}a^{5/2}b^{3/2}}{3\pi^{1/2}(a+b)^{7/2}}\exp\left[-\frac{2ab}{a+b}\langle AB\rangle^2\right]=0.0333.$$

APPENDIX III

Molecular Orbitals and Molecular Integrals for the Modified Polytetrafluoroethylene Chain

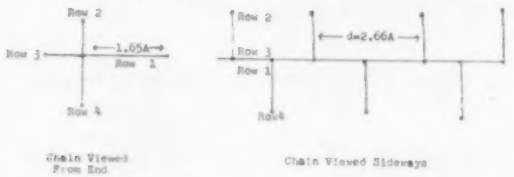

FIG. 2. Representation of the modified polytetrafluoroethylene chain.

Let orbital for Row 1 be Bloch sum b_1

$$b_1=\sum_{R_i^1}\exp(i\bar{k}\cdot\bar{R}_1^{(1)})\phi(\bar{r}-\bar{R}_i^1).$$

Similarly

$$b_2=\sum_{R_i^2}\exp(ik\cdot\bar{R}_i^{(2)})\phi(\bar{r}-\bar{R}_i^2)$$

$$b_3=\sum_{R_i^3}\exp(ik\cdot\bar{R}_i^{(3)})\phi(\bar{r}-\bar{R}_i^3)$$

$$b_4=\sum_{R_i^4}\exp(ik\cdot\bar{R}_i^{(4)})\phi(\bar{r}-\bar{R}_i^4).$$

For the $3s$ orbital

$$\phi=(4/15)^{\frac{1}{2}}\frac{(2a)^{7/4}}{(\pi)^{3/4}}r^2\exp(-ar^2),\quad a=0.15.$$

$$\frac{\langle b_i|-\Delta/2|b_j\rangle}{\langle b_i|b_j\rangle}=\frac{\sum_{m=-N}^{+N}\langle \underset{i0}{3s}|-\Delta/2|\underset{jm}{3s}\rangle}{\sum_{m=-N}^{+N}\langle \underset{i0}{3s}|\underset{jm}{3s}\rangle}$$

$$\langle 3s|3s\rangle=[1+0.1333aR^2+0.0666(aR^2)^2]\exp(-aR^2/2)$$

$$R^2\equiv R_{i0jm}{}^2=(X_{i0}-X_{jm})^2+(Y_{i0}-Y_{jm})^2+(Z_{i0}-Z_{jm})^2$$

$$\langle \underset{i0}{3s}|-\Delta/2|\underset{jm}{3s}\rangle=[1.1a-0.7a(aR^2)+0.3a(aR^2)^2-0.0333a(aR^2)^3]\exp(-aR^2/2).$$

For $2P_z$ orbitals, $a=1.132$,

$$\phi=(4a)^{\frac{1}{2}}(2a/\pi)^{\frac{3}{4}}(z-\underset{+N}{Z})\exp(-ar^2)$$

$$\frac{\langle b_i|-\Delta/2|b_j\rangle}{\langle b_i|b_j\rangle}=\frac{\sum_{m=-N}^{+N}\langle \underset{i0}{2p}|-\Delta/2|\underset{jm}{2p}\rangle}{\sum_{m=-N}^{+N}\langle \underset{i0}{2p}|\underset{jm}{2p}\rangle}$$

$$\frac{\left\langle b_i\left|\frac{1}{1r}\right|b_j\right\rangle}{\langle b_i|b_j\rangle}=\frac{\sum_{k=1,2,3,4}\sum_{n=-N}^{+N}\sum_{m=-N}^{+N}\left\langle \underset{i0}{2p}\left|\frac{1}{r_{kn}}\right|\underset{jm}{2p}\right\rangle}{\sum_{m=-N}^{N+}\langle \underset{i0}{2p}|\underset{jm}{2p}\rangle}$$

$$\langle \underset{i0}{2p}|\underset{jm}{2p}\rangle=(1-Z_{0m}{}^2a)\exp(-aR^2/2)$$

$$\langle \underset{i0}{2p}|-\Delta/2|\underset{jm}{2p}\rangle=1/2(5a-a^2R^2-7a^2Z_{0m}{}^2+a^3Z_{0m}{}^2R^2)\exp(-aR^2/2)$$

$$R^2\equiv R_{i0jm}{}^2\doteq(X_{i0}-X_{jm})^2+(Y_{80}-Y_{jm})^2+(Z_{80}-Z_{jm})^2$$

$$Z=(Z_{i0}-Z_{jm})^2.$$

Note: Subscripts $i0$ refer to orbital on ith row centered about fluorine atom 0; jm refers to orbital on jth row centered about fluorine atom m.

APPENDIX IV

Irreducible Representations of the Space Group of the Modified Poly-TFE Chain

	$D\{\epsilon\|R_n\}$	$D\{R\|R_n\}$	$D\{I\|R_n\}$	$D\{IR\|R_n\}$	$D\{\rho\|T+R_n\}$	$D\{\rho R\|T+R_n\}$	$D\{\rho I\|T+R_n\}$	$D\{\rho IR\|T+R_n\}$
(1)	1	1	1	1	1	1	1	1
(2)	1	1	1	1	−1	−1	−1	−1
(3)	1	1	−1	−1	1	1	−1	−1
(4)	1	1	−1	−1	−1	−1	1	1
(5)	1	−1	1	−1	1	−1	1	−1
(6)	1	−1	1	−1	−1	1	−1	1
(7)	1	−1	−1	1	1	−1	−1	1
(8)	1	−1	−1	1	−1	1	1	−1
(9)	$\begin{vmatrix} e^{ik_2R_n} & 0 \\ 0 & e^{ik_2R_n} \end{vmatrix}$	$\begin{vmatrix} e^{ik_2R_n} & 0 \\ 0 & e^{ik_2R_n} \end{vmatrix}$	$\begin{vmatrix} -e^{ik_2R_n} & 0 \\ 0 & e^{ik_2R_n} \end{vmatrix}$	$\begin{vmatrix} -e^{ik_2R_n} & 0 \\ 0 & e^{ik_2R_n} \end{vmatrix}$	$\begin{vmatrix} 0 & e^{ik_2R_n} \\ e^{ik_2R_n} & 0 \end{vmatrix}$	$\begin{vmatrix} 0 & e^{ik_2R_n} \\ e^{ik_2R_n} & 0 \end{vmatrix}$	$\begin{vmatrix} 0 & e^{ik_2R_n} \\ -e^{ik_2R_n} & 0 \end{vmatrix}$	$\begin{vmatrix} 0 & e^{ik_2R_n} \\ -e^{ik_2R_n} & 0 \end{vmatrix}$
(10)	$\begin{vmatrix} e^{ik_2R_n} & 0 \\ 0 & e^{ik_2R_n} \end{vmatrix}$	$\begin{vmatrix} -e^{ik_2R_n} & 0 \\ 0 & -e^{ik_2R_n} \end{vmatrix}$	$\begin{vmatrix} -e^{ik_2R_n} & 0 \\ 0 & e^{ik_2R_n} \end{vmatrix}$	$\begin{vmatrix} ee^{ik_2R_n} & 0 \\ e\ 0 & -e^{ik_2R_n} \end{vmatrix}$	$\begin{vmatrix} 0 & e^{ik_2R_n} \\ e^{ik_2R_n} & 0 \end{vmatrix}$	$\begin{vmatrix} 0 & -e^{ik_2R_n} \\ -e^{ik_2R_n} & 0 \end{vmatrix}$	$\begin{vmatrix} 0 & e^{ik_2R_n} \\ -e^{ik_2R_n} & 0 \end{vmatrix}$	$\begin{vmatrix} 0 & -e^{ik_2R_n} \\ e^{ik_2R_n} & 0 \end{vmatrix}$

ϵ = the identity operation, R_n = the nth translation, I = inversion through a center of symmetry.
ρ = notation about an axis normal to the chain axis.
T = a nonprimitive translation, $d/2$ chain axis and the axis for ρ.
R = reflection in the plane containing the $k_2 = \pi/d$.

APPENDIX V

Energy Eigenvalues for the Polytetrafluoroethylene Molecule

$2p$ Band		$3s$ Band	
Representations	Energies	Representations	Energies
D_2	2.8305863	D_1	0.0612498
D_4	2.8307815	D_3	0.1485455
D_5	2.8312030	D_6	0.2675215
D_7	2.8310078	D_8	0.1502842
D_9	2.8288947	D_9	0.370903
D_{10}	2.8293161	D_{10}	0.738750
(Isolated $2p$ orbital)	2.830	(Isolated $3s$ orbital)	0.1650

JOURNAL OF APPLIED PHYSICS VOLUME 31, NUMBER 11 NOVEMBER, 1960

Chain Folding and Free Energy Density in Polymer Crystals

ANTON PETERLIN
*Department of Chemistry, Wayne State University, Detroit, Michigan**†

Macromolecular chains in freely growing crystals very likely fold back at regular intervals in order to minimize the free energy density of the crystal. The surface energy contribution favors infinite thickness. The smearing out effect of interchain potential field, however, arising from the incoherent part of fluctuation of neighboring chains and increasing with the fold period, favors thin crystals. For sake of simplicity the longitudinal chain vibrations were considered in spite of the fact that in actual crystals the main contribution most likely comes from rotational oscillations. Since the general character of smearing out effect is nearly the same in both cases the present results may be applied at least qualitatively. They fairly well represent the general trend of temperature dependence of polymer crystal thickness and its change with intermolecular forces.

THE most striking phenomenon with polymer crystals, let us say of polyethylene, polypropylene, polyamides, and so on, is their finite and rather uniform thickness in the chain direction which requires the linear polymer chains to fold back at the crystal surface. In the same polymer series the fold period seems to be independent of chain length (molecular weight), provided the latter is great enough,[1,2] but it increases with temperature of crystal formation.[2] A similar increase is found on the heating of polyethylene crystals.[3] Above 110°C the crystals partly melt and rearrange into thicker crystals. Although the thickness at the beginning increases with annealing time—there is a net difference between values obtained after 30 min and 15 hr of annealing, respectively, but no further change after heating for 65 hr (one experiment at 125°C)—one may conclude that in nonbranched polyethylene very likely a limiting fold period exists depending merely on temperature. Very roughly the stable thickness d_3 varies as the inverse distance from melting point. With different polymers the thickness increases with smaller intermolecular forces, being the smallest with polyamides exhibiting hydrogen bonds and the largest with polytetrafluoroethylene showing the smallest interaction.

Explanation of the phenomenon must be based on some specific property of chain crystals which is not common to low molecular crystals. In any crystal the surface energy contribution favors large crystals with as small as possible surface to volume ratio. In polymer crystals, however, this tendency has to be overbalanced by some other effect so that the chain prefers to fold back after a while and does that with such uniformity that a rather constant crystal thickness results.

Kinetic explanations[4–8] concentrate on crystal nuclei formation and subsequent addition of new chains on the faces perpendicular to the a, b plane. In solution, supercooling by $\Delta T = T' - T$ (T' = temperature of crystal-solution equilibrium, T = temperature of actual crystallization) together with surface energy contribution $2S\sigma$ (S = area of chain cross section, σ = surface tension)

* On leave of absence from Physics Department, University Ljubljana, Yugoslavia. The author is indebted to SKNE, Beograd, Yugoslavia, for a research grant which made this work possible.

† Present address: Physikalisches Institut, Technische Hochschule, München, Germany.

[1] H. Zahn, International Symposium on Macromolecules, Wiesbaden, Germany, October, 1959.

[2] A. Keller, Discussions Faraday Soc. No. **25**, 112 (1958); A. Keller and A. O'Connor, International Symposium on Macromolecules, Wiesbaden, Germany, October, 1959; B. G. Ränby and F. F. Morehead, Am. Chem. Soc. Meeting, Boston, Massachusetts, April, 1959.

[3] W. O. Statton and P. H. Geil, Delaware Science Symposium, January, 1960.

[4] F. C. Frank, Discussions Faraday Soc. No. **25**, 208 (1958).

[5] R. Eppe, E. W. Fischer and H. A. Stuart, J. Polymer Sci. **34**, 721 (1959).

[6] J. I. Lauritzen and J. D. Hoffman, J. Research Natl. Bur. Standards **64a**, 73 (1960); J. Chem. Phys. **31**, 1680 (1959).

[7] F. P. Price, J. Chem. Phys. **31**, 1679 (1959).

[8] T.-P. Lin (to be published).

determines the most probable nucleus with the thickness

$$d_3 = \sigma V/\Delta F \sim \sigma/\Delta T. \quad (1)$$

$\Delta F/V$ is the difference of free energy per unit volume of solid due to supercooling. Larger or smaller nuclei are virtually excluded by the slow formation rate although the larger ones are favored thermodynamically. Addition of new chains on lateral faces of the growing crystal avoids extension over initial thickness d_3 of the nucleus in order not to increase the surface, and so the whole crystal becomes a thin platelet with uniform thickness.

Such an explanation first of all assumes that the supercooling is nearly proportional to the distance from melting point T_m

$$\Delta T \sim T_m - T \quad (2)$$

in order to agree with experiments on crystallization from solution. Further at annealing, according to kinetic theories, the crystals ought to grow indefinitely because no mechanism is provided for preventing their transformation into a thermodynamically stabler configuration. Moreover, the folding geometry in hollow pyramidal crystals of polyethylene as investigated by Niegisch and Swan[9] and Reneker and Geil[10] shows a shift by one repeat distance in c axis at every fold in spite of increased surface. By such experimentally observed shifts hence the nucleus would have the possibility to grow into a thermodynamically more favored thicker crystal—indeed the thickness ought to increase indefinitely—but does not do so.

Both cases require an additional explanation which very likely may be obtained from a more detailed consideration of free energy density of polymer crystals and its dependence on crystal thickness.[11] The main difference between polymer and low molecular crystals is the extreme anisotropy of a crystal force field in the former. In the chain direction the forces are nearly diamondlike; perpendicular to it, they are substantially smaller, let us say twenty times. However, the most marked decrease (by a factor of thousand) is found in forces between neighboring chains which prevent rotation around and translation along the chain axis. As a consequence, in paraffin crystals with 20 to 40 carbon atoms, a high degree of rotational freedom occurs below the melting point. The rotation is still "hindered," however, accompanied already by transition from orthorhombic and monoclinic, respectively, to hexagonal lattice. Nuclear magnetic resonance investigation[12–14] of crystallized polymers already shows far below the melting point a substantial narrowing of absorption line so that it becomes identical with that observed in the melt, indicating a high degree of incoherent rotational and translational motion of chains in the crystal. Irreversible changes in linewidth of polymer crystals occur at nearly the same temperatures, and to a similar extent, as the previously mentioned crystal transformation to larger thickness during annealing. A rather anisotropic smearing out of electron density in paraffin crystals was derived by Smith[15] from x-ray diffraction patterns. The amplitudes are larger in the direction perpendicular to the chain axis than parallel to it and are appreciably larger at the ends than at the center of the chain.

All these observations indicate the special role of rotational and longitudinal oscillations in chain crystals due to the exceptional small forces opposing such movements. Moreover, the fluctuations of neighboring chains must be to a large extent incoherent above the temperature at which the sharp transition in the NMR linewidth and the growth of crystal thickness at annealing occur. Very likely, the rotational vibrations are excited to a higher degree than the longitudinal. But since it is much easier to treat longitudinal vibrations—one can start with a rather simple point lattice, proposed by Stockmayer and Hecht[16] for the study of heat capacity of polymer crystals, and treat only the set of waves having elongations in the chain axis—this was the case investigated by Peterlin and Fischer.[17]

In the simplest tetragonal point lattice the strong force constants f, f', and κ are in the chain direction, perpendicular to it, and against chain bending, respectively, small forces g between second neighbors preventing longitudinal translation of the whole chain such that in the resulting secular determinant, the nondiagonal terms may be neglected.[18] The mean square longitudinal fluctuation s^2 of chain atoms (groups CH_2) against the center of mass turns out to be

$$s^2 = \langle s_3^2 \rangle_{av} = (kT/Nm) \sum_{j=1}^{N} 1/\omega_j^2 \quad N = N_1 N_2 N_3; \quad (3)$$

where N_1, N_2, N_3 are the number of chain atoms in the a, b, c axes, respectively; m is the mass of the chain atom, and ω_j is found from

$$\omega_j^2 = (2f/m)(1-\cos\phi_3) + (4g/m)(2-\cos\phi_1 \cos\phi_3 - \cos\phi_2 \cos\phi_3). \quad (4)$$

The eigenfrequencies of lattice waves with elongation

[9] W. D. Niegisch and P. R. Swan, Am. Phys. Soc. Meeting, Detroit, March, 1960.
[10] D. H. Reneker and P. H. Geil, Am. Phys. Soc. Meeting, Detroit, March, 1960.
[11] E. W. Fischer, Z. Naturw. **14a**, 584 (1959).
[12] W. P. Slichter, Am. Phys. Soc. Meeting, Detroit, Michigan, March, 1960.
[13] C. M. Huggins, L. E. St. Pierre and A. M. Bueche, Am. Chem. Soc. Meeting, Boston, Massachusetts, April, 1959.
[14] A. Peterlin and E. Pirkmajer, J. Polymer Sci. (to be published); A. Peterlin, F. Krašovec, E. Pirkmajer, and I. Levstek, Makromol. Chem. **37**, 231 (1960), International Symposium on Macromolecules, Wiesbaden, Germany, October, 1959.
[15] A. E. Smith, J. Chem. Phys. **21**, 2229 (1953) and private communication.
[16] W. H. Stockmayer and C. E. Hecht, J. Chem. Phys. **21**, 1954 (1953).
[17] A. Peterlin and E. W. Fischer, International Symposium on Macromolecules, Wiesbaden, Germany, October, 1959.
[18] Stockmayer and Hecht assume $f:f':\kappa:g = 0.992:0.03968:0.0992:0.002$.

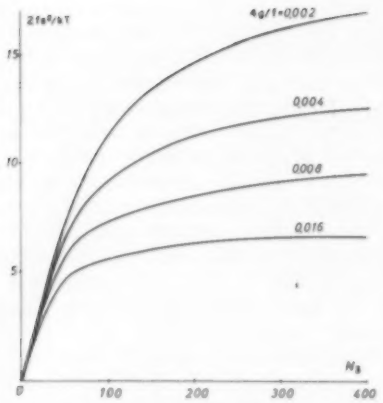

FIG. 1. Mean square longitudinal fluctuation $s^2 \cdot 2f/kT$ in a chain lattice as function of number N_3 of chain atoms in the straight section between the surfaces. The parameter $4g/f$ is 0.008 in the case treated by Stockmayer and Hecht.

in the chain direction are

$$\phi_t = 2\, n_t a_t / N_t$$
$$n_t = 1, 2, \cdots N_t \quad t = 1, 2, 3.$$

With the ratio of $f : f' : \varkappa$ (as given by Stockmayer and Hecht) and four different values of g, the resulting $2fs^2/kT$ is plotted in Fig. 1 as a function of N_3, the number of chain atoms in the straight section between the surfaces. After the initial linear increase with crystal thickness which persists longer the smaller $4g/f$ is, it bends downward rather sharply and very slowly approaches a limit $s_\infty^2 m/kT$, which again is higher the smaller $4g/f$ is, i.e., the higher the anisotropy of crystal forces.[19] But it is remarkable at what large values of N_3 there is still a net dependence of longitudinal fluctuation on crystal thickness. Moreover, the fluctuations as calculated from the harmonic force field are indeed very small because of the great increase of potential energy $gz^2/2$ with respect to elongation z. A nonquadratic, e.g., sinusoidal, force field

$$(c^2 g/4\pi^2)(1-\cos 2\pi z/c) \tag{5}$$

better represents the potential distribution in the chain axis due to second neighbor interaction and yields a marked increase in s^2—one has a nearly linear dependence on N_3, similar to that in Eq. (9)—because in the partition function the large amplitudes are much less depressed than in the pure quadratic potential field.

The net dependence of fluctuation amplitude in chain direction on crystal thickness until rather high N_3 is a specific property of polymer crystals with extreme anisotropy of second neighbor lattice forces. The lattice points are strongly prevented from moving in the a, b plane, but find a nearly negligible force field opposing the translation of the whole chain in the direction of the c axis. (In this connection one must not forget that the lattice model chosen has no provision for treating rotational motion of chains.) In usual low-molecular crystals (e.g., ionic crystals or metals), however, the fluctuation amplitude very rapidly reaches the limiting value for an infinite crystal, i.e., small deviations from the limit existing merely with very low N_1, N_2, or N_3.[20]

This specific effect of chain crystals exhibiting such a persistent increase of longitudinal-fluctuation amplitude with N_3 and its influence on free energy density was studied by Peterlin and Fischer[21] in order to see whether there is a net dependence of the latter on crystal thickness which at least qualitatively could explain the observations on polymer crystals. The obtained results, however, can also be applied to some extent to rotational motion. Of course a more detailed analysis of incoherent rotational and longitudinal vibrations in combination with extensive Fourier mapping from the x-ray diffraction pattern of polymer crystals at different temperatures will be desired in order to have a good starting point for a quantitative theory.

Peterlin and Fischer treat a one-dimensional model under the simplifying assumptions that chains fluctuate independently and that the force field the neighboring chains create in the axis of the chain under consideration is a pure sinusoidal field

$$\phi_0 - \phi \cos 2\pi z/c. \tag{6}$$

The energy of the chain in such a field is the sum of kinetic energy and of potential energy of the springlike forces in the chain itself and of the interchain sinusoidal field of Eq. (6). It reads[22]

$$U = (m/2)\sum_{j=1}^{N} \dot{z}_j^2 + (f/2)\sum_{j=1}^{N-1} (z_j - z_{j+1})^2 + N\phi_0 - \phi \sum_{j=1}^{N} \cos 2\pi z_j/c. \tag{7}$$

This yields the free energy per chain atom[22]

$$F/N = -kT \ln(2kT/\hbar\omega_0) + \phi_0 - \phi + [0.6909 + \ln(kT/\hbar\omega_0) + 0.5 \ln N(1+N\beta A^2)]kT/N \tag{8}$$

and mean-square fluctuation against the center of mass

$$s^2 = (NkT/6f)[1 - 0.4/(1+1/4N\beta A^2)]. \tag{9}$$

[19] At $T = 100°C$ and $4g/f = 0.008$ (0.002) one obtains $s_\infty = 0.11$ A(0.15 A).

[20] See for instance, G. Leibfried, in *Handbuch der Physik* (Springer-Verlag, Berlin, Gottingen, Heidelberg, 1955), Vol. 7, part 1.

[21] A. Peterlin and E. W. Fischer, Z. Physik **159**, 272 (1960).

[22] In what follows, N_3 is replaced by N.

[23] Equation 8 may be considered as that part of free energy density of a polymer crystal which depends on vibration along the chain axis. All other contributions to free energy density with exception of that from surface energy are independent of crystal thickness. Further, according to the derivation of Eq. 8, N must not be too small.

Here $\omega_0^2=4f/m$, $\beta=\phi/kT$, and $A^2=NkT/fc^2$. If all the chains were at rest, one would have $\phi=\phi_0$. With independent fluctuation of neighboring chains,[24] however, their force field is smeared out to

$$\phi_0-\phi_0\exp(-2\pi s^2/c^2)\cos 2\pi z/c, \tag{10}$$

which yields

$$\phi=\phi_0\exp(-2\pi s^2/c^2). \tag{11}$$

As a consequence, ϕ in the expression of free energy per chain atom [Eq. (8)] contributes a term increasing with N which, together with the contribution of surface energy $2S\sigma/N$, gives rise to a minimum of F_{cr}/N at finite N^* (Fig. 2).[25] A plot of N^*, representing the thermodynamically stable crystal configuration as a function of $2S\sigma/kT$ with $\beta_0=\phi_0/kT$ as parameter is shown in Fig. 3. The higher β_0 is, i.e., the stronger the interchain forces are, the smaller the stable crystal thickness is, in fair agreement with experimental data on polyamides, polyethylene, and polytetrafluoroethylene.

With increasing temperature the crystal mainly expands in the directions perpendicular to the chain axes, hence decreasing the interchain potential energy amplitude ϕ_0. In Fig. 3 one has to go to lower values β_0 at the nearly unchanged abscissa $2S\sigma/kT$, because the changes in T are small compared with T itself, and one obtains an increase in thickness of thermodynamically stable crystal, the increase being more rapid if the initial β_0 is smaller, i.e., the higher the starting temperature. This means that with increasing temperature the thickness increases faster, the higher the temperature, in good qualitative agreement with the rough experimental estimate that it varies nearly as the inverse distance from the melting point. In order to see how well the theory may agree with experimental data some arbitrary functional connections between β_0 and T were tried. In Fig. 4 a plot of N^* corresponding to an exponential decrease in β_0 with temperature

$$\beta_0(T)=B\exp(-CT) \tag{12}$$

is s[illegible] (the corresponding points in Fig. 3 are marked by small circles) together with the values observed by Statton and Geil. One sees from the upper abscissa that close to the melting point the decrease in β_0 is less steep than suggested by Eq. (12). The low precision of experimental data and the qualitative character of the present theory, of course, prohibit any far-reaching conclusion from this partial fit.

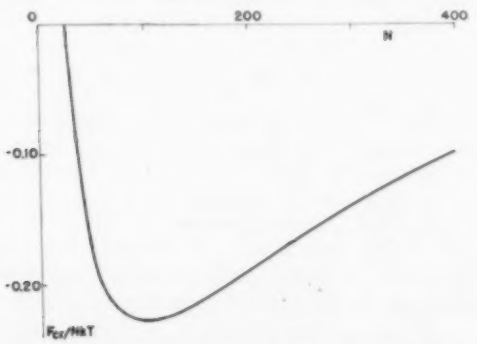

FIG. 2. Free energy of chain crystal per chain atom as function of N. All terms independent of N are omitted. Note the steep increase on the left and the low slope on the right side of minimum.

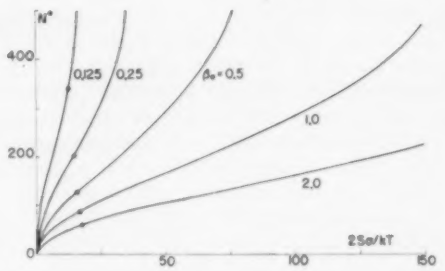

FIG. 3. Number of chain atoms N^* corresponding to stable crystal configuration as a function of surface energy contribution $2S\sigma/kT$ and with $\beta_0=\phi_0/kT$ as parameter. Circles (○) indicate points used for construction of temperature-thickness curve in Fig. 4 according to Eq. 12 and experimental data of Statton and Geil.

Since the crystal just grows with the thermodynamically most favored number of chain atoms in the c axis, its thickness remains uniform and independent of lateral dimensions. At heating, the steep increase (at the left side of free energy per chain atom curve in Fig. 2) rather strongly pushes the chains into the new stable configuration with longer straight sections. The transformation[26] is helped by the accompanying decrease of interchain potential energy amplitude ϕ_0, which less strongly opposes chain translation and higher fluctuation amplitude, decreasing ϕ_0 to ϕ. On cooling, however, the chain mobility, fluctuation amplitude, and the driving force corresponding to the much lower slope of the free energy curve at the right side of the minimum are small so that the configuration with too thick crystals, corresponding to a higher temperature, is easily frozen in.

In spite of good qualitative agreement with experimental data the model is far from being satisfactory. It has some inherent insufficiencies. First of all, neighboring chains are not completely independent in their

[24] In the crystal the longitudinal fluctuations of single chains are the more independent the smaller $4\pi^2\phi/c^2f$, but they are always smaller than s^2, so that Eqs. 10 and 11 overestimate the smearing out effect.

[25] All plots in this and in subsequent figures correspond to $T=100$°C, $f=2.10^5$ d/cm, $c=1.25$ A.

[26] Electron microscope (footnote 3) and x-ray observations (E. W. Fischer, Conference on Thermodynamics and Mechanics of Polymer Systems, New York Academy of Sciences, May 27, 1960) give the impression that during annealing at higher temperature the crystals which are too thin melt first, the crystal diffraction pattern completely disappears, and then the melt recrystallizes into thicker crystals.

longitudinal fluctuations so that the reduction of ϕ_0 to ϕ is less drastic, and hence the minimum in Fig. 2 less deep and the right side slopes still lower. The ratio of incoherent to total fluctuation is surely substantially lower than 1, but it very likely does not decrease with N. Such a correction would only reduce the abscissa, i.e., the surface energy $2S\sigma/kT$ in Fig. 3, by a corresponding factor without changing the general character of thickness dependence on ϕ_0/kT and σ. Further, the sinusoidal potential field in the actual crystal ends sharply, with a rather steep upward slope at the crystal surface (Fig. 5), whereas in the form of Eq. (6) it

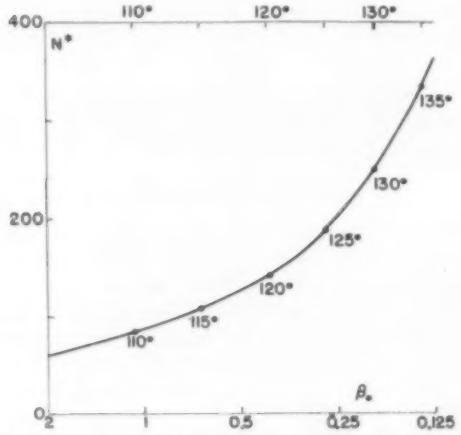

FIG. 4. Stable crystal thickness N^* as function of β_0. With assumption Eq. 12 the abscissa is a linear temperature scale. Temperatures corresponding to values found by Statton and Geil are written on the curve and yield the scale at the top. It slightly contracts on approaching the melting point, indicating that β_0 there decreases slower than assumed in Eq. 12.

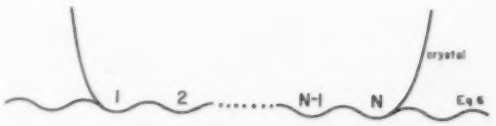

FIG. 5. Interchain potential energy according to Eq. 6 (sinusoidal curve extending on both sides to infinity) and the steep increase of actual crystal energy at the surface. Numbers indicate the minima occupied by single chain atoms.

stretches out to infinity. As a consequence the fluctuation amplitude in Eq. (9) is overestimated. This neglect does not matter very much as long as $s<c/2$ and this is the case with $N<900$. And finally one must not forget the fact, mentioned at the beginning, that rotational oscillations are very likely excited to a higher degree than longitudinal vibrations and hence contribute more to the smearing out effect of interchain potential energy than translation. All these facts require a more precise investigation of chain motion in polymer crystal[27] in order to obtain a satisfactory quantitative agreement with experiment. That such an extension of the program is worthwhile was just demonstrated by this simple model where we considered only the longitudinal vibrations which very roughly demonstrated the feasibility of thermodynamic explanation of finite folding periods in polymer crystals. In this connection one may also mention that a nonquadratic energy potential field is a basic condition for a sufficiently high positive term increasing with N in free energy per chain atom which is needed for the appearance of minimum at finite N^*. A purely quadratic field gives too small a contribution. This fact agrees well with recent observations of phonon distribution in real crystals.

[27] Work in this direction is under way and will be published soon.

Regular Articles

Effect of Random Inhomogeneities on Electrical and Galvanomagnetic Measurements

CONYERS HERRING
Bell Telephone Laboratories, Murray Hill, New Jersey
(Received June 20, 1960)

This paper is designed to supplement the existing extensive literature on the conductivity of a randomly inhomogeneous medium, by treating the effects of inhomogeneities on piezoelectric, galvanomagnetic, and thermoelectric measurements. The scale of the inhomogeneities is supposed small compared with the dimensions of the specimen being measured, but large compared with mean free path, Debye length, etc. Formulas for all the effects are derived which are asymptotically exact in the limit of small fractional fluctuations in the local conductivity, etc. Comparison with other approximations and application to various exactly soluble cases show that these formulas are often roughly valid for quite sizable fluctuations. For material which, if uniform, would show a high field saturation of transverse magnetoresistance, the presence of appreciable inhomogeneities in the Hall constant will cause the magnetoresistance to increase indefinitely with field. This effect is due to the current distortions arising from the large and fluctuating Hall fields. For the special case of an isolated inclusion, these distortions are shown to extend, at high fields, to distances in the direction of the magnetic field which are many times the diameter of the inclusion. Under some conditions it appears that even the random distribution of impurities in a semiconductor can give rise to perceptible fluctuations on a scale large enough for concepts of macroscopic conduction to be applicable. Since fluctuations of even smaller scale are still larger, the total effect of fluctuations cannot be properly treated by the present methods; however, when the macroscopic part of the fluctuations is large, conventional impurity-scattering theories must be inadequate. Applications to polycrystalline metals and semiconductors are discussed briefly.

1. INTRODUCTION

BULK electrical properties of semiconductors are usually related to a theoretical model based on a transport equation in crystal-momentum space, or to other models which also assume spatial homogeneity of all the fields and currents. By now this correlation of theory and experiment has become so detailed and so quantitative that it behooves us to consider carefully and, if possible, try to correct for, all the more or less trivial factors which may spoil the applicability of the models to actual experiments. Among such factors are surface conduction,[1] distortion of current lines near electrodes or sidearms,[1,2] and inhomogeneities.[1] Although with the best present day materials the latter factor is perhaps the least troublesome of the ones mentioned, inhomogeneity of a much more serious degree can undoubtedly occur; moreover, the theory of the effects of inhomogeneities has some physically and mathematically interesting features. These facts provided the original motivation for the present study. As the work progressed, it became evident that there are actually a wide variety of areas in which the type of analysis we have undertaken may prove useful, e.g., multiphase systems and, especially, polycrystalline metals and semiconductors. However, we shall attempt no more than a very sketchy discussion of most of these.

There is, of course, very extensive literature on the conductivities or, equivalently, the dielectric constants of inhomogeneous aggregates.[3] This literature has concerned itself mainly with the effective conductivity of a medium consisting of two or more distinct phases, separated by sharp boundaries. The present work differs from this in that we shall assume weak but continuously variable fluctuations in electrical properties, and in that we shall give principal attention to the effects of magnetic fields, anisotropic stress, thermal gradients, etc. Except for brief discussions of Hall effect[4] and thermoelectric power,[5] such effects have received little attention hitherto. The simple conduction problem has, however, been treated by Brown[6] via a systematic expansion in powers of the inhomogeneity, a method closely related to ours; a similar treatment, less extensively developed but applicable to anisotropic conductivity tensors, has been given by Nedoluha.[7]

This paper will be limited to a discussion of inhomogeneities whose scale is small compared with the size of the specimen but large compared with such things as a Debye length or a (suitably defined) mean free path. These limitations are imposed only to make the discussion tractable: inhomogeneities of larger scale cannot be treated in any general sense, but must be considered in relation to the boundary conditions of a specific geometry, while those of smaller scale cannot be treated by macroscopic theory, but require solution of

[1] The experimental studies which have suggested to us the need for careful consideration of these perturbing factors include: F. J. Morin, T. H. Geballe, and C. Herring, Phys. Rev. **105**, 525 (1957) (piezoresistance); C. Herring, T. H. Geballe, and J. E. Kunzler, Phys. Rev. **111**, 36 (1958), Bell System Tech. J. **38**, 657 (1959) (thermomagnetic effects). The latter paper gives the most detailed discussion.

[2] I. Isenberg, B. R. Russell, and R. F. Green, Rev. Sci. Inst. **19**, 685 (1948); R. F. Wick, J. Appl. Phys. **25**, 748 (1956); H. J. Lippmann and F. Kuhrt, Z. Naturforschung **13a**, 462 (1958); R. F. Brown, Proc. Phys. Soc. (London) **71**, 500 (1958); N. E. Alekseevski, N. B. Brandt, and T. I. Kostina, J. Exptl. Theoret. Phys. (U.S.S.R.) **34**, 1339 (1958) [translation: Soviet Phys. JETP 7, 924 (1958)].

[3] A concise summary of the various formulas and a list of the major references has been given by J. A. Reynolds and J. M. Hough, Proc. Phys. Soc. (London) **B70**, 769 (1957).

[4] J. Volger, Phys. Rev. **79**, 1023 (1950); H. Juretschke, R. Landauer, and J. A. Swanson, J. Appl. Phys. **27**, 838 (1936).

[5] S. V. Ayrapetyants, J. Tech. Phys. (U.S.S.R.) **27**, 478 (1957) [English translation: Soviet Phys.-Tech. Phys. **2**, 429 (1958)]; S. V. Ayrapetyants and M. S. Bresler, J. Tech. Phys. (U.S.S.R.) 28, 1934 (1958) [English translation: Soviet Phys.—Tech. Phys. **3**, 1778 (1958)].

[6] W. F. Brown, Jr., J. Chem. Phys. **23**, 1514 (1955).

[7] A. Nedoluha, Z. Physik **148**, 248 (1957).

an atomistic transport problem in which position as well as momentum variables must be retained. Most of our formulas (those of Sec. 2) will be based on the further assumption that the inhomogeneities are slight, so that the current lines in the experiment under consideration are almost uniform. Section 3 will discuss removal of this limitation for certain special situations. The small-fluctuation formulas will turn out, surprisingly, to be fair approximations for many, though not all, cases with moderately large fluctuations. For this reason, and because many materials are nearly homogeneous, the restriction to slight inhomogeneities does not greatly impair applicability of the results to many cases of interest. Inhomogeneities occurring over larger or smaller distances than those considered here are, however, often important; some speculations on the role of very small-scale inhomogeneities will be given in our discussion of applications in Sec. 4.

2. FOURIER APPROACH. WEAK CURRENT DISTORTIONS

Basic Concepts

Let the medium have a conductivity tensor $\boldsymbol{\sigma}(\mathbf{r})$, or a resistivity tensor $\boldsymbol{\rho}(\mathbf{r})$, dependent on position $\mathbf{r}$ in a random manner such that the fluctuations, though they may be arbitrarily anisotropic, have no long-range trend. The electric field $\mathbf{E}$ and the current density $\mathbf{j}$ are determined by the equations

$$\mathbf{E}=\boldsymbol{\rho}\cdot\mathbf{j} \quad \text{or} \quad \mathbf{j}=\boldsymbol{\sigma}\cdot\mathbf{E} \tag{1}$$

$$\nabla\cdot\mathbf{j}=0 \tag{2}$$

$$\nabla\cdot\mathbf{E}=0 \tag{3}$$

and the boundary condition that the macroscopic field $\langle\mathbf{E}\rangle$ or macroscopic current $\langle\mathbf{j}\rangle$ be given. (Here and henceforth we use angular brackets to denote spatial averages, which we assume to exist by virtue of our assumed statistical uniformity of $\boldsymbol{\rho}$ or $\boldsymbol{\sigma}$.) The effective conductivity tensor $\boldsymbol{\sigma}_{\text{eff}}$, or the effective resistivity tensor $\boldsymbol{\rho}_{\text{eff}}$, is defined by

$$\langle\mathbf{j}\rangle=\boldsymbol{\sigma}_{\text{eff}}\cdot\langle\mathbf{E}\rangle \quad \text{or} \quad \langle\mathbf{E}\rangle=\boldsymbol{\rho}_{\text{eff}}\cdot\langle\mathbf{j}\rangle. \tag{4}$$

We can convert the differential Eqs. (2), (3) into algebraic equations by Fourier transformation, at the cost of replacing the simple relations (1) by convolutions. For the most general kind of inhomogeneities this would be of little help, but if $\boldsymbol{\rho}$ and $\boldsymbol{\sigma}$ are each equal to a constant mean value plus a small fluctuating term, the Fourier transforms of the first-order fluctuations in $\mathbf{E}$ and $\mathbf{j}$ are related in a very simple manner. Specifically, let us choose some large parallelepiped in our medium, of volume V, and develop all quantities into Fourier series inside this volume:

$$\boldsymbol{\sigma}(\mathbf{r})=\langle\boldsymbol{\rho}\rangle+\sum_k{}'\,\boldsymbol{\sigma}_k e^{i\mathbf{k}\cdot\mathbf{r}}, \tag{5}$$

and likewise for $\boldsymbol{\rho}$, $\mathbf{E}$, $\mathbf{j}$; here $\sum'$ means a summation over a closely spaced lattice of points in $\mathbf{k}$ space, omitting the point $\mathbf{k}=0$. The phases of the $\boldsymbol{\sigma}_k$, etc., may be expected to depend randomly on the size and location of V, but their absolute magnitudes will approach proportionality to $V^{\frac{1}{2}}$ as $V\to\infty$. From (1) we have for $\mathbf{k}\neq 0$

$$\mathbf{j}_k=\langle\boldsymbol{\sigma}\rangle\cdot\mathbf{E}_k+\boldsymbol{\sigma}_k\cdot\langle\mathbf{E}\rangle+\text{second-order terms}, \tag{6}$$

and for $\mathbf{k}=0$,

$$\langle\mathbf{j}\rangle=\langle\boldsymbol{\sigma}\rangle\cdot\langle\mathbf{E}\rangle+\sum_k{}'\,\boldsymbol{\sigma}_k\cdot\mathbf{E}_{-k}. \tag{7}$$

Since Eqs. (2) and (3) show that $\mathbf{j}_k$ is transverse to $\mathbf{k}$ (two components), and that $\mathbf{E}_k$ is longitudinal (one component) the three components of Eq. (6) allow us to solve for $\mathbf{E}_k$ and $\mathbf{j}_k$ to the first order. These determine the second term of Eq. (7) to the second order, hence determine $\boldsymbol{\sigma}_{\text{eff}}$ to the second order in the fluctuations. In the following subsections we shall carry this out for cases of successively greater complexity.

Scalar Conductivity

As the first example let us consider the effective conductivity of a medium in which the local conductivity, though spatially fluctuating, is at each point isotropic. From the dot product of Eq. (6) with $_k$ we get, for this case,

$$\mathbf{E}_k=-\mathbf{f}\,\mathbf{f}\cdot\langle\mathbf{E}\rangle\sigma_k/\langle\sigma\rangle,$$

where $\mathbf{f}=\mathbf{k}/k$ is the unit vector along $\mathbf{k}$. Substitution in Eq. (7) gives finally, to second order

$$\sigma_{\text{eff}}=\langle\sigma\rangle[1-\textstyle\sum_k{}'\,\mathbf{f}_E^2|\sigma_k|^2/\langle\sigma\rangle^2], \tag{8}$$

where $\mathbf{f}_E$ is the component of $\mathbf{f}$ in the direction of $\langle\mathbf{E}\rangle$. If the fluctuations are statistically isotropic, the coefficient $\mathbf{f}_E^2$ in Eq. (8) can be replaced by $\frac{1}{3}$. Since the second term in square brackets is simply the mean square fractional departure of the local σ from the mean σ, we can rewrite Eq. (8), for the case of isotropic fluctuations, in the physically more appealing form

$$\sigma_{\text{eff}}=\langle\sigma\rangle[1-\tfrac{1}{3}(\langle(\sigma-\langle\sigma\rangle)^2\rangle/\langle\sigma\rangle^2)]. \tag{9}$$

A similar analysis can be made in terms of the mean value and fluctuations of the resistivity ρ, instead of the conductivity σ. For this case the equation corresponding to Eq. (8) contains the two components of $\mathbf{k}$ perpendicular to $\langle\mathbf{j}\rangle$, instead of the one along it. For the case of isotropic statistics the result is, again to second order,

$$\begin{aligned}\rho_{\text{eff}}&=\langle\rho\rangle[1-\tfrac{2}{3}\textstyle\sum_k{}'|\rho_k|^2/\langle\rho\rangle^2]\\&=\langle\rho\rangle[1-\tfrac{2}{3}(\langle(\rho-\langle\rho\rangle)^2\rangle/\langle\rho\rangle^2)].\end{aligned} \tag{10}$$

The fractional mean square fluctuation of ρ, occurring in (10), is, to second order, the same as that of σ, occurring in Eq. (9). The fact that $\rho_{\text{eff}}<\langle\rho\rangle$ while $\rho_{\text{eff}}^{-1}=\sigma_{\text{eff}}<\langle\sigma\rangle$ is, of course, due to the fact that $\langle\rho\rangle\neq\langle\sigma\rangle^{-1}$.

The present result (for the isotropic case) is identical with that of Brown[6] and Nedoluha,[7] obtained under equivalent assumptions. As Brown has pointed out, it involves only the mean square variation of σ, and is independent of other details of the association of σ with position. If the statistics of the fluctuations are not

isotropic, a different but still rather simple average occurs in Eq. (8). A calculation of σ_{eff} to higher orders in the fluctuations would, however, as Brown showed, involve more complicated details of the spatial distribution of σ.

General Case of Tensor Conductivity

When the local conductivity is anisotropic, as in crystals of low symmetry, or in cubic crystals in the presence of an anisotropic stress or a magnetic field, the effective conductivity tensor is still obtainable from Eq. (6) by use of the longitudinality of $\mathbf{E}_k$ and the transversality of $\mathbf{j}_k$. We find, to second order,

$$(\sigma_{eff})_{\mu\nu}=\langle\sigma_{\mu\nu}\rangle-\sum_k{}'\frac{\sum_{\alpha,\beta}(\sigma_{-k})_{\mu\alpha}k_\alpha k_\beta(\sigma_k)_{\beta\nu}}{\sum_{\alpha,\beta}k_\alpha\langle\sigma_{\alpha\beta}\rangle k_\beta}. \quad (11)$$

This holds even in a magnetic field $\mathbf{H}$, where the tensor $\boldsymbol{\sigma}$ has an antisymmetric part. If the statistics of the fluctuations are isotropic and $\langle\sigma_{\alpha\beta}\rangle$ is also isotropic, it reduces to the expression given by Nedoluha.[7] Note that local fulfillment of the Onsager relation $\sigma_{\mu\nu}(\mathbf{H})=\sigma_{\nu\mu}(-\mathbf{H})$ implies, as one expects, fulfillment of the same relations by the macroscopic conductivity $(\sigma_{eff})_{\mu\nu}$.

In most of the single-crystal applications we shall consider below, it will be possible to choose the coordinate system so that at all points

$$\boldsymbol{\sigma}=\begin{pmatrix}\sigma_{xx} & \sigma_{xy} & 0\\ -\sigma_{xy} & \sigma_{yy} & 0\\ 0 & 0 & \sigma_{zz}\end{pmatrix}. \quad (12)$$

When this holds we have from Eq. (11) the second-order expressions

$$(\sigma_{eff})_{xx}=\langle\sigma_{xx}\rangle+\sum_k{}'\left[\frac{k_y^2|(\sigma_k)_{xy}|^2-k_x^2|(\sigma_k)_{xx}|^2}{k_x^2\langle\sigma_{xx}\rangle+k_y^2\langle\sigma_{yy}\rangle+k_z^2\langle\sigma_{zz}\rangle}\right] \quad (13)$$

$$(\sigma_{eff})_{zz}=\langle\sigma_{zz}\rangle-\sum_k{}'\frac{k_z^2|(\sigma_k)_{zz}|^2}{k_x^2\langle\sigma_{xx}\rangle+k_y^2\langle\sigma_{yy}\rangle+k_z^2\langle\sigma_{zz}\rangle} \quad (14)$$

$$(\sigma_{eff})_{xy}=\langle\sigma_{xy}\rangle-\sum_k{}'\left[\frac{(\sigma_k)_{xy}(k_x^2(\sigma_{-k})_{xx}+k_y^2(\sigma_{-k})_{yy})+A_k}{k_x^2\langle\sigma_{xx}\rangle+k_y^2\langle\sigma_{yy}\rangle+k_z^2\langle\sigma_{zz}\rangle}\right], \quad (15)$$

where

$$A_k=k_xk_y[(\sigma_{-k})_{xx}(\sigma_k)_{yy}+|(\sigma_k)_{xy}|^2] \quad (16)$$

can be replaced by its expectation zero if the fluctuations are sufficiently symmetrical for the mean magnitudes of the Fourier coefficients to be unchanged when the sign of k_x or k_y is changed. The expression of $(\sigma_{eff})_{yy}$ is of course obtained from (13) by interchanging x and y.

Piezoresistance

Let a cubic crystal with inhomogeneous conductivity be homogeneously strained. Since the conductivity is much more sensitive to fluctuations of impurity content than is the piezoresistance constant, it will suffice to consider the case where, for suitable choice of the coordinate directions, Eq. (12) is everywhere valid and at each point

$$\sigma_{\mu\mu}=\sigma(1+\Pi_\mu X)(\mu=1\text{ to }3). \quad (17)$$

Here Π_μ is a piezoresistance constant, assumed independent of position, and X is the applied stress. We can get the effective piezoresistance constant in, say, the z direction by differentiating Eq. (14) with respect to X. Using Eq. (8) we find to the second order

$$\begin{aligned}(\Pi_{eff})_z&\equiv[1/(\sigma_{eff})_{zz}][\partial(\sigma_{eff})_{zz}/\partial X]\\&=\Pi_z[1+\sum_k{}'(\mathbf{f}_z^4-\mathbf{f}_z^2)|\sigma_k|^2/\langle\sigma\rangle^2]\\&\quad+\Pi_z\sum_k{}'\mathbf{f}_z^2\mathbf{f}_x^2|\sigma_k|^2/\langle\sigma\rangle^2\\&\quad+\Pi_y\sum_k{}'\mathbf{f}_z^2\mathbf{f}_y^2|\sigma_k|^2/\langle\sigma\rangle^2, \quad (18)\end{aligned}$$

where, as above, $\mathbf{f}$ is the unit vector in the direction of $\mathbf{k}$.

If the statistics of the fluctuations are isotropic and if $\Pi_x=\Pi_y=-\frac{1}{2}\Pi_z$, a case of common occurrence, Eq. (18) takes the simple form,

$$\begin{aligned}(\Pi_{eff})_z&=\Pi_z[1-\tfrac{1}{5}\sum_k{}'|\sigma_k|^2/\langle\sigma\rangle^2]\\&=\Pi_z\left[1-\tfrac{1}{5}\frac{\langle(\sigma-\langle\sigma\rangle)^2\rangle}{\langle\sigma\rangle^2}\right]. \quad (19)\end{aligned}$$

Thus, fluctuations alter the effective piezoresistance constant only three-fifths as much as they alter the effective conductivity. The reason for this lower sensitivity of the piezoresistance is that, as one can verify, the fluctuations in current density introduced by the inhomogeneity are larger for the component parallel to the mean current than for the component normal to the mean current; this in turn is due to the fact that σ_k's for $\mathbf{k}\|\langle\mathbf{j}\rangle$ or $\perp\langle\mathbf{j}\rangle$ give rise to no component of $\mathbf{j}_k\perp\langle\mathbf{j}\rangle$.

Hall Effect

Consider first the weak-field case. For a cubic crystal with the magnetic field $\mathbf{H}$ in the z direction, Eq. (12) always applies with neglect of terms of order H^2 in the conductivity tensor. To this order the neglect of the term A_k in (15) is always justified, if, as we are assuming, the fluctuations vary randomly over distances much smaller than the dimensions of the specimen;

they need not be at all isotropic. We may express σ_{xy} in terms of the Hall constant R by

$$\sigma_{xy}=R\sigma^2H. \tag{20}$$

If the current is in the x direction and the statistics of the fluctuations are such that σ_{eff} is also of the form of Eq. (12), we find easily, to the usual second order in the fluctuations,

$$R_{\text{eff}}(0)=\lim_{H\to 0}\left[(\sigma_{\text{eff}})_{xy}/(\sigma_{\text{eff}})_{xx}(\sigma_{\text{eff}})_{yy}H\right]$$
$$=\frac{\langle\sigma^2R\rangle}{\langle\sigma\rangle^2}\left[1+\textstyle\sum_k(\mathbf{f}_x^2+\mathbf{f}_y^2)\left(\dfrac{|\sigma_k|^2}{\langle\sigma\rangle^2}-\dfrac{(\sigma^2R)_k\sigma_{-k}}{\langle\sigma^2R\rangle\langle\sigma\rangle}\right)\right], \tag{21}$$

where as before $\mathbf{f}$ is the unit vector along $\mathbf{k}$.

The expression (21) takes a less cumbersome form if the fluctuations are fluctuations in carrier concentration n but not in mobility. For this case, which may often be approximated in semiconductors, we have

$$R_{\text{eff}}(0)=(\mu_H/\mu)/\langle n\rangle ec \text{ (fluctuations in } n \text{ only)}, \tag{22}$$

where μ_H and μ are the Hall and drift mobilities, respectively; thus the fluctuations simply reduce the effective Hall mobility by the same factor as the conductivity, i.e., the square-bracket expression in Eq. (9). In metals, on the other hand, it may happen that the carrier concentration and the ratio μ_H/μ do not fluctuate appreciably, but the mobility does. For this case, and for isotropic statistics of the fluctuations, we find

$$\mu_{H\text{eff}}=\langle\mu_H\rangle$$
(isotropic fluctuations in mobility only). (23)

In the high-field limit things are even simpler. Here σ_{xy} is of order H^{-1}, and if the local magnetoresistance saturates (as it should when the elementary form of transport theory is applicable), σ_{xx} and σ_{yy} will be of order H^{-2}. Therefore, the first term on the right of Eq. (15) is of order H^{-1}, the numerator of the second term is of order H^{-2} if A_k can be dropped, and the denominator is of order unity except when k_z is near zero. Since the range of solid angle in $\mathbf{k}$ space for which the last term of the denominator is $\leq$ the first two is of order H^{-1}, the total contribution of the second term of Eq. (15) for any case of reasonably random fluctuations will be of order $H^{-3}\cdot H^2\cdot H^{-1}=H^{-2}$. Therefore as $H\to\infty$ we have, to the second order in the fluctuations,

$$[R_{\text{eff}}(H)]^{-1}=\langle[R(H)]^{-1}\rangle+O(H^{-1}) \text{ (general fluctuations, saturating magnetoresistance)}. \tag{24}$$

If such things as nonclosed Fermi surfaces or quantization of the motion into Landau levels cause the local magnetoresistance to increase sufficiently rapidly with H, instead of saturating, Eq. (24) need not hold.

Low-Field Magnetoresistance

Let us again suppose Eq. (12) to be satisfied, and let

$$\sigma_{\mu\nu}=\sigma\delta_{\mu\nu}+\sigma_{\mu\nu}{}^{(1)}+\sigma_{\mu\nu}{}^{(2)}+\cdots, \tag{25}$$

where the superscripts (1), (2), $\cdots$, denote terms of order H, H^2, etc. From Eqs. (13), (14), and (9) we find easily the expressions for the low-field magnetoconductivity ratios. To the second order in the fluctuations, they are

$$\frac{(\sigma_{\text{eff}}{}^{(2)})_{xx}}{\sigma_{\text{eff}}}=\frac{\langle\sigma_{xx}{}^{(2)}\rangle}{\langle\sigma\rangle}\left\{1+\textstyle\sum_k{}'\,\mathbf{f}_x{}^2\dfrac{|\sigma_k|^2}{\langle\sigma\rangle^2}\left[1+\mathbf{f}_x{}^2+\mathbf{f}_y{}^2\dfrac{\langle\sigma_{yy}{}^{(2)}\rangle}{\langle\sigma_{xx}{}^{(2)}\rangle}+\mathbf{f}_z{}^2\dfrac{\langle\sigma_{zz}{}^{(2)}\rangle}{\langle\sigma_{xx}{}^{(2)}\rangle}\right]\right.$$
$$\left.-\textstyle\sum_k{}'\,\mathbf{f}_x{}^2\left[\dfrac{\sigma_k(\sigma_{-k}{}^{(2)})_{xx}}{\langle\sigma\rangle\langle\sigma_{xx}{}^{(2)}\rangle}+\dfrac{\sigma_{-k}(\sigma_k{}^{(2)})_{xx}}{\langle\sigma\rangle\langle\sigma_{xx}{}^{(2)}\rangle}\right]\right\}+\textstyle\sum_k{}'\,\mathbf{f}_y{}^2[|(\sigma_k{}^{(1)})_{xy}|^2/\langle\sigma\rangle^2], \tag{26}$$

$$\frac{(\sigma_{\text{eff}}{}^{(2)})_{zz}}{\sigma_{\text{eff}}}=\frac{\langle\sigma_{zz}{}^{(2)}\rangle}{\langle\sigma\rangle}\left\{1+\textstyle\sum_k{}'\,\mathbf{f}_z{}^2\dfrac{|\sigma_k|^2}{\langle\sigma\rangle^2}\left[1+\mathbf{f}_z{}^2+\mathbf{f}_x{}^2\dfrac{\langle\sigma_{xx}{}^{(2)}\rangle}{\langle\sigma_{zz}{}^{(2)}\rangle}+\mathbf{f}_y{}^2\dfrac{\langle\sigma_{yy}{}^{(2)}\rangle}{\langle\sigma_{zz}{}^{(2)}\rangle}\right]\right\}-\textstyle\sum_k{}'\,\mathbf{f}_z{}^2\left[\dfrac{\sigma_k(\sigma_{-k}{}^{(2)})_{zz}}{\langle\sigma\rangle\langle\sigma_{zz}{}^{(2)}\rangle}+\dfrac{\sigma_{-k}(\sigma_k{}^{(2)})_{zz}}{\langle\sigma\rangle\langle\sigma_{zz}{}^{(2)}\rangle}\right], \tag{27}$$

where, as before, $\mathbf{f}$ is the unit vector along $\mathbf{k}$.

These rather cumbersome general expressions simplify considerably in special cases. For example, if the fluctuations are statistically isotropic and affect only the carrier concentration n and not the mobilities, then

$$\frac{(\sigma_{\text{eff}}{}^{(2)})_{xx}}{\sigma_{\text{eff}}}=\frac{\sigma_{xx}{}^{(2)}}{\sigma}\left\{1+\left[-\frac{2}{15}+\frac{1}{15}\left(\frac{\sigma_{yy}{}^{(2)}+\sigma_{zz}{}^{(2)}}{\sigma_{xx}{}^{(2)}}\right)+\frac{1}{3}\frac{(\mu_HH/c)^2}{(\sigma_{zz}{}^{(2)}/\sigma}\right]\frac{\langle(n-\langle n\rangle)^2\rangle}{\langle n\rangle^2}\right\} \text{ (isotropic fluctuations in } n \text{ only)} \tag{28}$$

$$\frac{(\sigma_{\text{eff}}{}^{(2)})_{zz}}{\sigma_{\text{eff}}}=\frac{\sigma_{zz}{}^{(2)}}{\sigma}\left\{1+\left[-\frac{2}{15}+\frac{1}{15}\left(\frac{\sigma_{xx}{}^{(2)}+\sigma_{yy}{}^{(2)}}{\sigma_{zz}{}^{(2)}}\right)\right]\frac{\langle(n-\langle n\rangle)^2\rangle}{\langle n\rangle^2}\right\} \text{ (isotropic fluctuations in } n \text{ only)}. \tag{29}$$

Here we have done for n what we did for σ in Eqs. (9) and (19), namely, replaced $\sum_k{}'|n_k|^2$ by $\langle(n-\langle n\rangle)^2\rangle$. For

pure n-type germanium with $\mathbf{H}$ in a cube-edge direction, the square-bracketed coefficient of $\langle(n-\langle n\rangle)^2\rangle/\langle n\rangle^2$ in (28) (transverse magnetoconductivity) is about -0.22; that in (29) is about $+0.044$. The former figure can be converted into one for the effective modification of the transverse magnetoresistance $\rho_{xx}^{(2)}/\rho$ by using the modification factor for the Hall mobility; it turns out that the magnetoresistance is increased by about $0.2\langle(n-\langle n\rangle)^2\rangle/\langle n\rangle^2$.

High Field Magnetoresistance

As in the discussion of the Hall coefficient above, we shall give principal attention to the case where the local transverse magnetoresistance saturates as the magnetic field $H\rightarrow\infty$. We shall again take $\mathbf{H}$ in the z direction and assume (12) to hold both for the local $\boldsymbol{\sigma}$ and for $\boldsymbol{\sigma}_{\text{eff}}$. For the longitudinal magnetoresistance we have from Eqs. (14) and (8), to the second order in the fluctuations,

$$\frac{\rho_{\text{eff}}(\infty)}{\rho_{\text{eff}}(0)}=\frac{\sigma_{\text{eff}}(0)}{[\sigma_{\text{eff}}(\infty)]_{zz}}$$

$$=\frac{\langle\sigma(0)\rangle}{\langle\sigma_{zz}(\infty)\rangle}\left[1+\sum\nolimits_{k}{}'\left(\frac{|[\sigma_k(\infty)]_{zz}|^2}{\langle\sigma_{zz}(\infty)\rangle^2}-\frac{\mathbf{f}_z^2|\sigma_k(0)|^2}{\langle\sigma(0)\rangle^2}\right)\right], \tag{30}$$

independently of further assumptions regarding the directional preferences of the fluctuations; as before, $\mathbf{f}$ is the unit vector along $\mathbf{k}$. If the fluctuations are statistically isotropic and affect carrier concentration n but not mobility, Eq. (30) reduces to

$$\frac{\rho_{\text{eff}}(\infty)}{\rho_{\text{eff}}(0)}=\frac{\rho(\infty)}{\rho(0)}\left[1+\tfrac{2}{3}\frac{\langle(n-\langle n\rangle)^2\rangle}{\langle n\rangle^2}\right]$$

(longitudinal; isotropic fluctuations in n only). (31)

For the transverse case we encounter the fact that for small k_z the denominator of Eq. (13) can get very small without a corresponding reduction in the numerator; the directional distribution of the fluctuations is therefore important. (We shall see, in the following discussion of stratified media, an example of how the effect of fluctuations can change radically with a change in the orientation of the planes of constant n.) We shall therefore assume isotropic statistics for the fluctuations, so that the square bracket in Eq. (13) can be averaged on directions of $\mathbf{k}$ with $|(\sigma_k)_{xx}|^2$ and $|(\sigma_k)_{xy}|^2$ treated as constants. This directional average simplifies a little if, as we are assuming for large H, $\langle\sigma_{zz}\rangle\gg\langle\sigma_{xx}\rangle$ or $\langle\sigma_{yy}\rangle$; with neglect of terms of order $\langle\sigma_{zz}\rangle^{-1}$ one finds easily that

$$\left\langle\frac{k_y^2}{\langle\sigma_{xx}\rangle k_x^2+\langle\sigma_{yy}\rangle k_y^2+\langle\sigma_{zz}\rangle k_z^2}\right\rangle_{\text{dirs}}=[\langle\sigma_{zz}\rangle\langle\sigma_{xx}\rangle]^{-\frac{1}{2}}\left\{\frac{K\{[1-(\langle\sigma_{yy}\rangle/\langle\sigma_{xx}\rangle)]^{\frac{1}{2}}\}-E\{[1-\langle\sigma_{yy}\rangle/\langle\sigma_{xx}\rangle]^{\frac{1}{2}}\}}{1-(\langle\sigma_{yy}\rangle/\langle\sigma_{xx}\rangle)}\right\} \tag{32a}$$

if $\langle\sigma_{yy}\rangle<\langle\sigma_{xx}\rangle$, and

$$=[\langle\sigma_{zz}\rangle\langle\sigma_{yy}\rangle]^{-\frac{1}{2}}\left\{\frac{\{2-(\langle\sigma_{zz}\rangle/\langle\sigma_{yy}\rangle)\}E\{[1-(\langle\sigma_{zz}\rangle/\langle\sigma_{yy}\rangle)]^{\frac{1}{2}}\}-K\{[1-(\langle\sigma_{zz}\rangle/\langle\sigma_{yy}\rangle)]^{\frac{1}{2}}\}}{1-(\langle\sigma_{zz}\rangle/\langle\sigma_{yy}\rangle)}\right\} \tag{32b}$$

if $\langle\sigma_{yy}\rangle>\langle\sigma_{xx}\rangle$, where

$$K(u)=\int_0^{\pi/2}\frac{d\varphi}{(1-u^2\sin^2\varphi)^{\frac{1}{2}}},$$

$$E(u)=\int_0^{\pi/2}(1-u^2\sin^2\varphi)^{\frac{1}{2}}d\varphi,$$

are the complete elliptic integrals. If $\langle\sigma_{yy}\rangle=\langle\sigma_{xx}\rangle$, the curly-bracket expression in Eq. (32a) or (32b) takes the value $\frac{1}{4}\pi$.

Remembering that σ_{xx}, σ_{yy} are $O(H^{-2})$, that σ_{yz} is $O(H^{-1})$, and that σ_{zz} is $O(1)$, we see from Eq. (32) that the second term of Eq. (13) contains a part going as H^{-1}, whereas the first term is of order H^{-2}. This H^{-1} term will dominate the inhomogeneity correction at large H; however, we must remember that our whole method ceases to be valid when the second term of Eq. (13) becomes comparable with the first. When H is large enough to make σ_{xx} and $\sigma_{yy}\ll\sigma_{xy}\ll\sigma_{zz}$, but not so large as to out-weigh the smallness of the fluctuations and make the second term of Eq. (13) comparable with the first, we have

$$\frac{[\rho_{\text{eff}}(H)]_{yy}}{\rho_{\text{eff}}(0)}\sim[\sigma_{\text{eff}}(H)]_{xx}[R_{\text{eff}}(H)]^2[\sigma_{\text{eff}}(0)]H^2=\frac{\langle\sigma(0)\rangle\langle\sigma_{xx}(H)\rangle H^2}{\langle[R(H)]^{-1}\rangle^2}$$

$$\cdot\left[1-\frac{1}{3}\frac{\langle(\sigma-\langle\sigma\rangle)^2\rangle}{\langle\sigma\rangle^2}+\zeta\frac{\langle[\sigma_{xy}(H)-\langle\sigma_{xy}(H)\rangle]^2\rangle}{\langle\sigma_{xx}(H)\rangle[\langle\sigma_{xx}(H)\rangle\langle\sigma_{aa}(H)\rangle]^{\frac{1}{2}}}\right] \text{ (transverse; isotropic fluctuations)}, \tag{33}$$

where σ_{aa} is the larger of σ_{zz}, σ_{yy}, and ζ is the curly-bracket expression in Eq. (32a) or (32b), whichever is applicable. The last summation in Eq. (33) is asymptotically proportional to H, so to our approximation the inhomogeneity correction is a positive linear function of H. In this equation we have neglected not only terms of order H^{-1} and terms of higher than the second order in the fluctuations, but also some of the terms of second order in the fluctuations which are of zero order in H.

If the fluctuations are only in the carrier concentration n and not in the mobility, Eq. (33) reduces to

$$\frac{[\rho_{eff}(H)]_{yy}}{\rho_{eff}(0)} \sim \frac{\rho_{yy}(H)}{\rho(0)}\left[1+\left(\frac{RH}{\rho_{yy}(H)}\right)\left(\frac{\rho_{zz}(H)}{\rho_{\beta\beta}(H)}\right)^{1}\zeta\frac{\langle(n-\langle n\rangle)^2\rangle}{\langle n\rangle^2}\right] \text{ (transverse; isotropic fluctuations in } n \text{ only)}, \quad (34)$$

where we have dropped the middle term of Eq. (33) as of lower order, and where $\rho_{\beta\beta}$ is the smaller of ρ_{zz}, ρ_{yy}. As an example to illustrate orders of magnitude, we may again consider pure n-type germanium with H along a cubic axis. For this case the coefficient of $\langle(n-\langle n\rangle)^2\rangle/\langle n\rangle^2$ in Eq. (34) is about 0.9 times $\mu H/c$, the tangent of the Hall angle. This shows that when $\mu H/c$ is in the easily attainable range of 5–10, quite modest fluctuations can well have a serious effect on the transverse magnetoresistance.

This great sensitivity of the high field transverse magnetoresistance to inhomogeneities in n is due to the competition between the Hall fields of neighboring regions. If the distortion of the current lines by a slight inhomogeneity in n were to remain small as $H\to\infty$, the neighboring regions of different n would in general have to have different Hall fields, all of which would $\to\infty$. This would conflict with the requirement that $\nabla\times\mathbf{E}=0$. Thus, however slight the inhomogeneities in n, the distortion of current lines which they produce must, for most orientations of the fluctuations, become large as $H\to\infty$. Of course, when the distortions have become large we can no longer expect our formulas to be quantitatively accurate. We shall examine this point in more detail in Sec. 3, which follows.

If, as we have just argued, the culprit in Eqs. (33) and (34) is the inhomogeneity of the Hall constant, we might expect a more modest effect of inhomogeneities for the case, sometimes applicable to metals, where the mobility fluctuates but the Hall constant does not. This is indeed so. For in Eq. (13), if we neglect $|(\sigma_k)_{xy}|^2$, the summation becomes of order H^{-3} as $H\to\infty$, if the magnetoresistance is assumed to saturate. so the fractional correction to the transverse magnetoconductivity is of order $H^{-1}\times$ (fluctuations)^2.

Thermoelectric and Thermomagnetic Effects

Small fluctuations in carrier concentration or in impurity scattering generally have much less effect on the local thermoelectric power than on the local conductivity and Hall constant. Such fluctuations therefore have a much less serious effect on thermoelectric phenomena than on the conduction and galvanomagnetic phenomena we have just treated. However, it is worth while to list briefly some of the formulas obtainable by our method, as they are easily written down and as they provide a check on the validity of approximate expressions which have been or may be proposed to describe thermoelectric phenomena in highly inhomogenerous media (see Sec. 3, which follows).

For the present problem, we must consider the possibility of irregularities in the temperature distribution due to fluctuations in the local thermal conductivity. These fluctuations are given by equations analogous to Eqs. (1)–(3) with the thermal conductivity tensor $\boldsymbol{\kappa}$ replacing $\boldsymbol{\sigma}$, the temperature gradient ∇T replacing $\mathbf{E}$, and the heat flux replacing $\mathbf{j}$. (For simplicity we neglect Peltier heat transport by circulating thermoelectric currents arising from the inhomogeneities, an effect which may be appreciable in some heavily doped semiconductors,[5] though usually not in metals or purer semiconductors.) In terms of the kth Fourier coefficients $(\nabla T)_k$ and $\boldsymbol{\kappa}_k$, defined as in Eq. (5), the solution is, to first order in the fluctuations,

$$(\nabla T)_k=-\mathbf{k}\,\mathbf{k}\cdot\boldsymbol{\kappa}_k\cdot\langle\nabla T\rangle/\mathbf{k}\cdot\langle\boldsymbol{\kappa}\rangle\cdot\mathbf{k}. \quad (35)$$

For the electrical quantities, Eqs. (2) and (3) still hold, but Eq. (1) must be replaced by

$$\mathbf{E}=\mathbf{Q}\cdot\nabla T+\boldsymbol{\rho}\cdot\mathbf{j}, \quad (36)$$

where $\mathbf{Q}$ is the thermoelectric power tensor. (What we have called $\mathbf{E}$ is, strictly speaking, e^{-1} times the gradient of the electrochemical potential of the electrons.)

The effective thermoelectric power tensor $\mathbf{Q}_{eff}$ is defined by

$$\langle\mathbf{E}\rangle=\mathbf{Q}_{eff}\cdot\langle\nabla T\rangle \quad \text{for} \quad \langle\mathbf{j}\rangle=0. \quad (37)$$

The general expression for $\mathbf{Q}_{eff}$ is easily computed explicitly, to the second order in the fluctuations, from Eqs. (2), (3), (35), and (36). However, for brevity, we shall list only the formulas for some special cases. If $\mathbf{Q}$ and $\boldsymbol{\kappa}$ are locally isotropic, and if the fluctuations are statistically isotropic, we have to second order

$$Q_{eff}=\langle Q\rangle-\textstyle\sum_k{}' Q_{-k}\left[\frac{1}{3}\frac{\kappa_k}{\langle\kappa\rangle}+\frac{2}{3}\frac{\rho_k}{\langle\rho\rangle}\right]$$

$$=\langle Q\rangle-\left\langle(Q-\langle Q\rangle)\left(\frac{1}{3}\frac{\kappa}{\langle\kappa\rangle}+\frac{2}{3}\frac{\rho}{\langle\rho\rangle}\right)\right\rangle. \quad (38)$$

In other words, the departure of Q_{eff} from $\langle Q\rangle$ involves correlation coefficients of fluctuations of Q with fluctuations of κ and of ρ.

As an example of a formula involving an anisotropic $\mathbf{Q}$ tensor, we may give, finally, the formula for the effective low field Nernst coefficient B of a cubic extrinsic semiconductor with fluctuations in carrier concentration n but not in thermal conductivity or in mobility. This quantity is defined by the statement that for $\mathbf{j}=0$ in a magnetic field $\mathbf{H}$, the part of $\mathbf{E}$ transverse to ∇T is $-B\mathbf{H}\times\nabla T$. We have, to the second order in the fluctuations and in the limit $H\to 0$,

$$B_{\text{eff}}=\langle B\rangle+\sum_k{}'\frac{n_{-k}}{\langle n\rangle}\left[\tfrac{2}{3}B_k\pm\frac{1}{3}\frac{\mu_H}{c}Q_k\right]$$

$$=\langle B\rangle+\left\langle(n-\langle n\rangle)\left(\tfrac{2}{3}B\pm\frac{1}{3}\frac{\mu_H}{c}Q\right)\right\rangle$$

(isotropic fluctuations in n only), (39)

where μ_H is the low-field Hall mobility and the upper sign is for n type, the lower for p type.

Note that if $\mathbf{Q}$ does not fluctuate, $\mathbf{Q}_{\text{eff}}=\mathbf{Q}$ exactly, because the basic equations and boundary conditions are satisfied by $\mathbf{j}=0$.

3. COMPARISON WITH EXACT OR APPROXIMATE FORMULAS APPLICABLE TO LARGE FLUCTUATIONS

Our results so far are exact to the second order in the amplitude of small fluctuations. To assess the applicability of this order of approximation to actual materials, it is of interest to make a comparison with formulas, exact if possible, which do not assume the fluctuations to be small. Exact formulas of this sort exist of course only for special geometries of the fluctuations; we shall consider particularly the case of a stratified material, uniform within plane-parallel layers. However, some of the ways which have been discussed in the literature for approximating the effective scalar conductivity of a random mixture of two phases are known to be fairly good, so we shall start by comparing our formulas with these.

Approximate Formulas for Random Geometries

As good an equation as any with which to compare our formula in Eq. (9) is that which derives the σ_{eff} of a binary mixture from the assumption that the mean field in constituent 1 (or 2) is calculable by considering a sphere of 1 (or 2) embedded in an infinite medium of conductivity σ_{eff}[8,9]. If the single-phase conductivities are σ_1, σ_2 and the volume fractions are x_1, x_2, this formula is

$$x_1\left(\frac{\sigma_1-\sigma_{\text{eff}}}{\sigma_1+2\sigma_{\text{eff}}}\right)+x_2\left(\frac{\sigma_2-\sigma_{\text{eff}}}{\sigma_2+2\sigma_{\text{eff}}}\right)=0. \quad (40)$$

[8] V. I. Odelevski, J. Tech. Phys. (U.S.S.R.) **21**, 667, 678, 1379 (1951).
[9] R. Landauer, J. Appl. Phys. **23**, 779 (1952).

TABLE I. Comparison of thermoelectric powers predicted by Eqs. (41) and (38), for various binary mixtures with $x_1=x_2=\frac{1}{2}$.

σ_2/σ_1	κ_2/κ_1	Q_2/Q_1	Q_{eff}/Q_1 from (38)	Q_{eff}/Q_1 from (41)
3	1	$\frac{1}{3}$	0.667	0.662
3	1	-2	-1.00	-1.06
3	3	$\frac{1}{3}$	0.709	0.701
3	$\frac{1}{3}$	$\frac{1}{3}$	0.625	0.630
7	1	0	0.25	0.21

Landauer[9] has shown that this equation accounts fairly well for observed conductivities of two-phase alloys even when σ_1 and σ_2 differ by a factor of 5 or 10. In this range, the difference between the predictions of Eqs. (40) and (9), though quite perceptible, is not large; for example for $x_1=x_2=\frac{1}{2}$, $\sigma_2/\sigma_1=7$, Eq. (40) gives $\sigma_{\text{eff}}=0.77\langle\sigma\rangle$, while Eq. (9) gives $0.81\langle\sigma\rangle$, and Eq. (10) gives $0.70\langle\sigma\rangle$. Thus, it is likely that our formulas for vanishing and small magnetic fields are applicable to fluctuations of reasonable amplitude; we shall confirm this in other ways below.

A formula based on the same sort of assumptions as Eq. (40) has been given by Ayrapetyants[6] for the thermoelectric power of a mixture. For a mixture of any number of components i with electrical conductivities σ_i, thermal conductivities κ_i, thermoelectric powers Q_i, and volume fractions x_i, this formula is

$$Q_{\text{eff}}=\frac{\Sigma_i Q_i\sigma_i\gamma_i}{1-2\sigma_{\text{eff}}\Sigma_i\gamma_i}, \quad (41)$$

where

$$\gamma_i=3x_i\kappa_{\text{eff}}/(2\sigma_{\text{eff}}+\sigma_i)(2\kappa_{\text{eff}}+\kappa_i). \quad (42)$$

If σ_{eff}, κ_{eff} are taken to be given by the multicomponent extension of Eq. (40), one can easily verify that Eq. (41) agrees with our expression in Eq. (38) to the second order. As was the case with Eqs. (40) and (9), Eqs. (41) and (38) agree fairly well even at rather sizable amounts of inhomogeneity; Table I gives some typical comparisons for a binary mixture with $x_1=x_2=\frac{1}{2}$.

Stratified Medium

Encouraging though these comparisons are, they leave open the question of the accuracy of formulas like Eq. (34), which describe the effects of the distortions, extreme as $H\to\infty$, which the current lines undergo in consequence of inhomogeneities in the Hall constant. Let us therefore consider some special cases for which these distortions can be exactly calculated. The simplest such is a stratified medium, i.e., one in which the components of the local resistivity tensor ρ are functions only of a single coordinate, e.g., x. Although the equations we shall write presently will be valid for arbitrary orientations of the magnetic field $\mathbf{H}$, let us for the moment simply consider the qualitative behavior of the current lines when $\mathbf{H}$ is in the z direction and the macroscopic current $\langle\mathbf{j}\rangle$ is in the x direction. For this

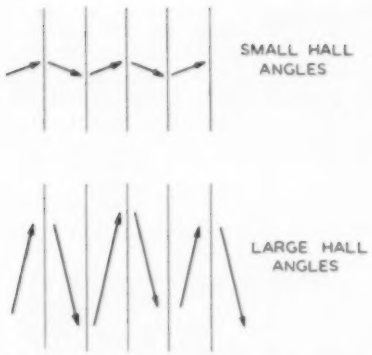

Fig. 1. Distortion of current lines as $H \to \infty$, for a stratified medium in which the Hall constant is a function of x, and for $\mathbf{H}$ in the z direction (normal to the paper) $\langle \mathbf{j} \rangle$ in the x direction. The arrows show the direction of $\mathbf{j}$.

case, the current component j_x must be the same in all strata. If the Hall constant varies from stratum to stratum, this j_x will give rise to a Hall contribution to E_y which varies from one stratum to the next and is proportional to H. Since the total E_y must be the same in all strata, there must be ohmic contributions to E_y arising from y components of $\mathbf{j}$, and these must also be proportional to H. Thus as $H \to \infty$ the current lines must distort as shown in Fig. 1. This distortion entails a dissipation which, for given $\langle j_x \rangle$, increases without limit as $H \to \infty$; thus the effective resistivity $(\rho_{\text{eff}})_{xx} \to \infty$. Its source, the shorting of Hall fields, is the same effect which causes like anomalies of magnetoresistance to arise from electrode end effects[2] or surface conduction.[1]

Let us develop this model quantitatively, for the general case of a tensor resistivity $\rho_{\mu\nu}(x)$, whose antisymmetrical part describes the Hall effect. Consider first the case where the orientation of the asymmetries of $\rho_{\mu\nu}$ is arbitrary, but where its fluctuations are due to fluctuations in the carrier concentration n only, so that $n\rho_{\mu\nu}$ is a nonfluctuating constant tensor. At each point we have

$$E_\mu(x) = \Sigma_\nu \rho_{\mu\nu}(x) j_\nu(x) \quad (\mu, \nu = x, y, z), \tag{43}$$

and because of $\nabla \cdot \mathbf{j} = 0$, $\nabla \times \mathbf{E} = 0$, we have, independently of x

$$j_x = \langle j_x \rangle \tag{44}$$

$$E_y = \langle E_y \rangle \tag{45}$$

$$E_z = \langle E_z \rangle. \tag{46}$$

Since $n\rho_{\mu\nu}$ is independent of x, we may write the volume average of Eq. (43) in the form

$$\langle E_\mu \rangle = \Sigma_\nu n\rho_{\mu\nu} \langle j_\nu / n \rangle. \tag{47}$$

We wish to relate $\langle \mathbf{E} \rangle$ to $\langle \mathbf{j} \rangle$; Eq. (47) contains the former, but it has $\langle \mathbf{j}/n \rangle$ instead of $\langle \mathbf{j} \rangle$, and the difference is bothersome for the y and z components. We can use Eqs. (45) and (46) to get $\langle j_{y,z}/n \rangle$ in terms of $\langle j_{y,z} \rangle$ by multiplying Eq. (43) by n and averaging: For $\mu = y,z$ (but not x),

$$E_\mu \langle n \rangle = \Sigma_\nu n\rho_{\mu\nu} \langle j_\nu \rangle. \tag{48}$$

Equating these two expressions to the y and z components of Eq. (47) gives tow equations in the two unknowns $\langle j_y/n \rangle$, $\langle j_z/n \rangle$. Solving for these we find

$$\langle j_{y,z}/n \rangle = \langle j_{y,z} \rangle / \langle n \rangle + F_{y,z} \langle j_x \rangle, \tag{49}$$

where $F_{y,z}$ are quantities dependent on the ratios of the $\rho_{\mu\nu}$ and on the statistics of the distribution of n. Inserting Eq. (49) into Eq. (47) gives equations of the form

$$\langle E_\mu \rangle = \Sigma_\nu (\rho_{\text{eff}})_{\mu\nu} \langle j_\nu \rangle, \tag{50}$$

where for every $\mu\nu$ pair except xx

$$(\rho_{\text{eff}})_{\mu\nu} = \frac{n\rho_{\mu\nu}}{\langle n \rangle}, \tag{51}$$

while it turns out that

$$(\rho_{\text{eff}})_{xx} = n\rho_{xx}\langle 1/n \rangle + n\left[\left\langle \frac{1}{n} \right\rangle - \frac{1}{\langle n \rangle}\right]\left[\frac{\rho_{xy}\rho_{yz}\rho_{zx} + \rho_{xz}\rho_{zy}\rho_{yx} - \rho_{xy}\rho_{yx}\rho_{zz} - \rho_{xz}\rho_{zx}\rho_{yy}}{\rho_{yy}\rho_{zz} - \rho_{yz}\rho_{zy}}\right]$$

(fluctuations in n only, arbitrary anisotropy of mobility). (52)

Other cases can be treated similarly. Omitting the derivations, we list here the results for the general case where the conductivity tensor $\sigma_{\mu\nu}$ is an arbitrary random function of x, subject only to the condition that there be no secular drift of the conductivity values with x; this is necessary in order that the equations $E_y = \text{constant}$, $E_z = \text{constant}$, be true. The formulas are a little more concise if expressed in terms of conductivities than in terms of resistivities; they are

μ or ν, or both, $= x$,

$$(\sigma_{\text{eff}})_{\mu\nu} = \langle 1/\sigma_{xx} \rangle^{-1} \langle \sigma_{\mu\nu}/\sigma_{xx} \rangle; \tag{53}$$

neither μ nor $\nu = x$,

$$(\sigma_{\text{eff}})_{\mu\nu} = \langle \sigma_{\mu\nu} \rangle + \langle 1/\sigma_{xx} \rangle^{-1} \langle \sigma_{\mu x}/\sigma_{xx} \rangle \langle \sigma_{x\nu}/\sigma_{xx} \rangle - \langle \sigma_{\mu x}\sigma_{x\nu}/\sigma_{xx} \rangle. \tag{54}$$

Equations (51) to (54), valid for fluctuations of arbitrary magnitude, can be compared in many ways with the small-fluctuation formulas of Sec. 2. For a laminated medium with scalar conductivities, Eq. (9) is exact for the conductivity parallel to the laminas (y and z directions), since $k_y = k_z = 0$ whenever $\sigma_k \neq 0$. More surprisingly, it turns out to be exact for the conductivity in the x direction for the case of two types of

laminas with equal volume fractions. If the volume fractions of the two types are widely unequal, say 0.1 and 0.9, the errors in Eq. (9) become appreciable when n_2/n_1 is of the order of 2, and serious by the time it is 5. Of more interest is the fact that Eq. (22) is exact for the Hall constant of the present laminar model. For Eq. (51) gives

$$R_{eff}=\langle 1/R\rangle^{-1} \text{ (fluctuations in } n \text{ only)}, \qquad (55)$$

for any value or orientation of **H**. When the mobility also fluctuates, Eqs. (53) and (54) shows that Eq. (24) is exact only when **H** is in the x direction, and that for **H** in the y or z direction $1/R_{eff}$ is an average of $1/R$ with weights proportional to $1/\sigma_{xx}$.

Most interesting of all, of course, is the high field transverse magnetoresistance of the laminar model. Let **H** be in the x–z plane, making an angle θ with the x axis. Suppose the medium such that as $H\rightarrow\infty$, the resistivity in any direction remains bounded, as does the Hall constant Then in Eq. (52) the diagonal ρ's and ρ_{xz} will be bounded, but ρ_{yz} and ρ_{xy} will increase as $H\cos\theta$ and $H\sin\theta$, respectively. The last term of Eq. (52) will therefore become independent of H unless $\cos\theta=0$. If $\cos\theta=0$, this term will increase as H^2. This is exactly the behavior we found in the small-fluctuation limit: the denominators in Eqs. (13) and (14) are of order unity as $H\rightarrow 0$ except when $k_z=0$, i.e., for those components of the fluctuations which are stratified in planes containing **H**. [Note that the choice of axis in Eqs. (13) and (14) is not in general the same as in Eq. (52).] If we compute $(\rho_{eff})_{zz}$, for **H** in the z direction, from Eq. (13) and the first line of Eq. (33), we find in the limit $H\rightarrow\infty$

$$(\rho_{eff})_{zz}\sim A+BH^2, \qquad (56)$$

from either Eq. (13) or (52), and

$$[A(13)/A(52)]=\frac{\langle\sigma_{yy}(H)\rangle R_{eff}^2H^2}{n\rho_{zz}\langle 1/n\rangle}=\frac{1}{\langle n\rangle\langle 1/n\rangle} \qquad (57)$$

$$[B(13)/B(52)]=\frac{\langle(n-\langle n\rangle)^2\rangle}{\langle n\rangle^3(\langle 1/n\rangle-1/\langle n\rangle)}. \qquad (58)$$

For an equal-volume binary mixture with $n_2/n_1=2$, Eqs. (57) and (58) each have the value 8/9. Thus, in spite of the large current distortions which take place as $H\rightarrow\infty$, the formulas of Sec. 2 not only continue to give the right qualitative behavior for the stratified medium, but are fairly good quantitatively for fair-sized fluctuations. The comparison turns out to be equally satisfactory, though less interesting, for $\langle\mathbf{j}\rangle$ in the plane of the laminas and $\perp\mathbf{H}$.

Rodlike Inclusions

Lest the preceding example leave too favorable an impression regarding the applicability of small fluctuation formulas at large magnetic fields, let us consider a case where the small fluctuation formulas break down seriously at large current distortions. As a simple example of this sort one may take the two-dimensional problem of the flow of current in a medium which is homogeneous except for occasional rod-shaped inclusions, the axes of the rods being along the magnetic field **H**. Let us suppose, as usual, that Hall constant R and resistivity ρ approach constant limits as $H\rightarrow\infty$, but that the limiting R of the material in the rods differs from that of the surrounding material. Using the subscripts t and n to designate the directions respectively tangential and normal to the boundary of a rod in the plane perpendicular to **H**, we have

$$E_t=RHj_n+\rho j_t. \qquad (59)$$

Since R is discontinuous across the boundary while E_t and j_n must be continuous, we must have $j_n\rightarrow 0$ as $H\rightarrow\infty$. In other words, for flow transverse to **H** the current lines in the limit simply avoid the rods as if they were nonconductors. This is consistent with the field Eqs. (1) to (3) for the present two-dimensional geometry, and can in fact be verified by explicit calculations for simple geometries.

For this model, the effective macroscopic transverse magnetoresistance therefore approaches a finite limit determined by the extent to which the current lines are squeezed in their avoidance of the rods. An evaluation of the small-fluctuation formula [Eq. (13)] for this case ($k_z=0$ whenever the numerator is nonvanishing) gives, however, a resistance increase proportional to H^2. Thus, this formula breaks down seriously when the current lines have been forced most of the way out of the rods.

As one might expect, the small-fluctuation formula [Eq. (24)] for the macroscopic Hall constant also breaks down for this case. Since the current lines avoid the rods as $H\rightarrow\infty$, the macroscopic Hall constant becomes identical with that of the continuous matrix, and is uninfluenced by the Hall constants of the rods. The behavior of the Hall constant as $H\rightarrow 0$ is of course somewhat better. This can be checked by a calculation, similar to that sketched by Juretschke, Landauer, and Swanson[4] for cylindrical pores. For cylindrical inclusions oriented either along or perpendicular to the magnetic field **H** and containing an infinitesimal fraction of the total volume, the calculation shows that, as $H\rightarrow 0$, R_{eff}/R_{matrix} is as given in the third column of Table II. The check with Eq. (22) is seen to be quite good if the conductivities of inclusion and matrix differ by no more than a factor two, but is poor for parallel inclusions of very high or very low conductivity. For inclusions perpendicular to **H**, however, Eq. (22) turns out to be exact if the mobilities are the same in both media; it turns out that this holds not only for widely separated inclusions but for any volume ratio.

It is interesting to consider the case where R and ρ are continuous functions of x and y, instead of simply having one value outside and another value inside the

TABLE II. Comparison of Eq. (22) with the exact low field Hall constant of a medium containing cylindrical inclusions of infinitesimal volume fraction f, inclusions and matrix being assumed to have the same value for the mobility $R\sigma$.

Orientation of inclusions	σ(inclusions)/σ(matrix)	$R_{\text{eff}}/R_{\text{matrix}}$ Exact	From (22)
$\parallel H$	$\frac{1}{2}$	$1+(4/9)f$	$1+\frac{1}{2}f$
	2	$1-(8/9)f$	$1-f$
	0	1	$1+f$
	∞	$1-4f$	$1-\infty f$
$\perp H$	Any (σ_i/σ_m)	$1+f[1-(\sigma_i/\sigma_m)]$	$1+f[1-(\sigma_i/\sigma_m)]$

rods, and where **H** is in the z direction. By a slight generalization of the argument given above, one can see that as H increases, the current lines transverse to **H** will be forced more and more out of regions of local maxima or minima of R, and will be confined more and more closely to the immediate neighborhood of the cylindrical surface $R(x,y)=R^*$ for that value of R^* for which this surface extends unbroken to infinity. This implies that if there are no connected regions of infinite extent where R is constant, the current lines will continue to be constricted more and more as $H\rightarrow\infty$, and the macroscopic resistivity will also $\rightarrow\infty$. The effective Hall constant will become R^*, which for fluctuations of modest range may well be close to the value of Eq. (24), though in general not identical with it. Thus, for the general case of this sort, the small-fluctuation formula is not so incorrect qualitatively as in the special case considered in the foregoing.

Isolated Inclusions in Three Dimensions

For a finite inclusion surrounded on all sides by a medium of different Hall constant, the current distribution at high values of the magnetic field H shows a new interesting feature. We shall again restrict ourselves to the case where both the Hall coefficient R and the symmetrical part $[\rho]$ of the resistivity tensor approach constant limits as $H\rightarrow\infty$. The new feature has to do with the fact that as $H\rightarrow\infty$, the current distribution tends to become more and more nearly two-dimensional. This follows from Eqs. (1), (2), and (3). With the notation $[\varrho]$ for the symmetrical part of the resistivity tensor we have, in any region of uniform R,

$$\begin{aligned}0&=\nabla\times(R\mathbf{H}\times\mathbf{j}+[\varrho]\cdot\mathbf{j})\\&=-R\mathbf{H}\cdot\nabla\mathbf{j}+\nabla\times([\varrho]\cdot\mathbf{j}).\end{aligned}\tag{60}$$

If we keep the macroscopic average of $\mathbf{j}$ fixed and let $H\rightarrow\infty$, the last term of Eq. (60) will remain bounded except in the neighborhood of certain singular points, and so, if the z direction is the direction of **H**, we must have

$$(\partial\mathbf{j}/\partial z)\rightarrow 0\tag{61}$$

almost everywhere.

Now the argument used above for rodlike inclusions can be applied to show that as $H\rightarrow\infty$, the current lines must tend to avoid crossing those parts of the surface of an inclusion of the present type which are tangent to the z direction. By expression (61), the resulting current distortions must then continue to occur for some distance above and below the inclusion in the z direction, this distance increasing without limit as $H\rightarrow\infty$. A slightly more detailed analysis, worked out in the Appendix for a cylindrical inclusion of finite height, shows that when a current transverse to **H** is imposed at infinity a strong current distortion persists above and below the perimeter of the cylinder for a distance in the z direction which is asymptotically of the order of

$$\Delta z\approx a(H/H_0)[\ln(H/H_0)]^{-1},\tag{62}$$

where a is the radius of the inclusion and H_0 is the field at which RH equals the resistivity. Throughout most of this region j_z is $\gg j_x$ and j_y. The extra dissipation introduced by this current distortion is, for fixed current density at infinity, proportional to Δz. Thus for a medium with a dilute sprinkling of such inclusions the macroscopic resistivity transverse to **H** should be a constant plus a term behaving like relation (62). This behavior resembles that of the weak-fluctuation expression (33) or (34), differing qualitatively only by the presence of the logarithmic factor.

General Three-Dimensional Fluctuations

When the inclusions are so numerous that their "shadows" interpenetrate, one can no longer compute the macroscopic resistivity from arguments about the current flow around an isolated inclusion. One can, however, make arguments regarding the orders of magnitude of the current fluctuations and their coherence distances along and normal to the magnetic field. These arguments, crude yet too complicated to be worth reproducing here in detail, seem to confirm two expectations suggested by the inclusion model just discussed. The first is that for the general case of three-dimensional fluctuations in Hall constant, the macroscopic resistivity transverse to a magnetic field H increases without limit when $H\rightarrow\infty$, if the local Hall constant and resistivity approach constant values at each point. The second feature is that the component of current along **H** becomes generally $\gg$ that normal to **H**, and the coherence distance of the current in the direction of **H** becomes $\gg$ that at right angles.

Thus it seems that the behavior of transverse magnetoresistance under conditions of large current distortion is usually qualitatively similar to that given by Eq. (33) or (34) for the case of small distortions. However, except for the example of the stratified medium, we have failed to get any quantitative comparison of Eq. (33) and (34) with an exact expression valid at moderate to large values of the distortion.

4. POSSIBLE APPLICATIONS

Macroscopically Inhomogeneous Semiconducting Crystals

The original motivation for this work was the suspicion that fluctuations in impurity density might sometimes have an important effect on measured properties of semiconducting single crystals. While it now seems quite possible, with the best modern techniques, to prepare silicon and germanium specimens free from appreciable random fluctuations over submillimeter distances, it is known[10] that pulled crystals can easily show quite sizable fluctuations on a scale determined by such factors as speed of rotation and the mechanism of temperature control. These are more apt to be striations than isotropic fluctuations. For such crystals the apparent and true Hall mobilities may differ by a considerable percentage, depending on the direction in which the specimen is cut, and a serious nonsaturation of transverse magnetoresistance may occur at high fields.

Crystals with Dislocations

It is known[11] that edge dislocations in n-type germanium, and doubtless in many other substances, are surrounded by cylindrical regions of positive space charge, from which conduction electrons are excluded. These cylinders have radii of the order of thousands of angstroms, which may, depending on temperature, etc., be either less than or greater than the mean free path. If the cylinder radius is much less than a mean free path, their effect on conduction is appropriately described as one of scattering the carriers[11]; if the radius is much more than a mean free path or a Debye length, however, it is more correct to think of the cylinders as regions of zero conductivity. For such a case the formulas of this paper, though not strictly valid for a fluctuation of the conductivity down to zero, can probably be used to obtain rough estimates of the effect which the dislocations produce on various properties such as piezoresistance, magnetoresistance, etc.

"Statistical Inhomogeneity" Effect

An interesting question, whose complete answer lies beyond the scope of this paper, is the following: Even if the impurities in a semiconductor are distributed completely randomly, i.e., with a three-dimensional Poisson distribution, their local density will fluctuate, i.e., the number of impurity atoms in a region of given dimensions will vary randomly with the location of this region. What effect do these fluctuations, whose scale extends down to the mean interimpurity distance, have on transport phenomena? One can, of course, use the concept of impurity scattering to describe the effect of that part of the fluctuations which has a scale small compared with an electronic mean free path. But fluctuations over larger distances cannot be taken into account by a transport equation in momentum space alone; the transport problem must be formulated in coordinate and momentum space together. For fluctuations on a scale well above that of the Debye length and mean free path, however, one can use the type of macroscopic theory we have been discussing in this paper. In the following paragraphs we shall make a few qualitative comments about this one aspect of the fluctuation problem.

To allow for the possibility of compensation, let us suppose the semiconductor to have, on the average, $\langle n \rangle$ carriers and $\langle n^{(I)} \rangle$ ionized impurity centers, per unit volume. The local density of the ions is

$$n^{(I)}(\mathbf{r}) = \sum \delta(\mathbf{r} - \mathbf{R}_i), \tag{63}$$

and if the ionic positions $\mathbf{R}_i$ are randomly distributed, the $\mathbf{k}$th Fourier coefficient of this has the mean square value

$$\langle |n_k^{(I)}|^2 \rangle = \langle n^{(I)} \rangle / V \tag{64}$$

independently of $\mathbf{k}$; here V is the volume of material over which the Fourier series development is being applied. The time-averaged Fourier coefficients of the carrier density n are related to those of $n^{(I)}$ by

$$n_k = n_k^{(I)} / (1 + \lambda^2 k^2), \tag{65}$$

where λ is the Debye length. For use in formulas such as Eqs. (28), (29), (31), (34), etc., we want $\sum_k' |n_k|^2$, summed up to some maximum k_1, of the order of the reciprocal of the least distance over which the concepts of macroscopic conduction are applicable. In other words, we want to compute $\langle (n - \langle n \rangle)^2 \rangle$ ignoring fluctuations of scale smaller than this least distance k_1^{-1}. In the absence of a magnetic field the most obvious limition on k_1^{-1} is that it be $\gtrsim$ the mean free path ℓ. At high magnetic fields, however, the distance an electron or hole is likely to move between scattering processes is of the order of ℓ only if it is moving along the magnetic field; perpendicular to the field the motion will not extend farther than twice the cyclotron radius R_c. Thus, if the appropriate value of k_1 in zero magnetic field is of order ℓ^{-1}, the appropriate value at high fields is greater, perhaps something like $(2R_c^2\ell)^{-\frac{1}{3}}$.

These statements do not mean, of course, that the n_k and $n_k^{(I)}$ for $k > k_1$ have no effect on transport, but merely that such effects cannot be calculated by the present method. However, it may well be true that these higher Fourier coefficients are of lesser importance than the lower ones for the high field magnetoresistance.

Figure 2 shows some typical numerical values for n-type germanium at 80°K and for degenerate n-type

[10] See, for example, the probe profiles reported by W. P. Slichter and J. A. Burton, in *Transistor Technology* (D. Van Nostrand Company, Inc., Princeton, New Jersey, 1958), Vol. 1, Sec. 6.4.

[11] W. T. Read, Phil. Mag. **45**, 775, 1119 (1954); **46**, 111 (1955); R. A. Logan, G. L. Pearson, and D. A. Kleinman, J. Appl. Phys. **30**, 885 (1959).

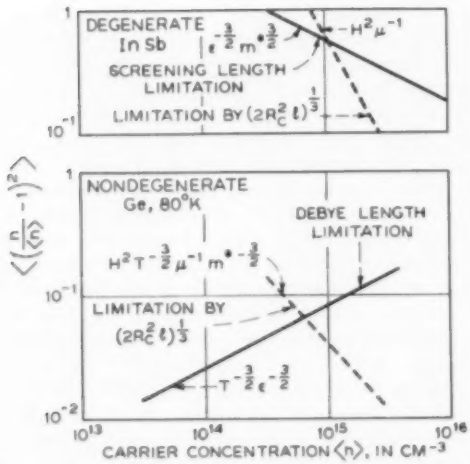

FIG. 2. Curves illustrating the order of magnitude of the "statistical inhomogeneity" effect. The ordinates are values of the mean square relative fluctuation of carrier density over distances greater than a Debye length or an effective mean free path. Bottom curves: uncompensated n-type germanium 80°K. The full curve has been calculated from Eq. (65), the dashed curve from a similar formula with λ replaced by $(2R_c^2\ell)^{\frac{1}{3}}$, where R_c is the cyclotron radius of an average carrier at 20 000 gauss and ℓ the mean free path along the magnetic field. Top curves: same for n-type indium antimonide at low temperature, degenerate but uncompensated. Here the Fermi-Thomas screening length has been used for λ. For all curves the dependence of the ordinates on temperature T, mobility μ, dielectric constant ϵ, effective mass m^*, and magnetic field H is indicated; for compensated specimens all ordinates go as the compensation ratio $\langle n^{(I)}\rangle/\langle n\rangle$.

indium antimonide.[12] The figure also indicates the rules for scaling to other materials and temperatures. The principal features of this "statistical inhomogeneity" effect are two: First, it is small for both very pure and very impure nondegenerate material, with a maximum at intermediate dopings, where the transition from Debye-length limitation to effective-free-path limitation occurs. Second, for given mean carrier concentration $\langle n\rangle$ the relative mean square fluctuation is proportional to the compensation ratio $\langle n^{(I)}\rangle/\langle n\rangle$, except when the modification of the mean free path by impurity scattering is of importance; this conclusion is obtained by using Eq. (64) in the evaluation of the square of Eq. (65). For heavily compensated material, the present effect on the high field transverse magnetoresistance can be quite perceptible. For example, the coefficient of $\langle(n-\langle n\rangle)^2\rangle/\langle n\rangle^2$ in the bracketed expression of Eq. (34) is about three for n germanium of mobility 2×10^4 cm^2/vsec, in a field of 20 000 gauss along the [001] direction. If $\langle(n-\langle n\rangle)^2\rangle/\langle n\rangle^2$ can become as large as, say, 0.1, as Fig. 2 suggests is possible for germanium at this field for $\langle n\rangle$ a few $\times10^{14}$ and $\langle n^{(I)}\rangle$ several times $\langle n\rangle$, then the second term in the bracketed factor of Eq. (34) can be a quarter of the first. For indium antimonide, quantum effects will prevent Eq. (34) from being applicable, but the large size of the ordinates in Fig. 2 suggests sizable effects.

Preliminary attempts[13] to find this effect experimentally have given inconclusive results. With magnetic field in a [100] direction the transverse magnetoresistance of n-type germanium specimens, extrapolated to infinite field, seems to show a maximum at a carrier concentration between 10^{14} and 10^{15} cm^{-3}, whereas conventional impurity-scattering theory predicts a shallow minimum. But measurements on a compensated specimen have failed to reveal as marked a rise in magnetoresistance as the above considerations would suggest. About all that can be said at present is that for a certain range of conditions there seem to be both theoretical and experimental reasons for distrusting impurity-scattering theories based on a transport equation in crystal-momentum space alone, especially where high-field magnetoresistance is concerned.

Magnetoresistance of Polycrystalline Media

The small-fluctuation formulas of Sec. 2 are useful for calculating the effect of polycrystallinity on various properties which in a single crystal would be moderately orientation-dependent. We shall give a few illustrations here, always on the assumption that the grain boundaries themselves offer no resistance. A trivial example, for which small-fluctuation theory is exact, is the low-field magnetoresistance of polycrystalline material of

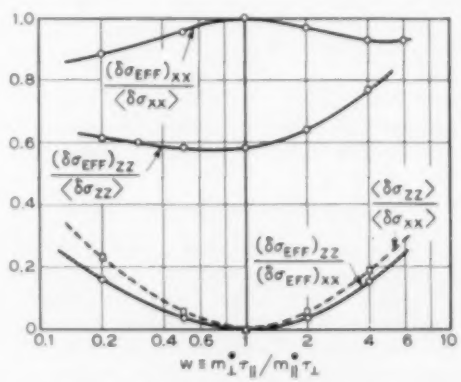

FIG. 3. Comparison of the H^2 term in the macroscopic magnetoconductivity of a polycrystal, $\delta\sigma_{eff}$, with the directional average $\langle\delta\sigma\rangle$ of the corresponding single-crystal magnetoconductivity, for measurements along and perpendicular to a magnetic field $\mathbf{H}$ in the z-direction. The individual grains are assumed to be uniaxial, with a single set of spheroidal energy surfaces characterized by effective masses $m_\parallel^*$, $m_\perp^*$, and relaxation times $\tau_\parallel$, $\tau_\perp$. The acoustic scattering law $\tau_{\parallel,\perp} \propto$ (energy)$^{-\frac{1}{2}}$ has been assumed.

[12] A recent paper by S. V. Ayrapetyants, J. Tech. Phys. (U.S.S.R.) 28, 1913 (1958) [English translation: Soviet Phys.—Tech. Phys. 3, 1758 (1958)], has independently called attention to the fact that purely random fluctuations in the impurity distribution in strongly compensated semiconductors can become quite appreciable over distances large enough to be treated macroscopically. Quantitative comparison of our estimates with his is impossible, since his expression (7), whose attainment of a value of order unity is supposed to signify sizable carrier fluctuations, does not seem to be dimensionless.

[13] T. H. Geballe and J. E. Kunzler (personal communication).

the cubic system. If the material is homogeneous in every respect except the orientations of the grains, the zero-field conductivity does not fluctuate, and the quantities $(\sigma_k)_{\delta\nu}$, etc.. in (11) are of the second order in the magnetic field H. Therefore,

$$(\sigma_{\text{eff}})_{\mu\nu}=\langle\sigma_{\mu\nu}\rangle+0(H^4). \tag{66}$$

With the z axis chosen along $\mathbf{H}$ and with the notation $\delta\sigma$, $\delta\rho$ for the changes in conductivity and resistivity, respectively, produced by H, we have, to order H^2,

$$(\delta\rho_{\text{eff}})_{zz}/\rho_0=-(\delta\sigma_{\text{eff}})_{zz}/\sigma_0=(b+c+\tfrac{1}{3}d)H^2 \tag{67}$$

$$(\delta\rho_{\text{eff}})_{xz}/\rho_0=-(\delta\sigma_{\text{eff}})_{xz}/\sigma_0-(\mu_H H/c)^2=(b+\tfrac{1}{3}d)H^2, \tag{68}$$

where σ_0, ρ_0 are the zero-field values, μ_H is the Hall mobility, and b, c, d are the three magnetoresistance constants introduced by Seitz.[14]

For crystals of lower than cubic symmetry, more interesting things occur, since the very fact of polycrystallinity makes the medium inhomogeneous even at zero magnetic field. Now Keyes[15] has recently pointed out that the mass-relaxation time anisotropy of a semiconductor with simple spheroidal energy surfaces can be determined from the directional average of the magnetoconductivity; identifying this directional average with the measured magnetoconductivity of polycrystalline black phosphorus, he has estimated that the mobility perpendicular to the layer planes is about a tenth that parallel to the planes. Keyes' assumption amounts to neglecting the second term on the right of Eq. (11). The value of this term for a macroscopically isotropic polycrystal can be computed by an elementary though tedious calculation, using the standard expressions for the terms of order 1, H, H^2 in the conductivity tensor of a valley with spheroidal energy surfaces.[16] The results, specialized to the acoustic scattering law, are shown in Figs. 3 and 4. The curves shown, being based on small-fluctuation theory, cease to be valid when the crystalline anisotropy of the zero-field conductivity becomes large. However, the examples discussed in Sec. 3 suggest that the curves of Figs. 3 and 4 will be fairly good even when the anisotropy ratio, or its reciprocal, is several times unity. It will be seen that the largest fractional correction to the assumption $\delta\sigma_{\text{eff}}=\langle\delta\sigma\rangle$ comes for the longitudinal magnetoconductivity when the anisotropy ratio w is near unity. But since the longitudinal magnetoconductivity $\delta\sigma_{zz}$ contains $(w-1)^2$ as a factor, the absolute error in $(\delta\sigma_{\text{eff}})_{zz}$ never gets very large. Table III gives a comparison of the true values of w with the values which would be inferred by various uses of the assumption $\delta\sigma_{\text{eff}}=\langle\delta\sigma\rangle$. It will be seen that the errors are not serious enough to prevent Keyes' uncorrected method from being a useful aid to the study of those semiconductors which are available only as polycrystals.

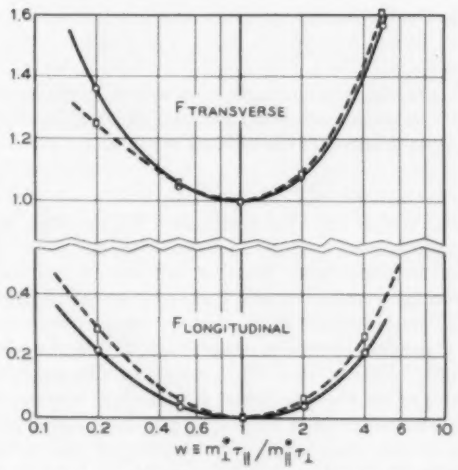

FIG. 4. Values of the dimensionless ratio F of the H^2 term in the fractional magnetoconductivity, $\delta\sigma_{\text{eff}}/\sigma_{\text{eff}}$, to the square of the Hall angle, as a function of the single crystal mass-relaxation time anisotropy ratio, for the case considered in Fig. 3. The full curves assume $\delta\boldsymbol{\sigma}_{\text{eff}}$, σ_{eff}, and $\mu_{H\text{eff}}$ to be given by the small-fluctuation formulas of Sec. 2, the dashed curves assume these to be given by $\boldsymbol{\sigma}_{\text{eff}}(\mathbf{H})=\langle\boldsymbol{\sigma}(\mathbf{H})\rangle$.

TABLE III. Illustrations of the errors involved in computing the anisotropy ratio w of a uniaxial material from the assumption that the magnetoconductivity of a polycrystal is the directional average of that of a single crystal. The z direction is to be taken along the magnetic field H. The acoustic law $\tau_{\text{III},\perp}\propto(\text{energy})^{-\frac{1}{2}}$ has been assumed, and small-fluctuation theory, as manifested in the curves of Fig. 4, has been taken as correct.

True $w\equiv m_\perp^*\tau_{\text{III}}/m_{\text{III}}^*\tau_\perp$	0.2	0.5	1.0	2.0	5.0
Value of w deduced assuming $\sigma_{\text{eff}}=\langle\sigma\rangle$ using:					
$\delta(\sigma_{\text{eff}})_{zz}/(\sigma_{\text{eff}})_{zz}$	0.27	0.61	1.0	1.7	4.4
$(\delta\sigma_{\text{eff}})_{zz}/\sigma_{\text{eff}}(\mu_{H\text{eff}}H/c)^2$	0.25	0.55	1.0	1.75	4.5
$(\delta\sigma_{\text{eff}})_{xz}/\sigma_{\text{eff}}(\mu_{H\text{eff}}H/c)^2$	0.13	0.48	1.0	1.95	4.7

At high magnetic fields H the expressions for the magnetoresistance of a polycrystal again become simple, if one can assume the validity of the relations

$$\tfrac{1}{2}(\sigma_{\mu\nu}+\sigma_{\nu\mu})\sim\sigma_{zz}\ (\text{orientation})\ \delta_{\mu z}\delta_{\nu z}+O(H^{-2}) \tag{69}$$

$$\tfrac{1}{2}(\sigma_{\mu\nu}-\sigma_{\nu\mu})\sim\delta_{\mu\nu z}/R_\infty H+O(H)^{-3}) \tag{70}$$

as $\mathbf{H}\to\infty$ in the z direction, with R_∞ the same for all grains. These relations follow from any transport theory in crystal-momentum space with closed energy surfaces, but in general fail if the effects of orbital quantization are important or if the material in question is a metal with a Fermi surface which can be continued periodically to infinity in crystal-momentum space. When Eqs. (69) and (70) hold, the denominator of Eq. (11) is $O(1)$ for most directions of $\mathbf{k}$, and $O(H^{-2})$ for a range of solid angle of order H^{-1}; the numerator is $O(H^{-4})$ if μ, ν are x, x, and $O(1)$ if μ, ν are z, z. Thus, to order H^{-2},

$$(\sigma_{\text{eff}})_{zz}=\langle\sigma_{zz}\rangle, \tag{71}$$

[14] F. Seitz, Phys. Rev. **79**, 372 (1950).
[15] R. W. Keyes, Phys. Rev. **109**, 43 (1958).
[16] See, for example, C. Herring and E. Vogt, Phys. Rev. **101**, 944 (1956), Eqs. (16), (18), (20).

while to order unity

$$(\sigma_{\rm eff})_{zz}=\langle\sigma_{zz}\rangle^{-1}[2\langle\sigma_{zz}\rangle^2-\langle\sigma_{zz}^2\rangle]. \quad (72)$$

The effective Hall constant is, of course, given by Eq. (24). The small-fluctuation formula [Eq. (72)] is clearly an approximation to the general relation

$$(\sigma_{\rm eff})_{zz}=\langle 1/\sigma_{zz}\rangle^{-1}. \quad (73)$$

Less trivial are the expressions for the high field magnetoresistance when, as for most metals, Eqs. (69) and (70) do not hold. We shall not discuss such cases here as they require careful consideration of the appropriate single-crystal expressions for magnetoresistance and Hall effect in various orientations. It is worth pointing out, however, that the methods of this paper are capable of providing a better relationship between the magnetoresistances of metallic single crystals and polycrystals than has been used in some of the current literature.[17]

ACKNOWLEDGMENTS

I am indebted to Drs. A. C. Beer, T. H. Geballe, and R. Wolfe for a number of comments and suggestions, and to Drs. T. H. Geballe and J. E. Kunzler for experimental measurements which have proved helpful in delimiting the field of this study.

APPENDIX

Current Flow Around an Isolated Inclusion in a Magnetic Field

Let the inclusion be a cylinder of radius a and height h, with axis parallel to the magnetic field $\mathbf{H}$. Take the z direction along $\mathbf{H}$, and suppose for simplicity that, both inside and outside, the conductivity tensor in the field $\mathbf{H}$ has the form

$$\sigma_{xx}=\sigma_{yy}=\sigma_\perp\propto H^{-2} \text{ as } H\to\infty, \quad (A.1)$$

$$\sigma_{xy}=-\sigma_{yx}\propto H^{-1} \text{ as } H\to\infty, \quad (A.2)$$

$$\sigma_{zz}\to \text{finite limit as } H\to\infty. \quad (A.3)$$

Define primed coordinates and current density components by the transformations

$$x'=x,\quad y'=y,\quad z'=z(\sigma_\perp/\sigma_{zz})^{\frac{1}{2}}, \quad (A.4)$$

$$j_x'=j_x,\quad j_y'=j_y,\quad j_z'=j_z(\sigma_\perp/\sigma_{zz})^{\frac{1}{2}}, \quad (A.5)$$

where $\sigma_\perp$, σ_{zz} refer to the region outside the inclusion. Then

$$\nabla'\cdot\mathbf{j}'=\nabla\cdot\mathbf{j}=0, \quad (A.6)$$

and if φ is the electrostatic potential,

$$\mathbf{j}'=-\boldsymbol{\sigma}'\cdot\nabla'\varphi,$$
$$\nabla'^2\varphi=0, \quad (A.7)$$
$$\sigma'=\sigma_\perp\mathbf{1}+\boldsymbol{\sigma}^{(H)'}, \quad (A.8)$$

$\boldsymbol{\sigma}^{(H)'}$ being a contravariant Hall conductivity tensor whose only components are

$$\sigma_{xy}{}^{(H)'}=-\sigma_{yx}{}^{(H)'}=\sigma_{xy}. \quad (A.9)$$

We shall undertake to derive the asymptotic behavior of the current flow as $H\to\infty$. Although, as we shall see, this asymptotic behavior is fully realized only at fields so high that Eqs. (A.1) to (A.3) are likely to break down, we shall hope to gain useful qualitative insights from this investigation.

In the primed system, the height h' of the cylinder is proportional to H^{-1}, so that as $H\to\infty$ the shape of the inclusion approaches that of a disc. Let us impose the boundary condition that at infinity $\mathbf{j}\to$ a constant vector $\mathbf{j}_\infty$, independent of H and oriented in the x direction. By Eqs. (A.7) to (A.9) and (A.2), this means that as $H\to\infty$,

$$\varphi\sim\text{constant}\cdot Hy \quad (A.10)$$

at infinite distance from the inclusion. The potential in the region external to the inclusion equals the sum of the potential which would obtain in the absence of the inclusion and the potential $\Delta\varphi$ due to a distribution of charges over the surface of the inclusion. The asymptotic form of this surface density, as $H\to\infty$, can be shown to be such as to make the periphery of the disk essentially an equipotential. The argument is as follows:

Consider first the special case where the symmetrical part of the conductivity tensor is the same inside the inclusion as outside, only the Hall conductivity being different. Then we can use the transformations (A.4), (A.5) everywhere. The potential will obey Laplace's equation everywhere except on the surface of the inclusion, where it will have sources. However, since $j_z'=-\sigma_\perp\partial\varphi/\partial z'$ must be continuous across the top and bottom faces of the disk, there can be no surface charges on these faces. Thus, to calculate the departure $\Delta\varphi$ of the potential from the form (A.10), which would obtain everywhere if the inclusion were absent, we need only calculate the potential due to surface charges on the cylindrical rim of the disk. Conservation of normal component of current across the latter surface requires that the discontinuity in the normal derivative $(\partial\varphi/\partial n)$ of the potential be given by

$$\sigma_\perp[(\partial\varphi/\partial n)_{\rm in}-(\partial\varphi/\partial n)_{\rm out}]$$
$$=(\partial\varphi/\partial s)[(\sigma_{xy})_{\rm in}-(\sigma_{xy})_{\rm out}], \quad (A.11)$$

where $\partial\varphi/\partial s$ is the tangential derivative of the potential in the $x-y$ plane. This quantity must be asymptotically independent of z as $H\to\infty$, so at distances from the rim $\ll$ the radius a of the disk the potential $\Delta\varphi$ must behave like the potential of a uniformly charged strip in two dimensions. Thus, on the rim,

$$\Delta\varphi\approx(h'/2\pi)[(\partial\varphi/\partial s)/\sigma_\perp]$$
$$\times[(\sigma_{xy})_{\rm in}-(\sigma_{xy})_{\rm out}]\ln(a/h'). \quad (A.12)$$

[17] J. M. Ziman, Phil. Mag. **3**, 1117 (1958); I. M. Lifshits and V. G. Peschanski, J. Exptl. Theoret. Phys. (U.S.S.R.) **35**, 1251 (1958) [English translation: Soviet Phys. JETP **8**, 875 (1959)].

At the same time, we must have

$$\partial\varphi/\partial s=(\partial\varphi/\partial y')_\infty(\partial y'/\partial s)+O(\Delta\varphi/a). \quad \text{(A.13)}$$

Since $h'\sigma_{xy}/a\sigma_\perp$ is of order 1 as $H\to\infty$, but $\ln(a/h')$ is $\gg 1$, Eqs. (A.12) and (A.13) require that $\partial\varphi/\partial s$ be of order $[\ln(a/h')]^{-1}$ times the first term of (A.13). To this order, then, the rim of the disk is an equipotential.

We have next to show that this argument can still be used when the symmetrical part of the conductivity is different in the two media. For this case we have again to express $\Delta\varphi$ in the external region as an integral over the surfaces of the inclusion, but now the contributions from the top and bottom surfaces will no longer vanish. It is not hard to show, however, that the contributions from regions not in the immediate neighborhood of the rim of the disk contribute a negligible amount to the potential field. The argument, which we omit for brevity, can be based on Laplace's equation in the primed coordinates of the interior medium. Now on the cylindrical rim an equation very similar to (A.11) must hold. The key question in the argument is whether an equation like (A.12) can still be written. That this is in fact the case follows from the fact that $\sigma_\perp$ times the flux of $\nabla\Delta\varphi$ into the neighborhood of a length dl of the rim must just cancel the difference between the current flux into this region from outside the cylindrical rim, due to $\boldsymbol{\sigma}^{(H)'}$, and the corresponding current flux within the inclusion at a moderate distance from the rim. The latter two fluxes will clearly be different when σ_{xy} is different in the two materials, regardless of equality or inequality of the symmetrical parts of the conductivity tensor. The occurrence of a logarithmic factor in an equation like (A.12) depends only on there being a nonvanishing flux of $\nabla\Delta\varphi$ into the rim region.

Let us now return to the calculation of the asymptotic behavior of the current flow at large magnetic fields. The discussion so far shows that at distances from the rim (in the primed space) which are $\gg h'$, the potential field will be very nearly that of a uniform field disturbed by a ring of radius a, made of conducting wire of diameter $\approx h'$. When $h'\ll a$, the solution of this problem gives a $\Delta\varphi$ which at points whose distance ξ from the rim of the disk is $\gg h'$ but $\ll a$ is of the order of

$$E_\infty' a[\ln(a/\xi)/\ln(a/h')], \quad \text{(A.14)}$$

where $E_\infty'=-(\partial\varphi/\partial y')_\infty$ is the field at infinity. Thus the electric field is changed away from E_∞' by a significant factor only at distances ξ from the rim which satisfy

$$\xi\lesssim a/\ln(a/h'). \quad \text{(A.15)}$$

Within this range, however, the distortion of the field, and hence of the current, is sizable, and, depending on the direction from the rim, j_z' can be of the same order of magnitude as j_z' and j_y'.

In the original (unprimed) coordinate system this means that there is great current distortion within a shell like region whose distance from the rim in the x-y plane satisfies expression (A.15), and which extends in the z direction for a distance $(\sigma_{zz}/\sigma_\perp)^{\frac{1}{2}}$ times expression (A.15). The current lines flowing outside the inclusion are almost undistorted until they reach this shell, but on entering it the current lines become enormously crowded together, and j_z becomes, at a general point of the shell, $\gg j_x$ or j_y. Inside the inner boundary of the shell, the current lines again behave almost as if the inclusion were not present.

The excess dissipation due to the presence of the inclusion is most simply described in terms of the volume ratio $V(H)/V_i$, where V_i is the volume of the inclusion and $V(H)$ is defined by

$$\begin{pmatrix}\text{dissipation}\\ \text{with}\\ \text{inclusion}\end{pmatrix}-\begin{pmatrix}\text{dissipation}\\ \text{without}\\ \text{inclusion}\end{pmatrix}=\begin{pmatrix}\text{dissipation per}\\ \text{unit volume}\\ \text{without inclusion}\end{pmatrix}\times V(H). \quad \text{(A.16)}$$

Thus, since $\mathbf{E}\cdot\mathbf{j}$ is the same in the primed and unprimed systems,

$$\begin{aligned}\sigma_\perp E_\infty'^2V(H)&=\sigma_\perp\int_{\text{ext}}[|\nabla'\varphi|^2-E_\infty'^2]dxdydz+I_{\text{int}}\\&=(\sigma_\perp\sigma_{zz})^{\frac{1}{2}}\int_{\text{ext}}[|\nabla'\varphi|^2-E_\infty'^2]\\&\qquad\times dx'dy'dz'+I_{\text{int}}, \quad \text{(A.17)}\end{aligned}$$

where the integration is over the region external to the inclusion, and I_{int} is a similar dissipation integral for the interior of the inclusion. From what has been said above, it is clear that as $H\to\infty$, I_{int} becomes negligible compared with the first term of Eq. (A.17). The integral in the first term can be expressed as an integral over the surface of the inclusion; with $\varphi=-E_\infty y+\Delta\varphi$, and with n designating the unit normal to the surface element dS,

$$\begin{aligned}\int_{\text{ext}}&=\int n\Delta\varphi\cdot[\nabla\Delta\varphi-2E_\infty']dS\\&\sim\int n\Delta\varphi\cdot\nabla\Delta\varphi dS,\end{aligned} \quad \text{(A.18)}$$

since by expression (A.14) the normal derivative of $\Delta\varphi$ on the rim must be $\gg E_\infty$. Using expression (A.14) we find, asymptotically as $H\to\infty$,

$$\int_{\text{ext}}\approx E_\infty'^2a^3/\ln(a/h'). \quad \text{(A.19)}$$

Thus Eq. (A.17) gives, finally, in this limit,

$$\frac{V(H)}{V_i}\approx\frac{a}{h\ln(a/h')}\left(\frac{\sigma_{zz}}{\sigma_\perp}\right)^{\frac{1}{2}}\propto\frac{H}{\ln(H/H_0)} \quad \text{(A.20)}$$

where we have written $a/h'=H/H_0$.

A Structural Study of the Compound $AgSbTe_2$

R. W. Armstrong, J. W. Faust, Jr., and W. A. Tiller
Westinghouse Research Laboratories, Churchill Borough, Beulah Road, Pittsburgh 35, Pennsylvania

X-ray, optical and electron microscope, and chemical etching techniques have been used to investigate a striated microstructure observed in zone refined single crystals of the $AgSbTe_2$ structure. This microstructure, originally thought to be fine twin lamellas, has been identified as a Widmanstatten precipitate of Sb_2Te_3 upon the {111} planes of the matrix face-centered cubic material. In addition, the evidence obtained from all the measurements made on this material indicates that the ternary compound of the $AgSbTe_2$ type does not melt congruently.

INTRODUCTION

CONSIDERABLE work on the structure, phase diagrams, and physical properties of ternary compounds of the $AgSbTe_2$ type has been carried out by J. Wernick and his co-workers.[1,2a,2b] This work indicated that the compounds in this family were congruent melting compounds and that, by zone refining, the maximum melting composition could be obtained in single crystal form. This should be particularly true for $AgSbTe_2$, which does not suffer a low temperature phase transition. However, when one carries out the zone melting operation on $AgSbTe_2$, it is observed that the single crystals contain a microstructure that appears to consist of a dense array of twin lamellas.[3] This microstructure is shown in Fig. 1.

Since the compound was considered to be congruently melting it was felt that only twin lamellas could produce such a microstructure. We set out to investigate the orientation, density, and cause for the occurrence of this twinlike defect. It was soon decided that the compound could not be congruently melting and that the defect was in fact a precipitate. The evidence for these conclusions is presented here.

EXPERIMENTAL DETAILS

Cast ingots of composition $AgSbTe_2$ were prepared from 99.999% pure starting elements and placed in either graphite or lavite boats which had been first coated with Aquadag and baked. The boats, which contained two parallel channels $22\times0.6\times0.6$ cm in dimension, were sealed in Vycor tubes with $\frac{1}{3}$ atm of He at room temperature. The zone refining operation consisted of placing the Vycor capsule in an ambient temperature of about 500°C, melting a zone of about 3 cm length with a resistance heater and making seven passes with this zone at 1/6 cm/hr. The ingots were then slowly cooled to room temperature. The first 50%–75% of each bar was invariably a single crystal; the remainder of the bars showed a rapid transition in grain size to a fine polycrystalline aggregate.

Mechanically polished surfaces and cleaved surfaces were both prepared for metallographic examination. Mechanically polished specimens were mounted in Kold Mount or in Ward's Bioplastic. Bulk specimens were easily cleaved with a knife edge at room temperature. Thin crystal slices could be cleaved from single crystal bars with a razor blade at room temperature.

The etchants that have been tried on $AgSbTe_2$ thus far are either the same etchants, or perturbations of the same etchants, that are used for etching pure samples of the individual constituent elements making up the compound.

Electron replica photomicrographs were made using an RCA No. EMU3 instrument. Two-stage replication, (1) Parlodion negative replica and (2) tungsten oxide shadowed under 30° carbon positive replica, was used to reproduce cleavage surface patterns and etched patterns on mechanically polished random surfaces. X-ray powder patterns were taken with Co $K\alpha$ radiation using a Phillips camera of 114.3 mm diameter. Laue back reflection and transmission photographs were taken using a molybdenum target with 20-mil collimators. Laue back reflection photographs were exposed for two hours at 20 kv and 10 ma, whereas Laue transmission photographs on specimens 0.15 to 0.32 mm thick required 0.25 hour exposure at 25 kv and 10 ma.

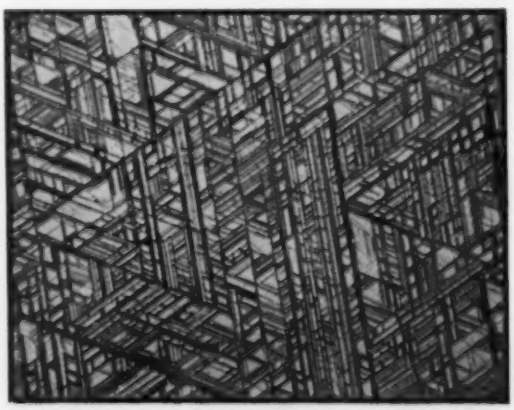

FIG. 1. Optical photomicrograph of lamella array; 432×, 20 sec in 55% HNO_3 aqueous solution.

[1] J. H. Wernick and K. E. Benson, J. Phys. Chem. Solids **3**, (1/2), 157 (1957).
[2a] J. H. Wernick, S. Geller, and K. E. Benson, J. Phys. Chem. Solids **4**, 154 and 240 (1958).
[2b] S. Geller and J. H. Wernick, Acta Cryst. **12**, 46 (1959).
[3] J. H. Wernick (private communication).

Cooling curves were taken on a series of alloys around the $AgSbTe_2$ composition to learn something of the liquidus surface in this region. Chemical analysis of the zone refined bars, some electrical measurements, and hardness measurements were also performed.

EXPERIMENTAL RESULTS

Fracture Studies

It was definitely established by measurement of the angles between cleavage planes with an optical goniometer, and measurements of the cleavage plane symmetry with Laue x-ray (back reflection and transmission) photography that the face-centered cubic crystals cleave on the close-packed planes, i.e., {111}. Almost macroscopic plane fracture surfaces showed that cleavage occurred on many parallel (111) planes of differing elevation bounded by ⟨110⟩ direction step heights which correspond to the intersection of other {111} planes with the major cleavage plane. The cleavage fracture surface frequently appeared layerlike, i.e., when one observed different grains in a cross section of a fractured polycrystalline sample, some grains could be viewed normal to the plane cleavage areas and others parallel to them, definitely showing this anisotropic fracture morphology.

A large variation in the dimensions of the cleavage pattern, i.e., step height, frequency of appearance of steps and the plane areas bounded by steps, was observed depending upon the growth history of the crystal. The intrinsic cleavage pattern exhibited by a single crystal bar was a function of both the number of zone passes and the position along the bar where cleavage was initiated. Although the beginning end of the crystal might cleave straight across on one macroscopic plane (few shallow cleavage steps), a few cms down the bar a cleavage surface might be so multiple faceted with small {111} planes that the fracture would appear noncrystallographic. Triangular ledge facets of 5 μ length per side and comparable step heights were microscopically observed in such multiple fracture surfaces.

ETCHING EFFECTS AND MICROSCOPY

Table I describes the etching results obtained on mechanically polished random surfaces and polished surfaces oriented parallel to the cleavage plane. An excellent etchant, 55% HNO_3 in aqueous solution (orientation etch for silver[4]), was obtained. This etchant did not stain the specimen and it was much superior in revealing microstructural details to CP4, Dash's etchant, H_2O_2 solutions, etc.

Figure 1 shows the etching pattern revealed on a mechanically polished surface nearly parallel to the cleavage plane. Random surfaces through a crystal showed four etch traces. The etch striations are ⟨110⟩ traces of the matrix close-packed plane, {111}; thus the striations were correlated with the observed cleavage patterns. Striation patterns have been observed thus far to vary from an interlamellar distance of less than

TABLE I. Etching results on $AgSbTe_2$.

Composition of etch[b]					Time of etch[a]	Remarks
HNO_3	HOAc	HF	Br_2	I_2		
5	3	3	1		1s	uneven etch, bad stain
5	0	3	1		2s	uneven etch, bad stain
5	3	3		1	5s	fair etch, brown stain
3	12	1			10s	light etch, stain
10	12	1			7.5s	medium etch, bad stain
4	2	1			1m	uneven etch, bad stain
5	0	3			2s	deep etch, stain
2	1				1.5m	good etch, faint stain
2	1.2				30s	light etch, faint stain
1	1				3m	good etch, faint stain
2	2.6				5m	good etch, light stain
1	4				6m	no etch, polish, or stain
HNO_3	H_2O	CH_2OH	HCl			
5.5	4.5				10–30s	excellent etch, no stain
1		3			30s	no etch, or stain (?)
2		2			1m	no etch
3		1			1m	faint etch
1			10		30s	unstab. etch, poor resolution
H_2O_2	HNO_3	H_2O	HF	Tartaric acid		
1		4	1		6m	faint etch
1	1			1	20s	poor etch, stain

[a] s is seconds; m is minutes.
[b] All reagents are analytical grade. HNO_3, HF, H_2O_2 are concentrated; Br_2 is liquid and I_2 solid; HOAc is glacial acetic acid; tartaric acid is used as a saturated water solution.

[4] H. E. Farnsworth, Phys. Rev. **40**, 684 (1932).

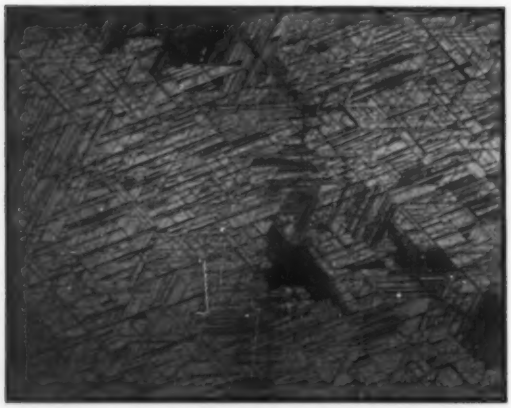

FIG. 2. Optical photomicrograph exhibiting enhanced array formation in the vicinity of subboundaries.

0.5 μ (resolvable at 1000×) on polished surfaces to 25 μ on etched large cleavage surfaces. The etch striation pattern, always smaller than the cleavage step pattern, varied in the same fashion with specimen growth history as the cleavage pattern.

Two separate and subsidiary observations made with the optical microscope concerned mosaic boundary delineation during etching and polyhedron detachment from the etching surface. Mosaic boundary delineation superimposed on the etch pattern of mechanically polished specimens was observed because of a high local density of striations in their vicinity (see Fig. 2). Polyhedrons bounded by {111} planes with shapes varying from thin sheets to small tetrahedrons became detached from the specimen surfaces during etching. This observation indicated that certain {111} plane regions were being preferentially etched and the polyhedrons undercut.

Electron replica micrographs of a polished and etched random polycrystalline surface are shown in Figs. 3 and 4. Figure 3 shows the surface of a grain etched for 10 sec in 55% HNO_3 (normal etching time for optical microscopy) while Fig. 4 shows a surface etched for 4 sec in 55% HNO_3 (optically underetched). Two important observations are to be made: (1) the waviness and

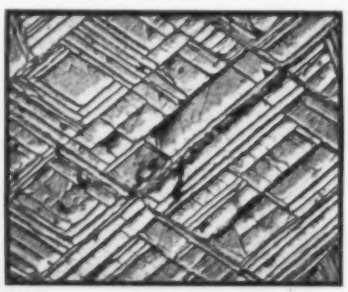

FIG. 3. Electron replica photomicrograph; 560×, 10 sec in 55% HNO_3 aqueous solution.

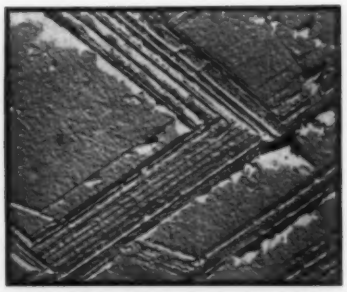

FIG. 4. Electron replica photomicrograph; 3200×, 4 sec in 55% HNO_3 aqueous solution.

intersections exhibited by the striations are characteristic of precipitation, and (2) a great difference in etching rate between the material within a striation lamella and the matrix material is indicated.

X-RAY ANALYSES

While using Laue back reflection photography to identify crystal orientations and the cleavage plane, considerable and unusual spot asterism was observed, i.e., some spots were sharply broken and displaced along certain zone axes while others appeared to be only generally distorted with their centers missing. It was not determined what part of this asterism was associated with the nature and distribution of the general striation pattern as compared to the particular mosaic pattern mentioned earlier, but that the asterism did seem to be associated with the striations suggested that transmission Laue photography might be used to further investigate their nature.

Laue transmission patterns of cleaved slices of the crystal are shown in Figs. 5 and 6. These photographs identify the striations as being caused by a Widman-

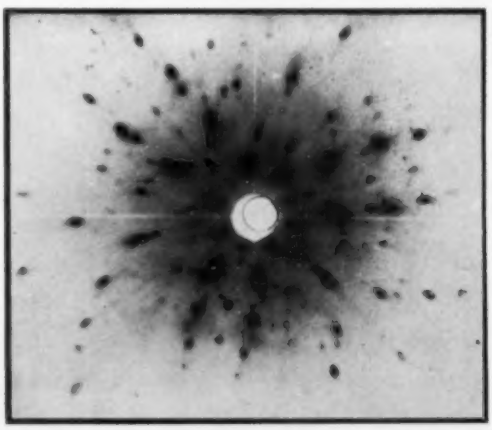

FIG. 5. Laue transmission photograph; specimen thickness 0.15 mm, Mo radiation, 20 mil collimator, 25 kv, 10 ma, 0.25 hr exposure.

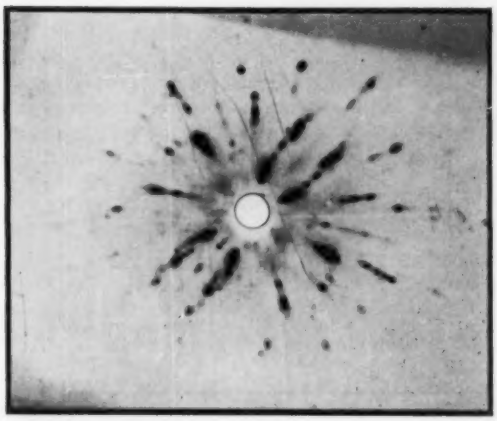

FIG. 6. Laue transmission photograph; specimen thickness 0.28 mm, Mo radiation, 20 mil collimator, 25 kv, 10 ma, 0.25 hr exposure.

statten precipitate.[5] A sterographic projection of the major plane poles observed in Fig. 6 is shown in Fig. 7 using the technique of Dunn and Martin.[6] In addition to the previous metallographic evidence concerning the striation habit plane, Fig. 7 shows that precipitation has occurred predominantly on one parallel set of the {111} plane family. Figure 5 indicates that precipitation has occurred on all three close packed planes. The orientation relationship in this system is apparently the same as that observed in the Widmanstatten precipitation of antimony from lead.[5f]

The results of powder photographs on as-grown material and annealed material (seven hours at 270°C) are shown in Table II and compared with previous results of Geller and Wernick.[2b]

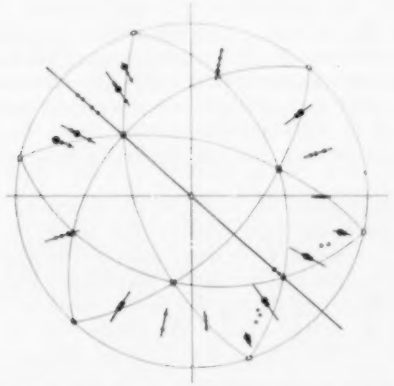

FIG. 7. Sterographic projection of major pole asterism due to (11$\bar{1}$) Widmanstatten precipitation.

[5] R. F. Mehl, Trans. AIME, (a) **93**, (b) **99**, (c) **105**, (d) **113**, (e) **117**, (f) **124**, 367 (1937).
[6] C. G. Dunn and W. W. Martin, Trans. AIME, **185**, 417 (1949).

TABLE II. *d* spacing and observed intensities from powder photography.

f.c.c.	As cast $AgSbTe_2$ Ref.,[b] Cu *K* rad.		Zone refined $AgSbTe_2$ Co $K\alpha$ radiation		Annealed $AgSbTe_2$[c] Co $K\alpha$ radiation	
hkl	Obs *d*(A)	*I*[a]	Obs *d*(A)	*I*[a]	Obs *d*(A)	*I*[a]
			3.11	w	3.10	s
200	3.04	vs	3.00	s	3.01	vvw
					2.63	vvw
					2.54	vvw
			2.26	vw	2.26	w, broad
					2.16	vw
220	2.14	s-vs	2.12	s	2.14	ms
					2.00	vvw
			1.92	vvw		
			1.86	vvw	1.86	vvw
311	1.83	vvvw			1.80	vvw
222	1.75	ms	1.76	vvw	1.76	m
			1.74	wm		
			1.70	vvw	1.70	vvw
			1.55	vvw	1.55	w
400	1.52	m	1.51	w		
					1.46	vvw
331	1.39	vvvw	1.42	vvw	1.42	vvw
420	1.36	s	1.35	m	1.36	wm
			1.32	vvw	1.33	vw
			1.27	vvw	1.26	w
422	1.24	ms	1.24	ms	1.23	m

[a] Visual intensity: s-strong, m-medium, w-weak, v-very.
[b] S. Geller & J. H. Wernick, Acta Cryst. **12**, 46 (1959).
[c] Annealed 7 hours at 270°C in ½ atm of argon.

CHEMICAL ANALYSIS AND METALLOGRAPHY

The zone refined bars were analyzed chemically at various positions along their length. It was found that the concentration changed greatly from point to point and was of the form $Ag_xSb_yTe_z$. It was possible to analyse the composition $Ag_xSb_yTe_z$ into a pseudobinary of $Ag_2Te-Sb_2Te_3$, with *a* parts of Ag_2Te and *b* parts of Sb_2Te_3 within an error of $\pm 2\%$. We have plotted the ratio b/a as a function of position *x* along the bar before and after zone refining in Fig. 8. We have also indicated the temperature of the first and any subsequent thermal arrests found on the cooling curves of several alloys. In Fig. 9, photomicrographs of the microstructure at various positions along the length of the bar are presented to show the variation in the precipitate and other

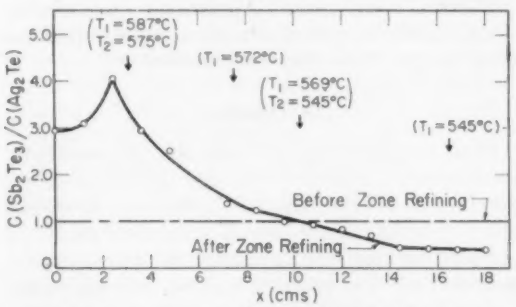

FIG. 8. Plot of the ratio $C(Sb_2Te_3)/C(Ag_2Te)=b/a$ at various positions along a zone refined bar originally of $AgSbTe_2$ concentration after 7 passes at 1/6 cm/hr. T_1= liquidus temperature, T_2= temperature of 2nd thermal arrest on cooling curve.

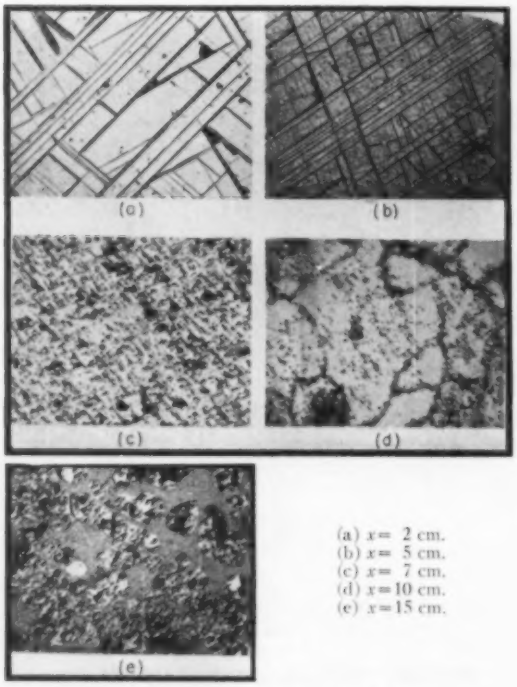

(a) $x = 2$ cm.
(b) $x = 5$ cm.
(c) $x = 7$ cm.
(d) $x = 10$ cm.
(e) $x = 15$ cm.

FIG. 9. Photomicrographs of various microstructures in zone refined bar. 40×.

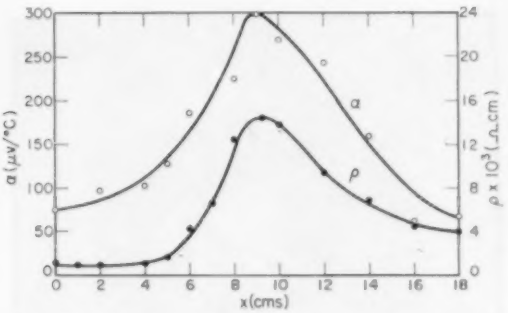

FIG. 10. Plot of resistivity, ρ, and thermoelectric power, α, along the length of the zone refined bar.

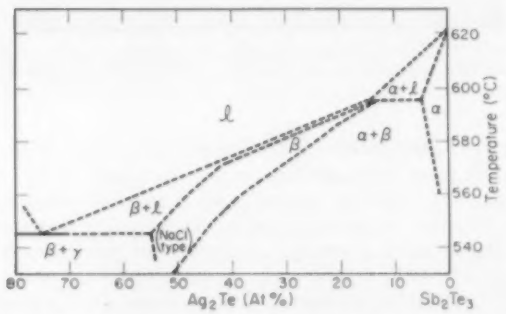

FIG. 11. Most probable pseudobinary $Ag_2Te - Sb_2Te_3$ phase diagram required to explain the results of this study.

phase particle morphology. It should be noted that the morphology of the precipitate changes from the Widmanstatten pattern of plates to tetrahedral shaped particles as the concentration of Ag_2Te in the alloy increases. Knopp hardness tests were made of the matrix material at $x = 2$ cm and $x = 10$ cm on the bar, yielding a hardness of 35 for the former and 110 for the latter. X-ray powder photographs at these positions showed the presence of Sb_2Te_3 and some Sb precipitation. The strength of the lines was much greater at $x = 2$ cm than at $x = 10$ cm. The matrix phase in the two regions exhibited the same lattice parameter.

Electrical measurements of resistivity, ρ, and thermoelectric power, α, were also made at various positions along the bar. These data are presented in Fig. 10.

DISCUSSION

From the metallographic and electron microscope studies alone it is quite obvious that the striated microstructure is due to a platelike precipitate formation rather than twin formation. The morphology of the precipitate is very characteristic of the Widmanstatten pattern. From the chemical analysis, melting points, metallography, and the fact that single crystals form so readily, the most plausible type of phase diagram cut in the ternary Ag, Sb, Te system which explains our results would be that shown schematically in Fig. 11. This figure is not meant to be exact, only representative.

The $AgSbTe_2$ phase may be considered to form as a result of the solution of Ag_2Te in Sb_2Te_3. The Widmanstatten precipitate will thus be Sb_2Te_3 plates nucleating on the {111} planes of the fcc structure. Although we could not unequivocally differentiate between precipitates of Sb and Sb_2Te_3 with our x-ray techniques, the volume fraction of the phases present would favor Sb_2Te_3. Since single crystals were easily obtained, one would expect that the equilibrium partition coefficient of Ag_2Te in $AgSbTe_2$ was close to unity; thus, the separation between the liquidus and solidus must be small.

The large plates of Sb_2Te_3 at the beginning of the sample probably form because the crystal is more perfect here, so that fewer nuclei exist, and because there is more time for diffusion to the plates since they most likely form during the refining of the remainder of the bar and not during cooling. The presence of the large Sb_2Te_3 plates in the beginning of the bar and the smaller Sb_2Te_3 plates in the remainder of the bar will account for the cleavage characteristics. The cleavage will occur on the weak Te-Te bond plane of the Sb_2Te_3 particles and give easy fracture. Large planar cleavage surfaces will occur in the regions of large Sb_2Te_3 plates, and small

faceted cleavage surfaces will occur in the regions of small Sb_2Te_3 plates and the tetrahedral precipitate particles.

The excessive precipitation of plates in the vicinity of dislocation boundaries indicates that this is either a favored site for nucleation or that the nucleation is a cooperative phenomenon.

CONCLUSIONS

1. The compound $AgSbTe_2$ does not appear to be a congruent melting compound, and thus the pseudobinary phase diagrams of Wernick *et al.*[2a] should be treated with caution. This compound forms peritectically in the pseudobinary $Ag_2Te-Sb_2Te_3$ system and is formed over a broad composition range.

2. The solid solubility of Sb_2Te_3 in $AgSbTe_2$ decreases with decrease in temperature and a Widmanstatten precipitate of Sb_2Te_3 plates form epitaxially with their close-packed plane parallel to the {111} planes of the $AgSbTe_2$ lattice.

3. Cleavage in the two-phase $AgSbTe_2-Sb_2Te_3$ crystals occurs most probably across the Te-Te bonds on the close-packed planes of Sb_2Te_3 plates.

4. Any physical property measurements made to date, by anyone, on the $AgSbTe_2$ compound were probably made on two-phase material.

ACKNOWLEDGMENTS

This work was carried out under contract to the Bureau of Ships. Sincere appreciation is due to Dr. R. Stickler for the electron micrographs, Brenda Kagle for the powder photography, and M. Lubell for electrical measurements.

JOURNAL OF APPLIED PHYSICS VOLUME 31, NUMBER 11 NOVEMBER, 1960

Anomalous Hall Effect in $AgSbTe_2$

R. Wolfe, J. H. Wernick, and S. E. Haszko
Bell Telephone Laboratories, Inc., Murray Hill, New Jersey

(Received April 13, 1960)

The Hall coefficient of the ternary semiconductor $AgSbTe_2$ near room temperature is positive in some specimens and negative in others, although the Seebeck coefficient is always positive. The negative Hall coefficient decreases as the temperature is lowered from 180°K to 70°K and changes sign in lower temperatures. This negative Hall coefficient is associated with the presence in the $AgSbTe_2$ of a second phase consisting of Ag_2Te. The properties of the two-phase material are interpreted in terms of the theory of the transport properties of inhomogeneous semiconductors. In single-phase $AgSbTe_2$ containing 3×10^{19} holes per cm^3, the hole mobility is 35 cm^2/v sec at 300°K and it varies approximately as $T^{-0.5}$. {*Note added in proof.* It has been suggested by Armstrong, Faust, and Tiller [J. Appl. Phys. **31**, 1954 (1960)] that the pattern in Fig. 3(a) is associated with the presence of Sb_2Te_3 as a Widmanstätten precipitate along {111} planes in the $AgSbTe_2$. This would indicate that none of the material was single phase. Even though the Sb_2Te_3 in the measured specimens is present in quantities too small to be detected in our x-ray powder photographs, it may have some effect on the measured properties. Therefore, the electrical properties of single-phase $AgSbTe_2$ have yet to be determined.} The lattice thermal conductivity is so low (0.0064 watts/cm°C at 290°K) that the calculated "phonon mean free path" is less than the nearest neighbor distance. The thermal conductivity of a specimen rich in $AgSbTe_2$-Ag_2Te eutectic is higher than that of either of the components. This excess thermal conductivity is attributed to circulating thermoelectric currents.

INTRODUCTION

SILVER antimony telluride is one of a group of ternary semiconducting compounds which have the NaCl type structure.[1,2] $AgSbTe_2$ is partially disordered, with tellurium atoms occupying the chlorine sites, and silver and antimony atoms arranged at random on the sodium sites. The phase relationships existing between this and some other isostructural ternary compounds, as well as some thermoelectric power data, have been reported[3] but very little information is available about the electrical properties.[4] The very low thermal conductivity[4,5] suggests that this material might find applications in thermoelectric refrigeration and generation if the mobilities and effective masses of the carriers are sufficiently high.

In an attempt to determine these parameters, the Hall effect was measured on a number of specimens and an anomaly was observed. Although the Seebeck coefficient was positive in every specimen, the Hall coefficient was positive in some samples and negative in others at room temperature. If this were due to mixed conduction, in a single phase semiconductor, then the

[1] J. H. Wernick and K. E. Benson, J. Phys. Chem. Solids **3**, 157 (1957).
[2] S. Geller and J. H. Wernick, Acta Cryst. **12**, 46 (1959).
[3] J. H. Wernick, S. Geller, and K. E. Benson, J. Phys. Chem. Solids **7**, 240 (1958).
[4] L. D. Dudkin and A. P. Ostranitsa, Doklady Akad. Nauk S.S.S.R. **124**, 94 (1959).
[5] E. F. Hockings, J. Phys. Chem. Solids **10**, 341 (1959).

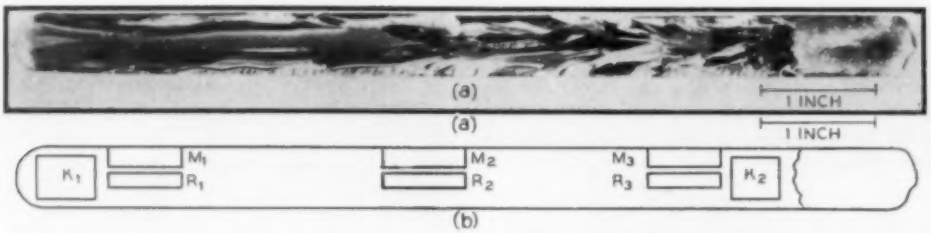

FIG. 1(a). Zone-refined ingot of $AgSbTe_2$ (lead end is on the left). (b). Location of specimens in the zone-refined ingot.

room temperature mobility of the small number of electrons would be greater than 50 000 cm^2/v sec. However, the variations of the negative Hall coefficient and the resistivity with temperature were not consistent with this model.

The measurements made on many specimens are typified by those made on a particular zone-refined ingot which was most carefully investigated [Fig. 1(a)].

EXPERIMENTAL PROCEDURE

The compound $AgSbTe_2$ was prepared by melting together the pure elements (99.999%) in stoichiometric proportion in a sealed quartz tube. The ingot was broken up and placed in a quartz boat, the inside surface of which was roughened by sandblasting with SiC, cleaned in $HF\text{-}H_2O$ solution, dried, and coated with lampblack. This boat was sealed in an evacuated Vycor tube for zone refining. The ingot was given 13 melting passes at about 2 in/hr. The lowest ambient temperature was approximately 200°C, corresponding to a Te vapor pressure of less than 10^{-7} mm Hg (as computed from published data). Another ingot, made under identical conditions, but with 58 passes, was very similar to the first one in all of its properties. These properties, as will be described, were the same within a small factor in all of the ingots which were prepared under various Te pressures up to 0.02 mm Hg, with departures from stoichiometry up to 2% in each of the elements or with the addition of many foreign elements, such as Cu, Sn, In, Ga, Pb, Se, etc., in amounts up to 0.5 wt%.

Measurements

The Seebeck coefficient relative to copper was measured at room temperature on the ingot shown in Fig. 1. Over most of its length the value was between +140 and +240 μv/°C. A small region near the last end to freeze had a smaller Seebeck coefficient of about +30 μv/°C but the sign remained positive everywhere. (On other ingots, the Seebeck coefficient was as high as +320 μv/°C and it was p type in every case.)

The resistivity at room temperature at various positions along this ingot varied from 0.005 to 0.009 ohm cm. On all specimens, prepared in a variety of ways with various additions and departures from stoichiometry, the room temperature resistivity showed only small variations, between 0.004 and 0.011 ohm cm. No correlation was observed between the resistivities and the thermoelectric powers of the various specimens.

The Hall coefficient was the property which showed the largest variations. Near the lead end of the ingot, the Hall coefficient was positive ($R \approx +0.2$ cm^3/coulomb). In specimens cut from the middle of the ingot, the Hall coefficient was too small to be measured with the available apparatus ($R < 0.003$ cm^3/coul). Near the last end to freeze, the Hall coefficient was negative at room temperature and its magnitude was much larger than the positive values. ($|R| \leq 11.0$ cm^3/coul).

Three very different types of Hall effect behavior are typified by the measurements made on three specimens, R_1, R_2, and R_3. The locations of these specimens in the ingot are shown in Fig. 1. At room temperature, these

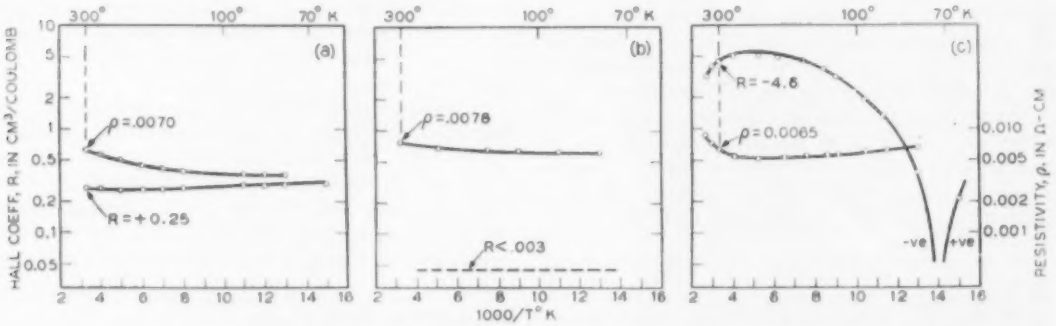

FIG. 2(a–c). Resistivity and Hall coefficient vs temperature measured on specimens R_1, R_2, and R_3.

specimens had the properties given in Table I. The variation with temperature of the resistivity and Hall coefficient of these specimens is shown in Fig. 2. Specimen R_1 behaved like a typical p-type semiconductor in the exhaustion range, with a hole concentration of about 3×10^{19}/cm³. The Hall coefficient remained essentially constant between 70°K and 350°K. In this range the resistivity rose with the temperature. The room temperature mobility was 35 cm²/v sec and it varied approximately as $T^{-\frac{1}{2}}$. For this specimen, the effective mass as calculated from the measured Hall and Seebeck coefficients was $m^*/m=1.1$.

In specimen R_2 the Hall coefficient was at least two orders of magnitude smaller than that of R_1 over the whole temperature range and the resistivity was slightly larger. The resistivity of specimen R_2 was similar to that of R_1, but it reached a minimum at about 180°K and rose slightly at lower temperatures. The negative Hall coefficient reached its maximum magnitude ($R=-5.6$ cm³/coul) at 180°K and then decreased to zero at about 70°K, changing sign at lower temperatures.

TABLE I.

Specimen	Seebeck coefficient (μv/°C)	Resistivity (ohm cm)	Hall coefficient (cm³/coul)
R_1	+170	0.0075	+0.25
R_2	+240	0.0078	<0.003
R_3	+165	0.0065	−4.7

Metallographic Examination

Specimens adjacent to each Hall-effect specimen were metallographically polished and etched for one minute in an acid etch (one part concentrated nitric acid, one part concentrated hydrochloric acid and two parts concentrated potassium persulphate solution). The results observed on specimens M_1, M_2 and M_3, which were located as shown in Fig. 1, are shown in Fig. 3.

In M_1, only one phase appears to be present. (See abstract for note added in proof.) In M_2 there is a small amount of a second phase which is darkly stained. In M_3 much more of this second phase is present and the higher magnification reveals a typical eutectic pattern. The fine structure in M_1, which is brought out by the etching, may be due to stacking faults or microtwinning in the crystal, or may indicate surface damage produced during the polishing operations. Similar etching effects were observed in the primary phase of the two-phase regions.

X-ray powder photographs of specimens near M_1 and M_2 were typical of the cubic silver antimony telluride. Only with a specimen taken from the eutectic-rich region near M_3 did lines corresponding to a second phase appear. This phase was identified as silver telluride (Ag_2Te). It comprised approximately 20% of specimen M_3 (and R_3) but only a small fraction of the whole ingot. (The presence of a small amount of Ag_2Te was also observed in an as-cast ingot by S. Geller.)

Thermal Conductivity

The thermal conductivity was measured near room temperature by an absolute (Lee's disk) method on two specimens from this ingot. Specimen K_1 (see Fig. 1) was

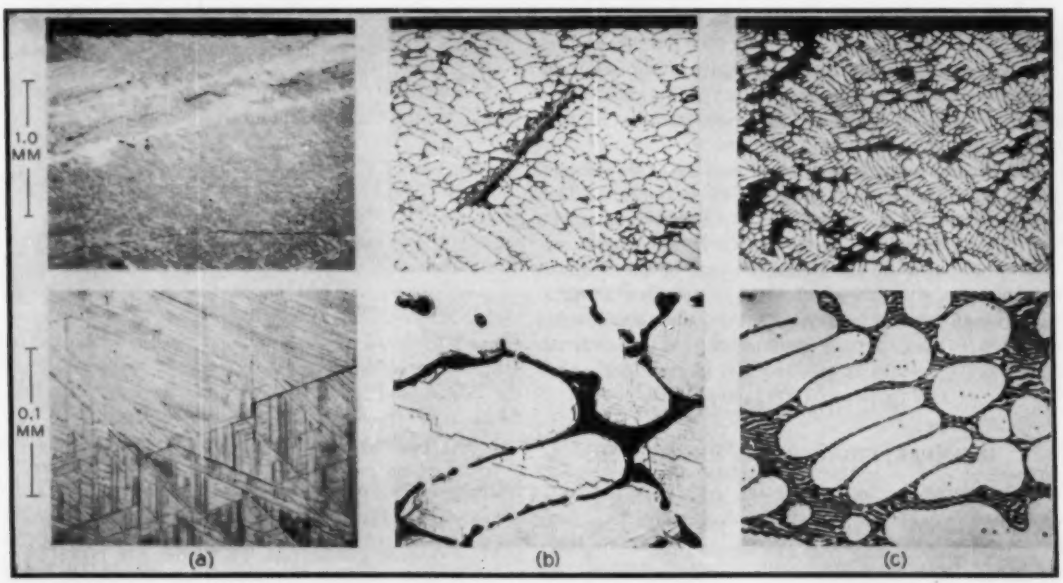

FIG. 3(a–c). Photomicrographs of polished and etched surfaces of specimens M_1, M_2, and M_3.

taken from the single-phase region. Specimen K_2 was rich in eutectic, and was estimated to be about 75% $AgSbTe_2$ and 25% Ag_2Te. The lattice component (κ_{ph}) of the thermal conductivity was determined by subtracting the electronic part from the measured total thermal conductivity of K_1. This electronic part (κ_{el}) was assumed to be proportional to the electrical conductivity with a factor of proportionality typical of a nondegenerate semiconductor, i.e.,

$$\kappa_{el}=2(k/e)^2\sigma T=4.5\times10^{-3}\sigma$$

at room temperature. The result was

$$\kappa_{ph}(AgSbTe_2)=0.0064 \text{ watt/cm°C}.$$

This value, which is assumed to be characteristic of $AgSbTe_2$, is in agreement with Hockings' measurements.[5] On the eutectic-rich specimen K_2, a higher thermal conductivity was measured although the electrical resistivity was approximately the same as that of K_1. The result in this case was

$$\kappa_{total}-\kappa_{el}=0.0075 \text{ watt/cm°C}.$$

The heat capacity of $AgSbTe_2$ as calculated from the usual formula ($C_v=3nR$) is 0.35 cal/°C cm³. A crude measurement gave approximately the same value. The velocity of sound v (longitudinal mode in a polycrystalline sample as measured by V. G. Chirba of these laboratories) was 4.8×10^5 cm/sec. The "phonon mean free path" λ was calculated from the formula

$$\kappa_{ph}=\tfrac{1}{3}C_v v\lambda,$$

using κ_{ph} measured on K_1, and the result was $\lambda=2.7\times10^{-8}$ cm. The nearest neighbor distance in $AgSbTe_2$ is $\frac{1}{2}$ the lattice parameter[2], or 3.04×10^{-8} cm. Therefore, the calculated phonon mean free path is shorter than the nearest neighbor distance. This type of anomaly has been reported by Ioffe[6] for materials such as In_2Te_3, which also has a disordered structure.

The thermal conductivity of a specimen of Ag_2Te was also measured. The result was 0.0109 watt/cm°C. The resistivity of this specimen was 0.0013 ohm cm, and its Seebeck coefficient was -98 μv/°C. It was, therefore, difficult to calculate the electronic part of the thermal conductivity with certainty. However, using the assumption of nondegeneracy, as before, the phonon contribution to the thermal conductivity was estimated to be

$$\kappa_{ph}(Ag_2Te)=0.007 \text{ watt/cm°C}.$$

INTERPRETATION OF THE RESULTS

In all of the specimens investigated, a positive Hall coefficient was found in single-phase $AgSbTe_2$ (see abstract for note added in proof), a very small Hall coefficient was associated with a small amount of second phase, and a negative Hall coefficient was found in specimens containing $AgSbTe_2$-Ag_2Te eutectic. It appears that the *p*-type $AgSbTe_2$ always dominates the thermoelectric properties, but that 10% or 20% of *n*-type Ag_2Te is enough to dominate the room temperature Hall coefficient.

This behavior is consistent with the theory of the transport properties of inhomogeneous systems, which has recently been investigated by Odelevskii,[7] Airapetiants,[8] and Herring.[9] The first two authors have calculated the conductivity, thermoelectric power, and excess thermal conductivity due to circulating thermoelectric currents of multiphase systems, using the model of spheres of each phase imbedded in an infinite medium with the average properties. Herring has calculated many of the transport properties, including the Hall effect, of inhomogeneous or multiphase systems in which the fluctuations in the properties are small. However, his expressions for the conductivity and Seebeck coefficient of a two-phase system agree fairly well with those of Odelevskii and Airapetiants even when the difference between the resistivities is large and even when the Seebeck coefficients of the two phases have opposite signs. It is probable that his Hall-effect result is also reasonably accurate for a two-phase system in which the two separate Hall coefficients are of opposite sign.

For convenience, the relevant formulas for a two-phase system are quoted here. In the expression for a property P, say, the properties of the individual phases are denoted by P_1 and P_2; P_A is the effective property of the system according to Airapetiants or Odelevskii; P_H is the effective property according to Herring, and $\langle P\rangle$ is the simple volume average $(x_1P_1+x_2P_2)$, where x_1 and x_2 are the volume fractions of the two phases.

1. Electrical conductivity σ (similar expressions apply for the thermal conductivity κ):

$$\sigma_H=\langle\sigma\rangle\left[1-\frac{x_1}{3}\frac{(\sigma_1-\langle\sigma\rangle)^2}{\langle\sigma\rangle^2}-\frac{x_2}{3}\frac{(\sigma_2-\langle\sigma\rangle)^2}{\langle\sigma\rangle^2}\right]. \quad (1)$$

$$\sigma_A:\ x_1(\sigma_1-\sigma_A)/(\sigma_1+2\sigma_A)+x_2(\sigma_2-\sigma_A)/(\sigma_2+2\sigma_A)=0. \quad (2)$$

2. Seebeck coefficient S:

$$S_H=\langle S\rangle-\sum_{i=1,2}S_ix_i\left(\frac{1}{3}\frac{\kappa_i-\langle\kappa\rangle}{\langle\kappa\rangle}+\frac{2}{3}\frac{\rho_i-\langle\rho\rangle}{\langle\rho\rangle}\right). \quad (3)$$

$$S_A=[S_1\sigma_1\gamma_1+S_2\sigma_2\gamma_2]/[1-2\sigma_A(\gamma_1+\gamma_2)], \quad (4)$$

where

$$\gamma_i=3\kappa_Ax_i/(2\sigma_A+\sigma_i)(2\kappa_A+\kappa_i).$$

[6] A. F. Ioffe, Soviet Phys.—Solid State **1**, 141 (1959).

[7] V. I. Odelevskii, Zhur. Tekh. Fiz. **21**, 667, 678, 1379 (1951).

[8] C. V. Airapetiants, Soviet Phys.—Tech. Phys. **2**, 429 (1957); C. V. Airapetiants and M. S. Bresler, *ibid.* **3**, 1778 (1958).

[9] C. Herring (to be published).

3. Hall coefficient R:

$$R_H=\frac{\langle\sigma^2R\rangle}{\langle\sigma\rangle^2}\left\{1+\tfrac{2}{3}\sum_{i=1,2}x_i\left[\frac{(\sigma_i-\langle\sigma\rangle)^2}{\langle\sigma\rangle^2}-\frac{(\sigma_i^2R_i-\langle\sigma^2R\rangle)(\sigma_i-\langle\sigma\rangle)}{\langle\sigma^2R\rangle\langle\sigma\rangle}\right]\right\}. \quad (5)$$

4. Excess thermal conductivity $\Delta\kappa$:

$$(\Delta\kappa)_A=\sum_{i=1,2}x_i\frac{2(S_i-S_A)^2}{(1+2\sigma_A/\sigma_i)}\sigma_AT. \quad (6)$$

The variation of the (negative) Hall coefficient with temperature of specimens such as R_3, the excess thermal conductivity of specimen K_2, and the consistently positive Seebeck coefficient can be understood qualitatively with the help of these equations. It may be assumed that the $AgSbTe_2$ in the two-phase specimens has properties similar to those measured on specimens R_1 and K_1, and that the Ag_2Te has properties similar to those reported by Appel.[10]

To account for the large negative Hall coefficient in R_3 at 180°K and the zero Hall coefficient at 70°K, the following assumptions were made about the hole mobility μ_h in $AgSbTe_2$ and the electron mobility μ_e in Ag_2Te.

	180°K	70°K
$AgSbTe_2$	$\mu_h=50$	$\mu_h=90$
Ag_2Te	$\mu_e=4000$	$\mu_e=4000$

It was estimated that the volume fraction of $AgSbTe_2$ was 0.8 and that of Ag_2Te was 0.2. From the measured values of the conductivity and Hall coefficient at the two temperatures, using Eqs. (1) and (5), the separate conductivities and Hall coefficients were calculated:

	180°K	70°K
$AgSbTe_2$	$\sigma_1=165\Omega^{-1}$ cm^{-1} $R_1=+0.30$ cm^3/coul	$\sigma_1=300$ $R_1=+0.30$
Ag_2Te	$\sigma_2=235$ $R_2=-17$	$\sigma_2=16$ $R_2=-250$

These calculated properties of $AgSbTe_2$ are close to those measured on the single-phase material. The calculated properties of Ag_2Te at these two temperatures are shown in Fig. 4. The dashed curves in this figure show the estimated resistivity of the Ag_2Te in specimen R_3 as a function of temperature. These properties, combined with the slowly varying properties of the $AgSbTe_2$, yield the effective properties measured on R_3. This behavior is very similar to that observed by Appel[10] (curve 1 of Fig. 4).

It appears that the Ag_2Te has a much larger negative Hall coefficient at low temperatures while the positive Hall coefficient of the $AgSbTe_2$ changes only slightly, and yet the resultant effective Hall coefficient becomes

[10] J. Appel and G. Lautz, Physica **20**, 1110 (1954); J. Appel, Z. Naturforsch. **10A**, 530 (1955).

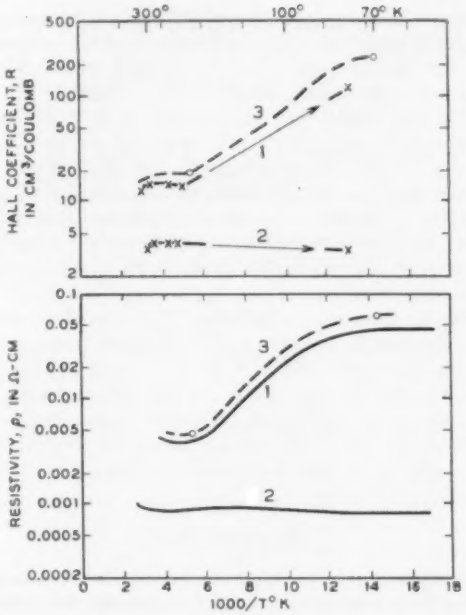

FIG. 4. Hall coefficient and resistivity vs temperature of Ag_2Te. Curves 1 and 2—measured by Appel; curves 3—estimated properties of second-phase material in specimen R_3.

positive. The reason for the sign reversal at low temperatures is that the resistivity of the Ag_2Te also rises by a large factor as the temperature is lowered, and the current flows mainly in the $AgSbTe_2$. In the expression for the effective Hall coefficient, Eq. (5), the conductivities are squared whereas only the first power of each Hall coefficient is involved.

In specimen K_2, $(\kappa_{\text{total}}-\kappa_{el})$ is greater than the lattice thermal conductivity of either of the components. The excess thermal conductivity is probably due to circulating currents and the associated Peltier heat flow as described by Airapetiants.[8] If it is assumed that the composition of the specimen is $\frac{3}{4}$ $AgSbTe_2$ and $\frac{1}{4}$ Ag_2Te, that the two thermal and electricity conductivities are equal ($\kappa_1=\kappa_2$; $\sigma_1=\sigma_2=180$ Ω^{-1} cm^{-1}), and that the Seebeck coefficients are $+200$ μv/°C and -200 μv/°C respectively, then the effective Seebeck coefficient according to Eq. (3) is $+100$ μv/°C as measured, and the excess thermal conductivity as given by Eq. (6) is

$$\Delta\kappa=0.0011 \text{ watts/cm°C},$$

in agreement with the measured value.

The effective Seebeck coefficient of the two-phase regions will be approximately equal to the simple volume average $\langle S\rangle$, if the resistivities and thermal conductivities of the two phases are similar [see Eqs. (3) and (4)]. This is the case for $AgSbTe_2$ and Ag_2Te at room temperature in eutectic-rich material. Since the $AgSbTe_2$ is always the major phase, and since the

negative Seebeck coefficient of the Ag_2Te is probably no larger in magnitude than the positive Seebeck coefficient of the $AgSbTe_2$, the effective Seebeck coefficient is positive at room temperature on all specimens.

The very small Hall effect observed in R_2 at room temperature indicates that the small volume fraction of Ag_2Te, with its relatively large negative Hall coefficient, is just sufficient to compensate the much larger volume fraction of $AgSbTe_2$ with its small positive Hall coefficient. The fact that the effective Hall coefficient remains very small over the whole temperature range suggests that the properties of the Ag_2Te must vary just as slowly as those of the $AgSbTe_2$. This type of behavior was observed by Appel in Ag_2Te with room temperature conductivity near $1000\,\Omega^{-1}\,cm^{-1}$ (see curve 2 of Fig. 4). It appears that zone melting not only moves the Ag_2Te toward the last end to freeze but also changes its doping level, so that the Ag_2Te which remains near the center of the ingot has a higher conductivity than that in the eutectic-rich region.

CONCLUSIONS

In $AgSbTe_2$, the presence of a second phase consisting of Ag_2Te in zone-refined ingots accounts for the anomalous Hall effect and the excess thermal conductivity observed in some specimens. A similar anomalous reversal in the sign of the Hall coefficient has been observed in p-type InAs at low temperatures, but this was attributed to the presence of microscopic n-type regions in the single-phase material.[11] In future work on this and other ternary compounds, it will be essential to verify that the samples studied are single phase before any of the basic properties of the semiconductor can be determined.

In the single-phase $AgSbTe_2$ specimens such as R_1 [Fig. 1(b)], the low mobility may be due to imperfections in the crystal which are associated with the crystallographic etching pattern shown in Fig. 3(a). It may be possible to eliminate these imperfections by changing the crystal growth conditions. The doping experiments will be repeated on single-phase $AgSbTe_2$ in an attempt to control the hole concentration and to produce n-type material.

The presence of Ag_2Te in these zone-melted ingots which were made from stoichiometric amounts of the pure elements suggests that the primary phase may depart from the stoichiometry of $AgSbTe_2$. The pseudobinary system Sb_2Te_3-Ag_2Te is being investigated to determine whether the maximum melting point is on the Sb_2Te_3 side of the $AgSbTe_2$ point.

ACKNOWLEDGMENTS

The authors are indebted to Conyers Herring for valuable suggestions about the interpretation of these experiments and permission to use his theoretical results before publication, and to E. E. Thomas and S. Preziosi for metallographic assistance.

[11] J. R. Dixon, J. Appl. Phys. **30**, 1412 (1959).

Diffusion of Ag^+, Cl^-, and Cd^{++} in Silver Chloride Single Crystals*

RICHARD F. READE AND DON S. MARTIN, JR.
Institute for Atomic Research and Department of Chemistry, Iowa State University, Ames, Iowa
(Received April 22, 1960)

The diffusion rates of silver, chlorine, and cadmium ions in single crystals of silver chloride have been investigated by means of a modification of the surface counting method. The diffusion coefficient of the silver ion from 200° to 400°C was represented by the equation $D=9.36\exp(-1.01\text{ ev}/kT)$ cm²/sec. Estimates of chloride ion activation energies gave a value of 1.57 ev between 350° and 400°C, and a value of 0.37 ev below 280°C. The silver and chloride ion diffusion data have been compared with results of workers who used sectioning methods. The diffusion coefficient of the cadmium ion may be expressed by the equation $D=32.8\exp(-1.36\text{ ev}/kT)$ cm²/sec $+2.35\times10^{-5}\exp(-0.56/kT)$ cm² sec.

INTRODUCTION

THE diffusion coefficients of Ag^+, Cl^-, and Cd^{++} in single crystals of silver chloride have been measured by a surface activity method. The procedure depends upon the fact that half-thicknesses for the absorption of beta radiation in the crystals correspond to migration distances which are readily obtainable.

In this procedure the diffusing ion, bearing a radioactive nuclide, is introduced onto a plane face of a cylindrical crystal. The radiation A_0 from the surface is measured with a window-type G-M counter mounted in a reproducible geometry over the face of the crystal. Next, the crystal is annealed in a furnace for a known time at a known temperature. Following the anneal, the radiation from the surface A is counted under identical conditions as before, and the ratio A/A_0 serves to characterize the degree of penetration of the radioactive ions into the crystal. The ratio of the surface radiation intensity before and after diffusion in a crystal of length L and cross section S may be expressed by the integral in Eq. (1).

$$A/A_0=\int_0^L \frac{C(x,t)S}{Q}\epsilon_x dx, \qquad (1)$$

where x is the depth below the surface, t is the time, $C(x,t)$ is the concentration of radioactive tracer at x and t, Q is the total activity deposited on the crystal face before diffusion, and ϵ_x is the ratio of the counting rate for a given amount of tracer a distance x below the surface to the counting rate of the same amount of tracer at the surface.

For a thick crystal, the solution of Fick's diffusion equation with appropriate boundary conditions is

$$[C(x,t)S]/Q=[\exp(-x^2/4Dt)]/(\pi Dt)^{\frac{1}{2}}, \qquad (2)$$

and Eq. (1) becomes

$$A/A_0=\frac{1}{(\pi Dt)^{\frac{1}{2}}}\int_0^x \exp(-x^2/4Dt)\epsilon_x dx, \qquad (3)$$

where D is the diffusion coefficient which is taken to be independent of concentration of the diffusing species.

During the diffusion anneal, a certain amount of tracer diffuses into the volume increment between x and $x+dx$ shown in Fig. 1(a). The activity in this increment is now $(a+x)$ cm away from the window of the counting tube. The emitted radiation must pass through the intervening thickness of silver chloride, where it is scattered and absorbed, before it is counted. The emergent radiation contributes differently to A than would radiation emitted from an equivalent amount of tracer at the surface. The ratio ϵ_x which is needed for this method can be evaluated empirically.

This evaluation of ϵ_x as a function of x must be very accurate to obtain satisfactory diffusion coefficients.

With activity upon an end face of a crystal, the radiation was counted with the G-M tube as shown in Fig. 1(a). The sample holder provided some degree of collimation and shielded the counter from the edges of the crystal. An absorber which was rolled from silver chloride was inserted before the crystal, and the radiation was counted as shown in Fig. 1(b). The absorber, identical with the crystal material, replaced the crystal between 0 and x, and the radioactive surface was a distance x behind the surface. In this way, the face of the crystal bearing the radioactivity lay behind the absorber in the identical position and environment relative to the counting tube as did the plane at x in the diffusion crystal.

Curves of ϵ_x vs absorber thickness are shown in Fig. 2. Values greater than 100% were obtained for ϵ_x with

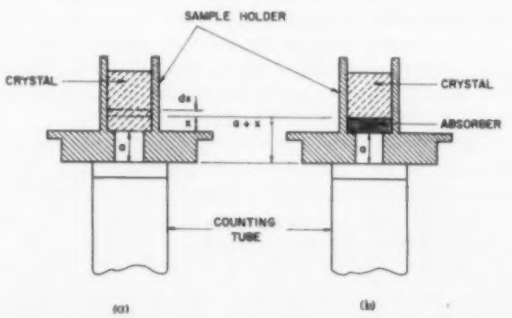

FIG. 1. Counting arrangement for single crystals. (a) Crystal without absorber. (b) Absorber inserted before crystal.

* Contribution No. 865. Work was performed in the Ames Laboratory of the U. S. Atomic Energy Commission.

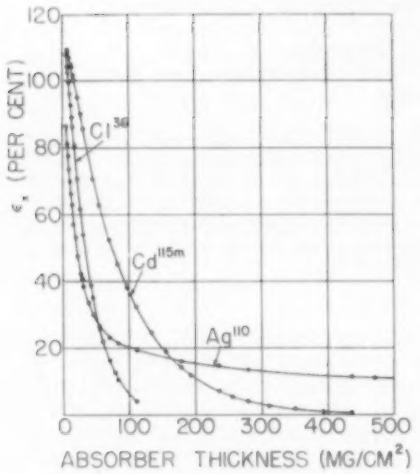

FIG. 2. Transmittancies of radiations in AgCl.

thin absorbers for the Cl^{36} and Cd^{115m} radiation. This feature is commonly encountered in the counting of beta rays, and it is caused by scattering of the beta rays by the absorbers into the detector which overshadows the absorption at these thicknesses. It has been discussed by Novey and Elliott.[1] Because of the shape of the curves, ϵ_x values could not be extrapolated satisfactorily to zero thickness of the absorber. In order to avoid the need for extrapolation, a thin reference absorber was positioned before the active face of the diffusion crystals for A and A_0 measurements. The experimentally determined values of ϵ_x and thickness for each absorber were standardized to the reference absorber. The integration indicated in Eq. (3) was performed numerically to provide an A/A_0 vs Dt plot for each of the isotopes. This procedure appears to be similar to that employed by Ruder and Birchenall[2] in studies of the diffusion of cobalt and nickel in cobalt.

The success of the surface activity method depends critically on a satisfactory evaluation of the function ϵ_x. However, in a number of attempts to use surface counting methods,[3] an absorption coefficient has been obtained under a geometry different from that of the diffusion measurements. In general, attempts in the past to use a surface activity method have yielded less satisfactory results for the evaluation of diffusion coefficients than recent sectioning techniques.

Carefully performed sectioning experiments for the diffusion of Ag^+ and Cl^- in silver chloride have been reported by Compton and Maurer,[4] and one important aim of the present work has been a comparison of the sectioning procedure with the surface activity method in which a valid absorption curve has been used.

[1] T. B. Novey and N. Elliott, *Radiochemical Studies: The Fission Products* (McGraw-Hill Book Company, Inc., New York, 1951), National Nuclear Energy Series, Vol. 9, Div. IV, Paper 3, Book I, p. 44.

[2] R. C. Ruder and C. E. Birchenall, J. Metals **3**, 142 (1951).

[3] See, for example, J. Steigman, W. Shockley, and F. C. Nix, Phys. Rev. **56**, 13 (1939).

[4] W. D. Compton and R. D. Maurer, Phys. and Chem. Solids **1**, 191 (1956).

EXPERIMENTAL

Crystal and Absorbers

The source of the single crystals was a large single crystal ingot of silver chloride supplied by the Harshaw Chemical Company. Diffusion and absorption crystals were cut from the ingot with a low-speed lathe. For silver and cadmium diffusion experiments cylindrical crystals 1.33 cm in diameter and about 2 cm long were used. For chloride diffusion and all the absorption measurements, the crystals were 1.33 cm in diameter and about 1 cm long. The flat crystal faces were hand-polished to a mirror surface and the crystals were then annealed in air at 400°C for 24 hr. They were furnace-cooled at the rate of 50°C/hr. Subsequently, they were stored in the dark and handled in a darkened room.

Silver chloride absorbers were prepared from scrap single crystal material. A hand-operated rolling mill was used to roll the specimens into thin sheets. After a few passes they were annealed at 400°C for a few hours and cooled in air to reduce brittleness. By repetition of the rolling-annealing cycle, sheets as thin as 15 mg/cm^2 were obtained. To obtain thinner foils, three sheets, stacked together, were rolled. The outer sheets were peeled away from the center sheet, which had been reduced to 5.0 to 15.0 mg/cm^2. Circular absorbers, to fit the counter mount, were cut from the sheets. They were then annealed in air for 24 hr. Diameters were measured with a Cambridge Universal Measuring Machine, and weights were obtained with a Volhard Model 560-D balance. Thicknesses, expressed in mg/cm^2, were accurate to within 1%.

Application of Radioactivity

Radioactive tracers were obtained from the Oak Ridge National Laboratory of the U. S. Atomic Energy Commission. The tracers, used without purification, were (1) Ag^{110} as $AgNO_3$ solution, (2) Cl^{36} as HCl solution, and (3) Cd^{115} as $Cd(NO_3)_2$ solution.

A large drop of the nitrate solution of Ag^* was placed on the crystal face for about 30 sec. The tracer was apparently deposited by an exchange mechanism.

To deposit chlorine activity, the crystal surface was first reduced to a thin metallic film by treatment with a drop of a dilute hydrazine solution. This film was then oxidized to the chloride by treatment with a solution of Cl_2 and HCl^*. With the rapid exchange between the Cl^- and the Cl_2, the silver deposit was converted into a layer of $AgCl^*$ whose thickness was about 1 μ.

For the cadmium activity, the surface of the silver chloride crystal was reduced by the hydrazine procedure. A solution of Cd^*Cl_2 solution was evaporated to dryness on the surface. The reduced silver was then

TABLE I. Experimental data.

Diffusing ion	Temperature, °C	A/A_0	Time, sec	Diffusion coefficient (D), cm²/sec
Silver	403	0.231	5130	2.65×10^{-7}
Silver	402	0.233	5130	2.51×10^{-7}
Silver	401	0.299	1530	2.35×10^{-7}
Silver	401	0.302	1530	2.26×10^{-7}
Silver	351	0.335	3330	6.13×10^{-8}
Silver	351	0.290	6990	5.96×10^{-8}
Silver	350	0.393	1530	5.86×10^{-8}
Silver	350	0.293	6990	5.74×10^{-8}
Silver	298	0.500	2130	1.18×10^{-8}
Silver	298	0.377	10 530	1.06×10^{-8}
Silver	297	0.372	10 530	1.05×10^{-8}
Silver	250	0.542	11 730	1.39×10^{-9}
Silver	249	0.516	11 730	1.82×10^{-9}
Silver	199	0.695	24 930	1.39×10^{-10}
Silver	199	0.705	24 930	1.24×10^{-10}
Silver	175	0.685	78 930	4.84×10^{-10}
Silver	148	0.847	43 590	1.20×10^{-11}
Silver	148	0.863	43 590	9.20×10^{-12}
Chloride	402	0.570	86 130	1.61×10^{-10}
Chloride	351	0.761	183 330	1.58×10^{-11}
Chloride	351	0.799	93 450	2.05×10^{-11}
Chloride	301	0.886	172 530	3.22×10^{-12}
Chloride	253	0.900	280 530	1.52×10^{-12}
Chloride	198	0.939	259 230	5.82×10^{-13}
Cadmium	402	0.534	28 530	4.00×10^{-9}
Cadmium	398	0.378	107 730	3.17×10^{-9}
Cadmium	350	0.683	33 930	1.09×10^{-9}
Cadmium	336	0.745	28 530	7.54×10^{-10}
Cadmium	300	0.813	39 930	2.70×10^{-10}
Cadmium	275	0.820	50 130	1.99×10^{-10}
Cadmium	249	0.857	78 930	7.83×10^{-11}
Cadmium	225	0.872	75 330	6.57×10^{-11}
Cadmium	199	0.908	93 330	2.76×10^{-11}
Cadmium	149	0.953	147 990	4.90×10^{-12}

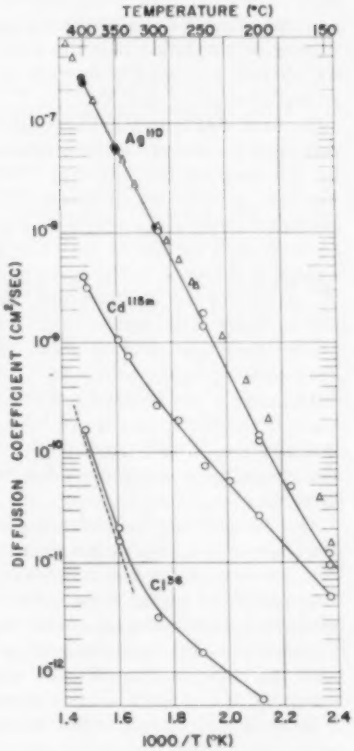

FIG. 3. Temperature dependence of diffusion coefficients in AgCl. ●: Present work—average of two points. ○: Present work—single point. Δ: Ag^+ data of Compton (footnote reference 5). – – – –: Expression reported by Compton and Maurer for the diffusion coefficient of the chloride ion in AgCl.

oxidized with dry chlorine gas. No more than 10^{-8} moles of Cd^*Cl_2 were deposited on the surface. The cadmium surface had to be handled carefully, for the activity was easily rubbed off.

Diffusion Anneals

Diffusion anneals were carried out in an air atmosphere. The core of the diffusion furnace consisted of an aluminum block to minimize thermal gradients in the vicinity of the sample. Temperature was controlled to within ±0.5°C for all runs and was measured with a calibrated chromel-alumel thermocouple. Appropriate heating time corrections were applied.

RESULTS AND DISCUSSION

Experimentally determined A/A_0 ratios and the corresponding values of the diffusion coefficient are shown in Table I. The uncertainties in the A/A_0 values were of the order of 1% to 2.5%. Uncertainties of this magnitude in A/A_0 introduce rather large uncertainties in the diffusion coefficients which are taken from the logDt vs A/A_0 plots. The estimated relative uncertainty for the silver diffusion coefficients was about 10% except for the 150°, point where it was 20%. For chlorine the relative uncertainty ranged from 8% at 400° to about 40% at 200°. The relative uncertainty for cadmium ranged from 8% at 400° to 28% at 200°. The cadmium diffusion coefficient at 150° had an apparent relative uncertainty of 58%. This large error resulted from the fact that the A/A_0 ratio was in the region of very steep slope on the logDt-A/A_0 curve. It is believed that a substantial reduction in the geometry and counting errors can not be achieved with G-M counters. Possible improvement may be achieved by the use of a counting system which incorporates a rigidly mounted gas-flow proportional counter. Preliminary results show that such a counter is much superior in performance to the G-M counter, and it is hoped that this new system will reduce the error in the diffusion coefficient to well below 10%.

Because of the large apparent uncertainty in the diffusion data, only qualitative or semiquantitative observations are presently possible. Plots of the temperature dependence of the diffusion coefficients for each of the ions are shown in Fig. 3. Data obtained by other investigators using the sectioning technique are illustrated for comparison. An inspection of the curves indicates that the diffusion of the chloride ion is much slower than that of the silver ion, a fact which is in

good agreement with the transport data of Tubandt[5] and the diffusion experiments of Compton and Maurer. It may be concluded that the silver ion is responsible for all but a negligible fraction of mass and charge transport in silver chloride.

Between 400°C and 200°C the Ag^+ diffusion coefficients from the present investigation are fitted very well by the equation $D=9.36\ \exp(-1.01\ \text{ev}/kT)\ \text{cm}^2/\text{sec}$. For the intrinsic region below 350°C, Compton and Maurer expressed Compton's[6] data by the equation $D=1.46\ \exp(-0.890\ \text{ev}/kT)\ \text{cm}^2/\text{sec}$. They noted a change in the slope of the curve of diffusion coefficient vs reciprocal of temperature in the vicinity of 350°C. Their curve agrees rather well with that of the present investigation from about 325°C to 400°C, but lies somewhat higher below 300°C. The reason for this discrepancy is not obvious, but it may be due to differences in the purity of the crystals. The results of this investigation do not conflict with the predictions of the interstitialcy mechanism for the diffusion of the silver ion.[7]

The temperature dependence plot of the diffusion coefficient of the chloride ion shows pronounced curvature. In view of the inaccuracies of the data and the continuously changing slope, a resolution of the temperature dependence plot could not be satisfactorily accomplished. The estimation of an activation energy from the slope of the diffusion coefficient curve between 350°C and 400°C gives a value of about 1.57 ev. A value of 0.37 ev was indicated for that part of the curve below 280°C. Compton and Maurer measured the diffusion coefficient of the chloride ion in silver chloride and expressed their data by the equation $D=133\ \exp(-1.61\ \text{ev}/kT)\ \text{cm}^2/\text{sec}$. The activation energy of 1.61 ev is in good agreement with the high temperature value noted above. It is unfortunate that these workers did not extend their studies to the region below 324°C where the present work indicates such a dramatic change in slope. Tannhauser[8] measured the diffusion coefficient of the bromide ion in silver bromide and found a definite curvature in the diffusion coefficient-temperature plot which he felt was not due to experimental error. From an investigation of the activation volume for bromide ion diffusion he concluded that a vacancy mechanism was followed, but he could not resolve the curvature. The high temperature activation of 1.57 ev found in this investigation is consistent with a vacancy mechanism, but the low temperature value of 0.37 ev seems too small to be associated with the volume diffusion of an individual chloride vacancy or ion. It may be indicative of the movement of silver vacancy-chlorine vacancy complexes, although the possibility of surface diffusion cannot be excluded.

In the diffusion of cadmium ion there was, of course, a concentration gradient in the crystals. The assumption has been made that the diffusion of cadmium was independent of the cadmium ion concentration in the range studied. If the greatest amount of cadmium used were distributed uniformly through a layer 1 μ in thickness, the Cd:Ag ratio would be 1:500. The concentration was much below this value for the greater part of the significant diffusion process. The consistency of the diffusion coefficients over the temperature range can be seen in Fig. 2 to be quite satisfactory. When it is recognized that A/A_0 ratios ranged from 0.38 to above 0.9 and that the total Cd content varied by a factor of two among the different experiments, it appears that possible vacancy currents and interactions between Cd^{++} were not influencing the processes within the experimental uncertainties.

The diffusion coefficient-temperature curve exhibits a change in slope at about 320°C. If the data are considered to indicate two competing diffusional modes, the following expression is obtained: $D=32.8\ \exp(-1.36/kT)\ \text{cm}^2/\text{sec}+2.35\times10^{-5}\ \exp(-0.56/kT)\ \text{cm}^2/\text{sec}$. It is now thought that the cadmium ion exists in the silver sublattice by occupying a silver lattice site with the introduction of an accompanying silver ion vacancy to maintain the electrical neutrality in the crystal. The small value of D_0 and the low activation energy (0.56 ev) for the low temperature process may characterize the movement of the cadmium ion in close association with a silver vacancy, i.e., as an uncharged complex. The high temperature process has a D_0 value and an activation energy which are in the range generally with volume ionic diffusion. This high temperature term may be indicative of the movement of an unassociated cadmium ion, but the mechanism of diffusion of this doubly positive ion is not understood. As in the case of the chlorine isotope, the possibility of a significant surface diffusion contribution at low temperatures should not be ignored.

The use of the surface counting technique for diffusion measurements should provide results of comparable accuracy to those obtained by sectioning procedures, if an empirical absorption curve is used and if all counting is done under sufficiently reproducible conditions. Comparison or results obtained in this investigation with the sectioning work of Compton and Maurer shows over-all qualitative agreement, although some discrepancies exist which have no apparent explanation. It is hoped that these discrepancies will be resolved by the use of an improved counting system.

[5] C. Tubandt, Z. anorg. u. allgem. Chem. **115**, 113 (1920).
[6] W. D. Compton, unpublished Ph.D. thesis (University of Illinois Library, Urbana, Illinois, 1955).
[7] C. W. McCombie and A. B. Lidiard, Phys. Rev. **101**, 1210 (1956).
[8] D. S. Tannhauser, Phys. and Chem. Solids **5**, 224 (1958).

Measurement of Orientation in Polypropylene Film

ZIGMOND W. WILCHINSKY
Esso Research and Engineering Company, Linden, New Jersey

(Received May 5, 1960; and in final form, June 16, 1960)

An average fiber axis orientation in polypropylene film was measured quantitatively from x-ray diffraction determination of orientation of two planes containing this axis. This orientation was expressed as the average square cosine of the angle between the fiber axis and a chosen reference direction in the sample. It was necessary to use an indirect method since there are no crystal planes perpendicular to the fiber axis. The nature of the fiber axis orientation thus determined was found to be consistent with birefringence measurements and qualitative deductions from pole figures. Films produced by flat die extrusion showed a double orientation in which the fiber axis is preferentially oriented in the extrusion direction, and the (010) crystal face is parallel to the film surface. Both components of the orientation tended to be of the same magnitude.

INTRODUCTION

ORIENTATION of the c axis (fiber axis) in crystalline polymers can be measured rather directly by x-ray diffraction methods if there is a plane of symmetry perpendicular to this axis, and if there is a convenient set of diffracting $00l$ planes. However, if the plane of symmetry is absent, as in the case of monoclinic polypropylene,[1] then there is no set of planes that reveals the c-axis orientation directly. In this case, it may be possible to obtain a measure of average orientation from measurements of diffraction from two sets of planes containing the c axis. The feasibility of this indirect method is evaluated here by quantitative diffraction measurements of polypropylene film. Measurements were also made of the b-axis orientation.

METHOD OF MEASUREMENT

A measure of average orientation of the c axis in a reference direction Q, fixed in a sample, can be expressed as the average square cosine of the angle σ between c and Q. This orientation parameter, $\langle\cos^2\sigma\rangle_{hl}$, was evaluated in terms of the orientation of plane normals similarly expressed as $\langle\cos^2\phi\rangle_{hl}$ where ϕ is the angle between Q and the normal P to a set of hkl planes. The direction of P is specified by the coordinates ϕ and ψ in a spherical coordinate system shown in Fig. 1, in which Q is the axis of the coordinate sphere.

Experimental values of $\langle\cos^2\phi\rangle_{hl}$ were determined by averaging $\cos^2\phi$ over the entire surface of the coordinate sphere. Because of symmetry relationships in the sample, averaging over one octant of the sphere was sufficient. This average is expressed mathematically by the following equation:

$$\langle\cos^2\phi\rangle_{hl}=\frac{\int_0^{\frac{1}{2}\pi}\int_0^{\frac{1}{2}\pi} I(\phi,\psi)\cos^2\phi\sin\phi d\psi d\phi}{\int_0^{\frac{1}{2}\pi}\int_0^{\frac{1}{2}\pi} I(\phi,\psi)\sin\phi d\psi d\phi}=\frac{\int_0^{\frac{1}{2}\pi} I(\phi)\cos^2\phi\sin\phi d\phi}{\int_0^{\frac{1}{2}\pi} I(\phi)\sin\phi d\phi}, \quad (1)$$

where $I(\phi,\psi)$ is the pole concentration representing the relative amount of crystalline material having plane normals in the direction ϕ,ψ, and

$$I(\phi)=\int_0^{\frac{1}{2}\pi} I(\phi,\psi)d\psi.$$

The intensity of the diffraction peak (corrected for background, absorption, sample geometry, etc.) at each position specified by the spherical coordinates was taken to be proportional to the pole concentration.

Since the b axis is perpendicular to the strongly reflecting 040 planes, its orientation parameter is given directly by Eq. (1); it is $\langle\cos^2\phi\rangle_{hl}$ for the 040 planes.

An expression for the c-axis orientation parameter was obtained from general relationships previously reported by the author.[2,3] It follows from these relationships that values of $\langle\cos^2\phi\rangle_{hl}$ for two planes containing the c axis are sufficient for evaluating $\langle\cos^2\sigma\rangle_{hl}$. The appropriate equation can be written in the form $\langle\cos^2\sigma\rangle_{hl}=1$

$$-\frac{(1-2\sin^2\rho_2)\langle\cos^2\phi_1\rangle_{hl}-(1-2\sin^2\rho_1)\langle\cos^2\phi_2\rangle_{hl}}{\sin^2\rho_1-\sin^2\rho_2}, \quad (2)$$

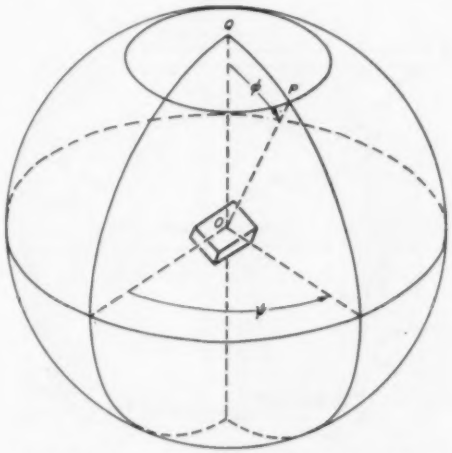

FIG. 1. Position of plane normal P specified by spherical coordinates ϕ and ψ.

[1] G. Natta, P. Corradini and M. Cesari, Atti accad. naz. Lincei. Rend. Classe fis. mat. e nat. **21**, 365 (1956).

[2] Z. W. Wilchinsky, Meeting of North Jersey Section, American Chemical Society, East Orange, New Jersey, January 26, 1959.

[3] Z. W. Wilchinsky, J. Appl. Phys. **30**, 792 (1959).

where the subscripts 1 and 2 refer to the two respective planes and ρ is the angle between a plane normal and the b axis. The values of ρ were calculated from the unit cell[4] and have the following values for the three main $hk0$ reflections:

Plane	Degrees
040	0
130	46.7
110	72.5

All three pairs of planes were used; however, the 040-110 pair was generally most satisfactory.

The orientation parameter $\langle\cos^2\sigma\rangle_{Av}$ has a simple physical interpretation. It has the value unity when all the crystals are oriented with their c axes parallel to Q, and a value zero when all the c axes are perpendicular to Q. This relationship holds only because the c axis is unique. If there were other equivalent directions in the crystal, it is obvious that they all could not be parallel to Q simultaneously, and consequently, the orientation parameter would be less than unity, even for perfect orientation. The b axis is also unique, and the value of its orientation parameter, $\langle\cos^2\phi_{040}\rangle_{Av}$, has a physical interpretation similar to that for $\langle\cos^2\sigma\rangle_{Av}$. For randomness, all orientation parameters have the value $\frac{1}{3}$.

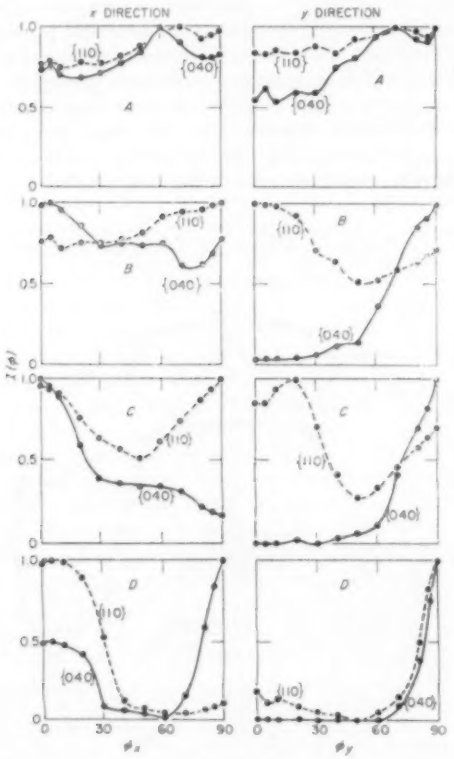

FIG. 2. Relative values of $I(\phi)$ for the samples A, B, C and D.

Experimental quantities in Eq. (1) were obtained by two procedures using a Norelco Geiger counter diffractometer. In one, a plane sample was used in the form of a pad built up of layers of film stacked parallel to each other. With the reference direction Q normal to the film surface, $I(\phi,\psi)$ was measured as a function of ψ while ϕ was held constant. The reflection technique of Schultz[5] was used for the lower range of ϕ and the transmission technique of Decker *et al.*[6] was used for the higher values. A sample thickness of about 1–1.5 mm was found satisfactory with Cu radiation. Absorption corrections were applied[5,6]; however, for the conditions that obtained in the reflection method, the maximum correction was about 0.5% for a 1 mm sample and 0.05% for a 1.5 mm sample. The corrected data by the two techniques were joined smoothly to cover the entire range of ϕ from 0 to 90°. Values of $I(\phi,\psi)$ were taken at sufficiently close intervals on the coordinate sphere to define the pole figure satisfactorily. From this pole figure, the distribution with respect to any other direction Q' in the sample can then be expressed in terms of the appropriate new set of spherical coordinates ϕ', ψ', with respect to Q' as axis of the coordinate sphere.

In the second procedure for evaluating $\langle\cos^2\phi\rangle_{Av}$, a portion of a film was rolled into a tight cylindrical rod about 1 mm in diameter with the reference direction Q parallel to the cylinder axis. This sample was examined by the x-ray technique of Cullity and Freda,[7] but without rotating the sample about its axis. The conditions were further modified by using a circular lead aperture in front of the sample so that the volume of sample material in the beam remained constant. Although this greatly reduced the variation in intensity due to purely geometric causes, it did not eliminate the variation completely. The effect of the geometric factors was evaluated empirically as a function of ϕ with the aid of a 1 mm diameter cylindrical rod carved out of a pad that showed negligible preferred orientation. The cylinders of film were sufficiently transparent so that $I(\phi)$ in Eq. (1) could be approximated by the diffracted intensity, after corrections were made for geometric factors. Measurements were made in two orthogonal directions in the film: y, or extrusion direction, and x, or transverse direction for films A, B, and C. For film D, the direction in the plane of the film showing the greatest fiber axis orientation was chosen as the y direction. The value of $\langle\cos^2\sigma\rangle_{Av}$ in the z direction, i.e., that normal to the film, was determined from the orthogonality relationship

$$\langle\cos^2\sigma_x\rangle_{Av}+\langle\cos^2\sigma_y\rangle_{Av}+\langle\cos^2\sigma_z\rangle_{Av}=1, \qquad (3)$$

where the subscripts refer to the three directions.

[4] The unit cell determined by the author has the following parameters: $a=6.64$ A, $b=20.88$ A, $c=6.51$ A, and $\beta=98.7°$.

[5] L. G. Schultz, J. Appl. Phys. **20**, 1030 (1949).

[6] B. F. Decker, E. T. Asp, and D. Harker, J. Appl. Phys. **19**, 388 (1948).

[7] B. D. Cullity and A. Freda, J. Appl. Phys. **29**, 25 (1958).

TABLE I. Orientation determined by the "rolled film" method in the x, y, z directions.

Sample	Crystalline content, Wt. %	b axis, $\langle\cos^2\phi_{040}\rangle_{Av}$ x	y	z	c axis, $\langle\cos^2\sigma\rangle_{Av}$ x	y	z
A	48	0.31	0.28	**0.41**	0.39	**0.41**	0.20
B	55	0.36	0.12	**0.52**	0.34	**0.49**	0.17
C	56	0.43	0.07	**0.50**	0.28	**0.53**	0.19
D	82	0.19	0.02	**0.79**	0.10	**0.87**	0.03

Finally, birefringence of the films was measured with a simple polariscope using a quarter-wave plate, according to the principles discussed by Gurnee *et al.*[8]

EXPERIMENTAL RESULTS

Orientation was measured by the rolled film technique from the {040} and {110} planes for four films

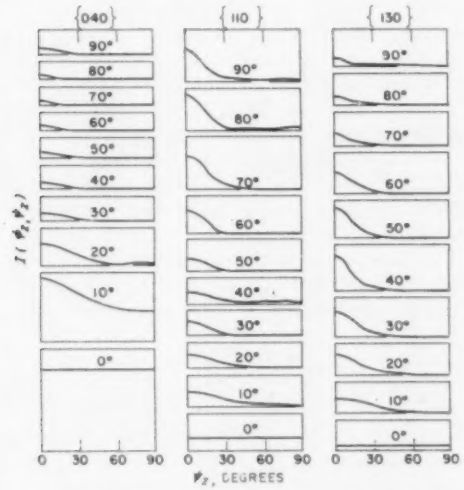

FIG. 3. Relative concentration of poles for the {040}, {110}, and {130} planes. Values of ϕ_z are indicated on curves. The angular coordinates for the three principal directions are: $\phi_z=0$ for z, $\phi_z=90°$ and $\psi_z=0$ for x, $\phi_z=90°$ and $\psi_z=90°$ for y.

having different degrees of orientation. The films *A*, *B*, and *C* were of Ziegler type polypropylene which had been synthesized and extruded through a flat die at this laboratory; the fourth film *D* was synthesized and prepared by another laboratory.[9]

Curves of $I(\phi)$ vs ϕ are shown in Fig. 2. It can be noted that $I(\phi)$ for the {040} planes is maximum for $\phi_y=90°$, i.e., the plane normals are preferentially oriented perpendicular to the y direction. Values of the orientation parameters in the three principal directions, calculated in accordance with Eqs. (1)–(3), are listed in

[8] E. F. Gurnee, L. T. Patterson, and R. D. Andrews, J. Appl. Phys. **26**, 1106 (1955).

[9] We thank the Minnesota Mining and Manufacturing Company for supplying this sample.

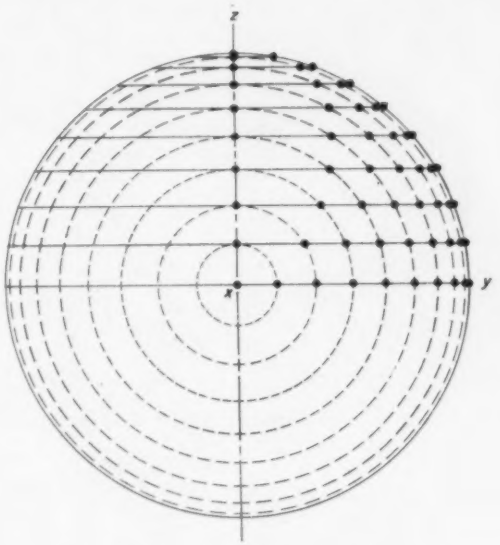

FIG. 4. Regions of coordinate sphere where pole concentrations were evaluated.

Table I. For samples *A*, *B*, and *C*, it can be noted that there is a preferred orientation of the c axis in the extrusion direction and of the b axis normal to the film surface. Also, the orientation parameters for these two axes in their preferred directions are of about the same magnitude. Sample *D* shows a similar orientation but to a higher degree.

The orientation of the film *D* was examined further

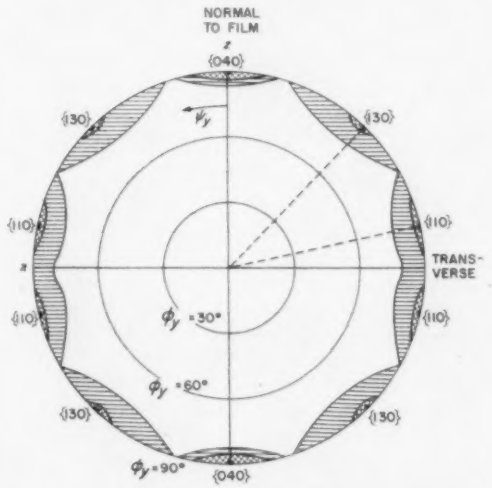

FIG. 5. Projection of hemisphere on xz plane showing pole distributions. In crosshatched region, concentration ranges from maximum, indicated by dark spot, to 90% of maximum; in horizontally hatched region concentration is 50–90% of maximum, and in clear region concentration is less than 50%.

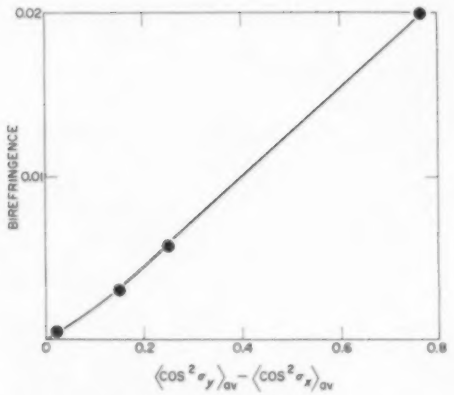

FIG. 6. Correlation of birefringence with difference of c-axis orientation in y and x directions.

by the complete pole figure method. With respect to the z direction, curves of $I(\phi_z,\psi_z)$ vs ψ_z at 10° intervals of ϕ_z were determined for the {040}, {110}, and {130} planes, and are shown in Fig. 3. The pole distribution with respect to the x direction was obtained by cross plotting the original data. Consider the x direction as the new axis of the sphere in Fig. 4. The broken lines indicate the lines of latitude with respect to this axis at intervals of 10° in ϕ_x. At each intersection of the ϕ_z and ϕ_x latitudes, the values of ψ_z and ψ_x were calculated from coordinate transformation relationships.[10] Then the value of $I(\phi_z,\psi_z)$ was read off the original curves at each intersection, and curves of $I(\phi_x,\psi_x)$ vs ψ_x were constructed for each of the values of ϕ_x. Curves for $I(\phi_y,\psi_y)$ were constructed in a similar manner.

The nature of the crystal orientation in the film can be depicted by the pole figure representation in Fig. 5, in which the y direction is the axis of the coordinate sphere. In the contour plots, it can be seen that the poles of the {hk0} planes are rather highly concentrated in the equatorial regions of the coordinate sphere. This would lead to the conclusion that the c axis concentration must, therefore, be rather high in the polar region of the sphere.

Orientation parameters for the b and c axes calculated from the original and transformed curves are listed in Table II. Mutual agreement of results from the various pairs of planes is quite satisfactory, considering the general accuracy of the x-ray intensity measurements and the computational operations involved. An additional check on these results is provided by the orthogonality relationship requiring the sum of the orientation parameters in the x, y and z directions to be unity. These sums shown in Table II are seen to be close to unity.

A comparison of results by the complete pole figure and rolled film methods for sample D shows that both methods indicate the same orientation characteristics. The agreement among the parameters is considered reasonable.

[10] W. F. Osgood and W. C. Graustein, *Plane and Solid Analytic Geometry* (The MacMillan Company, New York, 1930), p. 585.

TABLE II. Orientation determined by the complete pole figure method for sample D.

Direction in sample	b axis, $\langle\cos^2\phi_{040}\rangle_{Av}$	c axis, $\langle\cos^2\sigma\rangle_{Av}$ From {040} and {110}	From {040} and {130}	From {110} and {130}
x	0.23	0.09	0.05	0.03
y	0.06	0.83	0.88	0.89
z	0.71	0.09	0.08	0.06
	1.00	1.01	1.03	0.98

An independent partial confirmation of c-axis orientation was obtained through birefringence measurements. For strict accuracy, the crystalline orientation should be compared with the birefringence of the crystalline portion of a sample. However, for samples having a high degree of crystallinity, the total birefringence would be expected to be controlled to a large extent by the crystal orientation. In this case, a correlation between total birefringence and the difference of $\langle\cos^2\sigma\rangle_{Av}$ in the y and x directions should be expected. Such a plot in Fig. 6 shows an almost linear relationship for the samples in Table I for which the crystalline content measured by x-ray diffraction ranged from 48 to 82%. Extrapolation of the curve to complete c-axis orientation gives a value of about 0.026 for birefringence. This is in general agreement with the value of 0.030 reported by Keedy *et al.*,[11] and 0.027 by Padden and Keith.[12]

A correlation such as shown in Fig. 6 suggests a simplification in determining $\langle\cos^2\sigma\rangle_{Av}$ in the three principal directions. From a birefringence measurement which is easily made, the value $\langle\cos^2\sigma_y\rangle_{Av} - \langle\cos^2\sigma_z\rangle_{Av}$ is obtained from the correlation. This, together with a measurement of $\langle\cos^2\sigma\rangle_{Av}$ in either the x, y, or z direction, plus the orthogonality relationship, Eq. (3) is sufficient to permit evaluation of $\langle\cos^2\sigma\rangle_{Av}$ in all three directions.

CONCLUSIONS

It has been shown with polypropylene film that it is feasible to determine fiber axis orientation quantitatively in crystal systems which contain no planes perpendicular to the fiber axis. The procedures used, or suitable modifications of them, might also be applied to polypropylene in other physical forms or to other suitable polycrystalline materials.

ACKNOWLEDGMENT

The author wishes to thank Richard H. Hergert for assisting in the experimental work and data reduction.

[11] D. A. Keedy, J. Powers, and R. S. Stein, American Physical Society Meeting, Detroit, Michigan, March 21–24, 1960.

[12] F. J. Padden and H. D. Keith, J. Appl. Phys. **30**, 1479 (1959).

Transformation Studies of Gray Tin Single Crystals*

R. G. Wolfson, M. E. Fine, and A. W. Ewald
Departments of Materials Science and Physics, Northwestern University, Evanston, Illinois
(Received July 18, 1960)

Measurements of the linear growth rate of white tin into thin single-crystal wafers of gray tin, over the temperature range 24.2° to 46.5°C, are presented. The rate is not a single-valued function of the temperature. Imposed upon the strong temperature dependence of the average rate is a variation which is well defined at a given temperature; the spread in the observed values decreases sharply with increasing temperature. The variation is attributed to two observed stress-relaxation processes: cleavage in the gray tin and plastic deformation, accompanied by recrystallization, in the white tin.

INTRODUCTION

THE recent availability of large single crystals of gray tin[1] has made possible, for the first time, a detailed study of the interface motion during the gray (α) to white (β) tin transformation. Preliminary observations of Ewald and Tufte on the room temperature transformation of their crystals suggest that the phase change is martensitic in nature. The chief indication is the discontinuous motion of the interface, which appeared to advance by the conversion of distinct domains. This view is supported by the results of Burgers and Groen,[2] who performed the only previously reported study of the α-to-β growth kinetics. They found that the gross linear transformation rate in polycrystalline particles of the gray phase is much greater than that observed both in the reverse transformation and in the growth of recrystallized grains in deformed white tin. The rapid motion of the interface implies a coordinated movement of the atoms, but the surprisingly high apparent activation energy calculated from these data, 50 kcal/gm-atom, is inconsistent with such an interpretation.

The present investigation was in part undertaken in an attempt to resolve the anomalous association of a rapid and discontinuous mode of transformation with a high activation energy. This paper describes the measurement of the linear growth rate of white tin in single-crystal gray tin.

Initially, a qualitative study of the transformation was performed to determine certain of its general characteristics. Micrographic observations showed that both the parent and the product phases are distorted by the 21.4% volume decrease accompanying the transformation. The gray tin buckles visibly immediately in front of the advancing interface, and completely converted specimens exhibit a network of fine cracks. These features suggest that the brittle gray tin accomodates the accumulating strain by cleavage. In addition, the appearance of strain markings behind the interface indicates that the metallic white tin undergoes considerable plastic deformation. Both of these inferences were confirmed by Laue back-reflection patterns, which also revealed that single-crystal gray tin transforms into deformed polycrystalline white tin of fine grain size. Subsequently, rapid recrystallization occurs, going to completion in a few hours at room temperature.

SPECIMEN PREPARATION

The specimens used in this study were wafers of single-crystal gray tin, about $\frac{1}{8}$ in. across and 0.015 in. thick. A thin specimen was considered necessary in order to reduce the restraints imposed by the large transformation strains. The specimens were cut parallel to natural crystallographic faces, which are extremely smooth and splendent; all observations were made on these faces, and the necessity for polishing was thus avoided.

Although the crystals are highly perfect, they contain occasional pockets of occluded mercury, which goes into solid solution above 0°C and causes the immediate transformation of a comparable volume of the surrounding gray tin. Great care was taken to eliminate these nucleation centers for two reasons. First of all, the growth kinetics are quite sensitive to the presence of dissolved mercury because of the large transformation strain and the resultant importance of relaxation proc-

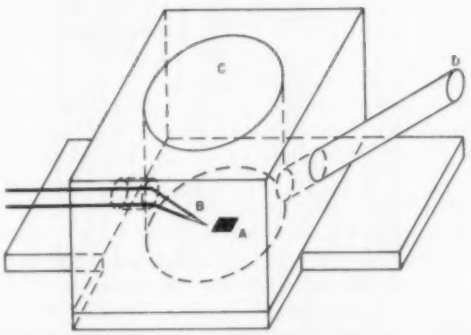

FIG. 1. Specimen chamber: *A* specimen, *B* thermocouple probe, *C* opening for microscope objective, *D* air line from constant-temperature bath.

* This research was supported by the Air Force Office of Scientific Research under contract, and is based upon the M. S. thesis of R. G. Wolfson, Northwestern University, June 1960.

[1] A. W. Ewald and O. N. Tufte, J. Appl. Phys. **29**, 1007 (1958).

[2] W. G. Burgers and L. J. Groen, Discussions Faraday Soc. No. 23, 183 (1957).

esses. Secondly, the incubation time for the initiation of the phase change is conveniently long in mercury-free material, up to several days at room temperature and about 15 minutes at 40°C. This delay is more than adequate to insure the attainment of thermal equilibrium between the specimen and the heating medium.

Briefly, a section about 0.015 in. thick was cut parallel to a prominent (111) face of the crystal by abrasive cutting. After all visible pockets of mercury had been trimmed off, the section was cleaved into fragments about ¼ in. across. As a final check, each piece was allowed to remain at room temperature for 10 minutes before use as a specimen; the absence of regions of white tin was taken as proof that no occluded mercury was present.

APPARATUS

The apparatus used for measuring the linear transformation rate consisted of a constant-temperature bath, a specimen chamber, and an optical system for micrographic observation; the specimen chamber is shown in Fig. 1. Air from the laboratory line was heated by passage through a copper coil suspended in the constant-temperature bath. The warm air was then conducted to the specimen chamber, where it was allowed to flow over the specimen; its temperature was determined by means of a movable Chromel-Alumel thermocouple probe. The specimen chamber was mounted directly on the mechanical stage of a Bausch & Lomb metallographic microscope. Motion-photomicrographs of the transformation were taken with a Cine-Kodak Special 16-mm camera, which was introduced into the optical system of the microscope by means of an image-splitter assembly designed specifically for the camera by the Bausch & Lomb Optical Company. Light for both the micrographic measurements and the motion-photomicrography was provided by the internal illumination system of the microscope.

The essential feature of the apparatus was the immersion of the specimen in a rapidly moving stream of heated air. This arrangement offered two important advantages: (1) the rapid fluid flow around the specimen insured effective heat exchange during the endothermic phase change and (2) the gaseous heating medium permitted the use of an open specimen chamber, which greatly facilitated micrography.

The variation of the temperature within the specimen chamber, with respect to both time and position, was repeatedly checked during the investigation. It was found that the temperature was constant, to better than 0.1C degree, for periods of an hour within a roughly cylindrical volume ½ in. in diam and ¼ in. high. Since a given series of measurements rarely lasted more than 5 min, once the transformation had started, and since the specimens were only about 1/8 in. across and 0.015 in. thick, a constant specimen temperature was thus maintained.

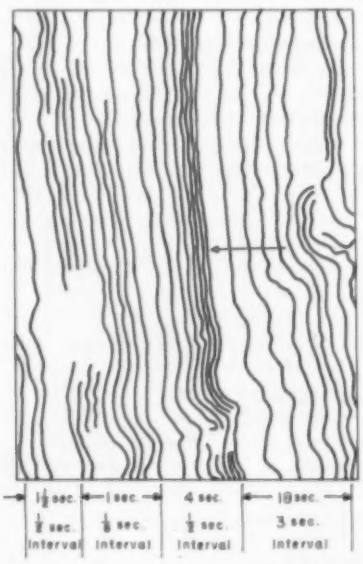

FIG. 2. Time-contour representation of interface motion at 34.8°C. The contour interval varies as shown; the magnification is 621.6×.

EXPERIMENTAL PROCEDURE

After the constant-temperature bath had reached equilibrium, the thermocouple probe was placed at the center of the specimen mount, and the temperature of the heated air was measured at 5-min intervals until no variation was observed for at least 15 min. The probe was then withdrawn slightly, and the specimen was attached to the mount with Apiezon "L" grease. Above 30°C, spontaneous nucleation of the transformation could be expected within a reasonable length of time (approximately 20 minutes at 35°C and less than one minute at 45°C). Below this temperature, the transformation was started by touching a hot wire to a corner of the specimen.

Because the average linear transformation rate increases by several orders of magnitude over the temperature range studied, two different measuring techniques were required. Between room temperature and 35°C, the measurements were made visually, at a magnification of 462.5 diam, by means of a micrometer eyepiece. Above this temperature, however, the rates were too great for direct determination. Instead, the interface motion was photographed on Kodak Tri-X Reversal film at a speed of 8 frames/sec; the magnification on the film was 60 diam. The photographs were subsequently analyzed at a total (projected) magnification of 1554 diameters by superimposing on a single map the interface positions recorded on successive frames. The result was a time-contour representation of the interface motion, which gave a detailed picture

of the rate variation. Portions of three such mappings are reproduced as Figs. 2–4. In both the micrographic and the motion-photomicrographic observations, the distance traveled by the interface was measured to within 1×10^{-4} cm.

RESULTS AND DISCUSSION

The experimental results are presented as Fig. 5, where the common logarithm of the linear transformation rate is plotted as a function of the reciprocal absolute temperature. The circles represent values obtained by the direct micrographic measurement of the interface motion, and the vertical arrows indicate the ranges of values observed by motion-photomicrography. Average values are denoted by triangles; those lying on vertical arrows are the measured average rates determined from the corresponding motion-photomicrographic observations, while the others are calculated averages of the visual readings.

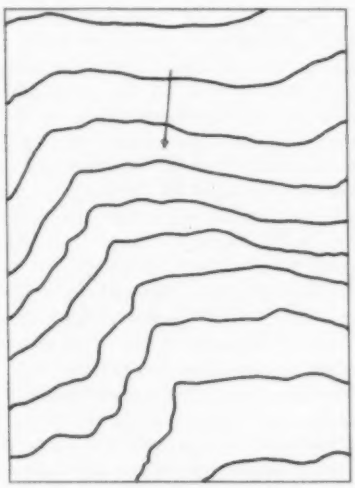

FIG. 3. Time-contour representation of interface motion at 40.4°C. The contour interval is 2 sec; the magnification is 621.6×.

The most salient feature of these data is that the linear transformation rate is not a single-valued function of the temperature. Imposed upon the strong temperature dependence of the average rate is a variation in the rate which itself decreases sharply with increasing temperature. The lower limit to the transformation rate is clearly delineated, and there also appears to be an upper limit, although this latter is not as well defined by the data.

The linearity of the extreme and average values of the transformation rate in the semi-logarithmic plot suggests that these data may be represented by Arrhenius type relations. It must be emphasized, however, that this treatment is introduced for purposes of comparison only, since the rate equation is obviously more complex. Consequently, the Arrhenius constants given below, which were obtained by least-squares analysis of the data, do not have the usual physical significance. The minimum rate expressed in cm/sec is given by

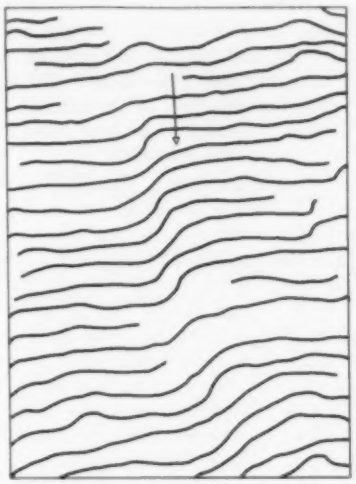

FIG. 4. Time-contour representation of interface motion at 46.5°C. The contour interval is ¼ sec; the magnification is 621.6×.

$$U_{\min}=6.38\times10^{11}\exp(-65.0/RT), \qquad (1)$$

where R is the gas constant in kcal/mole −°K and T is the absolute temperature. The 90% confidence limits on the apparent activation energy are 1.3 kcal/gm-atom, and the pre-exponential factor, within these limits, ranges from 7.7×10^{10} to 5.3×10^{12} cm/sec. The calculated average rate is given by

$$U_{av}=1.33\times10^{29}\exp(-46.1/RT), \qquad (2)$$

with 90% confidence limits on the apparent activation energy of 1.7 kcal/gm-atom and with a range of the pre-exponential factor of from 8×10^{27} to 2.2×10^{30} cm/sec. The maximum rate, U_{max}, is infrequently observed, and then only for brief intervals, so that the position of the upper limit cannot be fixed with great certainty. Nevertheless, the apparent activation energy corresponding to U_{max} may be estimated; its value is −22 kcal/gm-atom, with 90% confidence limits of 7 kcal/gm-atom.

These data show that the interface velocity in thin-wafer, single-crystal specimens has a definite minimum value which is not zero: once the boundary has started to move, it does not stop until the specimen has been completely transformed. This is also true for the transformation following nucleation by mercury, although there is an appreciable delay between the immediate and limited conversion associated with the solution of the mercury and the start of the continuous propagation

of the product phase. The temporary immobilization of the interface may be attributed to the strengthening of the white tin, and possibly the gray tin as well, by dissolved mercury,[3] which produces an increased resistance to the deformation accompanying the phase change. Evidently, a time-dependent relaxation process operates to decrease the restraint.

The last two observations illustrate an important point: unless the strain energy generated by the 21.4% volume decrease is relieved, the transformation cannot proceed. The uninterrupted propagation of the product phase, of course, is proof that the transformation strain is not allowed to accumulate. On the other hand, a certain amount of strain energy must be present in the immediate vicinity of the interface, since the two phases maintain contact at their common boundary. This nonchemical free energy adds algebraically to the chemical free energy difference driving the transformation.

The effect of the energy interaction upon the interface motion is most readily described in terms of the phenomenological theory of phase-boundary migration. For a transformation in which neither the composition nor the density changes, the linear growth rate, U, may be related to the difference between the frequencies of atom transfer in either direction across the boundary[4]:

$$U=\lambda\nu_0\exp[-\Delta G_a/RT]-\lambda\nu_0\exp[(-\Delta G_a+\Delta G_c)/RT], \quad (3)$$

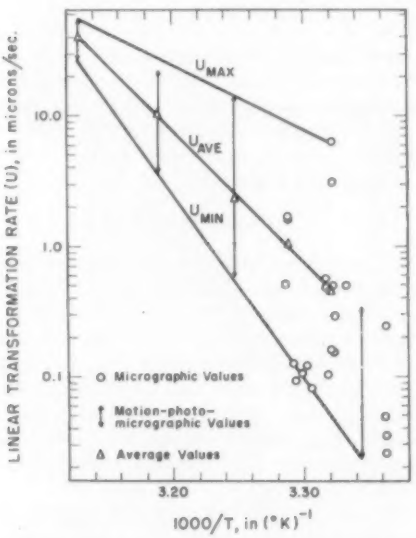

FIG. 5. Graphical representation of the experimental data. The common logarithm of the linear transformation rate is plotted as a function of the reciprocal absolute temperature. The straight lines for the minimum, average, and maximum rates were obtained by least-squares analysis of the data.

[3] E. O. Hall, *Symposium on the Mechanism of Phase Transformations in Metals* (The Institute of Metals, London, 1955), p.87.
[4] D. Turnbull, Solid State Physics **3**, 280 (1956).

where λ is the distance across the interface, ν_0 is usually taken as the atomic vibration frequency, ΔG_a is the activation free energy, and ΔG_c is the chemical free energy difference (suitably defined as to sign) between the two phases. This idealized expression may be extended to the case of a transformation involving a large density change by explicitly including the nonchemical free energies E_α and E_β stored, respectively, in the parent and product phases:

$$U=\lambda\nu_0\exp[(-\Delta G_c\pm E_\alpha)/RT]-\lambda\nu_0\exp[(-\Delta G_a+\Delta G_c\pm E_\alpha\pm E_\beta)/RT], \quad (4)$$

where the stored energies are defined as positive when they decrease the stability.

The energies E_α and E_β are produced by strain distributions which are, at best, extremely difficult to evaluate. In the gray-to-white tin transformation, they are determined not only by the crystallography of the interface, which is as yet unknown, but also by the macroscopic deformation of the specimen. Nevertheless, a qualitative explanation of the rate variation may be developed on the basis of the interaction between the chemical and the nonchemical free energies. It does seem certain that the strain energy terms generated by the transformation retard the transformation.

The observed variation in the linear transformation rate may be ascribed to the nature of the processes by which the 21.4% volume change is accommodated. Micrographic observations, supplemented by a Laue back-reflection study, have revealed that two relaxation mechanisms are active: plastic deformation accompanied by recrystallization in the white tin relieves E_β, and cleavage in the gray tin relieves E_α. The first process releases energy by the approximately continuous yielding of the newly formed white tin under the transformation stresses. The cleavage of the gray tin, to the contrary, can momentarily relieve the stored energy in the vicinity of the fracture. Moreover, if it occurs extensively on a fine scale, relatively large volumes of material may be affected. Since the cleavage is a discontinuous process, the stored energy varies locally from zero to some maximum value determined by the mechanical properties of the gray tin. A preliminary estimate, based upon an estimate of the critical resolved normal stress for cleavage, indicates that the elastic deformation energy stored by the gray tin may reach 40 cal/gm-atom, which is of the same order of magnitude as the free energy difference between the two phases.[5] Consequently, the fluctuation of the net driving energy may be very large, and the rate of interface movement will exhibit a correspondingly wide variation. The temperature dependence of the variation follows naturally, for, as the temperature increases, the free energy of the unstable phase continues to rise more rapidly than that of the stable phase. The nonchemical free energy terms in Eq. (4) become smaller in com-

[5] F. Lange, Z. physik. Chem. (Leipzig) **110**, 343 (1924).

parison, and the variation in the linear transformation rate decreases.

A rapid and discontinuous mode of propagation of the interface has previously been reported.[1,2] In thin wafers the interface motion is not truly discontinuous, for the rate does not fall to zero. However, the large variation in the rate (corresponding to a factor of about 150 at room temperature and 30 at 30°C) may give the impression of conversion by distinct domains. This variation negates the validity of kinetic constants derived from gross or average measurements. On the surface of massive samples a truly discontinuous mode may be observed due to the discontinuity at cleavage cracks.

Burgers and Groen previously reported an activation energy of about 50 kcal/gm-atom for growth of white tin into a polycrystalline gray tin matrix, which appears to agree with the apparent activation energy of 46.1 kcal/gm-atom of Eq. (2) for the average linear transformation rate observed in the present investigation. However, they only reported a single rate for each temperature. Their rates are much larger than the present average values and, in fact, are fairly close to the maximum values for which we found an activation energy of about 22 kcal/gm-atom. It should be noted that Burgers and Groen investigated only a narrow temperature range (30 to 36°C) and thus their activation energy determination was subject to considerable error. Their study was performed on gray tin granules, from 0.1 to 0.8 mm in diam, obtained by the reverse transformation from white tin. The specimens were polycrystalline aggregates of fine grain size, in which the release of the deformation energy may have been enhanced by the lack of crystallographic continuity of the matrix. This would reduce the maximum stored energy, thus suppressing the rate variation and permitting the more rapid movement of the interface. In contrast, the specimens used in the present study were thin wafers of relatively perfect, single-crystal gray tin. The coherence of the parent phase results in a discontinuous mode of energy release, which enables the stored energy to reach high values.

In summation, neither the gross activation energy nor the stepwise interface motion are fundamentally related to the atom movements occurring at the interface. The activation energy of 46.1 kcal/gm-atom is fictitious in the sense that it describes an average rate and has no direct physical significance. The actual thermodynamic barrier to growth is probably no greater than 22 kcal/gm-atom. The stepwise advance of the interface results from a discontinuous mode of stored energy release, that is, cleavage of the gray tin, rather than from a martensitic type transformation. However, in view of the large propagation rate it seems reasonable to still consider that the gray-to-white tin transformation proceeds by a coordinated movement of atoms across the interface. The maximum linear rate would then be determined by the stress-relaxation process of recrystallization, and the 22 kcal/gm-atom would correspond to this process.

ACKNOWLEDGMENT

The authors are pleased to acknowledge the helpful assistance of Dr. O. N. Tufte.

Effect of Magnetic Fields on Thermionic Power Generators

ALFRED SCHOCK
Republic Aviation Corporation, Farmingdale, New York
(Received April 5, 1960; and in final form June 14, 1960)

It is demonstrated that the high currents present in large thermionic power generators produce magnetic fields which result in a considerable reduction of electron transmission and energy conversion efficiency. To overcome the adverse effect of the self-induced field, the report presents the concept of a *magnetothermionic power generator*, employing an externally produced magnetic field parallel to the current direction. Analysis indicates that this concept will permit efficient operation of large generators. In addition, by use of a modulated field coil current, it offers the possibility of the direct generation of alternating current, at a controlled frequency.

INTRODUCTION

THE potential performance of low-pressure cesium plasma diodes in the direct conversion of heat to electricity was analyzed in a number of recent studies.[1-4] Although none of these discusses the effect of magnetic fields on electron transmission, the possible importance of this effect was recognized by several experimentalists,[1,5,6] as evidenced by their careful precautions to eliminate such fields.

While the prevention of magnetic fields is relatively easy in the small experimental devices tested to date, the problem is far more difficult in the case of a full-scale thermionic generator. Because of its inherently low operating voltage, a high-power generator must of necessity produce a very large current; and this, in turn, will induce a sizable magnetic field transverse to the direction of current flow. Such a field deflects the electrons, forcing some of them back to the emitter. The first half of the report examines the effect of these self-induced fields on thermionic current transmission.

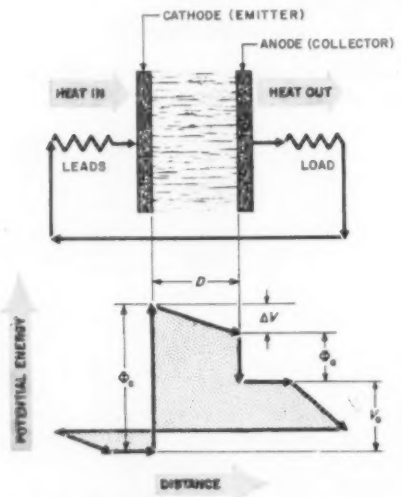

FIG. 1. Circuit and potential energy diagrams, assuming complete space charge neutralization. ΔV may be positive, zero, or negative.

EMISSION VELOCITY SPECTRUM

Assuming that the electrons within a metal have a Fermi-Dirac energy distribution, it can be shown[7,8] that the velocity spectrum of electrons emitted from the metal's xy face is given by

$$dJ=\frac{2em^3}{h^3}\exp\left[\frac{-e\Phi_c-\frac{1}{2}m(v_x^2+v_y^2+v_z^2)}{kT}\right]v_z dv_x dv_y dv_z, \quad (1)$$

where $dJ(v_x,v_y,v_z)$ is the current density of electrons with initial velocity components between v_x and v_x+dv_x, v_y and v_y+dv_y, v_z and v_z+dv_z; and where h and k designate Planck's and Boltzmann's constants, e and m represent the charge and mass of an electron, and Φ_c and T denote the work function and temperature of the cathode emitter. (Unless otherwise stated, MKS units are used throughout this report.)

Integration of Eq. (1) over the velocity limits $-\infty<v_x<\infty$, $-\infty<v_y<\infty$, $0<v_z<\infty$ results in the Richardson-Dushman equation for the saturation current density J_0:

$$J_0=[4\pi emk^2h^{-3}]T^2\exp(-e\Phi_c/kT), \quad (2)$$

where the square bracket has the well-known value of 120 amp/cm^{2}K^2. In terms of a dimensionless velocity $u\equiv(m/2kT)^{\frac{1}{2}}v$, Eq. (1) reduces to

$$dJ=(2J_0/\pi)\exp[-(u_x^2+u_y^2+u_z^2)]u_z du_x du_y du_z. \quad (3)$$

In the presence of a magnetic field, the fraction of emitted electrons which succeeds in reaching the collector is obtained by integration of Eq. (1) or (3) over appropriate velocity limits.

[1] K. G. Hernquist, M. Kanefsky, and F. M. Norman, R C A Rev. **19**, 244 (1958).
[2] P. L. Auer and J. Hurwitz, J. Appl. Phys. **30**, 161 (1959).
[3] J. M. Houston, J. Appl. Phys. **30**, 481 (1959).
[4] N. S. Rasor, J. Appl. Phys. **31**, 163 (1960).
[5] V. C. Wilson, J. Appl. Phys. **30**, 475 (1959).
[6] R. W. Pidd, G. M. Grover, E. W. Salmi, D. J. Roehling, and G. F. Erickson, J. Appl. Phys. **30**, 1861 (1959).
[7] J. Millman and S. Seely, *Electronics* (McGraw-Hill Book Company, Inc., New York, 1941), Chaps. 4 and 5.
[8] A. Schock, Rept. No. PPL-TR-60-1 (January 1960), Republic Aviation Corporation, Farmingdale, New York.

ASSUMPTIONS

To compute these integration limits, we shall confine our attention to the class of plasma diodes in which the cesium density is low enough so that collisions may be neglected. For this case, electron motion is governed by

$$m\dot{\mathbf{v}}=-e[(\mathbf{v}\times\mathbf{B})+\mathbf{E}]. \tag{4}$$

Note that relativistic corrections are negligible, since the average electron speed is of the order of $(kT/m)^{\frac{1}{2}}\approx 10^5$ m/sec.

Next, we assume that the positive ion density is everywhere adequate to neutralize the electron space charge. This assumption implies a uniform electric field $\mathbf{E}=E_z=-\Delta V/D$, where ΔV is the accelerating potential and D the distance between electrodes. As shown by Fig. 1, the accelerating potential ΔV depends on the cathode and anode work functions Φ_c, Φ_a, and on the external voltage drop V_0. Thus,

$$\Delta V=\Phi_c-\Phi_a-V_0. \tag{5}$$

Although the self-induced magnetic field $\mathbf{B}$ varies in both magnitude and direction, its variation over small distances is negligible. Since the average distance travelled by the electrons is of the order of the electrode spacing D (e.g., 1 mm), we may assume that each electron, throughout its life, sees a $\mathbf{B}$ field of essentially constant magnitude and direction.

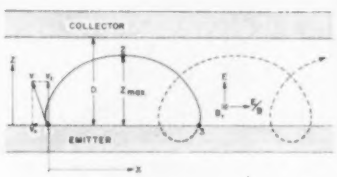

FIG. 2. Typical trochoidal electron trajectory, projected onto the xz plane.

TRANSVERSE FIELD EFFECT

For a given point of emission, we define the y coordinate to coincide with the direction of the transverse magnetic field. Consequently, Eq. (4) has the following components:

$$\ddot{x}=-\omega\dot{z}, \quad \ddot{y}=0, \quad \ddot{z}=\omega[\dot{x}-(E/B)], \tag{6}$$

where $\omega\equiv eB/m$. The boundary conditions at time $t=0$ are $x=y=z=0$, $\dot{x}=v_x$, $\dot{y}=v_y$, $\dot{z}=v_z$. On integrating each equation once,

$$\dot{x}=v_x-\omega z, \quad \dot{y}=v_y, \quad \dot{z}=v_z+\omega[x-(E/B)t]. \tag{7}$$

Inserting Eqs. (7) into (6) gives three separate equations, whose solutions are

$$x=(v_x-E/B)\omega^{-1}\sin\omega t-v_z\omega^{-1}(1-\cos\omega t)+(E/B)t, \tag{8a}$$

$$y=v_y t, \tag{8b}$$

$$z=v_z\omega^{-1}\sin\omega t+(v_x-E/B)\omega^{-1}(1-\cos\omega t). \tag{8c}$$

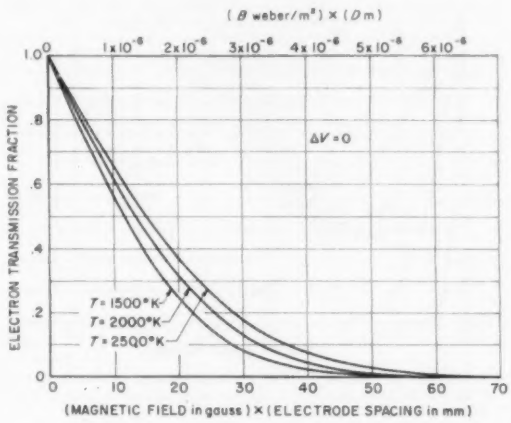

FIG. 3. Electron transmission vs the product BD, for the special case when $\Phi_c=\Phi_a+V_0$. Note that transmission is only weakly dependent on emitter temperature T.

The projection of the electron trajectory in the xz plane is a trochoid, a typical example of which is illustrated by Fig. 2. The electron has a cyclotron frequency of ω rad/sec, and a drift velocity E/B in the x direction. Clearly, an electron emitted at point 1 with velocity v will return to the emitter at point 3, unless its altitude z_{max} at point 2 exceeds the electrode spacing D. Therefore, to compute the integration limits for Eq. (1), we first solve Eq. (8c) for the maximum value of z;

$$z_{max}=\omega^{-1}\{[(v_x-E/B)^2+v_z^2]^{\frac{1}{2}}+(v_x-E/B)\}. \tag{9}$$

This equation shows that any electron whose $v_x>(\frac{1}{2}\omega D+E/B)$ will arrive at the collector, even if the electron's $v_z=0$. For all other electrons, the minimum value of v_z required for reaching the collector is obtained by setting $z_{max}=D$.

$$(v_x-E/B)^2+v_z^2=[\omega D-(v_x-E/B)]^2. \tag{10}$$

Electrons whose emission velocity satisfies Eq. (10) just graze the collector at the peak of their trajectory. As shown before, the lower limit on v_z is conditional on the value of v_x. Consequently, Eq. (1) must be integrated in two parts:

$$-\infty<v_x<(\tfrac{1}{2}\omega D+E/B), \quad -\infty<v_y<\infty,$$

$$\omega D\left[1-\frac{v_x-E/B}{\frac{1}{2}\omega D}\right]^{\frac{1}{2}}<v_z<\infty,$$

and

$$(\tfrac{1}{2}\omega D+E/B)<v_x<\infty, \quad -\infty<v_y<\infty, \quad 0<v_z<\infty.$$

Integration over the above velocity limits gives the transmitted current density J. Dividing the result by the saturation current J_0 [Eq. (2)] yields an expression for f, the fraction of the emitted electrons which reaches the collector in spite of the transverse B field:

$$f=\tfrac{1}{2}\operatorname{erfc}[\mathfrak{G}-(\mathfrak{V}/4\mathfrak{G})]+\tfrac{1}{2}\operatorname{erfc}[\mathfrak{G}+(\mathfrak{V}/4\mathfrak{G})]\exp\mathfrak{V}, \tag{11}$$

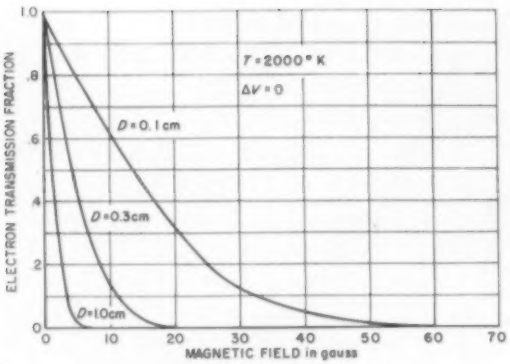

FIG. 4. Effect of transverse field strength B and electrode spacing D on electron transmission, for the special case $\Phi_c=\Phi_a+V_0$.

where $\mathfrak{B}\equiv[eD(8mkT)^{-1}]B$ and $\mathfrak{V}\equiv e\Delta V/kT$. Let us examine Eq. (11) in a number of special cases. First, in the absence of the transverse magnetic field Eq. (11) reduces to

$$f_{B=0,\Delta V>0}=1, \quad f_{B=0,\Delta V<0}=\exp(e\Delta V/kT). \quad (12)$$

As expected, with an accelerating voltage the transmitted current equals the saturation current; with a retarding voltage, the transmission current is reduced by the exponential term, i.e., the current is limited by the highest point of the energy barrier (Φ_a+V_0). In the special case of zero electric field, when $\Phi_c=\Phi_a+V_0$, Eq. (11) reduces to

$$f_{\Delta V=0}=\operatorname{erfc}\mathfrak{B}=\operatorname{erfc}[eBD(8mkT)^{-1}]. \quad (13)$$

Equation (13) is illustrated by Fig. 3, which depicts the variation of f as a function of the product BD, for three representative temperatures. As would be expected, increasing the field strength B decreases the transmitted current, since the electron trajectories are bent more sharply. Increasing the electrode spacing D also diminishes the transmitted current, since it makes it more difficult for electrons to reach the collector. Finally, raising the emitter temperature T increases the transmission fraction, by imparting a higher initial velocity to the emitted electrons.

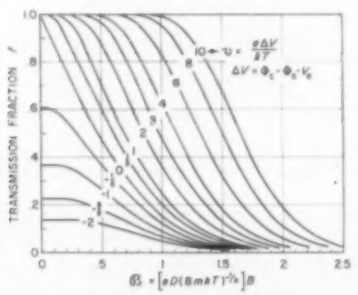

FIG. 5. Effect on electron transmission of a transverse magnetic field. General solution, showing the influence of the interelectrode potential ΔV.

For an emitter temperature of 2000°K, Fig. 4 illustrates the effect of the transverse field strength on transmission fraction, for various electrode spacings. Note that even modest field strengths reduce the electron transmission substantially.

The more general case, when $\Delta V\neq 0$, is illustrated by Figs. 5 and 6. Figure 5 depicts the solution of Eq. (11) in dimensionless form, and Fig. 6 presents a plot of f vs BD, for various values of ΔV (at a constant emitter temperature $T=1500$°K). As would be expected, increasing the accelerating voltage raises the electron transmission fraction at a given value of B. However, the adverse effect of the magnetic field is still present, particularly at the higher field strengths.

SELF-INDUCED FIELD EFFECT

Thus far we have examined the effect on electron transmission of a transverse magnetic field of arbitrary magnitude. Since this field is itself produced by the

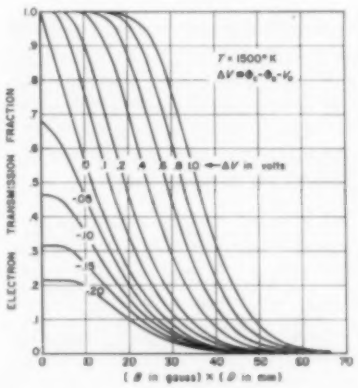

FIG. 6. Electron transmission versus transverse magnetic field B, electrode spacing D, and interelectrode potential ΔV.

electron current, a self-consistent coupled solution must exist. Consider, for example, a pair of parallel plane disk electrodes of radius R. From Maxwell's equation $\nabla\times\mathbf{B}=\mu_0\mathbf{J}$ and from the electrodes' radial symmetry we readily obtain a relation between the current density J and the induced magnetic field B at any radial position r,

$$2\pi rB_{(r)}=\mu_0\int_0^r J_{(r')}2\pi r'dr', \quad (14)$$

where μ_0 is the magnetic permeability, and J (the transmitted current density at position r') is given by $J=fJ_0$. As previously explained, we assume that $D\ll R$, so that each electron sees an essentially constant magnetic field, and Eq. (11) may be used to compute f. Upon inserting this in Eq. (14),

$$B_{(r)}=(\mu_0J_0/r)\int_0^r fr'dr'. \quad (15)$$

On differentiating, and defining the dimensionless radial position $\mathfrak{R}\equiv[\mu_0 J_0 eD(8mkT)^{-\frac{1}{2}}]r$, we obtain the generalized differential equation

$$(d\mathfrak{B}/d\mathfrak{R})=f-(\mathfrak{B}/\mathfrak{R}), \tag{16}$$

with initial boundary condition $\mathfrak{R}=0$, $\mathfrak{B}=0$, $\mathfrak{B}/\mathfrak{R}=\frac{1}{2}$. The system of Eqs. (11) and (16) was solved by digital computer, and the solutions for various values of $\mathfrak{U}$ are presented in Fig. 7. Upon inserting the values of $\mathfrak{B}$ and $\mathfrak{U}$ in Eq. (11), we solve for f, the electron-transmission fraction at radial position r. The results are illustrated by Fig. 8.

Of greater interest, however, is the value of the transmission fraction averaged over the entire electrode area. By making use of Eq. (14),

$$f_{av}\equiv\frac{\int_0^R J_{(r)}2\pi r dr}{\pi R^2 J_0}=\frac{2B_{(R)}}{\mu_0 J_0 R}=\frac{2\mathfrak{B}}{\mathfrak{R}}. \tag{17}$$

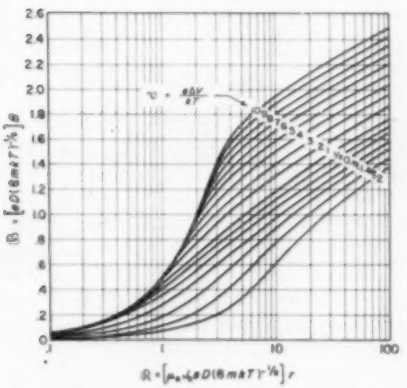

FIG. 7. Mutual interaction of electric current and the magnetic field it induces. General solution for plane, parallel disk electrodes, showing variation of field strength B vs radial position r, for various values of the interelectrode potential ΔV.

The generalized solution for f_{av} as a function of $\mathfrak{R}$ and $\mathfrak{U}$ is presented by Fig. 9. To assess the physical significance of the above results, consider some typical values. Figure 10 depicts the effect of electrode radius on average current transmission, for an emitter temperature $T=1500°K$, a saturation current $J_0=10$ amp/cm², an electrode spacing $D=0.3$ cm, and various values of the accelerating voltage ΔV.

It is seen that increasing ΔV improves the current transmission. However, for given electrode work functions, this increased current is obtained at the cost of a lowered output voltage, since $V_0=\Phi_c-\Phi_a-\Delta V$. The combined effect of ΔV on the power density $P=JV_0=J_0 f_{av}(\Phi_c-\Phi_a-\Delta V)$ is illustrated by Fig. 11 for electrode disks of 15-cm radius, typical values of $\Phi_c-\Phi_a$, and the same values of J_0, T, and D as before. Note that there is very little advantage in operating with a non-

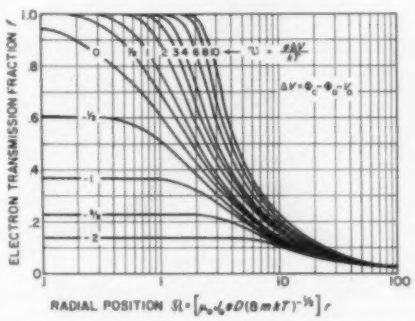

FIG. 8. Electron transmission versus radial position r. General solution for disk electrodes, showing the influence of the accelerating voltage ΔV.

zero ΔV. The special case $\Delta V=0$, i.e., when the external voltage drop V_0 equals the difference in the electrode work functions, is summarized by Fig. 12, which shows the effect of electrode radius on average transmission (for various electrode spacings). It is seen that, with a high emission current (10 amp/cm²) and reasonable electrode spacing (0.1–1 cm), even a relatively small electrode (e.g., 10-cm radius) will suffer a substantial reduction in current transmission, as a result of the self-induced B_y field.

In addition to parallel disk electrodes, the writer has also analyzed another geometry of interest[8]: coaxial cylindrical electrodes. It was found that the reduction of current transmission by the self-induced field in the latter case is even more pronounced than in the parallel disk case. This is illustrated by Fig. 13 for typical values of emission current, emitter temperature, and electrode spacing.

DISCUSSION

In a thermionic generator, a major portion of the energy input to the hot electrodes is required to compensate for radiative and conductive heat losses. These heat losses are, of course, independent of magnetic field strength and electron current. Consequently, the field-

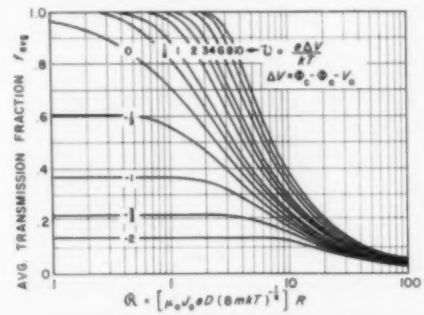

FIG. 9. Electron transmission averaged over the electrode area. General solution for disk electrodes, showing the effect of disk radius R and accelerating voltage ΔV.

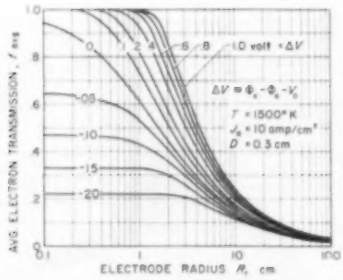

FIG. 10. Average electron transmission vs disk electrode radius R, for various values of the accelerating potential ΔV, and for typical values of emitter temperature T, emission current density J_0, and electrode spacing D.

induced reduction of the transmitted current will bring about a substantial decrease in the generator's power conversion efficiency, as demonstrated by the illustrative example presented in the Appendix. In fact, it is seen that the attainment of high current density (and efficiency) is only possible with relatively small electrodes. This severe restriction on allowable electrode size represents a highly undesirable limitation on the freedom of design. In particular, it may make it quite difficult to build an efficient high-power generator.

To avert this difficulty requires one of two things: either some electrode configuration which produces large currents without inducing a strong transverse magnetic field; or, a system permitting high current transmission in spite of the large transverse field. To attain the latter objective, we propose the concept of the *Magnetothermionic Generator*, in which an additional longitudinal magnetic field (B_z, i.e., parallel to the current flow) is superimposed on the self-induced transverse field (B_y).

EFFECT OF THE LONGITUDINAL FIELD

As illustrated by Fig. 14, the combined field $B=(B_y^2+B_z^2)^{\frac{1}{2}}$ intersects the emitting electrode at an angle α. To be conservative, assume no accelerating voltage; i.e., $\Delta V=0$. Hence, the equation of electron motion [Eq. (4)] has the following components:

$$m\ddot{x}=eB_z\dot{y}-eB_y\dot{z}, \quad m\ddot{y}=-eB_z\dot{x}, \quad m\ddot{z}=eB_y\dot{x}. \tag{18}$$

The boundary conditions are the same as for Eq. (6). Upon integrating each equation once,

$$\begin{aligned}\dot{x}&=v_x+(eB_z/m)y-(eB_y/m)z\\ \dot{y}&=v_y-(eB_z/m)x\\ \dot{z}&=v_z+(eB_y/m)x.\end{aligned} \tag{19}$$

By inserting Eqs. (19b) and (19c) in (18a), we obtain a differential equation in x and t, whose solution is

$$x=\frac{v_x}{\omega}\sin\omega t+\frac{v_y-\beta v_z}{\omega(1+\beta^2)^{\frac{1}{2}}}(1-\cos\omega t), \tag{20a}$$

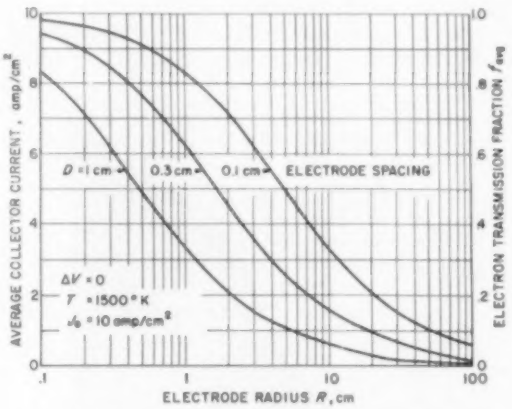

FIG. 12. Effect of electrode (disk) size on average current transmission, for the special case $\Phi_c=\Phi_e+V_0$.

where $\omega\equiv eB_z/m$ and β denotes the ratio of transverse to longitudinal field components [$\beta\equiv B_y/B_z=\cot\alpha$]. The insertion of Eq. (20a) in (19b) and (19c) gives differential equations for y and z, whose respective solutions are

$$y=\frac{(v_y-\beta v_z)\sin\omega t}{\omega(1+\beta^2)}-\frac{v_x(1-\cos\omega t)}{\omega(1+\beta^2)^{\frac{1}{2}}}+\frac{\beta^2v_y+\beta v_z}{1+\beta^2}t \tag{20b}$$

and

$$z=\frac{(\beta^2v_z-\beta v_y)\sin\omega t}{\omega(1+\beta^2)}+\frac{\beta v_x(1-\cos\omega t)}{\omega(1+\beta^2)^{\frac{1}{2}}}+\frac{\beta v_y+v_z}{1+\beta^2}t. \tag{20c}$$

These equations, in parametric form, define a helical electron motion at a rotational speed ω about an axis parallel to the magnetic field lines. Since we are primarily interested in the electron's position with respect to the emitting plane, we confine our attention to Eq. (20c). Let us define a dimensionless time $\tau\equiv\omega t$, and a dimensionless distance from the emitter

$$Z\equiv[(1+\beta^2)\omega(v_z+\beta v_y)^{-1}]z;$$

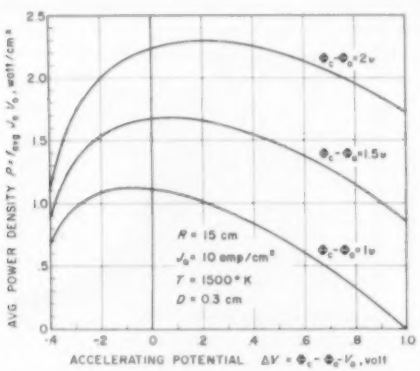

FIG. 11. Effect of accelerating voltage ΔV on power density (averaged over disk electrode area).

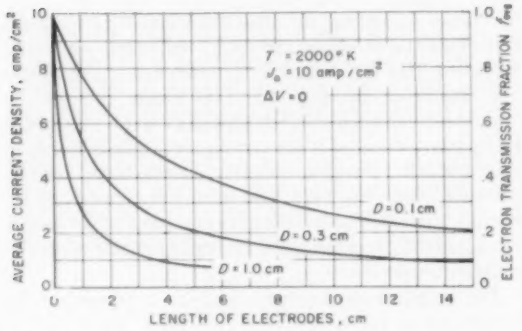

FIG. 13. Effect of cylindrical electrode length on average current transmission, for the special case $\Phi_c = \Phi_e + V_0$.

and let ξ and ψ be defined as functions of the magnetic field direction and the initial electron direction by

$$\xi \equiv \beta(\beta v_z - v_y)/(v_z + \beta v_y)$$
$$\psi \equiv \beta(1+\beta^2)^{\frac{1}{2}} v_x/(v_z + \beta v_y). \tag{21}$$

The rewriting of Eq. (20c) in terms of these dimensionless variables gives

$$Z = \xi \sin\tau + \psi(1-\cos\tau) + \tau. \tag{22}$$

The variation of Z with τ, i.e., the electron motion perpendicular to the emitter, is a sinusoidal function superimposed on a constantly ascending base line. Depending on their values of ξ and ψ, the emitted electrons may be divided into three groups, as illustrated by Fig. 15. Group I electrons have monotonically increasing Z, while Groups II and III pass through successive maxima and minima. Group II consists of those electrons whose first minimum value of Z is positive, while the electrons with negative Z_{min} belong to Group III.

Clearly, Groups I and II escape the emitting electrode. As for Group III, those electrons whose first maximum value of z exceeds the electrode spacing D will also reach the collector. In fact, when $B_z = 0$ these are

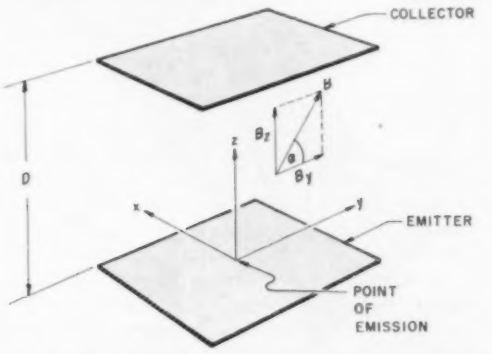

FIG. 14. Definition of Cartesian coordinates, showing their alignment with respect to the transverse and longitudinal magnetic field components.

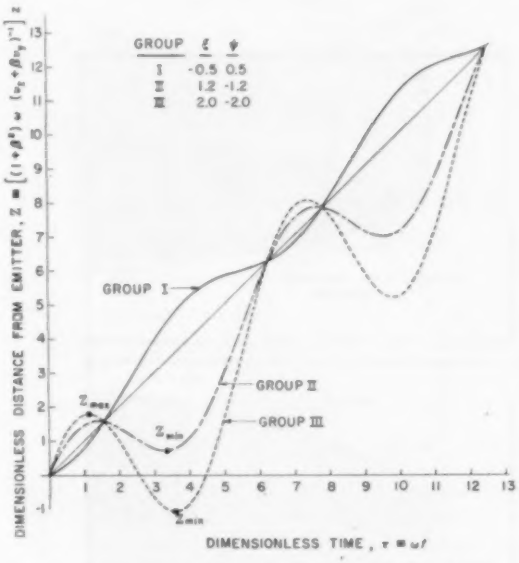

FIG. 15. Electron motion typical of Groups I, II, and III.

the *only* successful electrons, since Group I and II have no members. However, we are primarily interested in reasonably large electrode spacings, and in strong magnetic fields (i.e., small helical diameters). Under these conditions, the number of electrons whose $z_{max} > D$

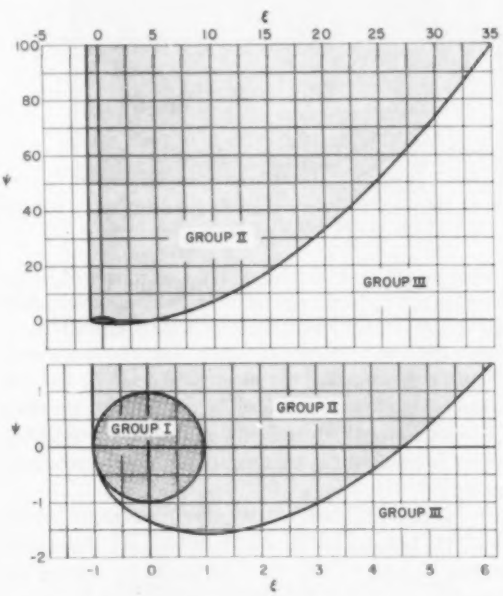

FIG. 16. Distribution of electron groups in ξ, ψ space. The boundary between Groups II and III represents the solution of Eq. (23). The lower section of the figure gives a magnified view of the area near the origin.

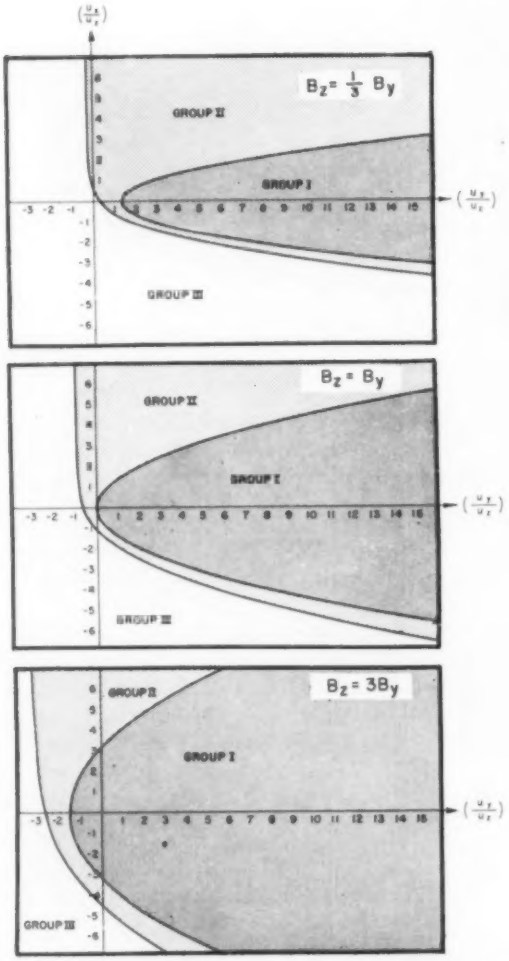

FIG. 17. Distribution of electron groups in velocity space. Note the effect of increasing the longitudinal field B_z.

is very small, and *all* Group III electrons will be assumed to return to the emitter. Since this approximation underestimates the fraction of electrons transmitted, the results obtained are conservative. The above assumption not only simplifies the subsequent analysis but also improves its generality, since the fractions of electrons in Groups I and II depend only on the field direction β, and are independent of the field strength B and electrode spacing D.

From Eq. (22) we find that all electrons whose $\xi^2+\psi^2<1$ belong to Group I, while the boundary between Groups II and III is obtained by solving for $Z_{\min}=0$.

$$(\xi^2+\psi^2-1)^{\frac{1}{2}}+\arccos[-(\xi^2+\psi^2)^{-\frac{1}{2}}] -\arctan(-\psi/\xi)+\psi=0. \quad (23)$$

Electrons which satisfy this transcendental equation just graze the emitting surface at their first minimum. Equation (23) was solved by computer, and the results are illustrated by Fig. 16. This figure depicts the boundaries between electron groups in terms of ξ and ψ. For a given value of β, the corresponding boundaries in terms of the emission velocity components can be computed from Eq. (21). The results are illustrated by Fig. 17 for three representative magnetic-field ratios. For a given B_y, it is clear that increasing B_z improves the electron transmission.

The transmission fraction $f=J/J_0$ is computed by integration of Eq. (3):

$$f=(2/\pi)\int\int\int \exp[-(u_x^2+u_y^2+u_z^2)]u_x du_x du_y du_z. \quad (24)$$

From Eqs. (21) and (23) we obtain the integration limits corresponding to the shaded areas of Fig. 17:

$$[\beta^{-1}(1+\beta^2)^{\frac{1}{2}}(\xi+1)^{-1}\psi u_z]<u_x<\infty,$$
$$(-\beta^{-1}u_z)<u_y<\infty, \quad 0<u_z<\infty,$$

where ξ is a function of u_y and u_z [Eq. (21)], and ψ is a function of ξ [Eq. (23)]. The integration of Eq. (24) is greatly simplified by converting from Cartesian to spherical velocity components, as illustrated by Fig. 18. Upon inserting $u_x=u\sin\theta\cos\phi$ and $du_x du_y du_z=u^2\sin\theta du d\theta d\phi$ in Eq. (24), we have

$$f=(2/\pi)\int\int\int u^3\exp(-u^2)\sin^2\theta\cos\phi\, du\, d\theta\, d\phi, \quad (25)$$

with the corresponding integration limits

$$0<u<\infty, \quad 0<\theta<\Theta \quad \text{and} \quad -\operatorname{arccot}\beta<\phi<\tfrac{1}{2}\pi,$$

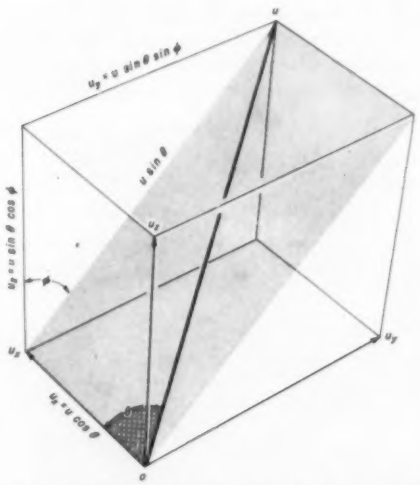

FIG. 18. Definition of spherical coordinates, showing the relation of the emission velocity's direction angles ϕ and θ to the Cartesian coordinates x, y, z.

where $\Theta=\arctan[\beta(1+\beta^2)^{\frac{1}{2}}\psi^{-1}(\cos\phi+\beta\sin\phi)^{-1}]$. Hence, the boundary between successful and unsuccessful electrons can be expressed in terms of their emission angles ϕ and θ. This is shown by Fig. 19, for several values of the field ratio β.

Finally, on integrating Eq. (25) over u and θ, and recalling that $\beta\equiv\cot\alpha$, we obtain an expression for computing the fraction of electrons in Groups I plus II, i.e., the fraction which arrives at the collector,

$$f_{(\alpha)}=\frac{1}{4\pi}\int_{-\alpha}^{\frac{1}{2}\pi}\cos\phi[2(\Theta-\sin 2(\Theta]d\phi, \qquad (26)$$

where

$$\Theta=\operatorname{arccot}[\psi\tan\alpha\sin(\alpha+\phi)]$$

$$(\xi^2+\psi^2-1)^{\frac{1}{2}}+\arccos[-(\xi^2+\psi^2)^{-\frac{1}{2}}]$$

$$-\arctan(-\psi/\xi)+\psi=0$$

$$\xi=\cot\alpha\cot(\alpha+\phi).$$

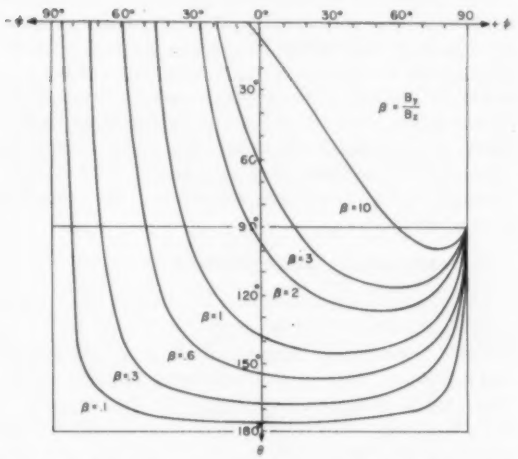

FIG. 19. Effect of emission direction on electron destination. For each magnetic field ratio β, the area above the curve represents the domain of the successful electrons, i.e., those reaching the collector. Actually, this graph should be plotted on a hemispherical surface, with ϕ denoting longitude and θ representing latitude.

By analogous methods, the writer has derived[8] an expression for the fraction of electrons in Group I. The electron fractions in Groups I and II were calculated by digital computer, with the results shown in Figs. 20 and 21. The latter figure shows that with matched fields ($B_z=B_y$) over 70% of the emitted electrons reach the collector, and that a longitudinal field of twice that magnitude ($B_z=2B_y$) permits 90% electron transmission. In other words, a longitudinal field of reasonable magnitude permits efficient operation in spite of the self-induced transverse field. This is illustrated by a typical example in the Appendix.

Examination of Fig. 21 reveals that there is a surprisingly simple relation between the transmission

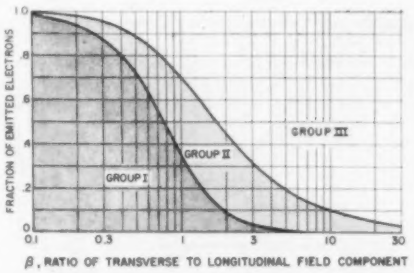

FIG. 20. Distribution of electron groups as a function of the magnetic field ratio. Note that with matched fields ($B_y=B_z$) the electron fractions in Groups I and II are each $\frac{1}{4}\sqrt{2}$.

fraction and the magnetic field direction

$$f=(1+\beta^2)^{-\frac{1}{2}}=\sin\alpha=B_z/(B_y^2+B_z^2)^{\frac{1}{2}}. \qquad (27)$$

The simplicity of the above equation suggests that there may be a direct, analytical method for proving it (i.e., without recourse to numerical computation). However, if such an analytical proof exists, it has so far eluded us.

We now proceed to couple the equation of current transmission with that of field induction, just as we did in the case of the pure transverse field. We shall assume plane parallel disk electrodes, with the longitudinal B_z field applied by means of a solenoidal field coil. Hence, B_z has a constant value. As before, the value of the self-induced field at radial position r is obtained from Eq. (14):

$$B_y=B_\theta=\frac{\mu_0 J_0}{r}\int_0^r fr'dr'. \qquad (28)$$

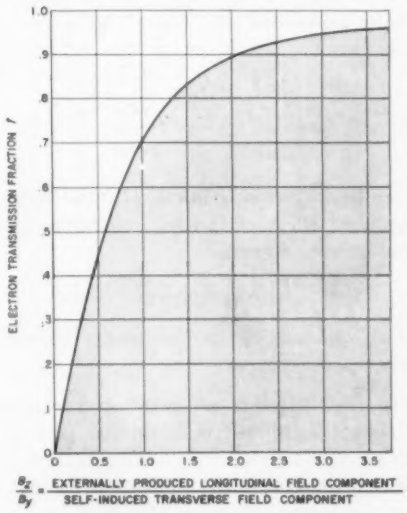

FIG. 21. Effect of perpendicular magnetic field on electron transmission. Note that the graph indicates that $f\to 0$ as $B_z\to 0$. This results from our assumption of a large transverse magnetic field and reasonable electrode spacing.

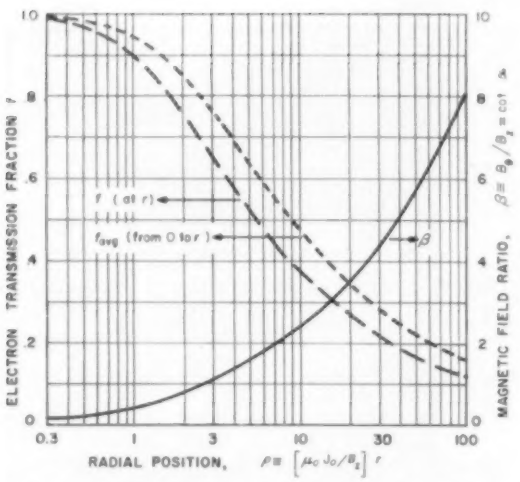

FIG. 22. Mutual interaction of the applied and self-induced magnetic fields with the transmitted current. General solution for plane parallel disk electrodes.

Dividing Eq. (28) by $B_z = B_y/\beta$, inserting Eq. (27) for f, and differentiating with respect to r, we obtain

$$(d\beta/d\rho) = (1+\beta^2)^{-1} - (\beta/\rho), \tag{29}$$

where ρ denotes a dimensionless radial position defined by $\rho \equiv [\mu_0 J_0/B_z]r$. The boundary condition at $\rho = 0$ is $\beta = 0$, $\beta/\rho = \frac{1}{2}$. Equation (29) was solved by digital computer, and its solution is depicted by the solid line in Fig. 22. From this, it is easy to compute the transmission fraction $f = (1+\beta^2)^{-1}$, and f_{av} (the transmission fraction averaged over the electrode area):

$$f_{av} = \frac{2\pi \int_0^r f r' dr'}{\pi r^2} = \frac{2B_y}{\mu_0 J_0 r} = \frac{2\beta}{\rho}. \tag{30}$$

These results are presented in Fig. 22, which summarizes the combined effect of the self-induced and applied fields on current transmission.

CONCLUSIONS

Theoretical analysis of the low density plasma diode indicates that:

1. The high currents generated induce transverse magnetic fields which deflect the emitted electrons.
2. Even modest field strengths force a large fraction of the current to return to the emitter, thus reducing the energy conversion efficiency.
3. As a result, cylindrical or plane electrodes, unless kept to a relatively small size, should prove quite inefficient.
4. This undesirable design limitation on electrode size is eliminated in the *magnetothermionic generator*, which employs external field coils to produce a longitudinal magnetic field parallel to the current flow.
5. With a longitudinal field of suitable magnitude, almost complete electron transmission can be achieved.

The magnetothermionic concept may not only minimize the undesirable magnetic field effects, but even offers the possibility of turning these effects to our advantage. By means of a modulated field coil current, a fluctuating dc output could be produced. Passing this output current through a suitable transformer would extract its ac component, and step up its voltage to match the load requirements.

ACKNOWLEDGMENTS

The author is indebted to the many investigators whose studies of thermionic power conversion developed the concepts and understanding which are the foundation of the present analysis. Among his colleagues at Republic Aviation, the writer wishes to thank A. E. Kunen and L. Kraus for their support and encouragement, L. Aronowitz for suggesting the possibility of using a perpendicular magnetic field, and L. Levin, J. Boggi, and B. Siegel for programming the numerical computations.

APPENDIX: ILLUSTRATIVE EXAMPLE

The example cited below is designed to illustrate a typical magnetothermionic generator. Its purpose is to examine the effect of magnetic fields on power density and efficiency, and to ascertain what fraction of the generated power is required to produce the longitudinal field. Since our main interest is in relative rather than absolute performance, any reasonable assumptions may be employed.

Consider a generator consisting of a 4-ft high stack of plane disk electrodes, 3 ft in diameter. Altogether, there are 50 unit cells connected in series, each cell consisting of one hot and two cold electrode disks (so that both sides of the emitters are utilized). The cathode disks are internally heated by means of a fissionable fuel. The fuel concentration is adjusted so that the entire assembly of stacked disks (together with the anode coolant-moderator and the external neutron reflector) constitutes a critical nuclear reactor. Assuming a cathode work function $\Phi_c = 2.2$ v and a temperature $T = 1491°\text{K}$, Eq. (2) gives a saturation current density $J_0 = 10$ amp/cm². If none of the emitted electrons were turned back by the self-induced magnetic field, such a generator would produce a current of 131 ka.

However, it is easily shown from Eq. (14) that a 3-ft electrode, operating at the current density J_0, would generate a transverse B_θ field of 572 gauss at the disk's periphery. As shown in Fig. 4, a transverse magnetic

TABLE I. Energy balance (with B_z field).

Heat input		Electric output	
Electron cooling	16 100 kw	Gross power produced	6850 kw
Lead conduction	1800 kw	Loss in leads	810 kw
Thermal radiation	3200 kw	Field coil power	57 kw
Total	21 100 kw	Net	5983 kw

Over-all efficiency = 5983/21 100 = 28.4%

field having even a small fraction of this strength would force practically all of the electrons back to the emitter. Actually, for a 0.3-cm spacing between 3-ft electrode disks (R=45.7 cm), Fig. 12 shows that only 4.5% of the emitted current (i.e., 5.9 ka) reaches the collector.

To avoid this difficulty, we wish to impose a longitudinal magnetic field B_z, perpendicular to the electrode disks. Assume that the cylindrical generator is surrounded by three closely wound coils of ½-in. aluminum tubing, connected in parallel with the electrical load. Such a coil, using less than 1% of the power generated, would produce a B_z field of 1130 gauss, which is twice the magnitude of the maximum B_θ field. This gives a value of $\rho \equiv \mu_0 J_0 R / B_z = 1.01$. Referring to the coupled solution presented in Fig. 22, we find that 95.0% of the emitted current will reach the collector, compared to the 4.5% transmission attainable without the B_z field.

Next, we assume that each hot electrode is connected to the previous cell by a number of tungsten leads,

TABLE II. Energy balance (without B_z field).

Heat input		Electric output	
Electron cooling	725 kw	Gross power produced	330 kw
Lead conduction	205 kw	Loss in leads	17 kw
Thermal radiation	3200 kw		
Total	4130 kw	Net	313 kw

Over-all efficiency = 313/4130 = 7.6%

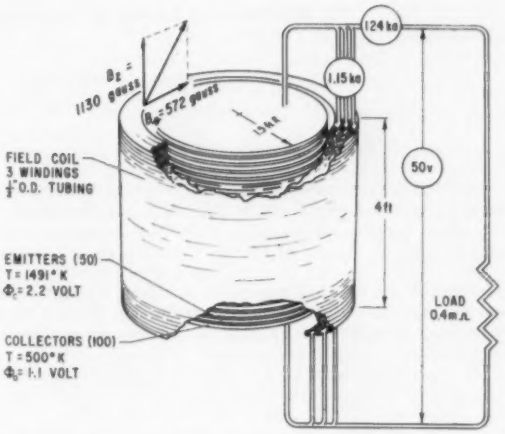

FIG. 23. Summary of the illustrative example, showing the postulated design and some of the computed results.

0.5 cm long. To optimize the system efficiency, these leads should have a *total* cross-sectional area of 15 cm² per electrode, giving a potential drop of 0.12 v per lead. Finally, we assume that the anode work function Φ_a = 1.08 v, and the accelerating voltage ΔV = 0. These assumptions give an external voltage drop of 2.2 − 0.12 − 1.08 = 1.0 v per cell, or a total load voltage of 50 v. The design postulated above is summarized by Fig. 23.

The system was analyzed[8] (assuming electrode emissivities of 0.3), and the results are shown in Table I. In the absence of the longitudinal magnetic field, the optimum lead cross section is reduced to 1.5 cm²/electrode, resulting in the performance shown in Table II.

To summarize, for the generator design postulated, the addition of the B_z field improves the efficiency from 7.6% to 28.4%, and increases the power production from 313 kw to 5983 kw.

Conservation Laws of Uniform Linear Homogeneous Systems

M. C. PEASE*
Sylvania Electric Products Inc., Mountain View, California
(Received March 1, 1960)

A generalized linear homogeneous system is analyzed for the quadratic forms that are invariant under it. Such forms lead to conservation laws that are properties of the system. If the system has n degrees of freedom, it will have at least n such conservation laws which together determine the "type" of the system. The analysis may be viewed as the determination of the metrics under which the operator becomes rotational. In such a metric, the square of the length of a vector is invariant. A conservation law is expressible as its appropriate metric. The Manley-Rowe relations for parametric devices, and Chu's kinetic power theorem for electron-beam devices are examples.

The analysis is related both to the system operator and to a possible system matrix differential equation. In the latter case, this allows a direct connection between the conservation laws and the physical construction of the system. The converse problem in which two metrics are specified is also considered. The range of possible matrix differential equations of a given type, and of system operators, is determined. Application is made to a uniform parametric line with "ideal forward coupling." Such a device will be stable in the sense that it avoids internal feedback. If it is matched either on the input or output side, it will not oscillate regardless of its gain or electrical length. The necessary and sufficient conditions for this ideal behavior are obtained by considering the invariant forms—the conservation laws—that it should obey.

THE problem studied here concerns the analysis of linear homogeneous systems by their quadratic invariances. These include the various conservation laws that the system obeys, and therefore specify its "type."

The systems that we are concerned with may be of various kinds. The method of analysis has been developed specifically for the study of parametric circuits in which there exists coupling between various related frequencies such as that described by Tien.[1] It is applicable, however, to many kinds of systems. The small signal theory of beams under various conditions may be cited as an example.[2,3]

Such systems always involve some conservation laws. For ordinary reactive networks, we have the conservation of energy. For reactive parametric circuits, we have the Manley-Rowe theorem[4] stating the conservation of a properly reduced power. For beam-type systems, we have Chu's theorem[5] on the conservation of kinetic power. For other classes of systems, there are other laws. And for subclasses of these classes, there are additional conservation theorems (e.g., an ordinary lossless transmission line can be defined as a device in which both total power and the power in a properly defined forward wave are conserved).

Our problem, then, is to determine all the conservation laws that may apply to a given type of system, and to determine the systems for which a given set of conservation laws apply.

We shall consider the system abstractly, without specific limitation to the physical situation. The basic requirements on it that permit this type of analysis are (a) that it be expressible as a linear homogeneous transformation on some suitable basis, (b) that its eigenvalues are restricted in a manner to be specified, and (c) that the basis on which we operate is discrete. The last requirement can be avoided by an integral formulation, but we shall here restrict ourselves to the discrete case so that we can use a matrix representation.

We need not limit ourselves to a finite basis although we shall do so here. If it is infinite, the matrix operators are infinite. Properly speaking, this creates some special difficulties of convergence and rigor. However, the number of observable degrees of freedom of any laboratory system is necessarily finite, although possibly large. It has, therefore, appeared to us better to ignore these added complications that arise only in the purely mathematical problem.

We shall, then, first consider the problem abstractly. Before doing this, however, we shall discuss the system itself to define more precisely the type of system being considered, and to establish the abstract formalism on which the analysis is based.

After having done this, we shall proceed with the analysis for the invariants of the system. We shall do this abstractly to obtain generality, hoping thereby not to sacrifice too much intelligibility.

Finally, we shall apply the analysis to determining the necessary conditions for a distributed parametric line with certain "ideal" characteristics. Specifically, we shall study how we may design such a line so as to avoid internal reflections. Can we, in other words, design an amplifier such that, if we match to the input terminals, the behavior will be stable regardless of the connections to the output terminals? We shall find that we can, and that the conditions for accomplishing this are theoretically quite straightforward.

The study of an "ideal" distributed parametric amplifier is an important and practical problem in its own right. It will also serve to illustrate the significance

* Now at Stanford Research Institute, Menlo Park, California.
[1] P. K. Tien, J. Appl. Phys. **29**, 1347 (1958).
[2] W. H. Louisell and C. F. Quate, Proc. I.R.E. **46**, 707 (1958).
[3] H. A. Haus, Massachusetts Inst. Technol. Tech. Rept. No. 316 (April, 1958).
[4] J. M. Manley and H. E. Rowe, Proc. I.R.E. **44**, 904 (1956).
[5] L. J. Chu, "A kinetic power theorem," paper presented at the I.R.E-P.G.E.D. Electron Tube Research Conference, Durham, New Hampshire (June, 1951). See also footnote reference 3.

and application of the analytic method which otherwise may be too generalized to be intelligible.

I. THE SYSTEM

As we have stated above, we are considering systems which are linear, homogeneous, and contain a discrete and finite number of degrees of freedom. For such a system, the matrix formulation[6] is convenient. We describe the state of the system by means of a column matrix $\mathbf{x}(z)$, whose elements are functions of z, and which together serve to describe the state of the system at that value of z. The manner in which these coefficients combine to describe the physical state of the system is the "basis" of the representation. The basis is not unique but is, within limits of appropriateness, a matter of convenience.

As an example, in an ordinary 2-port network, we may represent the state of the system by listing, in order, the voltage and current amplitudes as functions of z. Or we may take the amplitudes of the forward and backward waves, referred to some designated characteristic impedance, giving a wave basis.

In a distributed parametric circuit, in which the pump power is large compared to all other signals so that its effect may be included in the description of the device, we may take the voltages and currents at the various frequencies, $\omega_n=\omega_0+n\omega_p$, ω_p being the pump frequency. Alternatively again, we may define the basis in terms of forward and backward waves, referred to a characteristic impedance at each frequency. We could even, if there were value in it, define various mixed frequency impedances, leading to a generalized wave basis.

In a beam-type device, $\mathbf{x}$ may list the (complex) amplitudes of the various parameters that are considered to be significant to the problem—e.g., the rf longitudinal and transverse velocities, rf space charge, and the circuit parameters. Or, if we have a suitable modal description, $\mathbf{x}$ may list the complex amplitudes of these modes.

We shall assume that the time dependence has been removed. With some additional complexity, we could retain it, and show more general conditions under which the present approach is applicable, but to do so does not seem to be particularly profitable.

For the present purposes, we shall assume that $\mathbf{x}$ is a function of a single spatial variable z only.

We assume, then, that the differential equation of the system is of the form

$$d\mathbf{x}(z)/dz=-j\mathbf{W}\mathbf{R}\mathbf{x}(z), \tag{1}$$

where $\mathbf{W}$ and $\mathbf{R}$ are constant square matrices. $\mathbf{R}$ may be considered as the "coupling matrix" of the system. The operator $j\mathbf{W}$ then contains the effect of time variation. If, for example, the basis is a sequence of variables that are related to the physical state of the system with a time dependence of the form $\exp(j\omega_n t)$, then $\mathbf{W}$ is a diagonal matrix with the sequence ω_n along the diagonal.

The advantage of separating out the factor $\mathbf{W}$ lies in the fact that it is common to many systems with different $\mathbf{R}$ matrices and that the $\mathbf{R}$ factor is thereby much simplified. $\mathbf{W}$ is, in fact, determined by the basis, given the form of (1), and is therefore common to all problems of this type to which the basis is appropriate.

It should be recognized, however, that (1) is not always appropriate. It applies to those systems in which, if we retain the time factor, the z partial derivatives are homogeneous in the time derivatives. We may properly call such systems "purely reactive." If, instead, the time derivatives do not appear in the differential equations for the time varying functions, then we have the "purely resistive" case and (1) is not appropriate. In this case, instead of (1), we use

$$d\mathbf{x}(z)/dz=\mathbf{S}\mathbf{x}(z). \tag{2}$$

If, in the equations for the space derivatives of the time varying functions, both the time derivatives and the functions themselves enter, then we have the "lossy reactive" case, intermediate between the two previous cases. We then write

$$d\mathbf{x}(z)/dz=(\mathbf{S}-j\mathbf{W}\mathbf{R})\mathbf{x}(z). \tag{3}$$

While cases (2) and (3) can be analyzed by methods that are similar to what follows, we shall restrict our attention to those cases where (1) applies. These cases include many of the situations of greatest practical interest—lossless parametric circuits, linearized electron beams coupled to lossless circuits, linearized plasma problems where we can neglect inelastic collisions, etc.

Equation (1) may be recognized as a generalization of the equations for a uniform lossless transmission lines. It is also a formalistic way of writing the coupled mode equations[7] where the coupling is uniform, i.e., where it does not vary with z.

Equation (1) can be put into an alternate form which is a consequence of the linearity and homogeneity of the system. The $\mathbf{x}$ at any z is linearly related to the $\mathbf{x}$ at any other z, say $z=0$. Hence there exists a matrix $\mathbf{M}$, which is a function of z, such that

$$\mathbf{x}(z)=\mathbf{M}(z)\mathbf{x}(0). \tag{4}$$

On substituting this in (1), and since the resultant equation must hold for any $x(0)$,

$$d\mathbf{M}(z)/dz=-j\mathbf{W}\mathbf{R}\mathbf{M}(z). \tag{5}$$

The vector differential equation, (1), implies the matrix differential Eq. (5). This may not seem like a simplification since it replaces the n scalar differential

[6] As general references to the theorems of matrix algebra used here, we may cite *Principles and Techniques of Applied Mathematics*, by B. Friedman (John Wiley & Sons, Inc., New York, 1956); and *Algebraic Theories*, by L. E. Dickson (Dover Publications, New York, 1959).

[7] J. R. Pierce, J. Appl. Phys. **25**, 179 (1954).

equations of (1) by n^2 equations. Its significance, however, is that it removes the boundary conditions from the immediate problem. It is, therefore, with (5) that we shall principally concern ourselves.

II. THE METRICS OF THE SYSTEM OPERATOR

If we are given the operator **M**, on a suitable basis, we wish to know if we can find scalar forms s expressible as

$$s = \mathbf{x}^\dagger \mathbf{K} \mathbf{x}, \tag{6}$$

which are unchanged by replacing **x** by **Mx**. By $(\ )^\dagger$ we mean the "Hermitian conjugate" (i.e., the complex conjugate of its transpose) so that $\mathbf{x}^\dagger$ is a row matrix whose elements are the complex conjugates of the elements of the column matrix **x**. **K** is a square matrix. s is, then, a scalar quantity.

This is not an arbitrary choice of form. The form of (6) is a general expression for a "quadratic form." It may be noted that most of the known conservation laws are of this form, or are expressible in terms of such forms. For example, the conservation of energy in a nonparametric 2-port expresses the invariance of $\frac{1}{2}(EI^*+E^*I)$. The Manley-Rowe relation in its linearized form (large pump) and Chu's kinetic power theorem both express the constancy of a quadratic form. Hence, it is reasonable to search for the general existance of invariants of this form.

There is also another possible interpretation of (6) which may be of value. We may regard **K** as the "metric" of the space in which the vector **x** is "embedded." Since the definition of the vector in terms of the physical problem implies nothing about what we may mean by the "length" of **x**, we are at liberty to choose the metric of the vector space as we wish. Then s becomes, by definition of metric, the length, squared, of the vector **X**. The invariance of a s under the operation **M** then means that, in the space so defined, **M** is a rotational operator.

The problem of determining the conservation laws of an operator **M** is the problem of determining those metrics under which **M** is rotational. If we substitute (4) into (6) giving $s(z)$, and require that the results be constant for all z for any $\mathbf{x}(0)$, then we must have

$$\mathbf{M}^\dagger \mathbf{K} \mathbf{M} = \mathbf{K} \tag{7}$$

or

$$\mathbf{M}^{\dagger -1} = \mathbf{K} \mathbf{M} \mathbf{K}^{-1}. \tag{8}$$

Equation (8) expresses $\mathbf{M}^\dagger$ as a "simularity transformation" on $\mathbf{M}^{-1}$. It is a well-known theorem of matrix algebra that similar matrices must have the same eigenvalues with the same multiplicity and rank. Hence the eigenvalues of **M** must either be of unit magnitude, or else occur in pairs such that one is the conjugate reciprocal of the other. It may be shown that, if **M** is nonsingular, this condition on the eigenvalues is not only necessary, but sufficient for the existence of **K**'s satisfying (7).

The solution of (7) is given, briefly, in the appendix, and has been discussed elsewhere in greater detail. From the method used in the appendix, we can deduce that, if these conditions are met, then there will be at least n independent solutions for **K**—more if **M** is degenerate.

Consequently, if **M** is of this type, there is a multiplicity of quadratic forms (6) which are invariant under a given **M**. Each such form is a "conservation law" of the system.

The profusion of conservation laws may at first seem startling. However, we may note that most of these invariants are specific to a restricted class of **M**'s and do not have the generality of what is usually called a "conservation law."

To cite a simple example, consider a lossless transmission line, without parametric variation. One conservation law of this system is the conservation of energy. This law is, of course, common to all lossless networks. A second exists, however, which states the conservation of energy in the forward wave alone, or in the backward wave alone, the waves being defined with reference to the characteristic impedance of the line. This invariant is also common to a class of networks.

Each of these two invariances lead to a different **K** for the system. Each **K** defines a class of structures. A transmission line of the specified impedance can be considered as being essentially defined by the intersection of these two classes.

Hence these other invariants of the system are significant and reflect real properties of the system. Whether or not they are also useful depends, of course, on what use we want to make of them.

III. THE METRICS OF THE DIFFERENTIAL EQUATION

We now wish to relate the **K**'s as defined in terms of the **M** operator to the differential Eq. (5). To do so will eliminate the need for determining the **M** operator itself when we only seek those properties of the system that are implied by the set of **K**'s.

To do this, we differentiate (7) with respect to z, requiring that **K** be independent of z.

$$(d\mathbf{M}^\dagger/dz)\mathbf{K}\mathbf{M} + \mathbf{M}^\dagger \mathbf{K}(d\mathbf{M}/dz) = 0. \tag{9}$$

Equation (9), by itself, assures only that $\mathbf{M}^\dagger \mathbf{K} \mathbf{M}$ be a constant matrix. However, (4) requires that $\mathbf{M}(z)$ become the identity matrix at $z=0$. Hence the constant of integration must be **K**.

On substituting (5) in (9), premultiplying by $\mathbf{M}^{\dagger -1}$, and postmultiplying by $\mathbf{M}^{-1}$, we obtain

$$(\mathbf{W}\mathbf{R})^\dagger \mathbf{K} = \mathbf{K}(\mathbf{W}\mathbf{R}). \tag{10}$$

This may be solved, formally at least, by putting **WR** into diagonal form.

Equation (10) relates the metrics to the operator

appearing in the differential equation. It permits the determination of the invariants of the system—its conservation laws—from the differential equation without requiring a specific solution for **M**.

The solution to (10) is given in Appendix II. Again, there are at least n solutions, providing the general condition cited in Appendix II is satisfied.

One solution is of particular interest since it leads to the conservation of energy in single-frequency 2-ports, the linearized Manley-Rowe relation, and to Chu's kinetic power theorem. Under the various conditions, in other words, it leads to a metric that is common to large and important classes of systems.

This metric arises when there exists a matrix **A** whose square is the identity matrix and which commutes with **W**, and which transforms the **R** in Eqs. (1) or (5) into $\mathbf{R}^\dagger$:

$$\mathbf{R}^\dagger = \mathbf{A}^{-1}\mathbf{R}\mathbf{A} = \mathbf{A}\mathbf{R}\mathbf{A}. \tag{11}$$

If these conditions are met, then

$$\mathbf{K} = \mathbf{A}\mathbf{W}^{-1} = \mathbf{W}^{-1}\mathbf{A} \tag{12}$$

is a solution of (10).

In the parametric case, for example, where we may take as the basis the voltages at the various frequencies and the currents,

$$x = \begin{pmatrix} \vdots \\ E_n \\ \vdots \\ \vdots \\ I_n \\ \vdots \end{pmatrix}, \tag{13}$$

then, as mentioned before, **W** is the diagonal matrix of the angular frequencies ω_n. The **R** matrix has the form

$$\mathbf{R} = \begin{pmatrix} \mathbf{O} & \mathbf{L} \\ \mathbf{C} & \mathbf{O} \end{pmatrix}, \tag{14}$$

where **L** and **C** are themselves Hermitian matrices. If, now we set

$$\mathbf{A} = \begin{pmatrix} \mathbf{O} & \mathbf{I} \\ \mathbf{I} & \mathbf{O} \end{pmatrix}, \tag{15}$$

where **I** is the identity matrix, the conditions are met and (12) leads to the linearized Manley-Rowe condition.

The **K** so obtained does not contain the parameters of **R**. Hence this metric is appropriate to any parametric circuit such that **R** has the form of (14) with **L** and **C** Hermitian.

On the other hand, if the elements are lossy, and the form of the differential equation is that of (3) instead of (1), we might attempt to force it into the form of (1). If we did, maintaining **W** as a real diagonal matrix of some sort, **R** would still have the form of (14), but **L** and **C** would not be Hermitian, and (15) would not satisfy (11). Hence the Manley-Rowe condition is limited, as is known, to the lossless case.

The determination of one metric facilitates the determination of the others. Specifically, it serves as the $\mathbf{K}_0$ of Appendix II.

Thus, we are able to determine the metrics of the system from the differential equation without explicitly obtaining the system matrix operator itself. Each metric so obtained leads to an invariance of the system, i.e., some quadratic combination of the system variables that is constant throughout the system, or is conserved by the system.

Again, we may regard each metric as determining a class of possible systems. The specific type of system that is represented by the differential equation is then the type selected by the intersection of the classes appropriate to the metrics.

IV. THE SYSTEM AS DETERMINED BY THE METRICS

The point of view that has developed here requires a more detailed analysis of the converse problem. Given one or more metrics, is it possible to construct a device which will have these conservation laws? What should be the design parameters for it?

We shall consider this problem in several steps. We shall discuss first the significance of specifying that the given metrics shall be Hermitian. Then, we shall show that the specification of two independent Hermitian metrics implies a set of metrics. This implied set does not necessarily contain any additional metrics. It is important, however, since if it does contain additional independent metrics, then the original specification of two metrics is, by that extent, limiting. If we wish to obtain the broadest possible class of devices with certain properties expressed as conservation laws, then the **K**'s that are specified must be chosen so that the implied set of **K**'s is as small as possible.

We can next determine the set of **R** matrices which, when substituted in the differential Eq. (6), will describe a system with these metrics. This is probably the most useful form of the solution since it relates the metrics, and hence the conservation laws, directly to the physical properties that determine the differential equation.

Finally we can obtain a set of **M** matrices which are solutions of (6) with the derived set of **R** matrices. We will not discuss the completeness of this set although it appears to be complete. But it does at least give us a range of system operators that have the given metrics.

A. Hermitian K

We have not so far restricted **K** to Hermitian form or otherwise. Of principal interest, however, are those **K**'s that are Hermitian. For if **K** is nonHermitian,

then it can be written

$$\mathbf{K}=\mathbf{K}'+j\mathbf{K}'', \tag{16}$$

where $\mathbf{K}'$ and $\mathbf{K}''$ are Hermitian. These may be found from

$$\mathbf{K}'=(\mathbf{K}+\mathbf{K}^\dagger)/2 \tag{17}$$

$$\mathbf{K}''=-j(\mathbf{K}-\mathbf{K}^\dagger)/2. \tag{18}$$

If we take the conjugate transpose of Eq. (7),

$$\mathbf{M}^\dagger\mathbf{K}^\dagger\mathbf{M}=\mathbf{K}^\dagger. \tag{19}$$

We find that $\mathbf{K}^\dagger$ is also a metric.

Since any linear combination of metrics is also an acceptable metric, $\mathbf{K}'$ and $\mathbf{K}''$ are also acceptable metrics. Hence, if $\mathbf{K}$ is nonHermitian, and not a scalar times a Hermitian metric, then its specification is equivalent to the specification of two independent Hermitian metrics. The specification of such a metric is a much tighter restriction than the specification of a Hermitian metric.

In what follows we shall therefore assume that all metrics have been reduced to Hermitian form.

B. Implied Set of K's

If given two independent Hermitian $\mathbf{K}$'s, $\mathbf{K}_1$ and $\mathbf{K}_2$, associated with a given operator $\mathbf{M}$, we can generate a set of $\mathbf{K}$'s which must also be acceptable to $\mathbf{M}$. This set may contain no additional $\mathbf{K}$'s, or it may contain up to n $\mathbf{K}$'s. We are given nonsingular Hermitian $\mathbf{K}_1$ and $\mathbf{K}_2$ such that

$$\mathbf{M}^\dagger\mathbf{K}_1\mathbf{M}=\mathbf{K}_1 \tag{20}$$

and

$$\mathbf{M}^\dagger\mathbf{K}_2\mathbf{M}=\mathbf{K}_2. \tag{21}$$

We can solve (21) for

$$\mathbf{M}^\dagger=\mathbf{K}_2\mathbf{M}^{-1}\mathbf{K}_2^{-1}$$

and

$$\mathbf{M}=\mathbf{K}_2^{-1}\mathbf{M}^{\dagger\,-1}\mathbf{K}_2. \tag{22}$$

On substituting these expressions in (20) and taking the inverse, we have

$$\mathbf{M}^\dagger(\mathbf{K}_2\mathbf{K}_1^{-1}\mathbf{K}_2)\mathbf{M}=\mathbf{K}_2\mathbf{K}_1^{-1}\mathbf{K}_2. \tag{23}$$

Hence we have a possibly new metric $\mathbf{K}_3$,

$$\begin{aligned}\mathbf{K}_3&=\mathbf{K}_2\mathbf{K}_1^{-1}\mathbf{K}_2=\mathbf{K}_2\mathbf{J}\\&=\mathbf{K}_1(\mathbf{K}_1^{-1}\mathbf{K}_2)^2=\mathbf{K}_1\mathbf{J}^2,\end{aligned} \tag{24}$$

$$\mathbf{J}=\mathbf{K}_1^{-1}\mathbf{K}_2. \tag{25}$$

$\mathbf{K}_3$ is Hermitian if $\mathbf{K}_1$ and $\mathbf{K}_2$ are ($\mathbf{J}$, however, is not in general Hermitian). This is a specific application of the theorem that, if $\mathbf{A}$, $\mathbf{B}$, and $\mathbf{C}$ are acceptable metrics for $\mathbf{M}$, then so is $(\mathbf{AB}^{-1}\mathbf{C})$. For

$$\begin{aligned}&\mathbf{M}^\dagger\mathbf{AB}^{-1}\mathbf{CM}\\&\quad=(\mathbf{M}^\dagger\mathbf{AM})(\mathbf{M}^{-1}\mathbf{B}^{-1}\mathbf{M}^{\dagger\,-1})(\mathbf{M}^\dagger\mathbf{CM})=\mathbf{AB}^{-1}\mathbf{C}.\end{aligned} \tag{26}$$

From (24) by induction, we find that

$$\mathbf{K}_n=\mathbf{K}_1\mathbf{J}^{n-1} \tag{27}$$

is an acceptable metric. Hence the set $(\mathbf{K}_n)$ is a set of acceptable metrics.

This set can also be written

$$\mathbf{K}_n=(\mathbf{J}^\dagger)^{n-1}\mathbf{K}_1. \tag{28}$$

The matrix $\mathbf{J}$, defined by (25) is, then, of central importance in determining the extent of implication contained in the specification of $\mathbf{K}_1$ and $\mathbf{K}_2$. The set $\mathbf{J}^k$ may contain anywhere from two to n independent forms, where n is the number of degrees of freedom of the system. It cannot contain less than two, since $\mathbf{K}_1$ and $\mathbf{K}_2$ are assumed independent. It cannot contain more than n since any matrix satisfies its characteristic equation so that $\mathbf{J}^n$ can always be written in terms of the first $n-1$ powers of $\mathbf{J}$ and $\mathbf{I}$.

The number of independent forms in the set $\mathbf{J}^k$ determine how much the range of possible systems is restricted by the specification of $\mathbf{K}_1$ and $\mathbf{K}_2$. If we are to obtain the largest possible range, then $\mathbf{K}_1$ and $\mathbf{K}_2$ should be chosen so as to give $\mathbf{J}$ the maximum amount of degeneracy, so that $\mathbf{J}^2$ is a linear function of $\mathbf{I}$ and $\mathbf{J}$.

C. The R Set

On having obtained the set $\mathbf{K}_n$ of implied metrics, we can ask what operators $\mathbf{R}$, for the differential Eqs. (2) or (6), are possible. This is an important problem since its solution will allow us to design a distributed system that will obey the desired conservation laws.

The basic relation that $\mathbf{R}$ must satisfy is (10). This is both necessary and sufficient providing we assume the form (5) for the differential equation. It must furthermore satisfy (10), where $\mathbf{K}$ is each of the implied $\mathbf{K}_n$ although it is sufficient to obtain it for $\mathbf{K}_1$ and $\mathbf{K}_2$.

Let us define an $\mathbf{S}$ operator by

$$\mathbf{S}=\mathbf{K}_1\mathbf{WR}. \tag{29}$$

Then if $\mathbf{W}$, $\mathbf{K}_1$, and $\mathbf{K}_2$ are Hermitian, (10) becomes

$$\mathbf{K}_n\mathbf{K}_1^{-1}\mathbf{S}=\mathbf{S}^\dagger\mathbf{K}_1^{-1}\mathbf{K}_n. \tag{30}$$

Letting $\mathbf{K}_n$ equal $\mathbf{K}_1$ in (30) shows that $\mathbf{S}$ must be Hermitian. Letting $\mathbf{K}_n$ equal $\mathbf{K}_2=\mathbf{K}_1\mathbf{J}=\mathbf{J}^\dagger\mathbf{K}_1$ shows that

$$\begin{aligned}&\mathbf{J}^\dagger\mathbf{S}=\mathbf{S}^\dagger\mathbf{J}=\mathbf{SJ},\\&\mathbf{J}^\dagger=\mathbf{SJS}^{-1}.\end{aligned} \tag{31}$$

$\mathbf{J}^\dagger$ must be related by a similarity transformation to $\mathbf{J}$. We can then find an operator $\mathbf{Q}$ such that

$$\mathbf{J}^\dagger=\mathbf{QJQ}^{-1}. \tag{32}$$

By putting (32) in (31) we find

$$\mathbf{J}(\mathbf{Q}^{-1}\mathbf{S})=(\mathbf{Q}^{-1}\mathbf{S})\mathbf{J}. \tag{33}$$

Hence, the necessary and sufficient conditions on $\mathbf{S}$ are that it be Hermitian and that $\mathbf{Q}^{-1}\mathbf{S}$ commute with $\mathbf{J}$. Having found the range of $\mathbf{S}$, then the range of $\mathbf{R}$ is given by (29). Explicitly, then

$$\mathbf{R}=(\mathbf{K}_1\mathbf{W})^{-1}\mathbf{S} \tag{34}$$

D. The M Set

We may now derive a set of possible $\mathbf{M}$ operators. We note first that if $\mathbf{M}_1$ and $\mathbf{M}_2$ are acceptable $\mathbf{M}$ operators, so is $\mathbf{M}_1\mathbf{M}_2$. Hence the $\mathbf{M}$ set is a group. It is therefore only necessary to find a set of generators of the group.

With the help of (10), it is now straightforward to show that if

$$\begin{aligned}\mathbf{M}_1&=\exp(-j\theta\mathbf{W}\mathbf{R}_1)\\&=\mathbf{I}-j\theta\mathbf{W}\mathbf{R}_1-\tfrac{1}{2}\theta^2\mathbf{W}\mathbf{R}_1\mathbf{W}\mathbf{R}_1+\cdots\end{aligned} \tag{35}$$

converges to a limit, then $\mathbf{M}_1$ satisfies (7) for $\mathbf{K}=\mathbf{K}_n$ if θ is a real scalar. It may be noted that this form is the formal solution to (5), except for the presence of the scalar term θ. It is therefore, a plausible one to investigate. θ may be a function of z, say βz, so that we are thus able to introduce a spatial dependence into $\mathbf{M}$. If we require that this also be a solution to (5), then the dependency on z must be obtained from (5). However, we are discussing here the operators that have the specified $\mathbf{K}_1$ and $\mathbf{K}_2$, and this problem is a different one from asking for those that satisfy (5) as written. For this purpose, any scalar function of z is suitable.

If we take the set $\mathbf{R}_n$ as a maximal independent subset of the total $\mathbf{R}$ set, Eq. (35) generates a set of $\mathbf{M}_n$. This set can then be used as the generators of the total $\mathbf{M}$ set.

[A word of caution is perhaps necessary here. The exponential form of M_n as given in (35) is formal only. The product of two such series is not in general obtained as the expansion of the exponential of the sum of the exponents. For the exponential product law to apply, the exponents must commute. If $\mathbf{R}_1$ and $\mathbf{R}_2$ are independent, they will not in general commute.]

This gives us a set of $\mathbf{M}$ operators associated with the given $\mathbf{K}_1$ and $\mathbf{K}_2$. We have not here shown that this set is complete, i.e., that it includes all possible such $\mathbf{M}$'s. It appears likely that it is. Certainly it is sufficiently complete for most purposes.

We have thus been able to start with two independent nonsingular Hermitian metrics and deduce the appropriate differential equation and system operator. The results are not necessarily unique. Two metrics may or may not be enough to specify completely the type of the system. (We have used the word "type" before without more than an implied definition. By "type" we mean that the behavior of the system is determined within a set of scalar quantities that can be identified as the electrical lengths that are involved in the system.) The extent to which two metrics limit the type is determined by the "rank" of $\mathbf{J}$, which is defined by (25).

This analysis can then be used to determine either the form of the system operators, or the differential equation of the systems that will exhibit the invariances determined by the specified metrics.

V. UNIFORMLY DISTRIBUTED PARAMETRIC LINES

We shall apply these techniques now to a problem that has considerable importance for itself, and that will illustrate the application of the method.

We shall ask ourselves if it is possible to design a uniformly distributed parametric line which is lossless and in which there is no coupling between the forward and backward waves. We shall call such behavior "ideal forward coupling." If, as we shall find, it is possible, then we shall want to know the design requirement for obtaining it.

The importance of this problem arises from the consideration of the stability of such a device when used as an amplifier. If the forward and backward waves are completely decoupled, then it is only necessary to match one end or the other to assure that there is no positive feedback, and hence that oscillations do not occur. If, on the other hand, there is coupling, then internal feedback occurs, and we would expect a limiting gain to exist beyond which it is not possible to prevent oscillations. Hence, for many applications, it is very desirable to obtain such ideal coupling.

We may also generalize this concept of ideal coupling. If it is possible to couple only the forward waves at one set of frequencies to the backward waves at a second set, then again stability can be assured. It can be shown that this is possible providing the frequencies alternate. That is, if $\omega_n=\omega_0+n\omega_p$, then the forward waves at ω_n for n even are coupled to the backward waves, but not the forward waves at ω_n for n odd, and vice versa. We may call this situation "ideal backward coupling." This, too, is possible, and we can obtain the necessary conditions for it to occur.

However, we shall only give the analysis here for ideal forward coupling. That for ideal backward coupling is essentially the same.

We consider the problem by choosing appropriate $\mathbf{K}_1$ and $\mathbf{K}_2$ and determining what this implies for the $\mathbf{R}$ matrix of the differential equation.

First, we choose $\mathbf{K}_1$. We do this so as to obtain the "lossless" condition. The term is, of course anomalous. As is usual in parametric devices, there may be energy conversion to or from the pump signal. Since, in our analysis, we do not record the effect of the system on the pump generator, we do not actually obtain or want a lossless operator. What we want is one that is lossless if the pump power is included in the calculation. The condition that this implies is known to be the Manley-Rowe relation. Hence, for our $\mathbf{K}_1$ metric, we take the fundamental metric given by (12) with $\mathbf{A}$ as

in (15) and

$$\mathbf{W}=\begin{pmatrix}\mathbf{W}_1 & \mathbf{O}\\ \mathbf{O} & \mathbf{W}_1\end{pmatrix}\quad \mathbf{W}_1=\begin{pmatrix}\ddots & 0 & 0\\ 0 & \omega_n & 0\\ 0 & 0 & \ddots\end{pmatrix}. \tag{36}$$

This implies that the basis involves the voltages and currents at the frequencies ω_n, ordered by increasing n as indicated in (13). As is usual in parametric problems, the frequencies corresponding to n less than some value are negative.

For $\mathbf{K}_2$ we take

$$\mathbf{K}_2=\mathbf{W}^{-1}\begin{pmatrix}\mathbf{Z}^{-1} & \mathbf{O}\\ \mathbf{O} & \mathbf{Z}\end{pmatrix}, \tag{37}$$

where $\mathbf{Z}$ is a real diagonal matrix.

This has been selected by a generalization of the wave concept. Since $\mathbf{Z}$, $\mathbf{Z}^{-1}$, and $\mathbf{W}_1$ are diagonal they commute. Hence, if we define a "wave" basis with the impedance values $\mathbf{Z}$ as

$$\begin{pmatrix}\mathbf{F}\\ \mathbf{B}\end{pmatrix}=(1/\sqrt{2})\begin{pmatrix}\mathbf{1} & \mathbf{Z}\\ \mathbf{1} & -\mathbf{Z}\end{pmatrix}\cdot\begin{pmatrix}\mathbf{E}\\ \mathbf{I}\end{pmatrix}, \tag{38}$$

(where we use "$\mathbf{1}$" for the identity matrix so as not to confuse it with $\mathbf{I}$, the current matrix), then the resultant invariant forms (6) are

$$s(\mathbf{K}_1)=\mathbf{F}^\dagger\mathbf{W}_1^{-1}\mathbf{Z}^{-1}\mathbf{F}-\mathbf{B}^\dagger\mathbf{W}_1^{-1}\mathbf{Z}^{-1}\mathbf{B} \tag{39}$$

and

$$s(\mathbf{K}_2)=\mathbf{F}^\dagger\mathbf{W}_1^{-1}\mathbf{Z}^{-1}\mathbf{F}+\mathbf{B}^\dagger\mathbf{W}_1^{-1}\mathbf{Z}^{-1}\mathbf{B}. \tag{40}$$

Hence, with this $\mathbf{K}_2$, the Manley-Rowe relation applies separately to the set of forward waves and to the set of backward waves. This may be taken as the condition of "ideal forward coupling."

Given $\mathbf{K}_1$ and $\mathbf{K}_2$ as defined, then

$$\mathbf{J}=\mathbf{K}_1^{-1}\mathbf{K}_2=\begin{pmatrix}\mathbf{O} & \mathbf{Z}\\ \mathbf{Z}^{-1} & \mathbf{O}\end{pmatrix}. \tag{41}$$

Because $\mathbf{J}^\dagger$ is similar to $\mathbf{J}$ since $\mathbf{Z}$ is diagonal and real, $\mathbf{K}_1$ and $\mathbf{K}_2$ are mutually consistent. We note that $\mathbf{J}^2$ is the identity matrix. Hence the implied $\mathbf{K}$ set contains only $\mathbf{K}_1$ and $\mathbf{K}_2$. Thus we have managed to choose $\mathbf{K}_2$ so as to leave ourselves with the widest possible latitude for the determination of the system.

The most general $\mathbf{S}$ that is Hermitian is

$$\mathbf{S}=\begin{pmatrix}\mathbf{S}_1 & \mathbf{S}_{12}\\ \mathbf{S}_{12}^\dagger & \mathbf{S}_2\end{pmatrix}, \tag{42}$$

where $\mathbf{S}_1$ and $\mathbf{S}_2$, but not $\mathbf{S}_{12}$, are Hermitian.

To express $\mathbf{J}^\dagger$ as a similarity transformation of $\mathbf{J}$, as in (32), we may set $\mathbf{Q}$ equal to $\mathbf{A}$, as given by (15). Then

$$\mathbf{Q}^{-1}\mathbf{S}=\begin{pmatrix}\mathbf{S}_{12}^\dagger & \mathbf{S}_2\\ \mathbf{S}_1 & \mathbf{S}_{12}\end{pmatrix}. \tag{43}$$

Equation (33) now requires that $\mathbf{Q}^{-1}\mathbf{S}$ commute with $\mathbf{J}$. The necessary and sufficient conditions for this to be true are that

$$\mathbf{S}_2=\mathbf{Z}\mathbf{S}_1\mathbf{Z} \tag{44}$$

$$\mathbf{Z}\mathbf{S}_{12}=(\mathbf{Z}\mathbf{S}_{12})^\dagger. \tag{45}$$

From (34), then, the most general $\mathbf{R}$ is

$$\mathbf{R}=\begin{pmatrix}\mathbf{Z}\mathbf{R}_1 & \mathbf{Z}\mathbf{R}_0\mathbf{Z}\\ \mathbf{R}_0 & \mathbf{R}_1\mathbf{Z}\end{pmatrix}, \tag{46}$$

where $\mathbf{R}_0$ and $\mathbf{R}_1$ are Hermitian.

We have observed before that, for a distributed parametric line, $\mathbf{R}$ has the form of (14), i.e., it is contradiagonal with Hermitian submatrices. Hence, the solution in terms of $\mathbf{R}_1$ is extraneous to this particular problem. The solution in terms of $\mathbf{R}_0$ specify a relation between the $\mathbf{L}$ and $\mathbf{C}$ matrices of (14)

$$\mathbf{L}=\mathbf{Z}\mathbf{C}\mathbf{Z}. \tag{47}$$

To obtain forward coupling in a parametric line, we must vary both $\mathbf{L}$ and $\mathbf{C}$ and the variations must be of magnitude proportional to the product of the impedances of the coupled frequencies and at the same phase. These relations must apply throughout the line.

A little further study will show that this requires a transmission line in which both the instantaneous inductance and capacity are varied by the pump signal. If $\mathbf{Z}$ is the same for all frequencies, this variation must be such that the instantaneous value of the impedance does not change. Only the propagation constant is affected by the pump signal.

The condition expressed by (47) is, then, a necessary one for an ideally forward coupled parametric line. Conversely, it is a sufficient condition.

VI. CONCLUSIONS

Our principle purpose here has been to explore the possibility of analyzing a linear homogeneous system in terms of its quadratic invariants. For this purpose we have found it more convenient to study, not the invariants themselves, but the associated metrics. The problem is reduced to considering the metrics in which a given operator may be considered rotational. Given any such metric, then, by the definition of "rotational," the length of the vector to which the operator is applied is unchanged by the operator, and is an invariant of the system. The significance of this lies in the fact that the known conservation laws of such systems can be expressed in terms of such invariants.

This method of analysis gives us the means of determining the complete set of quadratic invariants that apply to a system.

We have also found methods of applying these concepts to a differential matrix equation of the (lossless) transmission-line or coupled-mode type. This

allows us to determine the conservation laws of the system under circumstances where it is inconvenient or impractical to obtain the system operator itself. The applicable conservation laws can be obtained directly from the equation.

Turning the problem around, we have investigated the extent to which a pair of metrics determine the type of the system. Given a pair of conservation laws, what operators are possible, and what differential matrix equations? We have chosen to study a pair of such laws, rather than a single one, for two reasons. Firstly, the reverse problem for a single (Hermitian) law is simply the classical problem of finding the rotational operators corresponding to a given metric. The problem of finding operators that are simultaneously rotational in two metrics is one that we have not previously seen.

Secondly, and perhaps more importantly, the problems of interest do often involve two conservation laws. One is imposed by some broad requirement such as that of conformance to the Manley-Rowe relations. The other is imposed by a more restrictive requirement which defines in some manner the type of solution we want.

As an illustration of this latter process we have considered a parametric line in which we require that there be no coupling, except externally, between the forward and backward waves. We have called this condition "ideal forward coupling." We have been able to show that such a line must involve similar parametric variations of both the capacity and the inductance. By "similar" we mean that the variations have the same shape and phase. It is, in principle, impossible to obtain ideal coupling by variation of only one of the line parameters.

APPENDIX I

Solution for $\mathbf{K}_1$, Given M

The formal solution to (7) of the text is readily obtained. If $\mathbf{M}$ is a matrix with a complete set of eigenvectors, then we can obtain a matrix $\mathbf{P}$ whose columns are the eigenvectors of $\mathbf{M}$. Then

$$\mathbf{M}' = \mathbf{P}^{-1}\mathbf{M}\mathbf{P} \tag{A1}$$

is the diagonal matrix of the eigenvalues. On substituting (A1) in (7) of the text, premultiplying by $\mathbf{P}^{\dagger}$, postmultiplying by $\mathbf{P}$, and setting

$$\mathbf{K}' = \mathbf{P}^{\dagger}\mathbf{K}\mathbf{P}, \tag{A2}$$

we obtain

$$\mathbf{M}'^{\dagger}\mathbf{K}'\mathbf{M}' = \mathbf{K}'. \tag{A3}$$

Now, as before, $\mathbf{M}'^{\dagger-1}$ is similar to $\mathbf{M}'$. Therefore we can find a $\mathbf{K}_0'$ such that

$$\mathbf{M}'^{\dagger-1} = \mathbf{K}_0'^{-1}\mathbf{M}'\mathbf{K}_0'. \tag{A4}$$

This $\mathbf{K}_0'$ is an acceptable $\mathbf{K}'$. Since $\mathbf{M}'$ is diagonal, it is not difficult to find a suitable $\mathbf{K}_0'$. It is, in fact, a matrix whose columns are the eigenvectors of $\mathbf{M}'^{\dagger-1}$, arranged in the order of their eigenvalues that appears in $\mathbf{M}'$. On substituting (A4) in (A3), and premultiplying by $\mathbf{K}_0'$,

$$(\mathbf{K}_0'\mathbf{K}')\mathbf{M}' = \mathbf{M}'(\mathbf{K}_0'\mathbf{K}'). \tag{A5}$$

Equation (A5) is a commutation law. Since $\mathbf{M}'$ is diagonal, it is simple to solve.

If $\mathbf{M}'$ is nondegenerate so that all of its eigenvalues are distinct, then $\mathbf{K}_0'\mathbf{K}'$ must be diagonal, but can have any values along the diagonal. By knowing the permissible forms of $(\mathbf{K}_0'\mathbf{K}')$, we can reconstruct the solutions of (7) of the text from (A2) and the known $\mathbf{K}_0'$

$$\mathbf{K} = \mathbf{P}^{\dagger-1}\mathbf{K}_0'^{-1}(\mathbf{K}_0'\mathbf{K}')\mathbf{P}^{-1}. \tag{A6}$$

If $\mathbf{M}'$ is degenerate such that one or more eigenvalues are repeated, then additional cross terms may be introduced into $(\mathbf{K}_0'\mathbf{K}')$. Equation (A6) still applies.

If $\mathbf{M}$ is of the limiting case for which the set of eigenvectors is not complete, then $\mathbf{P}$ is constructed from the eigenvectors and generalized eigenvectors. In this case $\mathbf{M}$ is not diagonalized by (A1), but is put into Jordan canonical form. While this situation is not as simple, it can still be handled and the general $\mathbf{K}$ obtained.

This, then, is a formal solution to the problem. It is formal in the sense that, while it does give the solution in computable form, it is often tedious to do so. It is, however, of value in giving some insight into the formal relation between $\mathbf{M}$ and $\mathbf{K}$.

APPENDIX II

Solution for K from the Differential Equation

The solutions to (10) of the text are obtainable, at least in a formal sense, by methods similar to those of Appendix I.

We note first that (10) of the text implies that $(\mathbf{WR})^{\dagger}$ is similar to $\mathbf{WR}$. We can, then, find a $\mathbf{K}_0^{-1}$ such that

$$(\mathbf{WR})^{\dagger} = (\mathbf{K}_0^{-1})^{-1} \quad (\mathbf{WR})(\mathbf{K}_0^{-1}) = \mathbf{K}_0\mathbf{WR}\mathbf{K}_0^{-1}, \tag{A'1}$$

where we have defined it this way to exhibit the fact that $\mathbf{K}_0$ is itself one solution for $\mathbf{K}$.

We can now find a nonsingular matrix $\mathbf{P}$ which diagonalizes $(\mathbf{WR})$. We use the same symbol as in Appendix I since it can be taken as the same operator as diagonalized $\mathbf{M}$. It can be shown that, if we take the eigenvectors of $\mathbf{M}$ independent of z, including the z dependence of $\mathbf{M}$ wholly within its eigenvalues, then its eigenvectors are also eigenvectors of $(\mathbf{WR})$. Since $\mathbf{P}$ is a matrix of eigenvectors, it will diagonalize both $\mathbf{M}$ and $\mathbf{WR}$.

On letting

$$\mathbf{D} = \mathbf{P}^{-1}\mathbf{WRP}, \tag{A'2}$$

where **D** is diagonal (assuming the eigenvectors of **WR** are a complete set), and using (A'1),

$$\mathbf{D}(\mathbf{P}^{-1}\mathbf{K}_0^{-1}\mathbf{K}\mathbf{P}) = (\mathbf{P}^{-1}\mathbf{K}_0^{-1}\mathbf{K}\mathbf{P})\mathbf{D}, \qquad (A'3)$$

which is a commutation law with a diagonal (or, at least, canonical) matrix. The general solution to this is an arbitrary diagonal matrix plus arbitrary cross terms involving the intersections of degeneracies of **D**, if any.

It is interesting to observe the difference in the conditions on the eigenvalues of **WR** from that on **M**. We have seen that, since $\mathbf{M}^{t-t'}$ is similar to **M**, the eigenvalues of **M** are either of unit magnitude or else occur in pairs that are conjugate reciprocals. It is, however (**WR**)^t that is similar to (**WR**). Hence the eigenvalues of **WR** must be either real or else occur in conjugate pairs. This results from the fact, which can be shown, that if the eigenvalues of WR are λ_n, then the eigenvalues of **M** have the form $\exp(-j\lambda_n z)$.

The condition on the eigenvalues of (**WR**) implies that the characteristic equation of **WR** has only real coefficients which, in turn, imposes a rather broad condition on the form of **WR**.

JOURNAL OF APPLIED PHYSICS VOLUME 31, NUMBER 11 NOVEMBER, 1960

Orientation-Dependent Dissolution of Germanium

F. C. Frank
H. H. Wills Physical Laboratory, University of Bristol, Bristol, England

AND

M. B. Ives
Metals Research Laboratory, Carnegie Institute of Technology, Pittsburgh, Pennsylvania

(Received May 26, 1960)

The dissolution of single crystals of undoped germanium in Superoxol etchant is shown to be very closely completely orientation-dependent by the applicability of recent theorems on crystal dissolution shapes. The results of the theory are outlined, and the method of application is described in detail.

I. INTRODUCTION

THIS paper describes the first application to physical data of the theorems of orientation-dependent solution of crystals, recently developed by Frank.[1] It is here applied to the experimental results on the dissolution of single-crystal germanium obtained by Batterman.[2] The Frank dissolution theory is responsible for the enunciation of two theorems, on which all applications are based. The first of the dissolution (or growth) theorems states that if the rate of dissolution (or growth) of a crystal surface is a function only of orientation (or depends on time only through an orientation-independent factor) then the locus in space of a particular orientation of crystal surface on dissolution (or growth) is a straight line. Further, the orientation dependence of the etch rate allows the complete dissolution properties of the crystal in a given solvent to be described in terms of a polar diagram of the reciprocal normal etch rate as a function of orientation, yielding a polar "reluctance." This surface is generated by the reciprocal normal dissolution rate, vector **P**, as a function of crystal orientation. The reluctance diagram is invoked in the second dissolution theorem, which states that the vector **Q**, defining the locus in space of a given crystal surface orientation is parallel to the normal drawn from the reluctance surface at the corresponding orientation. The situation is summarized diagrammatically in Fig. 1, for a two-dimensional case.

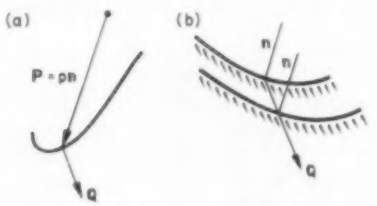

FIG. 1. (a) Portion of a polar diagram of reciprocal normal dissolution rate **P** for a hypothetical crystal. (b) Corresponding subsequent dissolution surfaces for the crystal, showing a straight line orientation trajectory **Q**, expected if dissolution is completely described by (a). **n** is also a vector.

When two or more dissolution trajectories intersect in space, an orientation discontinuity (i.e., a crystal edge) is produced. The sharpness of the discontinuity depends on the range of orientation trajectories which have intersected to produce it. The analysis also predicts the trajectory of such a crystal edge in terms of the reluctance diagram. It can be shown that **Q**, the trajectory of a point in the crystal edge, is parallel to the normal to the chord joining $\mathbf{P}_1$ and $\mathbf{P}_2$, reluctance

[1] F. C. Frank, *Growth and Perfection of Crystals* (John Wiley & Sons, Inc., New York, 1958), p. 411.
[2] B. W. Batterman, J. Appl. Phys. **28**, 1236 (1957).

vectors corresponding to the orientations adjacent to the edge.

The published derivation of the theory is two-dimensional only. While it can be extended into three dimensions, the theorems as stated remaining true, this is not required for the present application. The two-dimensional theory suffices for a cylindrical specimen, and also for the profile on a plane of cross section which is simultaneously a symmetry plane for the crystal structure and for the initial form of the specimen, provided that the dissolution (or growth) process does not generate any edge parallel to this plane. For all surface elements in this profile belong to the same zone, with a zone axis normal to the plane and, by symmetry, follow trajectories in this plane. It follows from the hypothesis that dissolution rates are a function of orientation only, that these trajectories are uninfluenced by adjacent surface elements not belonging to this zone, except insofar as they are eliminated by these, which would contravene the proviso that edges parallel to the plane of cross section are not generated. The detailed, fully three-dimensional analysis would in any case present considerable practical difficulties.

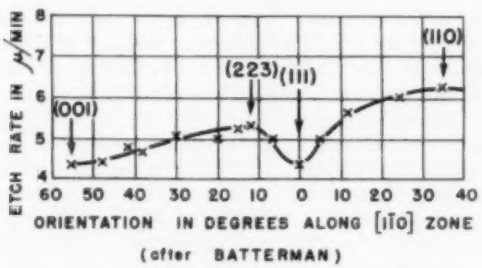

FIG. 2. Etch rates of germanium in Superoxol etchant for orientations along the [1$\bar{1}$0] zone.

In the present application, the theorems have been used to predict dissolution shapes of germanium, using known etch rate values. The converse use of the theory—to determine dissolution data from observed dissolution shapes—is also possible, although in this case the reluctance diagram is not usually reproduced completely, since only those crystal orientations present in the dissolution shapes can be measured.

II. GERMANIUM ETCH RATE

Batterman[2] has published values for the etch rates in Superoxol etchant[3] of single crystals of undoped germanium. Sets of parallel plate specimens representing a range of orientations were etched, ten at a time, for 4-min intervals. After each etch the crystal thicknesses were measured, and the dissolution rates determined graphically. Batterman has reproduced (Fig. 2), the variation in etch rate for crystal orientations with a common ⟨110⟩ zone axis. The authors have been furnished with the actual numerical values of the rates determined in that zone.[4]

[3] Superoxol etchant: 1:1:4 volume parts of H_2O_2(30%), HF (49%), and H_2O, respectively. U. S. Patent No. 2,542,727, H. C. Theuerer.

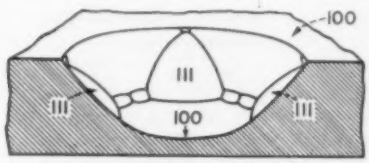

FIG. 3. Surface formed on etching a spherical hollow of germanium (after Batterman).

Some dissolution shapes of single-crystal germanium were also determined by Batterman.[2] In one experiment, a 1-cm diam hemispherical hollow was ground in a {100} face of a germanium single crystal and etched by dropping Superoxol at a fixed rate into the hollow. After 3 hr the hollow was found to have the form shown in Fig. 3. This dissolution shape exhibits triangular regions that are {111} planes, and a region at the center of the bowl which is near the (100) orientation but is not yet truly planar.

The purpose of this paper is to show how the theorems of footnote reference 1 predict the dissolution shapes of such a hollow by the geometric constructions described in the following sections, and thereby demonstrate whether the dissolution of germanium in Superoxol etchant is solely orientation-dependent, or not. For the reason noted, the treatment is reduced to two dimensions by considering the dissolution profile of a {110} symmetry section through the hollow.

III. THE DISSOLUTION RELUCTANCE DIAGRAM

The derivation of successive dissolution shapes of the hemispherical hollow from the known etch rate data can be accomplished by application of the dissolution theorems, once the dissolution reluctance diagram for the appropriate crystal zone is established. The reluctance diagram may be constructed directly from the etch rate values supplied by Batterman,[4] and used to plot the curve of Fig. 2, by plotting the reciprocals of the normal etch rates on polar graph paper. Because of the symmetry of the {110} section the data of Fig. 2 suffice to determine the entire reluctance diagram for the planes of a ⟨110⟩ zone, as is reproduced in Fig. 4. This figure shows the reciprocal points plotted for half the diagram. The curve has been drawn through all the plotted points in the upper half of the diagram, but approximated to the best smooth curve in the lower half, in an attempt to demonstrate the effect of the secondary maxima and minima due to the scatter of the etch rate values between (111) and (001), and to compare it with that due to the averaged curve.

[4] B. W. Batterman (private communication).

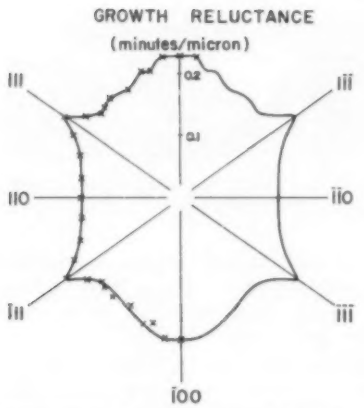

FIG. 4. Polar diagram of reciprocal normal dissolution rate for orientations of a (110) zone of germanium.

IV. PREDICTION OF DISSOLUTION SHAPES

Given a particular starting shape, we are now able to deduce the successive dissolution shapes of {110} sections of single-crystal germanium from the reluctance diagram. For the case of the spherical hollow we start, in two dimensions, with a circular section. The dissolution trajectories corresponding to the properties represented by Fig. 4 have been constructed as illustrated in Fig. 5.

The circular starting shape is indicated at the center of the diagram, although it has not been delineated for the sake of clarity. The original construction was made on polar graph paper, but here only the position of the origin is reproduced. The reluctance diagram of Fig. 4 was first added to the paper on a suitable scale. The scale itself is immaterial to the application of the curve to the problem, since it is the *direction* of the normal to the curve at a given orientation which is required. The reluctance curve was, in fact, fitted at the position where it was most easily accessible for measurement without impeding the construction, and is shown in the reproduction as a dashed curve. The next and principal step is the drawing of the orientation trajectories which obey the dissolution theorems. The trajectories are drawn in the *outward* sense from the starting shape, since we are considering the dissolution of a hole. For a given point on the initial surface the radius vector corresponding to this point was extended until it intersected the reluctance curve and a parallel rule was placed tangentially to the curve at the intersection. A right-angle triangle was then placed against the rule, determining the direction of the normal to the curve, which by the second theorem is the direction of the trajectory corresponding to the particular orientation. Hence by sliding the triangle along the rule, and sidestepping the rule if necessary, it was possible to draw a line in this direction from the point first chosen on the starting circle. This line is the orientation trajectory for subsequent dissolution. An adjacent point was then taken, and its corresponding trajectory determined in the same way. Similarly, trajectories at 2° intervals (and less where the divergence is great) were determined for the whole of the initial shape.

As noted in the foregoing, crystal edges form when trajectories intersect. Hence, when two trajectories were found to meet, their lines were erased beyond the meeting point, and the direction of the resulting (edge) trajectory determined in the manner already described, i.e., by drawing it normal to the chord joining points on the reluctance curve corresponding to the orientations immediately adjacent to the edge. On the trajectory diagram the sharpness of the edges formed is suggested by the width of the lines representing their trajectories.

This sketching method of trajectory determination is believed to be sufficiently accurate for deriving shapes qualitatively. The principal source of error must be in the determination of the slope of the reluctance curve, but by constructing the trajectories progressively around the starting figure, any appreciable error in determining the tangents will be noticed when a trajectory is compared with its neighbor. A test of the method is afforded by the symmetry of the trajectories deduced in Fig. 5. Apart from minor adjustments to the meeting of some very long trajectories, the whole diagram throughout the four quadrants has been derived independently. Small variations may be seen in the formations provided by the highly convergent trajectories but, in general, symmetry is preserved. An indication of the accuracy is the coincidence of the intersections of the edges (untouched for reproduction) at either side of (110), such that the intersections occur exactly on the radius vector for the consequent formation of an edge along ⟨110⟩. These subsidiary edges have each been evolved from numerous meetings and consequent step-by-step changes of direction, and that they finally intersect on the symmetry axis is sufficient testimony to the accuracy of the construction.

The final step is to derive resultant dissolution shapes from the trajectory array constructed. This has been done in the present case for two stages in the etching. Figure 5 shows the shapes expected at an early stage, and at a time corresponding to a large degree of dissolution (the outermost line of the figure). These shapes are determined by taking an orientation in the starting profile, placing the parallel rule as a tangent, and sidestepping the rule along the trajectory from that orientation for a distance appropriate to the dissolution time required. The rule is then, from the first theorem, still a tangent to the dissolving surface, and this portion of the new surface can then be drawn. Similar procedure with the other nonmeeting trajectories allows the complete shape to be determined.

From the profiles obtained we can predict that:

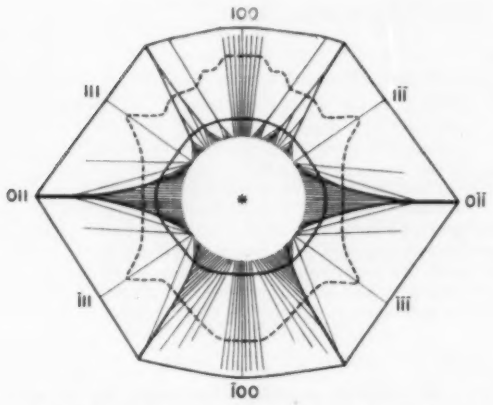

FIG. 5. Dissolution trajectories and derived profiles for the dissolution of a {110} circular section of germanium.

(i) Almost plane {111} faces are formed quite early and widen, rapidly at first and then more slowly after longer etching.

(ii) The {100} curvature is slowly reduced, until after prolonged dissolution mildly curved faces, symmetric about ⟨100⟩, remain. The trajectories show that curvature effecting a change in direction of 14° through the {100} orientations is never lost.

(iii) The alternate progress of the crystal orientations around ⟨100⟩, as deduced from the reluctance curve which followed every point (upper portion), includes the early formation of weak edges instead of a smooth curve to the sides of the {100} orientations. These edges are eventually lost in the expanding {111} faces, and the effect of the deviations is similarly lost.

(iv) The curvature around the {110} orientations is only slightly modified in the early stages, but in time the edges bounding the adjacent "{111}" areas advance and after continued dissolution meet to produce a sharp edge separating two {111} planes, which then travels undeviated along the ⟨110⟩ directions.

(v) Apart from the persisting curvature around {100}, the eventual profile of the crystal is seen to be of hexagonal form. Four of the sides are plane {111} faces, and two are the {100} faces.

V. CORRELATION OF THE DERIVED AND OBSERVED SHAPES

From the numerical etch rates it is possible to construct, by the same methods as used in Fig. 5, the crystal profile corresponding to the 3-hr dissolution of a spherical hollow of germanium (Fig. 3). This is a relatively early dissolution shape—produced in less than half the time required for the inner of the two profiles deduced in Fig. 5. It will be seen that there is good agreement between the {111} planes and between the persisting curvatures around ⟨100⟩, but there is one property not predicted. The surface around the {110} orientations is continuous. In the deduced profile there is no edge at ⟨110⟩ to form the characteristic pair of small facets (ignored by Batterman[2]) seen in Fig. 3.

For an early edge at ⟨110⟩ it is necessary for the dissolution trajectories to be convergent around ⟨110⟩. The amount of convergence must also be such that an edge is formed after 3-hr etching. This condition requires a small-scale concavity in the polar diagram at ⟨110⟩. Such a concavity is quite possible, since the etch rate values are widely spaced in this range of orientations, and their reliability has been quoted at only 2%.[4] Analytical curve fitting shows that the present etch rate values are not sufficient or accurate enough to predict the existence or nonexistence of a small concavity in the polar diagram around {110}. We therefore infer that the dissolution data in this region are insufficient to allow the theorems to predict the crystal dissolution shapes completely, although the larger scale features are adequately described.

VI. CONCLUSIONS

The dissolution theorems of Frank are shown to apply to the Batterman results for the dissolution of single-crystal undoped germanium in Superoxol. Derived dissolution profiles are found to correspond to those obtained in the experiment, within the accuracies of the method and the theoretical treatment.

We infer that the etch rate for germanium in the particular solvent considered is, to a first approximation, only dependent on crystal orientation.

VII. ACKNOWLEDGMENTS

One of us (M. B. I.) acknowledges the tenure of a D.S.I.R. Studentship during the solution of this problem, which has been included in a degree dissertation submitted to the University of Bristol, England. We are grateful to B. W. Batterman for helpful criticism during the preparation of the manuscript and permission to use his figures.

Neutron and Optical Studies of Domains in NiO

W. L. Roth
General Electric Research Laboratory, Schenectady, New York

(Received June 2, 1960)

Antiferromagnetic domains in NiO have been studied by neutron diffraction and optical observation of single crystals. There are two kinds of antiferromagnetic domain walls, T (twin) and S (spin-rotation). A T wall is produced by rotation of the antiferromagnetic pattern of magnetic moments and an S wall by rotation of the direction of the magnetic moments. The T walls can be observed with polarized light, and both T- and S-type domains can be studied by neutron diffraction. Crystals with simple T-wall structures are produced by annealing at high temperature. The crystallography of the T walls can be understood in terms of a small rhombohedral deformation which accompanies the antiferromagnetic ordering. The T walls are easily displaced by the application of small mechanical stresses or magnetic fields. A crystal without T walls may still contain S walls, and these S walls also are displaced or rotated by magnetic fields.

INTRODUCTION

THE antiferromagnetic ordering of magnetic moments in the series MnO, FeO, CoO, and NiO has been established by neutron diffraction.[1-3] In this previous work interest was centered on the arrangement of moments in the ideal crystal and the relation of the magnetic structures to the crystal deformations which occur on magnetic ordering.[4-6] The effects of magnetic imperfections, i.e., deviations from the ideal periodic magnetic structure, is less well understood. Magnetic imperfections may be classified as short range, such as point defects where the interaction extends over relatively few magnetic neighbors, and long range, in which the disturbance extends an appreciable distance in the crystal. As an example of the former, the effect of vacancies and interstitial cations on the antiferromagnetic ordering in ferrous oxide (Wüstite) was studied.[7,8] In this paper some aspects of the behavior of longer range defects, such as twins and antiferromagnetic domains in nickelous oxide, will be given.

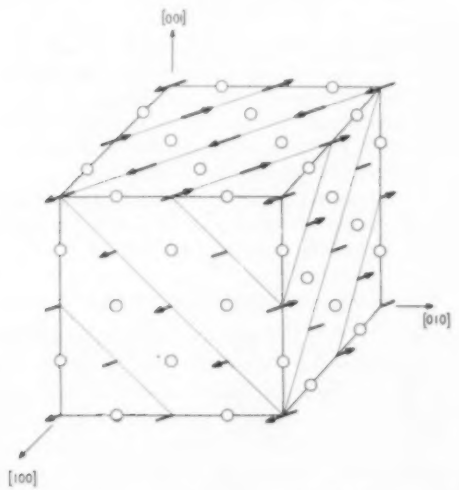

FIG. 1. Antiferromagnetic structure of NiO. The open circles are oxygen atoms. The spins lie in (111) but the direction within the ferromagnetic (111) plane is not specified. The contraction axis is [111] and the rhombohedral cell shown has $\alpha = 90°4'$.

In a simple antiferromagnet, the moments are arranged in antiparallel order on an atomic scale. An antiferromagnetic domain may be defined as a region in a crystal in which the antiferromagnetic pattern of atomic moments is triply periodic throughout the volume. There is a close relationship between ordinary crystal defects and defects in the magnetic structure: for example, crystallographic twins, small-angle grain boundaries, dislocations, and stacking faults produce corresponding disturbances in the magnetic arrangement.

At temperatures above $T_N = 523°K$, the Néel temperature,[9-11] NiO is paramagnetic and the crystal structure is cubic. Below T_N, the antiferromagnetic ordering results in a slight rhombohedral deformation of the crystal, which consists of a contraction of the original cubic unit cell along one of the ⟨111⟩ axes. Because this contraction may occur along any of four equivalent directions in the parent cubic crystal, crystallographic twinning which is related to the antiferromagnetic ordering may take place. These twins describe a type of antiferromagnetic domain wall which can be studied by the usual crystallographic methods. A report of optical studies of domains in thin sections of NiO has previously been given, while the growth of large domains by heat treatment and the movement of domain walls by the application of stresses and magnetic fields[12] was described.

Methods for producing large (several mm in all

[1] C. G. Shull, W. A. Strauser, and E. D. Wollan, Phys. Rev. **83**, 333 (1951).
[2] W. L. Roth, Phys. Rev. **110**, 1333 (1958).
[3] W. L. Roth, Phys. Rev. **111**, 772 (1958).
[4] H. P. Rooksby, Acta Cryst. **1**, 226 (1948).
[5] S. Greenwald and J. S. Smart, Nature **166**, 523 (1950).
[6] J. Kanamori, Progr. Theoret. Phys. (Kyoto) **17**, 197 (1957).
[7] W. L. Roth, J. Appl. Phys. Suppl. **30**, 303S (1959).
[8] W. L. Roth, Acta Cryst. **13**, 140 (1960).
[9] M. Foex, Compt. rend. **227**, 193 (1948).
[10] C. H. LaBlanchetais, J. phys. radium **12**, 765 (1951).
[11] H. Kondoh, E. Uchida, Y. Nakazumi, and T. Nagamiya, J. Phys. Soc. Japan **13**, 579 (1958).
[12] W. L. Roth, Fourth International Congress, International Union of Crystallography, Montreal, Canada, paper 15.6 (1957).

dimensions) crystals which are essentially untwinned have been developed by Slack,[13] and this has made possible the measurement of such properties as the stresses required to move domain walls, the magnetic anisotropies, and hysteresis effects which accompany the rotation of the magnetic moments in the crystal.[14] The present paper describes the phenomenology of antiferromagnetic domains in NiO and gives the results of the optical transmission and neutron diffraction studies of domains. The work on the detwinning and the crystallographic properties of domain walls is described in the companion paper by Slack.[13]

IDEAL MAGNETIC CRYSTAL

The magnetic structure of NiO below T_N, as determined from neutron diffraction,[1,2] is shown in Fig. 1. The atomic spins are arrayed in ferromagnetic sheets which are parallel to (111) and the direction of magnetization in neighboring planes is reversed. The antiferromagnetic pattern of moments is explained by the superexchange interaction between nickel ions on opposite sides of an oxygen ion.[15] The configuration with parallel spins lying in (111) is consistent with calculations of the minimum dipolar energy.[16,17] The first neutron diffraction measurements were made on powder specimens, and it was not possible to discriminate between various spin directions within the (111) plane. Neutron diffraction studies from single crystals were undertaken to resolve this problem, and the spin direction in annealed crystals was found to be $[1\bar{1}0]$.[3] The annealed crystals were twinned, and as will be shown later in this paper, the spin direction in twinned crystals may be determined by the line of intersection of the ferromagnetic (111) sheets.

The antiferromagnetic ordering is accompanied by a slight contraction of the cubic cell along one of the body diagonals. Neutron diffraction from an untwinned crystal has shown that the contraction axis is perpendicular to the ferromagnetic sheet.[14] Rooksby[4] has shown from x-ray studies that the rhombohedral deformation increases with decreasing temperature and that at room temperature the rhombohedral angle is 60°4.2′.

Based on the neutron diffraction determination of the magnetic structure, the true symmetry of NiO in the antiferromagnetic state is orthorhombic, rather than rhombohedral, but the additional distortion related to the direction of the spins in the ferromagnetic sheet is very small and has not been observed in the x-ray patterns. In the present work, since only the rhombohedral distortion was observed, the coordinate system defined in Fig. 1 will be retained. It is convenient to use the multiple rhombohedral cell containing 4 NiO with a rhombohedral angle $\alpha = 90°4'$ at room temperature rather than the monomolecular unit given by Rooksby. In this description, the superexchange antiferromagnetic coupling occurs along ⟨100⟩ and the ferromagnetic sheet is parallel to (111).

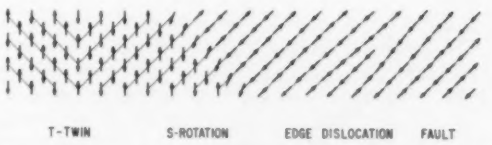

FIG. 2. Long range imperfections in the antiferromagnetic order of NiO. The section is parallel to (100) and the oxygens are omitted for clarity. The traces of the ferromagnetic (111) sheets are shown and all of the spins lie within (111).

ANTIFERROMAGNETIC DOMAINS

A single domain of NiO is a single magnetic crystal generated by the periodic repetition in three dimensions of the magnetic unit cell shown in Fig. 1. Antiferromagnetic domain walls result either if there is a rotation of the direction of moments within the ferromagnetic sheet, or if there is a change in crystallographic orientation of the ferromagnetic sheets. There is an observable contraction of the crystal normal to the ferromagnetic sheet, and domain walls of the second variety are rhombohedral twin walls which may be observed by normal crystallographic methods. In the work that follows, these will be termed *T* (twin) domain walls. The twinning planes which separate regions with different contraction axes are called *T* walls. The other kind of domain wall is called an *S* (spin-rotation) variety of wall, and separates regions of the crystal in which there is no change in contraction axis, but merely a rotation of the spin direction within the ferromagnetic sheet. The *S* walls have not been observed directly, but their properties have been studied by rotational torque and neutron diffraction measurements on single crystals in magnetic fields.[14] The relation between *T* and *S* type domain walls to dislocations and magnetic

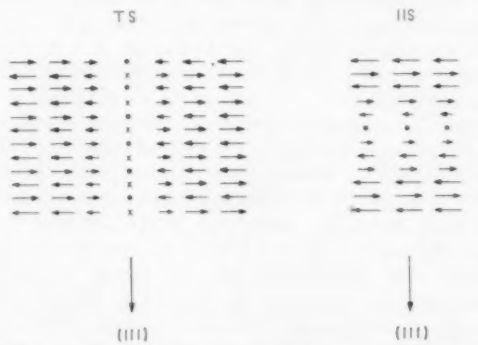

FIG. 3. *S* type domain walls. The magnetization changes direction in S_{II} by the rotation of adjacent ferromagnetic sheets. The rotation in $S_{\perp}$ occurs within the ferromagnetic sheet. A spin rotation of π is shown for clarity.

[13] G. A. Slack, J. Appl. Phys. **31**, 1571 (1960).
[14] W. L. Roth and G. A. Slack, J. Appl. Phys. **31**, 352S (1960).
[15] P. W. Anderson, Phys. Rev. **79**, 350 (1950).
[16] J. I. Kaplan, J. Chem. Phys. **22**, 1709 (1954).
[17] F. Keffer and W. O. Sullivan, Phys. Rev. **108**, 637 (1957).

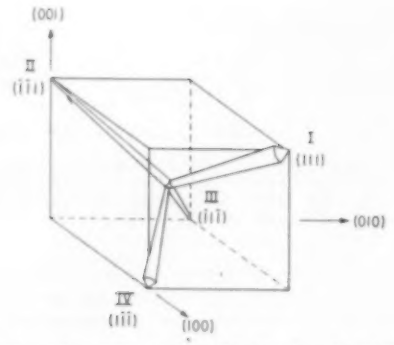

FIG. 4. Orientation of T regions in NiO. The direction of the rhombohedral axis with respect to the parent cube is shown.

stacking faults is shown in Fig. 2. Only the domain type of imperfection is presently considered. In the remainder of this paper, the term "crystal" signifies a morphological entity which possesses many of the attributes of a true single crystal, but which may contain either T or S domain walls. "Single domain," on the other hand, refers to a true single crystal in both the atomic and magnetic sense.

S Domain Walls

Consider a crystal with a single contraction axis, i.e., without T walls. There are continuous ferromagnetic sheets parallel to (111) in crystals which contain S domain walls and a multidomain crystal will appear to have rhombohedral symmetry. There are two types of mirror plane in the rhombohedral crystal: (111), which is perpendicular, and $(\bar{1}10)$, $(0\bar{1}1)$, $(10\bar{1})$, which are parallel to the rhombohedral axis. The symmetry in (111) is destroyed by the antiferromagnetic ordering and the mirror planes become possible twin planes. Consequently, two kinds of S wall result from the reduced symmetry when there is a unique magnetization direction within (111): S_{II}, in which the wall is parallel to the ferromagnetic sheets, and $S_{\perp}$, in which the wall is perpendicular to the ferromagnetic sheet and contains the rhombohedral axis. The two types of S walls are described in Fig. 3. In the S_{II} wall the magnetization direction within each ferromagnetic sheet remains constant. The orientation of magnetic moments in adjacent sheets changes direction as one proceeds along the $[111]$ axis through the domain wall. In the $S_{\perp}$ wall, the rotation of magnetization is accomplished within the ferromagnetic sheet. The anisotropy in (111) is very small and although a variety of S walls are possible, the most stable walls should form between regions where the angle between spins is $1/3\pi$, $2/3\pi$, or π. The exchange energy is reduced if there is a gradual rotation of magnetization on passing through the wall, so an S boundary probably is a thick transition layer similar to a ferromagnetic domain wall. It may be noted that the S_{II} wall bears a small magnetic moment, whereas $S_{\perp}$ does not. It may be possible to differentiate these walls by their behavior in magnetic fields.

TABLE I. T type walls between antiferromagnetic domains.

Domain Orientations	I-IV $(111)(1\bar{1}\bar{1})$	I-III $(111)(\bar{1}1\bar{1})$	I-II $(111)(\bar{1}\bar{1}1)$
Magnetic axis	$[01\bar{1}]$	$[\bar{1}01]$	$[1\bar{1}0]$
Domain Walls	(100) (011)	(010) (101)	(001) (110)
Domain Orientations	II-III $(\bar{1}1\bar{1})(\bar{1}\bar{1}1)$	II-IV $(\bar{1}1\bar{1})(1\bar{1}\bar{1})$	III-IV $(\bar{1}\bar{1}1)(1\bar{1}\bar{1})$
Magnetic axis	$[0\bar{1}\bar{1}]$	$[\bar{1}01]$	$[\bar{1}10]$
Domain Walls	(100) $(0\bar{1}1)$	(010) $(\bar{1}01)$	(001) $(\bar{1}\bar{1}0)$

T Domain Walls

When nickel oxide is cooled below T_N, the rhombohedral axis may alternatively be parallel to $[111]$, $[\bar{1}\bar{1}1]$, $[\bar{1}1\bar{1}]$, or $[1\bar{1}\bar{1}]$, where the directions refer to those in the original cube. For convenience, these four possible orientations are described by I-$[111]$, II-$[\bar{1}\bar{1}1]$, III-$[\bar{1}1\bar{1}]$, and IV-$[1\bar{1}\bar{1}]$ (Fig. 4). A domain wall is the composition plane joining two orientations; thus I(100)IV describes a domain wall parallel to (100) separating two individuals with rhombohedral axes parallel to $[111]$ and $[1\bar{1}\bar{1}]$.

The kinds of T walls between regions with different contraction axes are deduced by taking the initial state as that of a perfect cubic crystal and realizing that, since the deformation accompanying magnetic ordering is small, T walls of lowest energy should be parallel to mirror planes in the original cubic crystal whose symmetry is lowered as a consequence of the antiferromagnetic ordering. The T domains are rhombohedral twins related such that the magnetization vector passes continuously and without alteration of direction from one domain to another. This has been experimentally verified by neutron diffraction from a multidomain crystal.[3] Low energy T walls are restricted by the conditions that (*a*) the ferromagnetic sheets in adjoining domains intersect along a common magnetization direction, and (*b*) the domain wall contains this direction and be parallel to a mirror plane in the original cubic crystal. The antiferromagnetic domain walls predicted by these criteria are summarized in Table I. The six columns give the possible combinations of two domains. The first row describes the orientations of the ferromagnetic sheets, the second row the magnetic axis, and the last two rows the possible domain walls.

The two types of T walls are illustrated by I(001)II and I(110)II in Fig. 5. In both cases the magnetic axis is along $[1\bar{1}0]$ and the ferromagnetic sheet is rotated from (111) to $(\bar{1}\bar{1}1)$. However, the composition plane is parallel to (001) for case *A* and (110) for case *B*. It may be noted that the T walls shown are really glide planes and not mirror planes in the magnetic crystal,

TABLE II. Distribution of T regions in NiO crystals.

Crystal	Percent T region I	II	III	IV
1. Verneuil[a]; cleaved only	23.4	24.7	23.5	28.4
2. Verneuil[a]; cleaved and annealed at 1500°C	33.4	66.6	0	0
3. Verneuil[a]; thin section annealed at 1500°C	0	0	69.5	30.5
4. Verneuil[a]; thin section annealed at 1500°C	0	0	36.1	63.9
5. Vapor deposit[b]; (100) plate	3.7	22.8	72.3	1.2
6. Verneuil[c]; annealed at 1500°C; stressed [111]	98.7	1.3	0	0

[a] Supplied by Linde Air Products Corporation.
[b] Supplied by R. Cech.
[c] Supplied by G. Slack, crystal 7-9B.

since reflection in a mirror reverses the polarization of the component of spin parallel to the wall.

NEUTRON DIFFRACTION

Information about both T and S type domain walls can be obtained from neutron diffraction. The neutron diffraction patterns expected for various spin configurations in NiO have been given previously.[3] The neutron scattering from {111} in the magnetic cell depends upon the crystallographic orientation of the ferromagnetic sheets and is independent of the direction of magnetization within the sheet. The determination of magnetic intensity at the various {111} positions in reciprocal space directly gives the relative distribution of I, II, III, and IV type regions in the crystal, regardless of the presence, or absence, of S walls. (This will no longer be true if the dimensions of the domains become very small, say less than 100 A.) On the other hand, the scattering of neutrons from planes that are not parallel to (111) varies with the direction of magnetization within the ferromagnetic sheet and may be used to determine the distribution of both T and S type domain walls.

T Walls

The magnetic scattering from the {111} planes of a number of crystals grown by the Verneuil method[18] and from the vapor phase[19] was measured using the G. E. neutron spectrometer located at the Brookhaven National Laboratory. Typical results, analyzed as percent of the various domain types, are given in Table II.

The distribution of magnetic intensity among {111} in crystals cleaved from several different boules was highly variable. The T regions in crystal 1 were nearly randomly distributed among the four possible types, but this is not necessarily characteristic of a boule since other "as cleaved" crystals had nonrandom textures. The domain structure was refined by heating crystals to $T \gtrsim 1500$°C. In general, only two of the four possible T type regions were found in annealed crystals (2, 3, 4). The same result was obtained from a crystal that had been made by deposition from the vapor phase on a single-crystal MgO substrate at 700°C (crystal 5). These observations agree with the predictions of Table I and suggest that there should be a single magnetic axis in an annealed crystal which contains T walls where the twinning is a simple one-wall pattern [see Fig. 5(a) of work cited in footnote 13]. This agrees with a previously reported neutron diffraction study in which it was shown that the magnetization direction was the same in the two T regions present in an annealed NiO crystal.[3] The more complex T wall configurations in crystals which have not been annealed requires a change in magnetization direction in some T walls. These walls are probably of slightly higher energy, and appear to be stabilized by small-angle grain boundaries and other crystal imperfections. A single crystal may be obtained by applying a stress to the crystal after annealing.[12] The movement of T walls by the application of an external stress is well known,[11,12,20,21] but up till now crystals without T walls had not been prepared. The neutron scattering from an annealed and stressed crystal (6) is shown in Table II. The neutron diffraction result proves that the ferromagnetic sheets are perpendicular to the stressed direction and confirms that the anneal-stress technique produces a NiO crystal without T walls.

S Walls

The effect of the presence of S type walls on the neutron scattering is studied by measurement of the magnetic reflections hkl. In a single T region, the magnetic intensity is proportional to $F_{(hkl)}{}^2 q_{(hkl)}{}^2$, where $F_{(hkl)}$ is the magnetic structure factor and $q_{(hkl)}{}^2$ de-

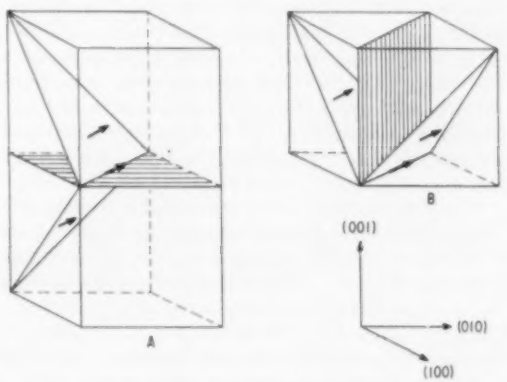

FIG. 5. T walls in NiO. The T walls are shaded. A single ferromagnetic sheet in adjoining T regions is shown and the magnetization in adjacent sheets is antiparallel. The magnetic axis is [110]. The wall in A is I(001)II and that in B is I(100)II.

[18] A. Verneuil, Compt. rend. **135**, 791 (1902).
[19] R. E. Cech and E. Alessandrini, Trans. Am. Soc. Metals **51**, 150 (1949).
[20] J. R. Singer, Phys. Rev. **104**, 929 (1956).
[21] R. Street and B. Lewis, Nature **168**, 1036 (1951).

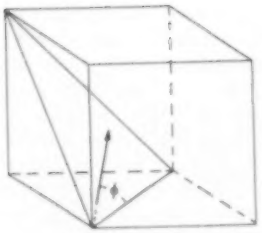

FIG. 6. Orientation of an S domain. The defining angle ϕ is measured in the ferromagnetic sheet.

pends on the relative orientation of the magnetic moments and the scattering plane. The structure factors of the allowed magnetic reflections from the NiO structure[3] are constant except for a gradual attenuation with $\sin\theta/\lambda$ due to the falloff of magnetic form factor, so the orientation of S domains can be obtained by determining $q_{(hkl)}^2$. The orientation of an S domain is defined by an angle ϕ, which measures the direction of spins within the domain (Fig. 6). Calculated curves for $q_{(hkl)}^2$ as a function of the azimuthal angle ϕ in the (111) ferromagnetic sheet are given in Fig. 7. Note that the $(11\bar{3})$ reflection is particularly sensitive to the spin orientation and a rotation of the spin axis by 90° causes a 97% reduction of the magnetic intensity. At $\phi=0$ the spin lies in $(11\bar{3})$; at 90° they are nearly perpendicular to $(11\bar{3})$. The (111) intensity is independent of the direction of spins in the plane and for this reason is particularly useful for analysis of the distribution of T regions in the crystal.

It should be possible by neutron diffraction to obtain the distribution of spins in (111) of a crystal which does not contain T walls. The magnetic scattering from crystal 7–9B (see Table II) was measured, and the results showed the crystal contained S type walls. The intensities are approximately satisfied by a model in which the spins are equally distributed among S type domains with magnetization directions $(\bar{1}10)$. This model predicts an isotropic magnetic susceptibility in (111), in agreement with the results of torque studies at low fields.[14] Alperin[22] has reported somewhat similar conclusions from a neutron diffraction study of a stressed NiO crystal obtained from Japan. An important difference is that the Japanese crystal apparently contained a distribution of both T type and S type walls.

An exact analysis of the distribution of S walls in crystal 7–9B was not made because the neutron intensities required excessively large corrections for secondary extinction. This is a natural consequence of the fact that the annealed and stressed crystals are quite perfect since secondary extinction is the result of dynamic scattering processes in nearly ideal crystals. Secondary extinction coefficients were calculated from the neutron intensities diffracted from the 111 (magnetic) and 222 (nuclear) reflections, since for these planes both F^2 and q^2 are known. Using the curves given by Bacon,[23] the mosaic spreads were found to be

$$\eta\ (\text{nuclear}) = 0.86'$$
$$\eta\ (\text{magnetic}) = 0.80'.$$

The perfections of the nuclear and magnetic structures are essentially the same, and very high. The large secondary extinction coefficient observed for the magnetic structure suggests that the density of S walls is small. In support of this, the width of the magnetic Bragg peaks appeared to be limited only by the resolution of the slit system of the spectrometer (about 20′ in 2θ), showing that the S regions probably are quite large.

Torque studies show that a magnetic anisotropy in annealed-stressed crystals of NiO is rotated by magnetic fields in excess of 2400 oe.[14] This suggested that small fields may induce spin rotation or movement of S walls. By measuring the effect of a magnetic field on the neutron scattering, it was established that the effect of H is to rotate the antiferromagnetic spins in (111) to a direction perpendicular to the applied field. Two experiments were carried out on crystal 7–9B. The geometry of the first experiment is shown in Fig. 8. The crystal is cut with faces parallel to (111), $(\bar{1}10)$, and $(\bar{1}\bar{1}2)$. The crystal was oriented such that the neutron scattering from $(\bar{1}13)$ could be observed while a magnetic field H was applied in a horizontal plane which nearly coincided with (111). The actual angle between (111) and the H plane was 10°. H could be rotated approximately ±25° about the $(\bar{1}13)$ scattering vector. The second experiment was similar except that the crystal rotation axis was $[1\bar{1}0]$ and H rotated in $(1\bar{1}0)$. The results are summarized in Table III. The first column describes the specimen history, the second the

TABLE III. Spin rotation and S wall displacement in an applied field.

	Treatment	∢[H][$\bar{1}13$]	H (oe)	Neutron intensity
(a)	Annealed crystal[a]; squeezed [111]; H approximately in (111).	···	0	3744
(b)		0°	2900	4277
(c)		0°	4300	4569
(d)		25°	4300	4040
(e)		0°	4800	4732
(f)	Crystal rotated in $H=4800$, H reduced when ∢[H][$\bar{1}13$]=90°.	···	0	3646
(g)	$H=4300$ applied along $[\bar{1}13]$; H reduced when ∢[H][$\bar{1}13$]=0.	···	0	4024
(h)		30°	4300	4166
(i)	Crystal remounted to rotate about [110].	···	0	3252
(j)		25°	4200	3945
(k)		0°	4200	3962
(l)		0°	0	3330
(m)		−20°	4200	3882
(n)	Crystal oscillated while H [111]; H reduced when ∢[H][$\bar{1}13$]=90°.	···	0	3393

[a] Crystal 7-9B. This crystal also was used in (6), Table II.

[22] H. Alperin, J. Appl. Phys. **31**, 354S (1960).
[23] G. E. Bacon and R. D. Lowde, Acta Cryst. **1**, 303 (1948).

angle between the applied field and the normal to the scattering plane, the third the magnetic field, and the fourth the integrated neutron intensity in arbitrary units. The neutron intensities in the two experiments should not be intercompared because the corrections for secondary extinction are quite different.

When H was applied normal to $(\bar{1}\bar{1}3)$, the antiferromagnetic spins rotated so they became perpendicular to H and therefore the neutron scattering increased (a,b). A significant rotation (or S wall displacement) took place when H was only 2900 oe, and additional rotation occurred as H increased (b,c,e). When H was maintained constant but rotated in (111) in a direction away from the scattering vector, the spins followed perpendicularly to H and the magnetic scattering from $(\bar{1}\bar{1}3)$ decreased (c,d). A similar alignment of the spins by H was observed when the rotation axis was $[\bar{1}10]$ (i,k). However, rotating H in $(\bar{1}10)$ from $-20°$ to $+25°$ had no effect on the neutron scattering (j,k,m). This is consistent with the fact that spin rotation occurs only within (111) and the magnetic moments remain aligned along $[\bar{1}10]$ as H is rotated in the $(\bar{1}10)$ plane.

The distribution of spins in zero field depends on the magnetic history. When H was applied along $[\bar{1}10]$, then reduced to zero, the distribution of spins in (111) was approximately the same as in the virgin crystal (f,a). On the other hand, when H was applied along $[\bar{1}\bar{1}3]$ and then reduced, there was a net rotation of spins toward $[\bar{1}10]$ (g). A similar rotation did not occur when H was rotated in $(\bar{1}10)$ (i,l,n). This again is consistent with the restriction of spin rotation to (111).

A spontaneous relaxation of the spins may take place when the H field is removed (i,k,l). The origin of the anisotropy in (111) is not clear at the present time and is currently under investigation. Torque curves obtained from this same crystal show a rotational hysteresis of 345 erg/cc-cycle when the magnetization is rotated in (111).[14] Since the anisotropy in (111) should be very small,[24] this rotational hysteresis probably is related to the defect structure in the crystal. The present crystals are slightly oxygen rich and probably are slightly ferromagnetic due to the Ni^{+2}–Ni^{+3} double exchange interaction. Perakis and Parravano[25] have observed a small ferromagnetic moment which increases with oxygen content in NiO powders. The excess anisotropy possibly originates from an exchange anisotropy[26] between the antiferromagnet and ferromagnetic regions associated with the trivalent nickel. A similar explanation has previously been given for the displaced hysteresis loop observed in nonstoichiometric FeO.[7]

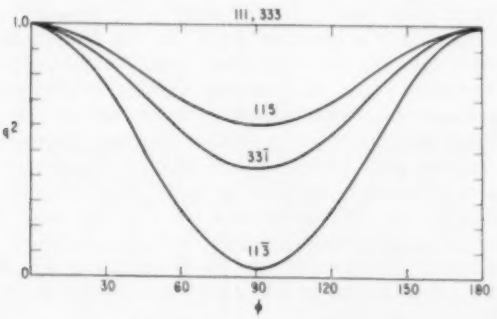

FIG. 7. Dependence of q^2 on spin direction within the ferromagnetic sheet.

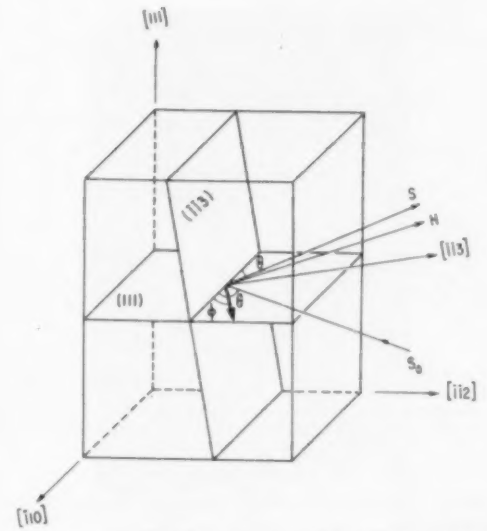

FIG. 8. Neutron diffraction in a magnetic field. The crystal faces are $(\bar{1}10)$, $(\bar{1}\bar{1}2)$, and (111). S_0 and S are parallel to the incident and diffracted beans, θ is the Bragg angle, and ϕ defines the spin direction in the ferromagnetic (111) sheet. S_0, S, H, and $[\bar{1}\bar{1}3]$ lie in a plane which is tipped 10° with respect to (111).

Rotation of the magnetization in (111) may take place either by coherent rotation within an S domain, or by the displacement of S type domain walls. The strength of the interaction between the four antiferromagnetic submotifs[3] which make up the antiferromagnetic structure of NiO is small and the coherent rotation of the submotifs may be relatively independent. Figure 9 illustrates the alternative rotation processes. The spin axes are taken along $\langle\bar{1}10\rangle$ and, since T walls are absent, the crystallographically equivalent spin directions have equal energy. Minimum energy is obtained in an antiferromagnet when the magnetic moments are perpendicular to the applied field so the spins either will rotate coherently (a), or by uncoupling the submotif system (b), or by the displacement of S walls to reduce the volume of crystal having spins with components parallel to H (c). Magnetic anisotropy studies[14] suggest that at intermediate fields $2400 < H < 8000$ (b) or (c) may be the predominant mechanisms for spin

[24] T. Nagamiya (private communication).

[25] N. Perakis and G. Parravano, Compt. rend. **250**, 677 (1960).

[26] W. H. Meiklejohn and C. P. Bean, Phys. Rev. **105**, 904 (1957).

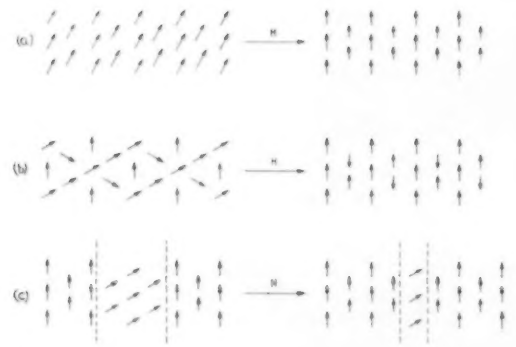

FIG. 9. Spin rotation in (111) of NiO. (a) Coherent rotation assuming coupling between antiferromagnetic submotifs is strong. (b) Coherent rotation, assuming weak coupling. This process leaves 180° S walls in the crystal. (c) Rotation by the displacement of S walls.

rotation, whereas at $H>8000$, the magnetization rotates coherently (a).

Estimates of the fractional alignment of spins perpendicular to the scattering vector were made from the data in Table III assuming spin rotation occurred by S type domain wall displacement. The magnetic orientations were restricted to $[\bar{1}10]$, $[0\bar{1}1]$, and $[\bar{1}01]$, and the intensities were normalized by assuming the spins were equally distributed among these directions when the neutron scattering was a minimum (f,i). The maximum alignment was 49% and this value was obtained for (e) when the applied field was 4800 oe. The failure of 4800 oe to completely align the antiferromagnetic spins agrees with magnetic anisotropy studies[14] on the same crystal. When a magnetic field was rotated in (111), rotational hysteresis appeared at a critical field of 2400 oe and increased linearly with H to a maximum value of 345 erg/cc-cycle at 7000 oe. At 4800 oe, only 213 erg/cc-cycle was developed. Making the reasonable assumption that the fraction of spins rotating is proportional to the energy dissipated, the torque studies suggest that 60% of the spins are rotated at $H=4800$ oe. in reasonable agreement with the neutron diffraction result.

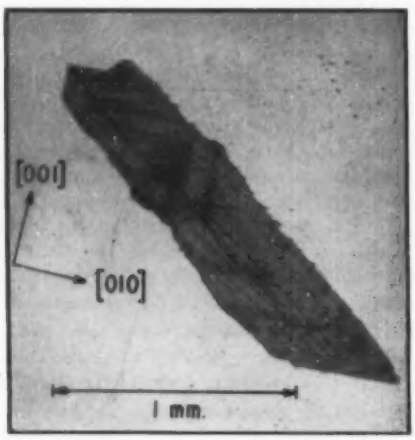

FIG. 10. NiO cleavage fragment. The dark areas are lamellar T regions. The curved surfaces are growth patterns.

OPTICAL PROPERTIES OF T WALLS

T walls are easily seen with transmitted polarized light in thin sections of crystal which are 100 μ or less thick.[12] The walls are visible because each domain is an optically uniaxial crystal with optic axis coincident with the contraction axis. The growth of domains by thermal annealing, the crystallographic orientations of T walls, and the displacement of walls by the application of a stress or a magnetic field can be observed with the microscope.

Thin sections of NiO are pale yellow (oxygen-rich) to green in transmitted unpolarized light. In polarized light the color saturation is increased and the crystals are slightly dichroic. The birefringence in a (100) thin

FIG. 11. Polished thin section before annealing, showing small T regions.

section was determined by measuring the retardation at λ5900 A with a Berek Compensator. In a crystal section 66 μ thick, the observed retardation was 193 mμ, corresponding to a birefringence $n_E-n_0\approx 0.003$. For these values of birefringence and thickness, the interference color should be first-order gray, whereas an intense yellow is observed. Since the thin crystals are nearly colorless in unpolarized light, the anomalous interference is due to dispersion. Uniaxial interference figures are observed in the single T regions and the [111] crystal direction coincides with the optic axis. By using a gypsum plate in conjunction with the interference figure, the domains were shown to be uniaxial positive, i.e., $n_E>n_0$. This agrees with the fact that NiO is slightly compressed along the optic axis, since the polarizability for vibrations parallel to the optic axis (the E ray) is greater than for vibrations perpendicular to the optic axis (the O ray).[27]

[27] N. H. Hartshorne and A. Stuart, *Crystals and the Polarizing Microscope* (Edward Arnold & Company, London, England, 1952), 2nd. ed., chap. IV, p. 89–159.

Preparation of Thin Specimens

A technique was developed for preparing thin polished sections of NiO, 20–50 μ thick, of any desired crystallographic orientation. The principal difficulty is that cleavage takes place very easily along {100}. The crystals first were cleaved parallel to {100}, then cast in a brass ring with either an Epon type resin or glycol phthalate. The crystal was easily oriented by reference to the 100 cleavage faces. The brass ring containing the crystal was mounted in a steel holder and one face of the crystal polished flat, using Precisionite on a wet wheel. The crystal-ring assembly was then recast, and the opposite face polished until the section had the desired thickness. The crystal thickness was estimated by the light transmission, or by a micrometer feed on the holder. The Epon resin was removed by digestion in hot 50% $H_2SO_4-HNO_3$, whereas the glycol phthalate could easily be removed by warming until the resin softened.

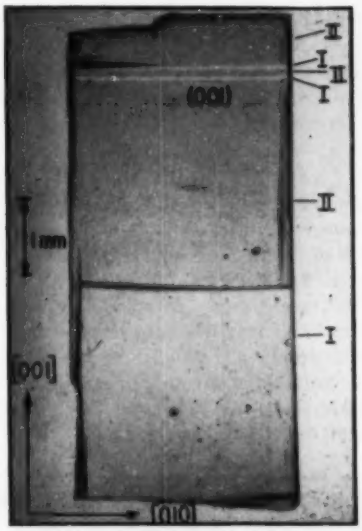

FIG. 12. Annealed crystal showing I(001)II walls. This pattern does not require spin rotation but *S* walls may be present. The curved boundary is probably due to strain.

Growth of *T* Regions

A photomicrograph of a cleavage fragment from a Verneuil-grown boule is shown in Fig. 10. The section is about 25 μ thick and the cleavage face is (100). The *T* wall texture is clearly visible when the crystal is viewed with [001] at 45° to crossed polaroids with a $\lambda/2$ gypsum plate in the 45° position. Each *T* region appears vivid yellow or green, depending on the orientation of the optic axis to the gypsum plate. Polishing of thin sections creates large numbers of domain walls, and the individual *T* regions in the (100) thin section shown in Fig. 11 are only a few microns in size.

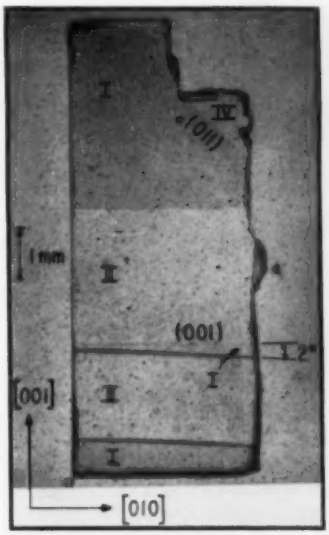

FIG. 13. Crystal containing both I(011)II and I(011)IV walls. The tilted walls are highly strained. *S* type domain walls must also be present.

The large domains shown in Figs. 12–20 were produced by annealing the crystals at high temperatures and cooling them slowly to room temperature. The domains are several mm in size and usually extend completely across the narrow width of the crystal. To produce the large domains, the crystals were supported on NiO powder contained in platinum boats and annealed at 1500°C for approximately one hour, then slowly cooled to room temperature. When an air atmosphere was used, the crystals were oxygen rich and had a yellow-brown color. The more nearly stoichio-

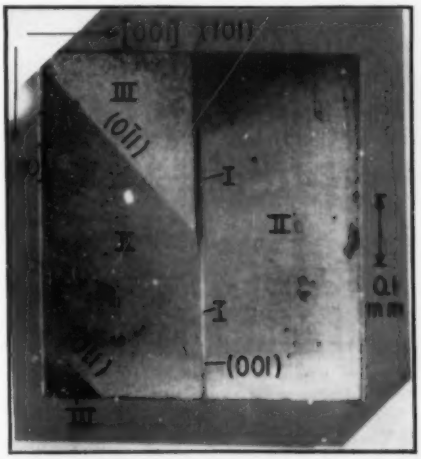

FIG. 14. Four wall pattern showing replacement of a (001) wall by a type III region which is bounded by $(0\bar{1}1)$ and (101) walls. There are probably *S* walls in the type III regions.

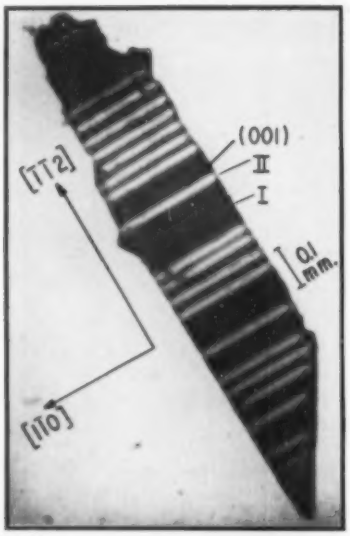

FIG. 15. Simple I(001)II walls in (111) section. *S* walls are not required by this pattern.

metric crystals, obtained by heating in CO_2 or in an atmosphere of *A* containing a trace of O_2, were pale green. The dependence of color on stoichiometry has been explained by Newman and Chrenko.[28] Domain growth was not obtained by heating at 1200°C. Apparently *T* walls nucleate on imperfections, such as grain

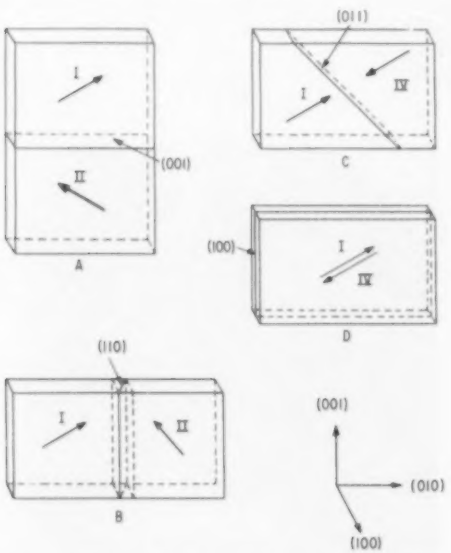

FIG. 16. The appearance of simple *T* walls in thin sections. The projection on (100) of the rhombohedral (optic) axis in each *T* region is shown.

[28] R. Newman and R. M. Chrenko, Phys. Rev. **115**, 7 (1959).

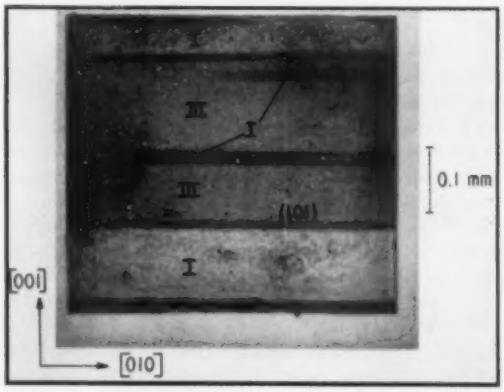

FIG. 17. Laminar *T* regions in (100) crystal. The laminar regions appear isotropic because of compensated birefringence.

boundaries or impurity particles, and the high temperature anneal clears the crystal from such defects by diffusion.[29]

Crystallography of *T* Domains and Walls

The orientation of *T* walls in annealed thin sections agrees in general with the predictions in Table I. The distribution of *T* walls in several representative crystals was analyzed. The black and white prints are made from color transparencies and the color differences which assisted in the assignment of domain type are not always visible in monochrome. The optical characteristics may be understood by reference to Fig. 16, which shows the appearance of the two types of walls consistent with a common spin direction across the *T* wall. If a I(001)II

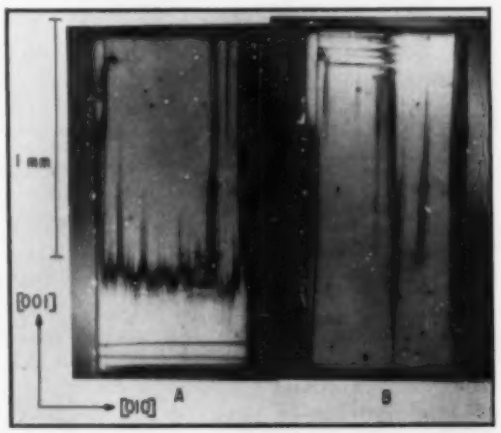

FIG. 18. Displacement and rotation of *T* walls by stress. The stress was applied along [001] and some (101) walls were displaced along [001], whereas others were converted into (010) walls. These are probably I-III regions and the conversion (101) → (010) does not require rotation of the spin axis.

[29] M. T. Shim and W. J. Moore, J. Chem. Phys. **26**, 802 (1957).

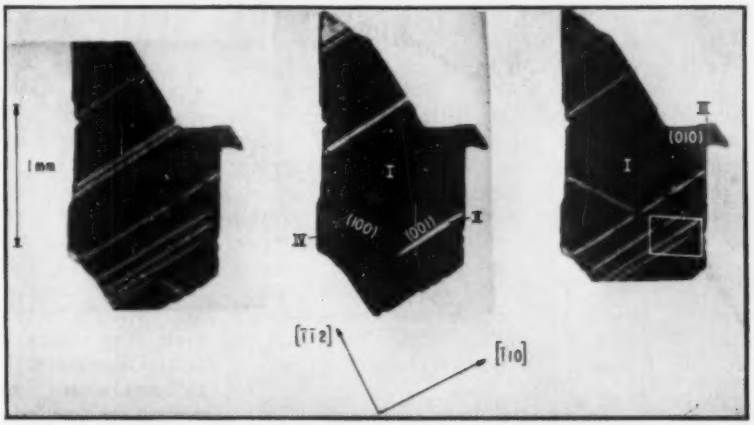

FIG. 19 Displacement of T walls by a magnetic field. The crystal face is (111) and $H = 25$ koe was first applied along $[11\bar{2}]$, then along $[\bar{1}10]$. A selected portion is shown at higher magnification in Fig. 20.

crystal is examined with plane polarized light transmitted along [100] or [010], the crystal may extinguish sharply enough to appear a single domain because the projection of the optic axes differs from 90° by only 6′. The identification of the two regions is easily made by inserting a $\lambda/2$ gypsum plate which differentiates between the directions of high and low index of refraction by a shift in the interference color. The orientation of the T regions across (110) is similarly established. The kind of T wall frequently can be identified by its appearance. For example, when the light path is along [001], the (001) wall is sharp, whereas the (110) wall is diffuse and seems to be optically isotropic. In this latter case, the light passes through overlapping wedges from two T regions. The wall has a projected thickness of $\sqrt{2}\times$ crystal thickness and appears isotropic because the birefringence of the overlapping crystals is compensated. The antiferromagnetic T walls resemble in many respects the domain structures in ferroelectric $BaTiO_3$.[30]

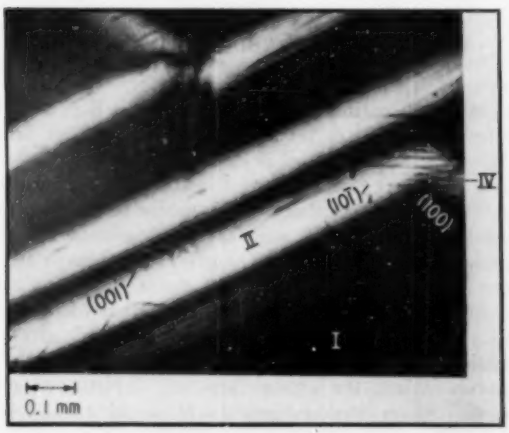

FIG. 20. Details of intersection of T regions in Fig. 19. Note strained region where II region is displaced, and smooth transition between II and IV accomplished by $(10\bar{1})$ walls.

Some T walls will be seen only if the crystal is tilted. The I(011)IV and I(100)IV walls as in Fig. 16 may not be detected if observed with light exactly along [100] because the projected optic axes are nearly coincident. They can be made visible by tilting the crystal with respect to the axis of the microscope. This clarifies an observation reported previously.[3] The neutron scattering from an annealed thin section indicated T regions were present although they had not been detected optically. The crystals used in the neutron diffraction work have been re-examined using a tilting stage on the microscope and the T walls required to explain the neutron data became visible.

A well annealed crystal usually has a simple domain pattern consisting of a few T walls parallel to one of the cube faces (Figs. 12, 15). The walls are most frequently parallel to the short dimension of the crystal plate. This probably reflects the adjustment of the domain configuration to minimize the T wall surface energy. Occasionally, T walls deviate slightly from simple crystallographic directions. For example, one of the walls in Fig. 12 is curved, although a mean plane through the wall is parallel to (010). Similarly, in Fig. 13, two of the T walls are tipped 2° from (010). In both of these cases, the deviate walls are diffuse and optically isotropic, indicating the T wall is highly strained. These effects seem to be due to internal strains produced when the crystals are cooled from 1500°C to room temperature. Further observations on the relation of stress to T walls is given in the next section.

As previously noted, the most stable domain configurations appear to develop from only two orientations of T regions. More complex domain patterns are observed and these require that S walls (spin-rotation) be present. In the crystal shown in Fig. 13, the magnetic axis probably is predominantly $[\bar{1}01]$, but rotation to $[01\bar{1}]$ must occur at the I(011)IV wall. An interesting example of a

[30] P. W. Forsbergh, Jr., Phys. Rev. **76**, 1187 (1949).

complex pattern is shown in Fig. 14. In the lower portion of the crystal, sharp (001) walls separate the type I and type II regions. In the upper portion, one of the (001) walls is replaced by a diffuse (101) wall [or a thin laminar region bounded by (101)] to accomplish the transition from type III to type I. Laminar regions, terminating in the middle of a crystal, are frequently seen (Fig. 17). The laminar T regions usually are observed in crystals which have been stressed, and probably are similar to the wedge-shaped laminar domains observed in $BaTiO_3$.[20] It is sometimes difficult to distinguish between 45° T walls and a thin laminar T region. However, identification of a laminar region is easily made if the region terminates within the crystal, or separates T regions with identical contraction axes.

Movement of T Walls by Stress and Heat Treatment

In a well annealed NiO crystal, the T walls are mobile and can easily be displaced by the application of a mechanical stress or magnetic field, or as the result of heating to temperature above T_N and cooling back to the antiferromagnetic state. The walls can be moved distances of several mm and the movement can be observed with polarized light and a microscope.

Since the antiferromagnetic ordering is accompanied by a contraction along (111), the elastic energy is lowest for those domains that have an appreciable component of their contraction axis parallel to the applied stress. When a moderate stress is applied, then removed after a fraction of a second, an elastic displacement of the T wall occurs and the boundary returns to the position it occupied in the unstressed state. On the other hand, if the wall is maintained in the displaced position for 10–20 sec, the movement is irreversible and the boundary remains in the new position until an additional stress is applied. The wall displacement experiments may be repeated many times, but eventually "work hardening" sets in, the motion becomes viscous, and the walls are immobilized. If the deformation is not too severe, the wall mobility is recovered when the crystal is left undisturbed at room temperature for a few days.

The force required to displace a T wall is very small[21] and their mobility is greatly reduced by crystal defects and imperfections. The work hardening and the recovery of wall mobility by annealing at room temperature suggest that T walls can be pinned by crystal or magnetic imperfections and that the quasi-equilibrium position of a T wall is determined by either the local stress or local magnetic field. Apparently the time required for the redistribution of the spins is large compared to the velocity of T wall movement.

The relation of the distribution of T domains to local stress was also seen by observing crystals on a microscope hot stage. The hot stage consisted of a conducting tin-oxide coating on a silica glass slide and the temperature was controlled by measuring the current passed as the voltage varied. The temperature scale was established by observing the melting of AgCl (465°C) and AgBr (434°C). When a crystal is heated it gradually becomes isotropic and the birefringence disappears at T_N. When the crystal is cooled, after being heated well into the paramagnetic region (500°C), the birefringence and domain pattern gradually reappear. In general, the T wall distribution will not be the same as before the heat treatment. If the experiment is repeated, the domain walls usually reappear in the same position—i.e., the walls move only during the first temperature cycle. The application of a very small stress to the crystal regenerates the sensitivity of the T wall pattern to temperature. These observations show that during cooling, the domains are nucleated at local inhomogeneities which are mobile at low temperature and can be moved by a small applied stress.

T walls may be transformed from one orientation to another by the application of stress. When the crystal shown in Fig. 18 was removed from the annealing furnace, the domain structure was very simple and consisted of several (011) walls similar to the diffuse walls in A. By applying a stress approximately normal to the wall, the boundary was converted into a complex zigzag with a principal component parallel to the direction of the stress (B). These complex boundaries appear to be laminar T regions formed by the convergence of nearly parallel T walls. The laminar T regions move easily through the crystal. In one type of motion, the angle between the T walls remains constant and the complex zigzag boundary is displaced parallel to itself. A second type of motion occurs when the angle between the T walls changes and the wedge advances into the adjoining region in the form of a long, thin spike.

Movement of T Walls by Magnetic Fields

Below T_N the magnetic susceptibility perpendicular to the antiferromagnetic spin axis is greater than the parallel susceptibility, and the energy is a minimum when the spins are perpendicular to an applied field. When magnetic fields of 20 to 30 kgauss are applied to well annealed crystals, the T walls are displaced or rotated to new positions. The response to H is highly erratic because the T walls are easily pinned by imperfections in the crystal. The effects of magnetic field are basically similar to those of stress, and again the position of T walls in a crystal appeared to be associated with local inhomogeneities. For example, after several applications of H, the T walls frequently become immobile. When the crystal was left undisturbed for several hours, the response to H would usually be restored.

The crystal in Fig. 19 was polished parallel to (111). The freshly annealed crystal was predominately type I,

[21] Slack has determined that the pressure required to move a T wall in a well annealed crystal is less than 10^6 d/cm^2.

with a few type II regions separated by (001) walls. Most of the (001) T walls were destroyed by the application of 25 kgauss along $[11\bar{2}]$. Some (001) walls were displaced from the crystal to form larger type II regions, and in other portions of the crystal, new type IV regions and (100) T walls were created. When the field was applied again, this time along $[\bar{2}11]$, many of the (001) walls were restored. The crystal is highly strained where two T regions appear to cross. This is clearly seen in the enlarged detail photomicrograph (Fig. 20) where the two halves of a type II region are displaced by intersection with a type IV. On the other hand, the transition from II to IV near the right edge of the crystal is accomplished smoothly by laminar T regions bounded by $(10\bar{1})$ T walls.

SUMMARY

The complete discussion of the properties of antiferromagnetic domains in NiO will be deferred until the results of magnetic anisotropy studies on detwinned crystals are presented. This paper has given the neutron diffraction evidence for the existence of two kinds of antiferromagnetic domain walls in NiO: T (twin) in which there is a change in the direction of the antiferromagnetic pattern of moments, and S (spin-rotation) in which there is a rotation in the direction of the moments. Optical studies of thin sections have shown that large T regions can be grown by annealing the crystals at 1500°C. The T walls in a well annealed crystal are highly mobile and can easily be displaced by applying a mechanical stress or a magnetic field. The S walls have not been observed directly, but some of their properties have been deduced from neutron diffraction studies. In a detwinned crystal, the distribution of S walls in zero field appears to be nearly random. Spin rotation or S wall displacements occur in moderate fields of 2400 oe or more. If T walls are present, a commonly occurring configuration is one in which there is no change in the magnetic axis between T regions. However, in more complex domain configurations both T and S walls exist. These latter, in particular, appear to be stabilized by defects or imperfections in the crystal.

The passage of a T-type domain wall through a crystal is accompanied by the rotation of spins into the wall and the magnetization direction in the immediate vicinity of the wall is determined by the intersection of the wall with the ferromagnetic (111) sheets. Proceeding away from the T wall, spin rotation (S walls) may occur. There appears to be a relaxation time of the order of seconds at room temperature associated with the spin rotation. This spin relaxation was observed in the neutron diffraction experiments with a detwinned crystal, and also was inferred from the optical studies of T wall mobility. The origin of the spin relaxation time is not clear at present. A possible interpretation is that it is due to the motion of dislocations through the crystal. An argument against the dislocation mechanism is that NiO is a hard crystal, and a dislocation velocity of the order of 10^{-1} cm/sec as a result of a stress of 10^6 d/cm^2 is surprisingly large. For example, W. G. Johnston has found that in MgO, a crystal of similar hardness, a stress of 4×10^8 d/cm^2 is required to produce a comparable velocity.[22] An alternate interpretation is that the spin relaxation is due to exchange anisotropy[7,26] between the antiferromagnetic spins and ferromagnetic inhomogeneities or impurities. The NiO crystals are oxygen rich and contain cation vacancies. Charge balance requires that 2 Ni^{+3} be produced for each cation vacancy, and the magnetic inhomogeneity could result from ferromagnetic exchange interaction between Ni^{+2} and Ni^{+3}. This latter mechanism suggests that the rotational hysteresis observed when the spins rotate in (111) and the spin relaxation time depend upon the crystal stoichiometry.

ACKNOWLEDGMENTS

The author is indebted to J. M. Hastings of the Brookhaven National Laboratory for cooperation in the experiment on the effect of a magnetic field on the neutron scattering. G. A. Slack provided the detwinned NiO crystal and contributed much valuable discussion. D. S. Hallgren prepared the NiO thin sections and A. Abrahamsen assisted with the neutron diffraction experiments.

[22] W. G. Johnston (private communication).

Temperature Dependence of the Debye Temperatures of Aluminum, Lead, and Beta Brass by an X-Ray Method*

D. R. CHIPMAN
Materials Research Laboratory, Ordnance Materials Research Office, Watertown, Massachusetts
(Received March 9, 1960)

The temperature dependence of the Debye temperature of aluminum, lead, and beta brass was determined by measuring the integrated intensity of a high angle x-ray diffraction peak from each of the materials as a function of temperature. This measured temperature dependence agrees well with the corresponding function obtained from elastic constant data, although it is determined by much higher lattice frequencies. In agreement with the elastic constant measurements, evidence is found for an explicit temperature dependence beyond that resulting from the simple dependence of Debye temperature on volume.

INTRODUCTION

THE integrated intensity of an x-ray Bragg reflection depends, through Debye-Waller theory, on the x-ray (or Debye-Waller equivalent) Debye characteristic temperature Θ of the material studied. Therefore a set of integrated intensities taken over a range of temperatures determines a curve of Θ vs temperature. Such curves have been measured for sodium chloride,[1] potassium chloride,[2] gold, copper, and aluminum.[3] All of these curves show the expected behavior; Θ decreases as the temperature increases. The detailed dependence of Θ on temperature seemed to be matched by theory[3-5] for all of the above materials except aluminum. These theories are nearly equivalent treatments of the dependence of Θ on temperature which results from the explicit dependence of Θ on the volume. It has since been shown, however, that the elastic constants of NaCl,[6] KCl,[6] CuZn,[6] Al,[6,7] Cu,[6,8] Ag,[9] Au,[9] and others, exhibit an additional explicit dependence on temperature about as important as that implicit in the volume dependence. Since Θ is related indirectly to the elastic constants, one might expect the simple theories[3-5] to be inadequate, as was the case for aluminum.[3] It is therefore surprising that these theories were able to match experiment as well as was claimed for the other materials. Consequently it was interesting to repeat some of the measurements. This paper reports some new x-ray measurements of the temperature dependence of the Debye temperatures of aluminum, lead, and beta brass.

EXPERIMENT

The x-ray intensity measurements reported here were made on a scintillation counter diffractometer using CuKα radiation monochromated by a doubly bent lithium fluoride crystal,[10] with pulse height analyzer set to eliminate the half-wavelength component from the beam. The samples were made from 400 mesh filings of 99.996% pure materials compressed into powder briquettes. The brass was 51.8 weight percent copper. The aluminum and lead briquettes were annealed for one-half hour each at 50 degrees below their melting points. The brass was annealed only for 20 minutes at 300°C to minimize zinc loss, but no further sharpening of the x-ray lines was observed during subsequent runs at higher temperatures.

Measurements below room temperature were made in an attachment which cooled the briquettes from the back by means of a circulated coolant. The data above room temperature were obtained using a vacuum furnace which employed four concentric radiation shields with nickel foil x-ray windows. Temperatures were measured with a calibrated thermocouple, and are good to plus or minus two degrees. Considerable difficulty was encountered due to zinc loss from the brass at higher temperatures. This was reduced by operating under an atmosphere of nitrogen gas, and by reducing to a minimum the time spent at temperature. This

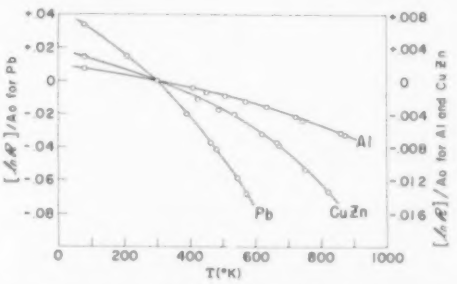

FIG. 1. The x-ray data $[\ln\theta]/A_0$ as a function of temperature for aluminum, lead, and beta brass. Steeper slopes mean lower values of Debye Θ.

* Portions of this work were presented at the Pittsburgh Diffraction Conference, Pittsburgh, Pennsylvania, on November 7, 1958.

[1] R. W. James and E. M. Firth, Proc. Roy. Soc. (London) **A117**, 62 (1927).

[2] R. W. James and G. W. Brindley, Proc. Roy. Soc. (London) **A121**, 155 (1928).

[3] E. A. Owen and R. W. Williams, Proc. Roy. Soc. (London) **A188**, 509 (1947).

[4] C. Zener and S. Bilinski, Phys. Rev. **50**, 101 (1936).

[5] A. Paskin, Acta Cryst. **10**, 667 (1957).

[6] D. Lazarus, Phys. Rev. **76**, 545 (1949).

[7] P. M. Sutton, Phys. Rev. **91**, 816 (1953); see also errata in Phys. Rev. **112**, 2139 (1958).

[8] W. C. Overton and J. Gaffney, Phys. Rev. **98**, 969 (1955).

[9] J. R. Neighbours and G. A. Alers, Phys. Rev. **111**, 707 (1958).

[10] D. R. Chipman, Rev. Sci. Instr. **27**, 164 (1956).

TABLE I. Coefficients used in Equation (5).

	Al	Pb	CuZn
$\alpha(°C^{-1})$	28×10^{-6}	29×10^{-6}	17×10^{-6}
$\gamma(°C^{-1})$	2.13×10^{-4}	0.76×10^{-4}	0.37×10^{-4}
$A_0(°K)$	295.0	27.93	98.7

principally accounts for the larger uncertainty given for the brass data.

One high angle reflection of each material was chosen, and its integrated intensity measured at the various temperatures reported. For aluminum, the (422) reflection was used, for lead the (511–333), and for brass the (310). The data were point counted so that the statistical accuracy in the final areas was held to about 1% for the Al and Pb, about 3% for CuZn. Each set of data consists of several runs at higher temperature interspersed between runs at room temperature. The room temperature value always repeated itself to within about 2% (5% for the brass). Figure 1, showing the $[\ln\Re]/A_0$ vs temperature, gives the results of these measurements. $\Re$ is the ratio of the integrated intensity of the reflection at temperature T to the corresponding intensity at room temperature, and A_0 is a constant defined in Eqs. (3) and (4). The estimated probable error is approximately given by the size of the circles.

ANALYSIS OF RESULTS

Using the notation of James[11] the integrated intensity, P, of a particular Bragg reflection from a powder is proportional to

$$P\propto\left(\frac{1+\cos^2 2\alpha\cos^2 2\theta}{\sin\theta\sin 2\theta}\right)Nf^2e^{-2M}=\mathrm{B}e^{-2M}. \quad (1)$$

N is the number of atoms per unit volume, f is the atomic scattering factor, $\exp[-2M]$ is the Debye-Waller factor, α is the Bragg angle at the monochromator, and θ the Bragg angle at the sample. If the peak is integrated above a straight line background, a correction for the peak in the temperature diffuse scattering occurring underneath can be made, following Chipman and Paskin,[12] by use of their factor β as follows:

$$P_{\mathrm{meas}}\cong\mathrm{P}e^{2M\beta}\propto\mathrm{B}e^{-2M(1-\beta)}, \quad (2)$$

where

$$2M(1-\beta)=\frac{12h^2}{mk}\frac{\sin^2\theta}{\lambda^2}(1-\beta)\left\{\frac{T\psi}{\Theta^2}\right\}=A\frac{T\psi}{\Theta^2}. \quad (3)$$

In this equation, ψ is written for the Debye function $\phi(x)+x/4$. The ratio $\Re$ of the measured peak area at temperature T to the area at room temperature, T_0, is given by

$$\ln\Re=\ln\left[\frac{P_T}{P_0}\right]_{\mathrm{meas}}=\ln\frac{B_T}{B_0}+A_0\left\{\frac{T_0\psi_0}{\Theta_0^2}-\frac{T\psi(\sin^2\theta/\lambda^2)_T}{\Theta^2(\sin^2\theta/\lambda^2)_0}\right\}, \quad (4)$$

where the subscripts T and 0 refer to the temperatures T and T_0 respectively. The ratio of $\sin^2\theta/\lambda^2$ at two temperatures can be expressed in terms of the linear thermal expansion coefficient α, and the equation rewritten as

$$\ln\Re-\ln\frac{B_T}{B_0}=A_0\left\{\frac{T_0\psi_0}{\Theta_0^2}-\frac{T\psi}{\Theta^2}[1-2\alpha(T-T_0)]\right\}. \quad (5)$$

Equation (5) is the final form used to obtain Θ. The ratio B_T/B_0 was computed to first order in the form

$$B_T/B_0=1-\gamma(T-T_0),$$

using only the values of the expansion coefficient α. The values of α, γ, and A_0 used for the different elements are given in Table I. Using these values, Eq. 5 was solved for Θ as a function of T for several choices of the parameter Θ_0. This was done by an electronic computer, the machine being required to solve for the different values of ψ from the series expansion,[13] and to iterate the calculation at each point until a value of ψ consistent with the final value of Θ was obtained.

A typical result of the above calculation, that for aluminum, is given in Fig. 2, which shows the family of curves resulting from small changes in the assumed room temperature value of Θ_0. To choose the correct curve from this family of curves requires additional information. Specifically, this could be either the absolute value of Θ at some temperature, or the shape of the Θ vs T curve. Unfortunately there is no general method available for determining the absolute value of Θ by x-ray means without recourse to theoretical calculations of intensity parameters such as the scattering

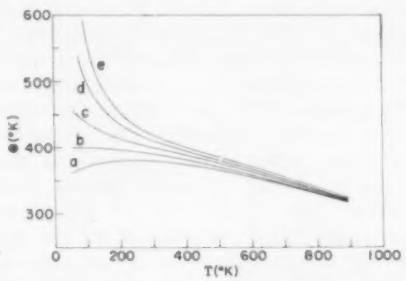

FIG. 2. The x-ray Debye Θ of aluminum as a function of temperature from the present x-ray intensity ratios. Curves *a*, *b*, *c*, *d*, and *e* obtained by choosing Θ_0 equal to 380°, 390°, 400°, 410°, and 420°K, respectively, at $T=300$°K.

[11] R. W. James, *The Optical Principles of the Diffraction of X Rays* (G. Bell and Sons, Ltd., London, England, 1948).

[12] D. R. Chipman and A. Paskin, J. Appl. Phys. **30**, 1998 (1959).

[13] P. Debye, *The Collected Papers of Peter J. W. Debye* (Interscience Publishers, Inc., New York, 1954), p. 31.

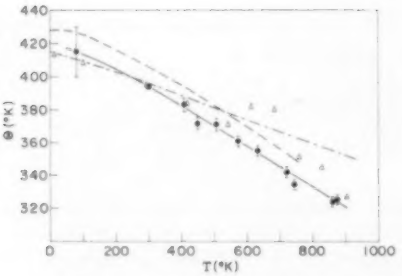

FIG. 3. Debye Θ of aluminum as a function of temperature. Solid line drawn through values (filled circles) obtained from present measurements using chosen value for Θ_0 at 300°K. Triangles are from Owen and Williams, also an x-ray technique. Dashed curve is from Sutton's elastic constant measurements. Dot-dashed curve is volume dependence only, from theory of Paskin.

factor and Hönl dispersion correction, or the intensity of Compton scattering.[14] For example, the integrated Bragg reflection measured in units of absolute intensity gives directly f^2e^{-2M}, but to separate the two factors, theoretical calculations of f^2 must be used. These quantities are not sufficiently well known to fix the value of Θ_0 for aluminum to better than about ± 10 degrees (for $\pm 1\frac{1}{2}\%$ uncertainty in f). Borie[15] has given a method by which f and Θ may be determined independently at one temperature by measuring the temperature diffuse scattering from the same sample. However, for most common materials this involves a fairly large (30% for copper) subtraction of the calculated Compton scattering. Assuming that the Compton scattering is known to an accuracy of about 10%, this again leads to uncertainties of the order of ± 10 degrees in the Θ_0 for copper, and larger errors for aluminum where a larger fraction of the diffuse scattering is Compton modified.

To determine, within the above limitations, an absolute value for Θ, the room temperature Bragg integrated intensities of aluminum and lead were measured in absolute units by comparison with the high angle scattering from Lucite. The x-ray Debye temperatures so obtained at $T=300°K$ were for aluminum $\Theta_0=407°K \pm 10°K$, and for lead $\Theta_0=86°K\pm 5°K$. In the case of beta brass, preferred orientation which always resulted from the pressing of the powder briquettes made absolute measurements impossible. The intensity ratio of a Bragg peak taken at two temperatures, however, should not be affected by a small amount of preferred orientation.

About equally good estimates of Θ_0 can be made immediately upon inspection of curves such as those shown in Fig. 2. Relying on a general knowledge of the shape of Θ vs T curves, d and e can be eliminated. Were the curves known accurately enough, one might also eliminate curves a and c. However, experimental error introduces an uncertainty in Θ which increases at lower temperatures so that, although the relative probable error within any one curve in Fig. 2 is only $\pm 2°C$ at high temperature and $\pm 3°C$ at room temperature, it rises to $\pm 15°C$ at 78°K. Hence the best value of the x-ray Θ_0 as determined by inspection of Fig. 2 would be $390°K\pm 10°K$, and for lead the corresponding value would be $84°K\pm 4°K$. These temperatures, however, agree fairly well with those obtained by direct standardization, and hence the method has been used as the sole standardization for the beta brass data from which Θ_0 was found to be $275°K\pm 15°K$, at $T=283°K$.

In Figs. 3–5, the x-ray Debye Θ's obtained as previously discussed for aluminum, lead, and beta brass are given as the solid curves drawn through filled circles. The relative probable errors for each curve are shown, but to each must be added the error in absolute standardization previously discussed. Thus the temperature dependence of Θ is determined better than the absolute value of Θ at any given temperature. In Fig. 3 the open triangles give the experimental results of Owen and Williams[3] (x-ray technique), the dashed curve gives the results of Sutton[7] from ultrasonic measurements of the elastic constants, and the dot-dashed curve is calculated from the theory of Paskin[5] which treats only the temperature dependence implicit in the volume dependence of Θ. Although there is considerable scatter in the data of Owen and Williams, there is still reasonable agreement among the experimentally determined slopes, which exceeds that given by the pure volume dependence.

Figure 4, giving the results for lead, shows also in the dashed curve the temperature dependence of Θ as

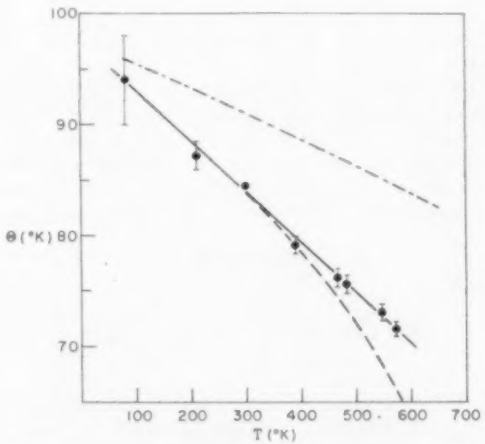

FIG. 4. Debye Θ of lead as a function of temperature. Solid line drawn through values (filled circles) obtained from present measurements using chosen value for Θ_0 at 300°K. Dashed curve is from Köster's measurements of Young's modulus. Dot-dashed curve is volume dependence only, from theory of Paskin.

[14] An exception would be any method in which the Compton scattering is first measured experimentally [C. B. Walker, Phys. Rev. **103**, 547 (1956)].

[15] B. S. Borie, Acta Cryst. **9**, 617 (1956).

calculated from data of Köster[16] on the temperature dependence of Young's modulus, normalized to match the present data at low temperature. The slopes agree well at low temperatures, but diverge badly at higher temperatures where Köster's data has been questioned in other materials.[17] The dot-dashed curve, as in Fig. 3, is calculated from Paskin's expression.

The data for beta brass are given in Fig. 5. The open square is a point calculated by Walker[18] from the elastic constant data of Lazarus[6] by the method of Quimby and Sutton.[19] The dashed curve is drawn through this point with a slope which can be calculated from the total temperature derivatives given by Lazarus[6] by making the assumption that $d\ln\Theta/dT=\frac{1}{2}d\ln C_{44}/dT$. The dot-dashed curve as before represents the volume dependent part only. This may also be calculated from the data of Lazarus, and by comparison with Paskin's expression, Grüneisen's constant for beta brass is found to be 2.23. It is interesting that in beta brass there is a downward curvature in the present data which seems to be outside of a reasonable estimate of error and which was not found in the other materials studied. There are two effects which could cause this behavior. As the temperature is raised, beta brass disorders, losing all long range order by about 730°K. This decrease in order probably causes an additional decrease in the Debye temperature.[20] Also, as the lattice becomes disordered, strains will be introduced because of the different sizes of copper and zinc atoms, which will cause a pseudotemperature effect of the type described by Huang.[21] This would cause an additional decrease in integrated intensity of the peaks, which the present analysis would attribute to an additional decrease in the Debye temperature.

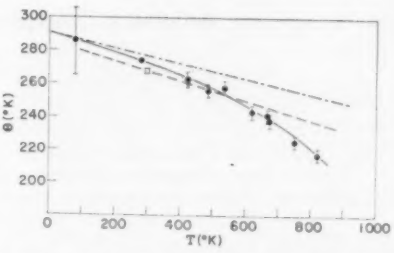

FIG. 5. Debye Θ of beta brass as a function of temperature. Solid line drawn through values (filled circles) obtained from present measurements using chosen value for Θ_0 at 283°K. Square is a point calculated from data of Lazarus, and dashed curve is from a slope given by Lazarus. Dot-dashed curve is volume dependence only, from theory of Paskin.

DISCUSSION

The Debye temperatures obtained from the present x-ray measurements have been given here directly as they come from the analysis of Eq. (5). These are referred to as x-ray (or Debye-Waller equivalent) Debye temperatures and, due to a difference in definition,[22] are expected to be larger by a few percent than the corresponding Debye temperatures obtained from specific heat data. In particular, the x-ray Debye temperature for aluminum will be about 3% higher, and for lead and beta brass about 4½% higher, than the standard Debye temperatures. Making these corrections, one obtains the room temperature Debye temperatures: for aluminum, 387°K±10°K; for lead, 81°K±5°K; and for beta brass, 263°K±15°K. Corresponding representative specific heat values would be[22]: for aluminum, 398°K; for lead, 88°K; (a specific heat value for beta brass is not available). As mentioned previously, the large uncertainties in the reported room temperature values of the x-ray Θ arise principally because of the present uncertainties in the individual atomic scattering factors concerned.

Although the present technique does not result in accurate absolute values of Debye Θ's, the method has allowed a fairly good measurement of the temperature dependence of Θ. It is worthy of note that the temperature dependencies of Θ obtained from the x-ray measurements agree quite well with those from elastic constant data, although the x-ray results are sensitive to lattice frequencies which are much higher than those employed in the elastic constant measurements. If this is indeed the case, it would imply that elastic wave velocities may depend on temperature in the same way over the entire range of the dispersion curve.

The measured temperature dependence is considerably stronger than the calculated slope implicit in the volume change alone, and is thus further evidence for the existence of an explicit dependence of Θ on temperature. Such an explicit temperature dependence is not predicted by any of the simple theories, and its understanding probably depends on a more exact treatment of the problem of anharmonicity.

ACKNOWLEDGMENTS

I thank Drs. A. Paskin and L. D. Jennings, and Professor C. B. Walker for helpful discussion and criticism.

[16] W. Z. Köster, Z. Metallk. **39**, 1 (1948).
[17] A. Paskin (private communication).
[18] C. B. Walker (private communication).
[19] S. L. Quimby and P. M. Sutton, Phys. Rev. **91**, 1122 (1953); P. M. Sutton, Phys. Rev. **99**, 1826 (1955).
[20] S. L. Quimby, Phys. Rev. **95**, 916 (1954).
[21] K. Huang, Proc. Roy. Soc. (London) **A190**, 102 (1947).
[22] See footnote 11, pp. 220–222, for a discussion of the difference in the averaging of longitudinal and transverse waves involved in the x-ray Debye Θ and the specific heat Debye Θ.
[22] C. Kittel, *Introduction to Solid State Physics* (John Wiley & Sons, Inc., New York, 1953), 1st. ed., p. 77.

Adiabatic Collapse of a Relativistic Electron Beam

T. F. GODLOVE AND D. C. DEPACKH
Nucleonics Division, U. S. Naval Research Laboratory, Washington 25, D. C.

(Received June 27, 1960)

Differential equations are derived and two computer solutions presented for the case of a relativistic electron beam injected into neutral gas. Processes included are ionization, scattering of electrons on atoms and ions, charge exchange, supply of neutrals to the beam by diffusion, and incoherent radiation by the electrons. A longitudinal electric field is assumed. The main restrictive assumptions are those of uniform densities and hydrodynamic stability. Solutions are given for an 1100-amp, 0.77-Mev, externally-focused beam injected into H_2 at pressures of 10^{-6} and 2×10^{-6} mm Hg. The beam contracts from an initial radius of 1.73 cm to an equilibrium radius of 7×10^{-4} cm in 3 and 0.5 msec, respectively. It is found in these cases that neutrality of the beam does not occur until *after* the radiation-scattering equilibrium, which was first studied by Budker, has occurred. Several difficulties connected with a neutralized beam are discussed. It is shown that a space-charge-limited beam of high phase-space density is the type most suitable for obtaining a small beam diameter in the shortest time. An approximate solution is derived which applies after a specified time near equilibrium and allows calculation of several parameters of interest without the necessity of computer integration.

I. INTRODUCTION

BUDKER[1] introduced the concept of a relativistic electron beam pinched by the focusing effect of positive ions in which an equilibrium is supposed to be established between scattering and radiation of the electrons. The underlying idea is that the scattering of electrons on positive ions which have been trapped in the beam causes a transfer of forward energy into transverse energy. Because of the small beam size (typically 10^{-2} cm) and consequent high frequency of transverse oscillation, this energy is radiated away. Thus if a strong forward electric field is present, an equilibrium exists in which the radiated energy is indirectly obtained from the electric field, leaving the electrons at a constant (average) energy and within very small cross-sectional radius.

Budker derived the formulas relating to the above process and discussed the application of such a beam to the acceleration of high-energy protons. He considered particularly the use of a neutralized beam, and gave a preliminary discussion of stability problems.

One of the present authors[2] analyzed these ideas in some detail and concluded that: (a) the kind of equilibrium envisioned by Budker would take a rather long time (the order of $10^{12}/n_+$ sec) to develop; (b) for application to a high-energy proton accelerator, in which the closed ring of electrons is supposed to provide the guide field for the accelerated particles, the number of protons which attain relativistic energy must be small compared with the total number of positive ions in the beam, because of bunching effects and the strong centrifugal force of large numbers of accelerated protons; and (c) several difficult theoretical questions arise in connection with a *neutralized* equilibrium. Lawson[3] points out several problems in connection with Budker's original proposal and also concludes that the time constant associated with a neutralized equilibrium is of the order of seconds.

Because of the difficult experimental problems and inherently low phase-space density connected with Budker and Naumov's accumulation method for obtaining kiloampere electron currents, footnote reference 2 suggests a rather direct experimental approach that requires no great extension of present techniques; namely, to inject directly the order of 1 kamp at about 1 Mev using a deflector which can be turned off quickly after a single loop of current has filled the accelerator torus. It is this approach to which the theory presented in this paper will most particularly apply. In order to obtain the positive ions which are necessary for small beam size, the torus can be filled with neutral gas, the most natural choice being hydrogen, although this is left open in the equations.

Another modification of Budker's original proposal which is implicit in the present work is the employment of external strong-focusing. This is necessary to counteract the defocusing effect of space-charge during injection time and during the appreciable time before positive-ion focusing dominates the behavior. It will be shown later that the kind of beam under consideration can be made to contract to the order of 10^{-2} cm without using positive ion focusing, i.e., by injecting the electron beam into a perfect vacuum. Such a contraction occurs when one accelerates a strongly-focused beam which has originated from a source of low temperature, of the order of 1 ev. Thus the experimental configuration to which the theory presented here applies directly is that of a high-energy strongly-focused betatron (typically several hundred Mev) which has been fitted with a 1-kamp, single-turn injection system, and into which

[1] G. I. Budker, *Proceedings of the European Congress on Nuclear Research (CERN) Symposium* (CERN, Information Service, Geneva 15, Switzerland, 1956), p. 68.

[2] D. C. dePackh, *Proceedings of the Third International Conference on Ionization Phenomena in Gases, Venice, Italy, 1957* (Fondazione "Giorgio Cini," Venice, Italy, 1957), p. 236.

[3] J. D. Lawson, Atomic Energy Research Establishment, Harwell, England, Rept. GP/M200, 1957; see also Rept. GP/M196, 1957.

some hydrogen has been introduced in order to obtain a further contraction of the beam. However, the theory permits a wide variation in the choice of parameters.

The philosophy of the present work has been to derive the basic differential equations including as many of the processes as are felt to be important short of solving the complete Boltzmann equation for the system. The equations are then integrated for two cases of interest. Section II contains the derivation of the equations. Section III summarizes the equations as actually programmed for the computer, lists the parameters chosen for computation, and describes the solutions, including the relative importance of various terms. In Sec. IV an approximate limiting solution is obtained, from which is derived the time to reach neutrality, the maximum electron energy, and the electron energy at neutrality. The increase in the transverse action integral due to scattering of electrons on neutral atoms and the general behavior of the electron energy vs time are also derived in this section. In Sec. V, the effect of various assumptions is discussed and comparison is made with a similar recent treatment given by Capps.[4]

It cannot be overemphasized that the equations presented here can give no predictions regarding the stability of the beam. Ehrman[5] has formulated the problem from the point of view of the Boltzmann equation. Some preliminary experimental studies on the self-contraction of a 10-amp, 80-kv electron beam have been reported;[6] and further work is planned using a 250-amp, 360-kv electron gun which was kindly lent to us by the High Energy Physics Laboratory at Stanford University.

The problems connected with acceleration of high-energy protons in the field of the beam are ignored in this work.

The following notation will be used throughout:

ω = electron angular frequency of transverse oscillation

$\mathbf{r}$ = position vector of an electron

x, y, z = Cartesian coordinates of a particle; z is the direction of motion of the electron stream

t = time

$a = \langle x_-^2 \rangle_{\text{av}}^{\frac{1}{2}}$ = radius of beam

$\mathbf{1}_x, \mathbf{1}_y, \mathbf{1}_z$ = unit vectors

$\boldsymbol{\varrho} = \mathbf{1}_x x + \mathbf{1}_y y$

e, r_o, m = charge (absolute value), classical radius, and rest mass of electron, respectively

c = velocity of light

N_- = linear density of electrons

$\nu = r_o N_-$

n_o = initial density of neutral gas

n_a = density of neutral gas within the beam

n_+, n_- = density of ions and electrons, respectively, within the beam

h = fractional neutralization (n_+/n_-)

z' = stream velocity of electrons, assumed nearly equal to c since the electrons are injected at near-relativistic velocity. (The prime denotes time differentiation)

v_+ = mean velocity of ion in potential well of electron beam

γ = ratio of electron total energy to mc^2 in laboratory system

$J = \gamma\omega a^2$ = transverse action integral for electrons

L_+, L_a = Coulomb logarithms appropriate to scattering by ions and neutral atoms, respectively

σ_+, σ_- = cross section for ionization of neutral gas by energetic ions and electrons, respectively

σ_x = cross section for charge exchange, wherein a fast ion captures an electron from a neutral atom, is lost from the beam, and leaves a slow ion

λ_β = betatron wavelength of free electron due to external focusing $(\lambda_\beta = \lambda_\beta/2\pi)$

E_z = longitudinal electric field strength (for simplicity the subscript z is dropped in the final equations)

$\delta(t)$ = Dirac δ function

$\delta_{-1}(t)$ = integral of Dirac δ function, 0 for $t<0$, 1 for $t>0$. Gaussian units are used throughout, except in a few specified formulas.

II. THEORY

The equations governing the slow contraction of the beam are based on a single particle model, and as such are incapable of describing any collective process; such a description must await a better theory than exists at present. The underlying assumptions in the present treatment are that:

(1) the individual electron trajectories are paraxial;

(2) the product of the linear electron density and the classical electron radius is substantially less than unity [it can be shown that this is a corollary of assumption (1)];

(3) the external focusing system can be described in terms of a simple restoring force proportional to the displacement of the particle from the beam axis;

(4) the densities within the beam of all component particles are uniform;

(5) the beam is assumed to be traveling in a torus of radius very large compared with the cross-sectional radius;

(6) there are no currents of positive charge;

(7) bremsstrahlung and frictional energy loss of electrons scattering on protons and neutrals is small and can be subsumed into the effective accelerating electric field, which must also

[4] R. H. Capps, Phys. Rev. **114**, 1203 (1959).
[5] J. B. Ehrman, Phys. Fluids **3**, 121 (1960); and **3**, 303 (1960).
[6] D. C. dePackh, *Proceedings of the Second United Nations International Conference on the Peaceful Uses of Atomic Energy, Geneva, September 1958* (United Nations Publication 1958), Vol. 30, p. 158.

supply the increasing electrostatic and magnetic energy required by the contracting beam;

(8) the beam does not become neutralized to an extent greater than about 10%, so that the mean-random-proton energy remains of the order of the electron space-charge potential and so that the proton self-force can be neglected;

(9) the electrons are relativistic;

(10) the proton orbits are such that their transverse action integral is conserved;

(11) the external focusing acts only on the electrons.

The basic equation governing the motion of a single electron in an external force $\mathbf{F}$ will be taken as[7]

$$\mathbf{F}=(\gamma m\mathbf{r}')'-(2\gamma^2/3)(e^2/c^3)[\mathbf{r}'''+(\gamma^2\mathbf{r}'\mathbf{r}'''\cdot\mathbf{r}'/c^2)]; \quad (1)$$

according to assumption (1), terms involving transverse velocity/c are neglected.

In addition to the restoring force described in assumption (3), the external force $\mathbf{F}$ is supposed to be made up of a longitudinal part, principally due to an external applied electric field, but including small residual nonparaxial components, bremsstrahlung, etc., all included in an effective forward electric field E_z [assumption (7)], and a transverse part due to the scattering of forward momentum into transverse motion.

Suppose that the change of transverse velocity of an electron resulting from an elementary electron-ion collision is $\Delta\boldsymbol{\varrho}'$, that collisions occur at the random times t_k, and that their durations are short compared with the transverse oscillation period. Then the contribution to the transverse force on the electron resulting from scattering is

$$\gamma m\sum_k\delta(t-t_k)\Delta\boldsymbol{\varrho}_k'. \quad (2)$$

If the constant of proportionality between the external restoring force and the displacement $\boldsymbol{\varrho}$ is introduced in terms of the oscillation frequency ω, Eq. (1) then becomes

$$-\gamma m\omega^2\boldsymbol{\varrho}+\gamma m\sum_k\delta(t-t_k)\Delta\boldsymbol{\varrho}_k'+\mathbf{1}_z eE_z = (\gamma m\boldsymbol{\varrho}')'-(2e^2/3c^3)\gamma^2[\mathbf{r}'''+(\gamma^2\mathbf{r}'\mathbf{r}'''\cdot\mathbf{r}'/c^2)]. \quad (3)$$

If the external focusing field is specified in terms of the betatron wavelength λ_β for a free electron (oscillating in the external focusing field only) and if the mean forces exerted by the electron and ion distributions are calculated in accordance with assumptions (3) and (4), then ω^2 is given by

$$\omega^2=\left(\pi n_+-\frac{N_-}{\gamma^2 g^2}\right)\frac{2e^2}{m\gamma}+\frac{c^2}{\lambda_\beta^2}, \quad (4)$$

setting $z'=c$.

Evidently the change of transverse velocity $\Delta\boldsymbol{\varrho}_k'$ in a collision depends on the particular event, but the increase of mean-square transverse velocity/sec is easily obtained;[8] if this quantity is denoted by $\langle(\Delta\boldsymbol{\varrho}')^2\rangle'_{av}$, then

$$\langle(\Delta\boldsymbol{\varrho}')^2\rangle_{av}'=(8\pi r_a^2c^3L_+n_+)/\gamma^2$$

if only electron-ion scattering is considered. In general, there is neutral gas in the system as well, so that this expression is inadequate, but account can be taken of the neutrals by writing

$$\langle(\Delta\boldsymbol{\varrho}')^2\rangle_{av}'=[(8\pi r_a^2c^3)/\gamma^2](L_+n_++L_an_a), \quad (5)$$

where L_a reflects the shielding of the scattering nucleus by the orbital electrons and is therefore less than L_+.

On separating Eq. (3) into transverse and forward components, one obtains

$$\boldsymbol{\varrho}''+[\alpha+(\gamma'/\gamma)]\boldsymbol{\varrho}'+\omega^2\boldsymbol{\varrho}=\sum_k\delta(t-t_k)\Delta\boldsymbol{\varrho}_k' \quad (6)$$

and

$$(\gamma z')'=eE_z-(2e^2/3mc^5)\gamma^4z'(\rho'')^2, \quad (7)$$

in which we have put

$$\mathbf{r}'''\cdot\mathbf{r}'=\boldsymbol{\varrho}'''\cdot\boldsymbol{\varrho}'+z'''z'=\boldsymbol{\varrho}'''\cdot\boldsymbol{\varrho}'-z'(\boldsymbol{\varrho}''\cdot\boldsymbol{\varrho}'/z')'\approx-(\rho'')^2,$$

since $(\rho')^2\ll(z')^2$, and

$$\alpha=(2r_a\gamma\omega^2/3c)[1+(2\gamma^2\omega^2a^2/c^2)]$$

in accordance with assumption (1). On taking as an example the x component of Eq. (6), one has

$$x''+[\alpha+(\gamma'/\gamma)]x'+\omega^2x=\sum_k\mathbf{1}_x\cdot\Delta\boldsymbol{\varrho}_k'\delta(t-t_k) \quad (8)$$

which, on the assumption of slow variation of γ, α, and ω^2, can be solved by variation of constants,[9] giving

$$x=\sum_k\mathbf{1}_x\cdot\Delta\boldsymbol{\varrho}_k'\delta_{-1}(t-t_k) \times\frac{\exp\left[-\int_{t_k}^{t}\tfrac{1}{2}[\alpha+(\gamma'/\gamma)]d\tau\right]}{[\omega(t)\omega(t_k)]^{\frac{1}{2}}}\sin\int_{t_k}^{t}\omega d\tau. \quad (9)$$

Therefore the mean square departure of the electron from the axis, here taken as the effective beam radius squared, is

$$a^2=\sum_k\tfrac{1}{4}(\Delta\boldsymbol{\varrho}')^2\delta_{-1}(t-t_k)\frac{\exp\left[-\int_{t_k}^{t}[\alpha+(\gamma'/\gamma)]d\tau\right]}{\omega(t)\omega(t_k)} \to\int_{-\infty}^{t}\tfrac{1}{4}\langle(\Delta\boldsymbol{\varrho}')^2\rangle'_{av} \times\exp\left[-\int_{t_k}^{t}[\alpha+(\gamma'/\gamma)]d\tau\right]\frac{dt_k}{\omega(t)\omega(t_k)} \quad (10)$$

on passage to the definite integral limit. It is now convenient to use the transverse action integral $J=\gamma\omega a^2$;

[7] A. O'Rahilly, *Electromagnetics* (Longman's Green and Company, Ltd., London, 1938), p. 251.

[8] L. Spitzer, *Physics of Fully Ionized Gases* (Interscience Publishers, Inc., New York, 1956), Chap. 5.

[9] E. Madelung, *Mathematische Hilfsmittel des Physikers* (Dover Publications, New York, 1943), p. 182.

by differentiation of Eq. (10) with respect to t, the secular variation of this quantity is found to be given by

$$J'+\alpha J=[(2\pi r_e^2c^3)/\gamma\omega](L_+n_++L_an_a) \quad (11)$$

on applying Eq. (5).

The forward equation is obtained from Eq. (7) on taking $z'\approx c$ in the second term, and putting $\langle(\rho'')^2\rangle_{av}=2\omega^4a^2$; one then has

$$(\gamma z')'=(eE_z/m)-\tfrac{1}{2}[(r_e\gamma^4\omega^4a^2)/c^2]. \quad (12)$$

Equations (4), (11), and (12) do not form a closed set because n_+ has not been determined. In order to get an idea of the behavior of this quantity, suppose that only the ions whose orbits are confined within the electron beam are effective in focusing the latter. If the linear ion density (consisting of ions both inside and outside the electron beam) is constant, then $n_+\propto 1/\langle x_+^2\rangle_{av}$, where $\langle x_+^2\rangle_{av}$ is the mean square amplitude of a typical ion orbit; this will refer explicitly to an ion whose orbit remains confined within the electron beam. We have assumed [assumption (10)] that the transverse action integral for such an ion is conserved, so that $\langle x_+^2\rangle_{av}\propto 1/\omega_+$, ω_+ being the ion oscillation frequency. By analogy with Eq. (4), using assumptions (8) and (11), one has $\omega_+^2\propto N_-/a^2$, whence $a^2n_+^2=$constant. Thus one has the result that many of the ions are left behind in the contraction and that the ion density is inverse with the *radius* rather than with the area of the electron beam. According to this conclusion, one has

$$dn_+=-n_+(da/a)+[\sigma_+n_+v_++\sigma_-(cN_-/\pi a^2)]n_adt, \quad (13)$$

in which the first term represents the concentration of ions in the electron beam due to contraction and the last two represent the creation of fresh ions from available neutrals by ions and electrons, respectively. This leaves the variable n_a, the neutral density within the beam, to be determined; the equation governing this will be taken to be

$$dn_a=-\left(\sigma_+n_+v_++\sigma_-\frac{cN_-}{\pi a^2}\right)n_adt -\sigma_zn_+v_+n_adt+(n_o-n_a)\frac{2v_sdt}{a}. \quad (14)$$

The first term represents the loss of neutrals by ionization, the second the loss by charge exchange, and the last represents the diffusion of neutral gas into the beam. Here n_o is the external neutral density, assumed constant, and v_s is the thermal velocity of the external gas.

It will be found in the numerical solutions developed below that the transverse action integral J does not vary greatly over an operating cycle, and this fact furnishes an idea of the general behavior of the system. Suppose that at a time late in the cycle, the ion focusing is the dominant mechanism. Then in accordance with Eq. (4),

$$\omega^2=(2\pi e^2n_+)/(m\gamma)=(2e^2N_-h)/(a^2m\gamma).$$

The fractional neutralization h has been assumed held to an upper limit [assumption (8)]. Therefore the particle density at such a time is proportional to

$$N_-/a^2=(N_-\gamma\omega)/J=(2e^2\gamma N_-^2h)/(mJ^2).$$

J^{-2} is proportional to the phase space density of the entering beam; by equating the mean-oscillatory-transverse energy in one direction to the thermal energy $\frac{1}{2}kT_o$ of the injected beam on the assumption of two-dimensional adiabatic compression, one has $J=(2kT_oa_o^2/m)^{\frac{1}{2}}$. This quantity depends only on the source, and it is clear that any source not operating close to the space-charge limit will be inefficient for this application. If J is initially large, it must be reduced by radiation if the current density is to become large, and this is likely to take a relatively long time.[4]

III. COMPUTER SOLUTIONS

Rearrangement of the equations, a necessity for numerical or computer integration, is summarized below. The action integral J is used whenever possible, and the frequency ω is eliminated. The combination n_+a is used instead of n_+ in order to reduce the range of the variables.

The summarized equations are as follows:

$$\frac{1}{a}=\frac{a\gamma^3}{\nu\lambda_\beta^2}-\frac{\pi r_en_+a\gamma^2}{\nu}-\frac{\gamma J^2}{2\nu c^2a^2}; \quad (15)$$

$$\frac{d(J^2)}{dt}=4\pi r_e^2c^3(L_+n_++L_an_a)a^2-\frac{8r_eJ^6}{3c^3\gamma a^6}; \quad (16)$$

$$\frac{d\gamma}{dt}=\frac{eE}{mc}-\frac{4r_eJ^4}{3c^3a^6}; \quad (17)$$

$$\frac{d(n_+a)}{dt}=\sigma_+v_+n_an_+a+\frac{\sigma_-cvn_a}{\pi r_ea}; \quad (18)$$

and

$$\frac{dn_a}{dt}=\frac{1}{a}\left[2v_sn_o-(\sigma_zv_+n_+a+2v_s)n_a-\frac{d}{dt}(n_+a)\right]. \quad (19)$$

Equation (15) follows from (4) after elimination of ω and is used to obtain the radius for given values of γ, J, and n_+a. Equation (16) is obtained from (11) by using the approximation

$$\alpha=(4r_eJ^4)/(3c^3\gamma a^6),$$

which is a good approximation if $(J/ca)^2\gg\frac{1}{2}$. In general, radiation becomes important when $a\lesssim 2\times10^{-3}$ cm, in which case $(J/ca)^2\gtrsim 10$ for $J=2\times10^8$. In this connection it is interesting to note the inverse sixth-power dependence of the radiation terms in (16) and (17) on the radius.

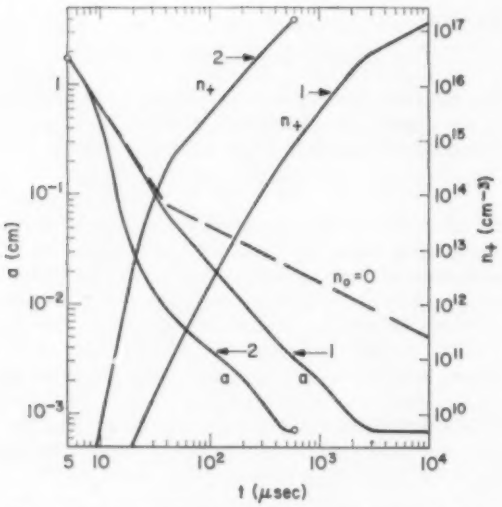

FIG. 1. Two computer solutions of the equations governing the collapse in radius of a 1100-amp, 0.77-Mev electron beam injected into hydrogen at pressures of 10^{-6} mm Hg (solution 1) and 2×10^{-5} mm Hg (solution 2). The electrons are assumed to have a free betatron wavelength of 120 cm and an initial transverse energy of 3.8 ev. The dashed lines represent injection of the same beam into a vacuum.

Equations (17)–(19) are straightforward results of (12)–(14), respectively, assuming $z'=c$ in (12).

The parameters chosen for computation are as follows:

(a) $\nu=0.0638$, corresponding to an electron-gun current of 1100 amp.

(b) γ_o at injection $=2.50$, corresponding to an injection voltage of 0.77 Mev. Combined with the current above, it gives a gun perveance of 1.6×10^{-6} amp/v$^{\frac{3}{2}}$.

(c) Betatron field strength $E=8.53$ v/cm. Note that the injection time of 5.0 μsec is used so as to eliminate an arbitrary constant in the integral of Eq. (17).

(d) Initial $J_o=2.0\times10^8$, corresponding to an initial transverse energy of 3.8 ev. According to discussions with several designers[10] of electron guns, careful design of a Pierce-type converging gun can yield transverse temperatures in the vicinity of 1–3 ev and perveance up to 2 or 3×10^{-6} amp/v$^{\frac{3}{2}}$.

(e) External strong focusing sufficient to give a betatron wavelength for a free electron of $\lambda_\beta=120$ cm. The radius of the beam under the injection conditions given above is calculated to be $a_o=1.73$ cm in the space-charge limited condition.

(f) The two values of initial atomic hydrogen density are $n_o=7.6\times10^{10}$ cm^{-3} (solution 1) and 1.47×10^{12} cm^{-3} (solution 2). These figures correspond to hydrogen pressures of about 10^{-6} and 2×10^{-5} mm Hg, respectively. Impurities are assumed to be small compared with the values above.

[10] G. Merdinian, Dr. Oscar Heil, and G. Badger, of the Eitel-McCullough Company, San Carlos, California.

A summary of the values of cross sections and other parameters is as follows:

$\sigma_-=1.0\times10^{-19}$ cm^2; $\sigma_+=\sigma_x=3.6\times10^{-16}$ cm^2;

$v_+=4.4\times10^8$ cm/sec; $v_o=1.3\times10^5$ cm/sec;

$L_+=28$; $L_\infty=10$.[11]

The computer solutions are shown in Fig. 1. They were obtained by using a Litton-40 digital differential analyzer.[12] A brief description of the computer and the programming has been given.[13] The large range of the variables required that the solutions be done in steps, with suitable rescaling and fitting of boundary conditions at the end of each step. In general, each step was a factor of two in the radius, making a total of ten steps for each solution. The integration interval in the time varied from 10^{-10} to 10^{-5} sec. The interval in radius varied from 10^{-3} cm to 10^{-5} cm. The total computer time was of the order of 30 hr.

A brief description of the computer solutions follows. With $n_+=0$ throughout, the radius decreases initially according to

$$a^2=2\nu\lambda_\beta^2(mc/eE)^2t^{-3}, \tag{20}$$

which goes over smoothly into the form

$$a^2=(mJ\lambda_\beta)/eE)t^{-1} \tag{21}$$

at a later time. The latter equation corresponds to the familiar betatron damping. The general form of (20) and (21) has been derived by Ehrman[5] using the Boltzmann-equation approach. In Fig. 1 this behavior is shown as two dashed lines. For our parameters, $a=0.16$ mm at 1 msec, and the energy of such a betatron would be 250 Mev.

Solution 1, with 10^{-6} mm hydrogen pressure, follows the t^{-1} law closely because of the low ion density. However, at the point where the pure-electron-beam radius would begin to obey the t^{-1} law, the proton density has built up sufficiently so that the proton focusing begins to dominate the behavior. For solution 2, the proton force dominates the focusing after 5–10 μsec have elapsed.

Ionization by the trapped energetic protons turns out to be comparable in importance to ionization by electrons throughout most of the collapse. Note that if one sets $n_a=n_o$ and neglects the second term in (18), then n_+a increases exponentially with the time. However, this accelerated production rate is slowed down because of the loss of neutrals via charge exchange and the finite diffusion rate of neutral atoms into the beam.

The relative neutral density thus decreases markedly in the central portion of these curves. The computer

[11] The authors are indebted to Dr. J. B. Ehrman for determining the cross sections involved in these processes.

[12] Litton Industries, 336 North Foothill Road, Beverly Hills, California.

[13] T. F. Godlove, NRL Quart. on Nuclear Science and Technol., January, 1958 (limited circulation report; reprints are available from author).

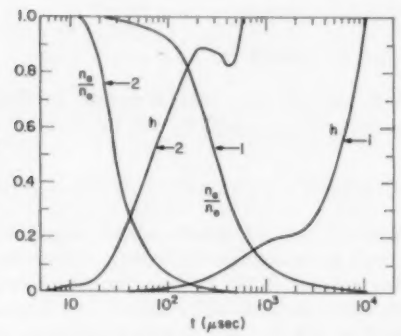

FIG. 2. Variation with time of (1) the fractional neutralization $h=n_+/n_-$ and (2) the ratio of hydrogen density in the beam n_a to the initial hydrogen density n_o for the two solutions discussed in the text. The solutions are terminated at $h=1$.

solutions for n_a/n_o and also the fractional neutralization h are shown in Fig. 2. For both solutions, $n_a/n_o=0.5$ when $n_+\approx 10^{14}$. At the end of the curves, $n_a/n_o \ll 1$.

The latter result is substantiated when one calculates that at $a=2\times10^{-3}$ cm, the lifetime of a neutral in such a beam is $\sim 10^{-9}$ sec, whereas the diffusion transit time across the beam is $\sim 2\times10^{-8}$ sec. In Sec. IV an approximate solution to Eqs. (18) and (19) is given which is also consistent with the above result.

Because of the low neutral density within the beam, the ion production rate decreases and n_+a becomes linear with the time as the beam approaches equilibrium. Again, this result is verified in Sec. IV. The rather odd behavior of the relative neutralization h for solution 2 of Fig. 2 between 200 and 400 μsec can be explained qualitatively as follows. In the region just before 200 μsec, the ion production rate has decreased to the linear rate mentioned above. In the region after 150 to 200 μsec, the radiation terms rather suddenly become important. This has the effect of reducing the action integral J, and hence the radius, rather sharply. Thus between 200 and 400 μsec the electron density increases faster than the proton density. Then, just after 400 μsec, the radius becomes constant at the Budker equilibrium value. Since n_+ is still increasing, h then increases until neutrality is reached. The same behavior is reflected in solution 1 in the region 1–3 msec, but to a lesser degree.

The action integral J remains nearly constant in each solution for $a>4\times10^{-3}$ cm. Below this point, scattering of electrons on protons becomes important. Then below $\sim 2\times10^{-3}$ cm, radiation predominates, as discussed previously. The final value of J is 4.5×10^7 cm²/sec, or 22% of the initial value.

The electron energy γ increases linearly until radiation becomes important, at about $a=2\times10^{-3}$ cm. Then γ reaches a maximum, starts decreasing, and continues to do so even after the Budker radius is reached until neutralization occurs. This behavior is discussed in Sec. IV, where an approximate general solution is given.

It may be noted that the solutions are continued until neutrality, violating assumption (8) of Sec. II. However, this is not believed to be a serious limitation. Its effect is discussed in Sec. V.

IV. APPROXIMATE LIMITING SOLUTION

If one assumes that the neutral density is in an equilibrium situation in which n_a varies slowly compared with the characteristic ionization and diffusion times, then one can set $dn_a/dt=0$ in (19) and solve for n_a. This procedure gives

$$\frac{n_a}{n_o}=\left[1+\frac{(\sigma_++\sigma_z)v_+}{2v_en_+a}+\frac{\sigma_-cv}{2\pi r_e v_e a}\right]^{-1}. \tag{22}$$

This equation can also be derived by starting from the form

$$\frac{n_a}{n_o}=\left[1+\frac{\text{mean transit time}}{\text{mean lifetime}}\right]^{-1}.$$

Equation (22) is certainly valid for $n_a\approx n_o$ and for $n_a\ll n_o$, and is probably valid throughout, although this has not been proved. The curves of Fig. 2, obtained by computer integration, agree with the predictions of (22). If one now substitutes (22) into (18), one obtains for the proton density

$$\frac{d(n_+a)}{dt}=\frac{2v_en_e\sigma_+}{\sigma_++\sigma_z}\left[n_+a^2+\frac{\sigma_-cv}{\pi r_e\sigma_+v_+}\right]\times\left[n_+a^2+\frac{\sigma_-cv}{\pi r_e v_+(\sigma_++\sigma_z)}+\frac{2v_ea}{v_+(\sigma_++\sigma_z)}\right]^{-1},$$

which for $n_+a^2\gg10^9$, $a\lesssim10^{-3}$, and $\sigma_+=\sigma_z$, becomes simply

$$(d/dt)(n_+a)\approx v_en_o.$$

Even at $a=2\times10^{-3}$, this rate differs from the computer-indicated rate by only 6% and 1% for solutions 1 and 2, respectively. Upon integrating, one obtains

$$n_+a=v_en_o(t-t_1) \quad \text{for } t>t_m, \tag{23}$$

where the integration constant t_1 can ideally only be found from a computer solution by integrating (18) up to the time t_m at which (23) becomes valid. However, it turns out that t_1 is generally substantially less than t_m; hence, the approximate formulas given subsequently are useful for a rough idea of the behavior when computer solutions are not available. The value of t_m is somewhat arbitrary and will be estimated below.

We now evaluate (4) for the case in which the frequency ω is so large (because of positive ion focusing) that the last two terms (representing electron repulsion and external focusing) are negligible. One obtains

$$a^2=J^2/(2\pi r_e^2\gamma n_+a). \tag{24}$$

This equation can now be substituted in (16) and (17) to obtain (25) and (26). This is a valid procedure,

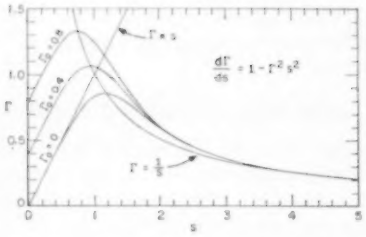

FIG. 3. Three solutions to Eq. (27) in the text. These curves give the normalized electron energy Γ as a function of the normalized time s for a wide range of initial parameters. The equation becomes separable when n_+a = constant, which in general is valid near and beyond $s=1$. The curves are applicable when the inequality $t_N > t_m$, or $\nu E^{\frac{1}{2}} n_o^{-1} > 1.3\times10^{-9}$ is satisfied. Γ_o is defined in the text.

because the radiation terms in (16) and (17) are important only in the region where (24) is a good approximation. Thus

$$d(J^2)/dt = 4\pi c r_o^2[(c^2 L_+ a) - (8/3)\pi r_o(\gamma n_+ a)J^2]n_+ a, \quad (25)$$

and

$$d\gamma/dt = (eE/mc) - (16/3)\pi^2 r_o^3 c(\gamma n_+ a)^2. \quad (26)$$

The term $L_o n_o$ has been dropped in (16), since $L_o n_o \ll L_+ n_+$ in the region we are considering.

By putting (23) into (26), Eq. (26) can be separated, giving an equation in γ and t only of the form

$$d\Gamma/ds = 1 - \Gamma^2 s^2, \quad (27)$$

where

$$\Gamma \equiv (mc/eE)K\gamma, \quad (28)$$

and

$$s \equiv K(t - t_1). \quad (29)$$

In the latter two definitions, K is defined as follows:

$$K^4 \equiv (16/3)\pi^2 (eE/m) r_o^3 v_o^2 n_o^2.$$

Three computer solutions[14] of (27) are shown in Fig. 3, taken directly from the output plotter of the Litton digital differential analyzer. Solutions are given for $\Gamma_o = 0$, 0.40, and 0.80. Γ_o is related to t_1 by $\Gamma_o = Kt_1$. For solutions 1 and 2 of Sec. III, $\Gamma_o = 0.40$ and 0.20, respectively, corresponding to $t_1 = 0.35$ and 0.04 msec. Although the curves of Fig. 3 give the correct qualitative behavior for the initial linear increase of γ, they are primarily meant to convey the behavior near and beyond the peak, where radiation becomes important and (23) becomes valid.

By setting $t_1 = 0$ and $s = 1$ in (29), we can obtain the time (within 20%) at which maximum γ occurs. This is the same time at which the radiation terms become important and also the approximate time at which (23) becomes valid; hence the symbol t_m will be used.

$$t_m \approx K^{-1} \approx 411 E^{-\frac{1}{2}} n_o^{-\frac{1}{4}} \text{ sec} \quad (E \text{ in v/cm}).$$

Similarly the maximum value of γ, designated γ_m, can be obtained within ~20% by setting $\Gamma = 1$ in (28), giving

$$\gamma_m \approx (eE/mc)K^{-1} \approx 2.4\times10^7 E^{\frac{1}{2}} n_o^{-\frac{1}{4}}, \quad (E \text{ in v/cm}).$$

For solutions 1 and 2, $\gamma_m = 440$ and 100, respectively.

To complete the solution at time t_m, the radius may be calculated from (24) by inserting γ_m above and $(n_+ a)$ as obtained from (23), with $t_1 = 0$. The initial value of J should be used in this connection, unless scattering on neutrals increases J significantly. If this does occur, the increase may be computed as derived in a subsequent paragraph. The radius as calculated in the above manner is 1.9×10^{-3} cm for solutions 1 and 2, in agreement with the curves of Fig. 1.

The equilibrium proposed by Budker is reached when $d(J^2)/dt$ in (25) and $d\gamma/dt$ in (26) become small. By setting them equal to zero, solving for J^2 and γ^2, then solving the resulting two equations simultaneously with (24), one obtains

$$a_B^2 = (mc^2 r_o L_+)/eE, \quad J_B^2 = (\sqrt{3}/2) r_o L_+^{\frac{1}{2}} (mc^4/eE),$$

and

$$(\gamma n_+)_B = (\sqrt{3}/4\pi)[eE/(mc^2 r_o^2 L_+^{\frac{1}{2}})],$$

which for $E = 8.53$ v/cm give

$$a_B = 6.9\times10^{-4} \text{ cm}, \quad J_B = 4.46\times10^7 \text{ cm}^2/\text{sec},$$

and $(\gamma n_+)_B = 5.4\times10^{18}$ cm^{-3}. Note that the field strength is the only adjustable parameter in the above equations.

For the parameters considered here, neutrality is attained after equilibrium. Using $n_- = \nu/(\pi r_o a_B^2)$, setting $n_+ = n_-$, and using (23), one obtains for the time t_N to reach neutrality,

$$t_N = \nu/(v_o n_o \pi r_o a_B) + t_1,$$

where, in general, the contribution from t_1 will be small. For solutions 1 and 2, $t_N = 11$ and 0.6 msec, respectively, with t_1 contributing $<7\%$. Similarly, γ at neutrality is

$$\gamma_N = (3L_+)^{\frac{1}{2}}/(4\nu),$$

which for both solutions is 36.

Scattering of electrons by neutrals turns out to be a small effect in these solutions. The computer results indicate that in solution 1 it is negligible, and in solution 2, J is increased by 1.6%. The increase takes place in the first part of the collapse, where $L_o n_o \gg L_+ n_+$ and the radiation term is negligible. Using these two assumptions and the additional assumptions that $n_o = n_o$ and that the radius varies according to (20), an upper limit to the increase in J may be calculated. It is an upper limit because the radius may decrease faster than (20) indicates and because n_o may be less than n_o. Carrying out

[14] An analytic solution of (27) exists in terms of Bessel functions; for $\Gamma_o = 0$ this gives

$$\Gamma = -\frac{i\, J_{1/4}(\frac{1}{2}is^2)}{s\, J_{-3/4}(\frac{1}{2}is^2)}.$$

the integration gives

$$\Delta(J^2) \leqslant 4\pi r_e^2 c^3 L_a n_o \int_{\gamma_o}^{\gamma} a^2 dt = 4\pi r_e^2 c^3 \nu \lambda_\beta^2 L_a n_o (mc/eE\gamma_o^2),$$

using $\gamma_o^2 \ll \gamma^2$. This formula gives an increase of 1.5% in J for solution 2, in good agreement with the computer result. Thus for many combinations of initial parameters, J may be assumed to be constant in order to obtain the qualitative behavior. In another computer solution not discussed here, $\Delta J/J$ turned out to be 40% for $n_o = 8\times10^{12}$ cm^{-3} and $J_o = 2.4\times10^8$, whereas the computer gave an increase of 58%.

It has been shown in this section that a limiting solution (for $t > t_m$) of the equations of Sec. II can be established in many cases of interest without recourse to numerical integration. Since the initial rate of collapse can be obtained from (20), the complete solution can be roughly ascertained by interpolation. The only unknown in this procedure is the integration constant t_1 in Eq. (23). The criterion for the validity of this procedure is that $t_N > t_m$, which can be written $\nu E^4 n_o^{-4} > 1.3\times10^{-9}$.

V. DISCUSSION

Both the electron and the proton densities are assumed to be uniform in this analysis. Alternative assumptions would affect the rate of collapse and the final equilibrium values somewhat. However, such assumptions would make the analysis a good deal more complicated, especially when one considers that the distributions would be time-dependent, and self-consistent methods would have to be employed. At injection, a "rectangular" distribution for the electron density is a good approximation.[5] Near neutrality, a "bell-shaped" distribution would be better. Also near the end, where $n_a \ll n_o$, protons are preferentially formed at the edge of the beam, and more may be lost as the beam collapses than is indicated in Eq. (13). The latter effect would tend to slow down the collapse near equilibrium and increase t_N. Furthermore, as neutrality is approached, the average kinetic energy of the protons diminishes, resulting in larger oscillation amplitudes and further loss of protons. Again this tends to increase t_N.

The cross sections σ_x and σ_+ may be expected to be reduced somewhat for the lower proton energy near equilibrium. However, the parameter which determines the proton production rate in this region is $\sigma_+/(\sigma_+ + \sigma_x)$, as can be seen in the derivation of Eq. (23). This ratio evidently does not change by more than about 20–30%, even for reduction in proton energy by a factor of ten.

At exact neutrality the beam loses its ability to cast off cold electrons formed in the ionization process. The beam may then collect cold electrons (trapped by the large magnetic fields) and protons (to maintain neutrality), resulting in an increase in scattering with no net increase in restoring force, as pointed out previously.[6] For this reason, J (and a) will probably increase slowly after neutrality.

In view of some uncertainty in the approach to neutrality and a greater uncertainty in what happens after neutrality, it is not deemed worthwhile to carry the present solutions further at this time. This is especially true when one considers the unresolved problems of resonances and instability, which this analysis ignores.

Capps[4] has made a study of relativistic electron beams injected into hydrogen gas. Four cases were chosen by him for computation, in which combinations of the following parameters were used: injection current and energy, 150 to 15 000 amp at 2 or 8 Mev; initial radius, 0.5 to 2 cm; $\lambda_\beta = 100$ cm; $E = 1$, 4, and 10 v/cm; and $n_o = 10^{12}$ or 10^{13} cm^{-3}. His values for L_+ and L_a are 25 and 11, respectively.

Capps also uses the adiabatic invariant J (Z in his notation) which is changed only by radiation and scattering processes. His value for the equilibrium radius a_B is somewhat larger than ours.

One major point of difference between the two treatments is that Capps assumes that the initial transverse temperature is rather large and of such a value that the beam at injection is temperature limited rather than space-charge limited as in our case. Such a beam collapses in a perfect vacuum as $t^{-\frac{1}{2}}$ given by (21) and not initially as $t^{-\frac{1}{4}}$ given by (20). One can use (21) and show that Capps' initial values of J range from 30 to 200 times our value of $J = 2\times10^8$ cm^2/sec. As mentioned in Sec. III, electron guns of large current can be designed which have transverse temperatures of a few electron volts or less. Experimentally, we favor a single-turn injection method,[15] wherein it is easier in principle to keep the field inhomogeneities and initial oscillations to a minimum. It is felt that the combination of a well-designed gun and single-turn injection system can yield an initial J close to our assumed value. In this connection, a review of phase-space concepts as applied to accelerator problems has been given by Judd.[16]

Because of the large J_o, Capps requires a relatively long "radiation" stage of operation, during which time the beam is supposed to be neutral, in order to reduce J and obtain small beam radii. One serious objection to this type of operation is the apparent accumulation of cold electrons (and protons) after neutrality, as mentioned before. Scattering of these electrons out of the beam may help in this regard.

Only secondary consideration has been given here to

[15] D. dePackh, H. R. Roess, and T. Godlove, NRL Quart. on Nuclear Science and Technol., July, 1956; and T. F. Godlove, H. F. Kaiser, D. C. dePackh, H. R. Roess, and W. Mayes, NRL Quart. on Nuclear Science and Technol., October, 1958 (limited circulation reports; reprints are available from authors).

[16] D. L. Judd, *Annual Review of Nuclear Science* (Annual Reviews, Inc., Palo Alto, California, 1958), Vol. 8, p. 192.

a neutralized type of operation, not only for the reasons given above but also because of the tremendous amount of power which would have to be provided to maintain E constant for many milliseconds. If protons are to be accelerated in the magnetic field of the beam, then the question arises: Why not accelerate the protons during the collapse, making sure that the beam is small enough at each point to hold them at that point? Although there is an assumption in the derivation of the equations that only a small fraction of the total number of protons in the beam would be accelerated, this type of operation would be preferable anyway for the reasons mentioned in the introduction. On the other hand, the study of intense relativistic electron beams is considered to be self-justifying and a detailed discussion of the possible applications of such beams is somewhat premature at the present time.

ACKNOWLEDGMENTS

Acknowledgment is gratefully given to beneficial discussions with Dr. J. B. Ehrman during the course of this analysis. In addition, the continuing support of Dr. M. M. Shapiro of the Nucleonics Division has been encouraging.

JOURNAL OF APPLIED PHYSICS VOLUME 31, NUMBER 11 NOVEMBER, 1960

Hole Mobility and Crystal Size in Lead Sulfide Photoconductive Films*

H. E. SPENCER† AND J. V. MORGAN‡
Apparatus and Optical Division, Eastman Kodak Company, Rochester, New York

(Received June 15, 1960)

A correlation has been found between the size of the microcrystals in photoconductive lead sulfide films and hole mobility calculated from Hall, signal, and noise measurements. Films composed of larger microcrystals exhibit larger mobilities. Field-effect mobility as a function of frequency has also been measured. The data indicate that the surfaces as well as the bulk of the films are p type. The lead sulfide-air interface of the films changes from exhaustion type to enhancement type as the film thickness increases.

INTRODUCTION

THE microcrystalline structure of photoconductive films of lead sulfide has a profound influence on the electrical properties of the films. Previous studies of such films made in this laboratory have been reported by Eastman Kodak Company[1–4] and by the Naval Ordnance Laboratory at White Oak, Maryland.[5–9] References to other studies of microcrystalline films are given in the footnotes cited, particularly in footnote reference 6. Extensive work has been done on films, even though their structure and their properties are complex, both for scientific reasons and because of their technological importance.

Briefly reported here are (1) a correlation between crystal size and mobility calculated from Hall, noise, and signal measurements, and (2) field-effect mobility studies. Both of these studies aid in the interpretation of the properties of photoconductive films produced in this laboratory.

It is appropriate to comment here that much of the conflicting data on microcrystalline films obtained by different investigators over the years were due, in part at least, to real differences in the films studied. Photoconductive deposits of lead sulfide are produced and sensitized in different ways by different laboratories and manufacturers. Since the electrical properties of the films depend so critically on the techniques of

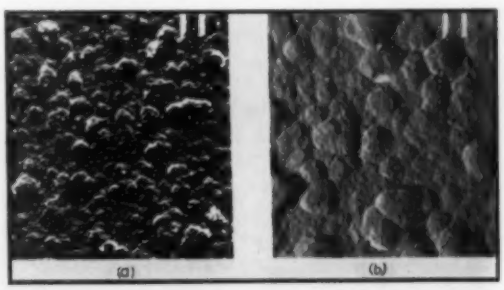

FIG. 1. Electron photomicrographs of the lead-sulfide-air interface of two films. Film 1(a) is 0.33 μ thick; film 1(b) is 0.88 μ thick. The distance between centers of the two lines at the top of each photomicrograph is 1 μ.

* This work was supported by a contract with the U. S. Navy Bureau of Ordnance.

† Present address, Research Laboratories, Eastman Kodak Company, Rochester, New York.

‡ Present address, Hughes Products, Semiconductor Division, Newport Beach, California.

[1] H. E. Spencer, Phys. Rev. **109**, 1074 (1958).
[2] H. E. Spencer, J. Appl. Phys. **30**, 927 (1959).
[3] H. E. Spencer, Phys. Rev. **113**, 1417 (1959).
[4] H. E. Spencer, Bull. Am. Phys. Soc. Ser. II, **3**, 410 (1958); J. Appl. Phys. **31**, 505 (1960).
[5] F. L. Lummis and R. L. Petritz, Phys. Rev. **105**, 502 (1957).
[6] R. L. Petritz, Phys. Rev. **104**, 1508 (1956).
[7] J. F. Woods, Phys. Rev. **106**, 235 (1957).
[8] R. L. Petritz, F. L. Lummis, H. E. Sorrows, and J. F. Woods in *Semiconductor Surface Physics*, edited by R. H. Kingston (University of Pennsylvania Press, Philadelphia, Pennsylvania, 1957), p. 229.
[9] H. E. Sorrows, Bull. Am. Phys. Soc., Ser. II, **3**, 131 (1957).

production, the results reported here do not necessarily apply to other films. It is expected, however, that at least some of the results are applicable to other films. In any case, the large number of studies of Eastman Kodak films make it worthwhile to continue to clarify the properties of these particular photoconductive films.

CRYSTAL SIZE

Figure 1 shows electron photomicrographs of the lead sulfide-air interfaces of two films, one 0.33 and one 0.88 μ thick. The technique of calculating thickness from optical interference effects has been described in footnote 3. All films were chemically deposited on glass or quartz substrates. It can be seen in Fig. 1 that the thicker film has the larger microcrystals. In fact, the edge dimensions of the larger microcrystals are approximately equal to the thickness of the films. Other films of thicknesses ranging between those of the two films illustrated in Fig. 1 show the same correlation between crystal dimensions and film thickness. Electron photomicrographs of the other interface of a film stripped from the substrate, i.e., the former lead sulfide-glass interface, show little or no crystalline structure.[10] The mechanism of crystal growth from solution appears to determine the difference between the two interfaces; this mechanism is not understood.

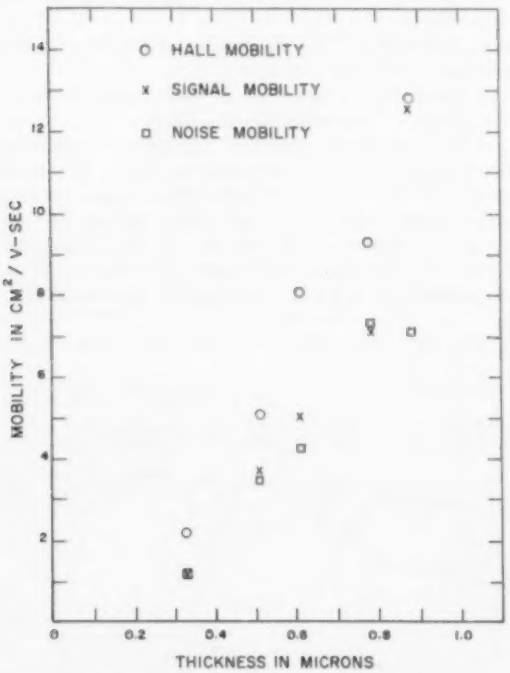

FIG. 2. Hole mobility as a function of film thickness.

[10] R. G. Devaney, Tennessee Eastman Company (private communication).

TABLE I. Hall, noise, and signal mobility equations.

	Equation	Reference
Hall mobility	$\mu_H = R_H \sigma$	11
Noise mobility	$\mu_n = 4L^2\Delta V_n^2 A / R\tau e \Delta f / E^2$	6
Signal mobility	$\mu_s = 4L^2\Delta V_s / R\tau e F E$	2

R_H = Hall constant, σ = conductivity, L = interelectrode spacing, n = noise voltage, s = signal voltage, A = area of film, R = resistance of film, τ = photoconductive time constant, e = electronic charge, f = bandwidth of amplifier, E = dc bias voltage across film and matching ballast resistor, F = rate of optical generation of hole-electron pairs.

MOBILITY

Plotted in Fig. 2 are values of mobility calculated from Hall, noise, and signal measurements for a series of films of increasing thicknesses. The equations used to calculate the mobilities are given in Table I. There is approximate agreement among the three mobility values for each film, although three completely different phenomena are used to obtain mobilities. The Hall measurements indicate that the majority carriers are holes.

The data in Fig. 2 show that the mobility is approximately proportional to the film thickness. The electron photomicrographs of Fig. 1 show that the crystal dimensions are about equal to the film thickness. Thus the hole mobility is approximately proportional to the crystal size. Petritz[6] has analyzed the effects of the intercrystalline barriers on mobility and concluded that the Hall mobility should vary inversely with the number per centimeter of such intercrystalline barriers. This conclusion is entirely consistent with the results reported here, viz., hole mobility is approximately proportional to the crystal size.

Table II lists the hole concentrations for the films of various thicknesses. The hole concentration was calculated from Hall measurements and was assumed equal to the conductivity divided by the product of the Hall mobility and the electronic charge. It has been shown[2] that the hole concentration (but usually not the hole mobility) changes with variations in ambient conditions such as relative humidity. Thus the hole concentrations listed in Table II represent the values at the time of the Hall measurements.

FIELD-EFFECT MOBILITY

The mobility of carriers near the surface of a semiconductor can be determined by inducing excess carriers in the semiconductor with an electric field

TABLE II. Hall mobility, hole concentration, and film thickness.

Film thickness in μ	Hall mobility $cm^2v^{-1}sec^{-1}$	Hole concentration 10^{-16} cm^3
0.33	2.2	3.8
0.51	5.1	1.8
0.61	8.1	1.3
0.78	9.3	1.8
0.88	12.8	2.1

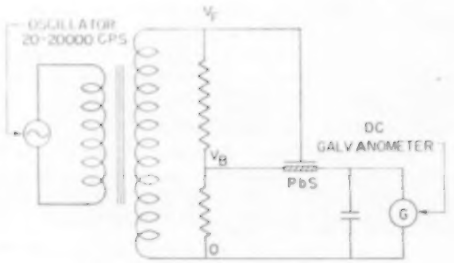

FIG. 3. Alternating current field-effect circuit.

normal to the surface and measuring the resulting increase in conductance parallel to the surface. Since the excess carriers are constrained by the field to move near the surface, their mobility can be strongly influenced by a number of surface effects, i.e., scattering, trapping, and recombination.

Surface effects can exert a major influence on the photoconductive properties of thin films. For this reason, data on the electrical properties of film surfaces for different methods of deposition and for different film thicknesses are particularly helpful in the interpretation of the photoconductive properties of the films. It is not possible at present to interpret the field-effect mobility of microcrystalline films in as complete detail as has been done for single crystals of germanium,[12,13] primarily because the influence of the complex film structure on field-effect mobility is not yet understood. In particular, the possible effects of minority-carrier trapping[14] on field-effect mobility and on photoconductivity are not yet clear. Nevertheless, the field-effect measurements reported here, together with a tentative interpretation based on the work of Montgomery[12] and Garrett[13] do suggest several possible conclusions of interest.

The circuit, first used by Aigrain *et al.*[15] is shown in Fig. 3. An ac field potential of 120 to 160 v rms was supplied by an audio oscillator coupled to the field electrode through a stepup transformer. The equation used for calculating field-effect mobility from the measured quantities is

$$\mu_{FE}=1.1\times10^{13}dLi/KWV_BV_F,$$

where

$\mu_{FE}=$ field-effect mobility in $cm^2v^{-1}sec^{-1}$
$d=$ distance between field electrode and surface to be studied in cm
$L=$ interelectrode spacing in cm
$i=$ dc current through the galvanometer in amperes
$K=$ dielectric constant of material separating field electrode from the lead sulfide surface; Mylar film was used for the air-PbS interface and the quartz substrate for the quartz-PbS interface
$W=$ film width in cm
$V_B=$ bias potential in v rms
$V_F=$ field potential in v rms.

It is assumed that the phase difference between V_F and V_B and between the electric field and the induced conductance are negligible.

Figure 4 shows typical field-effect mobility vs frequency curves given by Montgomery[12] and Garrett[13] for single crystals of germanium. Curves A, B, and C relate to *p*-type bulk with increasing negative surface potential as follows: A, *n*-type inversion layer; B, *p*-type exhaustion layer; and C, *p*-type enhancement layer. Three similar curves for an *n*-type bulk and increasing positive surface potential could be drawn, but only the first, a *p*-type inversion layer shown by curve D, suffices to illustrate the general behavior.

Figure 5 shows the experimental curves for field-effect mobility measured at the air-lead sulfide and quartz-lead sulfide interfaces of five films of various thicknesses. Comparison of Fig. 5 with Fig. 4, coupled with the interpretation of Fig. 4 according to Montgomery[12] and Garrett[13], suggests the following conclusions:

1. The bulk is always *p*-type in agreement with Hall measurements given earlier.

2. No inversion layers are formed; both the air and the quartz interfaces are always *p*-type.

3. The electrical properties of the lead sulfide-air interface change markedly with increasing film thickness. For thin films (0.42 and 0.54 μ thick) the field-effect dispersion curves are characteristic of mild exhaustion layers, both for the air and the quartz interfaces. For thick films (0.82 and 1.0 μ thick) the dispersion curves for the air interface flatten out in a

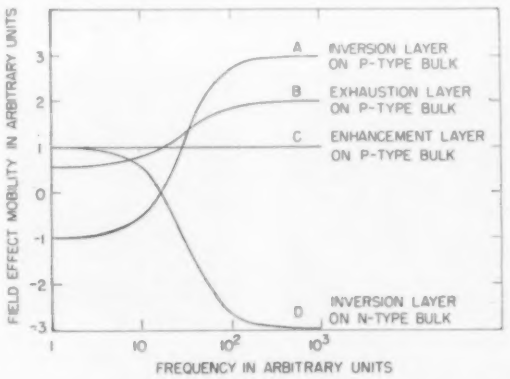

FIG. 4. Idealized representation of field-effect mobility-frequency measurements.

[11] W. Shockley, *Electrons and Holes in Semiconductors* (D. Van Nostrand Company, Inc., Princeton, New Jersey, 1950) p. 214.
[12] H. C. Montgomery, Phys. Rev. **106**, 441 (1957).
[13] C. G. B. Garrett, Phys. Rev. **107**, 478 (1957).
[14] For a brief discussion of the evidence for trapped electrons see footnote 2.
[15] P. Aigrain, J. Lagrenaudie, and G. Liandrat, J. phys. radium **13**, 587 (1952).

manner characteristic of enhancement layers; the curves for the quartz interface remain exhaustion type with increased dispersion. It has been found that the field-effect mobility of the quartz interface at the highest frequency of measurement approximately equals the signal mobility. This is not true for the air interface for the thicker films.

The differences between the quartz and the air interfaces for the thicker films as shown in Fig. 5 suggest that the exhaustion and enhancement layers which determine the shapes of the curves in Fig. 5 are relatively thin, perhaps of the order of one-tenth of a micron in thickness. No explanation of the physical nature of the interfaces is offered at this time. The approximate agreement of Hall, noise, and signal mobilities as shown in Fig. 2, and the fact that the high frequency field-effect mobility of the quartz interface is always about equal to the signal mobility indicates that each film may be characterized by a certain effective hole mobility. The air interface apparently plays little part in determining the magnitude of this effective hole mobility.

4. There is a point of inflection approximately at the frequency corresponding to the photoconductive time constant[16] in agreement with the interpretation for germanium.[12,13] Sorrows[9] also found this correspondence between point of inflection and time constant. No inflection point is exhibited, of course, by a field-effect mobility curve which has little or no dispersion, such as curve C of Fig. 4. It should be noted that the points of inflection for the two interfaces of the same film always occur at approximately the same frequency.

No *n*-type material, either in the bulk or on the surface, is evident from any of the measurements. Various ambient treatments including sparked oxygen, dry oxygen, wet nitrogen, and room air were tried; these ambients did change the potential of the air interface, but none produced sufficient change to drive the surface *n*-type. This result is in marked contrast to several theories[17] which have assumed an *n*-type bulk and *p*-type surface for photoconductive lead-sulfide films. For reasons given earlier it is concluded that such theories do not hold for the chemically deposited films studied here; the theories may hold for films produced by vacuum evaporation.

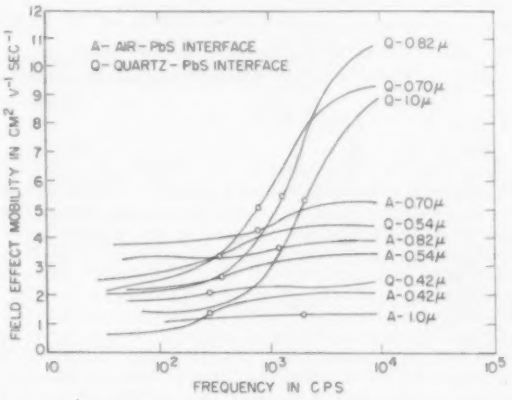

FIG. 5. Experimental measurements of field-effect mobility-frequency curves. The dimensions listed are thicknesses of the films. The open circles on the curves are drawn at the frequencies calculated from photoconductive time constants.

Finally, brief mention should be made of the effects of high intensity light on the films. Experimentally it is found that the effect of high intensity light on the shape of the field-effect mobility vs frequency curve is to change an exhaustion curve (curve B in Fig. 4) into an enhancement curve (curve C in Fig. 4). A curve corresponding to an enhancement surface (curve C) is not charged by light. Apparently the flood of carriers produced by the absorption of high intensity light washes out the potential gradient near an exhaustion surface. This occurs only when the intensity is high enough to appreciably change the resistance of the film, for example, by the order of a factor of two.

ACKNOWLEDGMENTS

We wish to thank Carl Oster of the Research Laboratories of Eastman Kodak Company for the electron photomicrographs. The encouragement and the many helpful discussions with George Koch have been greatly appreciated.

[16] The frequency f is calculated from $f=\frac{1}{2}\pi^{-1}\tau$, where τ is the photoconductive time constant.

[17] H. T. Minden, J. Chem. Phys. **25**, 241 (1956). Additional references are given by Minden (*ibid.*) and by Petritz in footnote 6.

JOURNAL OF APPLIED PHYSICS VOLUME 31, NUMBER 11 NOVEMBER, 1960

Conservation Laws of an Interacting Electron Beam

MARSHALL C. PEASE*
Stanford Research Institute, Menlo Park, California
(Received April 14, 1960)

The linearized theory of electron beams interacting with a circuit is studied. Such systems may be considered as coupling the modes of, for example, the beam and the circuit. It has been found, previously, that if these modes are properly defined, then there is a conservation law which states the constancy of the total power in these individual modes, independent of the extent of coupling. In single-frequency beam-type devices, this conservation law is Chu's kinetic power theorem. In multiple-frequency parametric systems, it is the linearized Manley-Rowe relation. The problem of such an interpretation is to determine what is an appropriate modal description that will lead to a convenient and useful conservation law. To obtain a systematic means of finding such a representation, we observe that any linear homogeneous system with n degrees of freedom has n quadratic invariances. The kinetic power theorem and the linearized Manley-Rowe relation are examples of such quadratic invariances, which are distinguished from the others by being independent of certain of the parameters of the system. Methods are obtained for determining, from the differential equations of the system expressed in any appropriate variables, the quadratic invariance, if it exists, which is independent of a given parameter. If the basis is now changed to one which diagonalizes this invariance, then we will have determined a modal, or wave, description in terms of which the invariance becomes a kinetic power law, as it is usually written. This method of analysis is illustrated by application to the infinite-plane parallel beam, the interaction of a longitudinal thin beam with an incompletely coupled circuit, and the interaction of a weakly constrained filamentary beam with a transverse-field circuit.

IN other papers[1,2] we have discussed procedures for obtaining the conservation laws of a linear homogeneous system from either the matrix-system operator or the matrix-differential equation. Such laws are expressible as quadratic forms that are invariant under the transformation that the system imposes.

For a system with n degrees of freedom, there are at least n such invariants, and more if the system is degenerate. Each such invariant determines a class of systems. The "type" of a system is determined by the intersection of the classes determined by its separate invariants. Taken together with a set of scalar quantities that can be identified as the pertinent "electrical lengths," they specify in detail the system being considered.

One such invariant is Chu's kinetic power theorem.[3,4] This states that, if we properly define the circuit and beam modes of the system, the algebraic sum of the powers in these various modes, taken with proper sign, is constant. Since a slow wave in general has negative "kinetic power," its interaction with a positively powered circuit wave permits amplification.

The difficulty that arises in the application of this theorem is in the determination of what is the "proper" way to define the modes that are coupled by the system. If this can be done, then the problem is largely solved.[5,6] In some cases—e.g., a one-dimensional beam with longitudinal velocity perturbation[7]—the general form is obvious and a suitable wave representation can be obtained readily. In other cases it is not obvious. We shall, for example, discuss the transverse interaction of a circuit with a filamentary beam as formulated by Siegman.[8] He was able to find an appropriate wave formalism—and hence a kinetic power theorem—but it is not clear how he obtained it. In more involved systems, the problem can be expected to become still more difficult.

The specific difficulty that arises is a consequence of the fact that the initial analysis[9] of the system is normally undertaken on a set of variables of quite mixed character. We have the voltage and current on the circuit, or else the forward and backward waves there. The beam is described by the longitudinal- and transverse-velocity perturbations and the perturbation of space charge on current density. The transverse displacements of the beam may also be involved. To obtain a proper wave formalism for the system as a whole, it is necessary to combine these various quantities in some suitable manner. In some cases it is not at all obvious how this can best be done.

As an example, we can again cite Siegman's analysis[8] of transverse interaction with a filamentary beam. The waves that he has found are of two types. One involves circularly polarized transverse-displacement and velocity waves; the other, circularly polarized displacement waves only. Of each type, there is a fast and a slow wave depending on the directions of polarization and of the magnetic field.

The difficulty is also compounded when we wish to

* Formerly of Sylvania Electric Products, Inc., Mountain View, California.

[1] M. C. Pease, "The quadratic invariances of a generalized network," Proc. IRE (to be published).

[2] M. C. Pease, J. Appl. Phys. **31**, 1988 (1960).

[3] L. J. Chu, "A kinetic power theorem," presented at the IRE-PGED Electron Tube Research Conference, Durham, New Hampshire, June, 1951.

[4] H. A. Haus, "Electron beam waves in microwave tubes," Mass. Inst. of Technol. Rept. No. 316 (April 8, 1958); see also footnote reference 3.

[5] J. R. Pierce, J. Appl. Phys. **25**, 179–183 (1954).

[6] W. H. Louisell and J. R. Pierce, Proc. IRE **43**, 425–427 (1955).

[7] L. D. Smullin and H. A. Haus, *Noise in Electron Devices* (Technology Press, Cambridge, Massachusetts, and John Wiley & Sons, Inc., New York, 1959). See Chap. 3, by H. A. Haus.

[8] A. E. Siegman, J. Appl. Phys. **31**, 17–26 (1960).

[9] J. R. Pierce, *Traveling-Wave Tubes* (D. Van Nostrand Company, Inc., New York, 1950).

consider electron beams for parametric amplification, thus requiring the analysis to account for two or more frequencies simultaneously. This problem has been studied by Louisell and Quate,[10] Haus,[11] and Johnson[12] for one-dimensional or longitudinal motion on the beam. In this case, the power theorem must include the effect of the linearized Manley-Rowe relations[13] governing power conversion between different frequencies.

The analytic complexity that is sometimes found in systems that physically seem relatively simple may be further illustrated by reference to the small-signal analyses by Gould,[14] Wightman,[15] Doehler, *et al.*,[16] and Macfarlane and Hay[17] of the crossed-field interaction.

It appears to us that there is need for a systematic method for determining a suitable basis for wave analysis.

The method to be followed here may be regarded as the reverse of the usual procedure. Normally, one starts by finding a convenient definition of the waves or modes of the system and shows that, on this basis, the system obeys a kinetic power law. Here we start by considering the quadratic invariants of the system. One of these we select as being the most convenient in that its form is independent of certain of the system parameters. From this we can then deduce the appropriate wave formulation.

GENERAL METHOD OF ANALYSIS

The general method of analysis that we shall use here will be the formal one that we have used before for other purposes. We assume that we have chosen a suitable set of variables such that, if we know the values of these variables along the tube, then we know the state of the tube as completely as is significant for our purposes. We arrange the values of these variables at a given cross section in a column matrix which we call the "state vector" $\mathbf{X}(z)$, the z axis being along the beam.

In this analysis we assume linearity and homogeneity. Then the state vectors at two different values of z are connected by a matrix operator $\mathbf{M}$.

$$\mathbf{X}(z_1)=\mathbf{M}(z_1,z_2)\mathbf{X}(z_2). \tag{1}$$

$\mathbf{M}$ will generally be a square matrix although this is not strictly necessary.

We want the quadratic forms which are invariant under $\mathbf{M}$. These will be the conservation laws of the system defined by $\mathbf{M}$. A quadratic form can be written in terms of the state vector $\mathbf{X}$, and a square matrix $\mathbf{K}$, as

$$s(\mathbf{K})=\mathbf{X}^\dagger\mathbf{K}\mathbf{X}, \tag{2}$$

where $(\ )^\dagger$ indicates the Hermitian conjugate—i.e., the complex conjugate of the transposed matrix. Hence $\mathbf{X}^\dagger$ is a row matrix and s a scalar quantity.

The scalar $s(\mathbf{K})$ is invariant under $\mathbf{M}$, and hence is a conservation law of the system if, and only if

$$\mathbf{M}^\dagger\mathbf{K}\mathbf{M}=\mathbf{K}. \tag{3}$$

We may interpret these results by calling $\mathbf{K}$ the "metric" of the space in which we regard $\mathbf{X}$ to be "embedded." That is, we have called $\mathbf{X}$ a vector. A vector, however, may be visualized as an oriented line segment in a space of appropriate dimension. However, there is nothing in the physical problem that determines what is the character of this space. It may be "Euclidean"; it may not be. We do not know until we define how a length is measured in this space. This definition can be conveniently expressed in terms of the "metric." Then (2) becomes the *definition* of the length squared of the vector $\mathbf{X}$ in the space whose metric is $\mathbf{K}$.

For s to be invariant under $\mathbf{M}$, we require then that the length squared of a vector be unchanged by operating on $\mathbf{X}$ with $\mathbf{M}$, whatever $\mathbf{X}$. Hence, we can describe our search for the conservation laws of the system as the problem of determining the metrics in which $\mathbf{M}$ is a rotational operator.

The necessary and sufficient condition that $\mathbf{M}$ be rotational in a space with metric $\mathbf{K}$ is Eq. (3).

This geometric description of the significance of $\mathbf{K}$ is intended as an aid to its interpretation. Alternatively, one can view the whole problem as a formal one. One simply substitutes $\mathbf{MX}$ for $\mathbf{X}$ in (2) and requires that s be unchanged. If the result is to hold for all $\mathbf{X}$, then (3) must hold.

While it is valid, and for many problems useful, to determine the $\mathbf{K}$'s from the $\mathbf{M}$ operator, it does depend upon specific knowledge of the operator $\mathbf{M}$. In most beam problems, and in certain other types, we may not know $\mathbf{M}$. Instead we have a set of differential equations that express the state vector as a function of distance only. (For beam problems and others involving a single frequency, we can assume the time dependency has been removed as a factor in $\exp j\omega t$.) It is therefore more convenient to be able to derive the $\mathbf{K}$'s from these differential equations.

We can assume that these equations are all of first order (i.e., involving only $\partial/\partial z$, not the higher derivatives). If this is not so, we can introduce additional variables which describe the lower derivatives and reduce to a set of first-order equations. For example, if one variable, say u, occurs as $\partial^2 u/\partial z^2$ plus,

[10] W. H. Louisell and C. F. Quate, Proc. IRE **46**, 707–716 (1958).
[11] H. A. Haus, IRE Trans. on Electron Devices, **ED-5**, 225–232 (1958).
[12] C. C. Johnson, J. Appl. Phys. **31**, 338–345 (1960).
[13] J. M. Manley and H. E. Rowe, Proc. IRE **44**, 904 (1956).
[14] R. W. Gould, J. Appl. Phys. **28**, 599–604 (1957).
[15] B. A. Wightman, "An investigation of the magnetron amplifier," Stamford Electronics Lab. Tech. Rept. No. 52 (February, 1959).
[16] O. Doehler, J. Brossart, and G. Mourier, "Les tubes à propagation d'onde à champ magnetique constant," Ann. de Rad. **5**, 293–307 (1950).
[17] G. G. Macfarlane and H. G. Hay, Proc. Phys. Soc. (London) **B63**, 409–427 (1950).

perhaps $\partial u/\partial z$ and u, then we define a new variable $v=\partial u/\partial z$. This gives us a new equation that is first-order in v. The original equation then can be written in terms of $\partial v/\partial z$, v, and u. It is first-order in v. Hence, the whole set of differential equations can be reduced by proper choice of the variables to a set of first-order equations.

Since the system is assumed to be linear and homogeneous, so are the differential equations. Hence we can write them as a single-matrix differential equation

$$\partial \mathbf{X}/\partial z = -j\mathbf{R}\mathbf{X}, \tag{4}$$

where $\mathbf{R}$ is an appropriate constant matrix. [The removal of the factor $(-j)$ is a convenience.]

If we write $\mathbf{X}$ as $\mathbf{M}\mathbf{X}_0$, where $\mathbf{X}_0$ is the state vector at a defined origin, then the z dependence is contained wholly in $\mathbf{M}$. Since (4) must apply for any $\mathbf{X}_0$, it becomes

$$\partial \mathbf{M}/\partial z = -j\mathbf{R}\mathbf{M}. \tag{5}$$

Now (3) can be differentiated with respect to z. $\mathbf{K}$ is required to be constant, independent of z. If we substitute (5) into the result of this differentiation, we find that the necessary and sufficient condition on the metric $\mathbf{K}$ is

$$\mathbf{R}^t\mathbf{K} = \mathbf{K}\mathbf{R}. \tag{6}$$

Equation (6) determines the metrics under which $\mathbf{M}$ is rotational in terms, not of $\mathbf{M}$ itself, but of the operator $\mathbf{R}$ that appears in the differential Eq. (4) that determines $\mathbf{M}$.

Given the differential Eq. (4), we have then the conditions that determine the conservation laws of the system. We determine the possible $\mathbf{K}$'s from (6). We then immediately write down the quadratic forms (2) that are the conservation laws of the system.

So far this involves nothing that we have not done before. However, in our previous application to parametric devices, we found that the structure of $\mathbf{R}$ was strongly and obviously restricted. We could use this fact to obtain one possible metric which, in turn, could be used to obtain others.

In the present problem the restrictive structural relation of $\mathbf{R}$ may not be obvious at all, as we shall later see. We must have some better way to determine the metric that we seek.

Once we have a single metric $\mathbf{K}_1$ of the system, other metrics are easily obtained. For, if $\mathbf{K}_1$ solves (6), so does $\mathbf{K}_1\mathbf{R}$. We can, for example, simply postmultiply (6) with $\mathbf{K}_1$ for $\mathbf{K}$ by $\mathbf{R}$,

$$\mathbf{R}^t(\mathbf{K}_1\mathbf{R}) = \mathbf{K}_1\mathbf{R}^2 = (\mathbf{K}_1\mathbf{R})\mathbf{R}. \tag{7}$$

Hence, if $\mathbf{K}$ is a metric, the set

$$\mathbf{K}_n = \mathbf{K}_1\mathbf{R}^{n-1}, \tag{8}$$

where n is any integer, is a set of metrics.

We may note that if $\mathbf{R}$ is $n\times n$ matrix, this set contains at most n independent $\mathbf{K}$'s. By the Cayley-Hamilton theorem, any matrix satisfies its characteristic equation. Hence, at worst, $\mathbf{R}^n$ is expressible as a linear combination of all lower powers of $\mathbf{R}$.

The set may contain less than n independent $\mathbf{K}$'s. There may also be more than n independent solutions to (6) if $\mathbf{R}$ is degenerate. Hence the set may not be the complete set of $\mathbf{K}$'s. We can only say that these $\mathbf{K}$'s are solutions of (6), not that they are all solutions of (6). If they are not complete, then there will be more than one such set. This is a situation that we have not found occurring except under very special conditions, but it is a possibility that should be kept in mind.

There remains then the determination of the first metric. This requires that we decide what special properties this metric can and should have (i.e., what property distinguishes this metric from the others). That $\mathbf{K}_1$ is a metric of the system is not sufficient to define it. There are, as we have stated, at least n independent metrics that fit the system, including at least those given by (8). Therefore we are at liberty to apply other conditions to $\mathbf{K}_1$.

It is a common and useful point of view to consider such a system as coupling certain sets of modes. We may have, for example, space charge modes and circuit modes which are coupled through the interaction mechanism. This concept, if it is to be interpreted in terms of our viewpoint, requires that the system have an $\mathbf{R}$ operator which may be written

$$\mathbf{R} = \begin{pmatrix} \mathbf{R}_{11} & \phi\mathbf{R}_{12} \\ \phi\mathbf{R}_{21} & \mathbf{R}_{22} \end{pmatrix}, \tag{9}$$

where the terms of $\mathbf{R}$ are themselves matrices. Then, if $\mathbf{R}_{11}$ is an $m\times m$ matrix, it provides the basic mode structure among the first m variables and $\mathbf{R}_{22}$, that among the remaining $(n\text{-}m)$ variables. ϕ is a scalar coupling parameter which does not appear in any of the submatrices, and $\mathbf{R}_{12}$ and $\mathbf{R}_{21}$ provide the cross-coupling between the sets of modes. The possibility of so ordering the variables and choosing ϕ as to permit writing $\mathbf{R}$ in this form is clearly implied by the modal concept.

Chu's kinetic power theorem has the form of the sum of the appropriately defined power flows in these various coupled modes. For it to be significant and useful, it must be independent of the coupling parameter. Hence it must be derived from a $\mathbf{K}_1$ of the form

$$\mathbf{K}_1 = \begin{pmatrix} \mathbf{K}_{11} & 0 \\ 0 & \mathbf{K}_{22} \end{pmatrix}, \tag{10}$$

where $\mathbf{K}_{11}$ and $\mathbf{K}_{22}$ are metrics of $\mathbf{R}_{11}$ and $\mathbf{R}_{22}$, respectively, independent of ϕ.

We cannot state that such a metric must necessarily exist. We only assert that a theorem of this sort exists only if a metric of this type can be found.

We shall call this metric the "principle metric for the specified coupling." We note that it may be

dependent on the choice of the modal sets. On occasion, this choice may be made in different ways, leading to different $\mathbf{K}_1$'s. Hence it is not "fundamental" to the system, but is determined by the definition of what variables are considered to be cross coupled, rather than simply coupled.

If $\mathbf{K}_1$, defined by (10) is to be a metric of an $\mathbf{R}$ of the form of (9) for all values of ϕ, then it must be a metric separately of $\mathbf{R}_1$ and $\mathbf{R}_2$, where

$$\mathbf{R}_1=\begin{pmatrix}\mathbf{R}_{11} & 0\\ 0 & \mathbf{R}_{22}\end{pmatrix} \tag{11}$$

and

$$\mathbf{R}_2=\begin{pmatrix}0 & \mathbf{R}_{12}\\ \mathbf{R}_{21} & 0\end{pmatrix}, \tag{12}$$

so that

$$\mathbf{R}=\mathbf{R}_1+\phi\mathbf{R}_2. \tag{13}$$

That it shall be a metric of $\mathbf{R}_1$ requires that $\mathbf{K}_{11}$ be a metric of $\mathbf{R}_{11}$ and $\mathbf{K}_{22}$ of $\mathbf{R}_{22}$. This, however, leaves considerable room for maneuver. If $\mathbf{R}_{11}$ is $m\times m$, then $\mathbf{K}_{11}$ can be any linear combination of the m metrics of $\mathbf{R}_{11}$. And similarly for $\mathbf{K}_{22}$. The additional requirement that $\mathbf{K}_1$ shall also be a metric of $\mathbf{R}_2$ specifies, generally within a scalar constant, which of these combinations are to be used.

One can, in principle, solve this problem by the simultaneous diagonalization of $\mathbf{R}_1$ and $\mathbf{R}_2$. This, however, is rarely practical to do.

A more practical, if less systematic, procedure depends on the usual circumstance that $\mathbf{R}_2$ is a highly singular operator. (Many of its rows and columns are filled with zeros.) We also note the general theorem that, if $\mathbf{K}_1$ solves $\mathbf{R}_1$ and $\mathbf{R}_2$, whatever their relation, then it also solves $\mathbf{R}_2\mathbf{R}_1\mathbf{R}_2$ and $\mathbf{R}_1\mathbf{R}_2\mathbf{R}_1$. The first of these, for example, is shown by repeated application of (6).

$$\begin{aligned}(\mathbf{R}_2\mathbf{R}_1\mathbf{R}_2)^\dagger\mathbf{K}_1&=\mathbf{R}_2^\dagger\mathbf{R}_1^\dagger\mathbf{R}_2^\dagger\mathbf{K}_1\\ &=\mathbf{R}_2^\dagger\mathbf{R}_1^\dagger\mathbf{K}_1\mathbf{R}_2\\ &=\mathbf{R}_2^\dagger\mathbf{K}_1\mathbf{R}_1\mathbf{R}_2=\mathbf{K}_1(\mathbf{R}_2\mathbf{R}_1\mathbf{R}_2).\end{aligned} \tag{14}$$

With the form of (11) and (12), $\mathbf{R}_2\mathbf{R}_1\mathbf{R}_2$ is diagonal in the submatrices,

$$\mathbf{R}_2\mathbf{R}_1\mathbf{R}_2=\begin{pmatrix}\mathbf{R}_{12}\mathbf{R}_{22}\mathbf{R}_{21} & 0\\ 0 & \mathbf{R}_{21}\mathbf{R}_{11}\mathbf{R}_{12}\end{pmatrix}. \tag{15}$$

Hence $\mathbf{K}_{11}$ must solve not only $\mathbf{R}_{11}$ but also $\mathbf{R}_{12}\mathbf{R}_{22}\mathbf{R}_{21}$. $\mathbf{K}_{22}$ must likewise solve both $\mathbf{R}_{22}$ and $\mathbf{R}_{21}\mathbf{R}_{11}\mathbf{R}_{12}$. This usually determines, within scalar constants, the form of $\mathbf{K}_{11}$, $\mathbf{K}_{22}$ or both, depending on the singularity of $\mathbf{R}_2$.

Likewise

$$\mathbf{R}_1\mathbf{R}_2\mathbf{R}_1=\begin{pmatrix}0 & \mathbf{R}_{11}\mathbf{R}_{12}\mathbf{R}_{22}\\ \mathbf{R}_{22}\mathbf{R}_{21}\mathbf{R}_{11} & 0\end{pmatrix}, \tag{16}$$

so that it has the role of $\mathbf{R}_2$. Either this or $\mathbf{R}_2$ itself provides the link between $\mathbf{K}_{11}$ and $\mathbf{K}_{22}$.

We may also note, as a possibly useful fact, that $\mathbf{R}_1^2$ and $\mathbf{R}_2^2$ are also suitable operators for the metric $\mathbf{K}_1$.

By manipulation of these various forms, it is usually possible to obtain the form of $\mathbf{K}_1$, either completely or within narrow limits, without excessive complication.

The methods discussed here are not confined to situations where the concept of coupled sets of modes are applicable. Whenever we can write $\mathbf{R}$ as $\mathbf{R}_1+\phi\mathbf{R}_2$, where ϕ is a parameter that does not otherwise appear, then we can, if we wish, ask if there exists a $\mathbf{K}_1$ for the system $\mathbf{R}$ that is independent of ϕ, and apply (15) and (16) to aid in obtaining that $\mathbf{K}_1$ if it exists.

We may also extend this procedure to more than a pair of modal sets. In this case we have a set of $\mathbf{R}$'s $(\mathbf{R}_1,\mathbf{R}_2,\mathbf{R}_3\cdots)$ which must be independently solved by $\mathbf{K}_1$. Again any combination of the form $\mathbf{R}_i\mathbf{R}_k\mathbf{R}_i$ is an operator that is solved by $\mathbf{K}_1$.

Finally, we repeat that we have no guarantee that a solution exists. The coupling parameter (or the modal sets) may have been chosen so that there is no $\mathbf{K}_1$ that is independent of ϕ. This usually shows up rapidly by finding, for example, that $\mathbf{R}_{12}\mathbf{R}_{22}\mathbf{R}_{21}$ in (15) is not solved by any $\mathbf{K}_{11}$ that solves $\mathbf{R}_{11}$. If this happens, one can only search for some more appropriate modal description.

We shall proceed now to illustrate this rather abstract discussion in some specific examples.

INFINITE PARALLEL-PLANE BEAM

We shall discuss first the infinite parallel-plane beam. This does not require the coupling of modal sets that we have been discussing, but it does illustrate the basic viewpoint of the metrical approach.

As Haus has shown,[7] the basic linearized differential equations are:

$$\begin{aligned}\partial a/\partial z&=j\beta_p^2(2V_0/\beta_eJ_0)i-j\beta_e a,\\ \partial i/\partial z&=j\beta_e(J_0/2V_0)a-j\beta_e i,\end{aligned} \tag{17}$$

where $a=u_0v/\eta$ the "kinetic voltage" of the beam, u_0=time average velocity, v=rf velocity, $\eta=|e/m|$ of electron, J_0=time average current density defined positively, V_0=dc beam voltage, i=rf current density, $\beta_e=\omega/u_0$ the electron propagation constant, $\beta_p=\omega_p/u_0$ the plasma propagation constant, and $\omega_p^2=\eta|\rho_0|/\epsilon$ the plasma frequency.

By taking as the state vector

$$\mathbf{X}=\begin{pmatrix}a\\ i\end{pmatrix}, \tag{18}$$

Eqs. (17) can be written in the form of (4) if

$$\mathbf{R}=\begin{pmatrix}\beta_e & -\beta_p^2(2V_0/\beta_eJ_0)\\ -\beta_eJ_0/2V_0 & \beta_e\end{pmatrix}. \tag{19}$$

Equation (6) with $\mathbf{R}$ as in (19) has two independent solutions. These may conveniently be taken as

$$\mathbf{K}_1=\begin{pmatrix}0 & 1\\ 1 & 0\end{pmatrix}, \tag{20}$$

$$\mathbf{K}_2=\begin{pmatrix}1/Z & 0\\ 0 & Z\end{pmatrix}, \tag{21}$$

where

$$Z=2\beta_p V_0/\beta_e J_0. \tag{22}$$

This may be readily confirmed either by direct substitution of (19) and (20) or (21) in (6), or by noting that (6) requires that if $\mathbf{K}$ is Hermitian ($\mathbf{K}^\dagger=\mathbf{K}$, so that the diagonal terms are real and opposite off-diagonal terms are complex conjugates of each other), then $\mathbf{KR}$ must also be Hermitian. $\mathbf{K}_1$ and $\mathbf{K}_2$ are Hermitian, being real and symmetrical. It is immediately found that $\mathbf{K}_1\mathbf{R}$ and $\mathbf{K}_2\mathbf{R}$ are also Hermitian. In fact, as may be easily seen,

$$\mathbf{K}_1\mathbf{R}=\beta_e\mathbf{K}_1-\beta_p\mathbf{K}_2. \tag{23}$$

[$\mathbf{K}_2$, as given in (21), is not the second member of the set (8) defined by the $\mathbf{K}_1$ of (20). The $\mathbf{K}_2$ of (21) is a linear combination of this derived $\mathbf{K}$ and $\mathbf{K}_1$.]

The resultant conservation laws are obtained from (2) with the state vector (18):

$$\begin{aligned} s(\mathbf{K}_1)&=a^*i+ai^*\\ s(\mathbf{K}_2)&=(aa^*/Z)+Zii^*. \end{aligned} \tag{24}$$

The scalar $s(\mathbf{K}_1)$ can be recognized as the real kinetic power flow at z. That it is conserved is Chu's kinetic power theorem.

The significance of $s(\mathbf{K}_2)$ is shown by changing to a wave basis. If we change the basis to

$$\begin{aligned} A_1&=(a-Zi)/\sqrt{2}\\ A_2&=(a+Zi)/\sqrt{2}, \end{aligned} \tag{25}$$

then we can easily find that Eqs. (24) become

$$\begin{aligned} s(\mathbf{K}_1)&=(|A_1|^2-|A_2|^2)/Z\\ s(\mathbf{K}_1)&=(|A_1|^2+|A_2|^2)/Z. \end{aligned} \tag{26}$$

Since each of these is conserved, both $|\mathbf{A}_1|^2$ and $|\mathbf{A}_2|^2$ must be conserved separately. The power in each wave is independently conserved. If we write

$$\mathbf{Y}=\begin{pmatrix}A_1\\ A_2\end{pmatrix}=\frac{1}{\sqrt{2}}\begin{pmatrix}1 & -Z\\ 1 & Z\end{pmatrix}\begin{pmatrix}a\\ i\end{pmatrix}=\mathbf{PX}, \tag{27}$$

then the substitution of $\mathbf{P}^{-1}\mathbf{Y}$ for $\mathbf{X}$ in (4) shows that $\mathbf{R}$ on the a,i basis is changed to $\mathbf{R}'$ on the A_1,A_2 basis

$$\mathbf{R}'=\mathbf{PRP}^{-1}=\begin{pmatrix}\beta_e+\beta_p & 0\\ 0 & \beta_e-\beta_p\end{pmatrix}, \tag{28}$$

so that $\mathbf{R}'$ is diagonal, indicating no coupling between the waves A_1 and A_2.

It is seen that the essential character of the system is contained in the two metrics $\mathbf{K}_1$ and $\mathbf{K}_2$. These, together with the lengths of the system for the slow and fast waves, are sufficient to define the system.

LONGITUDINAL SMALL BEAM

We now consider a slightly more complicated case that will involve a coupled-mode description. We consider a small beam constrained to longitudinal motion, interacting with a single transmission line. The situation is essentially that given by Pierce,[9] Chap. II, except that we do not assume close coupling. We use, instead, the concept of the effective space charge and voltage that he develops in Chap. XIII.

The circuit equations then are

$$\partial V/\partial z=-jk\beta_1 I, \tag{29}$$

$$\partial I/\partial z=J-j\beta_1 V/k=-\phi(\partial i/\partial z)-j\beta_1 V/k. \tag{30}$$

(We use k, instead of K, for the "cold" impedance of the line, and β_1 for its cold propagation constant.) J is the displacement current. ϕ is the coupling parameter that here relates the displacement current at the line to the rf current on the beam.

The linearized equation of motion is

$$j\omega v+u_0(\partial v/\partial z)=\eta\phi(\partial V/\partial z)=-j\eta k\beta_1\phi I, \tag{31}$$

where ϕ again enters as a decoupling effect.

The linearized equation of continuity is

$$\partial i/\partial z=-j\omega\rho=-j\beta_e(i-\rho_0 v). \tag{32}$$

Equation (32) can now be combined with (30):

$$\partial I/\partial z=-j\beta_1 V/k+j\phi\beta_e(i-\rho_0 v). \tag{33}$$

Using as the state vector

$$\mathbf{X}=\begin{pmatrix}V\\ I\\ v\\ i\end{pmatrix}, \tag{34}$$

Eqs. (29), (33), (31), (32) can be written in the form (4) with

$$\mathbf{R}=\begin{pmatrix}0 & k\beta_1 & 0 & 0\\ \beta_1/k & 0 & \phi\beta_e\rho_0 & -\phi\beta_e\\ 0 & \eta k\beta_1\phi/u_0 & \beta_e & 0\\ 0 & 0 & -\beta_e\rho_0 & \beta_e\end{pmatrix}. \tag{35}$$

We may consider ϕ as the coupling parameter, as implied by the name we have given it. We see that $\mathbf{R}$ has the form of (13) where the $\mathbf{R}_2$ provides the coupling between two sets of modes, one of which are the normal modes on the transmission line, and the other the modes within the beam.

We have

$$\mathbf{R}_{11}=\begin{pmatrix}0 & k\beta_1\\ \beta_1/k & 0\end{pmatrix} \tag{36}$$

and

$$\mathbf{R}_{22}=\begin{pmatrix}\beta_e & 0\\ -\beta_e\rho_0 & \beta_e\end{pmatrix}.$$

Two independent $\mathbf{K}$'s for $\mathbf{R}_{11}$ are easily seen to be

$$\mathbf{K}_{11,1}=\begin{pmatrix}0 & 1\\ 1 & 0\end{pmatrix},$$

$$\mathbf{K}_{11,2}=\begin{pmatrix}1/k & 0\\ 0 & k\end{pmatrix};$$

and for $\mathbf{R}_{22}$,

$$\mathbf{K}_{22,1}=\begin{pmatrix}0 & 1\\ 1 & 0\end{pmatrix}, \tag{38}$$

$$\mathbf{K}_{22,2}=\begin{pmatrix}1 & 0\\ 0 & 0\end{pmatrix}.$$

Now

$$\mathbf{R}_{12}=\begin{pmatrix}0 & 0\\ \beta_e\rho_0 & -\beta_e\end{pmatrix}, \tag{39}$$

$$\mathbf{R}_{21}=\begin{pmatrix}0 & \eta k\beta_1/\mu_0\\ 0 & 0\end{pmatrix},$$

and

$$\mathbf{R}_{12}\mathbf{R}_{22}\mathbf{R}_{21}=2\eta k\beta_1\beta_e^2(\rho_0/u_0)\begin{pmatrix}0 & 0\\ 0 & 1\end{pmatrix}. \tag{40}$$

We see that $\mathbf{K}_{11,2}$ is a suitable metric for this, but $\mathbf{K}_{11,1}$ is not. Hence

$$\mathbf{K}_{11}=\begin{pmatrix}1/k & 0\\ 0 & k\end{pmatrix}. \tag{41}$$

$\mathbf{R}_{21}\mathbf{R}_{11}\mathbf{R}_{12}$ vanishes identically, so that the other term of (15) contributes nothing. Likewise the powers of $\mathbf{R}_{11}$ and $\mathbf{R}_{22}$ contribute nothing.

Form (16) is no simpler to work with than is $\mathbf{R}_2$ itself. Hence, in this case, we proceed directly to $\mathbf{R}_2$. In order to write $\mathbf{K}_1$ in the most general form allowed by (41), we require that

$$\mathbf{K}_1\mathbf{R}_2=\begin{bmatrix}1/k & 0 & 0 & 0\\ 0 & k & 0 & 0\\ 0 & 0 & A & a\\ 0 & 0 & a & 0\end{bmatrix}\begin{bmatrix}0 & 0 & 0 & 0\\ 0 & 0 & \beta_e\rho_0 & -\beta_e\\ 0 & \eta k\beta_1/u_0 & 0 & 0\\ 0 & 0 & 0 & 0\end{bmatrix} \tag{42}$$

$$=\begin{bmatrix}0 & 0 & 0 & 0\\ 0 & 0 & k\beta_e\rho_0 & -k\beta_e\\ 0 & \eta k\beta_1 A/u_0 & 0 & 0\\ 0 & \eta k\beta_1 a/u_0 & 0 & 0\end{bmatrix}$$

be Hermitian if A and a are real so that $\mathbf{K}_1$ is Hermitian. This requires that a be $(-u_0\beta_e/\eta\beta_1)$, A be $(u_0\beta_e\rho_0/\eta\beta_1)$, and

$$\mathbf{K}_1=\begin{bmatrix}\eta\beta_1/k & 0 & 0 & 0\\ 0 & \eta\beta_1 k & 0 & 0\\ 0 & 0 & \beta_e u_0\rho_0 & -u_0\beta_e\\ 0 & 0 & -u_0\beta_e & 0\end{bmatrix}. \tag{43}$$

It can be directly verified that (43) is a solution of (6) with $\mathbf{R}$ given by (35). It is the only solution that does not contain ϕ.

If we had used either β_1 or β_e as the formal coupling parameter (although in this case, the concept of sets of modes coupled together becomes obscure), we would have found

$$\mathbf{K}_1'=\begin{bmatrix}0 & 1 & 0 & \phi\\ 1 & 0 & 0 & 0\\ 0 & 0 & 0 & -u_0/\eta\\ \phi & 0 & -u_0/\eta & 0\end{bmatrix}. \tag{44}$$

This is related to $\mathbf{K}_1$, as in (43), by

$$\mathbf{K}_1'\mathbf{R}=\mathbf{K}_1/\eta, \tag{45}$$

so that $\mathbf{K}_1$ is the second term, times a scalar, of the set generated by $\mathbf{K}_1'$.

If, on the other hand, we had used $1/u_0$ as a formal coupling parameter, even though the modal-set concept again becomes obscure, we would not have found it possible to obtain any solution. There is no $\mathbf{K}$ that is independent of u_0.

These statements, which can be verified, illustrate the point that which metric is the principal one depends on which system parameter we consider to be the coupling one.

$\mathbf{K}_1$ does not have the appearance of the usual power law. This derives from the fact that we have ignored the self-influence of the beam. We have ignored the fields due to space-charge bunching as being negligible compared to the effect of the circuit. In consequence $\mathbf{R}_{22}$ is a limiting case. Mathematically $\mathbf{R}_{22}$ has only a single eigenvector plus a "generalized eigenvector of rank two."[18] $\mathbf{R}_{22}$ cannot be diagonalized. Hence the beam part of the system is not expressible as a complete set of modes.

The formation of a power law, however, is still valid. Specifically, it is

$$s(\mathbf{K}_1)=\eta\beta_1(VV^*/k+kII^*)+u_0\beta_e(\rho_0 vv^*-vi^*-v^*i). \tag{46}$$

This is the expression that is conserved over the length of the interaction independently of ϕ.

$\mathbf{K}_1'$ actually leads to a more normal looking expression. Its conservation law is

$$s(\mathbf{K}_1')=V^*(I+\phi i)+V(I+\phi i)^*-u_0 vi^*/\eta-u_0 v^*i/\eta. \tag{47}$$

[18] As a reference for the significance and properties of generalized eigenvectors, we may cite *Principles and Techniques of Applied Mathematics*, by B. Friedman (John Wiley & Sons, Inc., New York, 1956), Chaps. 1 and 2.

The first two terms are the real power flow on the circuit if we consider the current on the circuit to be augmented by ϕi. The last two terms are the kinetic power flow on the beam.

Both of these, plus two more besides, are conservation laws of a particular system of this sort. Expression (46) is common to all such systems with the same β_1, β_e, u_0, ρ_0, and k, but with different ϕ. Expression (47) is common to all systems with the same ϕ and u_0, but with possibly different β_1, β_e, ρ_0, and k.

TRANSVERSE INTERACTION WITH A FILAMENTARY BEAM

As our final example, we shall consider the more complex situation analyzed in conventional terms by Siegman.[8] This assumes a filamentary beam interacting with a circuit that produces a purely transverse field at the average beam position but not necessarily at the perturbed beam position. Radio-frequency longitudinal motions and displacements are assumed negligible. The field produced by the beam is again assumed to have negligible effect on the beam.

The rf field is described in terms of the right- and left-hand circularly polarized components through the coupling terms f_+ and f_-, which may be complex. That is, one circularly polarized component is assumed to be describable as

$$E_+ = -f_+ V/D,$$

and the other as

$$E_- = -f_- V/D,$$

where D is a normalizing distance and

$$f_+ f_+^* + f_- f_-^* = 1.$$

As Siegman shows, the equations of this system are

$$\partial V/\partial z = \mp j\beta_0 k I$$

and

$$\partial I/\partial z = \mp j(\beta_0/k)V - (2\rho_0\omega/D)(f_+^* r_+ + f_-^* r_-), \quad (48)$$

where the upper sign is for a forward-wave circuit, the lower for a backward-wave one.

$$\partial^2 r_+/\partial z^2 + j(2\beta_e+\beta_c)\partial r_+/\partial z - \beta_e(\beta_e+\beta_c)r_+ = \eta f_+ V/u_0^2 D, \quad (49)$$

and

$$\partial^2 r_-/\partial z^2 + {}_4(2\beta_e-\beta_c)\partial r_-/\partial z - \beta_e(\beta_e-\beta_c)r_- = \eta f_- V/u_0^2 D, \quad (50)$$

where r_+ and r_- are the radial displacement of an electron expressed in the polarization coordinates; β_c is the cyclotron propagation constant ω_c/u_0 in which ω_c is ηB_0; B_0 is the dc axial-magnetic field.

These are Siegman's Eqs. (5) with (6) and (12). Equations (49) and (50) are second-order equations. However, if we define two new variables

$$w_+ = -j\partial r_+/\partial z, \qquad w_- = -j\partial r_-/\partial z, \quad (51)$$

then (49) and (50) become first-order.

$$\partial w_+/\partial z = -j\{(2\beta_e+\beta_c)w_+ + \beta_e(\beta_e+\beta_c)r_+ + \eta f_+ V/u_0^2 D\},$$

$$\partial w_-/\partial z = -j\{(2\beta_e-\beta_c)w_- + \beta_e(\beta_e-\beta_c)r_- + \eta f_- V/u_0^2 D\}. \quad (52)$$

If we take as the state vector

$$\mathbf{X} = \begin{bmatrix} V \\ I \\ w_+ \\ r_+ \\ w_- \\ r_- \end{bmatrix}, \quad (53)$$

then $\mathbf{R}$ is

$$\mathbf{R} = \begin{bmatrix} 0 & \pm\beta_0 k & 0 & 0 & 0 & 0 \\ \pm\beta_0/k & 0 & 0 & -2\rho_0\omega f_+^*/D & 0 & -2\rho_0\omega f_-^*/D \\ \eta f_+/u_0^2 D & 0 & (2\beta_e+\beta_c) & \beta_e(\beta_e+\beta_c) & 0 & 0 \\ 0 & 0 & -1 & 0 & 0 & 0 \\ \eta f_-/u_0^2 D & 0 & 0 & 0 & (2\beta_e+\beta_c) & \beta_e(\beta_e-\beta_c) \\ 0 & 0 & 0 & 0 & -1 & 0 \end{bmatrix}. \quad (54)$$

This rather monstrous looking thing can be considered as coupling between three modal sets. We set

$$\mathbf{R}_{11} = \begin{pmatrix} 0 & \pm\beta_0 k \\ \pm\beta_0/k & 0 \end{pmatrix}$$

$$\mathbf{R}_{22} = \begin{pmatrix} 2\beta_e+\beta_c & \beta_e(\beta_e+\beta_c) \\ -1 & 0 \end{pmatrix} \quad (55)$$

$$\mathbf{R}_{33} = \begin{pmatrix} 2\beta_e-\beta_c & \beta_e(\beta_e-\beta_c) \\ -1 & 0 \end{pmatrix},$$

and

$$\mathbf{R}_1 = \begin{bmatrix} \mathbf{R}_{11} & 0 & 0 \\ 0 & \mathbf{R}_{22} & 0 \\ 0 & 0 & \mathbf{R}_{33} \end{bmatrix}.$$

We let

$$\mathbf{R} = \mathbf{R}_1 + |f_+|\mathbf{R}_2 + |f_-|\mathbf{R}_3, \quad (56)$$

so that we have two coupling parameters $|f_+|$ and $|f_-|$. If we set

$$\nu = f_+/|f_+|, \qquad \mu = f_-/|f_-|, \quad (57)$$

then

$$\mathbf{R}_2=\begin{bmatrix} 0 & 0 & 0 & 0 & 0 & 0 \\ 0 & 0 & 0 & -2\rho_0\omega v^*/D & 0 & 0 \\ \eta v/u_0^2 D & 0 & 0 & 0 & 0 & 0 \\ 0 & 0 & 0 & 0 & 0 & 0 \\ 0 & 0 & 0 & 0 & 0 & 0 \\ 0 & 0 & 0 & 0 & 0 & 0 \end{bmatrix}, \tag{58}$$

$$\mathbf{R}_3=\begin{bmatrix} 0 & 0 & 0 & 0 & 0 & 0 \\ 0 & 0 & 0 & 0 & 0 & -2\rho_0\omega\mu^*/D \\ 0 & 0 & 0 & 0 & 0 & 0 \\ 0 & 0 & 0 & 0 & 0 & 0 \\ \eta\mu/u_0^2 D & 0 & 0 & 0 & 0 & 0 \\ 0 & 0 & 0 & 0 & 0 & 0 \end{bmatrix}$$

Appropriate $\mathbf{K}$'s for $\mathbf{R}_{11}$ are given by (37). For $\mathbf{R}_{22}$ we can easily find

$$\mathbf{K}_{22,1}=\begin{pmatrix} 0 & 1 \\ 1 & 2\beta_e+\beta_c \end{pmatrix} \tag{59}$$

and

$$\mathbf{K}_{22,2}=\begin{pmatrix} 1 & 0 \\ 0 & -\beta_c(\beta_e+\beta_c) \end{pmatrix}. \tag{60}$$

For $\mathbf{R}_{33}$ we have the same thing with $(-\beta_c)$ in place of β_c.

If now we form $\mathbf{R}_2\mathbf{R}_1\mathbf{R}_2$ and $\mathbf{R}_3\mathbf{R}_1\mathbf{R}_3$, we find that $\mathbf{K}$ must be constructed from $\mathbf{K}_{11,1}$, $\mathbf{K}_{22,1}$, and $\mathbf{K}_{33,1}$. This does not tell us the scalar multipliers. These are found by writing the general $\mathbf{K}$ of this type and testing it against $\mathbf{R}_2$ and $\mathbf{R}_3$. We find

$$\mathbf{K}_1=\begin{bmatrix} 0 & 1 & 0 & 0 & 0 & 0 \\ 1 & 0 & 0 & 0 & 0 & 0 \\ 0 & 0 & 0 & a & 0 & 0 \\ 0 & 0 & a & a(2\beta_e+\beta_c) & 0 & 0 \\ 0 & 0 & 0 & 0 & 0 & a \\ 0 & 0 & 0 & 0 & a & a(2\beta_e-\beta_c) \end{bmatrix}, \tag{61}$$

where

$$a=-2u_0^2\omega(\rho_0/\eta).$$

It may be directly verified that $\mathbf{K}_1$ is a metric for the $\mathbf{R}$ of (54). Except for a scalar factor, it is the only $\mathbf{K}$ that is independent of the coupling factors $|f_+|$ and $|f_-|$.

The resultant scalar invariant is

$$\begin{aligned} s(\mathbf{K}_1)=&V^*I+VI^* \\ &+a\{(2\beta_e+\beta_c)r_+r_+^*+jr_+(\partial r_+/\partial z)^* \\ &-jr_+^*(\partial r_+/\partial z)\}+a\{(2\beta_e-\beta_c)r_-r_-^* \\ &+jr_-(\partial r_-/\partial z)^*-jr_-^*(\partial r_-/\partial z)\}. \end{aligned} \tag{62}$$

It may be verified that this is the same conservation law (within a scalar factor, and considering the fact that we have retained the backward-circuit wave) that Siegman finds in terms of his modal description. In fact, his modal description can now be obtained from (61) by finding the appropriate transformation to the basis that will diagonalize $\mathbf{K}_1$.

CONCLUSION

We have been concerned here with the development of an analytic technique that will allow us to determine the appropriate power law for a complex system. From this we can then determine the appropriate "coupled mode" description of the system that will exhibit this conservation law as the sum and differences of the powers flowing in these coupled modes.

The power theorem so obtained is analogous to, and a generalization of, Chu's kinetic power law for a system comprising a beam and circuit at a single frequency. If multiple frequencies are involved, and other conditions met, it is analogous to the Manley-Rowe condition for a parametric circuit with linearized time dependence. (Pump signal large compared to those at the frequencies of interest.) It provides a powerful tool for the analysis of the possible behavior of such a system.

This "principle" conservation law is not the only one of the given system. It, in fact, generates a whole set of conservation laws, all of which apply to the system. These other laws, however, depend on the coupling parameter. Moreover, they are likely to depend on all the parameters of the system, although it is possible that one or more linear combinations of them may be independent of other system parameters. If this occurs, then these other laws could have been found as the principle law by a different definition of the "uncoupled" state. Thus the determination of the principle law may depend on our point of view.

We have illustrated this method of analysis in three situations. We have considered first the infinite parallel-plane beam, showing that it leads precisely to the well-known transmission line analogue. We have then considered a thin longitudinal beam loosely coupled to a transmission line and have obtained the appropriate power law for this case. Finally, we have considered the transverse-field situation discussed recently by Siegman.

The previous analyses of these cases have been reasonably complete. One may therefore ask what has been accomplished by recasting them into this unfamiliar form. The answer, we believe, is twofold. Insofar as these particular situations are concerned, this analysis elucidates the significance and interrelation of the coupled-mode representations that have been used. It exhibits explicitly the role of the particular parameter selected as the coupling one, giving insight into the physical significance of the representation. In particular, it emphasizes the choice that one has in the designation of what we consider to be the uncoupled state.

Our second purpose has been the development of

the analytic technique itself and its illustration. It provides a tool for the analysis of still more complicated situations where conventional methods are wholly inadequate. To determine, by conventional means, the analogue of Chu's kinetic theorem for an unknown system involving many degrees of freedom requires considerable inspiration to find the appropriate coupled-mode basis. The analysis presented here gives a usable method of doing this without intuitive guesswork.

We believe that this method provides a powerful tool for the analysis of complicated systems of this kind.

JOURNAL OF APPLIED PHYSICS VOLUME 31, NUMBER 11 NOVEMBER, 1960

Secondary Electron Emission of MgO Crystals Bombarded by Relativistic Electrons*

MARTIN A. POMERANTZ, ROMAS A. SHATAS,† AND WILLIAM C. SCHIEVE
Bartol Research Foundation of the Franklin Institute, Swarthmore, Pennsylvania

(Received November 30, 1959; and in final form July 25, 1960)

The yield of single crystals of MgO has been determined at a primary energy of 1.3 Mev, utilizing a modification of the "sandwich" technique developed earlier for investigating the secondary electron emission of metals at high primary energies. The value of δ for Al was measured concurrently under identical conditions.

The accumulation of surface charges usually encountered with insulators is prevented by the bombardment-induced conductivity of MgO. The influence of multiple scattering and energy loss of the primary beam, as well as of δ-ray production, must be considered when the targets are relatively thick as in the present case. An empirical correction for normalizing the thick target measurements to thin target conditions was determined.

The result is: $\delta_{MgO}=0.09\pm0.02$ as compared with $\delta_{Al}=0.023\pm0.003$.

I. INTRODUCTION

INASMUCH as MgO surfaces provide the highest reported secondary yields,[1] there has been much interest in understanding the nature of the mechanism which makes this material a considerably more copious emitter under electron bombardment than all the others which have been investigated. Measurements of the secondary electron emission in single crystals of MgO have revealed maximum values of $\delta=I_s/I_p$ ranging between 7[2] and 25[3,4] at a primary energy of 1100–1200 ev. Since the earlier experiments have been confined to primary energies below 10 kev, it is of interest to extend the measurements to the Mev region.

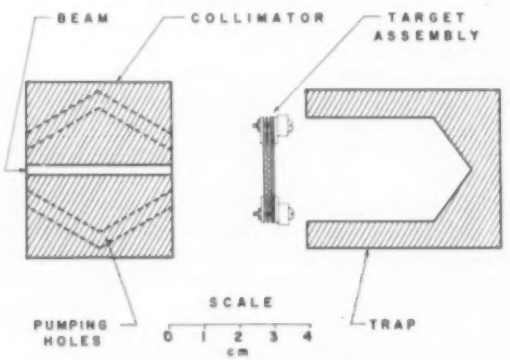

FIG. 1. Schematic diagram of experimental arrangement.

To eliminate the effects of the accumulation of surface charges produced by the emission of secondaries from insulators, techniques such as heating the target to increase the electrical conductivity, or bombardment with low energy electrons, have been utilized in previous experiments at low primary energies.[5] The purpose of the present investigation was to develop methods for measuring the secondary electron emission from nonconducting targets bombarded by relativistic primary electrons, and to compare the yields from MgO and a reference metal under identical vacuum conditions at these primary energies.

Previous investigations of bombardment-induced conductivity in MgO[6] had suggested that this phenomenon itself might prevent the buildup of surface charges. The "sandwich" arrangement,[7] utilized previously in investigations of secondary emission produced by 1.3

* Assisted in part by the U.S. Army Office of Ordnance Research.

† Present address: Philco Corporation, Research Division, Philadelphia 34, Pennsylvania.

[1] See, for example, A. J. Dekker in *Solid State Physics*, edited by F. Seitz and D. Turnbull (Academic Press, Inc., New York, 1959), p. 259.

[2] J. B. Johnson and K. G. McKay, Phys. Rev. **91**, 582 (1953).

[3] R. G. Lye, Phys. Rev. **99**, 1647 (1955).

[4] N. R. Whetten and A. B. Laponsky, J. Appl. Phys. **28**, 515 (1957).

[5] N. R. Whetten and A. B. Laponsky, Phys. Rev. **107**, 1521 (1957).

[6] M. A. Pomerantz, R. A. Shatas, and J. F. Marshall, Phys. Rev. **99**, 489 (1955).

[7] R. A. Shatas, J. F. Marshall, and M. A. Pomerantz, Phys. Rev. **102**, 682 (1956).

Mev electrons from a multiple-cavity linear accelerator, was readily adaptable for this purpose. However, this method had been applied only to thin targets (i.e., those characterized by negligible multiple-scattering of the primary beam). Since sufficiently thin MgO crystals are not available, it was expected that certain corrections would be required to reduce the measured yield to that characteristic of thin targets.

II. EXPERIMENTAL PROCEDURE

A. Target Assembly

The target arrangement utilized in the present measurements is shown schematically in Fig. 1. The collimated beam of 1.3 Mev primary electrons from the linear accelerator passes through the "sandwich" assembly, and is collected by the carbon trap. Both trap and target current pulses were displayed oscillographically and recorded photographically. The sandwich arrangement was chosen because it prevents collection by the target of stray low energy electrons either produced by primaries impinging upon the collimator and trap, or scattered onto the walls of the secondary emission tube. Furthermore, it also provides an electrostatic shielding of the target against the electric field of the pulsed-injection gun cathode, as well as against stray electric fields created by modulators driving the pulsed magnetron of the accelerator. As shown in Fig. 2, the electrode structure consists of two MgO wafers (total thickness, 203 mg/cm²) and three Al foils (total thickness 21 mg/cm²). Because the yield of the internal faces of the assembly can be determined, a direct comparison of the secondary emission properties of metals and insulating crystals under identical vacuum conditions is realized.

The MgO crystals, approximately 1 cm on a side, were cleaved to thicknesses of the order of 0.04 cm from large single crystals of commercially produced periclase.[8] After cleaving, they were ground down by hand to approximately 0.025 cm. Although desirable, a further reduction in thickness by mechanical means proved to be unsuccessful, because thinner wafers were found to have little strength and broke readily into sizes too small for targets.

Prior to the measurements, the ground wafers were vacuum fired for 12 hours at 1100°C. The target assembly was mounted in a demountable tube attached to the output end of the linear accelerator, and was pumped continuously by its vacuum system to 5×10^{-6} mm of Hg.

B. Method of Measurement

The schematic diagram of target arrangement and instrumentation employed in measuring the yield of secondaries is shown in Fig. 3. The voltage pulses

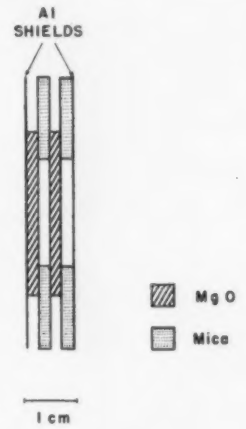

FIG. 2. Details of "sandwich" assembly. Conductive coating is applied to the faces of the MgO crystals in contact with the Al shields.

generated by target and trap current, I_T and I_P respectively, passing through resistors R_T and R_P, were amplified in a two-channel linear amplifier and displayed by a sequential dual-trace cathode ray oscillograph.

The target current I_T, at a given set of potential differences V_1 and V_2 of the shield electrodes (1 and 2) with respect to the target electrode (0), can be expressed as a sum of emitted and collected electrons. Since nine combinations of polarities of V_1 and V_2 are possible, we thus obtain nine equations. However, the precision of the measurements with MgO are enhanced by utilizing only those potential combinations which either collect or retard all of the low energy secondaries from the respective internal faces of the two crystals. This requirement excludes combinations which result in zero or nearly zero potential difference between the opposite MgO faces. As a consequence, only the composite yield, i.e., the sum of yields from both MgO faces, is determined. This restriction is of small practical significance since it has been demonstrated earlier that, with relativistic primaries, the ratio of forward to backward secondary emission is unity, at least in the case of metal targets.[7]

The current of low energy secondary electrons from MgO is determined from the measurements by means of the following equations:

$$I_T(V_1>0;\ V_2=0) = I_{01}{}^l+I_{01}{}^h+I_{02}{}^l+I_{02}{}^h-I_{10}{}^h-I_{20}{}^l-I_{20}{}^h-I_0{}^P \quad (1)$$

$$I_T(V_1<0;\ V_2=0) = I_{01}{}^h+I_{02}{}^l+I_{02}{}^h-I_{10}{}^l-I_{10}{}^h-I_{20}{}^l-I_{20}{}^h-I_0{}^P. \quad (2)$$

Here, $I_{mn}{}^l$ designates the low energy secondaries (i.e., less than 50 ev), $I_{mn}{}^h$ the high energy secondaries, and $I_0{}^P$ the primaries stopped within the target. Indices m and n denote the emitting and collecting faces of the sandwich assembly respectively (Fig. 3).

The composite secondary emission yield is given by

$$\delta'=[I_T(V_1>0;\ V_2=0)-I_T(V_1<0;\ V_2=0)]/I_P. \quad (3)$$

[8] Optical quality, produced by the Norton Company, Worcester, Massachusetts, under the trade name "Magnorite."

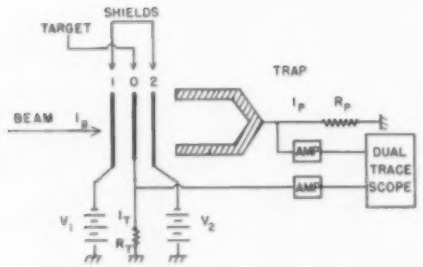

FIG. 3. Schematic diagram of the "sandwich" arrangement and the instrumentation utilized in measurements of secondary electron emission produced by high energy primaries.

Since δ' represents the sum of the low energy secondary yields from two opposite surfaces, the average yield of a single face is $\delta=\delta'/2$.

With respect to the primary current I_P, it should be pointed out that, as a consequence of multiple scattering, not all of the primaries which were effective in the production of secondaries reach the trap. In the computation of the yield this was taken into account on the basis of data obtained in an auxiliary experiment.

Concurrently with the measurements of MgO, the secondary yield of the Al surfaces was determined by a similar procedure.

C. Surface Charge Neutralization

The method of avoiding the accumulation of surface charges in the present experiments differs from any of the techniques utilized previously. The phenomenon of bombardment-induced conductivity in MgO[6] makes it unnecessary to neutralize the surfaces of the targets by auxiliary means.

During the 2 μsec primary current pulses (repetition rate-10pps, peak pulse current-0.2mA) a conductivity ($\sim 10^{-6}\Omega^{-1}$ cm^{-1}) is induced in the normally nonconducting ($\sim 10^{-16}\Omega^{-1}$ cm^{-1}) MgO crystals as a consequence of the production of mobile charge carriers. Since this phenomenon has been discussed previously, a detailed description will not be presented here. However, for the understanding of certain transient effects which are described below, it is essential to recall that the external current resulting from electron bombardment arises from an internal displacement of charge, and that Ohm's law is followed.

Prior to electron bombardment, an electric field exists in the crystal as a result of the application of a fixed voltage (100 to 700 v) between the electrodes. Consequently, during the initial pulses, the component of the target current attributable to bombardment-induced conductivity alone is quite large compared with the portion representing secondary emission. This is confirmed quantitatively by (a) the magnitude of the current, (b) the linear voltage dependence and lack of saturation, and (c) the variation of the pulse height with the crystal spacing. These are all in accordance with prediction on the basis of our previous investigations of bombardment-induced conductivity.

However, the development of a surface charge subsequently reduces the internal fields, thereby eliminating the relative contribution of bombardment-induced conductivity to the measured target current. The subsequent charging of the surface in the opposite sense as a result of the emission of secondary electrons is thus compensated by the residual bombardment-induced crystal current.

After equilibrium has been attained (20 μsec total pulse time in a typical case), the pulse height remains constant and independent of the previously applied potential. The bombardment-induced conductivity required to prevent the charging up of the surface caused by secondary emission then introduces a negligible contribution to the measured target current.

III. THICK TARGET EFFECTS

A. Nature of Corrections

When the elements of the "sandwich" are relatively thick, owing to the above mentioned difficulties of preparing sufficiently thin MgO crystals, the influence of multiple scattering and energy loss of the primary beam as well as of δ-ray production might alter the secondary emission yield from that characteristic of thin targets with the primary beam at normal incidence.

(1) *As a consequence of scattering, the primary electrons generally do not impinge upon the target at normal incidence.*

It has been demonstrated previously that the secondary electron emission produced by high energy electrons follows the relationship $\delta(\theta)=\delta_0 \sec\theta$, where θ is the angle of incidence of the primary beam, and δ_0 is the yield at normal incidence.[7] When the primary beam is characterized by a distribution of angle of incidence, the ratio of the measured yield to that corresponding to normal incidence is

$$\delta/\delta_n=\int\int d\theta d\phi\Phi(\theta,\phi)\Big/\int\int d\theta d\phi\Phi(\theta,\phi)\cos\theta. \quad (4)$$

Here $\Phi(o,\phi)$ is the angular distribution of the incident beam on the crystal surface, and ϕ is the azimuthal angle. Thus, for example, in the case of an isotropic distribution of primaries in the forward direction, neglecting backscattering of primaries, $\delta/\delta_n=\pi/2$.

(2) *The primaries are not monoenergetic after passing through an appreciable thickness of absorber, but are characterized by an energy distribution with low energy tail.*

Under the present circumstances, the measured yield is given by

$$\delta=\int_0^{E_{max}}(dI_p/dE)\delta(E)dE\Big/\int_0^{E_{max}}(dI_p/dE)dE, \quad (5)$$

where I_p represents the primary current, and E the primary energy.

However, on the basis of a direct measurement indicating that less than 1.5% of the primary beam effective in producing secondary electrons is in the energy range below 60 kev, together with an extrapolation of published data on the yield of MgO crystals at low primary energies, it is estimated that the contribution by the low energy tail amounts to less than 15% of the measured value of δ.

(3) *High energy secondaries (δ rays) are produced copiously, and may contribute appreciably to the secondary emission through the production of tertiaries.*

Data concerning the emission of energetic secondary electrons have been reported previously.[9] The δ-ray yield increases as a function of target thickness. However, the effects of energetic secondaries would be indistinguishable from those of scattered primaries.

B. Determination of Correction Factor

In order to establish an empirical correction for the three aforementioned effects, a series of runs was conducted with aluminum targets of different thicknesses. First, the secondary emission of Al was measured under thin target conditions. The arrangement was identical with that shown in Fig. 2, but with the MgO samples removed, leaving only the three Al electrodes of 21 mg/cm² total thickness. Secondly, two Al scatterers of 203 mg/cm² total thickness (equal to the MgO crystals) were inserted into the target assembly, one in front of the electrode nearest the collimator and the other after the third electrode nearest the trap. Thus, the geometrical and the scattering conditions applying to the MgO faces inside the sandwich were essentially reproduced (cf. Figs. 1 and 2). The measured ratio of the secondary emission of Al with the scatterers in, to that with the scatterers out, was 1.5 ± 0.2.

This factor has been applied to the present MgO measurements to obtain the yield characteristic of thin targets. It is evident that the correction determined in this manner provides a rigorous normalization of the thick target measurements to thin target conditions only in the case of Al. However, neglecting a small uncertainty arising from the fact that the shapes of the yield vs energy curves of Al and MgO are not identical, this single empirical correction takes into account the three effects enumerated above.

To gain further insight into the influence of scattering, the position of the Al scatterers in the above measurements was rearranged. With 203 mg/cm² of Al in front of the electrode nearest the collimator, and none behind the thin third Al electrode, the ratio of the thick target Al yield to the thin target yield as measured without the scatterer was 1.5 ± 0.1. Thus, the position of the thick scatterers does not affect the results.

IV. RESULTS

The thick target yield of MgO at 1.3 Mev primary energy was 0.130 ± 0.005; division by the normalization factor cited in the preceding section gives the value for the thin target yield of MgO at this energy, $\delta_{MgO}=0.09\pm0.02$. The yield corresponding to the latter for Al is $\delta_{Al}=0.023\pm0.003$. This agrees with the results of earlier measurements.

It is interesting to note that the relatively high secondary electron emission of MgO observed at low primary energies persists at relativistic energies. It would be desirable to conduct similar measurements under ultra-high vacuum conditions.

ACKNOWLEDGMENT

It is a pleasure to thank Dr. J. F. Marshall for helpful discussions.

[9] R. A. Shatas, J. F. Marshall and M. A. Pomerantz, Phys. Rev. **96**, 1199 (1954).

JOURNAL OF APPLIED PHYSICS VOLUME 31, NUMBER 11 NOVEMBER, 1960

Growth from the Melt. Part II. Cellular Interface Morphology

G. F. Bolling and W. A. Tiller
Westinghouse Research Laboratories, Churchill Borough, Beulah Road, Pittsburgh 35, Pennsylvania
(Received May 24, 1960)

The microscopic shape of a solid-liquid interface has been examined theoretically for those growth conditions which give rise to a cellular morphology. The method of obtaining a general solution is set forth, and approximate treatments are used to compare the theoretical approach with experimental data. The variation of cell size with temperature gradients, growth velocity, stirring in the liquid, interfacial free energy, and solute content is examined, and the conditions governing the stability of a cellular interface compared to that of a smooth interface are predicted.

INTRODUCTION

SINGLE crystals of a variety of metals and semiconductors grown from the melt exhibit a fibrous substructure for a wide range of freezing conditions. This manifests itself as a cellular network of solute segregation in the plane perpendicular to the growth axis and a columnar network in perpendicular planes. The cell diameter in this network is generally in the range 10^{-3}–10^{-2} cm.

It was first postulated by Rutter and Chalmers[1] that this cellular substructure, which could be observed on the solid-liquid interface by a decanting technique, arises as a consequence of the formation of a zone of constitutionally supercooled liquid adjacent to the interface. They also showed how this substructure could be affected by the freezing conditions. Tiller *et al.*[2] developed a quantitative condition for the onset of this constitutional supercooling which can be expressed as

$$\frac{G}{V} \leqslant \frac{-mC_0(1-k_0)}{Dk_0}, \qquad (1)$$

where G is the temperature gradient in the liquid, V is the freezing velocity, C_0 is the initial concentration of solute in the melt, D is the diffusion coefficient of this solute, k_0 is its partition coefficient, and m is the liquidus slope. It was further postulated that a smooth solid-liquid interface would become unstable when Eq. (1) was satisfied.

Walton *et al.*[3] and Tiller and Rutter[4] showed experimentally that the onset of constitutional supercooling in tin and lead, respectively, led to the instability of a smooth interface in agreement with Eq. (1). However, they observed that the initial instability did not immediately produce the cellular interface morphology, but that a finite degree of constitutional supercooling was necessary before the cellular morphology became the stable form. Herman and Damiano[5] found that a larger degree of constitutional supercooling was needed to stabilize the cellular interface morphology in zinc, and Bolling *et al.*[6] observed that a much larger degree was required to produce cells in germanium. This is best illustrated with the aid of Fig. 1, which shows the equilibrium temperature distribution, T_E, ahead of an interface of Pb, Sn, Zn, or Ge. Constitutional supercooling will occur when the actual temperature distribution, T_A, is less than $T_A(0)$. The cellular morphology will be the stable form for Pb, Sn, Zn, and Ge when $T_A = T_A(1)$, $T_A(2)$, $T_A(3)$, $T_A(4)$, respectively. A trend suggested from these observations is that the magnitude of constitutional supercooling necessary to stabilize the cellular interface morphology increases with the solid-liquid interfacial energy γ_{SL}. A postulate of this nature is supported by the observations of Boček *et al.*[7] who find that in zinc, a metal which should exhibit an anisotropy of γ_{SL}, the cell size for fixed freezing conditions is a function of the orientation of the solid-liquid interface.

Our present state of knowledge of crystal growth allows a quantitative description of the onset of constitutional supercooling, but it has not provided the same degree of understanding concerning the formation of the cellular interface morphology or the variation of the cell dimensions with the freezing conditions. In this paper

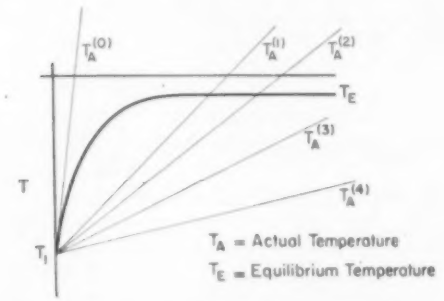

FIG. 1. Schematic illustration of the difference in the magnitude of constitutional supercooling required for the cellular interface morphology to be the stable growth form for Pb, Sn, Zn, and Ge.

[1] J. W. Rutter and B. Chalmers, Can. J. Phys. **31**, 15 (1953).
[2] W. A. Tiller, K. A. Jackson, J. W. Rutter, and B. Chalmers, Acta Met. **1**, 428 (1953).
[3] D. Walton, W. A. Tiller, J. W. Rutter, and W. C. Winegard, Trans. AIME **7**, 1023 (1955).
[4] W. A. Tiller and J. W. Rutter, Can. J. Phys. **34**, 96 (1956).
[5] M. Herman and V. Damiano (private communication).
[6] G. F. Bolling, W. A. Tiller, and J. W. Rutter, Can. J. Phys. **34**, 234 (1956).
[7] M. Boček, P. Kratochvil, and M. Valouch, Czech. J. Phys. **8**, 557 (1958).

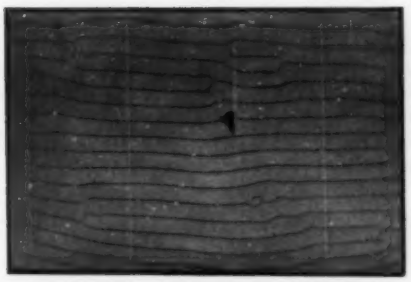

FIG. 2. Photomicrograph of the two-dimensional cell morphology on a decanted interface of Pb. 42×.

we attempt to enhance our quantitative understanding of the cellular morphology by developing an expression for the cell size, a, of elongated cells, as a function of the freezing conditions and the material parameters, and by developing an expression which determines the stability of the cellular morphology.

THEORY

Equilibrium Shape

The type of cellular interface that we intend to treat is shown in Fig. 2 and may be considered as a singly periodic system. The approximate shape of the cell caps, $x=f(y)$, in the initial stages of their formation is as depicted in Fig. 3, with the cell walls having an almost infinite slope at the points $[\pm x^*, y^*]$. In general some curvature K_c will exist at the point $[0,0]$ and, if $T(xy)$ and $C(xy)$ represent the temperature distribution and solute distribution, respectively, in the liquid, the condition of equilibrium at the interface leads to the following defining equation for $x=f(y)$:

$$\{T[0,0]-T[f(y),y]\}=m\{C[0,0]-C[f(y),y]\}-\frac{\gamma}{\Delta S}\{K_c-K[f(y),y]\}, \quad (2)$$

where K is the curvature, ΔS is the entropy of fusion per unit volume, and γ may be a function of y.

The temperature distribution is determined as the solution to the steady-state differential equations,

$$\left(\frac{\partial^2}{\partial x^2}+\frac{\partial^2}{\partial y^2}\right)T_i+\frac{V}{\alpha_i}\frac{\partial T_i}{\partial x}=0, \quad i=S, L, \quad (3)$$

with the boundary conditions

$$\left.\begin{aligned} &T_S=T_L, \\ \text{and}\quad &\kappa_L\frac{\partial T_L}{\partial n}+LV_n=\kappa_S\frac{\partial T_S}{\partial n} \end{aligned}\right\} \text{ on } x=f(y),$$

where the subscript $i=S$ or L, refers to solid or liquid, α is the thermal diffusivity, κ the thermal conductivity, L is the latent heat per unit volume, and V_n is the normal component of the growth velocity. The general solution to Eq. (3) is

$$\frac{T_i}{T_\infty}=1+\sum_{n=0}^{\infty}T_{in}\cos\left(\frac{2\pi n}{a}x\right)e^{-\beta_{in}y}, \quad (4)$$

where

$$\beta_{in}=\frac{V}{2\alpha_i}+\left[\left(\frac{V}{2\alpha_i}\right)^2+\left(\frac{2\pi n}{a}\right)^2\right]^{\frac{1}{2}}.$$

The determination of a particular solution of Eq. (3) is a very difficult problem and will not be treated here. However, on $x=f(y)$ we can expand $T[f(y),y]$ as a polynomial in y so that

$$\{T[0,0]-T[f(y),y]\}=-\sum_{n=1}^{\infty}G_{n-1}y^n. \quad (5)$$

We will use $T[f(y),y]$ in this form later.

The solute distribution is similarly determined as the solution to the steady-state differential equations

$$\left(\frac{\partial^2}{\partial x^2}+\frac{\partial^2}{\partial y^2}\right)C_i+\frac{V}{D_i}\frac{\partial C_i}{\partial x}=0, i=S, L, \quad (6)$$

with the boundary conditions on $x=f(y)$

$$C_S=k_0C_L$$

and

$$V_n(1-k_0)C_L=-\left[D_S\frac{\partial C_S}{\partial n}+D_L\frac{\partial C_L}{\partial n}\right].$$

The general solution to Eq. (6) is

$$\frac{C_i}{C_\infty}=1+\sum_{n=0}^{\infty}C_{in}\cos\left(\frac{2\pi n}{a}x\right)e^{-\tilde{\beta}_{in}y}, \quad (7)$$

where

$$\tilde{\beta}_{in}=\frac{V}{2D_i}+\left[\left(\frac{V}{2D_i}\right)^2+\left(\frac{2\pi n}{a}\right)^2\right]^{\frac{1}{2}}.$$

Again the particular solution to Eq. (6) is very difficult to obtain and will not be treated here. However, we will

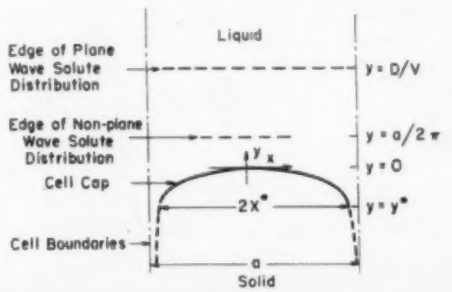

FIG. 3. Schematic representation of the cell cap morphology, the coordinate axes and the extent of plane wave and non-plane wave solute distributions in the liquid ahead of the cell cap.

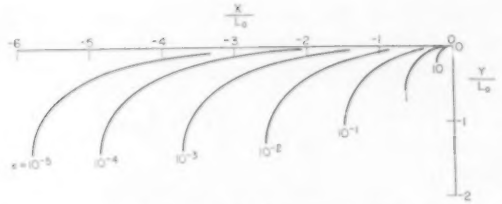

FIG. 4. Plot of the predicted cell cap morphology from Eq. (11) using the dimensionless coordinates X/L_0 and Y/L_0 for several values of the material parameter $\epsilon=L_0^2K_c^2/2$ ($L_0^2=\gamma/\Delta SG_0'$).

expand $C[f(y),y]$ as a polynomial in y so that

$$\{C[0,0]-C[f(y),y]\}=-\frac{1}{m}\sum_{n=1}^{\infty}\phi_{n-1}y^n. \qquad (8)$$

Using Eqs. (5) and (8), Eq. (2) becomes

$$\theta_0+\sum_{n=1}^{\infty}G_{n-1}'y^n=\frac{\gamma}{\Delta S}\left\{\frac{y''}{(1+y'^2)^{\frac{3}{2}}}\right\}, \qquad (9)$$

where $\theta_0=-\gamma(0)K_c/\Delta S$ and $G_{n-1}'=G_{n-1}-\phi_{n-1}$. Solutions for $x=f(y)$ can be found from Eq. (9) in the form of elliptic integrals if $G_{n-1}'=0$ for $n>1$. If the $G_{n-1}'\neq 0$ for $n>1$, the equation has solutions in the form of hyperelliptic integrals. In general then, we can say that if the G_{n-1}' are known, $x=f(y)$ can be found in terms of θ_0. If $x=f(y)$ is known, the solute flux equation will yield both $C[0,0]$ and all the ϕ_{n-1}, likewise the equation of continuity of heat flow will yield all the G_{n-1}. Equilibrium at $[0,0]$ will yield $T[0,0]$ in terms of θ_0 so that it appears that the cell shape can be completely specified in terms of θ_0 and that this is a free variable in the problem.

Returning to Eq. (9), we determine a first order approximation to the cell shape by choosing the $G_{n-1}'=0$ for $n>1$. Thus, Eq. (9) becomes

$$y+\theta_0'=L_0^2y''/(1+y'^2)^{\frac{3}{2}}, \qquad (10)$$

where $L_0^2=\gamma/\Delta SG_0'$ and $\theta_0'=\theta_0/G_0'$. With γ assumed independent of y, Eq. (10) can be integrated using a Legendre transformation[8] to yield

$$\frac{x}{L_0}=\pm\left(\frac{2}{2+\epsilon}\right)^{\frac{1}{2}}\left\{(1+\epsilon)\left[F(r,s)-F\left(r,\frac{\pi}{2}\right)\right]-(2+\epsilon)\left[E(r,s)-E\left(r,\frac{\pi}{2}\right)\right]\right\}, \qquad (11)$$

where

$$r=\sin^{-1}\left(\frac{2}{2+\epsilon}\right)^{\frac{1}{2}},\quad s=\cos^{-1}\left[\left(\frac{y+\theta_0'}{2L_0}\right)^2-\frac{\epsilon}{2}\right]^{\frac{1}{2}},\quad \epsilon=\frac{L_0^2K_c^2}{2}$$

in the region $2L_0^2\epsilon\leqslant(y+\theta_0')^2\leqslant 2L_0^2(2+\epsilon)$.

In Eq. (11), $F(r,s)$ and $E(r,s)$ are elliptic integrals of the first and second kinds, respectively. Equation (11) is plotted in Fig. 4 as x/L_0 vs y/L_0, and we can see that the general shape of the dimensionless curves agrees with the shape of elongated cell caps observed in practice. The dimensions of the cell will, of course, depend upon ϵ and L_0.

From Eq. (11) and the development of Eq. (10), the points $[\pm x^*, y^*]$ are given by

$$\frac{x^*}{L_0}=\pm\left(\frac{2}{2+\epsilon}\right)^{\frac{1}{2}}\left\{(1+\epsilon)\left[F\left(r,\frac{\pi}{4}\right)-F\left(r,\frac{\pi}{2}\right)\right]-(2+\epsilon)\left[E\left(r,\frac{\pi}{4}\right)-E\left(r,\frac{\pi}{2}\right)\right]\right\}, \qquad (12)$$

$$\frac{y^*}{L_0}=-\{(2+2\epsilon)^{\frac{1}{2}}-(2\epsilon)^{\frac{1}{2}}\}.$$

Equation (12) is plotted in Fig. 5 as x^*/L_0 vs ϵ and y^*/L_0 vs x^*/L_0, and we can see that in the region $\epsilon\ll 1$,

$$\frac{x^*}{L_0}=\pm\left\{0.5\ln\left(\frac{1}{\epsilon}\right)+0.23\right\},\quad \frac{y^*}{L_0}=-\sqrt{2}. \qquad (13)$$

We know that, in practice, $x^*\approx 0.9a/2$, but we cannot evaluate a from Eq. (13) since we do not know K_c for a certain set of growth conditions. However, we can gain an expression for a by the following approximate treatment.

Approximate Cell Size

The solute distribution in the liquid ahead of the cell caps is described by Eq. (7) and consists of a plane wave term plus a series of non-plane wave terms. The terms which cause lateral diffusion ahead of the cell caps are the non-plane wave terms which extend into the liquid an effective distance $y'=pa/2\pi$, where p is a function which depends upon the relative magnitude of C_n in Eq. (7). We will choose $p=\frac{1}{2}$ as an average value for our calculations. Knowing that solute can diffuse a distance x in the time $t\approx x^2/D$, we will postulate that the cell size is determined by the distance through which solute in the layer $0<y<y'$, $x\approx 0$ can diffuse laterally, before the cell cap reaches it. Since the allowable time for diffusion is $t\approx[(pa/2\pi)+|y^+|]/V'$, we have

$$a\approx\frac{4D}{V'}\left[\frac{p}{2\pi}+\frac{|y^+|}{a}\right], \qquad (14)$$

where $V'=V$ for quiescent liquids and $V'\equiv V$ plus an effective flow velocity for stirred liquids and y^+ is that value of y at which $dy/dx=\pm 1$. The magnitude of this effective flow velocity will be discussed later. Solving Eq. (14) as a quadratic and using $|y^+|\approx(0.6)^{\frac{1}{2}}L_0$ from the first integration of Eq. (10), we have

$$a\approx\frac{pD}{\pi V'}\left\{1+\left[1+\frac{4\pi^2V'}{p^2D}\left(\frac{0.6\gamma}{\Delta SG_0'}\right)^{\frac{1}{2}}\right]^{\frac{1}{2}}\right\}. \qquad (15)$$

[8] G. F. Bolling and W. A. Tiller, J. Appl. Phys. **31**, 1345 (1960).

The most difficult parameter to assess in Eq. (15) is G_0'. When the cell caps are very flat, (i.e., when K_c is small) G_0' is determined by G_L, and when the cells are well developed (when K_c is large), G_0' is determined by G_s. Thus we have

$$G_0' = G_L - \phi_0, \qquad K_c \text{ small}; \tag{16}$$

$$G_0' = \frac{\kappa_L}{\kappa_S} G_L + \frac{LV}{\kappa_S} - \phi_0, \qquad K_c \text{ large}.$$

We have made the oversimplification that ϕ is constant, whereas in general, it must be expected that ϕ will vary with the growth conditions. However, it is interesting to see how Eq. (15) fits Boček *et al*'s[7] data for zinc. Using the values in cgs units $\gamma=90$, $\Delta S=0.15$, $L=180$, $\kappa_S=0.25$, $\kappa_L=0.125$, $\phi_0=8$, $D=5\times10^{-5}$, and G_0' for well-developed cells, the theoretical value of a is plotted in Fig. 6 vs G_L and compared to Boček's data. In spite of the very approximate treatments the theoretical curves exhibit the same character as the experimental curves, showing a very sensitive G_L dependence for low V, this sensitivity decreasing as V increases. The curves could be brought into closer agreement at high G_L by using G_0' for cells with K_c small since this variation of G_0' should apply at high G_L. However, no close fit could possibly be expected from such an approximate treatment and it is gratifying to see that even this amount of agreement is obtained.

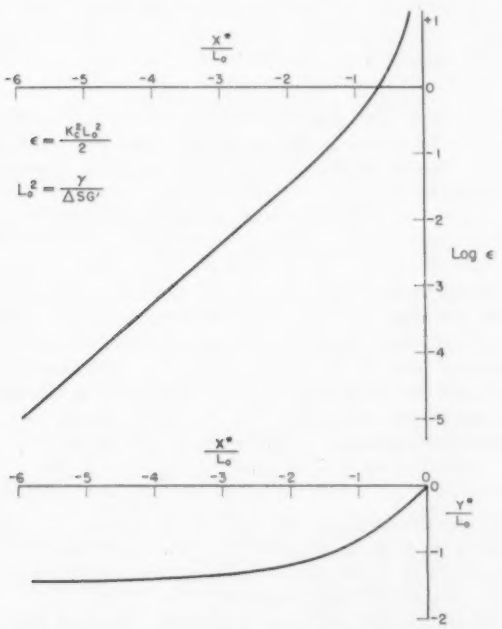

FIG. 5. Plot of the critical dimensionless coordinate, X^*/L_0 as a function of the material parameter ϵ and X^*/L_0 vs Y^*/L_0. The critical coordinates $[X^*,Y^*]$ occur at the points where the cell walls have almost an infinite slope.

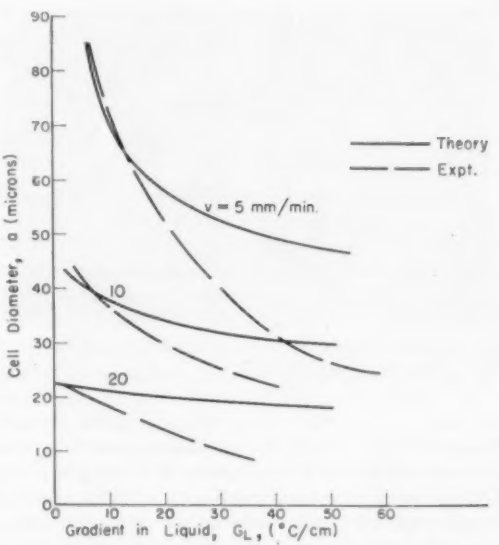

FIG. 6. Comparison of the approximate treatment for cell size, a, as a function of the freezing conditions, with Boček *et al*'s data[7] as a function of the gradient in the liquid, G_L.

Aside from the variation of a with the freezing conditions we can see that a will depend upon γ as observed by Boček *et al.*[7] and will increase as γ increases. We can also see that G' will decrease as ϕ_0 increases and ϕ_0 will increase as C_∞ increases. Thus, a will increase as C_∞ increases, as observed by Tiller[9] and Kratochvil *et al.*[10]

If the melt is stirred during crystal growth the fluid flow can penetrate the solute-rich layer, and inhibit the solute that leaves the cell cap region from reaching the cell boundary region by carrying some of this solute out into the bulk liquid. Because of this, V' must include a term which takes account of this flow velocity. This can also be seen from Eq. (6), where the diffusion equation must have V replaced by $V+W(y)$, where $W(y)$ is the fluid flow velocity at the position y ahead of the interface. Close to the interface $W(y)=Ay^2$, where A is a constant which depends upon the kinematic viscosity of the liquid and the flow velocity of the liquid far from the interface. This equation has a solution in the form of an integral error function which is difficult to use for illustrative purposes; however, it is possible to solve it simply if we assume an average flow velocity over the whole of the solute-rich layer. If we let this average value, $\bar{W}$, be one half the value of W at the boundary of the solute layer, i.e., at $y=\delta$, we have, for small values of $V\delta/D$,

$$\bar{W} \approx D/\delta \tag{17}$$

for the case of fluid flow caused by rotating the crystal

[9] W. A. Tiller, Ph.D. thesis, University of Toronto, Toronto, Canada, (1955).

[10] P. Kratochvil, P. Lukac, and M. Valouch, Czech. J. Phys. **B10**, 48 (1960).

during crystal growth as in the Czochralski technique.[11] In general we must apply a correction factor b when relating $\bar{W}$ to D/δ for other types of stirring so that

$$V'=V+bD/\delta. \tag{18}$$

Cell Formation

A shape perturbation will develop on the interface only if some regions of the surface can be stable at a higher temperature than that of a planar interface. This means that no stable shape perturbation is possible for a pure material if the temperature increases with distance in the liquid. As a curved projection forms on the interface its equilibrium temperature is reduced according to the Gibbs-Thomson relationship, and the surface must relax to the planar state. However, with an alloy liquid, the curved projection also produces a lateral diffusion of solute which depletes the interface concentration and increases the equilibrium temperature of the projection. For the projection to be stable at a higher interface temperature, the magnitude of the curvature effect, δT_K, must be less than the magnitude of the solute effect, δT_c. We shall make the postulate that cells will form only if the following condition is satisfied:

$$\delta T_K+\delta T_c>0. \tag{19}$$

The equilibrium temperature distribution ahead of a planar interface, $T_E(0)$ (due to the solute distribution $C_p(y)$), and $T_E(K)$ for a body of curvature K and the same solute distribution, are illustrated schematically in Fig. 7. Since lateral diffusion from a cell cap requires that the cap concentration be higher than that at $x=a/2$ for the same value of y, it is obvious that cells could not form with an average cap curvature of $\bar{K}$ if the temperature distribution, T_A, has a steeper slope than G_2. In fact, the slope G_3 is required in order for the cell cap to move ahead of the planar surface some average distance $\bar{y}$ with an average concentration greater than $C_p(\bar{y})$.

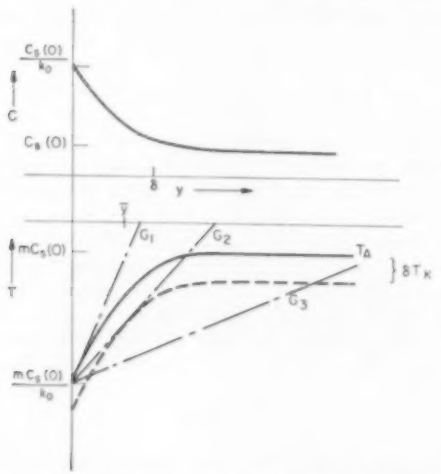

FIG. 7. Schematic representation of the effect of solid-liquid interfacial free energy, γ, on the stability of the cell morphology.

[11] J. Czochralski, Z. physik. Chem. **92**, 219 (1917).

Let the cell cap move ahead an average distance $\bar{y}$ and be in equilibrium at this temperature. The equilibrium condition is then

$$G\bar{y}=\left[\frac{-mC_s(0)(1-\bar{\alpha})}{k_0}-\frac{\gamma}{\Delta S}\bar{K}\right], \tag{20}$$

where $C_s(0)$ is the concentration in the solid at a planar interface and $\bar{\alpha}C_s(0)$ is the average concentration in the solid over the cell cap. Equation (20) can be readily transformed for comparison with Eq. (1) to give

$$\frac{G}{V}=\frac{-mC_s(0)(1-k_0)}{Dk_0}-\frac{1}{V\bar{y}}\left[\frac{\gamma\bar{K}}{\Delta S}-m\Delta C\right], \tag{21}$$

with

$$\Delta C=\frac{C_s(0)}{k_0}\left[\frac{V\bar{y}}{D}(1-k_0)-(1-\bar{\alpha})\right].$$

In Eq. (21) $C_s(0)\equiv C_0$ for unstirred liquids, and the last term has been absent in previous discussions of interface stability. Before discussing Eq. (20) let us estimate the magnitude of $\bar{\alpha}$ and $\bar{K}$.

The average curvature of the cap of the two-dimensional cells, $\bar{K}$, is given by

$$\bar{K}=\frac{2\tan^{-1}\psi}{l}, \tag{22}$$

where ψ is the slope of the cap at the cell groove ($\psi\approx-\infty$) and l is the arc length over the cell cap ($a<l<\pi a/2$). Equation (22) may be given approximately by

$$\begin{aligned}\bar{K}&\approx\pi/a \quad \text{for} \quad K_c \text{ small},\\ \bar{K}&\approx 2/a \quad \text{for} \quad K_c \text{ large}.\end{aligned} \tag{23}$$

Steady-state diffusion in the liquid requires that the average concentration freezing into the solid be $C_s(0)=C_\infty$. From growth experiments in quiescent liquids (Fig. 1) $x^*\approx 0.45a$; thus, the concentration excess $0.9a\,C_s(0)(1-\bar{\alpha})$ must be segregated to the cell boundaries of width $0.1a$. The average concentration at the cell boundaries, C_B, must then be given by

$$C_B\approx C_s(0)[1+9(1-\bar{\alpha})]. \tag{24}$$

The maximum excess at the cell boundaries may be estimated to be between $0.1\,C_s(0)$ and $C_s(0)$ and, since this is about twice the average excess, we may estimate $\bar{\alpha}$ to be between 0.995 and 0.95.

If we turn our attention to Eq. (20), although $\bar{y}$ and $\bar{\alpha}$ are unknowns, we can see two important things. First, the amount of constitutional supercooling necessary for cells to be stable will increase as γ increases.

This may be seen from Eq. (20), since if $\bar{\alpha}$ and $\bar{y}$ are approximately constant and G and V are held constant, $C_s(0)$ must increase linearly with increase of $\gamma/\Delta S$ to make the cells stable. The degree of constitutional supercooling for constant G and V will therefore increase almost linearly with $\gamma/\Delta S$. Thus, we can see one reason why more constitutional supercooling is required to stabilize the cellular morphology in germanium than in lead. Secondly, and more important, since $\bar{K} \alpha D/\delta$ it can be increased by increasing the stirring and reducing δ. Thus, no matter how large $C_s(0)$ becomes (~ 50 at %), the right-hand side of Eq. (20) can be made less than the left-hand side and the cellular morphology will not be the stable morphology. This value of $1/\delta$ may be given as

$$\frac{1}{\delta} \gtrsim \frac{1}{b}\left[\frac{-m\Delta SC_s(0)(1-\bar{\alpha})(p+2\pi|y^+|/a)}{\pi\gamma k_0} - \frac{V}{D}\right], \quad (25)$$

where $\bar{\alpha}$ is that average cap concentration and $|y^+|/a$ that ratio that would exist if δ were increased to the point that cells formed for the other growth conditions held constant. Equation (25) has not yet been examined experimentally but the principle has been tested. Figure 8 presents photomicrographs of sections of two crystals of Bi_2Te_3 +20 wt% Bi_2Se_3 grown under the same freezing conditions but different stirring conditions. The crystal on the left, which exhibits severe segregation indicating that the stable interface morphology was cellular, was grown at 10^{-4} cm/sec from a quiescent liquid; whereas the crystal on the right, which exhibits only grain boundary segregation indicating that the stable interface morphology was planar, was grown at $V = 10^{-4}$ cm/sec with $\delta \approx 100D$.

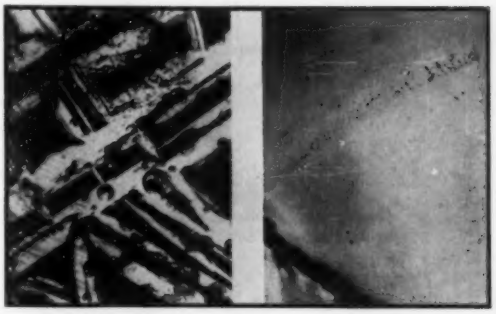

FIG. 8. Photomicrographs of $Bi_2Te_{2.4}Se_{0.6}$ crystals grown at a rate of 2×10^{-4} cm/sec. (a) Melt inadequately mixed; pronounced segregation. (b) Melt adequately mixed; segregation absent. 25×.

DISCUSSION

The first quantitative investigations on the formation of cells and the introduction of the concept of constitutional supercooling[1-4] established Eq. (1) as a reasonable approximation for the breakdown of a planar interface. It was also realized that the cell size to be expected when the cellular morphology was established would be of the order of D/v; this can be shown from the most simple diffusion argument. These conditions may be thought of as a zeroth order approximation, both in derivation and extent of agreement with experiment.

The description of equilibrium shapes presented in Eqs. (2) to (9) is completely general and capable of providing real solutions to the problem of cell formation and cell morphology. Since observations of cell boundaries on exterior[1] and microtomed[12] surfaces show the boundaries to extend, unperturbed, over distances of the order 10^2 a cm, it is reasonable to consider the cell morphology as a steady-state morphology under constant growth conditions. A two-dimensional treatment has been presented to illustrate the method of morphology prediction for elongated cells. The natural extension to three dimensions for treatment of the general cell shape can be made; however, it is sufficiently complicated that a better estimate of the G_{n-1} and ϕ_{n-1} are needed before such a treatment can be meaningful. It is for this reason that the present solutions were not extended to consideration of the general polynomial in Eq. (9). There is little advantage until some method of determining the G_{n-1}' can be devised. We are attempting to determine these parameters from particular solutions of Eqs. (3) and (6). When these parameters are known, numerical methods may be used to yield the hyperelliptic integral solutions.

An important concept that must be considered before a complete solution can be obtained concerns the choice of an optimization principle to determine the particular value of θ_0 that applies. Without this, θ_0 is still a free variable in the solution. An application of the principle of minimum rate of entropy production as the driving force for cell formation has been suggested by Kirkaldy.[13] However, this principle has not been validated for such growth processes[14] and cannot lead to a tractable solution without unwarranted assumptions. We prefer to choose, without proof, the following optimization principle: The cells will adopt that stable morphology which produces the maximum interface temperature over the cell caps. From this, constitutional supercooling is a necessary requirement before the cellular morphology could be preferred over the planar interface morphology.

The present treatment can be considered as a useful first-order approximation to an exact quantitative treatment of cell formation and the stable cell morphology as a function of the crystal parameters and the growth conditions.

[12] A. T. Maroun, S. S. Sheinin, and A. Rosenberg, Acta Met. **5**, 117 (1957).

[13] J. S. Kirkaldy, Can. J. Phys. **37**, 739 (1959).

[14] W. A. Tiller, Can. J. Phys. **37**, 1204 (1959).

Effect of Neutron Bombardment on the Magnetic Properties of Very High Permeability Iron*

G. Biorci, A. Ferro,† and G. Montalenti
Istituto Elettrotecnico Nazionale "Galileo Ferraris," Centro Studi per l'Elettrofisica, Torino, Italy
(Received June 15, 1960)

Rings of iron with permeability of about 150 000, after neutron bombardment (1×10^{18} nvt), show lower permeability and higher coercive force. This effect can be interpreted as due to large defects giving long range internal stresses, or as due to anisotropic defects interacting with the magnetization vector at each point of the specimen.

IT has recently been shown that strong changes in magnetic properties are produced by fast neutron bombardment on magnetic materials.[1–4] For instance, for doses of about 10^{17} nvt, permeability of permalloy is already greatly reduced. These changes can be interpreted[4,5] as mainly due to variations of directional short-range order according to the theories of Néel[6] and Taniguchi.[7] Irradiation allows atomic diffusion also at room temperature.

However, it may be interesting to see whether, apart from these ordering effects in alloys, some other effects of irradiation on magnetic properties could also be present.

Permeability and coercive force, as is well known,[8] are extremely sensitive to any small internal strain when the volumes affected by the strains are at least about the same, or not too much smaller than, the domain wall thickness. For iron this is about 1000 A.

From this standpoint the examination of the changes in magnetic properties seems to be a useful method to check whether irradiation actually produces some large size defects. The experimental results on radiation damage are related to point defects, while large defects such as displacement spikes, dislocation rings, and other defects produced by clustering of point defects, even if foreseen theoretically, have very little experimental evidence so far.

The most suitable material for determining the presence of these effects, which from early measurements[1,9] are expected to be rather small, is pure iron. It can be prepared with a very high permeability of 100 000 to 300 000 by long annealing at 1480°C in pure H_2, according to the technique suggested by Cioffi.[5] Alloys cannot be used as the ordering effects, discussed previously, may entirely mask the phenomenon.

Several $35\times7\times3.5$-mm iron rings have been prepared in this way. After such treatment the permeability is about 150 000 and the O, C, and N content, controlled by micrographic and internal friction methods, is smaller than 0.001%. The windings were made after heat treatment and each ring was enclosed in an aluminum container. The specimens with their windings were aged for four days at 150°C before irradiation, and no changes in the magnetic properties were observed. Since the irradiation is performed at a much lower temperature, and since the specimen is pure iron, any aging effect in the course of irradiation can be excluded.

A first group of specimens was irradiated in the BEPO reactor at Harwell, England, with an integrated flux of about 2×10^{18} nvt. The flux of fast neutrons ($\geqslant1$ Mev) was 4×10^{17} nvt. Temperature of specimens during irradiation was presumably somewhat above room temperature (60° to 80°C). A second group of specimens was irradiated in the Melusine swimming pool reactor at Grenoble, France, with an integrated flux of about 1.24×10^{19} nvt and a fast neutron flux of 1.2×10^{18} nvt. The specimen was directly immersed in the water.

A typical result is shown in Figs. 1 and 2. As is seen, the maximum permeability decreases by about 30% and the coercive force increases by about 0.005 oe. The two groups of specimens irradiated in the two reactors show about the same results in spite of the different doses. The interpretation of the observed results is not completely unequivocal.

As previously suggested from the theory of the magnetization processes, the size of the defects revealed by the observed variations of permeability and coercive force should be at least the same as, or not too much smaller than, the domain wall thickness, in our case about 1000 A. From the well known expression[8] which relates the coercive force to the internal stresses we can also say that the average effect of these defects is

* The research reported in this document has been sponsored by the Air Force Office of Scientific Research of the Air Research and Development Command, U. S. Air Force, through its European Office, under contract.

† Istituto Nazionale di Fisica Nucleare, Sezione di Torino.

[1] R. S. Sery, R. E. Fishell, and D. J. Gordon, "Effects of nuclear radiation on magnetic properties of core materials," Navord Rept. 4381 (December 16, 1956) and Nucleonics **16**, 73 (1958).

[2] D. J. Gordon and R. S. Sery, *Congr. Intern. sur la Physique de l'Etat Solide, Bruxelles, June 1958* (Academic Press, Inc., New York, 1960).

[3] R. E. Alley, J. Appl. Phys. Suppl. **30**, 284 S (1959).

[4] A. I. Schindler, E. I. Salkovitz, and G. S. Ansell, J. Appl. Phys. Suppl. **30**, 282 S (1959).

[5] A. I. Schindler and E. I. Salkovitz, J. Appl. Phys. Suppl. **31**, 245 S (1960).

[6] L. Néel, J. phys. radium **15**, 225 (1954).

[7] S. Taniguchi, Sci. Repts. Research Insts. Tohoku Univ. Ser. A **1**, 269 (1955).

[8] R. M. Bozorth, *Ferromagnetism* (D. Van Nostrand Company, Inc., Princeton, New Jersey, 1950).

[9] G. Biorci, A. Ferro, and G. Montalenti, ARDC Technical Note 1b (September 1958).

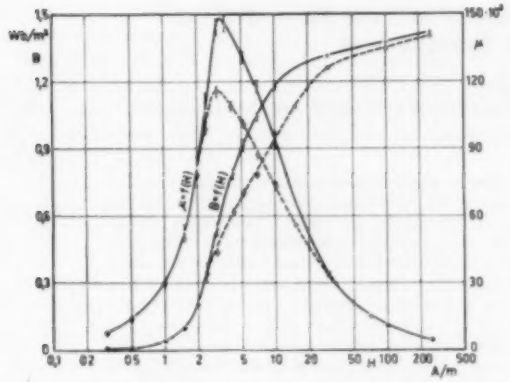

FIG. 1. Magnetization and permeability curves. Fe specimen annealed in H_2 at 1480°C for 18 hr. Irradiation with fast neutrons (>1 Mev). dose: 1.2×10^{18} fast and 1.24×10^{19} nvt (Melusine, Grenoble). Solid lines: before irradiation; dotted lines: after irradiation.

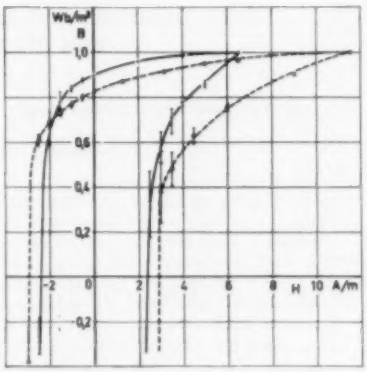

FIG. 2. Same as Fig. 1. Hysteresis loops with vertex at 1 Weber/m².

equivalent to that of weak fluctuating internal stresses of about 0.01 kg/mm² as an order of magnitude.

However, in addition to this possibility, the observed effects could also be due to some class of anisotropic defects which may interact with the magnetization vector. These defects distribute themselves anisotropically during irradiation according to the magnetization direction present at that time in each domain. In this condition, if the specimen could be tested with exactly the same domain distribution present during irradiation, we would observe an increased coercive force due to the additional field required to overcome the induced anisotropy energy present in each domain and wall. The effect would be strictly analogous to the one due to the pairs of solute atoms in alloys[6,7] when they are cooled slowly in the absence of field. If, as in our case, the specimens are demagnetized, the effect will be much smaller, but will still be present. In fact the new domain pattern will be completely random with respect to the previous one; however, in the material there is still an uniaxial anisotropy energy distributed at random according to the domain pattern present during irradiation. This random anisotropy energy, like an internal stress, can give rise to decreased permeability and increased coercive force.

Only successive experiments of recovery of the damage will clear the relative importance of the two contributions.

A preliminary experiment of annealing at 100°C, which already shows some recovery of the maximum permeability while the coercive force remains nearly the same, seems to suggest that both effects are present. A full discussion on this point will be given when these experiments are completed.

The presence of large defects, mainly dislocation rings produced by irradiation, has now been shown by the first results of the electron microscope transmission observations on irradiated aluminum, of Smallman and Westmacott[10] and of Hirsch and Silcox[11] on irradiated copper.

Our present results contribute to the demonstration, for iron, of the presence of such types of large defects by a completely different method. These results also show that this type of contribution is in any case very small from the point of influencing the magnetic properties of ferromagnetic alloys.

[10] R. E. Smallman and K. H. Westmacott, J. Appl. Phys. **30**, 603 (1959).

[11] J. Silcox and P. B. Hirsch, Phil. Mag. **4**, 1356 (1959).

Determination of Streaming Velocity and the Flow of Heat and Mass in High-Current Arcs

T. B. REED*
Speedway Laboratories, Linde Company, Division of Union Carbide Corporation, Indianapolis, Indiana
(Received May 2, 1960)

Arc plasma streaming velocities were calculated from previously unpublished experimental data obtained by H. N. Olsen on total pressure distributions at the anodes in 100- to 300-amp argon and helium arcs. The dynamic streaming component of pressure was calculated by subtracting the magnetic component (due to the self-magnetic field of the arc) from this total pressure. Arc temperatures also measured by Olsen were then used to calculate densities and heat contents of the plasma, and these were used with the streaming pressure to calculate velocities and mass and heat flow distributions. These in turn were integrated to give total mass and heat flows. The results compare reasonably with other measurements and estimates in the literature. Peak velocities range from 16 000 to 60 000 cm/sec, mass flows from 0.04 to 0.23 g/sec. The plasma heat flow distribution shows a close similarity in shape to values of heat transfer intensity at the anode measured by O. H. Nestor. A comparison of the total heat flow in the plasma to the total heat transfer due to streaming at a series of currents shows heat transfer proportional to (heat flow)$^{0.62}$ which agrees with correlations used for heat transfer from gases and flames. A simplified model of arc pumping is presented which suggests that heat and mass flow should increase as (current)^{1}. A simple analog experiment in mercury is described which illustrates graphically the streaming caused by a divergent current path in a conductor.

INTRODUCTION

IT has long been observed that unconfined high-current arcs are accompanied by a considerable flow of plasma, as evidenced by cathode and anode "flames," motions of particles in the arc, and forces exerted on the electrodes. Finkelnburg and Maecker[1] give a number of qualitative examples of this plasma streaming and a qualitative explanation of its origin. Wienecke[2] has measured these velocities by particle flow photographs and by measuring the time required to reinitiate an arc after the current has been stopped momentarily.

The purpose of this paper is to show that pressure distributions measured at the anode of a high-current atmospheric pressure arc can be combined with measured temperatures to give velocity of plasma streaming, heat and mass flux density, and total heat and mass flow in the anode region of the arc. The dependence of heat and mass flow on current is investigated and compared with measured anode heat transfer. A discussion of possible reasons for the observed functional dependence is included.

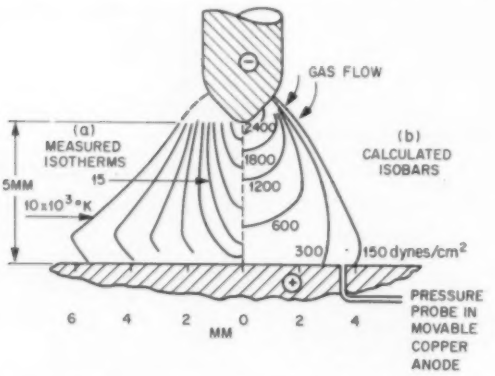

FIG. 1. (a) Measured temperatures in 200-amp normal mode argon arc according to footnote reference 3. (b) Isobars calculated from Eq. (3). Probe tube used in measuring stagnation pressures shown.

ORIGINS OF PLASMA STREAMING—MAGNETIC PRESSURES IN THE ARC

The plasma streaming is caused by Lorentz forces generated by the arc's self-magnetic field. These forces are related by the magnetohydrodynamic equation

$$(\vec{j}\times\vec{H})/c=\text{grad}\,p+\rho d\bar{v}/dt, \qquad (1)$$

i.e., the forces will produce a pressure gradient and streaming.

An exact knowledge of temperature and the physical properties of the plasma as a function of temperature enables one to understand better the origins of plasma streaming. Recent measurements in this Laboratory (see next section) give quantitative data on the temperatures in the arc, Fig. 1(a), and current densities at the anode. These measurements show that the current density in the arc can be closely approximated with a Gaussian distribution of the form

$$j(r)=(I/\pi R_0^2)\exp[-(r/R_0)^2], \qquad (2)$$

where $j(r)$ is the current distribution at a distance r from the axis, R_0 is the radius at which the current density falls to $1/e$ of its peak value, and I is the total current. For a static cylindrical plasma (see the following), Eq. (1) can be integrated using Eq. (2) to give the magnetically generated plasma pressure $p_m(r)$:

$$p_m(r)=(I j_0/c^2)[-Ei(-r^2/R_0^2)+Ei(-2r^2/R_0^2)], \qquad (3)$$

* Now at the Lincoln Laboratory, Massachusetts Institute of Technology, Lexington 73, Massachusetts.

[1] W. Finkelnburg and H. Maecker, *Handbuch der Physik* (Springer-Verlag, Berlin, Germany, 1956), Vol. 22, p. 296.

[2] R. Wienecke, Z. Physik, 143, 128 (1955).

where $Ei(-x)$ is the exponential integral and j_0 is the value of j at r equals zero.

Equation (3) will be used to calculate the magnetically generated plasma pressure in the anode region (where the arc is substantially cylindrical). The balance of the measured total pressure can then be attributed to the acceleration term.

Equation (3) was also used to give an approximate picture, Fig. 1(b), of the equivalent pressure gradients leading to the plasma streaming. Figure 1(b) was calculated from the measured current densities in the arc (discussed in the next section) by assuming that the z dependence of Eq. (1) can be neglected and integrating at each value of z as an ordinary differential equation dependent on r only. The vertical gradients in Fig. 1(b) are of the right magnitude to produce the observed streaming. The radial gas pressure gradient is, of course, balanced by the gradient of magnetic pressure, wherever radial acceleration can be neglected.

The appendix contains a description of an analog experiment which graphically illustrates the manner in which a divergent current path produces pumping (see Fig. 5).

MEASUREMENT OF ARC TEMPERATURES, CURRENT DISTRIBUTIONS, AND TOTAL ANODE PRESSURES

In the last few years a number of detailed measurements of arc temperatures have been made by H. N. Olsen[3] using spectral techniques. Figure 1(a) shows temperatures measured in a 200-amp normal mode argon arc. Detailed knowledge of temperatures thus obtained for the arcs studied was used to calculate densities, heat contents, and current distributions. A Gaussian distribution was fitted to the current distribution, and Eq. (3) was used to calculate magnetic pressures for each arc studied. Figure 1(b) shows a plot of the isobars for the same arc calculated from Eq. (3) and shows a vertical pressure gradient due to changing cross section. Measurements of current distributions at the anode surface have been made by Nestor[4] using a split anode; the radial distribution of current was derived by numerical integration of the Abel integral equation. Current distributions measured in this manner and those calculated from arc temperatures and conductivity data agree closely as shown in footnote reference 3.

Figure 1 shows a tube probe used to measure total pressure, $p_T(r)$ at the anode of an arc. A series of measurements were made by Olsen[5] of these pressures for three kinds of arcs, and the results are shown in Fig. 2. Most of the measurements were made on an argon arc operating in what is termed the contracted mode of operation. This is characterized by a very small cathode spot, higher voltages, higher temperatures in the cathode region, and, as will be seen, higher streaming

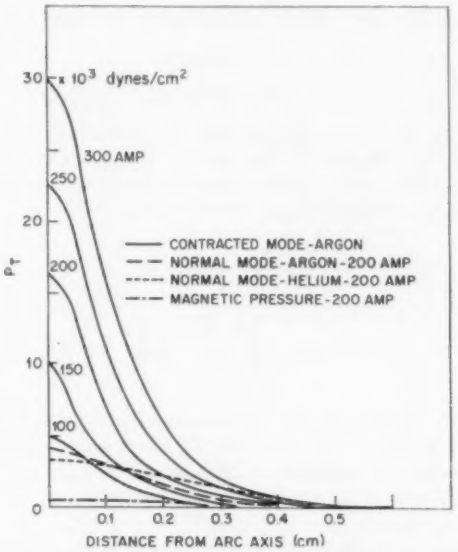

FIG. 2. Measured pressures for argon and helium arcs (footnote reference 5). Magnetic pressure correction p_m calculated from the equation for both 200-amp argon arcs shown ($\frac{1}{4}$-in. diam tungsten cathode, water-cooled copper anode, arc 0.5 cm long).

velocities than are found in the normal mode arc. Pressure measurements were also made on the normal mode, argon arc (more diffuse cathode attachment) and a normal mode helium arc, both at 200 amp. All arcs were run between a $\frac{1}{8}$-in. diam pure tungsten cathode and a water-cooled anode in a chamber at atmospheric pressure with a 0.5-cm arc length. No temperature measurement was available for the helium arc and so an average temperature of 18 000°K—the temperature at which the ionization is similar to that near the anode in argon arcs—was chosen for calculations.

CALCULATION OF PLASMA VELOCITIES AND FLOWS

Figure 2 also shows a typical example of the magnetic pressure which would exist at the anode as calculated from measured current distributions, using Eq. (3). These magnetic pressures p_m are considerably lower than the measured pressures on the axis, but become important near the edge of the arc, and the assumption will be made here that the balance of the pressure p_s is due to plasma streaming;

$$p_T(r)=p_m(r)+p_s(r). \tag{4}$$

It is assumed here that the component of velocity normal to the anode $v(r)$ can be computed from the Bernoulli equation, using the streaming pressure p_s and plasma density.

$$v(r)=[2p_s(r)/\rho(r)]^{\frac{1}{2}}. \tag{5}$$

A knowledge of velocity enables one to calculate the

[3] H. N. Olsen, Phys. Fluids **2**, 614 (1959).
[4] O. H. Nestor, Ph.D. thesis submitted to University of Buffalo.
[5] H. N. Olsen (private communication).

mass flow $g(r)$ and plasma streaming heat flow $q_s(r)$:

$$g(r)=v(r)\rho(r), \tag{6}$$

$$q_s(r)=v(r)h(r), \tag{7}$$

where $\rho(r)$ is the density and $h(r)$ is the heat content per unit volume of the plasma temperature. These equations can in turn be integrated to give total mass flow G and total plasma heat flow Q_s:

$$G=2\int_0^\infty \pi g(r)r\,dr, \tag{8}$$

$$Q_s=2\int_0^\infty \pi q_s(r)r\,dr. \tag{9}$$

The arc temperature distributions were used at the widest portion of the arc (Fig. 1). since current distributions are the same here as at the anode and the streaming plasma is not yet cooled and diverted by the anode.

RESULTS OF CALCULATIONS

Velocities

Figure 3 shows the velocity distribution at the widest part of the argon arc, both in contracted and normal mode operation, and for the helium arc. Peak velocities range from 1.6 to 6×10^4 cm/sec. The higher velocities for the contracted mode are due to higher current densities at the cathode. Finkelnburg and Maecker[1] estimate peak velocities in a 200-amp carbon arc to be 3.5×10^4 cm/sec and Wienecke[2] measured values in the cathode region which exceed 2×10^4 cm/sec. However, at the anodes of these fairly long arcs, peak velocities were about 0.25×10^4 cm/sec.

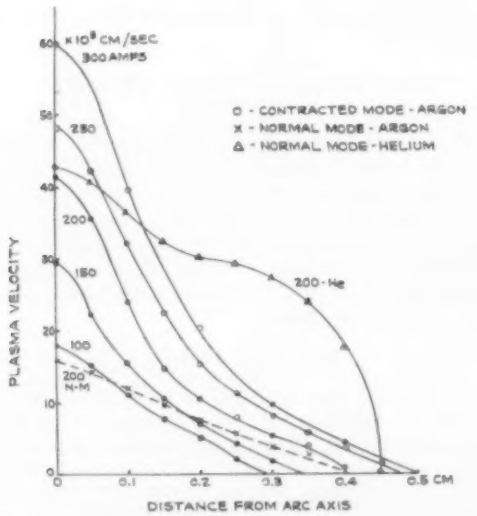

FIG. 3. Arc velocities calculated from Eq. (5) using measured pressures of Fig. 2 corrected for magnetic pressure.

Heat Transfer from Plasma Streaming

In footnote reference 4, the current distribution $j(r)$ and the anode heat transfer distribution $q_a(r)$ in arcs of this type have been measured. The measured heat transfer to the anode q_a is thought to be due partly to electron condensation q_{ac} [about 6.5 w/amp (v)], the combined effect of work function, about 4.5 v, and electron temperature and anode fall,[6,7] and partly to gaseous heat transfer from the high-velocity plasma streaming q_{as}. Figure 4 shows the heat flow at the widest point of the arc q_s calculated from Eq. (7), and the plasma heat transfer intensity calculated from the relation $q_a=q_{as}+6.5j$. Note that the distribution of the heat flow q_s is similar in shape to that of the heat transfer intensity q_{as} for the three different arcs.

Figure 5 shows a plot of total heat flow due to streaming in the arc plasma, Q_s, versus arc current. It also shows the total heat transfer due to streaming Q_{as} calculated from the measured total heat transfer by subtracting the electron condensation contribution Q_{ac} estimated as in the foregoing. From this it can be seen that heat transfer goes up as (heat flow)$^{0.62}$. This result is similar to the engineering correlation used for heat transfer from gases and flames.

Mass Flow from Plasma Streaming

Integration of the velocities in Fig. 3, according to Eqs. (8) and (9), gives heat and mass flows Q_s and G for

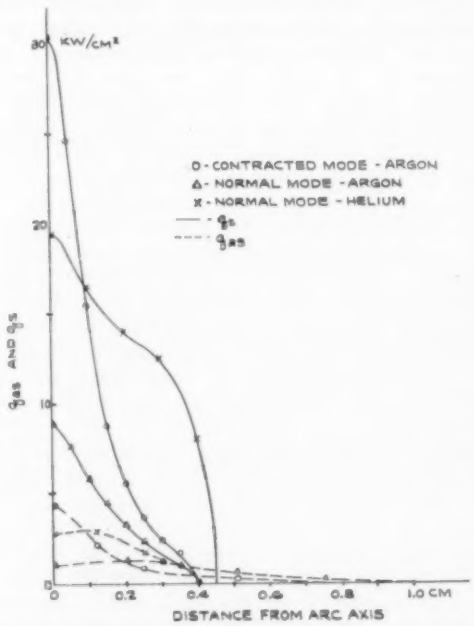

FIG. 4. Comparison of calculated heat flow distribution with heat transfer distribution as measured in footnote reference 4 for 200-amp arcs.

[6] J. F. Lancaster, Brit. Welding J. 1, 412 (1954).
[7] J. D. Cobine, *Gaseous Conductors* (Dover Publications, New York, 1958).

the various arcs. Table I summarizes the calculated flows in argon and helium arcs. The data on the contracted mode argon arc are plotted in Fig. 5, where mass flow is found to increase as (current)$^{1.52}$. The data in Table I and Fig. 5 for argon arcs agree in order of magnitude with related previous measurements. For example, Stresino[8] found that a minimum argon flow of about 0.1 g/sec was necessary to shield a tungsten welding arc from the atmosphere, and the author, using a null-pressure method[9] suggested by Morton,[10] measured mass flows in the region of the cathode of about 0.35 g/sec.

Table I shows that for the 300-amp arc, 5.15 kw of heat passes the widest point of the arc while 5.07 kw is generated electrically. This seems at first unreasonable, since electron condensation energy probably accounts (see the foregoing) for 2 kw of the total arc energy. An interesting explanation is possible. Since the arc is so short, it would seem reasonable that the hot gases rise from the anode and are drawn into the arc considerably above room temperature. This recirculation also makes it difficult to compare mass flow in the arc region with mass flow around the arc.

A word of caution is needed here in connection with this method of determining velocities. Measurements in footnote references 3 and 4 show that for argon arcs the current density at the anode surface is essentially the same as that at the widest part of the plasma. Arcs in diatomic gases, however, often develop an "anode foot," i.e., a contracted area at the anode which produces an anode flame moving toward the cathode which meets the cathode flame in the middle of the arc. In this case probe and temperature measurements would give the magnetic pressure p_m and another term due to the reaction pressure of the gases streaming away. These reaction pressures have been observed (see Finkelnburg and Maecker[1]).

Dependence of Flows on Current

Although interaction between plasma flow and current is too complex for a simple analytical explanation, the following model of arc pumping is offered to give a semiquantitative explanation of the observed dependence of mass and heat flow on current shown in Fig. 5.

The total flow is a function of both the pressures in the arc and the areas through which the gas streams. It is commonly observed that the cross-sectional area of

TABLE I. Calculated mass and energy flow in high-pressure arc plasmas.

Arc mode	Current amp	Total arc potential v	Mass flow G g/sec	Heat flow Q_e kw
Argon-contracted	100	18.2	0.046	0.57
	150	16.2	0.067	1.01
	200	16.2	0.136	2.36
	250	16.6	0.177	3.23
	300	16.9	0.226	5.15
Argon-normal	200	12.8	0.097	1.22
Helium-normal	200	22.5	0.038	6.74

[8] E. F. Stresino (private communication).

[9] These measurements were made with a loosely fitting chamber surrounding the cathode. Gas was supplied to the chamber and the mass flow was taken as that flow at which the pressure inside the chamber equaled the pressure outside.

[10] H. S. Morton (private communication).

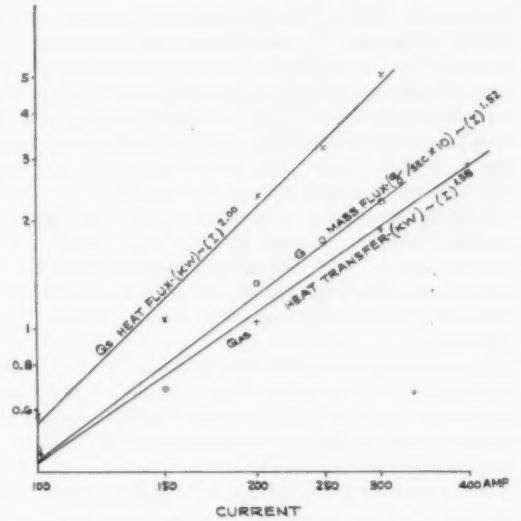

FIG. 5. Variation of total heat (Q) and mass (G) flow (across widest part of contracted argon arc) and estimated heat transfer to anode due to plasma streaming (Q_{ea}) with current.

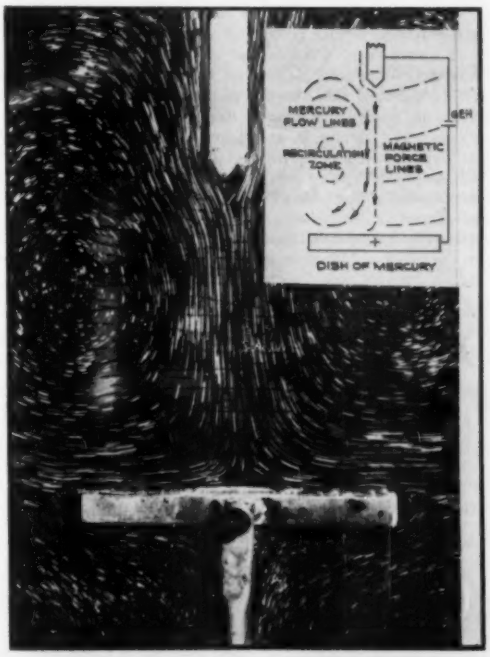

FIG. 6. Analog experiment showing flow induced in mercury by divergent current path.

the unconstricted arc is approximately proportional to current while peak current densities are independent of current. Then, according to Eq. (3), the pressure available to produce streaming is proportional to (current), and according to Eq. (5) the velocities resulting will be then proportional to (current)$^{\frac{1}{2}}$. Since the cross-sectional area is directly proportional to (current), this suggests that total flows should increase as (current)$^{\frac{1}{2}}$.

This simple picture is modified by the fact that as current increases in this range, temperatures also increase, so that velocity and heat flow should increase somewhat faster, while mass flow should increase slower than suggested by the foregoing. The data show this trend.

In conclusion it can be said that the magnetically produced streaming in the high current arc plays an important role in the over-all behavior of the arc and makes a very considerable contribution to the heat and mass transfer of the arc. The mechanism for the heat transfer appears to be analogous to that observed in flames.

I would like to thank H. N. Olsen and O. H. Nestor for supplying unpublished data for this work.

SIMPLE ANALOG EXPERIMENT DEMONSTRATING ARC PUMPING

A two-dimensional analog experiment was run in mercury to demonstrate the pumping which occurs in a divergent current path. A flat dish was filled to a depth of $\frac{1}{2}$ cm with mercury, and a small area electrode and large area electrode were connected to a generator to simulate the geometry existing in the arc (Fig. 6). With a current of 500 amp passing through the mercury, a vigorous streaming of mercury away from the small area electrode, with peak velocities of 5 cm/sec, was observed. A white powder on the surface shows the stream lines and velocities in a photograph exposed $\frac{1}{2}$ sec. A card was placed on the surface of the mercury and iron filings sprinkled on the surface to show the magnetic field lines. This was photographed and the two pictures superimposed in printing.

JOURNAL OF APPLIED PHYSICS VOLUME 31, NUMBER 11 NOVEMBER, 1960

In What Sense Do Slow Waves Carry Negative Energy?*

P. A. STURROCK
Microwave Laboratory, W. W. Hansen Laboratories of Physics, Stanford University, Stanford, California
(Received July 18, 1960)

It has been found in the theory of electron tubes that, according to the "small-amplitude power theorem," the fast and slow space-charge waves carry positive and negative energy, respectively. Similar analysis of different systems leads to similar results, leading one to conjecture that there is some sense in which one might assert that, for a wide class of dynamical systems, slow waves carry negative energy. In a one-dimensional model, "slow" and "fast" waves in a moving propagating medium refer to waves of which the phase velocity does or does not change sign, respectively, on transforming from the moving frame to the stationary frame. Small-amplitude disturbances of any dynamical system may be described by a quadratic Lagrangian function, from which one may form the canonical stress-tensor, elements of which are quadratic functions of the variables which appear in the linearized equations of motion. For any pure wave in this system, the energy density E and the momentum density P, as they appear in the canonical stress tensor, are related to the frequency ω and wave number k by $E=J\omega$, $P=Jk$, where $2\pi J$ is the action density. The rules for Galilean transformation now show that the energy densities, as measured in the stationary frame, of fast and slow waves have positive and negative sign, respectively, if (as is usually the case) the energy densities of both waves are positive in the moving frame. Similar arguments explain the signs of the energy density of the two "synchronous" waves which arise in the analysis of transverse disturbances of an electron beam in a magnetic field.

I. INTRODUCTION

ONE of the most illuminating and useful concepts in the theory of microwave tubes is the so-called "small-amplitude power theorem"[1-3] which was first given, in a very restricted form, by L. J. Chu.[4] It was found that, in simple cases, it is possible to ascribe to the particles of a modulated electron beam a "kinetic power," the formula for which involves only terms which appear in the linearized equations for the system, and which, when added to the Poynting flux of the associated electromagnetic field, is properly conserved. In more complicated cases, interaction terms arise. Certain simple but acceptable models for electron beams make it possible to analyze an arbitrary disturbance of a free beam into a "fast wave" and a "slow wave," the phase velocities of which are greater and less, respectively, than the particle velocity. The kinetic power of the fast wave is positive, that of the slow wave is negative; since the group velocities have the direction of the beam velocity, one must conclude that the corresponding energy density of the fast wave is positive, whereas that of the slow wave is negative.

* The research reported in this document was supported jointly by the U. S. Army Signal Corps, the U. S. Air Force, and the U. S. Navy (Office of Naval Research).
[1] W. H. Louisell and J. R. Pierce, Proc. I.R.E. 43, 425–427 (1955).
[2] H. A. Haus, *Noise in Electron Devices*, edited by L. D. Smullin and H. A. Haus (John Wiley & Sons, Inc., New York, 1959), pp. 77–153.
[3] P. A. Sturrock, Ann. Phys. 4, 306–324 (1958).
[4] L. J. Chu, paper presented at the Institute of Radio Engineers Electron Devices Conference, University of New Hampshire, June, 1951.

The small-amplitude power theorem has been the subject of some controversy which might be dispersed if it were generally agreed that the power which, in the framework of this theorem, is ascribed to the particle motion is not necessarily the correct or "physical" kinetic power of the beam, and that the usefulness of the theorem does not rest upon the equivalence of these two quantities. In solving the equations of motion, terms such as v_1 appear (where v is velocity) which are of first order in the amplitude, and also higher-order terms such as v_2 which is of second order in the amplitude. Terms such as v_2 must normally be obtained by solving nonlinear forms of the equations. It is important to note that such nonlinear terms are not determined uniquely by the linear terms: one may either complete the specification in an arbitrary way or, as is appropriate in electron-tube problems, by examining the way in which the wave is set up. It follows at once that we cannot expect to assert that the physical energy of a slow wave is negative, only that the energy of a slow wave *generated in a specified way* is negative.

The above point may be clarified by consideration of an ideal experiment. Let us accept that an appropriate coupler, excited in a certain way, will give rise to a slow wave on an electron beam and will, in the process, extract energy from the beam; this is one argument used by Pierce[5] to demonstrate that slow waves carry negative energy. Now consider a more complicated coupler in which the rf energy extracted from a beam in setting up the slow wave is converted to dc and then used to accelerate the beam. Such a coupler excites a slow wave with the same "small-amplitude" parameters, but in this case we should ascribe zero physical power to the slow wave since the coupler has neither added power to nor removed power from the beam. The analysis of Walker,[6] which aims at demonstrating the equivalence of the small-amplitude power theorem with the "physical" power theorem, contains an undetermined constant, the presence of which represents the impossibility of determining second-order quantities uniquely from first-order quantities. It is commonly believed that the negative-energy attribute of slow waves is peculiar to systems in which the vibratory motion is parallel to the dc velocity. Pierce[7] makes this assertion but points to what appears to be a counter-example: the experiment performed by C. C. Cutler, C. F. Chapman, and W. E. Mathews[8] on coupled torsional vibrations of the rims of two bicycle wheels rotating at different speeds. The instability of this system lends weight to the belief that slow waves in a moving medium capable of transverse vibrations again has negative energy in some sense, although one can see that the physical energy of any such disturbance must be positive.

As we have seen in discussing space-charge waves, we should not expect the physical energy of slow waves to be negative, although this may be so in particular propagating systems when the wave is excited in a particular way. We should therefore not be deterred from looking for a sense in which a slow wave can carry negative energy even in a system such as that considered in the previous paragraph. Indeed, the fact that one would wish to ascribe such an energy to a wave which is determined only in linear approximation requires that we look for an appropriate generalization of the small-amplitude power theorem rather than investigate the physical power of a class of propagating systems.

That such a generalization exists has been pointed out elsewhere.[2] It is possible to set up a small-amplitude energy theorem for any dynamical system, that is, for any system which may be described by an action principle. The Lagrangian function describing such a system may be expanded in a series of homogeneous polynomials in the dynamical variables representing the disturbance of the system from its quiescent state:

$$L=L^{(0)}+L^{(1)}+L^{(2)}+\cdots. \tag{1}$$

Since the term $L^{(0)}$ is independent of the dynamical variables, it may be ignored. Since the quiescent state, described by setting all dynamical variables equal to zero, is a solution of the Euler-Lagrange equations, we may ignore $L^{(1)}$ also. The lowest-order nonvanishing term is therefore $L^{(2)}$ which yields the linearized equations for the system. The fact that we have found a Lagrangian function to describe the "linear" system makes it possible to obtain, by standard procedures, conservation theorems for this system. It has been shown[2] that one may assign a complete stress tensor to the small-amplitude disturbances of an arbitrary electrodynamical system: this leads to the familiar small-amplitude power theorem as a special case. We shall show that it is this generalization of the small-amplitude energy theorem, applicable to any dynamical system, which enables us to assert that all slow waves carry negative energy.

II. THE SMALL-AMPLITUDE STRESS TENSOR

Consider a continuous dynamical system described by the action principle

$$\delta\int \mathfrak{L}d^3x dt=0, \tag{2}$$

where the Lagrangian density $\mathfrak{L}$ is expressible as

$$\mathfrak{L}=\mathfrak{L}\left(\phi_\alpha, \frac{d\phi_\beta}{dt}, \frac{d\phi_\gamma}{dx_\tau}, t, x_\sigma\right), \tag{3}$$

in terms of the dynamical variables $\phi_\alpha(x_\tau,t)$. We write $x_\tau(\tau=1, 2, 3)$ for the spatial variables and reserve the partial differential sign for functional differentiation as in $\partial\mathfrak{L}/\partial t$. We may now introduce the following

[5] J. R. Pierce, Bell System Tech. J. **33**, 1343–1372 (1954).
[6] L. R. Walker, J. Appl. Phys. **26**, 1031–1033 (1955).
[7] J. R. Pierce, J. Appl. Phys. **25**, 179–183 (1954).
[8] W. E. Mathews, Proc. I.R.E. **39**, 1044–1051 (1951).

variables which are canonically conjugate to ϕ_α

$$\Pi_{\alpha,t}=\frac{\partial \mathfrak{L}}{\partial(d\phi_\alpha/dt)}, \quad \Pi_{\alpha,r}=\frac{\partial \mathfrak{L}}{\partial(d\phi_\alpha/dx_r)}. \tag{4}$$

Then the Euler-Lagrange equations[9] derivable from (2) are

$$\frac{d\Pi_{\alpha,r}}{dt}+\sum_r \frac{d\Pi_{\alpha,r}}{dx_r}=\frac{\partial \mathfrak{L}}{\partial \phi_\alpha}. \tag{5}$$

We may now form from the Lagrangian function the canonical stress tensor[10] which has the following components

$$\left.\begin{aligned} T_{tt}&=\sum_\alpha \Pi_{\alpha,t}\frac{d\phi_\alpha}{dt}-\mathfrak{L}, \\ T_{tr}&=\sum_\alpha \Pi_{\alpha,r}\frac{d\phi_\alpha}{dt}, \\ T_{rt}&=\sum_\alpha \Pi_{\alpha,t}\frac{d\phi_\alpha}{dx_r}, \\ T_{rs}&=\sum_\alpha \Pi_{\alpha,s}\frac{d\phi_\alpha}{dx_r}-\mathfrak{L}\delta_{rs}. \end{aligned}\right\} \tag{6}$$

It is convenient to introduce the following symbols:

$$E=T_{tt}, \quad S_r=T_{tr}, \quad P_r=-T_{rt}; \tag{7}$$

E is the energy density, S_r the energy-flow (or "power") vector, P_r the momentum density, and $-T_{rs}$ the momentum flow tensor. We may verify from (5) that the following relations are satisfied

$$\frac{dE}{dt}+\sum_r \frac{dS_r}{dx_r}=-\frac{\partial \mathfrak{L}}{\partial t}, \tag{8}$$

$$\frac{dP_r}{dt}=\sum_s \frac{dT_{rs}}{dx_s}+\frac{\partial \mathfrak{L}}{\partial x_r}. \tag{9}$$

We see from (8) that if the Lagrangian function does not depend explicitly on time, energy is conserved; similarly, we see from (9) that if the Lagrangian function does not depend explicitly on any spatial coordinate, the corresponding component of momentum is conserved.

We now wish to consider wave propagation in such a continuous dynamical system. We suppose the system to be time-independent and uniform in one or more spatial coordinates. We may remove other coordinates from the problem by an appropriate normal-mode analysis. We now consider a wave-like solution of the equations, for which every dynamical variable is expressible as a function of the combination $\sum_r k_r x_r-\omega t$ of period 2π in this argument. In the particular case which is of interest to us (that the Lagrangian function is quadratic in its arguments), these periodic functions will be circular functions.

It has been shown elsewhere[11] that, for such a wave propagating in such a medium, the mean values of the energy density and momentum density are related to a quantity $2\pi J$, the "action density," in the following way

$$E=J\omega, \quad P_r=Jk_r. \tag{10}$$

The quantity J is obtained by introducing a phase angle κ into the expression for the wave function, for instance by replacing ωt by $\omega t+\kappa$, and then evaluating the expression

$$J=\frac{1}{2\pi}\int d\kappa \sum_\alpha \pi_{\alpha,t}\frac{\partial \phi_\alpha}{\partial \kappa}. \tag{11}$$

The relations (10) involving the wave energy density and momentum density, which are identical in form with the familiar relations of quantum mechanics between energy and frequency, momentum, and wave vector,[12] enable us to establish a sense in which slow waves carry negative energy.

III. SLOW WAVES AND NEGATIVE ENERGY

In order to obtain an appropriate generalization of the idea of "fast" and "slow" waves, we consider a *convected* propagating medium. From now on, we consider only one spatial coordinate z. We introduce primed quantities, such as z', for quantities referred to a frame of reference which is convected along with the medium. We retain unprimed quantities for measurements with respect to a fixed frame, and suppose that the medium is moving with velocity v in the z direction. Then the time and space coordinates of the two frames are related as follows

$$t=t', \quad z=z'+vt', \tag{12}$$

so that frequencies and wave numbers are related as follows

$$\omega=\omega'+vk', \quad k=k'. \tag{13}$$

We now consider the energy and momentum densities in the two frames. According to (10), the following relations should hold

$$\left.\begin{aligned} E&=J\omega, \quad P=Jk, \\ E'&=J'\omega', \quad P'=J'k'. \end{aligned}\right\} \tag{14}$$

The usual rules for transformation of a stress tensor on

[9] H. Goldstein, *Classical Mechanics* (Addison-Wesley Publishing Company, Inc., Reading, Massachusetts, 1950), Sec. 11-2.

[10] L. Landau and E. Lifschitz, *The Classical Theory of Fields* (Addison-Wesley Publishing Company Inc., Reading, Massachusetts, 1942), Sec. 4-7.

[11] P. A. Sturrock, "Field-theory analogs of the Lagrange and Poincaré invariants," Microwave Laboratory Report M.L. 689 (Stanford University, Stanford, California, 1960).

[12] L. I. Schiff, *Quantum Mechanics* (McGraw-Hill Company, Inc., New York, 1955), p. 17.

going to a moving coordinate system [13] require that

$$P=P', \quad E=E'+vP'. \tag{15}$$

The relations (15) are indeed compatible with (13) and (14), and show that

$$J=J'. \tag{16}$$

If we denote by u the phase velocity of a wave, so that

$$u=\omega/k, \quad u'=\omega'/k', \tag{17}$$

the second of the relations (15) may be rewritten as

$$E=\frac{u}{u'}E'. \tag{18}$$

Now consider two waves, with the same wave number, which propagate in opposite directions with respect to the moving reference frame; then $u'>0$ for the "forward" wave and $u'<0$ for the "backward" wave. If $v>|u'|$, both waves appear to be going forward in the fixed frame of reference; one is a "fast wave," traveling faster than the convected medium, and the other is a "slow wave," which travels slower than the medium. It we assume that, when looked at from the comoving frame, the medium looks the same for a wave traveling to the right as for a wave traveling to the left, E' will have the same value for both waves, if they have the same amplitude. Hence we see that the energy of the fast wave E_f and the energy of the slow wave, E_s, will be given by

$$E_f=\frac{v+u'}{u'}E'. \quad E_s=-\frac{v-u'}{u'}E'. \tag{19}$$

We see that the fast and slow waves do indeed have energies of opposite signs with respect to the fixed coordinate system. It will frequently, but not invariably, be true that E' gives the correct expression for the physical energy density in the frame moving with the medium; in this case, E' must be positive. We then see from (19) that *the fast wave carries positive energy and the slow wave carries negative energy.* It is interesting to note from the second of relation (19) that if the convected velocity is not great enough to convert the backward wave of the moving frame into a forward wave of the fixed frame, then the slow wave (which is now a backward wave) has positive energy.

IV. DISCUSSION

It must be emphasized that the relations (10), which make it possible to assign negative energy to slow waves in a general way, hold for the energy and momentum of a wave as defined by the small-amplitude stress tensor. In the case that the exact equations for the system are linear, it is not in general true that the canonical stress tensor is identical with the physical stress tensor. Nevertheless, the mean values of these quantities are identical[11] under conditions which lead to the action relation (10); moreover, it may happen that certain contributions to the canonical stress tensor can be directly related to physically significant quantities—such as Poynting flux.

We see from (10) that evaluation of the small-amplitude energy and momentum densities is a simpler process than evaluation of the corresponding nonlinear quantities, since all components may be derived from the one quantity J. Formula (11) for J is usually simpler to evaluate than corresponding direct expressions for E and P_r. Indeed, we may write down simple expressions for the remaining terms S_r and T_{rs} of the stress tensor. If, as we are here assuming, $\partial\mathfrak{L}/\partial t$ and $\partial\mathfrak{L}/\partial x_r$ vanish, we may use the properties of group velocity[11,14] to establish from (8) and (9) the following relations

$$S_r=E\frac{\partial\omega}{\partial k_r}, \quad T_{rs}=-P_r\frac{\partial\omega}{\partial k_s}. \tag{20}$$

Hence, by combining (10) and (20), we may write down the following expressions relating the sixteen components of the stress tensor to the action density

$$\left.\begin{aligned} E&=J\omega \qquad S_r=J\omega\partial\omega/\partial k_r, \\ P_r&=Jk_r, \quad T_{rs}=-Jk_r\partial\omega/\partial k_s. \end{aligned}\right\} \tag{21}$$

There are a few further points which should be noted concerning the relationship of the small-amplitude[11] stress tensor, the canonical stress tensor and the physical stress tensor. In setting up the canonical stress tensor for small-amplitude disturbances of electrodynamical systems,[2] the usual difficulty was found to arise, that formulas for components of the tensor were gauge-dependent. It was therefore expedient to modify the canonical tensor by adding a term which did not impair the conservation relations (8) and (9). The necessary transformation is of a type[11] which does not invalidate the relation (21).

The negative energy carried by slow space-charge waves explains the operation of traveling-wave tubes[5]; it also explains the difficulty of removing noise from the slow wave of an electron beam.[2] In looking for a mechanism for removing this noise, one might direct attention to the physical energy represented by the slow wave of a beam but this would be inadvisable. The problem of removing noise is simply the problem of coupling different types of electrodynamic systems, a problem which may be discussed by means of the linearized equations. Study of the small-amplitude energy theorem therefore provides information about this coupling problem; study of the physical stress tensor, on the other hand, provides information also about nonlinear effects of the wave equations and coupling mechanisms which are irrelevant to the problem of noise removal.

[13] P. M. Morse and H. Feshbach, *Methods of Theoretical Physics* I (McGraw-Hill Company, Inc., New York, 1953), pp. 98–100.

[14] L. Brillouin, *Wave Propagation in Periodic Structures* (McGraw-Hill Company, Inc., New York, 1946).

It has been noticed[15] that the formulas for kinetic power of an electron beam can yield the correct expression for the physical power lost by an electron beam in an electron tube, and it is interesting to see when and why this is so. Suppose that the beam enters the interaction region with power $S_{b,i}$ and that the input coupler introduces an electromagnetic field with power $S_{f,i}$; suppose also that the beam leaves the interaction region with power $S_{b,f}$ and that the output coupler removes field power $S_{f,f}$. The equation of conservation of energy requires that

$$S_{b,i}+S_{f,i}=S_{b,f}+S_{f,f}. \tag{22}$$

We first interpret (22) as relating the "physical" powers involved. However, we may set up an analogous relation between the powers assigned to the beam and field by the small-amplitude energy theorem

$$S_{b,i}'+S_{f,i}'=S_{b,f}'+S_{f,f}'. \tag{23}$$

(If the beam is initially unmodulated, $S_{b,i}'=0$.) In the usual statement of the small-amplitude energy theorem for electron tubes,[1-3] the expression for the power of an electromagnetic field alone gives correctly the physical power carried by this field; hence

$$S_{f,i}'=S_{f,i}, \quad S_{f,f}'=S_{f,f}. \tag{24}$$

We note that interaction terms in the expressions for energy flow do not appear in our equations since we are evaluating the power carried by various components of the system outside of the interaction region. We now see from (22), (23), and (24) that

$$S_{b,f}-S_{b,i}=S_{b,f}'-S_{b,i}', \tag{25}$$

which states that the physical power lost by the beam is equal to the power loss as evaluated by the small-amplitude power theorem. We can see that it is generally true that if an electrodynamic system interacts with an "external" field for a finite length of space or time, the small-amplitude formulas give correctly the loss of power or energy by this system.

It is interesting to return to consideration of transverse torsional waves in a moving medium. The analysis of Sec. III would lead us to assign negative canonical energy to slow waves in such a system. This is compatible with results of the experiment of Cutler, Chapman, and Mathews.[8] However, Pierce[7] has stated that "an analysis shows that when a torsional wave on a fixed rod is coupled purely by couples about the axes to the slow torsional wave on a parallel rod moving axially with the respect to the first, no gaining wave results." Pierce resolves the discrepancy between this statement and the experiment referred to by pointing out that the interaction mechanism in the experiment involves longitudinal forces. If, on the other hand, one looks for a resolution of this paradox within the framework of the small-amplitude energy theorem, one is led to conjecture that the mathematical model considered by Pierce was not a valid model of a dynamical system in that the equations were not derivable from a Lagrangian function.

In conclusion, let us consider briefly the theory of transverse-field electron tubes. It has been shown[16] that the motion of a filamentary electron beam in a longitudinal dc magnetic field may be analyzed into four waves. One pair of these waves, which Siegman terms cyclotron waves, is similar to space-charge waves in that one is "fast" and carries positive energy and the other is "slow" and carries negative energy. This is as we should expect. The other pair is termed "synchronous waves" since its phase velocity is equal to the dc beam velocity. Of these, it is found that one carries positive energy and the other negative energy, but it is not immediately obvious from our theory why this should be so.

The synchronous waves have the form of right-hand and left-hand helices convected with the beam velocity. Hence, in the comoving frame, these waves have zero frequency and hence zero canonical energy. Evaluation of energy in the laboratory coordinate system therefore turns upon evaluation of the momentum of the two waves, which will be the same in the laboratory system and in the comoving coordinate system. However, the presence of the magnetic field makes the medium anisotropic so that we cannot assert that the action densities of the two waves in the comoving frame should be equal if their amplitudes are equal. This anisotropy may be removed by going to the Larmor frame,[17] which rotates with half the cyclotron frequency. Hence the two waves, which were of the form

$$x+iy=re^{\pm ik(z-vt)} \tag{26}$$

in the original coordinate system, have the form

$$x'+iy'=e^{-i\omega_L t'\pm ikz'}, \tag{27}$$

in the comoving Larmor frame if the appropriate transformation is written as

$$x+iy=(x'+iy')e^{i\omega_L t'}, \quad z=z'+vt', \quad t=t'. \tag{28}$$

If the field is so directed that ω_L is positive, the waves characterized by plus and minus signs may be termed "antirotating" and "corotating." We expect both waves to have energy of the same sign in the Larmor frame so that the action densities which we should assign to both waves have the same sign. The momentum in the comoving Larmor frame is $\pm Jk$; this is the same in the comoving nonrotating frame and in the stationary frame. Hence, from (26), the energy densities of the two waves in the stationary frame are $\pm Jvk$. If, as we should expect, $J>0$, we see that the antirotating wave has positive energy and the corotating wave has negative energy. This is in agreement with Siegman's analysis.

[15] M. Chodorow, private communication.

[16] A. E. Siegman, J. Appl. Phys. **31**, 17–26 (1960).

[17] H. Goldstein, *Classical Mechanics* (McGraw-Hill Company, Inc., New York, 1950), section 5–8.

On the Incorporation of Neodymium in Mixed Yttrium-Neodymium-Iron Garnets*

G. GOLDRING, M. SCHIEBER, AND Z. VAGER
The Weizmann Institute of Science, Rehovoth, Israel

(Received April 11, 1960)

The preparation and saturation magnetization of yttrium-iron garnets containing various amounts of neodymium was investigated. The amount of Nd which can be incorporated in the garnet structure was determined crystallographically and magnetically. The chemical analysis of the Nd/Y ratio was carried out by the counting of the characteristic x rays of Nd produced by proton bombardment in a Van de Graaff accelerator. A compound with a formula of $YNd_2Fe_5O_{12}$ was found to be the richest iron garnet containing Nd and has a saturation magnetization, at room temperature, of 4.25±0.13 Bohr magnetons per formula weight compared to that of 3.55±0.13 of $Y_3Fe_5O_{12}$ or $Sm_3Fe_5O_{12}$.

INTRODUCTION

THE rare earth ions which can be included in the garnet structure are limited to the group from Sm to Lu. The reason for this limitation is that the ionic size is favorable for garnet formation for elements in this group, but it is too large in the case of Nd and lighter rare earth ions. However, Nd can be included in the garnet structure if Y is also added.[1] The cell dimensions of such a compound with a formula $Y_{1.5}Nd_{1.5}Fe_5O_{12}$ were given by Bertaut and Forrat.[2]

We were interested in ferromagnetic garnets which contain the maximum amount of Nd, but the investigation of such mixed garnets is hampered by the difficulties of the quantitative chemical analysis of the Nd/Y ratio.

In this paper, a method is described for determining the amount of Nd in the garnet. The saturation magnetization at room temperature and the purity of the garnet phase for the various amounts of Nd is reported, and compared with samarium-yttrium garnets.

METHOD OF PREPARATION

Preliminary trials were made by using the method described by Wolf and Rodrigue,[3] i.e., the coprecipitation of the rare earths and iron nitrates by NH_4OH, presintered at 1.000°C for several hours and finally pressed to pellets and fired to the desired temperature.

Other tests were made, which consisted of thorough mixing of the various oxides into pellets and firing directly to the desired final temperature. The saturation magnetization obtained with the two methods were equal and therefore Wolf and Rodrigue's method was not further used. The chemicals used in the synthesis were Fisher's certified analytical Fe_2O_3 and the rare earth oxides were 99% pure, certified by the Lindsay Company.

Stochiometric mixtures corresponding to the formula $Y_{3(1-x)}Nd_{3x}Fe_5O_{12}$ and $Y_{3(1-x)}Sm_{3x}Fe_5O_{12}$ were prepared, with different values of x, from 0 to 1. A small iron oxide excess of 1% of the total weight was added in order to avoid any perovskit formation.

The samples were mixed, pressed, and fired on a platinum surface for 10 hr to various temperatures in an oxygen atmosphere, and were ground and washed in a magnetic field in order to eliminate completely the nonmagnetic phase.

ANALYSIS OF THE CHEMICAL COMPOSITION

The analysis described here is based on the fact that elements emit their characteristic x rays when bombarded by high energy particles. These x rays are readily observed for the heavier elements and afford an easy means of identification, particularly in cases where the various constituents of a compound have widely different atomic numbers. The analysis was carried out by bombarding samples of the garnet material with 2 Mev protons from a Van de Graaff accelerator. The x rays emitted from the target were counted in a NaI crystal and the pulses were analyzed in a 100-channel pulse height analyzer. An example of the pulse spectra obtained is given in Fig. 1.

The number of x rays produced per bombarding particle in a target which is thicker than the range of the particles is given by

$$N=\frac{L}{M}\alpha\int_0^{E_{\max}}\frac{\sigma(E)dE}{\kappa(E)},$$

where L is Loschmidt's number, M is the atomic weight of the element under investigation, and α its relative amount by weight in the compound. $\sigma(E)$ is the cross section of the reaction and $\kappa(E)$ the energy loss of the particles in the target material per g cm^{-2}. $E_{\max}$ is the bombarding energy.

The energy loss $\kappa(E)$ is different for different elements and therefore depends somewhat on α. The function $N(\alpha)$ is therefore not strictly linear. A specific empirical determination of $N(\alpha)$ was carried out by bombarding samples of different Nd content. The results are shown in Fig. 2, in which the number of counts in the channel of the peak are given as a function of the Nd weight percentage in the material α and also as a function of the

* Part of a thesis of one of the authors (M.S.) to be submitted to the Hebrew University, Jerusalem, in partial fulfillment of the requirements for a degree of Doctor of Philosophy.

[1] F. Bertaut and F. Forrat, J. phys. radium **18**, 305 (1957).
[2] F. Bertaut and F. Forrat, Compt. rend. **242**, 382 (1956).
[3] W. P. Wolf and G. P. Rodrigue, J. Appl. Phys. **29**, 105 (1958).

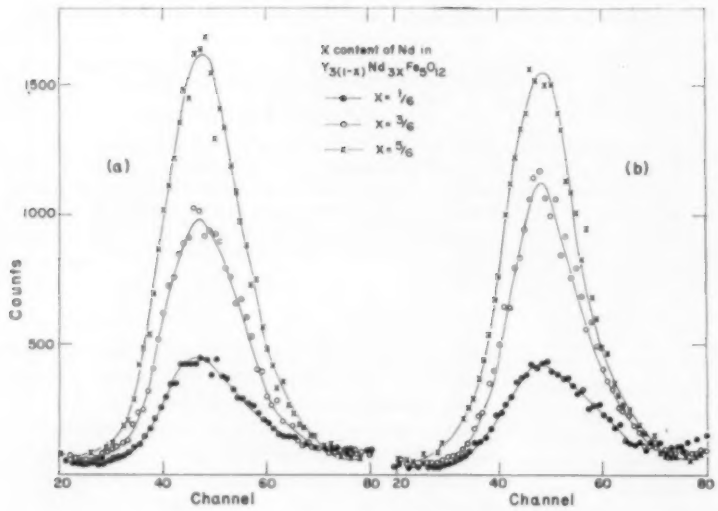

FIG. 1. Pulse spectra obtained for a mixture $Y_{3(1-x)}Nd_{3x}Fe_5O_{12}$ with $x=\frac{1}{6}$, $\frac{3}{6}$, and $\frac{5}{6}$ before and after garnet formation.

amount x of Nd in the composition $Y_{3(1-x)}Nd_{3x}Fe_5O_{12}$. It appears that within the accuracy of our measurements $N(\alpha)$ is linear.

Figure 1 shows the number of Nd x rays produced in some samples of garnet material both from the original mixture and then after firing. All the measurements were carried out with the same amount of charge falling on the target. It is obvious from Fig. 1 that the intensity of the x ray, and therefore the relative amount of Nd in the garnet, remained unchanged throughout the process of production. The same was found to hold true for all other samples.

RESULTS

Powder photographs were made in a Debye-Scherrer Camera of 57.5 mm diam, with CuK_α radiation filtered with nickel foil. It was found that a pure garnet phase was obtained only for amounts of Nd with x varying between 0 and $\frac{2}{3}$ of the Y-Nd combination.

The saturation magnetization moments compared with that of spectroscopic pure nickel were measured by the ponderometer method of Rathenau and Snoek[4] with spherical pole caps, at a field strength of about 9.000 oe. The saturation magnetization σ at room temperature of the neodymium- and samarium-containing samples is shown in Fig. 3. The optimum firing conditions for both series was at a temperature of 1340±20°C.

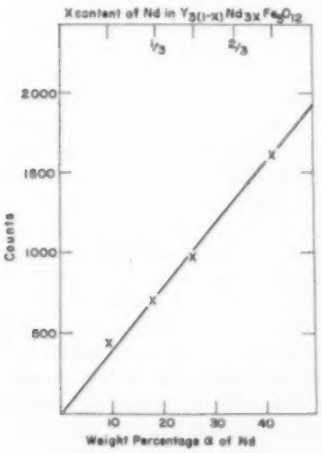

FIG. 2. Calibration curve, of counts in the channel of the peak vs Nd content x and weight percentage α for (a) the material before firing and (b) the material after firing.

FIG. 3. The saturation magnetization at room temperature σ in Bohr magnetons per formula weight as a function of the x content of neodymium or samarium R in the formula $Y_{3(1-x)}R_{3x}Fe_5O_{12}$.

[4] C. W. Rathenau and J. L. Snoek, Philips Research Repts. **1**, 239 (1946).

These results may be considered as unexpected. The substitutions of nonmagnetic ions like Y by the magnetic ions of Nd or Sm in the rare earth sublattice which is opposed to the two iron sublattices,[5] should reduce the magnetic moment.

However, our data for the samarium-yttrium-iron garnets series as given in Fig. 3 seem to agree with the results obtained by Cunningham and Anderson,[6] and are different from the neodymium-yttrium-iron garnet series prepared in the same conditions.

Traces of magnetite below the accuracy of x-ray measurements in our samples could have affected considerably the measured magnetic moments. However, the only opaque impurity found in the translucent petrographic garnet samples was some minor trace of hematite. As magnetite is also unstable in the oxygen atmosphere in the range of 700°C, another test was made.

[5] R. Pauthenet, thesis, University of Grenoble (1958).
[6] J. R. Cunningham, Jr., and E. E. Anderson, J. Appl. Phys. **31**, 45S (1960).

Our garnet samples and pure magnetite were treated for one hour with oxygen in a flow of 200 l/hr at a temperature of 700°C. The magnetic moments of the garnet samples after the treatment were practically unchanged, whereas the magnetite transformed itself into hematite and showed no ferrimagnetic moment.

It was found that, at 1450°, most of the neodymium-containing samples were melted. With the melting, the garnet structure was partially destroyed, but even at these firing temperatures, no appreciable losses of Nd were found.

The richer neodymium mixtures, with x values of $\frac{5}{6}$ and 1, showed no garnet structure in the x-ray analysis, but still exhibited magnetic moments.

ACKNOWLEDGMENTS

The authors wish to express their gratitude to Drs. S. Shtrikman and A. Aharoni for critical discussions of the work.

JOURNAL OF APPLIED PHYSICS VOLUME 31, NUMBER 11 NOVEMBER, 1960

Nonlinear Effects of Crystalline Anisotropy on Ferrimagnetic Resonance

PETER GOTTLIEB
Hughes Aircraft Company, Culver City, California
(Received February 12, 1960; and in final form, May 30, 1960)

The crystalline anisotropy of a ferrimagnetic solid will cause the magnetic resonance frequency to depend upon the angle of precession. It is shown that the resonance frequency depends quadratically upon the precession amplitude to lowest order. It is also shown that the dependence of this quadratic term upon the magnetic field orientation with respect to the crystal axis is the same as dependence of the usual zero-order resonance term upon orientation of the magnetic field. It is shown that the quadratic nonlinear term can cause a foldover of the resonance line, even in a spherical sample which is usually considered to have no foldover. The necessary conditions for the onset of this foldover are discussed, and some experimental results are mentioned.

INTRODUCTION

THE energy of an anisotropic ferrite depends upon the relative orientation of the magnetic field and the crystal axis. This anisotropy produces the well-known dependence of magnetic resonance frequency upon orientation of the applied field.[1] In Fig. 1 the field required for resonance is shown as a function of the angle in the $(1\bar{1}0)$ plane for a cubic crystal. (The experimental and theoretical sources of this type of curve are well known, but, for those unfamiliar with this work, a calculation of this linear anisotropy is included in the Appendix.) Now, if we consider the dc field to lie along the [100] direction, and we increase the rf driving field at the resonance frequency in the transverse plane, then the total magnetization will precess about the [100] direction at some finite angle of precession θ_1. Figure 1 shows that the resonance frequency changes as the precession angle goes from 0° to θ_1, and thus the resonance frequency is a function of rf signal amplitude. This means that the ferrite has a nonlinear response to the rf field.

Experimentally, one frequently encounters other nonlinear effects which mask the effect of anisotropy. The largest and most common nonlinear effect is due to the dependence of resonant frequency upon particular components of magnetization through the inequality of the demagnetizing factors along the principal axes of a nonspherical sample. Another nonlinear effect is due to the unstable amplification of spin waves, discussed by H. Suhl.[2] Another possibility is the g factor dependence on spin temperature, discussed by M. T. Weiss.[3] The choice of which of these factors is dominant is governed

[1] Joseph O. Artman, Proc. I.R.E. **44**, 1284 (1956).
[2] H. Suhl, J. Phys. Chem. Solids **1**, 209 (1957).
[3] M. T. Weiss, J. Appl. Phys. **30**, 2014 (1959).

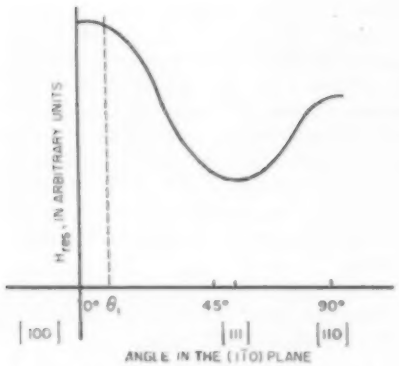

FIG. 1. Magnetic field required for resonance as a function of the angle between the crystal [100] axis and the applied dc field in the (1$\bar{1}$0) plane.

by the particular experimental situation. It is also possible to obtain conditions under which all of the above effects will be negligible compared to the effect of anisotropy. This has been mentioned by M. T. Weiss in the last paragraph of footnote reference 3, as occurring in single crystal YIG at 125°K.

After the intuitive discussion given in connection with Fig. 1, we would like to obtain more quantitative results. In patricular, we would like to find the lowest-order nonlinear term in the expression for resonance frequency. In general, we can write the resonance frequency, to lowest order in the nonlinearity, as

$$\omega_r=\gamma H_0-\kappa\theta^2=\omega_0-\kappa\theta^2, \tag{1}$$

where H_0 is the internal dc magnetic field, $\theta=|\bar{m}|/|\bar{M}_0|\,\hat{m}$, is the ac magnetization perpendicular to $\bar{M}_0$, and $\bar{M}_0$ is the dc magnetization. The constant (independent of θ) κ will depend on all the previously mentioned nonlinear effects. However, we can obtain the total effect of all the nonlinearities to this order simply by calculating the constant for each nonlinearity, disregarding the presence of the other nonlinearities, and adding all the constants together to get κ. In the following discussion we shall be concerned only with the effects of anisotropy; the value of κ depending only upon this factor is calculated for a cubic crystal in the Appendix. The result is given by Eq. (A8), and is seen to depend upon the orientation of the dc magnetic field. The meaning of this result will be discussed more fully subsequently.

ANALYSIS OF FOLDOVER[4]

We now wish to obtain the minimum value of h_0 which will give foldover (h_c will be defined as this minimum value of h_0). With the resonance frequency as shown in Eq. (1), we can write θ in the usual resonator equation

$$\theta^2=\frac{\gamma^2h_0^2}{(\omega-\omega_r)^2+(\gamma\Delta H)^2}, \tag{2}$$

where ΔH is the linewidth and h_0 is the incident signal magnetic field. We can eliminate ω_r between Eqs. (1) and (2) to obtain

$$\theta^2=\frac{\gamma^2h_0^2}{(\kappa\theta^2-\delta)^2+(\gamma\Delta H)^2}, \tag{3}$$

where $\delta=\omega_0-\omega$. The amplitude θ is obviously not a maximum for $\delta=0$ so the resonance frequency is shifted from ω_0. In fact, from Eq. (3) we can see that $d\theta/d\delta=0$ for $\delta=\kappa\theta^2$ and the resonance frequency is given by ω_r of Eq. (1). If we take the substitution $\kappa\theta^2=y+(2/3)\delta$, then Eq. (3) simplifies to the normal cubic form

$$y^3+y[(\gamma\Delta H)^2-(\delta^2/3)]+(2\delta^3/27)+(2\delta/3)(\gamma\Delta H)^2-\kappa\gamma^2h_0^2=0. \tag{4}$$

Foldover will occur when there are three real roots of this equation as shown in Fig. 2. The condition for three real roots is obtained from the formula for the solution of a cubic. Equation (4) will have three real roots when

$$\frac{[(2\delta^3/27)+(2\delta/3)(\gamma\Delta H)^2+(\kappa\gamma^2h_0^2)]^2}{4}+\frac{[(\gamma\Delta H)^2-(\delta^2/3)]^3}{27}\leq 0. \tag{5}$$

When the equality holds in Eq. (5), two of the roots become equal as at H_a and H_b in Fig. 2. The onset of foldover will occur for the minimum h_0 which gives three real roots of Eq. (4), or the h_0 which gives all three roots equal. In this case both terms of Eq. (3) are zero and

$$\delta=\pm\gamma\Delta H\sqrt{3}. \tag{6}$$

It is obvious that δ must have the same sign as κ in order for the first term of Eq. (5) to be zero. (There can only be foldover in one direction.) The minimum value of h_0 which will give foldover is found by substituting Eq. (6) in Eq. (5), with the equality holding, to obtain

$$\kappa\gamma^2h_c^2=\pm(8/9)\sqrt{3}(\gamma\Delta H)^3. \tag{7}$$

This form agrees with the result of an unpublished memorandum of H. Suhl.[5] The minus sign in Eq. (7) is used for negative κ and gives a negative value of δ as would be expected from Eq. (1).

In general, if Eq. (4) is solved for θ, the resulting expression is too cumbersome to provide any direct information. We can see, however, from the general formula for the solution of a cubic, that $d\theta/d\delta=\infty$ at H_a and H_b, as it is evident from Fig. 1.

Now, as shown in the Appendix, Eq. (A8), κ will be $9\gamma H_Au$, where H_A is the anisotropy field k_1/M and u is

[4] Foldover is the term used to signify the possibility of having more than one precession angle response to a given signal at a given dc field.

[5] H. Suhl (private communication).

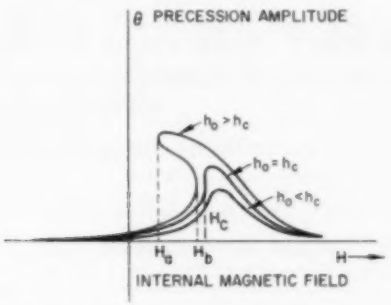

FIG. 2. Anharmonic response for positive κ.

a numerical factor [the factor in brackets in Eq. (A8)] which varies between $+1$ and $-\frac{2}{3}$ depending on crystal orientation. Since this analysis will apply only when h_0 is less than ΔH, we can see from Eq. (7) that the approximate requirement which the material must satisfy (in order to have large enough linewidth to give foldover) is

$$|uH_A| > |\Delta H|\,(8/81)\sqrt{3}.$$

(H_A is usually negative and will be assumed so here.) If H_A and the linewidth are given, then the threshold field for foldover can be calculated from Eq. (7). If we take the values for YIG at 125°K, $\Delta H = 2$ oe, $H_A = -100$ oe, then $h_c = 0.12$ oe in the [100] direction, $h_c = 0.15$ oe for the [111] direction, and $h_c = 0.23$ oe for the [110] direction. The direction of foldover shown in Fig. 2 is for positive κ, as can be seen from Eq. (1). From the expression for κ given in the Appendix we can see that the foldover will be toward the low field for magnetization in the hard (100) direction (negative κ), and toward the high field for the easy direction (positive κ). These results are in qualitative agreement with the experiments reported by M. T. Weiss (private communication).

APPENDIX[6]

The dependence of κ upon the magnetic field direction is calculated here by successive approximations of the nonlinear equations of motion. Damping is neglected, but this is consistent with the accuracy of Eq. (2) to the lowest order in damping. If the coordinate axes x, y, z lie along the crystal axes, then the energy of the magnetic-spin system can be written in the usual form (with the lowest-order anisotropy terms)

$$E = (M_x H_x + M_y H_y + M_z H_z) + k(M_x^4 + M_y^4 + M_z^4), \quad \text{(A1)}$$

where M is the magnetization, k is the anisotropy constant, and H is the applied magnetic field. For simplicity let the directions of cosines of M and H be (x,y,z) and (x_0,y_0,z_0), respectively.

$$E = MH(xx_0 + yy_0 + zz_0) + kM^4(x^4 + y^4 + z^4). \quad \text{(A2)}$$

The anisotropy term is frequently written as $-k_1(x^2y^2 + y^2z^2 + x^2z^2)$. Since the sum of the squares of the cosines is always equal to one (conservation of magnetization), it is seen that $2kM^4 = k_1$. The equations of motion for the magnetization M can be expressed conveniently in terms of the vector $\mathbf{r}$ with components x, y, z. The torque equations can then be written in the vector form

$$d\mathbf{r}/dt = (\mathbf{r} \times \nabla)E,$$

and the components are

$$\begin{aligned} \dot{x} &= c(yz_0 - zy_0) + b(yz^3 - zy^3) \\ \dot{y} &= c(zx_0 - xz_0) + b(zx^3 - xz^3) \\ \dot{z} &= c(xy_0 - yx_0) + b(xy^3 - yz^3), \end{aligned} \quad \text{(A3)}$$

where $c = \gamma H$ and $b = 4kM^3\gamma = 2\gamma k_1/M$. We could eliminate the third equation of (A3) by imposing the condition of conservation of magnetization (as is usually done), but for the present analysis it is advantageous to postpone this step in order to be able to treat all field orientations to the same degree of approximation. Now, for the equilibrium situation the time derivatives of x, y, z are zero. Then the well-known solution of Eq. (A3) will give (to zero order in the anisotropy constant b) $x = x_0$, $y = y_0$, $z = z_0$. To calculate the effects of the anisotropy it is simplest to go to the next highest order with the substitutions

$$\begin{aligned} x &= x_0 + a_1 e^{i\omega t} + a_1^* e^{-i\omega t} + g_1 + O_1(b) \\ y &= y_0 + a_2 e^{i\omega t} + a_2^* e^{-i\omega t} + g_2 + O_2(b) \\ z &= z_0 + a_3 e^{i\omega t} + a_3^* e^{-i\omega t} + g_3 + O_3(b). \end{aligned}$$

The constant terms $O(b)$ are linear in b and have been added so that the constant terms of Eq. (A3) will cancel to first order in b. The g's have been added to conserve M, they are constant in time and are quadratic in the a's. We then substitute these expressions into Eq. (A3) and retain only those terms with $e^{\pm i\omega t}$ time variation and containing a's up to the third order. The equations of motion then become

$$\begin{aligned} i\omega a_1 = {} & c(a_2 z_0 - a_3 y_0) + b\{y_0 a_3(3z_0^2 - y_0^2 \\ & + 3a_2 a_2^* - 6a_3 a_3^*) - 3y_0 a_3^* a_2^2 \\ & + a_2[3(z_0^2 - y_0^2)g_3 - 6y_0 z_0 g_2] \\ & + z_0 a_2(z_0^2 - 3y_0^2 + 6a_3 a_3^* - 3a_2 a_2^*) \\ & + 3z_0 a_2^* a_2^2 + a_3[3(z_0^2 - y_0^2)g_2 + 6y_0 z_0 g_2]\}, \\ i\omega a_2 = {} & c(a_3 x_0 - a_1 z_0) + b\{z_0 a_1(3x_0^2 - z_0^2 \\ & + 3a_1 a_1^* - 6a_3 a_3^*) - 3z_0 a_1^* a_3^2 \\ & + a[3(x_0^2 - z_0^2)g_3 + 6x_0 z_0 g_1] \\ & + x_0 a_3(x_0^2 - 3z_0^2 + 6a_1 a_1^* - 3a_2 a_2^*) \\ & + 3x_0 a_3^* a_2^2 + a_2[3(x_0^2 - z_0^2)g_1 - 6x_0 z_0 g_2]\}, \end{aligned}$$

[6] The results of this Appendix are strictly true for only spherical or infinite geometry. For nonspherical geometry the difference in demagnetizing factors will shift the resonance frequency. If this shift is small compared to the original resonance frequency, then the nonlinear effect of the demagnetizing factors can simply be found by making the appropriate change in κ, as is mentioned in the Introduction. If the frequency shift is not small compared to the resonance frequency, then any foldover will be mainly due to the difference in demagnetizing factors, and the calculation of that part due to the anisotropy will not be necessary.

$$i\omega a_3 = c(a_1y_0 - a_2x_0) + b\{x_0a_2(3y_0^2 - x_0^2 + 3a_2a_2^* - 6a_1a_1^*) - 3x_0a_2^*a_1^2 + a_1[3(y_0^2 - x_0^2)g_2 - 6x_0y_0g_1] + y_0a_1(y_0^2 - 3x_0^2 + 6a_2a_2^* - 3a_1a_1^*) + 3y_0a_1^*a_2^2 + a_2[3(y_0^2 - x_0^2)g_1 + 6x_0y_0g_2]\}. \quad (A4)$$

There are also three more equations which are the complex conjugates of the above three. The resonance condition that the determinant of the coefficients of the a's should vanish can be represented by

$$\begin{vmatrix} A & D \\ D^* & A^* \end{vmatrix} = 0, \quad (A5)$$

where A and D are 3 by 3 matrices. In this procedure there is some ambiguity concerning the terms of Eq. (A4), which are cubic in the a's. Any one of the a factors could be considered the variable, and the other two factors would contribute to the above coefficient matrix. However, the value of this determinant can be shown to be independent of which "a" factor plays the role of variable. Thus, for simplicity, Eq. (A5) was obtained by using the grouping already suggested in Eq. (A4). In this case it is evident that the terms of D are all linear in b. Thus the terms of D will enter into Eq. (A5) only in terms of order b^2. If we consider only frequency shifts of order b, then we can neglect D. This is consistent with choosing (x, y, z) so that the constant terms in the equation of motion will cancel to first order in b. Equation (A5) now factors into two cubic equations for ω. These equations are identical and can be further reduced by factoring ω from all the terms.

Interpretation of the resulting frequency equation requires the expression of all the aa^*'s and g's in terms of the transverse magnetization amplitude θ. We note that two of the a's can be expressed in terms of the third a through the use of the lowest order terms in the equations of motion (A3). The anisotropy terms will cause corrections of first order in b, but since the aa^* terms are already multiplied by b the extra correction can be neglected. We can then determine the a's in terms of θ from the definition

$$a_1a_1^* + a_2a_2^* + a_3a_3^* = \theta^2. \quad (A6)$$

The lowest-order terms in g in the equations of motion must cancel since they are constant in time. Thus we must have $g_1 = x_0G$, $g_2 = y_0G$, and $g_3 = z_0G$. In order to determine G in terms of θ, we impose the condition of conservation of magnetization

$$x^2 + y^2 + z^2 = 1.$$

To first order in b and second order in a, this can be written as

$$(x_0 + O_1)^2 + (y_0 + O_2)^2 + (z_0 + O_3)^2 + 2\theta^2 + 2(x_0^2 + y_0^2 + z_0^2)G = 1.$$

Since the O's just produce a rotation due to the static anisotropy,

$$(x_0 + O_1)^2 + (y_0 + O_2)^2 + (z_0 + O_3)^2 = 1.$$

Thus $G = -\theta^2$ and the characteristic equation can be written as

$$\omega^2 = c^2 + cb\{2 - 10(x_0^2y_0^2 + y_0^2z_0^2 + z_0^2x_0^2) + 9\theta^2 \times [-1 + 5(x_0^2y_0^2 + y_0^2z_0^2 + x_0^2z_0^2)]\}. \quad (A7)$$

If we take the square root of this expression and expand it to first order in b, we will find that the terms independent of θ^2 agree with the well-known expressions for the frequency shift due to anisotropy. (See, for example, the derivation of J. O. Artman.[1] The expression given there must, of course, be expanded to first order in the anisotropy constant in order to agree with the present one.) Then Eq. (A7) is seen to correspond to Eq. (1) with

$$\kappa = 9b/2[-5(x_0^2y_0^2 + y_0^2z_0^2 + x_0^2z_0^2) + 1], \quad (A8)$$

where $b = 2\gamma K_1/M = 2\gamma H_A$. It is rather surprising that the angular dependence of this expression is the same as that of the linear anisotropy effect, as can be seen from Eq. (A7). This general expression for κ agrees with the particular values in the (100) and (111) directions derived by E. Schlömann.[7]

By comparing Eq. (A7) and Eq. (A8) we can see why the choice of sign for κ in Eq. (1) was advantageous. The linear anisotropy effect is always opposite in sign from the nonlinear effect. This is to be expected from the intuitive description given in connection with Fig. 1. Near the maximum at $\theta = 0$ in Fig. 1 the linear effect has shifted the resonance field to a higher value than it would have had in the absence of anisotropy. Now the maximum has negative curvature so that the nonlinear effect will lower the resonance field. The same argument can be repeated in reverse for the minimum. This description cannot be applied to the maximum at $\theta = 90°$ in Fig. 1 because this point is a minimum as a function of angle in the (100) plane.

ACKNOWLEDGMENT

The author wishes to thank Dr. M. T. Weiss for suggesting this problem and for many helpful discussions concerning the solution.

[7] E. Schlömann, "Ferromagnetic resonance at high power levels," Raytheon Rept. No. R-48, Raytheon Company, Waltham, Massachusetts (1959).

Letters to the Editor

Modification in Technique for Growing Single Crystals of ZnF_2:Mn

L. M. Matarrese and F. L. Hughes
U. S. Naval Research Laboratory, Washington 25, D. C.
(Received July 26, 1960)

LATELY there has been a considerable amount of experimental and theoretical work on electron and nuclear magnetic resonance spectra involving single crystals of ZnF_2 containing transition metal ions as dilute substitutional impurities.[1,2] Large single crystals of pure MnF_2, FeF_2, and CoF_2 have been obtained[3,4] from the melt by the moving-crucible technique,[5] usually in an atmosphere of anhydrous HF and in graphite crucibles with conical tips. In utilizing the same technique to grow single crystals of ZnF_2 with small additions of MnF_2, we consistently obtained crystals of poor optical quality. Although the boules contained large crystals, they were uniformly clouded with striae of minute bubbles, except for the exterior, which consisted of a thin shell of clear material 1–2 mm thick. The same difficulty has been experienced by others[6] in the growth of ZnF_2:Co and pure CoF_2 crystals. The purpose of this letter is to describe a modification to the growing procedure that has eliminated the difficulty for us in three consecutive trials.

The modification consists of placing a grooved and slotted insert of graphite into the crucible along with the starting powder. Figure 1 shows this insert and its location in the crucible. Not shown are the crucible cover and a graphite stick between the cover and insert, which restrains the insert from floating on the melt. We have obtained good results also with a crucible that has a tip with a square cross section and flat bottom, rather than the conical tip shown in the figure. The crystal grows into the grooves and slot of the insert, and all the material, including that in the crucible tip and that above the insert, is clear and bubble-free.

Crystals were grown in an apparatus similar to that which had been used in growing crystals of the pure fluorides.[3,4] The crucible had an i.d. of $\frac{3}{4}$ in., an o.d. of 1 in., and an interior length of 4 in. It was supported on a nickel elevating rod that traveled along the axis of a vertical tube furnace about 3 ft long. The furnace tube is a nickel pipe with an o.d. of 2.875 in. and an i.d. of 2.469 in. In the lower part of the furnace the o.d. was reduced to 2.75 in. in an effort to improve the thermal gradient in the crystallization region between the upper and lower parts of the furnace. The nickel pipe is provided with a closely fitting carbon liner of 2 in. i.d. in order to reduce the infiltration of impurities from the nickel pipe. The crucible was started in the upper part of the furnace where the temperature was about 200°C in excess of the melting temperature, then lowered at the rate of 0.16 in./hr through a temperature gradient of about 150°C/in. near the middle of the furnace, where the temperature was maintained at the melting point of ZnF_2(870°C). The run continued for 72 hr, after which the power was turned off and the furnace allowed to cool. During the entire run a slow stream of dry HF was passed through the furnace tube, from bottom to top.

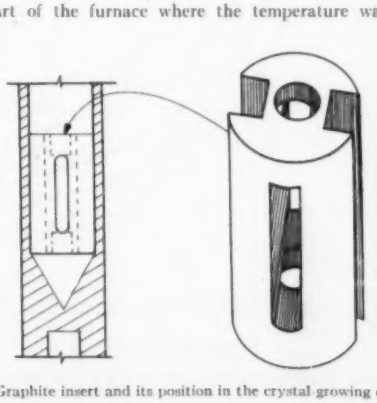

FIG. 1. Graphite insert and its position in the crystal-growing crucible.

TABLE I. Arc spectral analysis of a boule of ZnF_2:0.01 Mn.

Impurity	Top	Content, mole fraction Middle	Bottom
Mn	>	0.01	=
Ni	>	0.01–0.1	=
Fe	>	0.001–0.01	=
V, Al, Ca	>	0.0001–0.001	=
Co	=	0.0001–0.001	=
Mg	<	0.00001–0.0001	=
Si	=	0.00001–0.0001	=
Cu	>	0.000001	=
Cr, Cb	>	...	<

Initially, the crucible was charged with a mixture of 99 parts of ZnF_2 and 1 part of MnF_2 powder (cp grade). The ZnF_2 had been prepared by adding XX grade Horsehead ZnO (New Jersey Zinc Company) to cp semiconductor grade hydrofluoric acid and collecting the precipitate, which is $ZnF_2{\cdot}4H_2O$. Dehydration was accomplished by a preliminary heating at 200°C of powder mixture under HF atmosphere in the same crucible and furnace used for crystal growing, just prior to a run.

Table I gives an idea of the segregation of impurities in a boule grown under the foregoing conditions, using a crucible with a square tip. Specimens were taken from the square bottom of the boule, the middle of one of the sections grown in a side groove, and the top edge of the section that grew above the insert. The symbols in the "Top" and "Bottom" columns refer to the inequality or equality of the concentration of impurities in the top and bottom specimens compared to the impurity content of the middle specimen. The relatively large amounts of Ni and Fe evidently came from the furnace walls.

Our conjecture is that our previous failures with ZnF_2 were caused by an inability to maintain the proper critical temperature distribution within the crucible in spite of the similarities of our apparatus to that which had produced good results in the past with the other fluorides.[3,4] The insert, we believe, aids materially in achieving this distribution by providing a sink for the heat of crystallization, thus providing at the liquid-solid interface a sufficiently large thermal gradient to eliminate such imperfections as bubbles.

[1] M. Tinkham, Proc. Roy. Soc. (London) **A236**, 535, 549 (1956).
[2] A. M. Clogston *et al.*, Phys. Rev. **117**, 1222 (1960).
[3] M. Griffel and J. W. Stout, J. Am. Chem. Soc. **72**, 4351 (1950).
[4] L. M. Matarrese, Ph.D. dissertation, University of Chicago, Chicago, Illinois, 1954.
[5] D. Stockbarger, Rev. Sci. Instr. **7**, 133 (1936).
[6] E. Catalano (private communication).

Alkali Vapor Plasmas*

M. A. Hakeem and Harry S. Robertson
Department of Physics, University of Miami, Coral Gables, Florida
(Received May 26, 1960)

THE positive column of a glow discharge would be a convenient laboratory plasma for a variety of experimental purposes, if it were free of standing or moving striations. Molecular gases usually seem to show standing striations, and the noble gases and mercury vapor, as reported by Donahue and Dieke,[1] exhibit moving striations over the range of current and pressure most convenient for many experimental purposes. Since the alkali metals have no neutral-atom metastable states, it was expected[2] that alkali vapor glow discharges should be free of moving striations.

We have found, with the exceptions to be noted, no moving striations in alkali vapor positive columns. We have examined potassium, rubidium, and cesium, in the current range from 0 to 300 ma and the pressure range of about 0.01–2.0 mm Hg. Atom densities in this range are $3(10)^{14}$–$3(10)^{15}$ cm^{-3}. We have looked thoroughly over this range, both at the light emitted as a function of time and position, and at the tube voltage. We have used tubes of 1.8 cm and 3.0 cm diameter, 30 cm between tantalum electrodes. A pool of the metal is kept in a reservoir in a side arm of the sealed tube. The reservoir temperature, which is lower than that of the discharge tube, determines the vapor pressure in the tube. No metal was observed to have condensed on the walls of the discharge tube. No filler gas such as argon was used, and the tubes were sealed at a background gas pressure of about 10^{-5} mm Hg.

At the lowest operable pressures and at currents of 1 ma or less, very faint standing striations were sometimes seen, with spacing approximately 1 mm. At higher currents and pressures, these were not present. Also at low pressures and low currents, transient oscillatory phenomena are sometimes observable in the light from near the edge of the negative glow and in the tube current. These oscillations are rarely encountered and are not as yet reproducible.

The only common, reproducible oscillation observed by us is associated with anode spots, which we have described elsewhere.[3] Tube voltage and light from the plasma within 1 cm of the anode show periodic oscillations, but the phototube shows clearly that the striation which moves into the positive column from the anode is very quickly attenuated, and that the plasma is essentially unperturbed by this anode spot oscillation. For sufficiently high or low currents, anode spot oscillations are absent, and both the tube voltage and light emission are free of periodic or large amplitude perturbations.

Cesium seems to be the most convenient alkali to use since it reaches an operable vapor pressure at a lower temperature than the others. Neither cesium nor rubidium attack or combine with the Pyrex tubes to an annoying extent, but potassium quickly turns the tubes dark brown, interfering with light measurements.

* This work is supported in part by funds provided by the U. S. Atomic Energy Commission.

[1] T. M. Donahue and G. H. Dieke, Phys. Rev. **81**, 248 (1951).
[2] H. S. Robertson, Phys. Rev. **105**, 368 (1957).
[3] H. S. Robertson and M. A. Hakeem, Plasma Phys. Bull. **1**, 2 (1960), University of Miami. Copies may be obtained, as long as the supply lasts, by writing us.

Effect of Interelectrode Spacing on Cesium Thermionic Converter Performance

R. L. Hirsch
Atomics International, Canoga Park, California
(Received August 18, 1960)

In the cesium thermionic converter, energy dissipating interactions occur between emitted electrons and the "plasma," thus reducing the net electrical output. These interactions can be suppressed by reducing either the cesium pressure or the distance between electrodes. At very high emitter temperatures cesium is utilized primarily to neutralize space charge, and its effects on emitter work function are small. In this range the cesium pressure can be varied to approach emission limited performance. However, for operation in the moderate temperature range (1400° to 2000°C), cesium may be utilized to modify emitter work function as well as to reduce space charge. In this mode of operation the cesium pressure is fixed by these requirements, and departure from this optimum pressure results in drastic reductions in converter output. The interelectrode spacing then becomes a variable of great importance.

Experiments have been conducted with a variable spacing converter in this moderate temperature region, and the results affirm the importance of spacing. In this diode the plane-parallel electrodes were fabricated to arc cast molybdenum. The emitting surface was the bottom of a circular cylinder, the sides of which were shielded in an effort to minimize edge currents. During operation, the interelectrode spacing could be varied from zero to one-tenth of an inch through the use of a micrometer drive. The cesium reservoir and anode temperatures could be independently varied and were controlled by gaseous forced convection. The temperatures at these points were continuously monitored by thermocouples and a chart recorder. The emitter was heated by electron bombardment, and its temperature was determined through the use of an optical pyrometer.

The results of the first phases of this work are shown in Figs. 1 through 3. Figure 1 shows the observed effects of spacing on specific power output. At each cathode temperature and spacing the load resistance, the cesium temperature, and the anode temperature were varied to yield maximum power output. Generally,

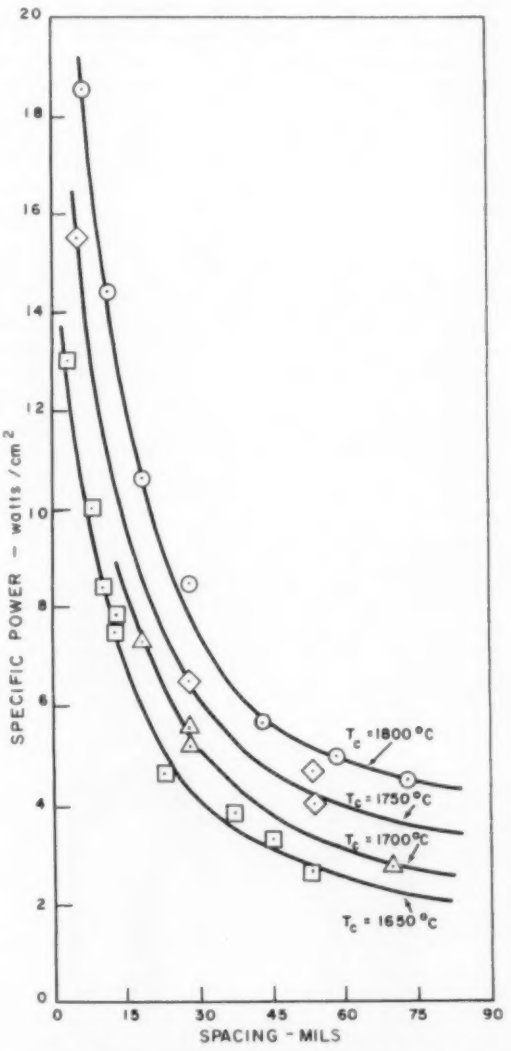

FIG. 1. The experimentally observed effects of electrode spacing on specific power output.

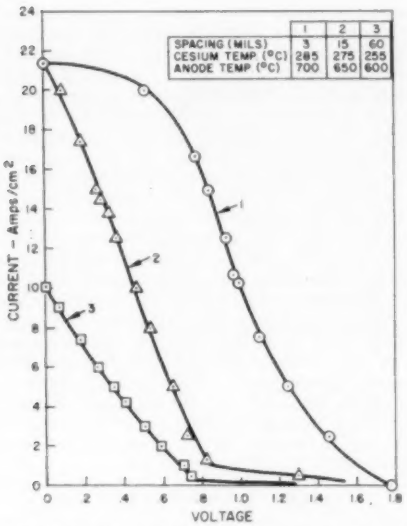

FIG. 2. The effects of electrode spacing on volt-ampere characteristics at a cathode temperature of 1650°C.

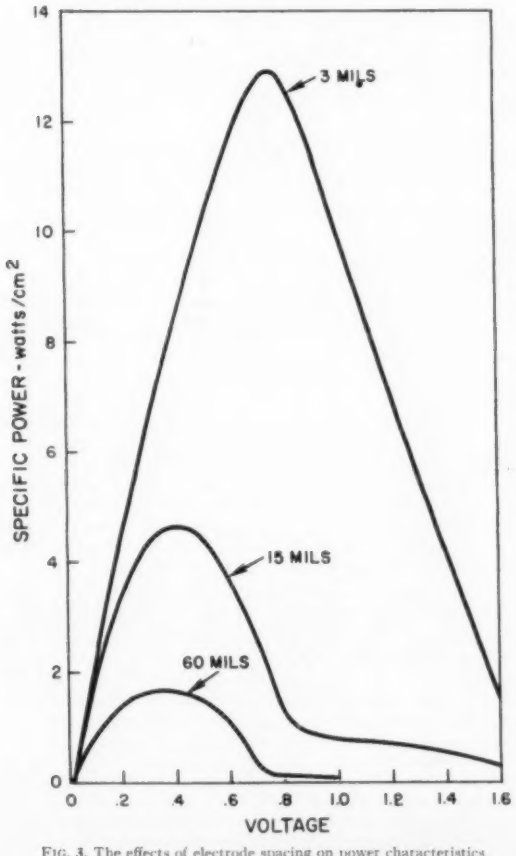

FIG. 3. The effects of electrode spacing on power characteristics at a cathode temperature of 1650°C.

the required variations in each of these parameters was small. Figures 2 and 3 indicate the changes in the volt-ampere and power characteristics as a function of spacing. The characteristic at 0.003 in. departs from the resistive characteristics seen at the larger spacings, and its form begins to resemble the characteristic of an emission limited converter. The fact that maximum power occurs at an emf approaching the difference in work functions (about 1.1 v) is a further indication of the approach to the emission limit.

At 1650°C and 17 amp/cm² it is interesting to note that the ratio of radiative to electronic cooling is less than 8%. This converter was built as a research tool and was not meant to provide high efficiency. Nevertheless, the ratio of power output to heater power input approached 9% at the high specific powers. In a more desirable geometry in which all parasitic losses have been minimized, this would correspond to over-all efficiencies near 25%.

The author gratefully acknowledges the assistance of Dr. N. S. Rasor and J. M. Nuding, H. G. Barrus, R. C. Dahleen, and C. C. Weeks, without whose help this work would not have been possible.

Influence of Arsenic Pressure on the Doping of Gallium Arsenide with Germanium

J. O. McCALDIN AND ROY HARADA
Hughes Semiconductors, Newport Beach, California
(Received May 23, 1960)

THE doping of III–V compounds with elements from the IVth column of the periodic table has been studied under standard conditions of preparation by several investigators.[1–6] In most cases, the IV element was found to act as an *n*-type dopant of low doping efficiency, a result that is usually interpreted to mean that more of the impurity atoms are located on the III element sublattice than on the V element sublattice. Causes for the unequal distribution of impurity atoms between the two sublattices have been sought in the sizes of the atoms and in their binding energies.[4] An additional influence on the impurity atom distribution, namely, the vapor pressure of the V element, is considered in this note. A simple estimate will be given of the magnitude expected for the pressure effect, followed by some qualitative results for Ge-doped GaAs.

Suppose the III–V compound is composed of a relatively nonvolatile element located at A sites of the lattice and a volatile element located at B sites. Qualitatively, one might expect that higher pressures P_B of the volatile element would reduce the concentration V_B of vacancies at the B sites; consequently, a IV element like germanium would tend to move to an A site, where it acts as a donor. Similarly, a reduced pressure P_B would shift the Ge atoms to B sites, where they behave as acceptors. The transfer of a Ge atom from an A site to a B site may occur with the participation of the appropriate vacancies V,

$$\mathrm{Ge}_A + V_B \rightleftharpoons \mathrm{Ge}_B + V_A. \tag{1}$$

The actual reaction may be more complicated than (1). The reacting species, for example, are probably ionized to a large extent. Let us assume that, at the high temperatures at which equilibrium is reached, the intrinsic concentration n_0 of conduction electrons is considerably larger than the concentrations of the reacting species, so that ionization reactions do not affect the equilibrium appreciably.[7] Writing a mass action relation for the equilibrium between vacancies and Ge atoms,

$$N_{\mathrm{Ge}A}/N_{\mathrm{Ge}B} = K_2 N_{VA}/N_{VB}. \tag{2}$$

The vacancy concentration N_{VB} depends[8] upon the pressure P_B

$$N_{VB} P_B = K_3 \tag{3}$$

assuming a monatomic gas. A similar relation can be written for the A (i.e., column III) species, and the two pressures P_B and P_A

can also be related[7]

$$A_{gas}+B_{gas}\rightleftharpoons AB_{solid}\cdots P_AP_B=K_4. \tag{4}$$

Assuming equilibrium, we may eliminate P_A and write Eq. (2) as

$$\frac{N_{GeA}}{N_{GeB}}\left(\frac{P_B}{P_{BO}}\right)^r, \tag{5}$$

where the exponent r is introduced to allow for a gas phase which is not monatomic (for arsenic vapor, $r=\frac{1}{2}$), and P_{BO} is the vapor pressure for which the impurity atoms are distributed equally between A and B sites. The last equation indicates that a tenfold increase or decrease of the pressure P_B from the reference pressure P_{BO} should make the IV impurity a rather effective donor or acceptor dopant, respectively.

The equilibrium relationships just described have been investigated qualitatively by diffusion treatments of Ge-doped GaAs. A GaAs ingot was grown from a melt doped with 2% Ge in a horizontal Bridgman furnace. The melt was contained in a carbonized quartz boat enclosed in an evacuated sealed quartz tube and was frozen directionally at a rate of about 1 in./hr. The arsenic vapor pressure was maintained at 0.9 atm.[9] The resulting ingot was p type at most places; it was polycrystalline with crystallites about 2 mm in size in some regions.

Slices about 0.075 cm thick were taken from the nose of the ingot. Some of the slices were treated 70 hr at 900°C at 5-mm arsenic pressure. These slices, which contained a few deep pits, were everywhere p type at the surface. Other slices were treated 70 hr at 1100°C at 5 atm arsenic pressure. These slices became everywhere n type at the surface. Metallographic sectioning followed by etching (1 pt. HF, 5 pts. HNO_3) revealed a p-n junction underlying the surface at a depth ranging from 30 μ to 70 μ at most places and penetrating considerably deeper at grain boundaries. The behavior at grain boundaries is probably related to the kinetics of vacancy formation. Also the junction within individual grains was scalloped, probably for similar reasons. Capacity vs reverse bias measurements made on some of these junctions indicate linear grading for the doping.

The experimental results agree qualitatively with relation (5); however, only the specimen surface, and perhaps some grain boundaries, could have been close to equilibrium under the experimental conditions. We are now engaged in preparing homogeneous specimens for quantitative measurements.

[1] C. Kolm, S. A. Kulin, and B. L. Averbach, Phys. Rev. **108**, 965 (1957).
[2] D. Jenny and R. Braunstein, J. Appl. Phys. **29**, 596 (1958).
[3] F. Schillman, Z. Naturforsch. **11a**, 463 (1956).
[4] O. G. Folberth and E. Schillman, Z. Naturforsch. **12a**, 943 (1957).
[5] J. T. Edmond, Proc. Phys. Soc. **73**, 622 (1959).
[6] J. M. Whelan, J. D. Struthers, and J. A. Ditzenberger, Bull. Am. Phys. Soc. **5**, 152 (1960).
[7] The effects of ionization on amphoteric impurities like the Ge atoms of the present case have been treated by R. L. Longini and R. F. Greene, Phys. Rev. **102**, 992 (1956).
[8] J. J. Lander and D. G. Thomas, in *Semiconductors*, edited by N. B. Hannay (Reinhold Publishing Corporation, New York, 1959), Chap. 2 and 7.
[9] J. van den Boomgaard and K. Schol, Philips Research Rept. **12**, 127 (1957).

Noise Propagation in Drifting Multivelocity Electron Beams

J. A. Morrison
Bell Telephone Laboratories, Inc., Murray Hill, New Jersey
(Received June 21, 1960)

Berghammer and Bloom[1] have recently published an approximate analysis (hereafter referred to as [1]), based on a macroscopic model, describing the behavior of the noise parameters in a multivelocity beam in which the velocity spread is assumed to be sufficiently small that the third-order moment (about the mean) of the distribution function may be neglected. They derived differential equations for the variation of the noise parameters with distance along the beam and in addition obtained two conservation laws. The differential equations were solved for the particular case of a drifting beam, with uncorrelated full shot noise being assumed at the input plane. The case of a half-Maxwellian dc density distribution was considered in detail. It is the purpose of this letter to point out that the formulas they give for the noise parameters S and H do not agree with the results of numerical computations based on the distribution function method of Siegman *et al.*,[2,3] which were carried out in the above case for a moderately high drift voltage, and were reported by J. R. Pierce.[4] These calculations are based on the same physical assumptions as [1], with uncorrelated full shot noise in each velocity class, but do not involve the approximations made in [1] because of the assumption of small velocity spread.

The computations were carried out in a manner similar to that adopted by Siegman, Watkins, and Hsieh and were programmed for the IBM 704 by D. E. Eastwood. The frequency ω was taken to be 3 kMc and the cathode temperature T_c to be 1000°K. The accompanying figures depict, for two different values of the dc beam current I_0, the variation of the normalized noise parameters with normalized distance along the beam, which is taken to be drifting at 1 v. In terms of the quantities in [1] the normalized noise parameters in Figs. 1(a) and (b) are

$$\varphi=\Phi/\Phi(0);\quad \psi=\Psi/\Psi(0);\quad \chi=\Lambda/S(0). \tag{1}$$

In Figs. 2(a) and (b) the normalizing factor is $S(0)$. The normal-

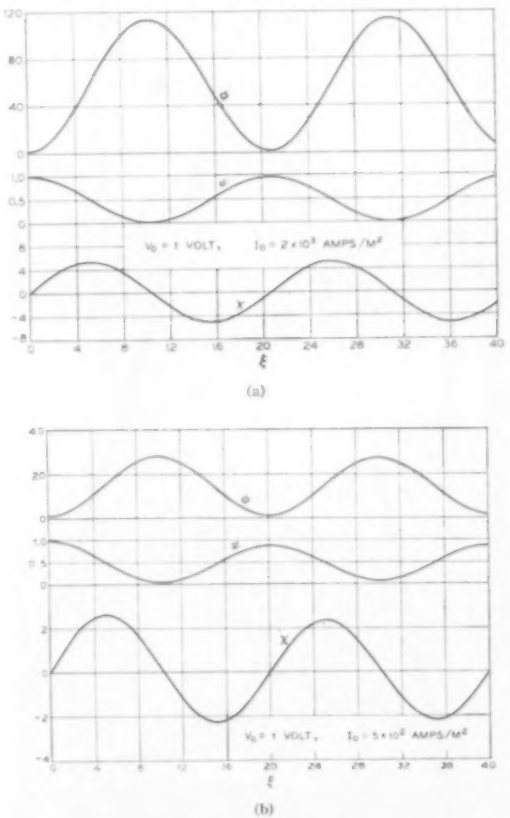

Fig. 1. Variation of the self-correlations, and of the imaginary part of the cross-correlation, of the current and voltage fluctuations with distance along the drifting beam. (a) dc beam current of 2×10^3 amp/m^2. (b) dc beam current of 5×10^2 amp/m^2.

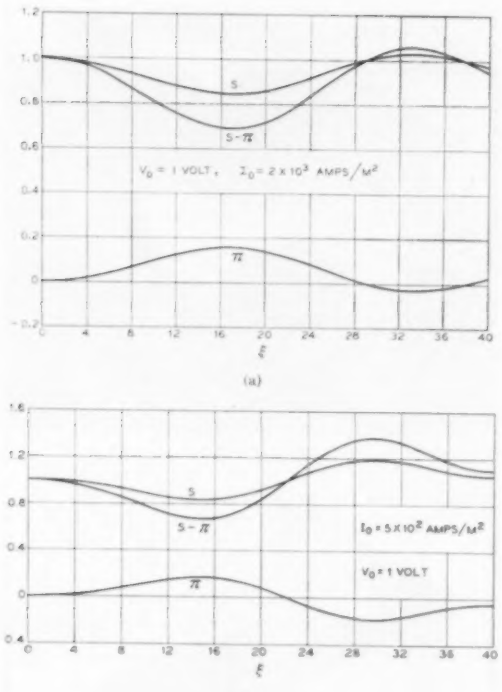

FIG. 2. Variation of the noise parameters S, Π, and (S−Π), normalized by the factor $kT_c/(2\pi)$, with distance along the drifting beam. (a) dc beam current of 2×10^3 amp/m². (b) dc beam current of 5×10^2 amp/m².

ized distance parameter ξ is given by

$$\xi=[m/(2kT_c)]^{\frac{1}{2}}[eI_0/(m\epsilon_0)]^{\frac{1}{2}}x. \tag{2}$$

It is seen from Figs. 1(a) and (b) that the noise parameters Φ, Ψ, and Λ are almost periodic and the period is quite close to that corresponding to twice the plasma wave number, which is in agreement with the results of [1]. Also it is seen that the wavelength in Fig. 1(a) is just a little longer than that in Fig. 1(b), the current I_0 being higher in the former case, and this is in accordance with the formula in [1]. Moreover, the amplitudes of the oscillations correspond fairly closely to those given by [1]. However, the discrepancy that occurs is seen by comparing Figs. 1 and 2, for then it is apparent that S and Π do not have the same oscillatory behavior as the other noise parameters, whereas according to [1] all the noise parameters are periodic with the same period. That Φ, Ψ, and Λ are not quite periodic is emphasized by the fact that

$$S=(\Phi\Psi-\Lambda^2)^{\frac{1}{2}}, \tag{3}$$

but that S does not have the same oscillatory behavior.

Since Γ^2 and Ψ do not have the same oscillatory behavior, it is clear that they cannot be linearly related (with constant coefficients) as they are according to one of the conservation laws in [1], for a drifting beam. Furthermore, it is seen from Figs. 2(a) and (b) that $(S+\Pi)$ is essentially constant along the beam, whereas the other conservation law in [1] states, for a drifting beam, that $(S^2-\Pi^2)$ is constant. It is interesting to note that the behavior of S (and Π) is different for the two values of the current I_0. It thus appears that the approximate linearized macroscopic analysis in [1] cannot be reconciled with the exact linearized microscopic analysis by the distribution function method, and in particular as far as the noise parameters S and Π are concerned, for a beam drifting at 1 v, in which case the parameter y defined in Eq. (31) of [1] is approximately 0.13. From what follows it will be seen that it is also questionable as to whether or not the two analyses can be reconciled for higher drift voltages, i.e., for smaller values of y.

Thus, for a drifting beam, an expansion in powers of x up to terms in x^2 was obtained for the noise parameters according to the microscopic theory of Siegman *et al.* We give here the results of this expansion for the case of large drift voltage. The dc density distribution function is taken in the form

$$f_0(u)=2\alpha I_0 S(u-u_s)g[\alpha(u^2-u_s^2)], \tag{4}$$

where, in the notation of [1], $u_s=(2\eta V_0)^{\frac{1}{2}}$. Also

$$\int_0^\infty g(w)dw=1; \quad \int_0^\infty wg(w)dw=\mu_1, \tag{5}$$

and

$$\mu_r=\int_0^\infty (w-\mu)^r g(w)dw, \quad (r=2, 3). \tag{6}$$

In the neighborhood of the input plane ($x=0$) we find that

$$\frac{\Phi(x)}{\Phi(0)}\sim1+\frac{4}{\mu_2}\left(\frac{\omega_p}{\omega}\right)^2\left(\frac{eV_0}{kT_c}\right)^2\left(\frac{\omega_p x}{u_s}\right)^2, \quad \frac{\Psi(x)}{\Psi(0)}\sim1-\left(\frac{\omega_p x}{u_s}\right)^2;$$
$$\frac{\Lambda(x)}{S(0)}\sim\frac{2}{(\mu_2)^{\frac{1}{2}}}\left(\frac{\omega_p}{\omega}\right)\left(\frac{eV_0}{kT_c}\right)\left(\frac{\omega_p x}{u_s}\right) \tag{7}$$

and

$$\frac{\Pi(x)}{S(0)}\sim\frac{3(\mu_2)^{\frac{1}{2}}}{4}\left(\frac{kT_c}{eV_0}\right)\left(\frac{\omega_p x}{u_s}\right)^2; \quad \frac{S(x)}{S(0)}\sim1-\frac{3\mu_3}{8\mu_2}\left(\frac{kT_c}{eV_0}\right)\left(\frac{\omega_p x}{u_s}\right)^2, \tag{8}$$

where ω_p is the plasma frequency and $[eV_0/(kT_c)]\gg1$.

Now, for the half-Maxwellian distribution

$$g(w)=\epsilon^{-w}; \quad \mu_1=1=\mu_2, \quad \mu_3=2. \tag{9}$$

It is readily verified that the results of [1] are in agreement with Eq. (7) for this case, but that there is disagreement with Eq. (8), for according to [1]

$$\frac{\Pi(x)}{S(0)}\sim\frac{3}{2}\left(\frac{kT_c}{eV_0}\right)\left(\frac{\omega_p x}{u_s}\right)^2; \quad \frac{S(x)}{S(0)}\sim1+0\left[\left(\frac{kT_c}{eV_0}\right)^2\left(\frac{\omega_p x}{u_s}\right)^4\right]. \tag{10}$$

It is interesting to note that, from Eq. (8),

$$[S(0)-S(x)]/\Pi(x)\sim\tfrac{1}{2}\mu_3(\mu_2)^{-1}, \tag{11}$$

and this is a measure of the skewness of the distribution $g(w)$. For the half-Maxwellian distribution, Eq. (9), it is seen that, in the neighborhood of the input plane,

$$S(x)+\Pi(x)\sim S(0). \tag{12}$$

Of course, these expansions are valid only part of the way to the first minimum of $(S-\Pi)$, but it has been seen from the numerical computations that, for a beam drifting at 1 v, Eq. (12) holds well past this first minimum.

It would thus seem that while the approximate macroscopic analysis in [1] gives acceptable approximations to the noise parameters Φ, Ψ, and Λ, it does not give satisfactory approximations to the parameters S and Π and hence not to the minimum attainable noise figure which is linearly related to $(S-\Pi)$. The approximations made in [1] because of the assumption of small velocity spread are tantamount to the supposition that the main portion of the noise is carried by the two space charge waves, the normal modes of the system. It is evident that the input condition of uncorrelated full shot noise in each velocity class cannot be satisfied in terms of just these two modes and essentially no input velocity class is distinguished from any other in the approximate macroscopic analysis in [1].

[1] J. Berghammer and S. Bloom, J. Appl. Phys. **31**, 454 (1960).
[2] A. E. Siegman, J. Appl. Phys. **28**, 1132 (1957).
[3] A. E. Siegman, D. A. Watkins, and H. C. Hsieh, J. Appl. Phys. **28**, 1138 (1957).
[4] J. R. Pierce, paper presented at the International Convention on Microwave Valves, London, May, 1958.

Solvent Evaporation Technique for the Growth of Arsenic-Doped Germanium Single Crystals for Esaki Diodes

F. A. Trumbore and E. M. Porbansky
Bell Telephone Laboratories, Inc., Murray Hill, New Jersey
(Received July 26, 1960)

THE growth of single-crystal, low resistivity arsenic-doped germanium is of considerable interest in Esaki diode work.[1] This note describes a solvent evaporation technique which has been applied successfully to the arsenic-germanium system and which should be applicable to a large variety of materials. The present method utilizes the relatively high volatility of arsenic, normally a source of difficulty in other growth techniques.

The method consists of dipping a rotating germanium seed crystal into an arsenic-germanium melt and allowing the seed to puddle at constant temperature. *The seed crystal is not pulled.* As arsenic evaporates from the melt, arsenic-doped germanium is precipitated or grown on the seed crystal. The experimental arrangement is shown schematically in Fig. 1. The process is analogous to the evaporation of the solvent water from a saturated salt solution at constant temperature. As the water (corresponding to the arsenic) evaporates, salt (corresponding to the germanium) precipitates out of the solution which would otherwise become supersaturated.

In one experiment a <111> germanium seed crystal, rotating at 144 rpm, was dipped into a melt containing about 5–10 at.% arsenic. A conventional crystal-pulling apparatus was used. After the seed contacted the melt, the growth temperature was attained by first lowering the temperature until growth occurred as in a conventional pulling experiment, then raising the temperature slightly to melt back the grown material. The rotating seed was then held in contact with the melt for about 18–19 hr. Removal of the seed after this period of time revealed the grown crystal, 30–34 g in weight, shown in Fig. 2. Resistivity profiles taken on rods cut perpendicular and parallel to the growth axis showed a total variation in resistivity from 0.00069 to 0.00080 ohm-cm. However, these profiles also indicated that perhaps three-quarters of the crystal was uniform in resistivity at 0.00071 ohm-cm to within ±3%. Microscopic examination revealed little or no evidence of germanium arsenide occlusions as frequently found in crystals grown by other techniques.[2] Esaki diodes have been made from this material by Dickten,[3] who alloyed aluminum wire to the germanium using a current pulse technique. Measurements on typical units with 20–25 ma peak currents yielded rc products of 5–10×10⁻¹¹ sec and peak current to valley current ratios of 4 to 1.

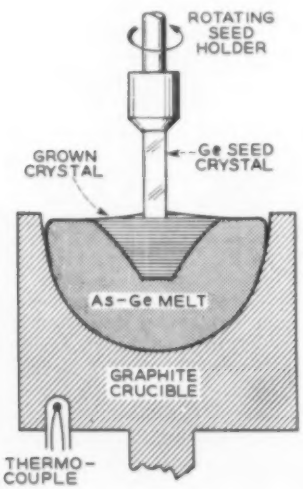

FIG. 1. Schematic diagram of solvent evaporation apparatus.

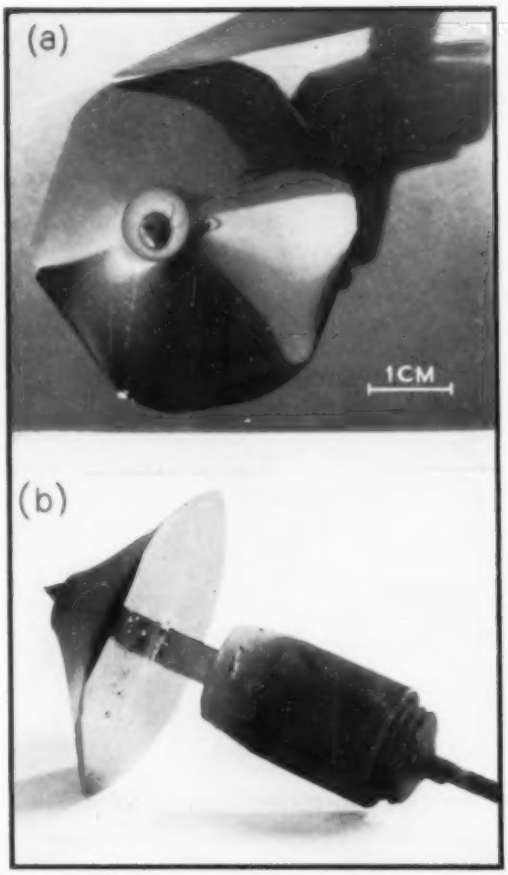

FIG. 2. (a) Bottom view of crystal showing (111) face on which a small droplet of melt adhered on removing from melt. The symmetry characteristic of the <111> orientation is apparent. (b) Top view of same crystal shown in Fig. 2 (a). The irregular features on the top surface were caused by bits of arsenic dropping back on the crystal, causing local melting and solidification.

This technique has a number of advantageous features. For example, since the growth is in principle an isothermal process, uniformly homogeneous material should be obtained. (Actually, a crystal pulling machine contains a built-in thermal gradient so that some nonuniformity is to be expected using such an apparatus.) A second feature is that, while retaining the advantages of the pulling technique (rotation, ease of seed orientation, etc.), there is no need for an elaborate pulling mechanism. Also, once sufficient experience has been obtained concerning growth parameters, relatively little or no attention is required on the part of the operator. Finally, since this method should be applicable, with suitable modifications, to any system where there is a volatile component or solvent, it should be possible to grow a wide variety of other materials such as, for example, III–V compounds.

We are indebted to Miss A. Mills for the resistivity measurements and to A. A. Tartaglia for metallurgical examination.

[1] See, for example, P. L. Moody and A. J. Strauss, Electrochem. Soc. Electronics Div. Abstracts **9**, No. 1, 167 (1960).
[2] F. A. Trumbore, Late Newspaper, Electrochem. Soc. Meeting, Chicago, May 2, 1960.
[3] E. Dickten (private communication).

Books Reviewed

Prompt, noncritical reviews appear in this column. Critical reviews of many of the books described here will appear in Physics Today, The Review of Scientific Instruments, *or* American Journal of Physics.

Methods in Geochemistry. A. A. SMALES AND L. R. WAGER, EDITORS. Pp. 434. Interscience Publishers, Inc., New York, 1960. Price $13.50.

Analytical techniques, used primarily in geochemistry to determine the composition of the earth and its parts, have traditionally been primarily chemical in nature. This book is a review of some of the more recently developed techniques based on radiochemistry, activation analysis, x-ray fluorescence, and other physical techniques.

Stress Wave Propagation in Materials. NORMAN DAVIDS, EDITOR. Pp. 327. Interscience Publishers, Inc., New York, 1960. Price $5.00.

This book is a collection of papers given at the Office of Ordnance Research sponsored by the Symposium on Stress Wave Propagation in Materials at the Pennsylvania State University on June 30–July 2, 1959. The particular subject of high-amplitude stress waves has been studied in many types of media from those approaching ideal elastic or viscoelastic media to complicated substances such as rocks. This is an up to date collection of both experimental and theoretical contributions to the field.

Solid State Physics (In Electronics and Telecommunications). Vol. 2: Semiconductors. M. DESIRANT AND J. L. MICHIELS, EDITORS. Pp. 1284. Academic Press, Inc., New York, 1960. Price $18.00.

This is the proceedings of a conference on solid state physics, as applied in electronics and telecommunications, held in Brussels in June, 1958. More attention toward techniques and applications was evident at this conference on semiconductors than in the usual conference on semiconductor physics. The 250 papers given constitute an extensive survey of the state of the art at the time of the conference.

Direct Conversion of Heat to Electricity. JOSEPH KAYE AND JOHN A. WELSH, EDITORS. Pp. 387. John Wiley & Sons, Inc., New York, 1960. Price $8.75.

The volume is an edited collection of papers which have been prepared by principal people in the new technology of direct conversion. It includes fundamental discussions in thermoelectric energy conversion (the thermocouple), thermionic energy conversion (the vacuum tube and the gaseous tube), magnetohydrodynamic conversion (separating the positive and negative charges in gas), and fuel cells (the separation of positive and negative charges during a chemical reaction). The contributors offer considerations of the practical applications and problems associated with each type of conversion scheme.

Histological Techniques for Electron Microscopy. DANIEL C. PEASE. Pp. 260. Academic Press, Inc., New York, 1960. Price $7.50.

This book is a handbook for the histologist who is a novice with the electron microscope. Material is presented on the mechanics and operation of the equipment and also on the handling and preparation of the samples.

Appendices are also included on the literature of electron microscopy and sources of equipment and materials.

Electrical Engineering Science. PRESTON R. CLEMENT AND WALTER C. JOHNSON. Princeton University Series. Pp. 574. McGraw-Hill Book Company, Inc., New York, 1960. Price $9.50.

This book is intended as a text for an introductory two-semester course in electrical engineering. It presumes a familiarity with the basic concepts of differential and integral calculus and a moderate competence in differentiating and integrating simple functions.

The aims of this volume are to provide an introduction to the field of electrical engineering via the basic concepts of electricity and magnetism, to apply these concepts in developing the fundamentals of energy conversion and circuit theory, and to carry forward, in a continuous and integrated way, a modern treatment of network analysis. It is intended to serve as a foundation for the subsequent study of topics such as electronic circuits, energy conversion and feedback control systems, advanced network analysis, and network synthesis. This book has been written with the purpose of providing the reader with a unifying point of view for these varied subjects.

Incompressible Aerodynamics. BRYAN THWAITES, EDITOR. Pp. 610. Oxford University Press, New York, 1960. Price $12.00.

This book, the first of a new series, the *Fluid Motion Memoirs*, sponsored by the Aeronautical Research Council, is a comprehensive review of certain flows of incompressible fluid, which are of special importance to aeronautics. The central theme of the book is the up to date theoretical and experimental treatment of the uniform flow of air and other viscous fluids past two-dimensional aerofoils and three-dimensional wings. Also grouped are various related topics such as flows past joined bodies, shear flows, rotary flows, and boundary-layer control.

Frozen Free Radicals. G. J. MINKOFF. Pp. 141. Interscience Publishers, Inc., New York, 1960. Price $5.00.

This is a brief, well-referenced, and current review of methods for production of trapped free radicals and techniques for studying their electronic, chemical, and optical properties.

Reactor Handbook. 2nd ed. Vol. 1. Materials. C. R. TIPTON, JR. Pp. 1148. Interscience Publishers, Inc., New York, 1960. Price $36.50.

This book is a revision of the first edition, extended to include liquids and gases as well as solids, which were the exclusive consideration of the original handbook.

Vibrations from Blasting Rock. L. DON LEET. Pp. 134. Harvard University Press, Cambridge, Massachusetts, 1960. Price $4.75.

This monograph on the character and effect of vibrations from explosives is important as a source of material recently published and includes reports and investigations not easily located elsewhere.

It covers the following:

A. Explosives and blasting caps
B. Rocks (their properties and effect of blasting)
C. Rupture of rock by blasting
D. Elastic-wave pattern
E. Safe limits for structures.

Most useful is a chapter devoted to the character of rocks, the nature of explosives, and techniques in the preparation for blasting. This book will be helpful to manufacturers of explosives, engineers, and contractors. The author, Professor of Geology at Harvard, has contributed other articles on physical geology, ground vibrations, and earth waves.

Extractive and Physical Metallurgy of Plutonium and Its Alloys. W. D. WILKINSON, EDITOR. Based on a symposium held in San Francisco, California, February 16–17, 1959, sponsored by Nuclear Metallurgy Committee, Institute of Metals Division, and Titanium, Uranium, and Uncommon Metals Committee, Extractive Metallurgy Division of the Metallurgical Society, American Institute of Mining, Metallurgical, and Petroleum Engineers. Pp. 314. Interscience Publishers, Inc., New York, 1960. Price $10.50.

These papers, resulting from a symposium on physical metallurgy of plutonium, present the work of several authors who are specialists in their field. This compilation is the first published volume on plutonium metallurgy. Papers from the session on extractive metallurgy and physical metallurgy of plutonium are included. An introduction describing the "general properties, allotropes, and transformation behavior of plutonium" is followed by chapters on the conversion of plutonium salts to metal, preparation of metallic plutonium, preparation of plutonium halides for fused salt studies, alloying behavior of plutonium, experiments in zone refining plutonium, and behavior of some delta-stabilized plutonium alloys at high pressures. A most important feature of the book is the annotated bibliography on plutonium metallurgy. Much of the material included was at one time classified information. That and the bibliography make this monograph doubly valuable.

Books Received

Progress in Elementary Particle and Cosmic Ray Physics. Vol. V. J. G. WILSON AND S. A. WOUTHUYSEN, EDITORS. Pp. 408. North Holland Publishing Company, Amsterdam, The Netherlands, 1960. Price $10.75.

Introduction Mathématique À La Mécanique Des Fluides. CAIUS JACOB. Pp. 1282. Gauthier-Villars, Paris, 1959.

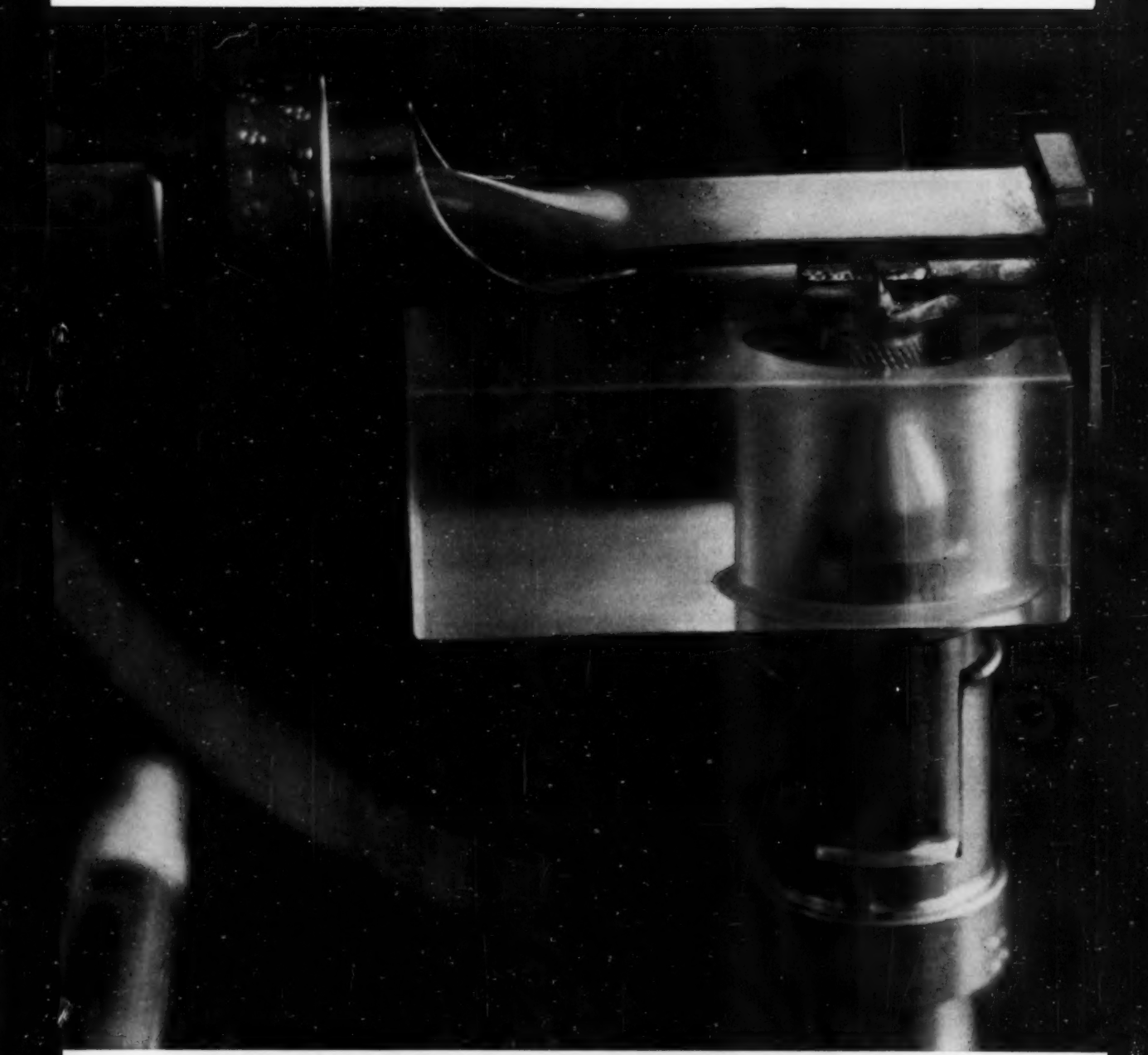

Special high-speed pulse equipment sets up a magnetic field in a fraction of one nanosecond to measure switching times in thin magnetic films.

Nanosecond switching in thin magnetic films

Switching in thin magnetic films takes place in the nanosecond range—10^{-9} seconds. Because of this, thin magnetic films—some just 100 atom-layers thick—promise many advantages over conventional magnetic elements in storage and switching applications.

The physical behavior of these thin films is now under investigation by a group of scientists at the IBM Research Laboratory in Zurich, Switzerland. A study is being conducted to determine how fast thin magnetic films can switch, and how this speed is related to fundamental magnetics.

To observe changes in magnetization, special high-speed pulse equipment had to be designed. The sample holder above is a part of the equipment which sets up a magnetic field in the film's plane in a fraction of a nanosecond. In addition, a pulse sampling oscilloscope, capable of a time resolution of 0.35 nanoseconds, was built to detect the switching.

Experiments using this equipment bring nanosecond switching one step closer to application in memory and logic units. This will help make possible greater speed and versatility in tomorrow's computers.

IBM. RESEARCH

Investigate the many career opportunities available in exciting new fields at IBM.
International Business Machines Corporation, Dept. 579Y, 590 Madison Avenue, New York 22, New York

THE 1960's WILL BE A DECADE OF TIME COMPRESSION . . .

More people will travel further in a shorter time—men will move in geocentric orbits at 18,000 mph—space probes will shrink our celestial environment. To accomplish these things, the time between research and application engineering will shrink dramatically.

Convair believes that the full potential of Technology in the Sixties will be realized through ideas originating in the minds of creative scientists and engineers. To implement this conviction, Convair-Fort Worth is pursuing an active research program in the engineering and physical sciences.

A position on the staff of the newly formed Applied Research Section offers opportunity rarely found for physicists and engineers at the doctorate level. Research programs in the fields of astrophysics, relativity, gravitation, physics of materials, and geophysics are in the formative stages of planning and activation. Active and mature programs in electronics, space mechanics, and thermodynamics are underway.

If you can qualify, a position within this section will offer unlimited growth potential. For further information, forward your personal resume to Dr. E. L. Secrest, Chief of Applied Research, Convair-Fort Worth, P. O. Box 748 J, Fort Worth, Texas.

CONVAIR/FORT WORTH
CONVAIR DIVISION OF
GENERAL DYNAMICS

Physicists:

SEVERAL POSITIONS OPEN IN NEW ADVANCED PROJECTS OPERATION FOR R & D OF NON-CONVENTIONAL DISPLAY DEVICES

Although details cannot be published here, one of the activities of this new group will concern development of an entire family of unusual information recording, storage and display systems.

Key Posts to be Filled in These Areas:

Electron Optics
Physical Optics
Vacuum Technology Development
Tube Development
Display System Analysis
Circuit Analysis
Physical Chemistry
Synthesis & Application of Organic Materials to Electronic Components

For more information, write informally or forward your resume in confidence to Mr. J. Wool, Dept. 37-MK. Your inquiry will receive prompt review and an early reply.

CATHODE RAY TUBE DEPARTMENT

GENERAL ELECTRIC

Electronics Park Syracuse, New York

A Superior Detector for Infra-Red Spectroscopy

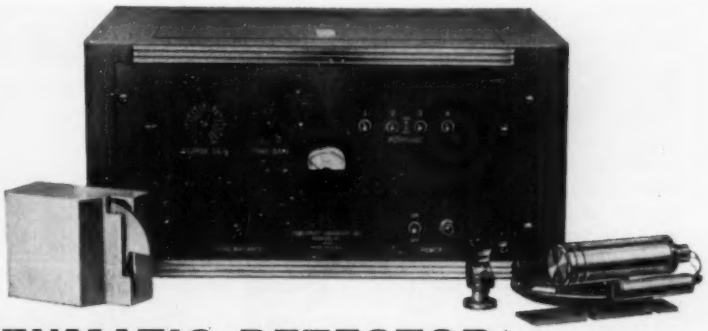

GOLAY PNEUMATIC DETECTOR*

Among the characteristics that render the Golay Detector superior to other types of detectors for use in infra-red spectroscopy are:

1. **An effective sensitive area $\frac{3}{32}$" in diameter.**
2. **Sensitivity of 6×10^{-11} watts RMS-ENI when used with "chopped beam" method and with recording time constant of 1.6 second.**
3. **Uniform sensitivity from the ultra-violet through the visible and the entire infra-red, and up to the micro-wave region.**
4. **Improved, drift-free, A. C. operated amplifier with step gain controls and four response periods.**

Write for EPLAB Bulletin No. 10

*Fundamental and experimental aspects of this detector are discussed in the following publications: Rev. Sci. Inst. *18*, 347 and 357 ('47); ibid. *20*, 816 ('49); Proc. IRE *40*, 1161 ('52).

278-S

THE EPPLEY LABORATORY, INC.
SCIENTIFIC INSTRUMENTS
6 Sheffield Ave. • Newport • Rhode Island • U.S.A.

QUALITY WITHOUT COMPROMISE

Performance
Flexibility
Reliability

HIGH VACUUM & LEAK DETECTION EQUIPMENT

EVAPORATORS

VEECO manufactures a complete *quality* line of time-proven vacuum components, Leak Detectors, Evaporators and High Vacuum Systems.

PUMPING STATIONS

For individual bulletins or complete catalog write Dept. J856

LEAK DETECTORS

Veeco

VACUUM-ELECTRONICS CORP.
TERMINAL DRIVE, PLAINVIEW, L. I., NEW YORK

Developed for use with thermocouples, thermopiles and similar type detectors.

The Amplifier operates on frequencies between 2 and 20 cycle signals. However, amplifiers are peaked for frequency response desired or most suitable for a particular application, therefore, any intermediate frequency response can be specified.

The Power Supply to operate the amplifier has sufficient regulation and freedom from noise to permit detection of first stage tube noise, and thereby, enables observation of lowest thermocouple noise.

Farrand

LOW FREQUENCY-HIGH GAIN AMPLIFIER

AND REGULATED POWER SUPPLY

Technical data available on request
Specify Bulletin No. 810AP

FARRAND OPTICAL CO., INC.
BRONX BLVD. AND EAST 238th STREET • NEW YORK 70, N. Y.
Engineering Research, Development, Design and Manufacture of Precision Optical, Electronic and Scientific Instruments

---

High Performance ELECTROMAGNETS and Power Supplies

ECONOMY
7" Electromagnet Type E (7" pole diameter). Fields up to 8,000 gauss. Homogeneity of at least 4 parts in 10^3 in ½ cc.

ROTATION
Rotating Base Type AE. 360° scale. Positive friction lock.

STABILITY
Current-Stabilized Power Supply Unit Type B. Two models:
B.4—Stability 1 part in 10^4.
B.5—Stability 1 part in 10^5.

Also available:—
1½" Electromagnet Type C—for Teaching purposes.
4" Electromagnet Type A—for all purposes.
8" Electromagnet Type D—for Electron Resonance and Nuclear Magnetic Resonance work.
Direct Reading Magnetometer Type G.
Proton Resonance Magnetometer Type P.

NEWPORT INSTRUMENTS
(Scientific & Mobile) Ltd.
3 CRAWLEY ROAD, NEWPORT PAGNELL, BUCKS, ENGLAND
Telephone: NEWPORT PAGNELL 401/2

To demonstrate transistor functions . . .

NEW CENCO TRANSISTOR ANALYZER

Graphically demonstrates three basic transistor configurations—common emitter, base and collector. May also be used for simple circuit experiments and plotting response curves. Utilizes any general purpose transistor. Mounted on "Lucite".

No. 80390
$37.50

cenco
Serving education since 1899.

CENTRAL SCIENTIFIC CO.
A Subsidiary of Cenco Instruments Corporation
1718-A Irving Park Road • Chicago 13, Illinois
Mountainside, N. J. Montreal Santa Clara
Somerville, Mass. Toronto Los Angeles
Birmingham, Ala. Ottawa Vancouver Houston
Cenco S.A., Breda, The Netherlands Tulsa

ILFORD

Q plates for spectrography

The special plates of this group are coated with unique emulsions possessing a high silver halide to gelatin ratio. Their relatively low gelatin content minimizes radiation absorption and makes Ilford Q Plates especially useful for spectrography below 2300 A.

To suit individual requirements, we offer these plates with three different speed, grain and contrast characteristics.

PLATE	SPEED	GRAIN	CONTRAST
Ilford Q1 Plate	Slowest	Very fine	Highest
Ilford Q2 Plate	Medium	Fine	Intermediate
Ilford Q3 Plate	Fastest	Intermediate	Lowest

Available in plate sizes and thicknesses to fit your needs.

ILFORD INC. 37 WEST 65th STREET, NEW YORK 23, N. Y.

For fast, accurate measurement of

SURFACE-INTERFACIAL TENSIONS

CENCO-du Nouy

the original

TENSIOMETER

Measures surface or interfacial tensions by the ring method. Precise determinations in a matter of minutes. Upward or downward forces are read directly—reproducible to within 0.05 dyne. (See ASTM D971-50)

With platinum ring and metal case.....$439.50

cenco

CENTRAL SCIENTIFIC CO.

A Subsidiary of Cenco Instruments Corporation

1718-A Irving Park Road • Chicago 13, Illinois

Mountainside, N. J. Montreal Santa Clara
Somerville, Mass. Toronto Los Angeles
Birmingham, Ala. Ottawa Vancouver Houston
Cenco S.A., Breda, The Netherlands Tulsa

THE FRANKLIN INSTITUTE

Philadelphia, Pa.

. . . has openings for expanding research programs in the following areas:

SEMICONDUCTORS
Exploration of Organic Materials

X-RAY CRYSTALLOGRAPHY
X-ray Scattering by Imperfect Lattices

STRUCTURE OF THIN FILMS
Structural Investigation of Thin Magnetic Films using Electron Microscopy and Electron Diffraction

DISLOCATION THEORY
Study of Dislocation Interactions, Surface Phenomena, Point Defects

DEFORMATION OF METALS
Investigation of Dislocation Patterns by Diffraction Electron Microscopy

These positions offer excellent opportunities for creative scientists who would enjoy basic research in an academic atmosphere. Publication of papers encouraged. Ph.D. or equivalent experience required. For further information write to Dr. H. G. F. Wilsdorf, Technical Director, or send resume to Mr. John Christ, Director of Personnel, The Franklin Institute, Philadelphia 3, Pa.

now from Librascope:

NARROW-BAND INTERFERENCE FILTERS

...with a new approach to side-band problems

Recent achievements at Librascope's Applied Research Center make it possible for you to now order high-precision, multilayer, narrow-band interference filters...custom-made to your specified wavelength, side-band requirement, and detector's spectral characteristics. Greater than 70% transmission and a half-bandwidth of approximately 1% at specified peak wavelength. Delivery from stock: set of 8 filters uniformly distributed over visible spectrum...as well as mercury and sodium lines. Send your requirements for quotation today.

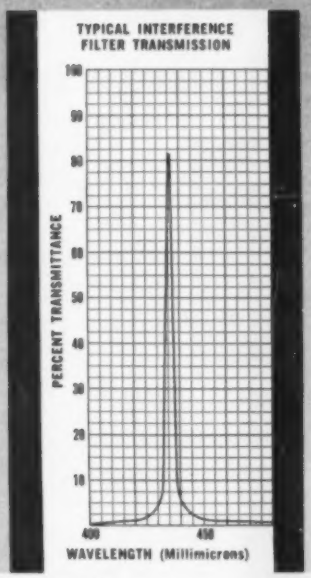

BURBANK BRANCH
LIBRASCOPE DIVISION
GENERAL PRECISION, INC.
100 East Tujunga • Burbank, Calif.

FOR YOUR SINGLE CRYSTAL REQUIREMENTS

- Aluminum
- Aluminum Oxide
- Barium Fluoride
- Barium Titanate
- Barium Titanate (Iron Doped)
- Cadmium Sulfide
- Cadmium Telluride
- Calcium Fluoride
- Cesium Bromide
- Cesium Chloride
- Cesium Iodide
- Copper
- Gadolinium Iron Garnets
- Germanium
- Lead
- Lithium Bromide
- Lithium Chloride
- Lithium Fluoride
- Magnesium Oxide
- Magnesium Oxide (Chromium Doped)
- Magnesium Oxide (Copper Doped)
- Magnesium Oxide (Iron Doped)
- Magnesium Oxide (Titanium Doped)
- Potassium Bromide
- Potassium Chloride
- Potassium Fluoride
- Potassium Iodide
- Potassium Iodide (Thallium Activated)
- Rubidium Bromide
- Rubidium Chloride
- Rubidium Iodide
- Silicon
- Silver Bromide
- Silver Chloride
- Sodium Bromide
- Sodium Chloride
- Sodium Fluoride
- Sodium Iodide
- Strontium Chloride
- Thallium Bromide
- Thallium Bromide Iodide
- Thallium Chloride
- Yttrium Iron Garnets
- Zinc

Also Custom Crystal Growing

SINGLE CRYSTAL DIVISION
SEMI-ELEMENTS INC.
SAXONBURG BOULEVARD SAXONBURG PA. USA

SENIOR PHYSICIST

Magnetics department of our Research Division offers an unusual opportunity for a physicist or engineer (Ph.D. desirable) to participate in and lead experimental and theoretical studies in various aspects of magnetism and magnetic materials. Company sponsored projects are underway on thin films, fine particles, magneto-optics and allied areas. Job environment emphasizes individual achievement.

AMPEX CORPORATION

World Leader in Magnetic Recording

Send resumes to:

Donald F. Eldridge
Head, Magnetics Department
934 Charter Street
Redwood City, California

THERMAL CONDUCTIVITY TESTERS

Alundum Guarded Hot Plate Console

Shown on either side are units for determining the K-factors or coefficients of thermal conductivity of various materials. The range on the Guarded Hot Plate Console is up to 1400° F and the Probe Unit is up to 250° F.

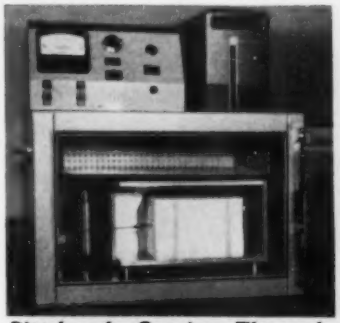

Pittsburgh Corning Thermal Conductivity Probe Unit

Write for information and brochure

CUSTOM SCIENTIFIC INSTRUMENTS, INC.

541 Devon St. Kearny, N. J.

Tel. WYman 1-6403

CHEMISTS
PHYSICISTS

Rapid and steady growth has created new openings in Melpar's Physical Sciences Laboratory for several experienced solid state chemists or physicists. Must be skilled in both theoretical and applied techniques, involving the selection, synthesis, application and testing of a wide variety of materials. Broad areas of interest include infrared, electroluminescence, semiconductors, nonlinear amplifiers, thermoelectricity, electro-chemistry, and fabrication of microcircuits.

Send complete resume to: **Professional Placement Manager**

MELPAR, INC.

A Subsidiary of Westinghouse Air Brake Co.

3343 Arlington Boulevard, Falls Church, Va.

In Historic Fairfax County. *(10 MILES FROM WASHINGTON, D.C.)*

a vacuum pump as quiet as a . . .

Steady and silent. That's the new Stokes Series H Microvac pump. Unique dynamic balancing provides hushed operation. And the compact Stokes pump saves up to 50% in valuable floor space.

Find out all the reasons why you get *more pumping performance per dollar* with Stokes Microvac pumps. Just write: Vacuum Equipment Division, F. J. STOKES CORPORATION, 5500 TABOR RD., PHILA. 20, PA.

STOKES

SEND TODAY
for your free
Vacuum Slide Calculator.

NEWS from the NRC Vacuum MICRONICLE*

New 6″ vacuum pump —70% more speed— no loss of reliability

Upgraded performance is but half the story on the new NRC Model H6-1500. Compared with its predecessor it assures: *Speed* — 1500 l/s, up 70%. *Forepressure Tolerance* — 700 microns, up 275%. *Backstreaming* — less than 0.03 mg/-cm²/min, down 40%. *Height* — 18½″, down 34%. *Blank-off* — as low as 10^{-10} mm Hg in trapped UHV system.

The other half is the way it can do all this without carefully regulated power and water supplies, oversized backing pumps, delicate pump oils, or frequent maintenance. Stainless steel body — 4-stage fractionating jet assembly (securely anchored yet demountable in 15 sec.) — easily removable, long-lived "cast-in" heater — silver soldered cooling coils — all keep operating and maintenance costs low. Original cost is low, only $495.

*Send for FREE periodical containing details on H6-1500 and other news about high vacuums. Dept. P-11, 160 Charlemont St., Newton 61, Mass.

NRC
EQUIPMENT CORPORATION

A Subsidiary of National Research Corporation

NEO-17

Soviet Physics—SOLID STATE

Monthly. A cover to cover translation of the USSR Academy of Sciences journal, "Fizika Tverdogo Tela."

Soviet Physics—TECHNICAL PHYSICS

Monthly. A cover to cover translation of the USSR Academy of Sciences journal, "Zhurnal Tekhnicheskoi Fiziki."

Soviet Physics—CRYSTALLOGRAPHY

Bimonthly. A cover to cover translation of the USSR Academy of Sciences journal, "Kristallografiya."

Please address orders and inquiries to the publisher:

AMERICAN INSTITUTE OF PHYSICS
335 East 45th Street, New York 17, N. Y.

HIGH IN RESOLVING POWER, EASIER TO MAINTAIN THAN ANY OTHER ELECTRON MICROSCOPE

BENDIX TRONSCOPE TRS-50 E1

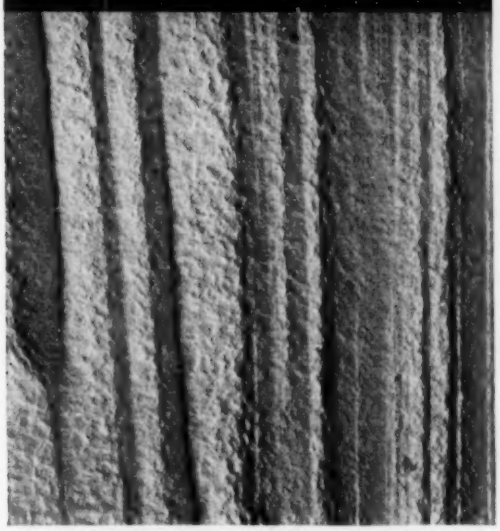

Dislocations in germanium transistor crystal. 12,000X.

BENDIX TRONSCOPE demonstrates 15-20Å resolving power with no adjustments.

BENDIX TRONSCOPE is first electron microscope with absolutely no decrease in resolving power from adjustments.

BENDIX TRONSCOPE is the most trouble-free electron microscope in the world.

BENDIX TRONSCOPE is *warranted* against defects in materials and workmanship. Service is available after warranty period on either a contract or a transportation, per diem, and parts basis.

FULL DETAILS can be obtained by writing Dept. S11.

Cincinnati Division
3130 Wasson Road • Cincinnati, Ohio

THE Bendix CORPORATION

Canada: Computing Devices of Canada, Ltd., Box 508, Ottawa 4, Ont.

Kinney® PRESENTS A NEW AND BETTER McLEOD GAGE

READS EASIER

•

USES LESS MERCURY

•

PANEL OR PORTABLE MOUNT

•

SEPARATE CAPILLARIES

•

2 SCALES
150 mm to 2 mm
2,000μ to 1μ

•

ACCURATE LIGHT IN WEIGHT COMPACT

The KINNEY McLeod Gage answers the many objections to other gages now in use. Its advanced design compacts superior performance into a rugged, versatile instrument that may be permanently mounted on bracket, tank, panel or pipe or, by affixing demountable legs, used as a portable unit.

The KINNEY McLeod Gage covers a broad range of pressures . . . accurate readings from 150 mm Hg to 1 Micron Hg. This exceptional range of pressure readings is achieved by incorporating two separate capillaries having separate compression ratios, making available measurements of 150 mm to 2 mm and 2,000 microns to 1 micron. Unlike other McLeod Gages, the reading capillary tubes are completely separate and replaceable—easily detached from the main body at the knurled sealing glands. Because these tubes are reproducible, complete accuracy between each gage is assured.

The KINNEY McLeod Gage requires less mercury and it is supremely simple to add mercury, remove it for cleaning or recharge the gage. Operation requires no special skill . . . readings are achieved quickly, easily and confidently. Write for full information and prices today.

Get all the facts on the NEW KINNEY McLEOD GAGE. Write today!

KINNEY VACUUM DIVISION
THE NEW YORK AIR BRAKE COMPANY
3556L WASHINGTON STREET • BOSTON 30 • MASS.

Please send me Bulletin No. 3821.1 and prices on the KINNEY McLeod Gage.

Name _____

Company _____

Address _____

City _____ State _____

INDEX TO ADVERTISERS

Name	*Page*
AMHERST LABORATORIES, SYLVANIA ELECTRONIC SYSTEMS	xviii
AMPEX CORPORATION	xxx, xxxv
ARNOLD ENGINEERING COMPANY	v
AUTONETICS, DIV. OF NORTH AMERICAN AVIATION	viii
BELL TELEPHONE LABORATORIES	vii
BENDIX CORPORATION CINCINNATI DIVISION	xxxiii
CENTRAL SCIENTIFIC COMPANY	xxviii, xxix
COLLINS RADIO COMPANY	xxi
CONVAIR/FORT WORTH DIV. OF GENERAL DYNAMICS	xxvi
CUSTOM SCIENTIFIC INSTRUMENTS, INC.	xxxi
DELCO RADIO DIV. OF GENERAL MOTORS	xxiii
DOW CORNING CORPORATION	ix
EASTMAN KODAK COMPANY	xi
EPPLEY LABORATORY, INC.	xxvii
FARRAND OPTICAL COMPANY	xxviii
THE FRANKLIN INSTITUTE	xxix
GENERAL ELECTRIC CATHODE RAY TUBE DEPT.	xxvi
GENERAL MAGNETICS, INC. INSERT AT PAGES	iii, iv
GENERAL RADIO COMPANY	Cover 4
HARSHAW CHEMICAL COMPANY	Cover 2
HARVEY-WELLS ELECTRONICS, INC.	vi
IBM CORPORATION	xxv, xxxiv
ILFORD, INC.	xxix
JET PROPULSION LABORATORY	x
KEITHLEY INSTRUMENTS, INC.	xv
KINNEY VACUUM DIVISION, N. Y. AIR BRAKE CO.	xxxiii
LIBRASCOPE DIV. OF GENERAL PRECISION	xxx
LOS ALAMOS SCIENTIFIC LAB.	xix
McGRAW-HILL BOOK CO., INC.	xx
MELPAR, INC.	xxxi
NRC EQUIPMENT CORP.	xxxii
NEWPORT INSTRUMENTS LTD.	xxviii
RADIO CORP. OF AMERICA	xvii
SEMI-ELEMENTS INC.	xxx
SPACE TECHNOLOGY LABORATORIES	Cover 3
STOKES CORP., F. J.	xxxii
STROMBERG-CARLSON DIV. OF GENERAL DYNAMICS	xiv
SYLVANIA ELECTRONIC SYSTEMS WALTHAM LABORATORIES	xxxvi
TESLA, REP., NATIONAL INSTRUMENTS LABS., INC.	xxii
VARIAN ASSOCIATES	xii, xiii, xxxv
VEECO VACUUM-ELECTRONICS CORP.	xxvii
WELCH SCIENTIFIC CO., W. M.	xxiv
JOHN WILEY & SONS, INC.	xvi

Key positions on new semiconductor studies with IBM Research

PHYSICISTS

Positions are now open on new semiconductor studies being undertaken at the IBM Research Center at Yorktown Heights, New York. These studies will present unique opportunities to do advanced work in your field.

Solid State Photo Devices: We have a unique opportunity for a man interested in studying the mechanisms governing the behavior of solid state photo devices covering the wide field of photoconductors, photo-junctions, and solid state light sources. The program is supported by close association with a well established materials group. You should have a Ph.D. or its equivalent, in physics, or physical chemistry, and a sound knowledge of semiconductor physics. Previous experience in solid state optical work would be desirable.

IBM's ultra-modern new research center is located in one of the most desirable parts of Westchester County, just forty miles north of New York City. All IBM benefits apply. Your relocation expenses paid.

For further information, please write, outlining your background and experience to:

Mr. K. J. Turner, Dept. 579Y1
IBM Research Center
Box 218
Yorktown Heights, N. Y.

IBM®

International Business Machines Corporation

MANAGER
PRODUCT ENGINEERING

We are looking for an outstanding man of proven leadership and long experience to head up product engineering in our successful and growing scientific instrument company. This man must be able to take product ideas proven out by research and development and convert them into sound manufacturable products. He must be experienced in working with both R & D and manufacturing people and must understand and appreciate their objectives and requirements. He must possess widely-recognized product engineering abilities along the lines of sophisticated electronic instrumentation for scientist/engineer/technician customers. He must be cost-conscious, yet imaginative, experienced in engineering products for production, with proven organization ability. If you believe that you are this man, send a full resume to

Mr. J. A. Kallgren, Employment Manager
VARIAN ASSOCIATES
611 Hansen Way Palo Alto, California

SENIOR PHYSICIST

Advanced Memory Department of our Research Division offers an unusual opportunity for a physicist or engineer (Ph.D. desirable) to lead experimental and theoretical studies in new information storage media and techniques. Background in information storage or in solid state materials (ferroelectrics, scotophors, energy sensors, semiconductors or optical devices) essential. Company sponsored projects are underway in these areas and others may be initiated and directed by this man. Job environment emphasizes individual achievement.

AMPEX CORPORATION

World Leader in Magnetic Recording

Send resumes to:
Skipwith W. Athey
Director, Research Lab.
934 Charter Street
Redwood City, California

RADIO ASTRONOMER

Large, space-oriented organization in San Francisco vicinity is seeking a scientist well-versed in Radio Astronomy. Applicant must have either a MS or PhD degree.

Work involves sky mapping techniques utilizing large aperture antennas and low noise detection and amplification circuitry to detect radio stars, determine spectral indices and establish thermal and non-thermal radiation sources.

Those scientists qualified for this position may send their resumes to:

Box 1160–A Journal of Applied Physics, 335 East 45th St. New York 17, N.Y.

POSITION OPEN

FERRITE SCIENTIST

PH.D. with experience in ferrite work and ability to do high level independent research. Send resumé to

Philip T. Forsling, Personnel Manager,
MAGNETICS, INC.
Butler, Pennsylvania.

PHYSICIST or PHYSICAL CHEMIST

Appointment for basic research and publication in reaction mechanisms and transport phenomena in gas-phase detonations and shock waves. Background in shock tube techniques, spectroscopy, chemical kinetics desirable.

Salary range $7,500–$10,000.

Send resume to:

OHIO STATE UNIVERSITY
RESEARCH FOUNDATION
1314 KINNEAR ROAD
COLUMBUS 12, OHIO

Experimental Physicists – MS & PhD

COLLISION STUDIES IN PLASMA PHYSICS

...Part of a broad program in radio physics attracting scientists to SYLVANIA

ARL
Applied Research Laboratory

New effectiveness for communication and detection systems in natural and man-made environments may result from current Sylvania efforts in the field of plasma physics.

In the Radio Physics Department of the Applied Research Laboratory, investigators are studying a variety of wave propagation and scattering techniques in ionized gases and conducting fluids. Of particular promise are experimental developments in microwave diagnostics of ionized gas flow.

Through microwave heating, inelastic collisions are being induced between free electrons in ionized air. To measure collision frequency, the fractional energy loss G per collision must be known. New experiments will measure the temperature dependence of G in the afterglow of a DC discharge in ionized air. Small shock tube environments are also being explored.

Additional programs involve electromagnetic phenomena associated with solar flares and aurora, propagation in non-uniform media, and formulation of a new microscopic electrodynamics theory of the ionosphere.

The Applied Research Laboratory's studies in radio physics offer important opportunities to advance your professional reputation in a genuine scientific environment. Qualified physicists will be invited to meet the manager of the Radio Physics Department to discuss programs in progress and the opportunities for initiating original studies.

Please write in confidence to Dr. Leonard Sheingold, Director, Applied Research Laboratory

Waltham Laboratories / **SYLVANIA ELECTRONIC SYSTEMS**
A Division of

SYLVANIA
Subsidiary of GENERAL TELEPHONE & ELECTRONICS

100 First Avenue—Room 11-B—Waltham 54, Massachusetts

A special breed of generalist for **S**pace **T**echnology **L**eadership

America's dramatic accomplishments in space technology are made possible not only by developments in science, but by advances in technical management concepts. A new type of generalist has emerged to meet the demands of systems engineering and technical direction of complex missile and space projects. This technical manager combines a broad knowledge of science and engineering with the leadership capability to fuse the disciplines of creative specialists into a dynamic, effective team ● In its six years as a principal contractor for the Air Force, NASA, and ARPA, STL's hard core of technical management generalists has set the pace in developing new members of this very scarce breed ● Their unique ability is the prime asset in Space Technology Leadership ● Scientists and engineers who would add this new management dimension to their professional careers are invited to submit their resumes to STL, where they will receive meticulous attention.

SPACE TECHNOLOGY LABORATORIES, INC. P.O. BOX 95005AA, LOS ANGELES 45, CALIFORNIA

a subsidiary of Thompson Ramo Wooldridge Inc.

Los Angeles • Santa Maria • Edwards Rocket Base • Cheyenne Cape Canaveral • Manchester, England • Singapore • Hawaii

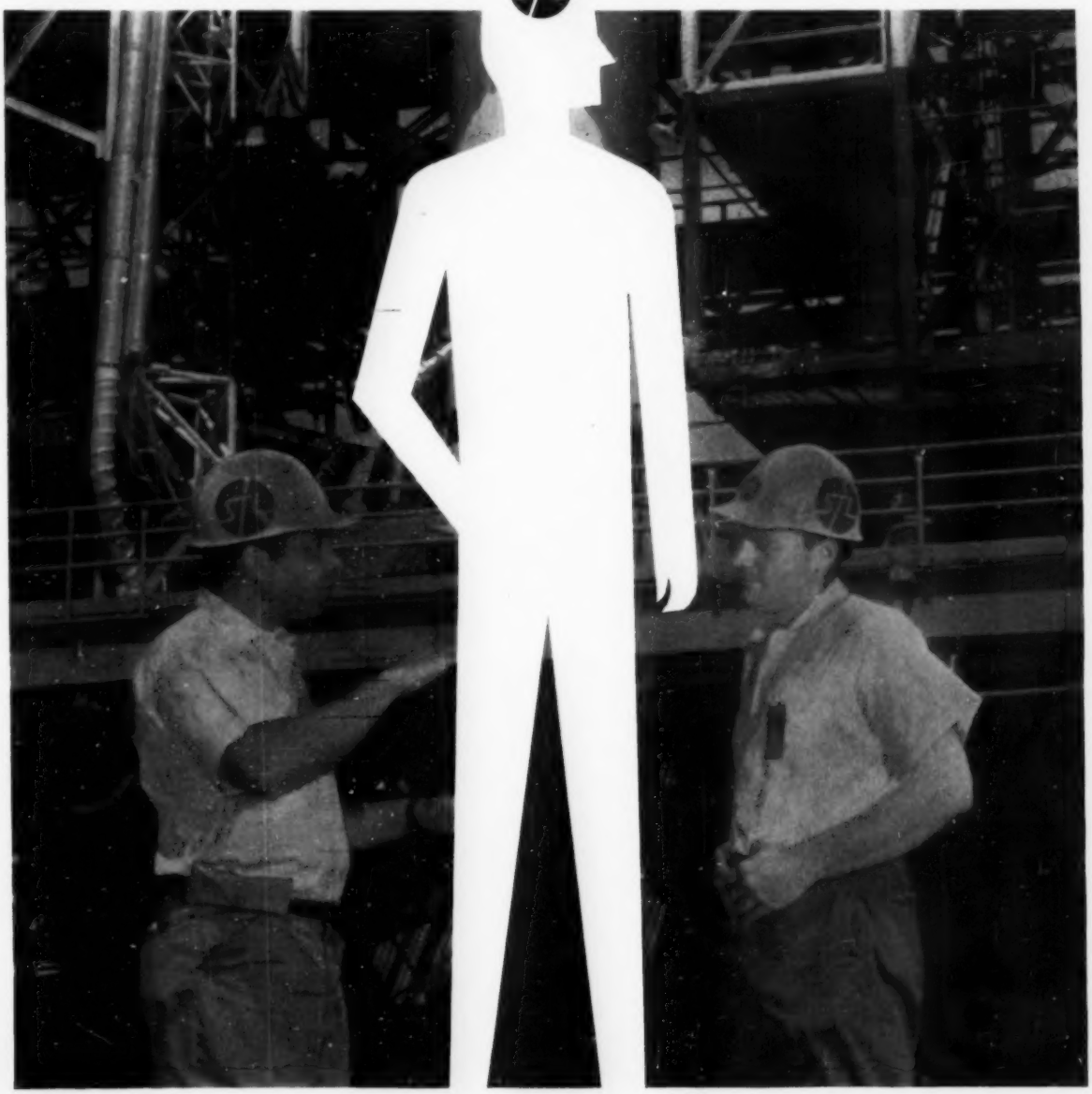

BASIC instruments for VHF-UHF Measurements

Type 874-LV Micrometer Vernier . . . $30

Type 874-LBA Slotted Line $230

ACCESSORIES:

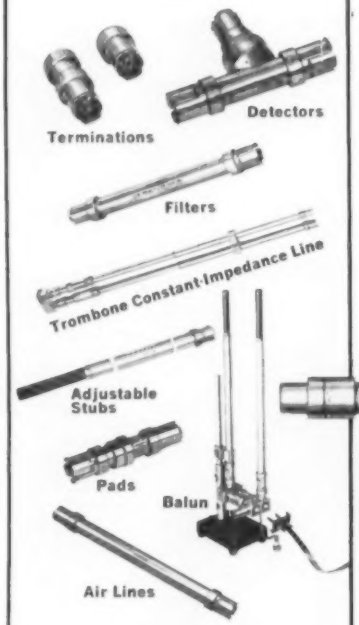

ADAPTORS
with low VSWR for all popular coaxial connector systems.

A 50-ohm line with a wide 300 Mc to 5000 Mc range . . . High accuracy: crystal-detector probe penetration is constant within ±1½% . . . Low residual VSWR: less than 1.025 at 1000 Mc, and less than 1.07 at 4000 Mc . . . A wide variety of accessories are available, including: terminations, adjustable stubs, filters, pads, air lines, detectors, and adaptors with low VSWR for all popular coaxial connector systems . . . Also available are an accessory Micrometer Vernier for measuring high VSWR ratios, and a motor drive for automatically sweeping the line to produce VSWR displays on scopes.

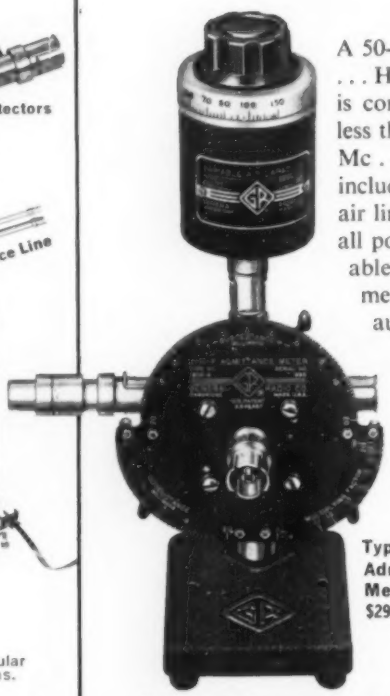

Type 1602-B Admittance Meter $295

For Impedance, Admittance and VSWR Measurements

Wide 20 Mc to 1500 Mc frequency range; useful to 2000 Mc for impedance matching . . . Direct reading in conductance (0.2 to 1000 millimhos) and susceptance (±0.2 to ±1000 millimhos) . . . with the addition of a one-quarter wavelength line between unknown and instrument, measurements can be readily made in terms of resistance (1 to 5000 ohms), and reactance (±1 to ±5000 ohms) . . . Basic ±3% accuracy . . . Uses same accessories as slotted line.

The DNT series of heterodyne detectors are recommended for use with the Slotted Line and Admittance Meter. Each system consists of a 30-Mc Type 1216-A Unit I-F Amplifier, Type 874-MR Mixer Rectifier, and appropriate Unit Oscillator and Low-Pass Filter. This general-purpose system is useful as a tuned voltmeter (2μv from 400-ohm source will produce a 1% meter deflection) as well as for insertion loss and attenuation measurements of cables and components.

Type	Frequency Range	Price
DNT-1	40 to 530 Mc	$665
DNT-2	40 to 280 Mc	$645
DNT-3	220 to 950 Mc	$693
DNT-4	870 to 2030 Mc	$898

Operation up to 5000 Mc possible by using oscillator harmonics. Any DNT system can be converted to any other by simply changing local oscillator and low-pass filter.

Write For Complete Information

GENERAL RADIO COMPANY
WEST CONCORD, MASSACHUSETTS

NEW YORK, WOrth 4-2722 **NEW JERSEY,** Ridgefield, WHitney 3-3140	**CHICAGO** Oak Park Village 8-9400	**PHILADELPHIA** Abington HAncock 4-7419	**WASHINGTON, D.C.** Silver Spring JUniper 5-1088	**SAN FRANCISCO** Los Altos WHitecliff 8-8233	**LOS ANGELES** Los Angeles HOllywood 9-6201	**IN CANADA** Toronto CHerry 6-2171